Summer 8-15-2013

Photosynthetic Chromophore Analogs and Biohybrid Antenna for Light Harvesting

Joseph William Springer
Washington University in St. Louis

WASHINGTON UNIVERSITY IN ST. LOUIS

Department of Chemistry

Dissertation Examination Committee:

Dewey Holten, Chair
Pratim Biswas
Ronald Lovett
Liviu Mirica
Lee Sobotka
Jay Turner

Photosynthetic Chromophore Analogs and Biohybrid Antenna for Light Harvesting

by

Joseph William Springer

A dissertation presented to the
Graduate School of Arts and Sciences
of Washington University in
partial fulfillment of the
requirements for the degree
of Doctor of Philosophy

August 2013

St. Louis, Missouri

Table of Contents

ACKNOWLEDGMENTS

I thank Washington University and the Department of Energy for financial support throughout my graduate studies. In particular, the Photosynthetic Antenna Research Center (PARC), an Energy Frontier Research Center funded by the U.S. Department of Energy, Office of Science, Office of Basic Energy Sciences, under Award No. DE-SC0001035, and the Division of Chemical Sciences, Geosciences and Biosciences Division, Office of Basic Energy Sciences of the U.S. Department of Energy, DE-FG02-05ER15661.

ABSTRACT OF THE DISSERTATION

Photosynthetic Chromophore Analogs and Biohybrid Antenna for Light Harvesting

By

Joseph William Springer

Doctor of Philosophy in Chemistry

Washington University in St. Louis, 2013

Professor Dewey Holten, Chair

Photosynthetic chromophore analogs are studied, starting with simplified structures and systematically building complexity to elucidate overarching design principles. The general goals are to achieve an artificial light-harvesting system that exhibits broad spectral coverage, including extension well into the photon rich red and near-infrared portions of the solar spectrum. For example, the spectral properties of chlorophylls are primarily a consequence of the 13^1-oxophorbine base macrocycle, with further tuning provided by the dramatic difference in auxochromic effects of a given substituent at the 7- versus 3-position, consistent with Gouterman's four-orbital model.

While light-harvesting antennas in photosynthetic bacteria generally have near-quantitative transfer of excitation energy among pigments, only a fraction of the solar spectrum is typically absorbed. The new biohybrid antennas retain the energy-transfer and self-assembly characteristics of the native antenna complexes, offer enhanced coverage of the solar spectrum, and illustrate a versatile paradigm for the construction of artificial light-harvesting systems. Such complexes can ultimately connect with complimentary efforts in the realms of energy conversion and storage towards a successful utilization of natural and bio-inspired photosynthesis for energy production.

Chapter 1

Introduction and Overview

I. Introduction

This body of work creates a fundamental molecular toolbox that can be employed to harness the sun's radiation and power artificial photosynthetic processes for the benefit of humankind. An extensive collection of intricately studied light absorbing chromophores and a platform to deploy them in biologically inspired light-harvesting antenna that can perform efficient, directed excitation energy transfer are developed herein.

To explore the unique characteristics of photosynthetic pigments, often the natural pigments are extracted and chemically manipulated to effect a desired structural and spectral change. The work here breaks new ground, powered by access to unique photosynthetic analogs synthesized from scratch by our collaborator Jonathan Lindsey, North Carolina State University. His novel synthetic routes allow for an ever expanding library of compounds, creating a large set of highly tunable and functionalizeable chromophores for fundamental studies of light harvesting. A recurring theme is the systematic study of different photosynthetic chromophore classes by starting with a simplified structure and building complexity with additional substituents one step at a time. In this manner the specific effects of each change can be understood and overarching design principles elucidated, with general goals of broad solar coverage and the extension of light-harvesting well into the photon rich red and near-infrared (NIR) portions of the solar spectrum. With the variety of novel chromophores studied here, and the vast prior knowledge of the research group and its collaborators, a molecular toolbox is neatly organized, ready to provide insight and the right light-harvesting chromophore for future applications related to artificial photosynthesis and solar energy production.

While there is continual and immediate focus on the spectral and photophysical properties of the native photosynthetic chromophores and synthetic analogs, there is also an

awareness of broader challenges, such as the long term increasing global energy demand. It is projected that the energy demand will essentially double from today's value to 30 TW by 2050.[1] Supplying this energy has dramatic implications for local and global societies and environments. Modern technological advances are now commonly assessed not only for their immediate impact, but also for their long term viability, or sustainability. Photosynthesis has the remarkable distinction of being so far beyond the base level of sustainability that it is more accurately described as sustaining, forming the basis of nearly all life on earth! There is no greener technology, and there is no power source more readily abundant than the sun, depositing 120,000 TW of radiation on the surface of the Earth. Societies can continue to drill, spill and burn, or transition to a sustainable path of harnessing the abundant sun for a clean energy future.

While photosynthesis provides an alluring inspiration for solar energy conversion, the immense and daunting challenge remains to translate these principles and processes that power the biosphere into powering the electrical grid and transportation network. Meeting future energy demands with clean energy sources will require prolonged, colossal efforts with an unprecedented degree of global commitment and cooperation not yet achieved by human society. The difficulty of this enterprise cannot be overstated and may only be eclipsed by its necessity.

The ultimate utilization of solar energy will require an intricate interplay of energy capture, conversion, and storage.[1] The research described herein is intimately connected to the first step in this process, the capture of solar radiation. Based upon a vast and growing knowledge concerning the synthesis and photophysical properties of photosynthetic pigments and analogs, coverage of the solar spectrum can be greatly expanded to provide the possibility for enhanced solar energy capture. For example, bio-hybrid antenna systems have been created that integrate such synthetic chromophores with native-like peptide scaffolding to organize the

light harvesting pigments and direct the excitation energy flow. Such strategies for light capture and energy funneling can connect with complimentary efforts in the realms of conversion and storage towards a successful utilization of natural and bio-inspired photosynthesis for energy production.

II. Overview.

The following research overview is a detailed, guided tour of the projects showcased in this thesis. It introduces the underlying motivations for the work, discusses important inter-project relationships, and highlights the exciting results encountered along the journey.

Basic Macrocycles. Photosynthetic pigments absorb energy from the sun and initiate the process of photosynthesis. They are very complex molecules, containing a planar hydrocarbon skeleton, or macrocycle, with a diverse arrangement of substituents around the perimeter. At the center of the macrocycle can be found a central metal (typically magnesium in natural systems and zinc in synthetic analogs), or two hydrogens (free base).

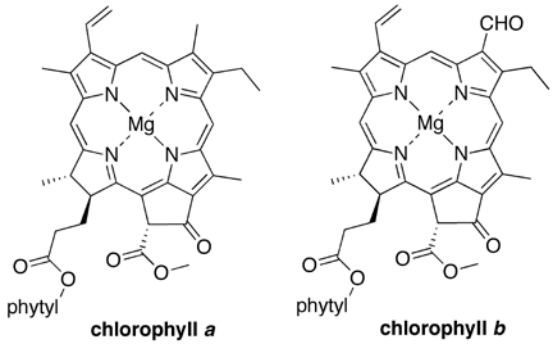

Figure 1. Structures of chlorophyll *a* and chlorophyll *b*.

What is responsible for the characteristic spectral and photophysical properties of natural chlorophylls? Chlorophylls *a* and *b* (Figure 1) each bear nine total substituents, most of which are unique and employed only once, plus an additional keto-bearing five-membered ring fused to the hydrocarbon skeleton and a magnesium central metal. Here we start with simplified versions

of these intricate chromophores and then build complexity in a systematic way to understand the key components that contribute to the properties of natural chlorophylls.

There are three classes of chromophores discussed in this work, collectively termed tetrapyrroles. They all contain the 18-electron conjugated pi system outlined in blue, but differ in the degree of saturation of the pyrrole rings. Porphyrins have completely saturated pyrrole rings, whereas chlorins and bacteriochlorins contain one and two reduced rings, respectively, as shown in Figure 2.

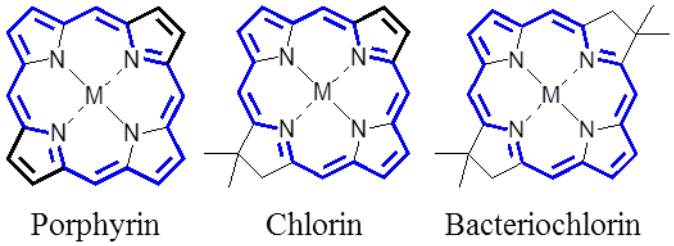

Figure 2. Three classes of tetrapyrroles. The central metal (M) is typically magnesium for natural tetrapyrroles, zinc for synthetic analogs, or two protons (free base).

The three distinct classes have remarkably unique electronic absorption spectra. While all three absorb strongly in the near-ultraviolet to blue region, the lowest energy (longest wavelength) absorption for porphyrin is weak and is found in the green to yellow spectral region. For chlorin, the lowest energy absorption is stronger and further to the red (~600-700 nm), while bacteriochlorin is stronger still, and shifting to the NIR region (~700-800 nm). The studies herein primarily focus on the fundamental properties of chlorins (Chapters 4-7) and porphyrins are used as reference points for some more detailed discussions (Chapters 2 and 4). Bacteriochlorins are employed in the study of amphiphilic tetrapyrroles (Chapter 6) and biohybrid light-harvesting constructs (Chapters 8 and 9).

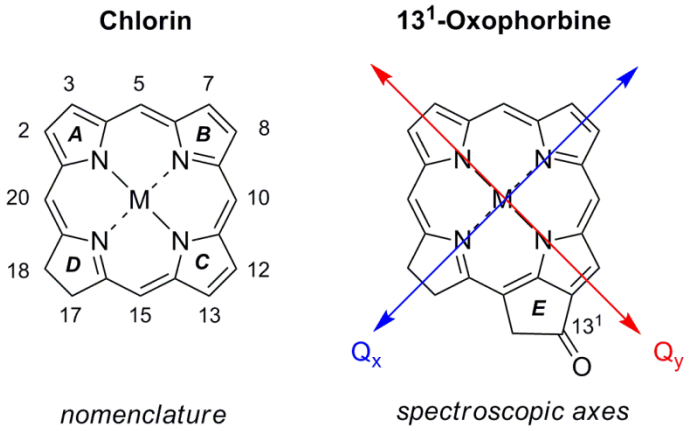

Figure 3. Nomenclature of chlorins (left) and 13^1-oxophorbines (right), along with spectroscopic axes.

Figure 3 introduces some key nomenclature and molecular axes that are particularly important for spectroscopic studies and analysis. The peripheral positions are numbered and the pyrrole rings are labeled A through D in a clockwise manner. On the right of Figure 3, the ring E is included, which spans the 13 and 15 positions. A keto group at the labeled 13^1-position in ring E is an extremely common moiety found in a range of natural photosynthetic pigments and synthetic analogs studied here. Addition of the keto-bearing five-membered ring to a chlorin produces the "oxophorbine" class of molecules.

The starting point for this exploration is the unsubstituted chlorin hydrocarbon skeleton, from which we start to build complexity with the addition of peripheral substituents (Figure 4). The unsubstituted zinc bearing chlorin has minimal spectral resemblance to the chlorophyll *a* analog for comparison (**ZnC** vs. **ZnPheo *a*** in Figure 4). The long wavelength absorption feature of **ZnC** is weak and at significantly higher energy. The addition of a five-membered hydrocarbon ring (ring E of figure 3 without the keto group) in the lower right quadrant of the macrocycle has little effect, with the long wavelength feature again at too high an energy, and even further reduced relative intensity compared to the unsubstituted chlorin. If a keto group is added to this isocyclic ring, to make the oxophorbine, the changes are substantial and the

spectrum of the molecule now starts to strongly resemble that of the zinc bearing chlorophyll *a* analog. In addition to the spectral changes, the fluorescence yield and singlet excited state lifetime also increase dramatically. Thus, the keto group in the isocyclic ring is a remarkably powerful component, which transforms the simplified macrocycle into a chromophore with properties very similar to those of chlorophyll *a*. These comparisons indicate that the peripheral substituents play a role in fine tuning the spectral properties. The role of specific substituents and their placement around the macrocycle are explored in further detail in this work, and form a basis for the comprehensive understanding of chlorin spectral and photophysical properties.

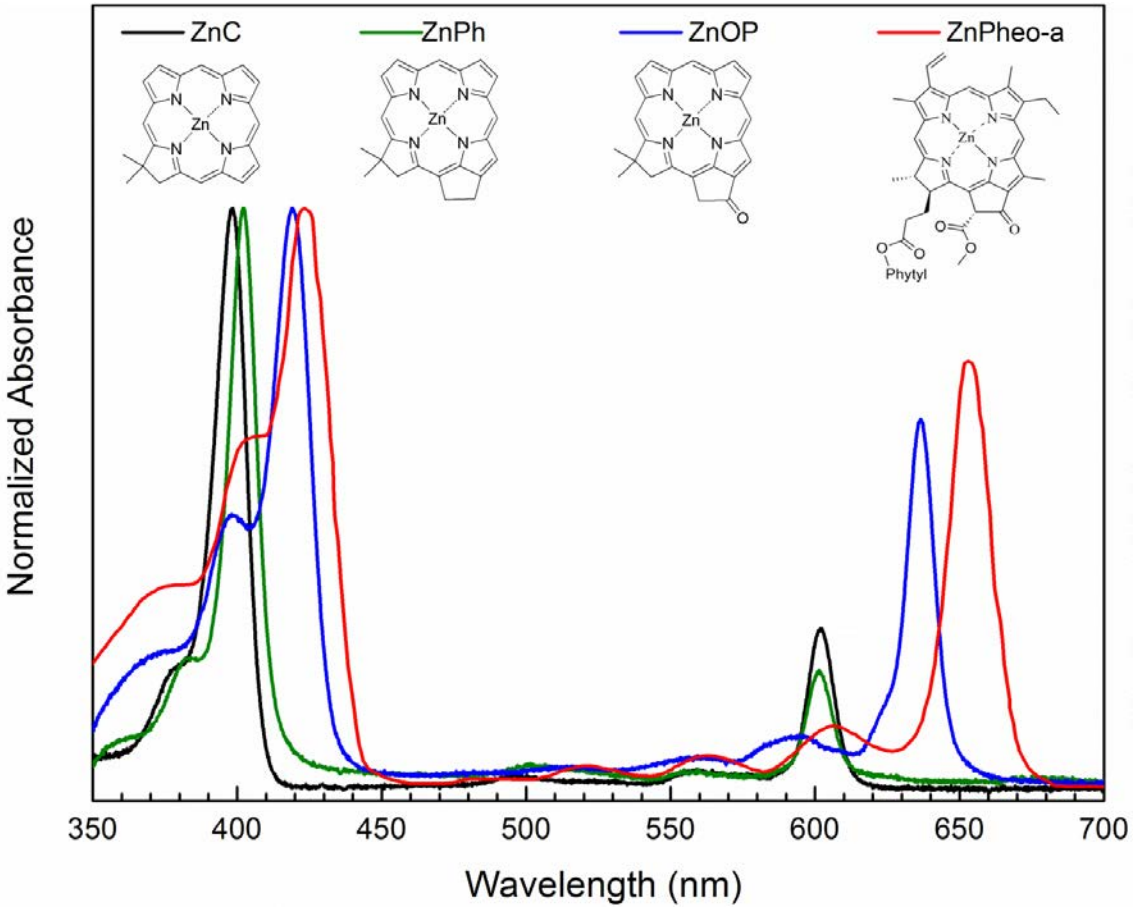

Figure 4. Absorption spectra and molecular structures of increasingly complex chlorins. Zinc chlorin (black, **ZnC**), zinc phorbine (Green, **ZnPh**), zinc oxophorbine (Blue, **ZnOP**), zinc pheophorbide *a* (red, **ZnPheo-a**, chlorophyll *a* with native magnesium replaced by zinc).

An additional comparison that can be made concerns a chlorin containing an acetyl group at the 13-position, which places a double bonded oxygen in a similar position (i.e., off the 13-position and molecular Q_y axis of Figure 3), but without the closed isocyclic ring structure. The effects of the acetyl group at this position are similar, but reduced in magnitude, compared to those of the keto-bearing isocyclic ring. The coplanarity of the keto group and macrocycle imposed by the isocyclic ring compared to the torsionaly less restricted carbonyl is likely a key aspect here. This comparison gives a further manifestation of the relationship between molecular composition and structure, electronic structure, and spectral characteristics.

The measured energy (wavelength) and relative intensity of the prominent long wavelength feature in the ~600-680 nm region (termed Q_y) is related to calculated energies of the frontier molecular orbitals through Gouterman's four orbital model. The key parameters in this model, for a given molecule or trends within a set of molecules, are that the energy (wavelength) trends with the average energy of the HOMO-LUMO and HOMO-1 – LUMO+1 energy gaps, and the intensity trends with the difference in the two orbital energy gaps. The HOMO-LUMO energy gap has the greatest impact on the Q_y position as the HOMO-1 – LUMO+1 energy gap is relatively constant for the set of chlorins studied. Closer examination of the individual orbital energies reveals that the LUMO has the greatest variability, exerting the greatest influence on the ultimate HOMO-LUMO energy gap, and both the average (wavelength) and difference (intensity). This fact is manifest in the absorption spectra for a set of chlorins (chlorophyll analogs), as the Q_y band moves to longer wavelength and lower energy, the Q_y band intensifies. A more in depth discussion of Gouterman's four orbital model is presented in Chapter 2 because the associated concepts are prevalent throughout this body of work. A major utility of this model

is the ability to not only predict the effects of substituents and other molecular details on the wavelength positions of the prominent absorption features, but also their relative intensities.

The relationships between observed spectra and calculated orbital energies, in conjunction with structural considerations, are an important tool set for the design of novel chromophores, and the understanding of roles played by macrocycle type and substituents in complex natural chlorophylls. By starting with the basic chlorin and zinc chlorin skeletons, the effects of the macrocycle are separated from those of the substituents and a powerful starting point is created for the fine tuning of spectra based on substituent type and placement. These facets of molecular design and spectral manifestations are explicitly explored in Chapters 3 and 5, and are also thematically relevant to other fundamental studies of chromophore properties found in Chapters 4, 6 and 7.

Chlorosomal Bacteriochlorophylls. Green photosynthetic bacteria have a unique light-harvesting antenna system. Densely packed and self-assembled chromophores form chlorosomes, with minimal protein scaffolding. This departs greatly from the light-harvesting apparatus of plants, cyanobacteria and purple bacteria, which employ large protein architectures to place and orient chromophores for efficient energy funneling.

The chlorosomes chiefly rely on the intermolecular interactions of the chromophores to construct an extended light-harvesting antenna. The chromophores found in chlorosomes, called "bacteriochlorophylls *c*, *d*, *e,*" are quite similar to the chlorophylls found in plants and purple bacteria (Figure 5).

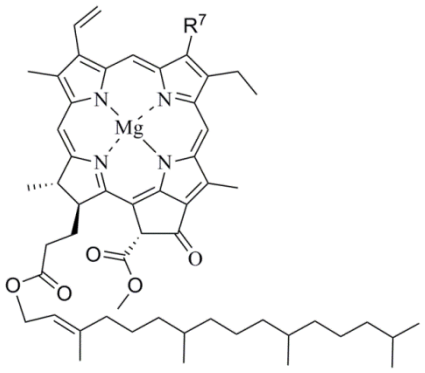

Plant Chlorophylls
chlorophyll *a* ($R^7 = CH_3$)
chlorophyll *b* ($R^7 = CHO$)

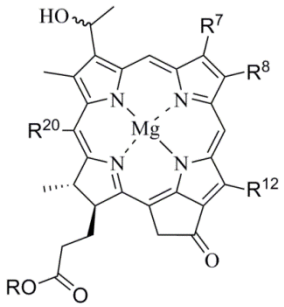

Chlorosomal bacteriochlorophylls
R = mixture of hydrocarbon chains
R^8 = Et, Pr, *iso*-Bu, neopentyl
R^{12} = Me, Et
bacteriochlorophyll *c* ($R^7 = R^{20} = CH_3$)
bacteriochlorophyll *d* ($R^7 = CH_3$, $R^{20} = H$)
bacteriochlorophyll *e* ($R^7 = CHO$, $R^{20} = CH_3$)

Figure 5. Structures of plant chlorophylls (left) and chlorosomal bacteriochlorophylls (right).

Looking at the structures of the chlorosomal "bacteriochlorophylls", one sees that they are actually chlorins, bearing only one reduced pyrrole ring (compared to none in porphyrins and two in "real" bacteriochlorophylls, see figure 2). Several unique characteristics of the chlorosomal bacteriochlorophylls are apparent: the incorporation of a hydroxyethyl group at the 3-position, the lack of additional substituents on the isocyclic ring, heterogeneous substituents at the 8-, 12- and 17-positions, and incorporation of a methyl group at the 20-position for bacteriochlorophylls *c* and *e*.[2]

What is unique about these chromophores that promotes self-assembly, and what are the key components involved in this process? Similar to the analysis of plant chlorophyll analogs, the investigation of Chapter 4 starts with simplified structures that are stripped of many of the peripheral substituents found in the natural systems. By varying substituents systematically at only a few select sites, the impact on absorption and emission spectra, along with fluorescence

yields and excited singlet state lifetimes are evaluated. The analysis of the isolated chromophores in solution forms a basis for investigating the propensity of these molecules to form extended, self-assembled structures analogous to natural chlorosomes. Such insights aid in elucidating the key structural components necessary to construct an extended light-harvesting apparatus that is essentially free of protein scaffolding and organized solely by intermolecular interactions of the chromophores themselves. Although such self-assembly studies have been accomplished previously using the native tetrapyrroles[3] and porphyrin analogs,[4,5] the new direction here is to use synthetic chlorin analogs of the chlorosomal bacteriochlorophylls to tune structural and electronic characteristics and explore the effects on assembly formation and spectral properties (Chapter 4).

The central metal is expected to play a fundamental role in the creation of an extended, self-assembled system. To evaluate this parameter, different solvents were used, with varying affinity for ligation to the central metal, which could disrupt a self-assembly process based on metal coordination. To this end, analogous free base compounds that lack the central metal were also analyzed for their unique properties and to help define the role of a central metal. The simplified, relative to natural bacteriochlorophyll *c*, model compound **ZnOP-He^{3}M^{10}** (see Figure 6) shows very typical absorption in tetrahydrofuran (THF), which is expected to ligate to the central zinc metal and prevent further coordinating interactions in solution. As the solvent is changed to predominantly hexane, a new peak forms that is substantially red-shifted and reminiscent of the chlorosome assembly. The similar free base compound, **FbOP-He^{3}M^{10}** (see Figure 6), without a central metal shows no such effect, confirming that the central metal is requisite for the formation of chlorosomal self-assembled structures. The results also expose a theme of natural systems −accessing different parts of the solar spectrum by tailoring the specific

environment around a light-harvesting chromophore. Here the photon-rich near infrared portion of the solar spectrum is accessed by inducing a substantial red-shift of the long wavelength absorption feature through complex chromophore-chromophore interactions in a natural chlorosome.

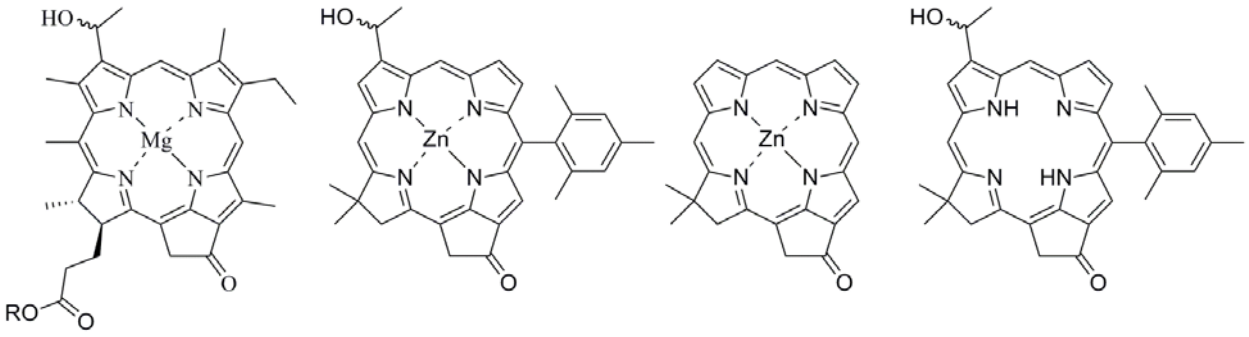

BChl *c* ZnOP-He^{3}M^{10} ZnOP FbOP-He^{3}M^{10}

Figure 6. Bacteriochlorophyll *c* (**BChl *c***) and related synthetic analogs. While **ZnOP-He^{3}M^{10}** mimics the self-assembly of the natural chlorosomal bacteriochlorophylls, further simplification to **ZnOP**, or removal of the central metal to yield **FbOP-He^{3}M^{10}**, are not prone to self-assembly, confirming the necessity of the 3-substituent and the central metal.

In Chapter 4 assembly formation of the model compound **ZnOP-He^{3}M^{10}** was dependent on the solvent environment and pigment concentration. Increasing the pigment concentration led to dominating chromophore-chromophore interactions and self-assembly in toluene, and increasing hexane portions led to the same in hexane:THF solvent mixtures. Again, self-assembly is not observed for a further simplified **ZnOP** or free base analog lacking the central metal (**FbOP-He^{3}M^{10}**, Figure 6), regardless of the concentration or solvent combination explored. Together the findings suggest a self-assembly mechanism that involves at least the central metal, keto group in the isocyclic ring, and hydroxyethyl group at the 3 position. Other substituents at meso positions (10 in our synthetic analogs, and 20 in the natural bacteriochlorins) could affect the propensity for self-assembly by fine tuning the steric hindrance as molecules pack together in the extended systems. To this end, synthetic analogs bearing

mesityl versus phenyl at the 10-position were explored to probe steric effects of meso substituents on assembly. Similarly 10-pentafluorophenyl was explored to uncover potential electronic effects of a meso substituent on assembly and spectral properties.

While the formation of the self-assembled structures was not really controllable in terms of size or rate of formation (which were not measured directly), the molecular structure requisites for self-assembly were identified by recreating chlorosomal-like absorption with a minimally substituted synthetic chromophore. Understanding some of the more subtle effects of each substituent will allow for the customization of bacteriochlorophyll *c* analogs for use in light-harvesting systems inspired by the natural chlorosome. The insights also demonstrate that further access to the near infrared can be accomplished through chromophore-chromophore interactions, but the ultimate utility of these constructs will be related to other photophysical properties-fluorescence yield and excited state lifetimes. In our studies the fluorescence from self-assembled synthetic pigments was not detected (fluorescence yield < ~10^{-4}) and the first excited singlet state had a predominant lifetime on the order of 1 picosecond. The prompt non-radiative decay back to the ground state severely limits the ability to get the absorbed energy out of an assembly. The ability of the natural chlorosome to circumvent, or at least accommodate these constraints is a fascinating aspect of chlorosome function that was not discerned from this work. This issue remains an overriding one for understanding how the native chlorosomal systems operate and how that key functional aspect can be elicited in artificial systems based on the same types of assemblies.

These solution studies (Chapter 4) provided a foundation for the investigation of surface deposition of synthetic bacteriochlorophyll *c* analogs by electrospray, in collaboration with the Biswas lab. Monomer solutions (645 nm peak) were applied to a glass surface and the long

wavelength absorption observed for self-assembled aggregates in solution was reproduced (~720 nm). Transient absorption spectroscopy also showed great similarities in excited state lifetimes (~1 ps) of self-assembled chromophores in solution and on a surface. The fundamental challenge of getting this excitation energy out of such an assembly has not yet been overcome, and this extensive effort is not described here. The translation of any light-harvesting system from a solution based formulation to a surface is extremely attractive in terms of large scale deployment for solar energy capture. Spray methods also seem inherently scalable, adding to the allure of a viable self-assembled solid antenna on a surface.

The molecular toolbox, already containing a variety of macrocycles (Chapter 3), from which natural plant chlorophylls can be closely mimicked, is expanded to include analogs of chlorosomal bacteriochlorophylls (which again are actually chlorins, Chapter 4). The addition of a hydrogen bonding hydroxyethyl group at the 3-position along with the zinc oxophorbine macrocycle produced bacteriochlorophyll *c* analogs that were induced to self-assemble, reproducing absorption characteristics of natural chlorosomes, one of the more mysterious and specialized natural light harvesting complexes.

Substituent Effects (7 vs 3 Position). Returning to the complexity and diversity of natural chlorophylls, with their myriad of peripheral substituents (Figures 1 and 5), we are prompted to build upon the fundamental characterization of the basic macrocycles and determine how molecular properties are fine-tuned by the addition of particular substituents at particular positions. A variety of new synthetic analogs and the natural chlorophylls *a*, *b*, *d* were studied in Chapter 5, along with previously studied key benchmarks, to address the effects of substituents on spectral and photophysical properties. The small set of natural chlorophylls (*a*, *b*, and *d*) have reasonably different absorption spectra despite some very minor differences in substituent

patterns. The spectral differences are dominated by the effect of a formyl group at the 7-position in chlorophyll *b*, the 3-position in chlorophyll *d*, and no formyl group in chlorophyll *a*.

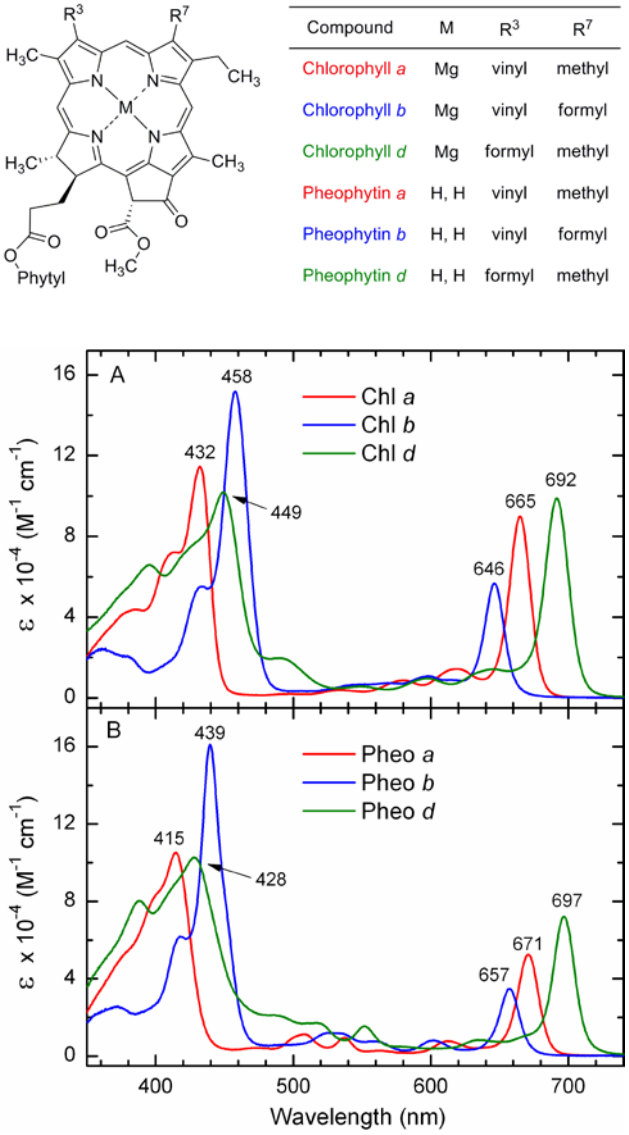

Figure 7. Chemical structure and absorption spectra of (A) chlorophyll *a* (red), chlorophyll *b* (blue), and chlorophyll *d* (green) and (B) the pheophytin analogs (no central metal) in toluene at room temperature. The spectra utilize the molar absorption coefficients reported in Reference 5 of chapter 5 (the ordinate has been multiplied by 10^{-4}). (The small absorption near 500 nm for Chl *d* and Pheo *d* is due to carotenoid.)

Remarkable spectral changes relative to chlorophyll *a* are achieved by placing a formyl group at the 3- or 7-position (Figure 7). Even more remarkable is that the placement of the same

group at these two different positions creates opposing effects on the Q_y band. The 3-formyl group produces a substantial red (bathochromic) shift and intensification of the Q_y band, while 7-formyl produces a blue (hypsochromic) shift and the intensity of the Q_y band is reduced, shifting intensity back to the Soret. These differing results are not accounted for with a one-electron particle-in-a-box model, which would suggest that adding a conjugated group, wherever the position, would extend the pi-electron system, increasing the box size and decreasing the energy of the lowest excited singlet state. The differing results, however, are completely accounted for by Gouterman's four orbital model and highlight the power and utility of this analysis, along with the rich science at the heart of chlorin spectral and photophysical properties. The four orbital model is presented in more detail in Chapter 2 to aid in understanding its use in other chapters, in particular the substituent effects that are the focus of Chapter 5.

Substituent placements, along with identity, are key parameters that must be considered when tailoring a chromophore for a specific role. Different cyanobacteria exploit these effects to fine tune their respective antennas and get out from the shadow of chlorophyll *a* absorption, accessing new portions of the solar spectrum. This tuning motif is greatly extended with a diverse set of synthetic substituents. The ability to construct these chromophores *de novo* creates a library of compounds with finely tuned absorption spectra, ready to meet the light-harvesting needs of eventual artificial photosynthesis applications.

Amphiphilic Tetrapyrroles. The studies described here on amphiphilic chlorins and bacteriochlorins expand an already extensive library of synthetic chromophores and are the subject of Chapter 6. The incorporation of both hydrophobic (non-polar) and hydrophilic (polar) parts on the same molecule impart the amphiphilic character. This specialization creates an initial set of compounds that can be incorporated into media where the typical chromophore

would be insoluble, expanding the potential range of use for synthetic chlorins and bacteriochlorins. This approach allows chlorins and bacteriochlorins to maintain their light-harvesting advantage over analogous porphyrins, which have limited to no absorption in the red and NIR regions. To ultimately be useful, these novel amphiphilic chromophores have to maintain their desirable light-harvesting characteristics (strong absorption bands), and potential for efficient excitation energy transfer (singlet excited-state lifetimes on the order of nanoseconds).

From the long developing understanding of substituent effects, the meso positions (5, 10, 15, 20 positions in Figure 3) arise as points on the macrocycle for inclusion of specialized substituents that do not greatly perturb the general spectral properties of the analogous macrocycle, most notably for chlorins and bacteriochlorins. Groups are added to greatly change the solubility, but maintain strong long wavelength absorption bands, appreciable first excited singlet state lifetimes and fluorescence yields. The chromophore toolbox continues to expand, as now there are pigments amenable for inclusion in micelles, membranes, proteins and synthetic peptides. With the distinct amphiphilic groups on opposite ends of the macrocycle, some directionality is created, which could lead to consistent orientation upon spontaneous self-assembly. In particular, the hydrophobic 'head' of the chromophore would be expected to insert itself into the lipophilic interior within the previously listed media.

Chlorin Chalcones. Photosynthetic systems in nature typically need to safely dissipate excess energy (how would you fare sitting in the full sun all day?). This function is often carried out by carotenoids, accepting energy from photosynthetic pigments like chlorophylls and bacteriochlorophylls and dissipating that excess energy through non-radiative internal conversion, producing heat. Carotenoids can also augment absorption, and transfer that absorbed

energy to chlorophylls. The ability to enhance energy capture, or dissipate excess energy hints at the complex and vital nature of carotenoids in photosynthetic antenna function. The studies of Chapter 7 introduce into the chlorin framework a synthetic retinyl moiety similar to a carotenoid. The retinyl benchmark has been studied on its own and also attached to chlorin macrocycles and analyzed for spectral and photophysical properties. A shorter chain analog was also produced. These have been designated chalcones. The structures and absorption spectra of the zinc chlorin chalcones are presented in Figure 8.

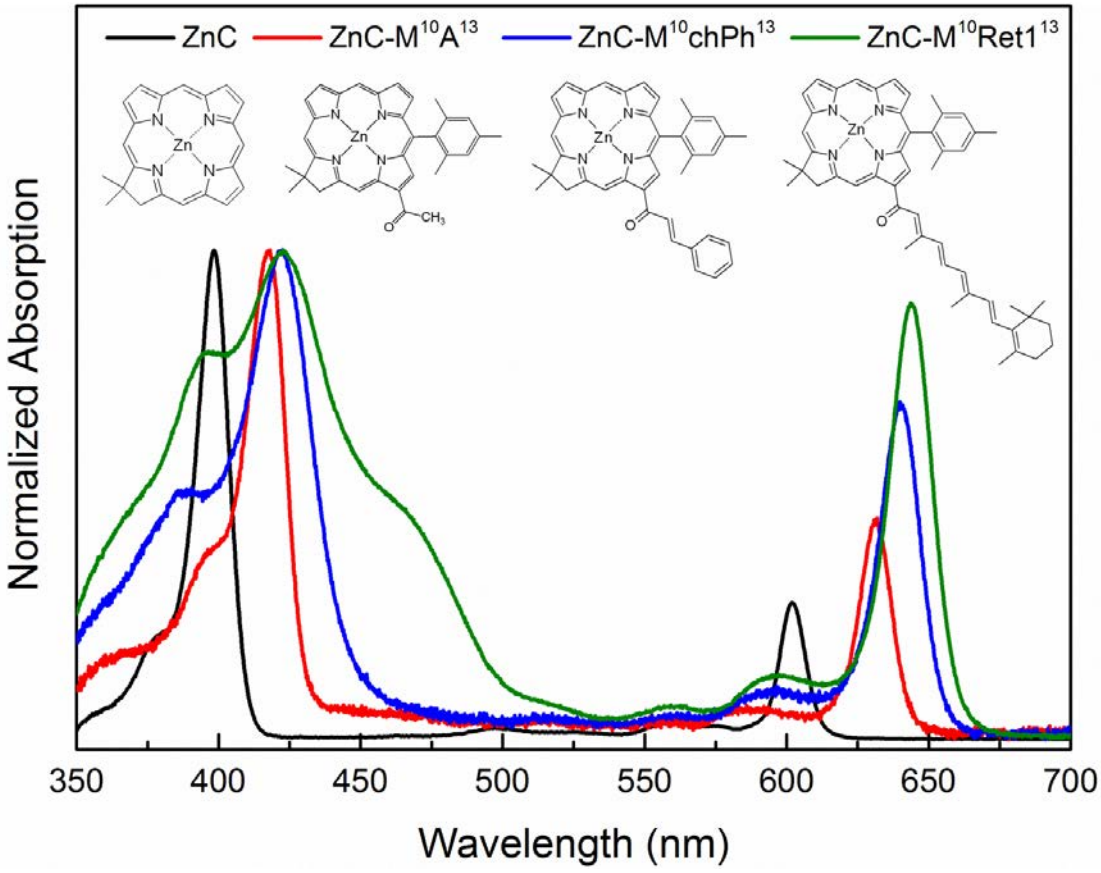

Figure 8. Normalized absorption spectra and molecular structures of simplified benchmarks **ZnC** (black), **ZnC-M^{10}A^{13}** (red) and novel chlorin chalcones **ZnC-M^{10}chPh^{13}** (blue), **ZnC-M^{10}Ret1^{13}** (green). Note the broadened absorption from 350-500 nm and the extremely intense long wavelength feature of the novel **ZnC-M^{10}Ret1^{13}**.

Zinc chlorin and free base chlorin chalcones were prepared (Lindsey lab) with both the shorter substituent and the longer retinyl attached to the macrocycle. A set of simpler benchmark

chlorins were also studied to establish a baseline of substituent effects as the complexity of the chromophore increases to the final zinc chlorin retinyl. For this thesis work, all compounds were studied in non-polar and polar media to assess the impact of the environment on the spectral and photophysical properties. The Q_y absorption band bathochromically (red) shifts, intensifies, and has increased peak width as the 13-substituent changes along the series: no substituent, acetyl, chalcone-phenyl (chPh), retinyl1 (ret1). The increase in the relative Q_y absorption is dramatic for the chlorin-chalcones, especially for **ZnC-M^{10}Ret1^{13}**, where the peak intensity ratio of the Q_y to B band approaches unity (0.89). This is the most intense chlorin Q_y band observed. The 13-retinyl substituent also has dramatic effects at the edge of the Soret region (350 – 450 nm), displaying a prominent shoulder consistent with the underlying absorption from the **Ret1** auxochrome. Similar spectral results are observed for the same set of compounds lacking the central metal (free base).

As will be detailed in Chapter 7, the photophysical properties of the chlorin chalcones are also quite interesting, exhibiting consistently high fluorescence yields in non-polar solvent (0.26-0.30), which approach that of native chlorophyll *a* (0.325). In highly polar solvent, the chlorin chalcones display some interesting properties not seen in the structurally simpler benchmarks, **ZnC** and **ZnC-M^{10}A^{13}** (Figure 8), the pinnacle of which is the extreme reduction in fluorescence yield of **ZnC-M^{10}Ret1^{13}**, where the retinyl appears to play the role of excitation quencher. These synthetic chlorin chalcones could emulate the dichotomous roles that carotenoids play by varying the local environmental conditions, performing great light-harvesting functions in a non-polar environment and excitation energy quenching in a quite polar setting. Both modalities are likely to be of use in artificial photosynthesis; devising schemes to manipulate and controllably switch between the divergent properties could be a future pursuit.

Biohybrid Antenna. The previous studies that comprise the material for Chapters 3-7 are all investigations into the fundamental properties of photosynthetic pigments, forming an extensive platform of light-harvesting. These studies typically involved the investigation of chromophores in solution where there is no appreciable interaction between chromophores, allowing for the analysis of their inherent molecular properties. An exception being the chlorosomal bacteriochlorophylls project were environmental conditions were manipulated to promote chromophore-chromophore interactions and self-assembly. In the biohybrid antenna project of Chapter 8, synthetic pigments along with native bacteriochlorophyll are incorporated into more elaborate environments and go beyond the initial process of energy capture and engage in the transfer of excitation energy from one unit to another within a model photosynthetic antenna.

Photosynthetic plants and bacteria share the same basic motif when it comes to using the sun's radiation as a primary energy source. Light is absorbed by an antenna function, and this energy is funneled to an active site (the reaction center), which initiates the charge separation and electron transfer events that culminate in chemistry taking place. The light-harvesting antenna is the primary focus for this project. This is where the initial photon absorption occurs, and starts the monumental process of photosynthesis. Energy donor and acceptor functions are created in our biohybrid antenna constructs, but there is no reaction center function coupled to the biohybrid complex (yet).

This project relies on past experience with synthetic chromophores and the previous work of others on the structure and function of antennas in natural photosynthetic (purple) bacteria[6-9] to design a new light-harvesting antenna that is inspired by the natural system yet contains synthetic components. The light-harvesting antennas in photosynthetic bacteria are composed of

peptide dyads containing a pair of bacteriochlorophyll chromophores. The bacteriochlorophyll dimers are held in place by a pair of peptides, which interact with each other to construct the ring-like formations. The peptide pairs that hold the bacteriochlorophyll dimer in place are both helical in structure but are not identical and are uniquely labeled as α and β. The dyads associate to form cyclic oligomers composed of 8 or 9 dyads (16 or 18 bacteriochlorophylls) in light-harvesting complex two (LH2) and 15 or 16 dyads in LH1, which houses the reaction center inside the ring. Figure 9 shows: (A) a side view of the structural model of 8 interacting αβ-subunits forming the light-harvesting oligomer of LH2, (B) top view of the same structural model with the bacteriochlorophylls removed, (C) a structural model of a single αβ-dyad, and (D) the relative orientation of the bacteriochlorophyll dimer found in each subunit. The αβ-dyad, with its bacteriochlorophyll dimer, has peak Q_y absorbance at 820 nm and can be generically referred to as B820. When the dyads, or subunits, interact with each other to form the oligomer, there is now an array of interacting bacteriochlorophyll pairs, and the Q_y absorbance is shifted to ~850 nm in LH2 (B850) and ~ 875 nm in LH1 (B875). LH2 also contain a ring of monomeric pigments (B800) that transfer energy to the B850 ring (B800 pigments omitted for clarity to focus on the general structures and acceptor function of the bacteriochlorophyll dimer).

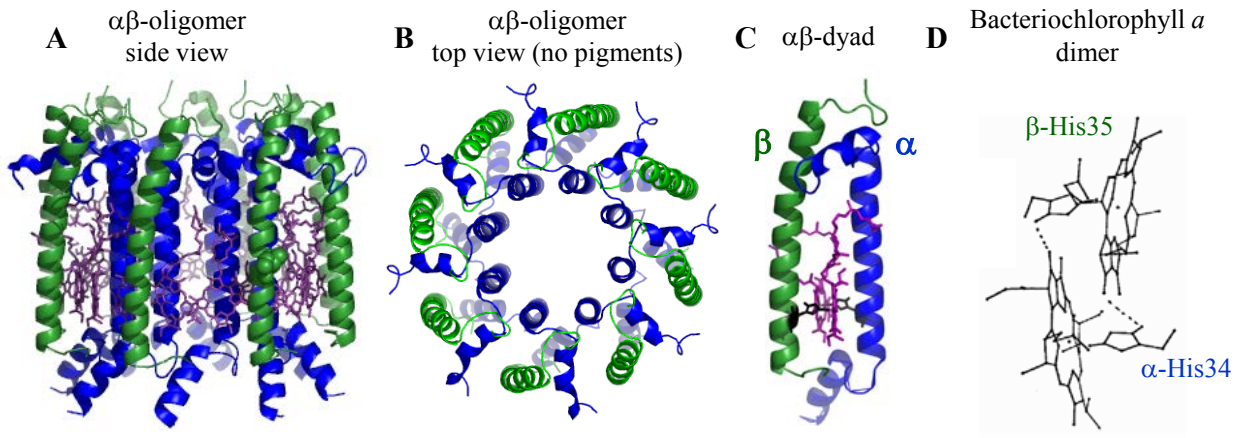

Figure 9. Light-harvesting structural models with α-peptides in blue, β-peptides in green, and bacteriochlorophylls in purple (black in right image). (A) Side view of the cyclic light harvesting oligomer, (B) top view with bacteriochlorophylls removed, (C) the αβ-dyad, and (D) relative orientation of the bacteriochlorophyll dimer.

The antennas of these native systems are composed of amazing ring like structures, with light absorbing chromophores held at specific distances and orientations to each other by proteins, which can also fine tune important energy levels. As noted above, Nature uses the interaction of two identical chromophores to construct a dimer, which creates a first excited singlet state at slightly lower energy than the single chromophore. In turn, the interaction between multiple dimers lowers this energy even further. In this way the native light-harvesting complex could be viewed as a ring of independent monomer donors (B800) that absorb light and transfer excitation energy to an acceptor ring-like array (B850) composed of strongly interacting dimers, creating the donor and acceptor relationship and downhill energy funnel.

Natural systems are remarkably efficient at taking the energy from an absorbed photon and funneling it to the reaction center to do work. While highly efficient, these native systems tend to absorb only a fraction of the solar spectrum. This appears adequate for bacteria and plants, which have actually developed complex systems to dissipate excess energy as they often receive more than they need. In a synthetic system that is focused solely on harvesting the

energy from the sun, there is no need to consider compromising antenna function with other biological necessities (like growing, reproducing, or even dissipating excess absorbed energy).

There are some primary questions driving this line of investigation. Can we recreate native-like light-harvesting antenna with minimal parts? Can chromophores be equipped with substituents for covalent attachment to peptides without compromising their desirable properties? Can excitation energy be transferred from a donor to acceptor, creating an energy funnel?

Here we take inspiration from the light-harvesting antennas of photosynthetic bacteria, which are highly efficient at funneling excitation energy, to construct our biohybrid antenna and improve solar coverage by attaching additional chromophores. These additional chromophores need to transfer their excitation energy efficiently. The bacteriochlorophyll pair, in dyad preparations, or bacteriochlorophyll array, in oligomer preparations, function as energy acceptor as in native bacterial photosynthetic light-harvesting complexes. Overall efficiency can be compromised if the radiation that is absorbed is not funneled to the target site, lost either through fluorescence or non-radiative decay (heat).

The subject of Chapter 8 is the fruit of a very interactive collaboration. Native-like B820 systems are constructed from two identical, truncated β polypeptide sequences (31 amino acid helix compared to about 50 in the native system) that produce absorption spectra identical to the analogous αβ B820. The matching spectra strongly suggest that the bacteriochlorophyll pair, which gives rise to the absorption features, has similar binding and relative orientation to the native systems. Dyads are prepared in the Loach lab at Northwestern University by the addition of bacteriochlorophyll to a detergent solution of the requisite peptide. The detergent concentration is then lowered by dilution, resulting in formation of dyads, viewed here as a model for the fundamental light-harvesting subunit. Upon chilling the preparations at ~4 C, or

reducing the detergent concentration further, the dyads are coerced to interact with each other to form oligomers. Our synthesized 31-mer peptide incorporates a change in one amino acid (to cysteine) to allow for covalent attachment of a donor chromophore (with a maleimide attachment site on a linker). The donor chromophores studied include synthetic bacteriochlorins prepared in the Lindsey lab at North Carolina State University. The site on the peptide for chromophore attachment was selected to minimize interference with dyad (and oligomer) formation. Figure 10 shows structural models of (1) the light harvesting oligomer (left), with potential binding sites for chromophore attachment highlighted in red and brown, (2) αβ dyad (again, generically described as B820 based on Q_y peak absorbance) with same highlighted binding sites labeled (center), and (3) the 31-mer ββ dyad (also B820) with approximate distances along the polypeptide chain from the histidine 0-position (right).

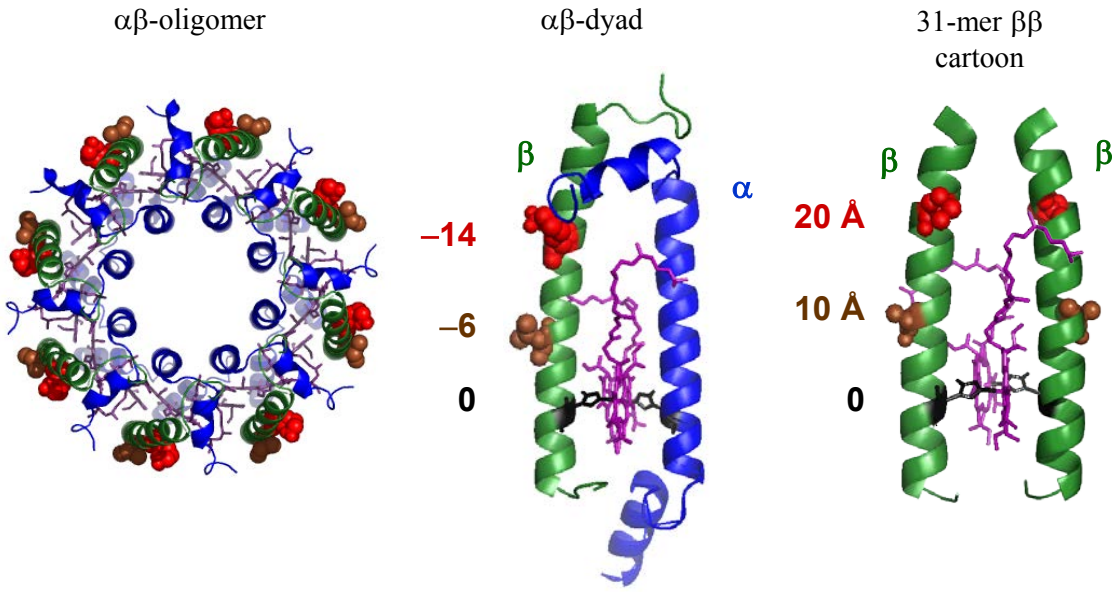

Figure 10. Top view of the cyclic light harvesting oligomer, B850 (left), the αβ B820 dyad (center), and a truncated 31-mer ββ B820 dyad (right). Two potential positions for donor chromophore attachment are colored in red (lysine residue at the -14 position, approximately 20 Å from histidine at zero position), and brown (isoleucine at the -6 position, approximately 10 Å). Bacteriochlorophylls are purple, with histidine coordination sites colored black.

The two peptides on their own do not assemble into a relevant dyad; the bacteriochlorophylls are essential for this process and there are multiple interactions, such as peptide-peptide, peptide-chromophore, and chromophore-chromophore that all contribute to making the self-assembled dyad. There is no covalent attachment of the bacteriochlorophylls to the peptide backbone, but rather they are delicately held in place, primarily through coordination of histidine sites on the peptide with the central metal (magnesium) of the bacteriochlorophyll (along with interactions between bacteriochlorophylls and with the peptides). In an effort to not upset this delicate balance, the sites for binding additional donor chromophores were selected to be on the outside of the helical peptides, to minimize any interference in the self-assembly of the dyad subunit. Under certain conditions the dyads can associate with each other and eventual oligomer ring-like formations are created. The binding site for the donor chromophores also took this into consideration, minimizing the impact an additional chromophore on each peptide would have on dyad and oligomer formation.

Our simplified model, with two identical, truncated β-peptides, can bind a bacteriochlorophyll pair and native-like B820 spectra are reproduced. The bacteriochlorophylls that form the dyad and oligomer energy acceptor sites in the biohybrid antenna are the same chromophores used in the native antenna. This connection back to the properties of the native system creates a strong foundation for further tailoring. The natural properties of the bacteriochlorophyll pair are held intact in the ββ-dyad, and can now be studied on their own, without the influence of neighboring pairs as would be found in the cyclic light-harvesting systems, where, again, the bacteriochlorophyll pairs essentially create a ring of dimers (B850 - B875). Studies on the ββ-dyad can be related back to the native systems, and can be carried forward, expanding solar coverage by attaching donor chromophores. Figure 11 shows a

representative biohybrid antenna system, with synthetic donor chromophores covalently bound to the peptide. The donor chromophores are excited and perform excitation energy transfer to the bacteriochlorophyll pair (B820).

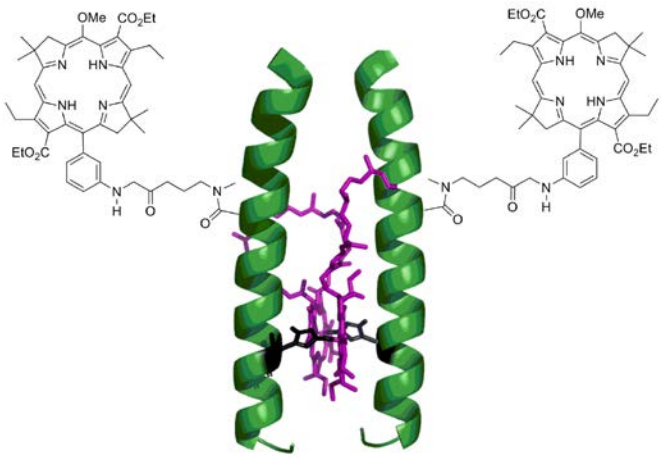

Figure 11. Light-harvesting biohybrid dyad, with synthetic donor chromophores and bacteriochlorophyll dimer acceptor.

Our biohybrid antennas contain an identical pair of β peptides, each with a designated place for donor chromophore attachment, which self-assemble in the presence of bacteriochlorophyll to create a fundamental light-harvesting B820 subunit. The conditions can be controlled such that the dyads are induced to interact with each other and form β_n oligomers that contain 2n bacteriochlorophylls in the acceptor array, presumably similar to the native cyclic light harvesting systems that contain on the order of 10 subunits. One difference is that the oligomeric form composed of our ββ dyads only shifts the Q_y wavelength to ~830-850 nm (collectively termed B850), opposed to the B875 of the native cyclic oligomer, which use full length peptides (about 50 amino acids in length) and αβ-dyads. Studies of ring-like oligomers are the ultimate goal in making the closest connection to and then extending the properties of the native antenna systems. This work is described in Chapter 8.

Palette of Lipophilic Bacteriochlorins. The initial success of the biohybrid antenna project prompted considerations of many directions to expand the research program. One direction was to include a larger variety of chromophores that could be bound to specific, controlled sites on the peptides (bioconjugatable). The increase in available synthetic chromophores creates a veritable palette of pigments that can be selected to absorb in a desirable region of the solar spectrum. With a variety of pigments and bioconjugation techniques, a robust and versatile platform begins to develop for the creation of highly tunable antennas. The ability to form cyclic oligomers from dyad subunits allows for further specialization as multiple complementary pigments can be used to fill out the solar spectrum and construct the energy funnel. This work is the focus of Chapter 9.

For all of these biohybrid antenna studies the final stop on the energy transfer path is the bacteriochlorophyll dimer or array, which is relatively unchanged from its native state in photosynthetic bacteria. Ultimately this antenna function could be connected to a natural or artificial reaction center to harness the initial excitation energy for direct current production or chemical work. The use of native bacteriochlorophylls and native-like peptides provided some assurance that effective antennas could be produced, and also limited the experimental phase space for these preliminary studies, allowing the focus to be on the bioconjugation of the peripheral chromophores and the transfer of excitation energy. This platform for biohybrid antenna design could be expanded with the use of full length peptides, creating oligomers to extend light-harvesting out to 875 nm like native systems. Also, the preparation of dyads from unique α and β polypeptides would allow each to be tailored independently, then assembled in the presence of bacteriochlorophyll to construct dyads or oligomers with multiple and distinct chromophores acting as excitation energy donors to expand solar coverage even further.

References.

(1) Report of the Basic Energy Science Workshop on Solar Energy Utilization; April, 2005.

(2) H. Scheer, in *Chlorophylls and Bacteriochlorophylls: Biochemistry, Biophysics, Functions and Applications*; ed. B. Grimm, R. J. Porra, W. Rüdiger and H. Scheer, Kluwer Academic Publishers, The Netherlands, 2006, pp 1–26.

(3) T. Miyatake and H. Tamiaki, *Coord. Chem. Rev.*, 2010, **254**, 2593–2602.

(4) T. S. Balaban, *Acc. Chem. Res.,* 2005, **38**, 612–623.

(5) T. S. Balaban, in *Handbook of Porphyrin Science,* ed. K. M. Kadish, K. M. Smith and R. Guilard, World Scientific Publishing Co., Singapore, vol. 1, 2010, pp 221–306.

(6) Papiz, M. Z.; Prince, S. M.; Howard, T.; Cogdell, R. J.; Isaacs, N. W. *J. Mol. Biol.* **2003**, *326*, 1523–1538.

(7) Roszak, A. W.; Howard, T. D.; Southall, J.; Gardiner, A. T.; Law, C. J.; Isaacs, N. W.; Cogdell, R. J. *Science* **2003**, *302*, 1969–1972.

(8) Koepke, J.; Hu, X.; Muenke, C.; Schulten, K.; Michel, H. *Structure* **1996**, *4*, 581–597.

(9) (a) Sturgis, J. N.; Tucker, J. D.; Olsen, J. D.; Hunter, C. N.; Niederman, R. A. *Biochemistry* **2009**, *48*, 3679–3698. (b) Sener, M. K.; Olsen, J. D.; Hunter, C. N.; Schulten, K. *Proc. Natl. Acad. Sci. USA* **2007**, *104*, 15723–15728.

Chapter 2.

Background, Methods, Contributions and Collaborations

I. Background

Absorption and fluorescence spectra are routinely acquired for all samples, so a brief introduction is worthwhile to describe common features, some points of interest, and commonly used terminology. A Jablonski diagram, with representative absorption and emission spectra correlated to the transitions symbolized by arrows (up for absorption, down for emission) is presented in Figure 1. Transitions from the ground state to S_3 (and S_4 not shown) are termed Soret bands, or B bands. Typically there are two prominent B bands, termed B_x and B_y, which tend to overlap in chlorins, along with vibronic bands of these electronic transitions, leading to the generalized Soret region, typically found from 350-400 nm. This is the most common region for excitation of the chromophores to monitor subsequent fluorescence or transient absorption. From here we can trace the energy as it makes its way back to the ground state. From S_3, we have a non-radiative transition, termed internal conversion (IC), to the S_2 state. The absorption band produced upon a transition from the ground state to S_2 is termed the Q_x band, with a typical range of 500-600 nm. There is again a non-radiative transition, IC, to the S_1 state. The absorption band produced upon a transition from the ground state to S_1 is termed the Q_y band, with a typical range of 600-680 nm for chlorins, extending to 800 nm and beyond for bacteriochlorins.

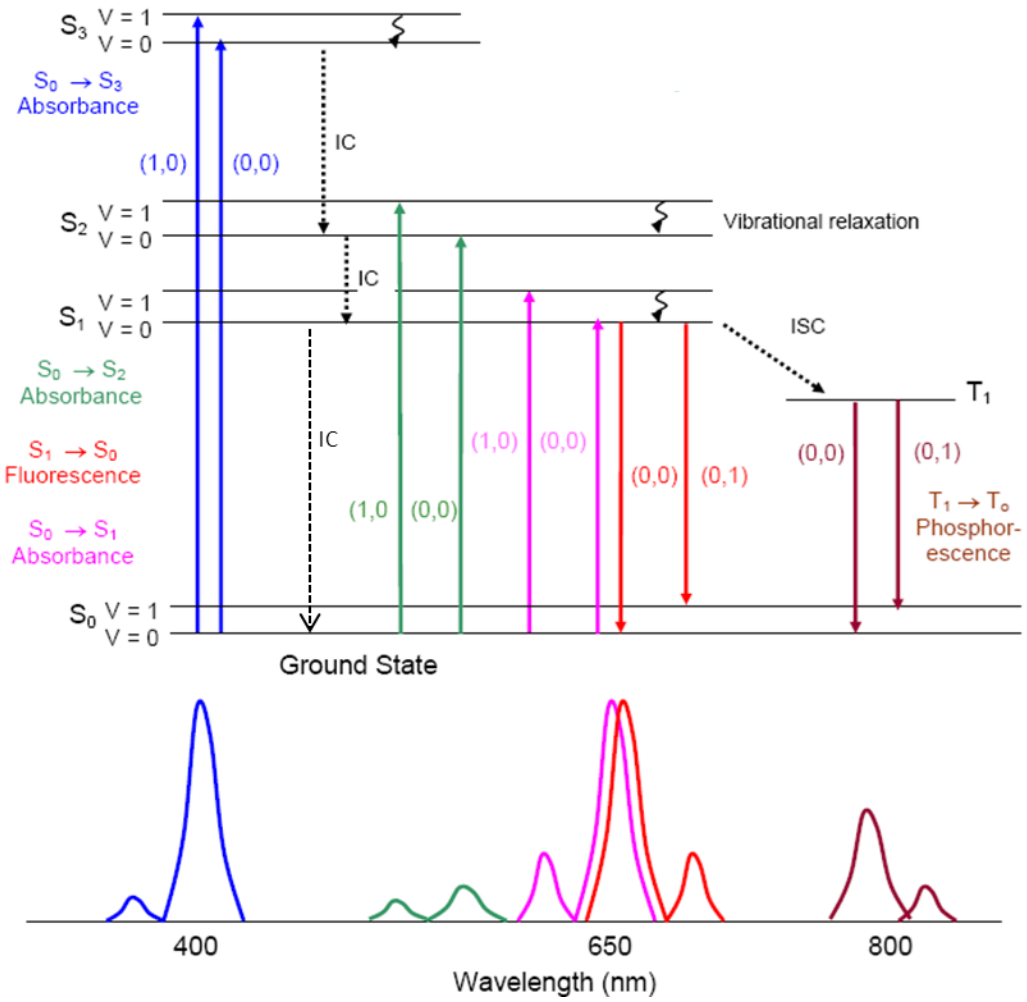

Figure 1. Jablonski diagram of a representative photosynthetic chromophore, with a correlated simulation of absorption and emission spectra below.

The S_1 state is of particular importance as this is where fluorescence originates from, and dictates important molecular properties of interest in light-harvesting, and directed excitation energy transfer. From the S_1 state there are three possible pathways the excitation energy can take (in the absence of other more complicated interactions). These are radiative S_1-S_0 transitions (fluorescence), non-radiative S_1-S_0 transitions (IC), and non-radiative S_1-T_1 transitions, termed intersystem-crossing (ISC), which additionally involve a change in spin. These pathways are described pictorially in Figure 2. Phosphorescence is the radiative decay from T_1-S_0, and was not studied.

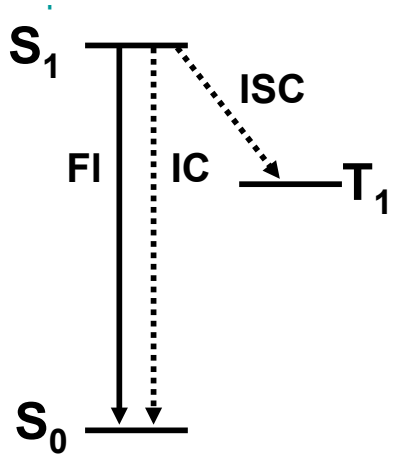

Figure 2. Possible pathways for energy relaxation from the S_1 state: fluorescence (Fl), internal conversion (IC) and intersystem crossing (ISC).

Complete characterization of the different pathways is possible via measurements of τ_S, Φ_f, and Φ_{isc} utilizing Equations (1) to (5).

$$\tau_S = (k_f + k_{ic} + k_{isc})^{-1} \quad (1)$$

$$\Phi_f = k_f / (k_f + k_{ic} + k_{isc}) \quad (2)$$

$$\Phi_{isc} = k_{isc} / (k_f + k_{ic} + k_{isc}) \quad (3)$$

$$\Phi_{ic} = 1 - \Phi_f - \Phi_{isc} \quad (4)$$

$$\Phi_i = k_i / \tau_S \quad (5)$$

τ_S and Φ_f are routinely measured, and taken together, a quick determination of the total non-radiative yield is trivial. Φ_{isc} determinations have been made by analyzing the data from transient absorption experiments, allowing for the determination of Φ_{ic} through Equation (4). Equations (1) and (2) are also an important stating point for the assement of excitation energy transfer yields, where effectively an additional pathway and rate constant are introduced (k_{ET}). A new lifetime expression (τ_S^q) is created to account for the additional decay pathway resulting in Equation (6). An expression for the the yield of energy transfer, Equation (7), is constructed, paralleling Equation (5), leading to an expression for the energy

transfer yield related to changes in $\tau_{S;}$ Equation (8).

$$\tau_S^q = (k_f + k_{ic} + k_{isc} + k_{ET})^{-1} \quad (6)$$

$$\Phi_{ET} = k_{ET} / \tau_S^q \quad (7)$$

$$\Phi_{ET} = 1 - \tau_S^q / \tau_S \quad (8)$$

In the exploration of excitation energy transfer, kinetic data is acquired for a donor molecule in the absence of an acceptor (τ_S) as a control. When the acceptor is present, k_{ET} is now active, and the new lifetime, τ_S^q, allows for a calculation of Φ_{ET}. Similar analysis can be performed using the reduction in donor Φ_f when an acceptor is present. These are two of several techniques used to establish energy transfer yields in biohybrid antennas, which are the subjects of Chapters 8 and 9.

The theoretical framework for the exploration of excitation energy transfer is Förster theory, where the interaction of donor and acceptor transition dipoles allow for through-space energy transfer. While demonstrating that the Förster mechanism provides for excitation energy transfer in our biohybrid systems was not a goal of the research, it does provide insight into important factors that affect energy tranfer efficiency, and was consistent with our experimental results. In the semi-classical treatment, distance, relative orientation of dipole moments, donor fluorescence yield, index of refraction of the media, and spectral overlap (donor emission overlap with acceptor absorption) are the explicit factors contributing to overall efficiency. An illustration of the spectral overlap considerations are presented in Figure 3. The acceptor is the bacteriochlorophyll *a* dyad B820, and overlap with donor emission spectra can be achieved in the weak Q_x region, or the strongly absorbing Q_y. The synthetic bacteriochlorin donors designed to overlap with the intense Q_y band of B820 show greater excitation energy transfer efficiencies than the commercial dyes that

overlap in the weaker Q_x region, again consistent with the theoretical treatment.

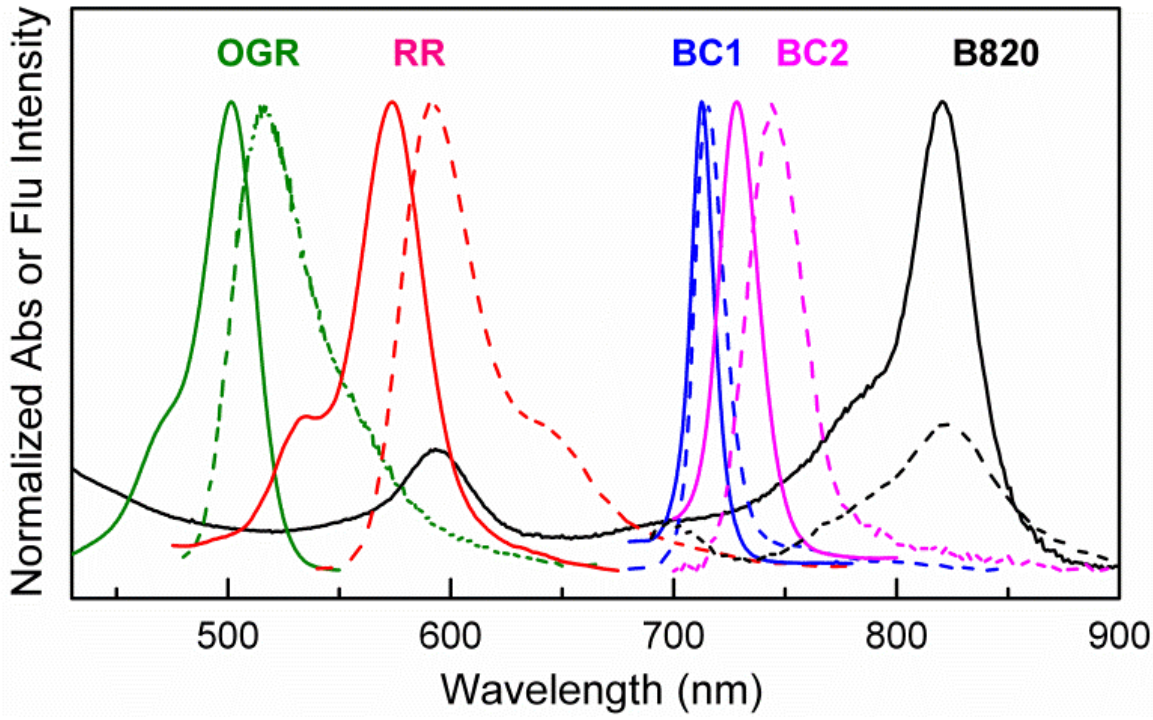

Figure 3. Illustration of spectral overlap in the biohybrid antennas. Normalized absorption (solid) and fluorescence (dashed) spectra of bioconjugatable dyes (colored) and the B820 dyad (black). The B820 fluorescence is scaled arbitrarily for clarity. OGR and RR emsision spectra overlap with the B820 Q_x, while the synthetic bioconjugatable bacteriochlorins BC1 and BC2 overlap with the more strongly absorbing Q_y.

Our calculations employed the point-dipole approximation and were useful to assess the impact of spectral overlap and distance on the expected efficiency. In this treatment, the efficiency is inversely proportional to the sixth power of the distance. With good spectral overlap and high donor fluorescence yields, appreciable energy transfer efficiencies are predicted for distances in excess of 40 Å, with efficiency dropping rapidly as the distance extends to 50 Å and greater. This is discussed in more detail in the Supporting Information of Chapter 8 and schematically represented with a simple illustration in Figure 4.

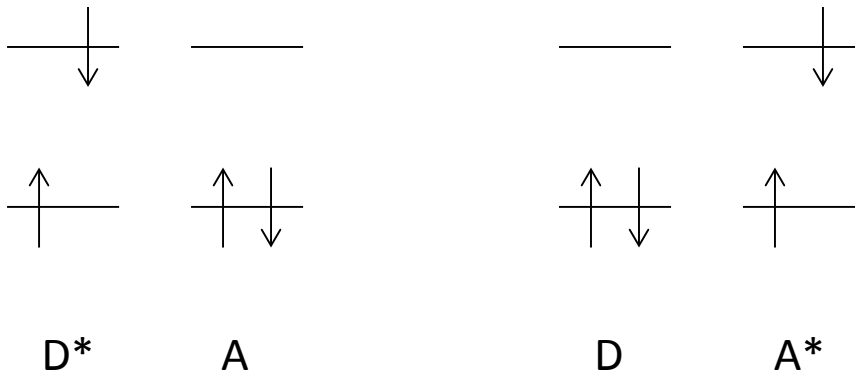

Figure 4. Schematic of Förster excitation energy transfer between a donor (D) and acceptor (A) pair. The donor is excited to produce the initial configuration of D* A (left), the excitation energy then migrates to the acceptor, producing the configuration of D A* (right).

With the introduction of spectral properties and terminology, along with a brief discussion of kinetics, and the importance of spectral overlap in the excitation energy transfer process, a more rigorous foundation for spectral and photophysical properties is required. This foundation is Gouterman's four orbital model[1-3], where the energies of the frontier MOs (HOMO−1, HOMO, LUMO, LUMO+1) are tantamount to the spectral properties of the synthetic tetrapyrroles studied here. Within this model, the B_y and Q_y states are comprised of linear combinations of the (y-polarized) electronic configurations that result from HOMO $\rightarrow$ LUMO and HOMO−1 $\rightarrow$ LUMO+1 one-electron promotions. (Similarly B_x and Q_x are derived from HOMO $\rightarrow$ LUMO+1 and HOMO-1 $\rightarrow$ LUMO.) The B_y state reflects the symmetric combination and the Q_y state the antisymmetric combination of the configurations. These transitions are pictured in Figure 5 (top panel), with actual spectra of the three modeled compounds in the lower panel.

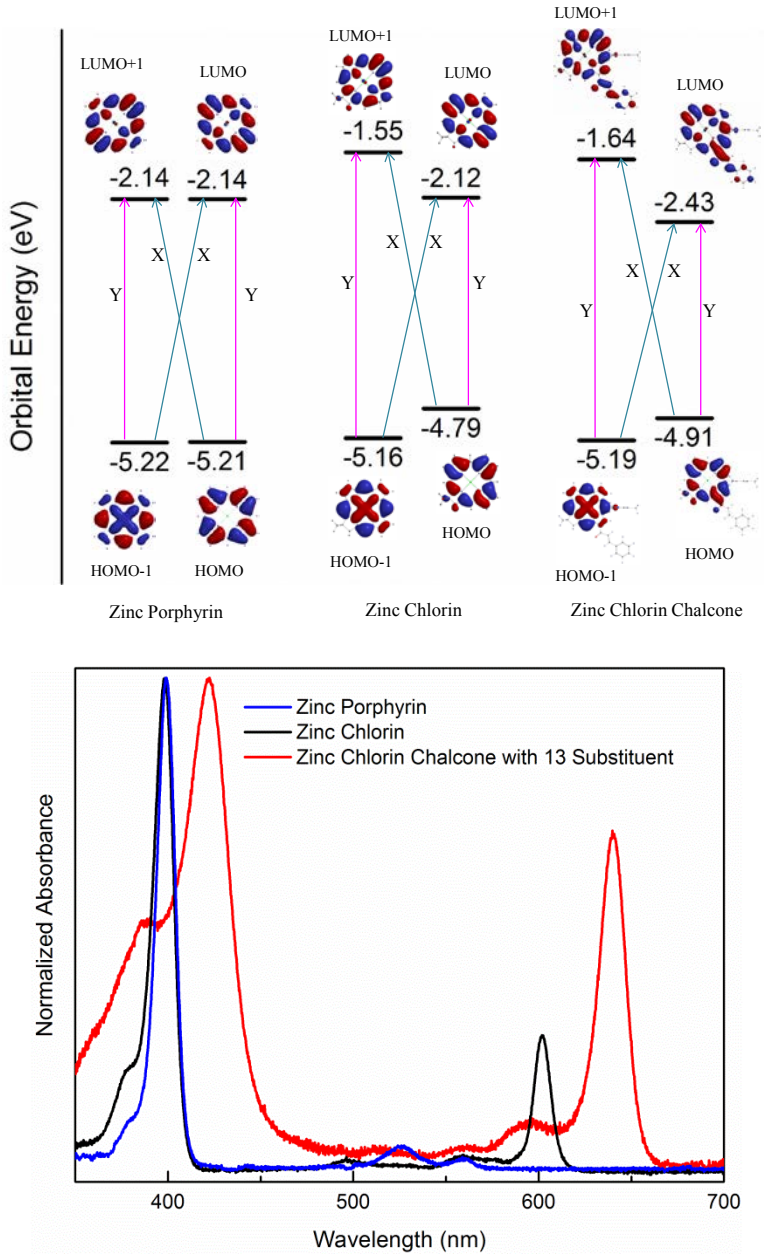

Figure 5. Top panel: one electron promotion basis states for the four orbital model. Zinc porphyrin (left), zinc chlorin (center), and zinc chlorin chalcone (right). Bottom panel: actual absorption spectra.

The key parameters that are most closely tied to the optical properties are the average energy (ΔE_{avg}) and difference in energy (ΔE_{dif}) of the [LUMO – HOMO] and [LUMO+1 – HOMO-1] energy gaps given in Equations 9.

$$\Delta E_{avg} = [\Delta E(\text{LUMO+1} - \text{HOMO-1}) + \Delta E(\text{LUMO} - \text{HOMO})]/2 \quad (9a)$$

$$\Delta E_{dif} = [\Delta E(\text{LUMO+1} - \text{HOMO-1}) - \Delta E(\text{LUMO} - \text{HOMO})] \quad (9b)$$

Parameter ΔE_{avg} places the energy center of gravity of the $B_y(0,0)$ and $Q_y(0,0)$ bands. The $Q_y(0,0)$ band lies lower and the $B_y(0,0)$ band higher than the average energy by one-half the magnitude of a splitting parameter (σ_y) that in turn depends on ΔE_{dif} and the configuration interaction energy (δ) as given by Equations 10 and 11.

$$E_{By} = \Delta E_{avg} + \sigma_y/2 \quad (10a)$$

$$E_{Qy} = \Delta E_{avg} - \sigma_y/2 \quad (10b)$$

$$\sigma_y = \Delta E_{dif} /[\sin(2\eta_y)] \quad (10c)$$

$$\eta_y = [\tan^{-1}(\Delta E_{dif}/2\delta)]/2 \quad (11)$$

The configuration-interaction energy derives from the electron-density distribution in the molecule (and thus electron-electron repulsion) and should be relatively constant for a series of related molecules. In addition to the $B_y - Q_y$ splitting (σ_y; Eq. (10c)), the relative intensities of the B_y and Q_y bands is driven by ΔE_{dif} via Eq. (12), using η_y in Equation (11).

$$\Sigma_{Qy}/\Sigma_{By} = [1-\cos(2\eta_y)]/[1+\cos(2\eta_y)] \quad (12)$$

The intensity relationship follows because the constructive (B_y) versus destructive (Q_y) interference of the (nominally equal) transition-dipole moments associated with the HOMO-1 $\rightarrow$ LUMO+1 and HOMO $\rightarrow$ LUMO configurations dictates the relative oscillator strengths of the B_y and Q_y absorption transitions. In particular, as ΔE_{dif} increases (e.g., due to substituents), the

transition-dipole cancellation for the Q_y state decreases and intensity is shifted from B_y to Q_y, and vice versa. Mathematically, as ΔE_{dif} increases, η_y in Eq. (10c) increases, $\cos(2\eta_y)$ decreases and the numerator in Eq. (12) grows at the expense of the denominator, and vice versa. According to Eqs. (10), this same increase in ΔE_{dif} increases the energy spacing between B_y and Q_y, and vice versa.

Figure 5 exemplifies that substituents along the molecular Y axis (e.g. 3- and 13-substituents) can particularly stabilize (more negative energy) the LUMO, substantially decreasing $\Delta E(\text{LUMO} - \text{HOMO})$ with little change to $\Delta E(\text{LUMO+1} - \text{HOMO-1})$, driving the increase in ΔE_{dif} which is prominently manifest in the increased relative intensity of the Q_y peak for the zinc chlorin chalcones. The four orbital model is an instructive lens through which spectral properties are aligned with design concepts for tuning the prominent wavelength features, adding functionality (like amphiphilic character or bioconjugating groups), as well as tuning important redox properties explored previously.[4,5] In addition to guiding the synthesis of chlorins with novel spectral properties, insight into natural chlorophylls has also been made with the help of the four orbital model (Chapters 3 and 5).

The basis for the variation in natural chlorophylls *a*, *b*, and *d* is elucidated by performing a series of molecular orbital calculations, placing a simple substituent at each position of the macrocycle with comparison to no group at all (recall that the spectral differences are dominated by the effect of a formyl group at the 7-position in chlorophyll *b*, the 3-position in chlorophyll *d*, and no formyl group in chlorophyll *a*). The molecular orbital energies, energy gaps, and simple four orbital parameters of ΔE_{avg} and ΔE_{dif} (Equation 9) are presented in Figure 6 for a zinc chlorin for which a single formyl, acetyl, vinyl, and ethynyl substituent is walked around the macrocycle.

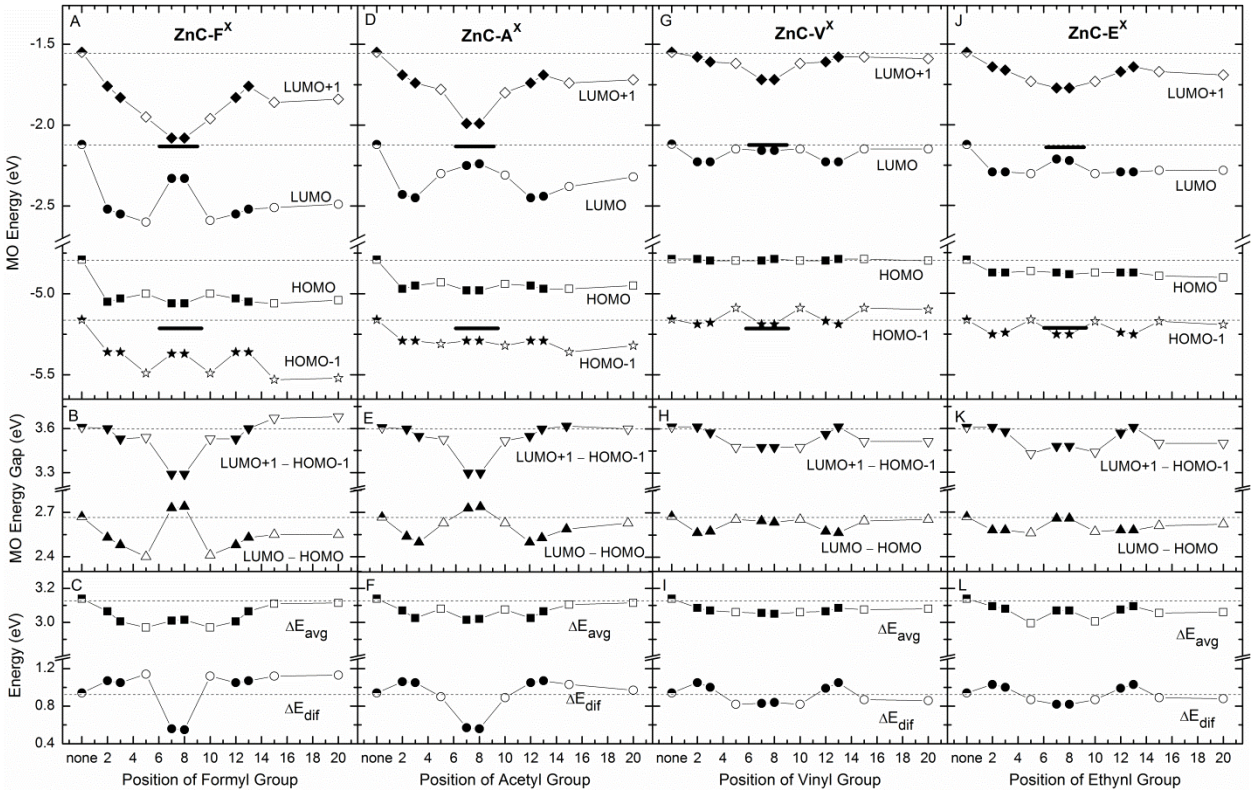

Figure 6. Walking a substituent around the zinc chlorin macrocycle. MO energies (top panels), energy gaps (middle panels) and four-orbital parameters (bottom panels) for a zinc chlorin containing a single formyl (A-C), acetyl (D-F), vinyl (G-I) or ethynyl (J-L) group at various macrocycle sites. The solid bar at –2.14 eV (under the points for the 7- and 8-positions) denotes the energy of the degenerate "LUMOs" of the unsubstituted zinc porphyrin and the solid bar at –5.21 eV denotes the energy of the accidentally degenerate porphyrin "HOMOs". The horizontal dashed lines denote the reference values for **ZnC** with no substituents.

A formyl group at the 7-position (7- and 8-positions being nearly identical) has the remarkable effect of stabilizing the LUMO+1 energy more than that group at any other position, and at the same time having the least impact on the LUMO. Similar results are seen for the acetyl group, with the vinyl and ethynyl exhibiting much weaker effects. The preferential stabilization of the LUMO+1 decreases the LUMO+1 – HOMO-1 energy gap, significantly decreasing ΔE_{dif}, leading to a decrease in the relative intensity of the Q_y band as oscillator strength is shifted back to the B_y (Equation 12), and also decreasing σ_y (Equation 10c), shifting

the prominent absorption bands closer together. In this manner chlorophyll *b* (and organism that have adopted its use) can get out from under the optical shadow of chlorophylls *a* and *d* as seen in Figure 7 of Chapter 1. A more extensive four orbital analysis is made in Chapter 5, exploring a variety of macrocycle types along with substituent identity and placement effects, detailing the rich science behind the spectral properties of native photosynthetic chromophores and related synthetic analogs.

Scales and units. Absorption, fluorescence and transient absorption spectra throughout this thesis utilize the convention of a wavelength scale (in nanometers). Energy is inversely proportional to wavelength through a form of the Planck relation for a photon ($E = hc/\lambda$), where h is Planck's constant, c the speed of light, and λ is the wavelength. Recognizing that energy units of electron volts (eV) or reciprocal centimeters (cm^{-1}) might be more familiar scales to some, identical absorption and fluorescence data for zinc oxophorbine is presented in Figure 7 to allow for some comparison between commonly used scales.

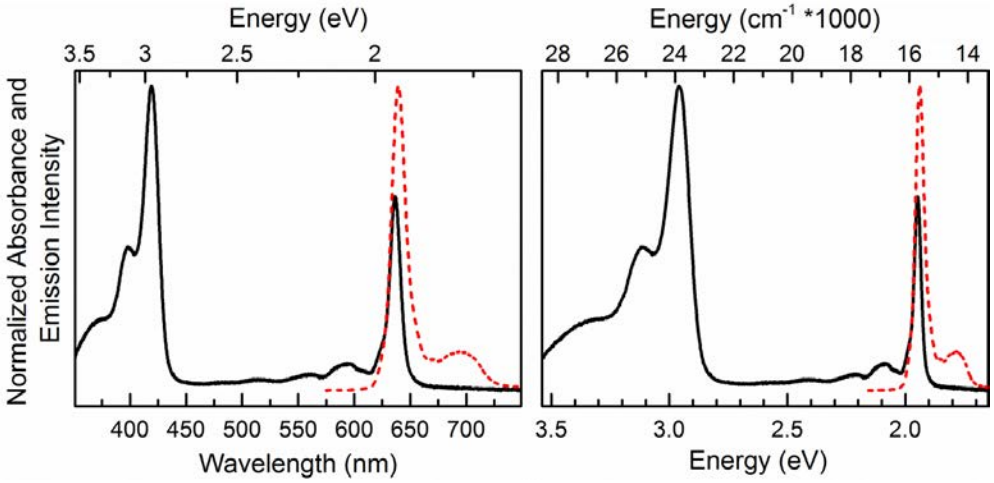

Figure 7. Representative normalized absorption (solid black line) and normalized emission (dashed red line) spectra for zinc oxophorbine. The left panel utilizes a wavelength (nm) scale typical of the data found in this thesis (with the reciprocal scaled eV on top axis for reference). The right panel shows the same data with a linear energy scale, eV on bottom and cm^{-1} on top. The x-axis spans the same energy space in both panels.

Several common parameters and spectral features are presented in the different units for comparison. For the primary absorption features, the Soret maximum is at 419 nm, 2.96 eV, or 23,870 cm^{-1}, and the Q_y maximum is at 637 nm, 1.95 eV, or 15,730 cm^{-1}. The full width at half maximum of the primary emission feature is 14 nm, 0.05 eV, or 360 cm^{-1}. While spectral information is typically presented with the wavelength scale, comparisons of molecular orbital energies employ the eV unit, and detailed analysis of peak widths and small energy shifts are often presented in the unit of cm^{-1}. Qualitatively, the linear energy scale accentuates the breadth of the Soret absorption and narrows the Q_y with respect to the linear wavelength scale.

II. Methods

Static Absorption and Fluorescence. Static absorption was performed on Varian Cary 100 or Shimadzu UV-1800, used interchangeably with equivalent capabilities. Spectra collected at 0.2 nm data intervals. Static fluorescence measurements were performed on one of two systems, typically depending on the desired detection range. One system (Spec Fluorolog Tau 2) employs a R928 photomultiplier tube for detection, which loses efficiency rapidly in the 850 nm - 900 nm range. This is more than sufficient for the analysis of chlorin spectra. The second system (PTI quantamaster 40) has capabilities for similar detection with an R928 photomultiplier, but with an added solid state InGaAs detector with lock-in detection and excitation light chopped at 30 Hz. This detector has an expanded range in the NIR, making it ideal for use with bacteriochlorins and biohybrid assemblies. Both systems utilize excitation and detection monochromators with adjustable bandwidths (2-4 nm is typical, detection increased to 8 nm for some measurements of weak NIR fluorescence). For both setups, the excitation light source is a xenon arc lamp and emission spectra were corrected for detection-system spectral response. Fluorescence yield determinations employ argon purged solutions having absorption <

0.1 at the excitation wavelength to prevent front-face and inner-filter effects. Fluorescence yields were determined relative to a known standard, corrected for index of refraction effects for the solvents used. These standards are (1) free base *meso*-tetraphenylporphyrin (**FbTPP**) in nondegassed toluene, for which $\Phi_f = 0.070$ was established with respect to the zinc chelate **ZnTPP** in nondegassed toluene ($\Phi_f = 0.030$),[6] consistent with prior results on **FbTPP**,[7] and (2) 8,8,18,18-tetramethylbacteriochlorin[8] in argon-purged toluene, for which $\Phi_f = 0.14$ was established with respect to **FbTPP** and chlorophyll *a* (**Chl *a***) in deoxygenated benzene[9] or toluene[10] (both with $\Phi_f = 0.325$).

The same apparatus can be used to obtain fluorescence excitation spectra, where the emission monochromator was trained on a specific wavelength and the excitation monochromator was scanned across a range. Fluorescence excitation spectra were particularly valuable for the determination of energy transfer yields in the biohybrid systems (along with fluorescence quenching data and transient absorption).

Fluorescence Lifetime. Two distinct and complementary techniques were used to obtain fluorescence lifetimes and the results were typically in good agreement and averaged. One is a frequency domain technique based on the modulation of the intensity of the excitation source (xenon lamp) while detecting the modulating fluorescence signal from the sample with a scattering reference (no inherent excited state lifetime). Samples were excited at various wavelengths in the Soret region and detected through appropriate colored glass filters (Spex Fluorolog Tau 2). Modulation frequencies from 5–200 MHz were typically utilized and both the fluorescence phase shift and modulation amplitude were analyzed. This technique has the very positive attributes of being integrated into the static fluorescence spectra system and requires no additional materials. The excitation source is modulated by a Pockels cell which requires

exceptionally little maintenance. The drawbacks are that no actual fluorescence decay profile is produced, it can be time consuming to perform accurate signal balancing with the scattering reference, and there is little recourse for dealing with a very weakly fluorescing sample. The optimal lifetime range for this technique is approximately 1-12 ns. Detection is performed with a photomultiplier tube (R928) with typical spectral limitations as the efficiency drops dramatically at wavelengths higher than 850 nm, which is typically not an issue with chlorins fluorescing in the 600-700 nm range.

The second technique is in the time domain and a laser source is used to excite the sample with time-correlated-single-photon-counting detection on an apparatus with an approximately Gaussian instrument response function with a full-width-at-half-maximum of ~1 nanosecond (Photon Technology International LaserStrobe TM-3). Samples were excited in the Soret or Q regions using excitation pulses at 337 nm from a nitrogen laser or in the blue to green spectral regions from a dye laser pumped by the nitrogen laser. Appropriate glass filters are again used to eliminate scattering effects. This instrument produces an actual fluorescence decay profile which can be analyzed visually and mathematically. With the added dye laser module the excitation wavelength can be finely tuned over a large range while maintaining plenty of power. The lifetime range that can be determined from this instrument is from less than 1 nanosecond to several seconds, although lifetimes shorter than the width of the instrument response function (< 1ns) become problematic to assess accurately. This technique provides rapid results and is quite flexible in terms of data acquisition parameters (time steps, averaging, and wavelength selection). The drawbacks are the need for laser dyes to gain the ability to tune the excitation wavelength. The system also uses non-trivial amounts of nitrogen gas and needs routine cleaning and maintenance. Actual detection is made by a photomultiplier tube (R928) with the

same limitations as above. Together, the two techniques help to establish reliable fluorescence lifetime results for chromophores and systems with lifetimes greater than 1 ns. For lifetimes below this threshold, ultrafast transient absorption spectroscopy is employed to resolve more prompt decay components, and is discussed below.

Transient absorption. Time-resolved pump-probe absorption experiments were carried out using a Helios femtosecond transient absorption spectrometer (Ultrafast Systems) coupled to a femtosecond laser system (Newport/Spectra-Physics). The one-box Solstice amplified ultrafast laser system consists of a Mai-Tai femtosecond oscillator whose output goes to a Spitfire Pro XP regenerative amplifier that is pumped by an Empower diode-pumped solid state pulsed green laser. The amplifier produces 800 nm pulses (~3.5 mJ, ~90 fs) at 1 kHz. The output beam is split into two and used to generate (i) the pump beam (90%) in a Topas-C optical parametric amplifier (Light Conversion, Lithuania) and (ii) probe pulses (10%) for the Helios transient-absorption spectrometer. The pump (excitation) pulses pass through a depolarizer to provide isotropic excitation of the sample and avoid pump-probe polarization effects. The resulting excitation pulses have a temporal resolution of ~130 fs and typically span a 20 nm range. Individual ΔA spectra are acquired using excitation light chopped at 0.5 kHz (to provide alternate accumulations of the probe light with and without excitation) and averaged over 0.1-5 s (depending on signal quality, typically 0.5 s). Final ΔA spectra represent the average of 1000 such individual spectra. The excitation pulses (typically of energy 0.5-2 μJ/pulse, or 0.25 to 1 mW) were adjusted to have a spot diameter of 1 mm. Two different probe and detection configurations are possible dependent on the spectral region of interest; 400-800 nm with 1.5 nm resolution and 800-1600 nm range with 3 nm resolution. The delay range extends to ~8 ns, with a minimum step of 20 fs.

The samples were typically excited near the peaks of the main absorption features (~400-450 nm for Soret excitation, 500-600 nm for Q_x band excitation). Samples were contained in 2-mm or 1-cm path cuvettes and were mixed continuously using a magnetic micro-stirrer to minimize photo-degradation. Sample absorbance at the excitation wavelength varied depending on the project, typically in the range of 0.05-0.3.

Contributions and Collaborations

I performed static absorption and emission spectroscopy, fluorescence yield determinations and excited singlet state lifetime analysis by multiple techniques (time- and frequency-domain) for the projects described in Chapters 3-8 (chlorin set only in Chapter 6). Interpretation of molecular orbital energies in terms of Gouterman's four-orbital model and the connection with spectral and photophysical properties, and trend analysis was performed for Chapters 4, 5 and 7. Detailed solution studies of assembly properties and formation were performed for Chapter 4. Transient absorption studies were performed for Chapters 6-9.

For the biohybrid project described in Chapter 8, I performed photophysical characterization of the biohybrid samples and controls, which includes static absorption and fluorescence (with multiple detection systems depending on sample properties), excited singlet state lifetime analysis, transient absorption as well as solution studies of dyad and oligomer properties and the conversion between the two forms. I also performed calculations of spectral overlap to aid in the interpretation of the excitation energy transfer results in the context of Förster energy transfer.

For Chapter 9, I performed low temperature static and time-resolved analysis for energy transfer within oligomers on select samples. I performed training and technology transfer as the viability of the project was demonstrated and the possibility to expand the scope was

increasingly realistic. This project served as a transition point for training and handing off the project to another student, which included training on sample receipt and handling, sample analysis and data processing, along with instrument setup. The close collaboration produced a successful transfer of knowledge and skills for the expanding research on this topic.

Resonance Raman spectroscopy was performed by the Bocian lab for Chapters 3, 4, and 8. Molecular orbital energies were calculated using density functional theory in the Bocian lab for Chapters 3, 5, and 7.

X-ray crystal structure analysis was performed by the Lindsey lab for Chapter 3. Chromophore synthesis was performed by the Lindsey Lab for Chapters 3-9, except for a few select cases described here. For Chapter 5, chlorophyll *a* and *b* were purchased and chlorophyll *d* was isolated from *chlorobium vibroforme* and gifted. Free base analogs were created from the native pigments in the Holten lab as described in Chapter 5. For Chapters 8 and 9, the dyes Oregon Green and Rhodamine Red were used as purchased.

For Chapters 8 and 9, synthetic polypeptides were synthesized by an outside source. Bacteriochlorophyll *a* was isolated by the Loach lab. Biohybrid samples and controls were prepared by the Loach lab.

References

(1) Gouterman, M. (1959) Study of the effects of substitution on the absorption spectra of porphin. *J. Chem. Phys.* **30**, 1139–1161.

(2) Gouterman, M. (1961) Spectra of porphyrins. J. Mol. Spectroscopy 6, 138–163.

(3) Gouterman, M. (1978) Optical spectra and electronic structure of porphyrins and related rings. In The Porphyrins Vol. 3 (Edited by D. Dolphin), pp 1–165. Academic Press, New York.

(4) H. L. Kee, C. Kirmaier, Q. Tang, J. R. Diers, C. Muthiah, M. Taniguchi, J. K. Laha, M. Ptaszek, J. S. Lindsey, D. F. Bocian and D. Holten, *Photochem. Photobiol*., 2007, **83**, 1110–1124.

(5) H. L. Kee, C. Kirmaier, Q. Tang, J. R. Diers, C. Muthiah, M. Taniguchi, J. K. Laha, M. Ptaszek, J. S. Lindsey, D. F. Bocian and D. Holten, *Photochem. Photobiol*., 2007, **83**, 1125–1143.

(6) Seybold, P. G.; Gouterman, M. *J. Mol. Spectrosc.* **1969**, *31*, 1–13.

(7) Gradyushko, A. T.; Sevchenko, A. N.; Solovyov, K. N.; Tsvirko, M. P. *Photochem. Photobiol.* **1970**, *11*, 387–400.

(8) Yang, E.; Kirmaier, C.; Krayer, M.; Taniguchi, M.; Kim, H.-J.; Diers, J. R.; Bocian, D. F.; Lindsey, J. S.; Holten, D. *J. Phys. Chem. B* **2011**, *115*, 10801–10816.

(9) Weber, G.; Teale, F. W. J. *Trans. Faraday Soc.* **1957**, *53*, 646–655.

(10) Mass, O.; Taniguchi, M.; Ptaszek, M.; Springer, J. W.; Faries, K. M.; Diers, J. R.; Bocian, D. F.; Holten, D.; Lindsey, J. S. *New J. Chem*. **2011**, *35*, 76–88.

Chapter 3.

Structural Characteristics that Make Chlorophylls Green: Interplay of Hydrocarbon Skeleton and Substituents

Reprinted with permission from the *New Journal of Chemistry*. Mass, O., M. Taniguchi, M. Ptaszek, J. W. Springer, K. M. Faries, J. R. Diers, D. F. Bocian, D. Holten and J. S. Lindsey (2011). *New J. Chem*. **35**, 76–88.

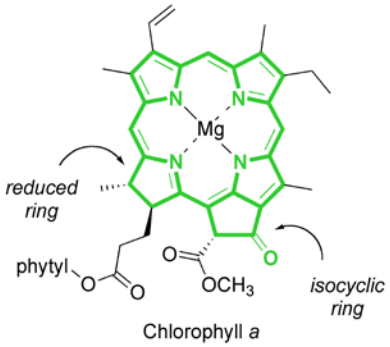

Chlorophyll *a*

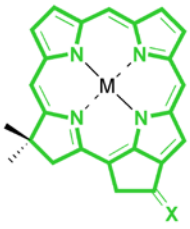

a 13^1-oxophorbine (X = O)
a phorbine (X = H, H)

Abstract

Understanding the effects of substituents on natural photosynthetic pigments is essential for gaining a deep understanding of why such pigments were selected over the course of evolution for use in photosynthetic systems. This knowledge should provide for a more thoughtful design of artificial light-harvesting systems. The hydrocarbon skeleton of all chlorophylls is phorbine, which contains an annulated five-membered (isocyclic) ring in addition to the reduced pyrrole ring characteristic of chlorins. A phorbine and a 13^1-oxophorbine (which bears an oxo group in the isocyclic ring) were synthesized as benchmark molecules for fundamental spectral and photophysical studies. The phorbine and 13^1-oxophorbine macrocycles lack peripheral substituents other than a geminal dimethyl group in the reduced ring to stabilize the chlorin chromophore. The spectral properties and electronic structure of the zinc or free base 13^1-oxophorbine closely resemble those of the corresponding analogues of chlorophyll *a*. Accordingly, the fundamental electronic properties of chlorophylls are primarily a consequence of the 13^1-oxophorbine base macrocycle.

Introduction

Chlorophylls are the most famous members of the chlorin family.[1] The chlorin designation stems from the presence of one reduced pyrrole ring in the tetrapyrrole macrocycle. However, the carbon skeleton of chlorophylls is not simply a cyclic tetrapyrrole, but also contains an annulated five-membered ring. This hydrocarbon framework is known as phorbine.[2] A phorbine that carries an oxo group at the 13^1-position, as is the case with all chlorophylls, is known as a 13^1-oxophorbine. The structures of chlorin, phorbine, 13^1-oxophorbine, chlorophyll *a* and chlorophyll *b* are shown in Chart 1. Inspection of the chlorophyll structure leads naturally to questions concerning the requirements for the fifth ring, the given set of peripheral substituents, and the extent to which such features contribute to the distinct spectral and electronic properties of the chlorophylls.

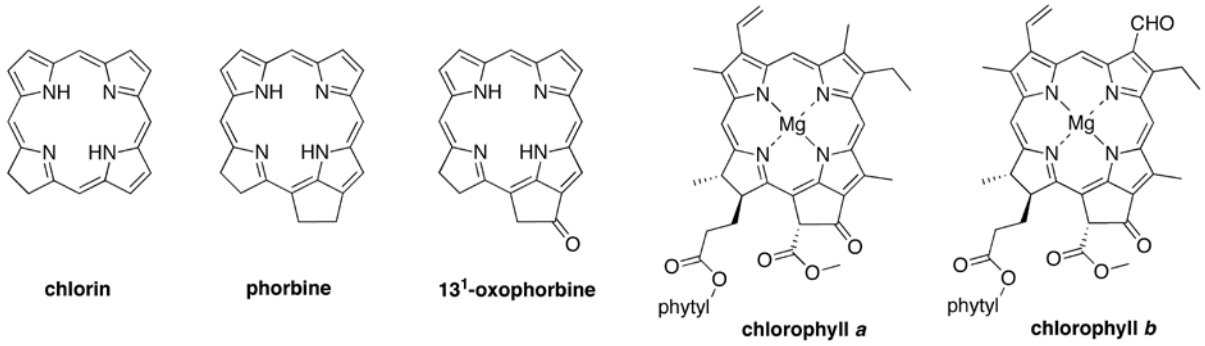

Chart 1. Building the skeleton of chlorophyll *a*.

The question of 'why chlorophyll?' has been asked a number of times from different perspectives. Mauzerall considered the features of chlorophyll with regards to the biosynthetic pathway, the electronic properties that give rise to spectral and photochemical properties, and how such properties are well matched for photosynthetic function.[3] A generation later the same question was addressed from the vantage point of a deeper molecular understanding of the diverse roles of chlorophylls in photosynthetic energy- and electron-transfer processes, including

the apparently unique role of chlorophyll *a* in oxygenic photosynthesis.[4] Björn considered the spectral matching of the chlorophyll absorption spectrum with solar radiation[5] and also the prospects for finding habitable exoplanets on the basis of chlorophyll spectral properties.[6] The spectroscopic properties of chlorophylls have been studied in detail.[7] Still, the role of the specific substituents about the perimeter of the tetrapyrrole macrocycle in engendering the characteristic features of chlorophylls has largely been unaddressed, at least in a systematic manner.

The presence of specific substituents at sites around the perimeter of the chlorophyll macrocycle can have a significant effect on the spectral, electronic, and photochemical properties. For example, the sole distinction between chlorophyll *a* and chlorophyll *b* is the presence of a 7-methyl versus 7-formyl group, yet this structural change results in a significant difference in spectral properties. This difference is exploited in nature, where chlorophylls *a* and *b* serve together to broaden spectral coverage in plant photosynthesis.[8]

The traditional route to probe the effects of substituents in chlorophylls has been to modify intact chlorophylls.[9-22] Such semisynthesis methods have resulted in structural changes such as hydrogenation of the 3-vinyl group, reduction of the 13-keto group, and insertion of other metals. However, achieving more global changes such as removing all alkyl groups (2, 7, 8, 12 positions) has not been feasible via semisynthesis. An alternative entails total synthesis, which has been used to prepare analogues of the naturally occurring chlorophylls. Our own work has been focused on the development of de novo synthetic methods for the preparation of stable synthetic analogues of the naturally occurring chlorophylls.[23-43]

Herein we report the use of recently developed synthetic methods to gain access to a series of benchmark analogues of chlorophylls that lack any substituents other than a stabilizing

geminal dimethyl group in the reduced ring. The compounds include phorbine **FbP**, chlorin **FbC-A**^{13}, and 13^{1}-oxophorbine **FbOP** (Chart 2), as well as their zinc chelates (**ZnP**, **ZnC-A**^{13}, and **ZnOP**). The analogous chlorins **FbC** and **ZnC** have been synthesized previously,[31] as has the 17-oxochlorin **FbOC**.[32] The spectral and photophysical properties of each compound are also presented and are accompanied by density functional theory (DFT) calculations aimed at characterizing the frontier molecular orbitals. Collectively, these studies systematically address the issue of how structural modifications to the base chlorin macrocycle contribute to the electronic and spectral characteristics of chlorophylls.

Chart 2. Benchmark molecules for chlorophylls.

Results and Discussion

I. Synthesis

A. Reconnaissance. A method for installing the isocyclic ring was first reported nearly three-quarters of a century ago, when Fischer subjected (hydroxymethylcarbonyl)porphyrin to dehydrating conditions to give "pheoporphyrin" **I** (Chart 3).[44] Fischer also used Dieckmann condensation to convert chlorin e_6 trimethyl ester to methyl pheophorbide *a* **II**.[45] Other methods for installing the isocyclic ring have been described.[30] To our knowledge, the first mention of formation of a phorbine (lacking the keto group) appears in Fischer's work, where deoxy-pyropheophorbide *a* **III** was reported (but not characterized) as a side product during

esterification of pheophorbide *a*.[46] Some 30 years later, Wolf reported the spectral properties of phorbine **III**.[47] The first report of the synthesis and characterization of a number of phorbines (**IV**) was provided by Brockmann, who reduced bacteriopheophorbide *d* methyl ester with $LiAlH_4$ in the presence of zinc chloride to deoxygenate the 13-keto group.[48] Lash reported the condensation of one dipyrromethane bearing an annulated ring with a second dipyrromethane to form a free base porphyrin containing the five-membered isocyclic ring (**V**, M = H,H).[49-51] Callot's group, drawing on the work of Kenner and Smith and coworkers,[52] reported the acid-catalyzed cyclization of a β-pyrrolic vinyl group to give the analogous nickel porphyrin (**V**, M = Ni).[53] However, in each of the studies by Lash and by Callot, the resulting macrocycle was a porphyrin, not a chlorin; in other words the skeleton was a 17,18-dehydrophorbine.

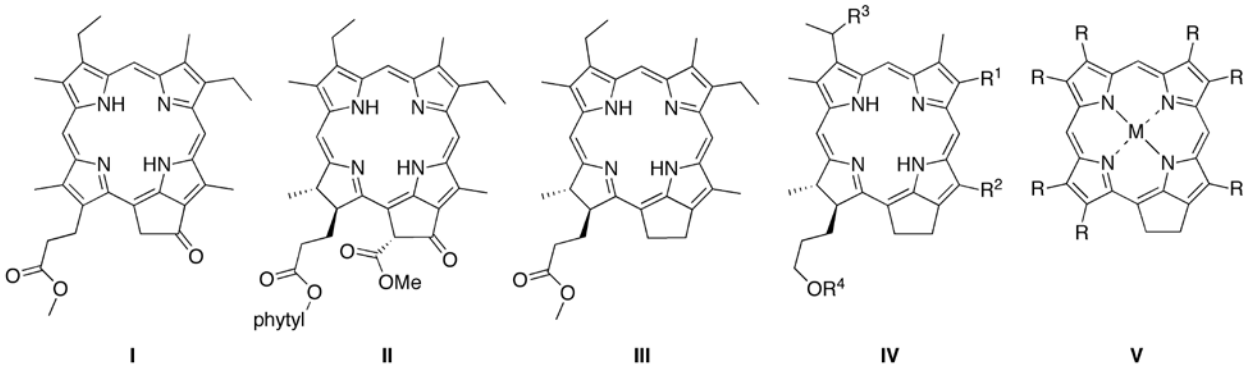

Chart 3. Historical precedents in 13^1-oxophorbine and phorbine chemistry.

Each of the aforementioned syntheses of phorbines, dehydrophorbines, and 13^1-oxophorbines affords a macrocycle that contains a full complement of substituents at the β-pyrrole positions. The de novo synthesis of chlorins that we developed joins an Eastern half (rings B and C) and a Western half (rings A and D), where the latter contains a geminal methyl group in the pyrroline ring to stabilize the resulting chlorin macrocycle toward adventitious dehydrogenation (Scheme 1).[23-43] The de novo route requires far more synthetic effort than semisynthetic methods that begin with chlorophylls,[9-22] yet affords greater versatility in the scope

and range of substituents that can be introduced. The available substituent pattern includes a benchmark chlorin (**FbC**) that differs from chlorin itself only in the presence of the geminal dimethyl group in the reduced ring.[31] Methodology also has been developed to convert a synthetic 13-acetylchlorin to the corresponding 13^1-oxophorbine (via 15-bromination and intramolecular α-arylation).[30] In this manner, seven free base 13^1-oxophorbines have been prepared, each of which bears a mesityl group at the 10-position and one or two other substituents. Four such 13^1-oxophorbines incorporate various substituents at the 7-position.[30,41] Nevertheless, a synthesis of the phorbine and 13^1-oxophorbine lacking any meso or β-pyrrole substituents has heretofore not been accomplished. Access to such macrocycles is fundamentally important because these molecules serve as benchmarks against which to compare the spectral and photophysical properties of the full library of synthetic chlorins, as well as the naturally occurring chlorophylls.

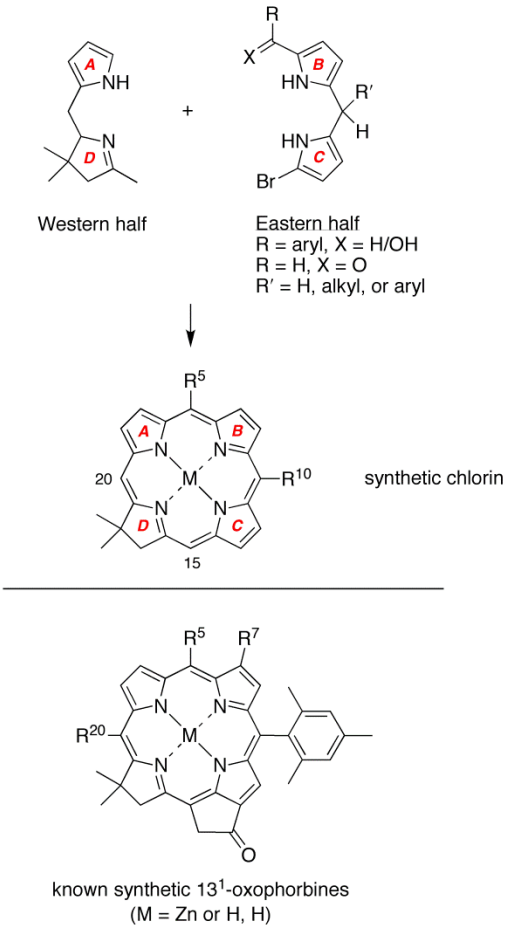

Scheme 1. De novo synthesis of chlorins (top). All prior known synthetic 13[1]-oxophorbines incorporate a 10-mesityl group and one or two other substituents (bottom).

B. Unsubstituted 13[1]-Oxophorbine. The de novo method was employed for the synthesis of the unsubstituted 13[1]-oxophorbine **FbOP**. The condensation of 8,9-dibromo-1-formyldipyrromethane **1**[42] (Eastern half) and **2**[28] (Western half) was carried out in CH_2Cl_2 upon treatment with a solution of $TsOH \cdot H_2O$ in anhydrous MeOH under argon. The resulting crude tetrahydrobilene-*a* was subjected to zinc-mediated oxidative cyclization in CH_3CN for 20 h at reflux exposed to air.[31,38] Filtration through a silica pad and column chromatography afforded chlorin **ZnC-Br[13]** in 16% yield, which upon demetalation with TFA in CH_2Cl_2 gave **FbC-Br[13]** in 87% yield (Scheme 2).

Stille coupling[54] of **FbC-Br**^{13} with tributyl(1-ethoxyvinyl)tin and $[(PPh_3)_2Pd]Cl_2$ in CH_3CN/DMF (3:2)[42] for 2.5 h at 85 °C followed by acidic workup afforded 13-acetylchlorin **FbC-A**^{13} in 81% yield. Regioselective 15-bromination of **FbC-A**^{13} was achieved with 1 molar equivalent of NBS under acidic conditions[41] for 1 h at room temperature to give **FbC-A**^{13}**Br**^{15} in 73% yield. Acidic conditions cause deactivation of ring B of the macrocycle and thus prevent bromination at the 7-position. Intramolecular α-arylation[30,55,56] of the 13-acetyl group in the presence of $(PPh_3)_2PdCl_2$ and Cs_2CO_3 in toluene installed the isocyclic ring (spanning positions 13 and 15) in 55% yield. Metalation of **FbC-A**^{13} and **FbOP** with $Zn(OAc)_2 \cdot 2H_2O$ gave **ZnC-A**^{13} and **ZnOP** in 70 and 79% yield, respectively. The zinc oxophorbine **ZnOP** was successfully purified by precipitation; however, other attempts to purify by column chromatography using 1% TEA resulted in complete decomposition.

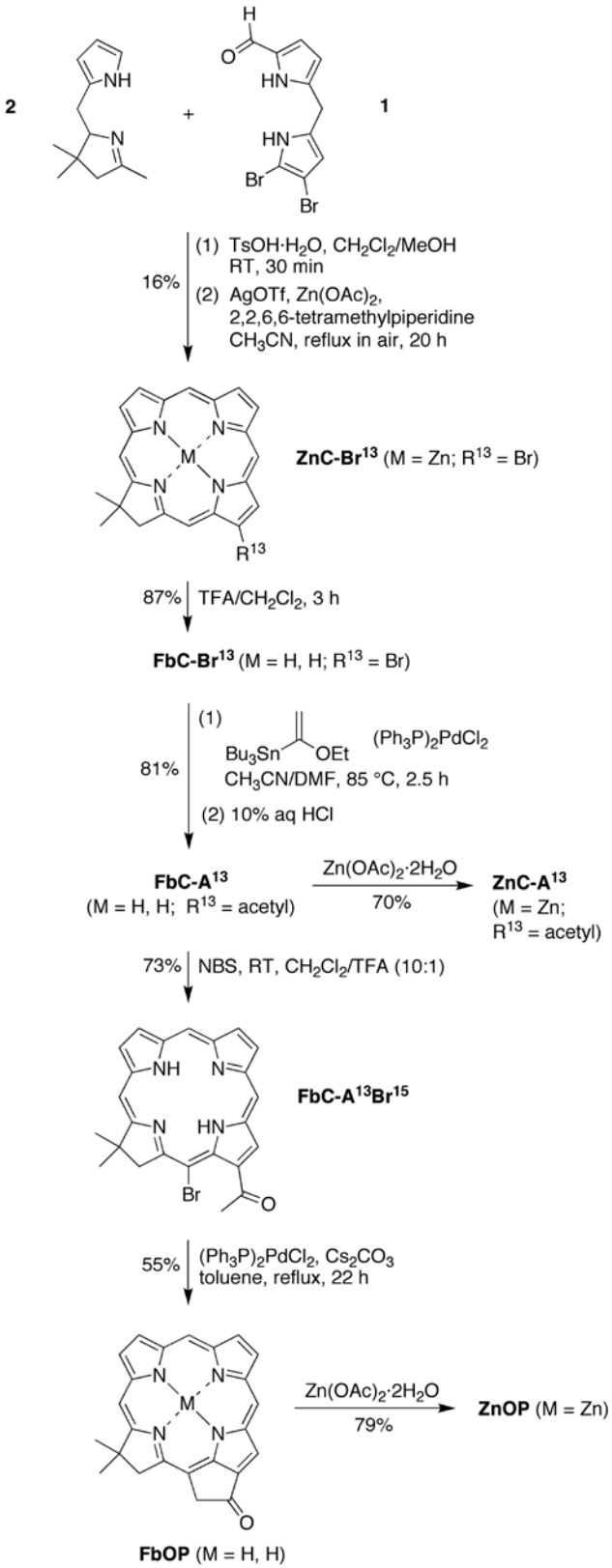

Scheme 2. Synthesis of the 13[1]-oxophorbines **FbOP** and **ZnOP**.

C. Conversion to Phorbine. The 13-keto group of naturally occurring chlorophylls has been reduced (predominantly in acidic media[46,48,57-69]) to the methylene group. However, the absence of peripheral substituents on **FbOP** makes this macrocycle somewhat susceptible to the vigorous conditions generally employed for reduction of the 13-keto group. Hence, we turned to the use of milder conditions via the reduction of an intermediate tosylhydrazone.[70,71] Treatment of oxophorbine **FbOP** with tosylhydrazide in $CHCl_3$/ethanol (1:1) at 65 °C afforded crude tosylhydrazone-**FbP**, which upon reduction with sodium cyanoborohydride in the presence of $TsOH \cdot H_2O$ in MeOH/THF gave tosylhydrazide-**FbP**. The latter was converted to the target phorbine **FbP** in 42% overall yield in EtOH/DMF for 5 h at 80 °C in the presence of sodium acetate trihydrate. Metalation of phorbine **FbP** with $Zn(OAc)_2 \cdot 2H_2O$ gave the zinc chelate phorbine **ZnP** in 90% yield (Scheme 3).

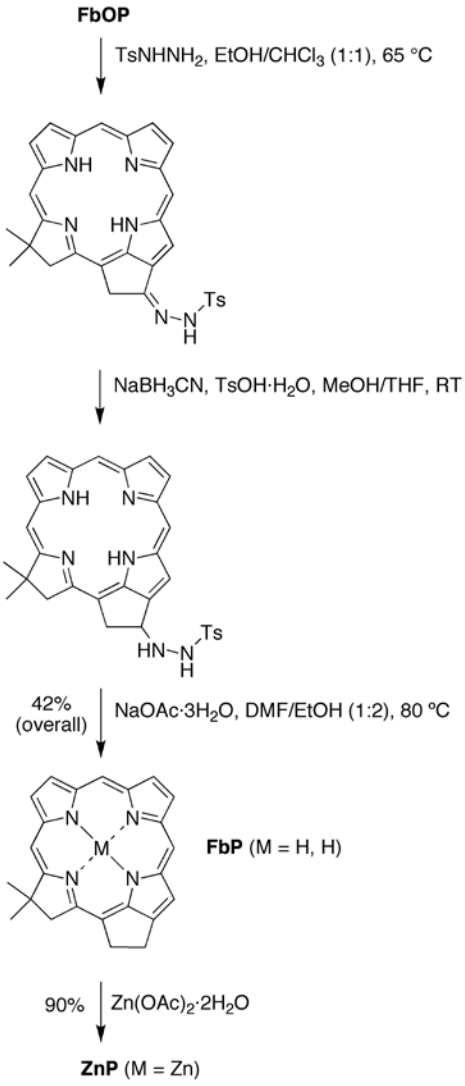

Scheme 3. Synthesis of the free base phorbine **FbP** and the zinc phorbine **ZnP**.

II. Characterization

A. Molecular Identification. All of the phorbines and analogues were characterized by ^{1}H NMR spectroscopy (including gCOSY and NOESY), ^{13}C NMR spectroscopy, laser desorption mass spectrometry [without a matrix or using a matrix of 1,4-bis(5-phenyloxazol-2-yl)benzene],[72] high-resolution electrospray ionization mass spectrometry, and absorption and

fluorescence spectroscopy.[73,74] Key electronic, spectral, and excited-state characteristics of the compounds are described in the following sections.

B. Absorption Spectra. The absorption spectra of the synthetic phorbine and 13^1-oxophorbine compounds are shown in Figure 1 in the free base form (top panel) and zinc chelate form (bottom panel). The spectra for **ZnC**, **FbC**, **ZnOC** and **FbOC** match those reported previously.[32,33] For comparison purposes, the spectral properties of sparsely substituted chlorins lacking any β-pyrrole substituents (**FbC** and **ZnC**) or only the 13-acetyl substituent (**FbC-A^{13}** and **ZnC-A^{13}**) also are provided. For exact comparison with species containing the full complement of substituents characteristic of chlorophylls, also displayed are the free base[75] and zinc[76] analogues of chlorophyll *a* [pheophytin *a* (**Pheo *a***) and zinc pheophytin *a* (**Zn-Pheo *a***); Chart 4].

The absorption spectrum of each compound is comprised of three main spectral regions. The strong red-region feature (600-670 nm) is the $Q_y(0,0)$ band; on average, this band lies ~30 nm to longer wavelength for the free base compound versus the corresponding zinc chelate. The weaker features in the blue-green to yellow spectral region (470-580 nm) are the Q_x bands; these features are somewhat stronger for the free base compounds than the zinc chelates. The intense bands in the near-ultraviolet region are the B_x and B_y features, also known as the Soret bands; these bands are generally superimposed for the zinc chelates but split for the free base compounds. The positions and relative intensities of the B and Q_y bands for the various macrocycles are listed in Table 1.

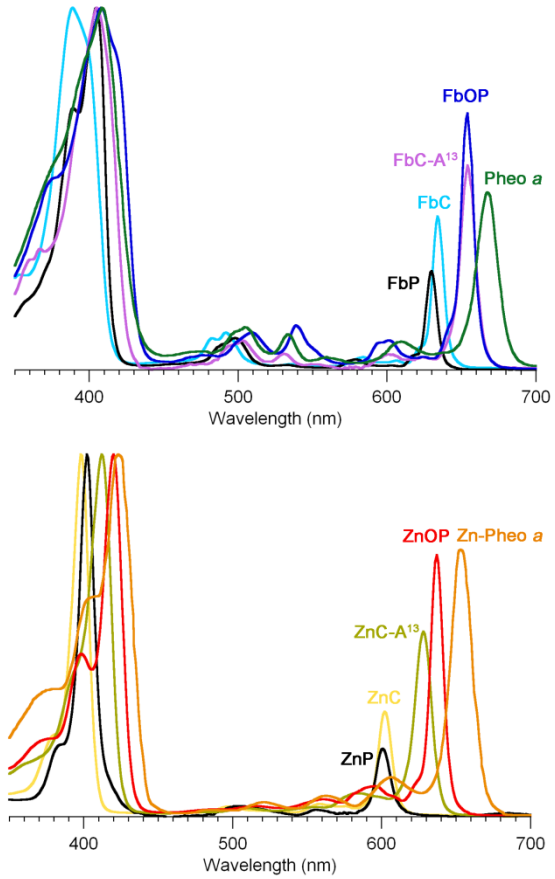

Figure 1. Absorption spectra of synthetic chlorins and phorbines versus pheophytins[75,76] (normalized at the B-band maxima). Top panel: free base macrocycles. Bottom panel: zinc chelates. The solvent is diethyl ether (**Pheo *a*** and **Zn-Pheo *a***) or toluene (all other compounds).

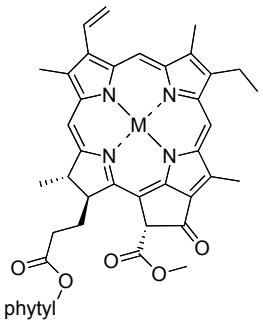

Pheophytin *a* (M = H, H)
Zinc Pheophytin *a* (M = Zn)

Chart 4. Analogues of chlorophyll *a*.

Table 1. Photophysical Properties of Oxophorbines and Analogues.[a]

Compound	λ_B [fwhm] (nm)	Δ_B (cm^{-1})[b]	λ_{Q_y} [fwhm] (nm)	ΔQ_y (cm^{-1})[b]	I_B/I_{Q_y}[c]	Σ_{Q_y}/Σ_B[d]	HOMO – LUMO (eV)[e]	Φ_f[f]	τ_s (ns)[g]
FbC	389 [33]	- -	633 [10]	- -	2.4	0.19	2.69	0.20	8.8
FbP	404 [30]	–950	629 [9]	100	3.6	0.15	2.72	0.28	10.6
FbOP	408 [55]	–1170	654 [11]	–490	1.5	0.24	2.58	0.30	11.5
FbC-A[13]	405 [34]	–970	654 [12]	–500	1.8	0.24	2.59	0.24	7.8
FbOC	400 [27]	–710	634 [9]	–10	4.6	0.09	2.76	0.12	8.4
Pheo *a* [h]	409 [53]	–1200	668 [17]	–810	2.0	0.25	2.47		
ZnC	398 [13]	- -	602 [11]	- -	3.6	0.24	2.67	0.062	1.7
ZnP	402 [2]	–240	601 [12]	11	4.6	0.27	2.69	0.064	1.7
ZnOP	419 [19]	–1230	637 [17]	–910	1.6	0.42	2.55	0.23	5.1
ZnC-A[13]	411 [21]	–760	627 [14]	–680	1.9	0.40	2.56	0.23	4.3
ZnOC	412 [14]	–810	602 [9]	–10	3.4	0.23	2.68	0.030	0.82
Zn-Pheo *a* [i]	423 [38]	–1480	653 [17]	–1300	1.4	0.40	2.43		
MgC	402 [10]	- -	607 [12]	- -	4.3	0.28	2.63[j]	0.26	6.9
Chl *a*	432 [40]	–1730	665 [18]	–1440	1.3	0.63	2.40	0.33	6.3[k]

[a]In toluene at room temperature unless noted otherwise. [b]The redshift of the band relative to the corresponding band of the parent chlorin (**FbC** or **ZnC**). [c]Ratio of the peak intensities of the B and Q_y bands. [d]Ratio of the integrated intensities of the Q_y manifold [$Q_y(0,0)$ and $Q_y(1,0)$ bands] and B manifold [B_x and B_y origins and first vibronic overtones]. [e]Energy gap between the HOMO and LUMO orbitals. [f]Fluorescence quantum yield (error ± 7%). [g]Lifetime of the singlet excited state measured using fluorescence techniques (error ± 8%). [h]Absorption data from ref. 75 (in diethyl ether). [i]Absorption data from ref. 76 (in diethyl ether). [j]Essentially the same value (2.65 eV) is obtained with an H_2O axial ligand. [k]From ref. 34.

The characteristics of the main absorption features (B_x, B_y, Q_x, Q_y) depend on the nature of the macrocycle and peripheral substituents. **Pheo *a*** bears two major auxochromes, the 13-keto group (embedded in the isocyclic ring) and the 3-vinyl group. The 13^1-oxophorbines **FbOP**

and **ZnOP** lack the 3-vinyl group; the phorbines **FbP** and **ZnP** additionally lack the 13-keto group; the chlorin **FbC-A**^{13} further lacks the five-membered ring; the base chlorins **FbC** and **ZnC** lack any substituents (except for the geminal dimethyl group in the reduced pyrrole ring common to all of the synthetic compounds examined here). Of major interest is the manner in which the nature of the macrocycle influences the position and intensity of the $Q_y(0,0)$ band. This is so because this feature corresponds to excitation to the lowest singlet excited state, from which key energy- and electron-transfer events of photosynthesis are initiated. The salient points concerning the $Q_y(0,0)$ band are as follows:

(1) In the free base series, **FbOP** has the most intense $Q_y(0,0)$ band (relative to the Soret maximum). The $Q_y(0,0)$ band of **FbC-A**^{13} exhibits the same (largest) bathochromic shift as **FbOP**, but is about 80% as intense. Both compounds nearly mimic the spectrum of **Pheo *a***. In the zinc-chelate series, **ZnOP** has the relatively most intense $Q_y(0,0)$ band and the largest bathochromic shift, with **ZnC-A**^{13} second in the series in both categories.

(2) The spectral properties of phorbines (**FbP** and **ZnP**) closely resemble those of chlorins (**FbC** or **ZnC**). Both sets of compounds exhibit a $Q_y(0,0)$ band that lacks the intensity and bathochromic shift of the keto-substituted analogues.

(3) The main absorption characteristics of unsubstituted chlorin **MgC**[33] closely resemble those of **ZnC** (Table 1). This similarity parallels that for the native magnesium-containing chlorophyll *a* (**Chl a**) and the zinc-bearing analogue **Zn-Pheo *a*** (Table 1).

In summary, the chlorin chromophore alone affords a poor mimic of the spectral properties of chlorophylls. However, the addition of a 13-keto group to the chlorin is essential (and suffices) to closely mimic the absorption spectrum of the naturally occurring chlorin

pigment; it is anticipated that the added effect of a 3-vinyl group would give a near complete match to the spectrum of chlorophyll *a*.

C. Fluorescence spectra and quantum yields and excited-state lifetimes. For each compound studied, the fluorescence spectrum (not shown) contains a prominent $Q_y(0,0)$ band and a much weaker $Q_y(0,1)$ band, which together are in approximate mirror symmetry to the $Q_y(0,0)$ and $Q_y(1,0)$ absorption features. The $Q_y(0,0)$ emission band has approximately the same spectral width as, and lies no more than 2 nm to longer wavelength of, the corresponding $Q_y(0,0)$ absorption feature. This very small (<60 cm^{-1}) absorption-fluorescence spacing (Stokes shift) indicates little change in the structure or solvent interactions of these macrocycles upon photoexcitation. The fluorescence quantum yields of **FbC**, **FbP**, **FbOP**, and **FbC-A**[13] are in the range 0.20-0.30, while the value for **FbOC** is somewhat smaller (0.12). For **ZnC**, **ZnP**, and **ZnOC**, the fluorescence yields are each about one-quarter of those for the corresponding free base form, while the values for **ZnOP** (0.23) and **ZnC-A**[13] (0.23) are closer to those for **FbOP** and **FbC-A**[13] (Table 1). The lifetime of the lowest singlet excited state (determined via fluorescence detection) is in the range 7.8 to 11.5 ns for all free base compounds. The values are considerably shorter for **ZnC** (1.7 ns), **ZnP** (1.7 ns) and **ZnOC** (0.82 ns), with the oxochlorin being the shortest. We have previously found such short excited-state lifetimes for peripherally substituted zinc oxochlorins,[26] and the current work shows that this effect is inherent to the parent macrocycle and does not stem from substituent effects. The excited-state lifetimes for **ZnOP** (5.1 ns) and **ZnC-A**[13] (4.3 ns) are much longer than for the other zinc chelates and are about half of those for the free base forms, **FbOP** (11.5 ns) and **FbC-A**[13] (7.8 ns).

The fluorescence yield of the magnesium chlorin **MgC** is larger than those for the free base form **FbC** and zinc chelate **ZnC** (0.26, 0.20, 0.062) while the singlet excited-state lifetime

is intermediate (6.9 ns, 8.8 ns, 1.7 ns). This trend follows those for the fluorescence yields (0.14, 0.09, 0.030) and excited-state lifetimes (13 ns, 8.9 ns, 2.1 ns) of magnesium, free base, and zinc tetraphenylporphyrins.[77-79]

The collective photophysical data show that the addition of a 13-keto group to the chlorin results in a more intense and bathochromically shifted $Q_y(0,0)$ absorption feature, accompanied by fluorescence yields and singlet excited-state lifetimes for the zinc chelates that are not nearly as diminished compared to the free base analogues as for the other macrocycles. The decreased excited-state energy and increased optical-transition strength affords better utilization of the red region of the solar spectrum. The 13-keto group also increases the excited-state lifetime, which is desirable for allowing a higher yield of the light-driven energy- or charge-transfer reactions of photosynthesis. The lengthening of the excited-state lifetime is unexpected in that the lower excited-state energy would normally (based on the energy-gap law[80]) lead to a shortening of the lifetime due to enhancement of the nonradiative (internal conversion) decay pathway. Thus, the incorporation of a 13-keto group in a chlorin or phorbine macrocycle results in a very favorable motif from a photophysical point of view.

D. Structural Studies. X-ray crystal structure analysis of the benchmark macrocycles porphine, **FbC**, **FbC-Br^{13}**, **FbP**, **FbOP** and **FbOC** allowed analysis of structural changes of the core macrocycle lacking any β- and *meso*-pyrrolic substituents along the series porphyrin, chlorin, phorbine, 13^1-oxophorbine and 17-oxochlorin.[33,81] Such studies were accompanied by resonance Raman spectroscopy and DFT calculations.[81] Moving from chlorin to phorbine (upon installation of the five-membered isocyclic ring) and, finally, from phorbine to oxophorbine (upon introduction of the 13-oxo group) causes numerous alterations in the core macrocycle size, shape and framework. The macrocycle changes from kite-shaped (**FbC**) to more trapezoid-like

(**FbP** and **FbOP**), and the size decreases along the series **FbC** > **FbP** ~ **FbOP**. Suprisingly, alterations (e.g., shortening of the C13-C13^1 bond length) caused by introduction of the keto group are very small indicating that the unsymmetrical nature of the isocyclic ring (ring E) is probably due to annulation with the macrocycle rather than conjugation with the 13-keto group.

E. Frontier Molecular Orbitals and Electronic Properties. The energies and electron-density distributions of the frontier molecular orbitals (MOs) of all the newly synthesized phorbins and chlorins were obtained from DFT calculations. Such methods were also applied to several fictive chlorins, incuding the 13,15-dimethylchlorin **FbC-Me^{13,15}** and the 13-acetyl-15-methylchlorin **FbC-A^{13}Me^{15}**, as well as the corresponding zinc chelates **ZnC-Me^{13,15}** and **ZnC-A^{13}Me^{15}** (Chart 5). Examination of such fictive chlorins provides deeper insight into the origin of the effects caused by the isocyclic ring and the 13-keto group. The key results of the DFT calculations for both the synthetic and fictive free base compounds are summarized in Figure 2, and the analogous results for the zinc chelates in Figure 3. These figures show the characteristics of the highest occupied molecular orbital (HOMO), the lowest unoccupied molecular orbital (LUMO), the HOMO-1, and LUMO+1. Below, we first discuss the relationship between the MO energies and the structure of the macrocycle, with connections to the anticipated redox properties of the molecules. We then discuss the relationship between the MO energies and position and intensity of the lowest-energy absorption feature of the molecules.

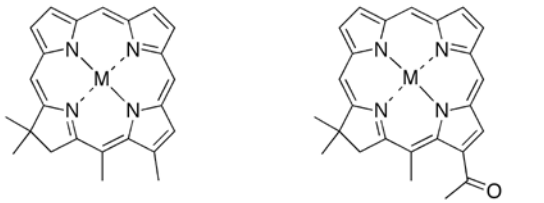

FbC-Me^{13,15} (M = H, H)
ZnC-Me^{13,15} (M = Zn)

FbC-A^{13}Me^{15} (M = H, H)
ZnC-A^{13}Me^{15} (M = Zn)

Chart 5. Fictive chlorins for which DFT calculations were performed.

	FbC	FbC-Me^{13,15}	FbP	FbOP	FbC-A^{13}	FbC-A^{13}Me^{15}	FbOC	Pheo *a*
LUMO+1	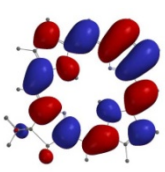	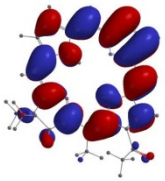	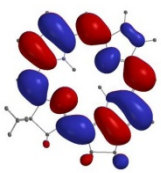	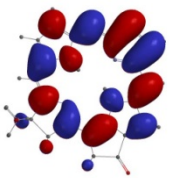	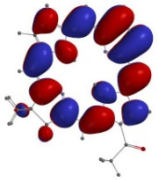	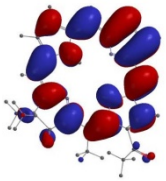	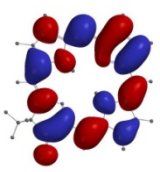	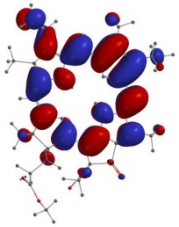
	–1.67	–1.60	–1.62	–1.93	–1.87	–1.83	–2.17	–1.99
LUMO	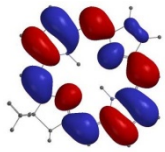	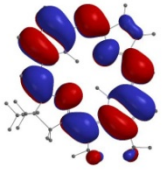	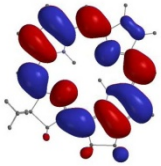	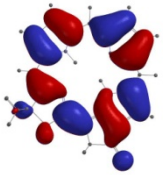	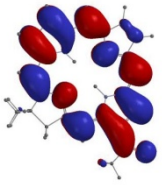	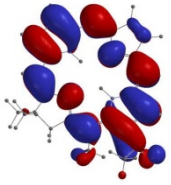	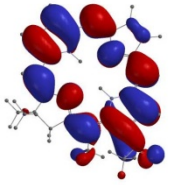	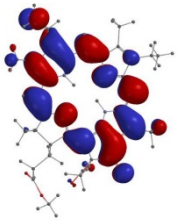
	–2.20	–2.12	–2.06	–2.62	–2.55	–2.44	–2.51	–2.69
HOMO	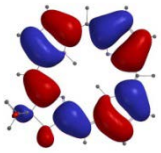	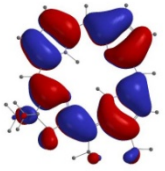	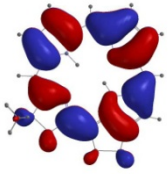	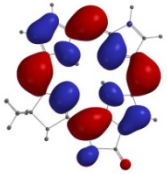	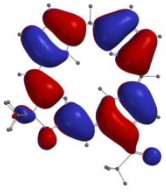	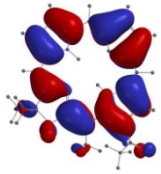	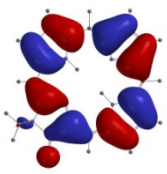	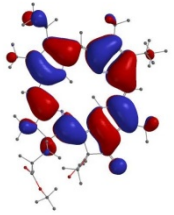
	–4.89	–4.80	–4.78	–5.20	–5.14	–5.06	–5.27	–5.16
HOMO-1	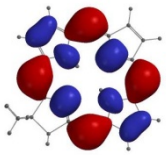	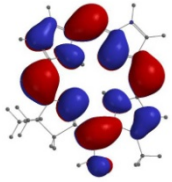	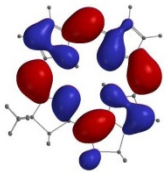	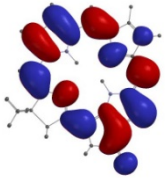	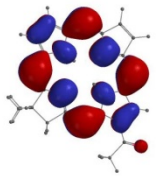	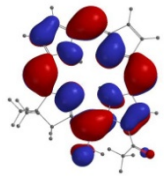	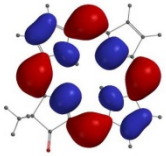	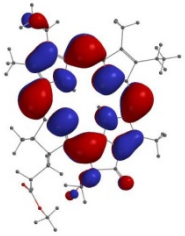
	–5.07	–4.94	–4.93	–5.26	–5.29	–5.17	–5.34	–5.34

Figure 2. Electron-density distributions and energies (eV) of the frontier MOs of the free base compounds.

	ZnC	ZnC-Me^{13,15}	ZnP	ZnOP	ZnC-A^{13}	ZnC-A^{13}Me^{15}	ZnOC	Zn-Pheo *a*
LUMO+1	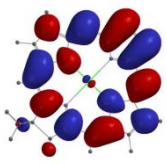	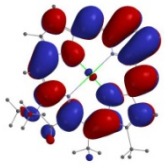	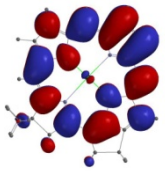	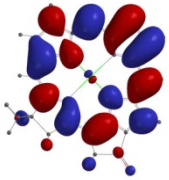	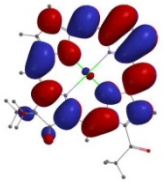	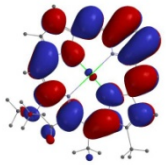	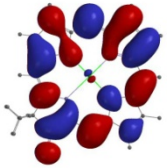	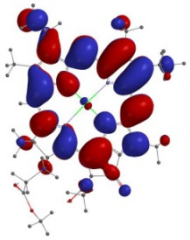
	–1.55	–1.48	–1.52	–1.83	–1.75	–1.71	–2.06	–1.89
LUMO	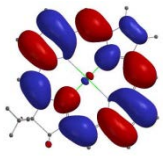	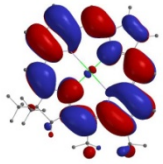	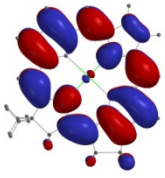	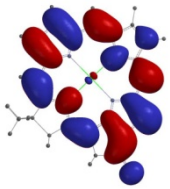	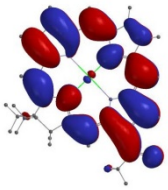	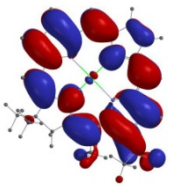	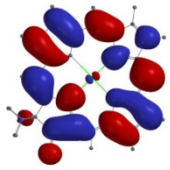	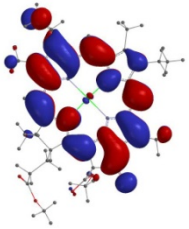
	–2.12	–2.07	–2.02	–2.57	–2.48	–2.39	–2.49	–2.64
HOMO	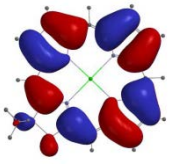	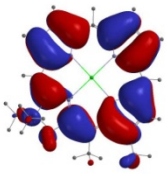	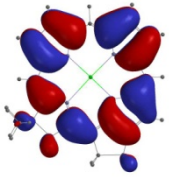	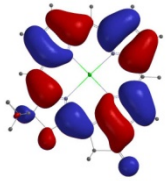	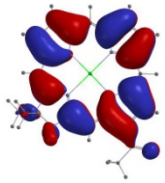	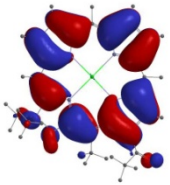	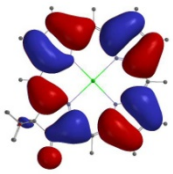	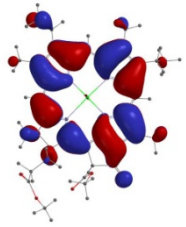
	–4.79	–4.71	–4.71	–5.12	–5.04	–4.98	–5.17	–5.07
HOMO-1	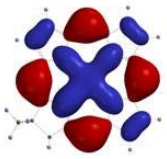	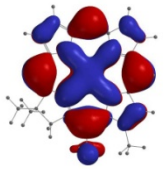	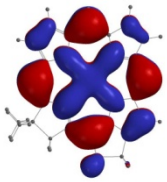	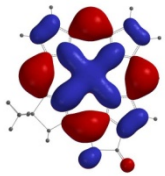	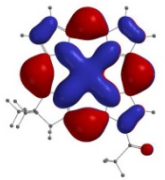	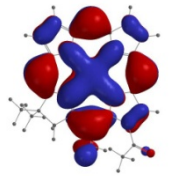	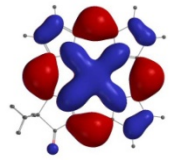	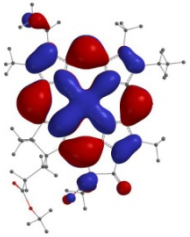
	–5.16	–5.03	–5.01	–5.35	–5.38	–5.27	–5.44	–5.43

Figure 3. Electron-density distributions and energies (eV) of frontier MOs of the zinc chelates.

Macrocycle structure and MO energies. The key findings from the MO calculations are as follows:

(1) The conversion of the chlorin to a phorbine results in a small (0.08-0.14 eV) shift in the HOMO and LUMO energies to less negative values. Such shifts correspond to the phorbine being slightly easier to oxidize and slightly harder to reduce than the chlorin. This connection follows from our prior studies on about two dozen synthetic zinc chlorins that showed linear correlations between the calculated MO energies and measured redox potentials.[34,35] Moreover, the calculations reported herein on the fictive chlorins **FbC-Me^{13,15}** and **ZnC-Me^{13,15}** suggest that about half (free base) or almost the entire (zinc chelate) MO-energy shifts can be accounted for simply by the presence of the 13- and 15-substituents and that closure to the five-membered ring (and associated ring strain) has only a small effect.

(2) Incorporation of a 13-keto group in a chlorin to produce **FbC-A^{13}** or **ZnC-A^{13}** gives a 0.25 eV shift in the HOMO energy and a 0.35-0.36 eV shift in the LUMO energy to more negative values. The analogous incorporation of an oxo group in a phorbine to produce the 13^1-oxophorbine (e.g., **FbP** to **FbOP**) gives an even larger 0.41-0.42 eV shift in the HOMO energy and a larger still 0.55-0.56 eV shift in the LUMO energy to more negative values. The direction of the shifts is such that the presence of the 13-keto group will make the molecule harder to oxidize and easier to reduce. The calculations on the fictive chlorin **ZnC-A^{13}M^{15}**, together with those described above for **ZnC-M^{13,15}**, suggest that closure to the five-membered ring (and associated ring strain) has a somewhat greater effect on the frontier-MO energies when the 13-keto group is present (e.g., **FbP** to **FbOP**) than in its absence (e.g., **FbC** to **FbC-A^{13}**).

(3) The effect of the 13-keto group on the LUMO energy is larger than the effect on the HOMO energy by an average of 0.11 eV for the four cases (13-keto addition to chlorin or 13^1-

oxo addition to phorbine and for free base and zinc forms). This effect can be understood by the generally larger electron density on the 13-keto group for the LUMO compared to the HOMO (Figures 2 and 3). The unequal effect of the 13-keto group on the LUMO and HOMO alters the HOMO - LUMO energy gap and thus affects the energy/wavelength of the $Q_y(0,0)$ absorption band, as described further below.

(4) The 13-keto substituted chlorins **FbC-A**[13] and **ZnC-A**[13] have HOMO energies that are only slightly (0.02-0.03 eV) less negative and LUMO energies that are modestly (0.14-0.16 eV) less negative than those of the corresponding natural pigments **Pheo *a*** and **Zn-Pheo *a***. Thus, the simple presence of a 13-keto group, without closure to the five-membered ring to give the oxophorbine, is sufficient to give a macrocycle which is slightly easier to oxidize and only modestly harder to reduce than the related photosynthetic pigment (i.e., **Pheo *a***). Carrying the comparison one step further, the unsubstituted oxophorbines **FbOP** and **ZnOP** have HOMO energies that are actually slightly (0.04-0.05 eV) more negative and LUMO energies that are slightly (0.07 eV) less negative than those of **Pheo *a*** and **Zn-Pheo *a***. Thus, the oxophorbine macrocycle encodes the primary electronic properties that dictate the redox potentials of the native photosynthetic pigments, with only small net adjustments due to the substituents at the six β-pyrrole positions.

Absorption spectra and MO energies. Figure 4 (top) plots the energies of the HOMO, LUMO, HOMO-1, and LUMO+1 versus $Q_y(0,0)$ absorption energy/wavelength (Table 1) for the various macrocycles, along with linear fits to the data and values indicating the slopes of the trend lines. For both the free base macrocycles (open symbols and dashed lines) and zinc chelates (closed symbols and solid lines), the LUMO exhibits a much greater dependence on macrocycle characteristics than the HOMO or other orbitals (HOMO-1 and LUMO+1). In

particular, the slope of the trend lines encompassing the addition of a 13-keto group to a chlorin (e.g. **FbC** to **FbC-A^{13}**) or a 13^1-oxo group to a phorbine (e.g. **FbP** to **FbOP**) is twice as large for the LUMO than for the other three frontier MOs.

Close inspection of the orbital energies listed in Figures 2 and 3 shows that the trends depicted in Figure 4 (top) reflect a correlation between a decrease in the $Q_y(0,0)$ absorption-band energy (an increase in wavelength) and a decrease in the LUMO – HOMO energy gap upon the presence of a 13-keto group (in either a chlorin or phorbine). This tracking of the $Q_y(0,0)$ energy/wavelength with the LUMO – HOMO energy gap is shown explicitly in Figure 4 (bottom) for the free base macrocycles (open downward triangles and dashed line) and zinc chelates (closed downward triangles and solid line). The bottom panel of Figure 4 also shows that, in contrast, the energy gap between the LUMO+1 and HOMO-1 increases slightly as the $Q_y(0,0)$ energy decreases (wavelength increases), and with a trend-line slope that is about one-third that of the LUMO – HOMO energy gap.

The collective results depicted in Figure 4 show that (1) the bathochromic shift in the position of the $Q_y(0,0)$ absorption band is driven by a reduction in the LUMO – HOMO energy gap. (2) The reduction in the LUMO – HOMO energy gap is in turn driven by a stronger effect of the 13-keto substituent on the LUMO energy than the HOMO energy. (3) These effects can be understood by the greater electron density on the 13-keto group for the LUMO compared to the other frontier MOs.

The results above can be taken one step further by application of Gouterman's four-orbital model.[82-84] Within this model, the energy/wavelength of the $Q_y(0,0)$ absorption band depends on the quantity ΔE_{avg} defined in Eq (1), namely the average of the LUMO – HOMO

and LUMO+1 – HOMO-1 energy gaps, whereas the intensity of the band depends on the quantity ΔE_{dif} defined in Eq (2), namely the difference in these two orbital energy gaps:

$$\Delta E_{avg} = [(LUMO+1 - HOMO-1) + (LUMO - HOMO)]/2 \quad (1)$$

$$\Delta E_{dif} = [(LUMO+1 - HOMO-1) - (LUMO - HOMO)] \quad (2)$$

Figure 5 (top) shows a good overall correlation between ΔE_{avg} and the $Q_y(0,0)$ absorption energy/wavelength for both the free base macrocycles and zinc chelates. Figure 5 (bottom) shows a good correlation between ΔE_{dif} and the integrated intensity of the $Q_y(0,0)$ absorption band (Table 1), especially for the free base compounds (open symbols and dashed line). We have previously utilized the four-orbital model to understand how the macrocycle-substituent pattern controls the MO energies and the spectral characteristics of a large set of synthetic free base and zinc chlorins.[34,35]

In the present study of unsubstituted parent macrocycles (chlorin, phorbine, oxophorbine), the use of the four-orbital framework (involving simple sums and differences of MO energy gaps) provides additional fundamental insights into the intimate relationship between the hydrocarbon skeleton, electronic structure, and characteristics of the long-wavelength absorption band of the natural photosynthetic pigments. Moreover, this framework and understanding has predictive value in aiding the design of synthetic analogues of the parent macrocycles and of the fully substituted photosynthetic pigments to allow better coverage of the solar spectrum for use in artificial systems for solar-energy conversion. The ability to mimic the spectral properties of chlorophylls with far simpler and synthetically accessible macrocycles augurs well for the use of such hydroporphyrins in a variety of artificial photosynthetic architectures.

Finally, we note that the studies here have employed zinc chelates rather than magnesium as is present in the chlorophylls. Compared with zinc, magnesium affords a bathochromic shift of the Q_y band of about 10 nm, a 3-4-fold longer singlet excited-state lifetime, more facile ground-state oxidation, a more potent excited-state reductant, and tighter binding of oxygenic apical ligands. On the other hand, magnesium is more susceptible to demetalation. Any application would need to balance the advantageous photophysical properties of magnesium chlorins versus the greater chemical stability of the zinc chelates.

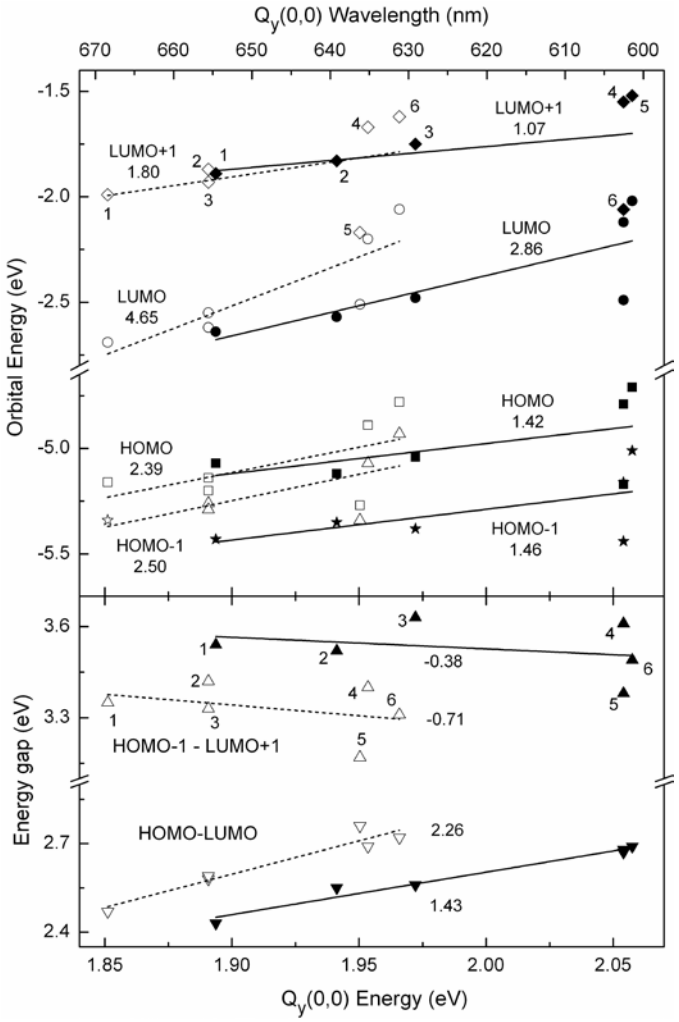

Figure 4. Calculated frontier MO energies (top panel) and energy gaps (bottom panel) versus the measured $Q_y(0,0)$ absorption-band energy (bottom axis) and wavelength (top axis) for free base macrocycles (open symbols) and zinc chelates (closed symbols). Top: energies LUMO+1 (diamonds), LUMO (circles), HOMO (squares), HOMO-1 (stars). Bottom: energy gaps HOMO-1 – LUMO+1 (up triangles), and HOMO – LUMO (down triangles). The indicated values are the slopes of the trend lines for free base macrocycles (dashed lines) and zinc chelates (solid lines). The points for the different macrocycles are labeled as follows: **Pheo *a*** (1), **FbC-A**[13] (2), **FbOP** (3), **FbC** (4), **FbOC** (5), and **FbP** (6), and similarly for the zinc chelates.

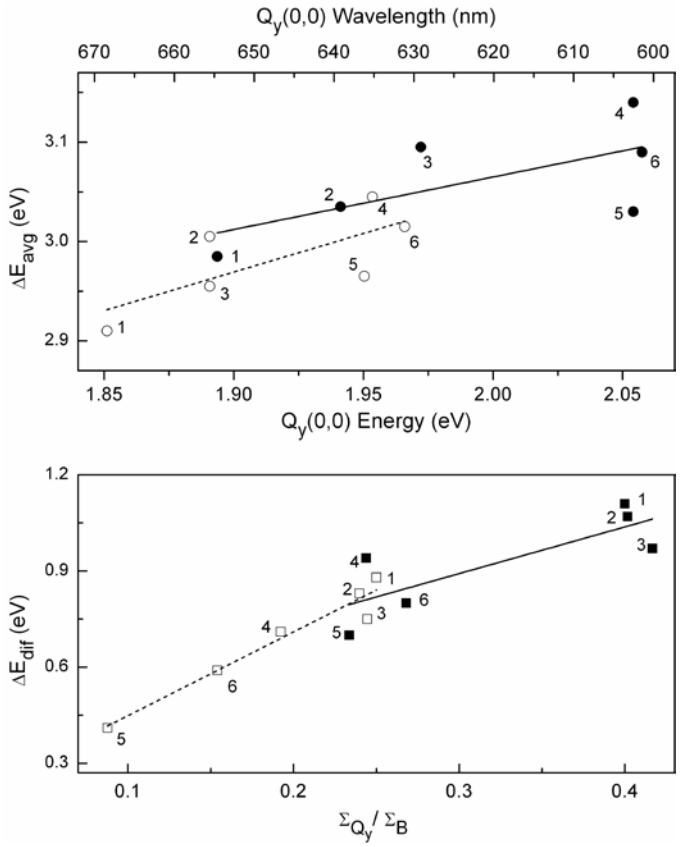

Figure 5. (Top) Calculated average of the HOMO-1 – LUMO+1 and HOMO – LUMO energy gaps versus the measured $Q_y(0,0)$ absorption-band energy (bottom axis) and wavelength (top axis) for free base macrocycles (open symbols and dashed trend line) and zinc chelates (closed symbols and solid trend line). (Bottom) Calculated difference in the HOMO-1 – LUMO+1 and HOMO – LUMO energy gaps versus the ratio of the integrated intensities of the Q_y and B absorption manifolds for the free base macrocycles (open symbols and dashed trend line) and zinc chelates (closed symbols and solid trend line). The points for the different macrocycles are labeled as follows: **Pheo *a*** (1), **FbC-A**[13] (2), **FbOP** (3), **FbC** (4), **FbOC** (5), and **FbP** (6), and similarly for the zinc chelates.

Experimental Section

General Synthetic Methods. All ^{1}H NMR (300 MHz and 400 MHz) and ^{13}C NMR (100 MHz) spectra were obtained in $CDCl_3$ unless noted otherwise. Mass spectra of chlorins were obtained via laser desorption ionization mass spectrometry without a matrix or using a matrix of 1,4-bis(5-phenyloxazol-2-yl)benzene. Electrospray ionization mass spectrometry (ESI-MS) data are reported for the molecule ion or protonated molecule ion. Column chromatography was performed with flash silica. NBS was recrystallized (water). All other commercially available materials were used as received. Absorption and fluorescence spectra were obtained in toluene at room temperature unless noted otherwise. All of the Pd-mediated coupling reactions were carried out under argon using standard Schlenk-line procedures (e.g., three freeze-pump-thaw cycles were performed prior to and after the addition of the palladium reagent, for a total of six such cycles).

Photophysical Measurements. Static absorption (Varian Cary 100) and fluorescence (Spex Fluorolog Tau 2 or PTI Quantamaster 40) measurements were performed as described previously.[73,74] Argon-purged solutions of the samples in toluene with an absorbance of ≤0.10 at the excitation wavelength were used for the fluorescence spectral, quantum yield, and lifetime measurements. Fluorescence lifetimes were obtained using a phase modulation technique and Soret-band excitation[74] (Spex Fluorolog Tau 2) or via decay measurements using excitation pulses at 337 nm from a nitrogen laser and time-correlate-single-photon-counting detection (Photon Technology International LaserStrobe TM-3). Emission measurements employed 2-4 nm excitation- and detection-monochromator bandwidths and 0.2 nm data intervals. Emission spectra were corrected for detection-system spectral response. Fluorescence quantum yields

were determined relative to chlorophyll *a* in benzene ($\Phi_f = 0.325$)[85] or chlorophyll *a* in toluene, which was found here to have the same value as in benzene.

Density Functional Theory Calculations. DFT calculations were performed with Spartan '08 for Windows (Wavefunction, Inc.) on a PC (Dell Optiplex GX270) equipped with a 3.2 GHz CPU and 3 GB of RAM.[86] The hybrid B3LYP functional and the 6-31G* basis set were employed. The equilibrium geometries were fully optimized using the default parameters of the Spartan '08 program. A methyl group was substituted for the phytyl chain in the calculations on **Pheo *a*** and **Zn-Pheo *a***.

Acknowledgment. This work was supported by grants from the Division of Chemical Sciences, Geosciences and Biosciences Division, Office of Basic Energy Sciences of the U.S. Department of Energy to D.F.B. (DE-FG02-05ER15660), D.H. (DE-FG02-05ER15661) and J.S.L. (DE-FG02-96ER14632). Mass spectra were obtained at the Mass Spectrometry Laboratory for Biotechnology at North Carolina State University. Partial funding for the facility was obtained from the North Carolina Biotechnology Center and the National Science Foundation.

References

(1) H. Scheer, in *Chlorophylls and Bacteriochlorophylls. Biochemistry, Biophysics, Functions and Applications*, ed. B. Grimm, R. J. Porra, W. Rüdiger and H. Scheer, Springer, Dordrecht, 2006, vol. 25, pp 1–26.
(2) G. P. Moss, *Pure Appl. Chem*., 1987, **59**, 779–832.
(3) D. Mauzerall, *Ann. N. Y. Acad. Sci.,* 1973, **206**, 483–494.
(4) L. O. Björn, G. C. Papageorgiou, R. E. Blankenship and Govindjee, *Photosyn. Res*., 2009, **99**, 85–98.
(5) L. O. Björn, *Photosynthetica,* 1976, **10**, 121–129.
(6) L. O. Björn, G. C. Papageorgiou, D. Dravins and Govindjee, *Curr. Sci.*, 2009, **96**, 1171–1175.
(7) M. Kobayashi, M. Akiyama, H. Kano and H. Kise, in *Chlorophylls and Bacteriochlorophylls. Biochemistry, Biophysics, Functions and Applications*, ed. B. Grimm, R. J. Porra, W. Rüdiger and H. Scheer, Springer, Dordrecht, 2006, vol. 25, pp 79–94.
(8) W. L. Butler, in *The Chlorophylls*, ed. L. P. Vernon and G. R. Seely, Academic Press, New York, 1966, pp 343–379.
(9) W. Flitsch, *Adv. Heterocyclic Chem*., 1988, **43**, 73–126.
(10) P. H. Hynninen, in *Chlorophylls*, ed. H. Scheer, CRC Press, Boca Raton, FL, 1991, pp. 145–209.
(11) K. M. Smith, in *Chlorophylls*, ed. H. Scheer, CRC Press, Boca Raton, FL, 1991, pp. 115–143.
(12) F.-P. Montforts, B. Gerlach and F. Höper, *Chem. Rev*., 1994, **94**, 327–347.
(13) F.-P. Montforts and M. Glasenapp-Breiling, *Prog. Heterocycl. Chem*., 1998, **10**, 1–24.
(14) L. Jaquinod, in *The Porphyrin Handbook*, ed. K. M. Kadish, K. M. Smith and R. Guilard, Academic Press, San Diego, CA, 2000, vol. 1, pp. 201–237.
(15) M. G. H. Vicente, in *The Porphyrin Handbook*, ed. K. M. Kadish, K. M. Smith and R. Guilard, Academic Press, San Diego, 2000, vol. 1, pp. 149–199.
(16) R. K. Pandey and G. Zheng, in *The Porphyrin Handbook*, ed. K. M. Kadish, K. M. Smith and R. Guilard, Academic Press, San Diego, 2000, vol. 6, pp. 157–230.
(17) F.-P. Montforts and M. Glasenapp-Breiling, *Fortschr. Chem. Org. Naturst*., 2002, **84**, 1–51.
(18) V. Y. Pavlov and G. V. Ponomarev, *Chem. Heterocycl. Cmpds*., 2004, **40**, 393–425.
(19) M. O. Senge, A. Wiehe and C. Ryppa, in *Chlorophylls and Bacteriochlorophylls. Biochemistry, Biophysics, Functions and Applications*, ed. B. Grimm, R. J. Porra, W. Rüdiger and H. Scheer, *Advances in Photosynthesis and Respiration*, Springer, Dordrecht, The Netherlands, 2006, vol. 25, pp 27–37.
(20) S. Fox and R. W. Boyle, *Tetrahedron,* 2006, **62**, 10039–10054.
(21) M. Galezowski and D. T. Gryko, *Curr. Org. Chem*., 2007, **11**, 1310–1338.
(22) A. M. G. Silva and J. A. S. Cavaleiro, in *Progress in Heterocyclic Chemistry*, ed. G. W. Gribble and J. A. Joule, Elsevier, Amsterdam, 2008, vol. 19, pp 44–69.
(23) J.-P. Strachan, D. F. O'Shea, T. Balasubramanian and J. S. Lindsey, *J. Org. Chem.*, 2000, **65**, 3160–3172.
(24) T. Balasubramanian, J.-P. Strachan, P. D. Boyle and J. S. Lindsey, *J. Org. Chem.*, 2000, **65**, 7919–7929.

(25) M. Taniguchi, D. Ra, G. Mo, T. Balasubramanian and J. S. Lindsey, *J. Org. Chem.*, 2001, **66**, 7342–7354.
(26) M. Taniguchi, H.-J. Kim, D. Ra, J. K. Schwartz, C. Kirmaier, E. Hindin, J. R. Diers, S. Prathapan, D. F. Bocian, D. Holten and J. S. Lindsey, *J. Org. Chem.*, 2002, **67**, 7329–7342.
(27) M. Taniguchi, M. N. Kim, D. Ra and J. S. Lindsey, *J. Org. Chem.*, 2005, **70**, 275–285.
(28) M. Ptaszek, J. Bhaumik, H.-J. Kim, M. Taniguchi and J. S. Lindsey, *Org. Process Res. Dev.*, 2005, **9**, 651–659.
(29) (a) J. K. Laha, C. Muthiah, M. Taniguchi, B. E. McDowell, M. Ptaszek and J. S. Lindsey, *J. Org. Chem.*, 2006, **71**, 4092–4102. (b) Ibid. *J. Org. Chem.,* 2009, **74**, 5122.
(30) J. K. Laha, C. Muthiah, M. Taniguchi and J. S. Lindsey, *J. Org. Chem.*, 2006, **71**, 7049–7052.
(31) M. Ptaszek, B. E. McDowell, M. Taniguchi, H.-J. Kim and J. S. Lindsey, *Tetrahedron*, 2007, **63**, 3826–3839.
(32) M. Taniguchi, M. Ptaszek, B. E. McDowell and J. S. Lindsey, *Tetrahedron*, 2007, **63**, 3840–3849.
(33) M. Taniguchi, M. Ptaszek, B. E. McDowell, P. D. Boyle and J. S. Lindsey, *Tetrahedron*, 2007, **63**, 3850–3863.
(34) H. L. Kee, C. Kirmaier, Q. Tang, J. R. Diers, C. Muthiah, M. Taniguchi, J. K. Laha, M. Ptaszek, J. S. Lindsey, D. F. Bocian and D. Holten, *Photochem. Photobiol*., 2007, **83**, 1110–1124.
(35) H. L. Kee, C. Kirmaier, Q. Tang, J. R. Diers, C. Muthiah, M. Taniguchi, J. K. Laha, M. Ptaszek, J. S. Lindsey, D. F. Bocian and D. Holten, *Photochem. Photobiol*., 2007, **83**, 1125–1143.
(36) C. Muthiah, J. Bhaumik and J. S. Lindsey, *J. Org. Chem*., 2007, **72**, 5839–5842.
(37) K. E. Borbas, V. Chandrashaker, C. Muthiah, H. L. Kee, D. Holten and J. S. Lindsey, *J. Org. Chem*., 2008, **73**, 3145–3158.
(38) C. Muthiah, M. Ptaszek, T. M. Nguyen, K. M. Flack and J. S. Lindsey, *J. Org. Chem*., 2007, **72**, 7736–7749.
(39) C. Muthiah, H. L. Kee, J. R. Diers, D. Fan, M. Ptaszek, D. F. Bocian, D. Holten and J. S. Lindsey, *Photochem. Photobiol.*, 2008, **84**, 786–801.
(40) C. Ruzié, M. Krayer and J. S. Lindsey, *Org. Lett*., 2009, **11**, 1761–1764.
(41) C. Muthiah, D. Lahaye, M. Taniguchi, M. Ptaszek and J. S. Lindsey, *J. Org. Chem*., 2009, **74**, 3237–3247.
(42) O. Mass, M. Ptaszek, M. Taniguchi, J. R. Diers, H. L. Kee, D. F. Bocian, D. Holten and J. S. Lindsey, *J. Org. Chem*., 2009, **74**, 5276–5289.
(43) M. Ptaszek, D. Lahaye, M. Krayer, C. Muthiah and J. S. Lindsey, *J. Org. Chem*., 2010, **75**, 1659–1673.
(44) H. Fischer and O. Laubereau, *Justus Liebigs Ann. Chem.*, 1938, **535**, 17–37.
(45) H. Fischer and A. Oestreicher, *Justus Liebigs Ann. Chem*., 1940, **546**, 49–57.
(46) H. Fischer and H. Siebel, *Justus Liebigs Ann. Chem*., 1932, **499**, 84–108.
(47) H. Wolf, *Liebigs Ann. Chem.*, 1966, **695**, 98–111.
(48) H. Brockmann Jr. and R. Tacke-Karimdadian, *Liebigs Ann. Chem.*, 1979, 419–430.
(49) T. D. Lash, R. P. Balasubramaniam, J. J. Catarello, M. C. Johnson, D. A. May Jr., K. A. Bladel, J. M. Feeley, M. C. Hoehner, T. G. Marron, T. H. Nguyen, T. J. Perun Jr., D. M. Quizon, C. M. Shiner and A. Watson, *Energy&Fuels*, 1990, **4**, 668–674.

(50) B. Zhang and T. D. Lash, *Tetrahedron Lett.*, 2003, **44**, 7253–7256.
(51) T. D. Lash, W. Li and D. M. Quizon-Colquitt, *Tetrahedron*, 2007, **63**, 12324–12342.
(52) G. W. Kenner, J. Rimmer, K. M. Smith and J. F. Unsworth, *J. Chem. Soc. Perkin Trans. 1*, 1978, 845–852.
(53) C. Bauder, R. Ocampo and H. J. Callot, *Tetrahedron*, 1992, **48**, 5135–5150.
(54) M. Kosugi, T. Sumiya, Y. Obara, M. Suzuki, H. Sano and T. Migita, *Bull. Chem. Soc. Jpn*., 1987, **60**, 767–768.
(55) H. Muratake and M. Natsume, *Tetrahedron Lett*., 1997, **38**, 7581–7582.
(56) H. Muratake, M. Natsume and H. Nakai, *Tetrahedron*, 2004, **60**, 11783–11803.
(57) H. Brockmann Jr. and J. Bode, *Liebigs Ann. Chem.*, 1974, 1017–1027.
(58) K. M. Smith and D. A. Goff, *J. Am. Chem. Soc.*, 1985, **107**, 4954–4964.
(59) K. Maruyama, H. Yamada and A. Osuka, *Chem. Lett.*, 1989, 833–836.
(60) N. W. Smith and K. M. Smith, *Energy&Fuels*, 1990, **4**, 675–688.
(61) K. Maruyama, H. Yamada and A. Osuka, *Photochem. Photobiol.*, 1991, **53**, 617–626.
(62) R. J. Abraham, A. E. Rowan, N. W. Smith and K. M. Smith, *J. Chem. Soc. Perkin Trans. 2*, 1993*,* 1047–1059.
(63) H. Tamiaki, M. Amakawa, Y. Shimono, R. Tanikaga, A. R. Holzwarth and K. Schaffner, *Photochem. Photobiol.*, 1996, **63**, 92–99.
(64) R. K. Pandey, S. Constantine, T. Tsuchida, G. Zheng, C. J. Medforth, M. Aoudia, A. N. Kozyrev, M. A. J. Rodgers, H. Kato, K. M. Smith and T. J. Dougherty, *J. Med. Chem.*, 1997, **40**, 2770–2779.
(65) H. Tamiaki, T. Miyatake and R. Tanikaga, *Tetrahedron Lett.*, 1997, **38**, 267–270.
(66) S. Mettath, M. Shibata, J. L. Alderfer, M. O. Senge, K. M. Smith, R. Rein, T. J. Dougherty and R. K. Pandey, *J. Org. Chem.*, 1998, **63**, 1646–1656.
(67) H. Tamiaki, S. Yagai and T. Miyatake, *Bioorg. Med. Chem.*, 1998, **6**, 2171–2178.
(68) M. Katterle, A. R. Holzwarth and A. Jesorka, *Eur. J. Org. Chem.*, 2006, 414–422.
(69) T. Miyatake, S. Tanigawa, S. Kato and H. Tamiaki, *Tetrahedron Lett.*, 2007, **48**, 2251–2254.
(70) R. O. Hutchins, C. A. Milewski and B. E. Maryanoff, *J. Am. Chem. Soc.*, 1973, **95**, 3662–3668.
(71) V. Nair and A. K. Sinhababu, *J. Org. Chem*., 1978, **43**, 5013–5017.
(72) N. Srinivasan, C. A. Haney, J. S. Lindsey, W. Zhang and B. T. Chait, *J. Porphyrins Phthalocyanines*, 1999, **3**, 283–291.
(73) F. Li, S. Gentemann, W. A. Kalsbeck, J. Seth, J. S. Lindsey, D. Holten and D. F. Bocian, *J. Mater. Chem.*, 1997, **7**, 1245–1262.
(74) H. L. Kee, C. Kirmaier, L. Yu, P. Thamyongkit, W. J. Youngblood, M. E. Calder, L. Ramos, B. C. Noll, D. F. Bocian, W. R. Scheidt, R. R. Birge, J. S. Lindsey and D. Holten, *J. Phys. Chem. B*, 2005, **109**, 20433–20443.
(75) E. Zass, H. P. Isenring, R. Etter and A. Eschenmoser, *Helv. Chim. Acta*, 1980, **63**, 1048–1067.
(76) I. D. Jones, R. C. White, E. Gibbs and C. D. Denard, *J. Agric. Food Chem*., 1968, **16**, 80–83.
(77) S. I. Yang, J. Seth, J.-P. Strachan, S. Gentemann, D. Kim, D. Holten, J. S. Lindsey and D. F. Bocian, *J. Porphyrins and Phthalocyanines*, 1999, **3**, 117–147.
(78) A. T. Gradyushko, A. N. Sevchenko, K. N. Solovyov and M. P. Tsvirko, *Photochem. Photobiol.*, 1970, **11**, 387–400.

(79) P. G. Seybold and M. Gouterman, *J. Mol. Spectrosc.*, 1969, **31**, 1–13.
(80) J. B. Birks, in *Photophysics of Aromatic Molecules*, Wiley-Interscience, London, 1970, pp 140–192.
(81) M. Taniguchi, O. Mass, P. D. Boyle, Q. Tang, J. R. Diers, D. F. Bocian, D. Holten and J. S. Lindsey, *J. Mol. Structure*, 2010, **979**, 27–45.
(82) M. Gouterman, in *The Porphyrins,* vol. 3, ed. D. Dolphin, Academic Press, New York, 1978, pp 1–165.
(83) M. Gouterman, *J. Chem. Phys.*, 1959, **30**, 1139–1161.
(84) M. Gouterman, *J. Mol. Spectroscopy*, 1961, **6**, 138–163.
(85) G. Weber and F. W. J. Teale, *Trans. Faraday Soc.*, 1957, **53**, 646–655.
(86) Except for molecular mechanics and semi-empirical models, the calculation methods used in Spartan have been documented in Y. Shao, L. F. Molnar, Y. Jung, J. Kussmann, C. Ochsenfeld, S. T. Brown, A. T. B. Gilbert, L. V. Slipchenko, S. V. Levchenko, D. P. O'Neill, R. A. DiStasio Jr., R. C. Lochan, T. Wang, G. J. O. Beran, N. A. Besley, J. M. Herbert, C. Y. Lin, T. Van Voorhis, S. H. Chien, A. Sodt, R. P. Steele, V. A. Rassolov, P. E. Maslen, P. P. Korambath, R. D. Adamson, B. Austin, J. Baker, E. F. C. Byrd, H. Dachsel, R. J. Doerksen, A. Dreuw, B. D. Dunietz, A. D. Dutoi, T. R. Furlani, S. R. Gwaltney, A. Heyden, S. Hirata, C.-P. Hsu, G. Kedziora, R. Z. Khalliulin, P. Klunzinger, A. M. Lee, M. S. Lee, W.-Z. Liang, I. Lotan, N. Nair, B. Peters, E. I. Proynov, P. A. Pieniazek, Y. M. Rhee, J. Ritchie, E. Rosta, C. D. Sherrill, A. C. Simmonett, J. E. Subotnik, H. L. Woodcock III, W. Zhang, A. T. Bell, A. K. Chakraborty, D. M. Chipman, F. J. Keil, A. Warshel, W. J. Hehre, H. F. Schaefer III, J. Kong, A. I. Krylov, P. M. W. Gill and M. Head-Gordon, *Phys. Chem. Chem. Phys.*, 2006, **8**, 3172–3191.

Chapter 4.

De novo Synthesis and Properties of Analogues of the Self-Assembling Chlorosomal Bacteriochlorophylls

Reprinted with permission from the *New Journal of Chemistry*. Mass, O., D. R. Pandithavidana, M. Ptaszek, K. Santiago, J. W. Springer, J. Jiao, Q. Tang, C. Kirmaier, D. F. Bocian, D. Holten and J. S. Lindsey (2011). *New J. Chem.* **35**, 2671–2690.

Abstract

Natural photosynthetic pigments bacteriochlorophylls *c*, *d* and *e* in green bacteria undergo self-assembly to create an organized antenna system known as the chlorosome, which collects photons and funnels the resulting excitation energy toward the reaction centers. Mimicry of chlorosome function is a central problem in supramolecular chemistry and artificial photosynthesis, and may have relevance for the design of photosynthesis-inspired solar cells. The main challenge in preparing artificial chlorosomes remains the synthesis of the appropriate pigment (chlorin) equipped with a set of functional groups suitable to direct the assembly and assure efficient energy transfer. Prior approaches have entailed derivatization of porphyrins or semisynthesis beginning with chlorophylls. This paper reports a third approach, the *de novo* synthesis of macrocycles that contain the same hydrocarbon skeleton as chlorosomal bacteriochlorophylls. The synthesis here of Zn(II) 3-(1-hydroxyethyl)-10-aryl-13^1-oxophorbines (the aryl group consists of phenyl, mesityl, or pentafluorophenyl) entails selective bromination of a 3,13-diacetyl-10-arylchlorin, palladium-catalyzed 13^1-oxophorbine formation, and selective reduction of the 3-acetyl group using $BH_3 \cdot {}^t BuNH_2$. Each macrocycle contains a geminal dimethyl group in the pyrroline ring to provide stability toward adventitious dehydrogenation. A Zn(II) 7-(1-hydroxyethyl)-10-phenyl-17-oxochlorin also has been prepared. Altogether, 30 new hydroporphyrins were synthesized. The UV-Vis absorption spectra of the new chlorosomal bacteriochlorophyll mimics reveal a bathochromic shift of ~1800 cm^{-1} of the Q_y band in nonpolar solvent, indicating extensive assembly in solution. The Zn(II) 3-(1-hydroxyethyl)-10-aryl-13^1-oxophorbines differ in the propensity to form assemblies based on the 10-substituent in the following order: mesityl < phenyl < pentafluorophenyl. Infrared spectra show that

assemblies also can be formed in solid media and likely involve hydrogen-bonding (or other) interactions of the ring E keto group.

Introduction

The light-harvesting antennas in photosynthetic organisms contain highly organized, three dimensional systems of pigments that absorb light and funnel the resulting excitation energy to the reaction centers.[1] In plants and purple bacteria, photosynthetic pigments (chlorophylls and bacteriochlorophylls) are bound to protein scaffolds to define the proper relative distances and orientations for efficient energy transfer. On the other hand, in green photosynthetic bacteria, the tetrapyrrole macrocycles are organized in self-assembled structures (chlorosomes) with little or no aid from a proteinaceous scaffolding.[2,3] This highly organized system encompassing as many as 250,000 pigment molecules collects light and supports rapid excitation energy migration. Chlorosomes are perhaps Nature's most spectacular light-harvesting antennas and enable photosynthesis under conditions of low ambient light intensity.

It is important to note that the tetrapyrrole macrocycles in the chlorosomes are termed bacteriochlorophylls but in fact are chlorins (i.e., dihydroporphyrins) rather than true bacteriochlorins (i.e., tetrahydroporphyrins). The chlorosomal bacteriochlorophylls (bacteriochlorophylls *c*, *d*, and *e*) are structurally heterogeneous (i.e., not pure compounds) yet differ only slightly from the plant photosynthetic pigments chlorophylls *a* and *b* (Chart 1). Key structural differences include the presence of a mixture of stereoisomeric 3-(1-hydroxyethyl) groups rather than the 3-vinyl unit; the absence of the 13^2-methoxycarbonyl substituent in the isocyclic ring; diverse substituents at the R^8, R^{12}, and propionate ester positions; and the presence of a methyl group at position 20 (bacteriochlorophyll *c* and *e*).[4]

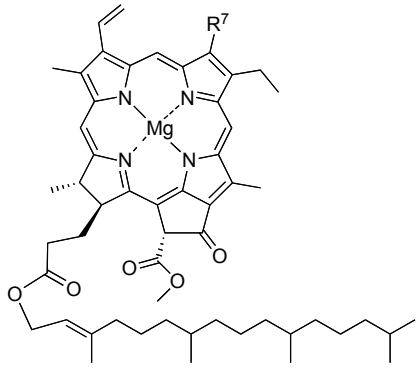

Plant chlorophylls
chlorophyll *a* ($R^7 = CH_3$)
chlorophyll *b* ($R^7 = CHO$)

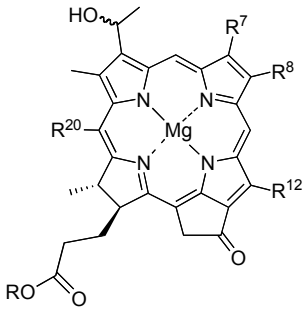

Chlorosomal bacteriochlorophylls

R = mixture of hydrocarbon chains
R^8 = Et, Pr, *iso*-Bu, neopentyl
R^{12} = Me, Et

bacteriochlorophyll *c* ($R^7 = R^{20} = CH_3$)
bacteriochlorophyll *d* ($R^7 = CH_3$, $R^{20} = H$)
bacteriochlorophyll *e* ($R^7 = CHO$, $R^{20} = CH_3$)

13^1-Oxophorbine

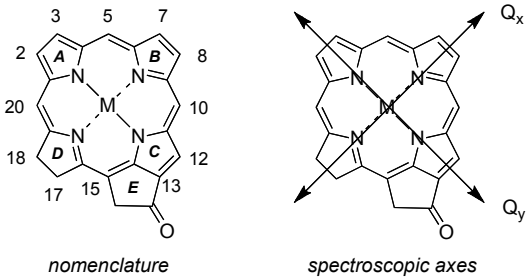

nomenclature *spectroscopic axes*

Chart 1. Chief pigments of plants (top) and green bacteria (middle). Nomenclature of 13^1-oxophorbine showing the reduced ring (D), isocyclic ring (E), and spectroscopic axes (bottom).

The structure of chlorosomes has been investigated by diverse methods including cryoelectron microscopy,[5-7] X-ray scattering,[5,7,8] absorption linear dichroism spectroscopy,[9]

resonance Raman spectroscopy,[10] and solid-state NMR spectroscopy.[8,11,12] The pattern of self-assembly of chlorosomal bacteriochlorophyll molecules – which may differ across diverse organisms – remains a subject of intense debate. One of the longstanding models proposed for the self-assembled architecture is illustrated in Figure 1.[13] In the proposed model, the hydroxy oxygen of one macrocycle coordinates to the apical Mg(II) site of a second macrocycle, and the hydroxy proton forms a hydrogen bond with the carbonyl oxygen from a third macrocycle. The resulting two-dimensional lattice results in π–π interactions between the chlorin macrocycles, which additionally stabilize the self-assembled system. The organization shown in Figure 1, which implies long-range order of crystal-like periodicity, likely represents an idealized limiting form given the heterogeneity of the bacteriochlorophylls themselves. Several alternative models have recently been proposed that retain key features of apical coordination (and typically hydrogen bonding) yet pack the macrocycles in other patterns.[12,14,15] Structural issues that remain poorly understood include the fundamental assembly pattern of the tetrapyrrole macrocycles; the role and effect of length of diverse long-chain alcohols incorporated to form the ester at the 17-propionate position;[7] the effects of stereoisomeric mixtures derived from the presence of *R/S* epimers of the 3-(1-hydroxyethyl substituent);[16] and the size, internal regularity, and relative orientations of self-assembled domains of bacteriochlorophylls within the chlorosome.[7]

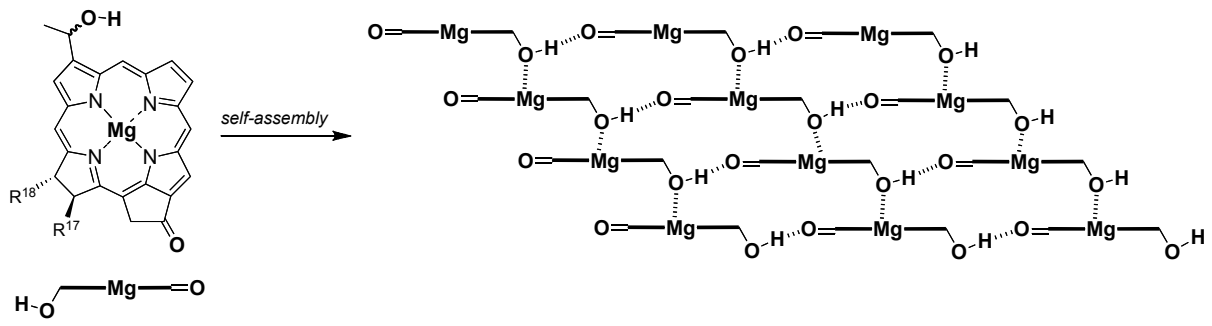

Figure 1. One model for the assembly pattern of chlorosomal bacteriochlorophylls, showing coordination of the hydroxy group to the apical site on magnesium, hydrogen bonding, and π–π stacking.

The complexity and size of the chlorosomes has prompted a large body of work on synthetic macrocycles to determine the essential features for self-assembly.[13,17-19] The groups of Tamiaki[13,18,20-25] and Würthner[26-29] extensively investigated semisynthetic chlorophyll and bacteriochlorophyll derivatives to probe the influence of the nature and position of substituents on the self-assembly pattern. Balaban[13,14,16,17,19,30-34] explored synthetic porphyrins bearing oxygenic (hydroxyalkyl and keto groups, **I**, Chart 2) at the meso or β-positions, as well as cyano substituents (**II**). Balaban also prepared chlorins by derivatization of porphyrins (**VIII**).[17] Tamiaki also developed methodology for converting octaethylporphyrin to porphyrin-based chlorosomal bacteriochlorophyll mimics (**III**-**VI**).[35] Almost all studies to date of wholly synthetic macrocycles have employed zinc(II) porphyrins, though a recent study of magnesium(II) porphyrins (analogues of **I**) was reported.[36] We synthesized porphyrin derivatives with two oxygenic substituents at the meso or β-positions (**VII**).[37] However, X-ray structural studies of **VII** (5-hydroxymethyl and 5,15-diphenyl; 3-hydroxymethyl- and 5,15-di-*p*-tolyl) revealed intermolecular interactions and packing patterns quite different from those

suggested in Figure 1. Balaban has reported similar results.[14,16] At a minimum, such results point to the subtlety of structural features that engender assembly.

To build informative structural and functional mimics of the chlorosomes requires access to model compounds that possess essential molecular features of the natural bacteriochlorophylls *c*, *d* and *e*. The minimum structural features appear to include an α-hydroxyalkyl group and carbonyl group at the perimeter of a metallochlorin. In the chlorosome neighboring tetrapyrrole macrocycles are believed to be oriented such that their respective Q_y transition dipole moments are close to collinear, thereby affording strong exciton coupling. Because porphyrins are planar oscillators whereas chlorins are linear oscillators,[38,39] it does not appear feasible to mimic the photophysical features of the chlorosome with porphyrins alone, though valuable insights concerning the structural requirements for assembly undoubtedly can be gleaned by examination of diverse tetrapyrrole macrocycles.

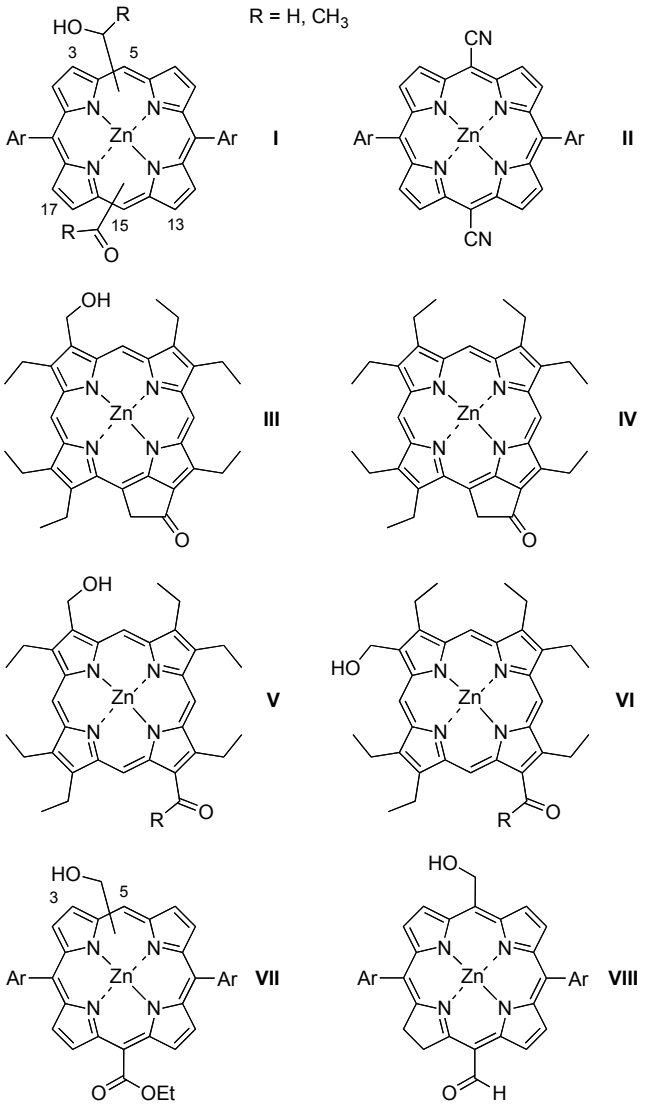

Chart 2. Synthetic porphyrin and chlorin mimics of chlorosomal bacteriochlorophylls.

Over the years we have been working to develop *de novo* synthetic methods for preparing chlorins. A key feature of the *de novo* methods is the ability to introduce substituents at will at the various β-pyrrolic and meso positions, and to install the 5-membered isocyclic ring (ring E, spanning positions 13 and 15).[40-45] Chlorins that contain the isocyclic ring are termed phorbines,[46] which is the hydrocarbon skeleton for all naturally occurring chlorophylls (including the chlorosomal bacteriochlorophylls).[4] Herein we report extension of this methodology to the

synthesis of mimics of chlorosomal bacteriochlorophylls. The resulting mimics are equipped with the structural features that are believed to be essential for self-assembly: (i) central metal with apical ligation site, (ii) coplanar keto group, and (iii) α-hydroxyethyl group, with the latter two substituents disposed on opposite sites of the macrocycle. For appropriate electronic coupling to give rise to efficient energy transfer, as in the natural systems, the α-hydroxyethyl and 13-keto groups are positioned along the Q_y axis. Three such 13^1-oxophorbines have been prepared, which differ only in the nature of a substituent (phenyl, mesityl, or pentafluorophenyl) at the 10-position. For comparison purposes, a chlorin was prepared that contains a coplanar keto group and an α-hydroxyethyl group located along the Q_x axis, which is perpendicular to the Q_y axis. This *de novo* approach to the synthesis of chlorin/13^1-oxophorbine macrocycles complements the existing strategies for the semisynthesis of naturally derived tetrapyrroles and the chemical synthesis of porphyrins.

Results and Discussion

A. Synthesis of 13^1-Oxophorbines.

(i) Retrosynthetic Analysis. Our approach to chlorosomal bacteriochlorophyll analogues relies on a *de novo* route to 3,13-dibromochlorins.[40] The route entails the directed formation of the chlorin macrocycle by reaction of an Eastern half and a Western half. Extension therefrom to the key precursor 3-acetyl-13^1-oxophorbine **FbOP-A^{3}R^{10}** includes (a) palladium-mediated acetylation of a 3,13-dibromochlorin (**FbC-Br^{3,13}R^{10}**),[40] (b) selective 15-bromination (under acidic conditions) of the resulting 3,13-diacetylchlorin,[44] and (c) installation of the isocyclic ring by palladium-mediated, intramolecular α-arylation.[41] The resulting 13^1-oxophorbine possesses two keto groups, one embedded in the isocyclic ring and the second as

the 3-acetyl substituent. Selective reduction of the carbonyl group at the 3-position of the chlorin will afford the target 3-(1-hydroxyethyl)-13^1-oxophorbine **FbOP-He^{3}R^{10}** (here we use "He" to denote the 1-hydroxyethyl unit).

(ii) Chlorins FbC-Br^{3,13}R^{10}. The requisite Western half (8-bromo-2,3,4,5-tetrahydro-1,3,3-trimethyldipyrrin, **1**) for the syntheses of the target 13^1-oxophorbines has been prepared in multigram quantities.[47] The Eastern halves for the phenyl (**2a**)[48] and mesityl (**2b**)[40] substituted target compounds also have been reported. The synthesis of the pentafluorophenyl substituted Eastern half (**2c**) is shown in Scheme 1. Treatment of 1-formyl-5-(pentafluorophenyl)dipyrromethane[49] with two equivalents of NBS at –78 °C afforded the corresponding 8,9-dibromo derivative **2c**.

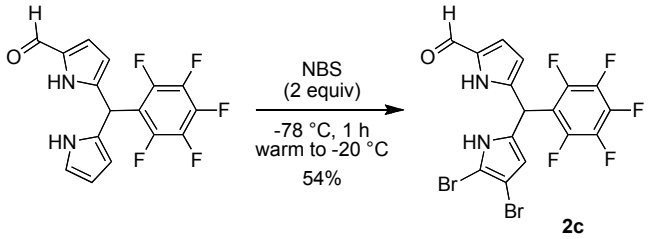

Scheme 1. Preparation of the Eastern half for the pentafluorophenyl-substituted 13^1-oxophorbine.

The dibromochlorin **FbC-Br^{3,13}M^{10}** was recently prepared via a streamlined procedure[45] from 0.5 mmol quantities of 8-bromo-2,3,4,5-tetrahydro-1,3,3-trimethyldipyrrin (**1**, Western half)[47] and 8,9-dibromo-1-formyl-5-mesityldipyrromethane (**2b**, Eastern half).[40] Here, the same procedure at the 1.7 mmol scale afforded **FbC-Br^{3,13}M^{10}** in 24% yield (versus 25% previously) (Scheme 2). Dibromochlorin **FbC-Br^{3,13}P^{10}** or **FbC-Br^{3,13}Pf^{10}** bearing a 10-phenyl or 10-(pentafluorophenyl) substituent was synthesized in the same manner in 29% or 9% yield,

respectively. It is noteworthy that the three dibromochlorins were prepared in 0.13–0.53-g quantities, facilitating subsequent elaboration.

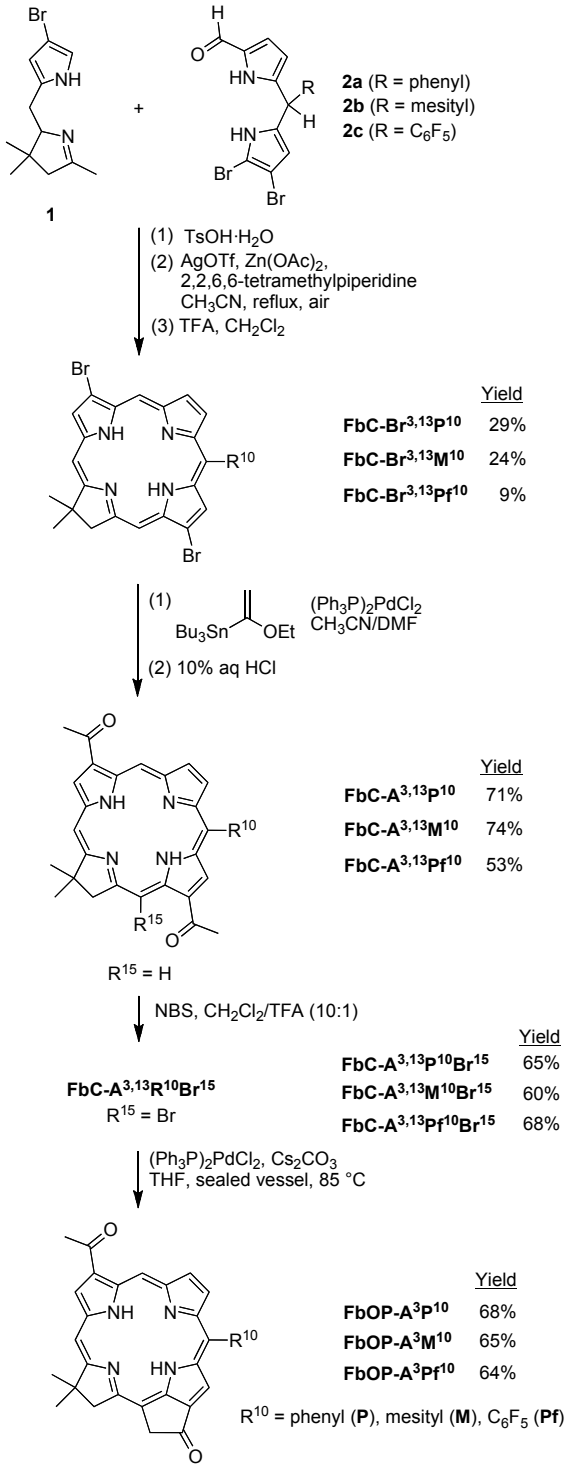

Scheme 2. Synthesis of 3-acetyl-13^1-oxophorbine compounds.

(iii) 3,13-Diacetylchlorins. The Pd-coupling of dibromochlorin **FbC-Br^{3,13}R^{10}** employed five mol equivalents of tributyl(1-ethoxyvinyl)tin[41] in the presence of 20 mol% of $(Ph_3P)_2PdCl_2$ in CH_3CN/DMF (3:2) at 83 °C for 3.5 – 4 h. Hydrolysis with 10% aqueous HCl and purification of the crude product gave 3,13-diacetylchlorin **FbC-A^{3,13}R^{10}** (53-74% yield). Note that the free base 3,13-diacetylchlorin **FbC-A^{3,13}M^{10}** was previously prepared from the zinc chelate **ZnC-A^{3,13}M^{10}** via demetalation,[42] and the latter was obtained from the zinc chelate of the dibromochlorin **ZnC-Br^{3,13}M^{10}** via a multistep procedure that includes demetalation, Pd-coupling, acidic work up, and remetalation.[40]

(iv) Synthesis of 3-Acetyl-13^1-oxophorbines. Installation of the isocyclic ring on the free base 3,13-diacetylchlorin **FbC-A^{3,13}R^{10}** was achieved by intramolecular ring closure of the 13-acetyl group and the 15-position of the chlorin macrocycle. The 15-bromo analogue of the 3,13-diacetylchlorin was synthesized using a selective bromination strategy.[44] The conditions of selective bromination were studied with **FbC-A^{3,13}M^{10}**. Thus, treatment of **FbC-A^{3,13}M^{10}** with 1 equiv of NBS in CH_2Cl_2/TFA (10:1) resulted in incomplete reaction, affording a ~2:1 ratio of starting material/**FbC-A^{3,13}M^{10}Br^{15}**. The mixture was not readily separable by column chromatography. Prolonged reaction or higher temperature (50 °C, 1,2-dichloroethane/TFA mixture) did not improve the outcome. The stepwise treatment of **FbC-A^{3,13}M^{10}** with 1.3 equiv of NBS in CH_2Cl_2/TFA (10:1) at room temperature provided complete consumption of the starting material and also yielded 30% of dibrominated side product (according to the ^{1}H NMR spectrum of the crude mixture). Analogous bromination of **FbC-A^{3,13}P^{10}** and **FbC-A^{3,13}Pf^{10}** afforded **FbC-A^{3,13}P^{10}Br^{15}** and **FbC-A^{3,13}Pf^{10}Br^{15}**, respectively (Scheme 2). With the 15-bromo-13-acetylchlorins in hand, intramolecular ring closure[41] upon treatment with $(Ph_3P)_2PdCl_2$

(20 mol%) in the presence of 5-6 mol equiv of Cs_2CO_3 in THF at 85 °C in a sealed Schlenk flask for 4 h gave in 64-68% yield the desired 3-acetyl-13[1]-oxophorbines **FbOP-A^{3}R^{10}**.

(v) Reduction of the 3-Acetyl Group. The selective reduction of the 3-acetyl group of oxophorbine **FbOP-A^{3}M^{10}** to give the macrocycle containing the 3-α-hydroxyethyl moiety (**FbOP-He^{3}M^{10}**) is shown in Scheme 3. Several methods have been described for the reduction (using $NaBH_4$,[24] BH_3·THF,[20] BH_3·Me_2S,[20] BH_3·^{t}BuNH$_2$,[25] and BH_3·$PhNEt_2$[20]) of the 3-acetyl group in chlorophylls and their derivatives. We examined a number of such reductants under various conditions to achieve selective reduction of the 3-acetyl moiety (Table 1).

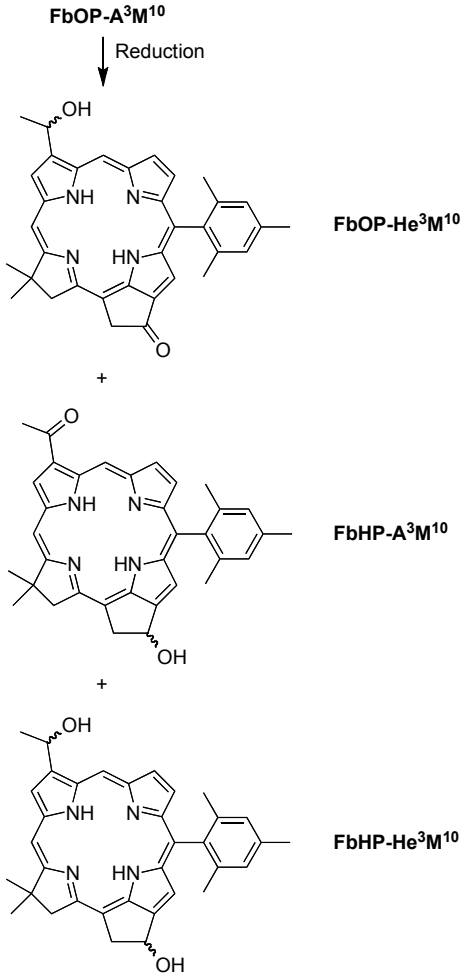

Scheme 3. Reduction to form a free base 3-(1-hydroxyethyl)-13[1]-oxophorbine.

Table 1. Reduction of **FbOP-A^{3}M^{10}**.

Entry	Reductant	Solvent	Temp.	Product(s)
1	$NaBH_4$, excess	THF/MeOH	RT	**FbHP-He^{3}M^{10}**
2	$NaBH_4$, excess	THF/MeOH	–78 °C	No reaction
3	$NaBH_4$, excess	THF/MeOH	–20 to 0 °C	**FbOP-He^{3}M^{10}** + **FbHP-A^{3}M^{10}** + **FbHP-He^{3}M^{10}** (~ 1:1:1)
4	BH_3·THF	THF	0 °C	**FbOP-He^{3}M^{10}** (42%)[a]
5	BH_3·^{t}BuNH$_2$	$CHCl_3$	RT	**FbOP-He^{3}M^{10}** (77%)[a]

[a]Isolated yield.

Treatment of **FbOP-A^{3}M^{10}** with excess $NaBH_4$ in THF/MeOH (10:1) at room temperature resulted in fast reduction of both keto groups to produce the corresponding diol **FbHP-He^{3}M^{10}** (Table 1, entry 1). Reaction of **FbOP-A^{3}M^{10}** with $NaBH_4$ did not proceed at –78 °C (entry 2) whereas at –20 °C to 0 °C (entry 3) a mixture of three products was obtained: expected **FbOP-He^{3}M^{10}** (presumably as a racemic mixture), 13^1-hydroxyphorbine **FbHP-A^{3}M^{10}** (presumably as a racemic mixture) and 3,13^1-dihydroxyphorbine **FbHP-He^{3}M^{10}** (presumably as a mixture of diastereomers). The expected product could be separated by column chromatography; however, it was difficult to obtain fully reproducible results, presumably due to the inaccuracy in temperature control and the relative amount of sodium borohydride employed in these vigorous, small-scale reactions. Stepwise treatment of **FbOP-A^{3}M^{10}** with 2 mol equiv of a 1 M solution of BH_3·THF in THF at 0 °C (entry 4) provided the expected **FbOP-He^{3}M^{10}** as the major product in 42% isolated yield, together with small amounts of **FbHP-A^{3}M^{10}** and **FbHP-He^{3}M^{10}**. The best selectivity upon reduction was achieved when **FbOP-A^{3}M^{10}** was

treated with 6 mol equiv of $BH_3 \cdot {}^t BuNH_2$ in anhydrous $CHCl_3$ at room temperature for 4.5 h (entry 5). Quenching the reaction mixture with 5% aqueous HCl and stirring for 20 minutes followed by organic extraction and column chromatography [silica, CH_2Cl_2, then CH_2Cl_2/ethyl acetate (9:1)] gave **FbOP-He^{3}M^{10}** in 77% isolated yield; the side products 3-acetyl-13^1-hydroxyphorbine **FbHP-A^{3}M^{10}** (10% yield) and diastereomers of 3,13^1-dihydroxyphorbine **FbHP-He^{3}M^{10}** (3% and 5% yield) also were isolated. The workup procedure proved critical to obtain the desired product: attempted quenching of the reaction with saturated aqueous NH_4Cl followed by the same workup described above resulted in full reduction of **FbOP-A^{3}M^{10}** to a diastereomeric mixture of 3,13^1-dihydroxyphorbine **FbHP-He^{3}M^{10}** (presumably because the excess $BH_3 \cdot {}^t BuNH_2$ was not removed completely). Application of the best conditions (6 mol equiv of $BH_3 \cdot {}^t BuNH_2$ in $CHCl_3$) to oxophorbines **FbOP-A^{3}P^{10}** and **FbOP-A^{3}Pf^{10}** afforded the corresponding free base analogues of the chlorosomal bacteriochlorophyll mimics **FbOP-He^{3}P^{10}** and **FbOP-He^{3}Pf^{10}** in 72% and 55% yield respectively (Chart 3).

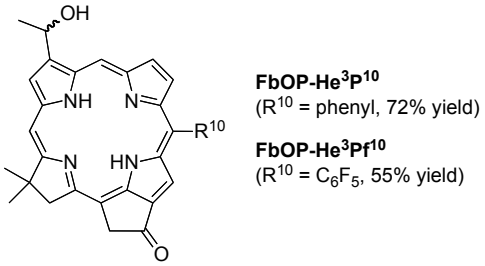

Chart 3. Free base 3-(1-hydroxyethyl)-13^1-oxophorbines with various R^{10} substituents.

(vi) Zinc Insertion. Metalation of each of the three hydroxyethyl–oxophorbines (**FbOP-He^{3}R^{10}**) with 15 mol equiv of zinc acetate in $CHCl_3$/MeOH afforded the corresponding zinc(II) chelate. Thus, **ZnOP-He^{3}P^{10}**, **ZnOP-He^{3}M^{10}** and **ZnOP-He^{3}Pf^{10}** were obtained in good yield (Chart 4). The zinc chelates (**ZnOP-He^{3}R^{10}**) are unstable in solution, especially in chlorinated

solvents (CH_2Cl_2, $CHCl_3$) resulting in demetalation and decomposition. Compound **ZnOP-He^{3}Pf^{10}** turned out to be poorly soluble in organic solvents (CH_2Cl_2, THF, ethyl acetate, MeOH, DMF), and hence the failure to obtain a ^{1}H NMR spectrum. For spectroscopic studies, the 3-acetyl-10-phenyl-13^1-oxophorbine **FbOP-A^{3}P^{10}** also was converted to the zinc chelate **ZnOP-A^{3}P^{10}**.

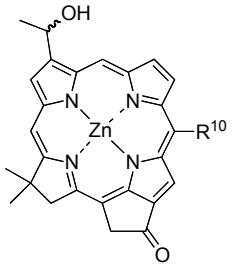

ZnOP-He^{3}P^{10}
(R^{10} = phenyl, 80% yield)

ZnOP-He^{3}M^{10}
(R^{10} = mesityl, 70% yield)

ZnOP-He^{3}Pf^{10}
(R^{10} = C_6F_5, 80% yield)

Chart 4. Target zinc(II) 3-(1-hydroxethyl)-13^1-oxophorbines.

B. Synthesis of a 7-Substituted Oxochlorin.

(i) Selective Bromination of Oxochlorins. Chlorins that contain a keto group integral to the reduced ring (ring D) are known as oxochlorins. Oxochlorins exhibit greater redox stability than chlorins.[50] Retrosynthetic analysis of a chlorosomal bacteriochlorophyll analogue built around a 17-oxochlorin macrocycle relies on: (1) regioselective bromination at the 7-position of the macrocycle; (2) selective reduction of the 7-acetyl group in the presence of the 17-keto group. Results concerning the interplay of electronic and steric factors in dictating the regioselectivity of bromination warrant mention as a preface to the studies described below. First, bromination of the chlorin **FbC** (which bears no substituents other than the 18,18-dimethyl group) with 1 mol equiv of NBS at room temperature proceeds selectively at the 15-position given the hindrance of the 20-position owing to the 18,18-dimethyl group, while the second preferable sites of bromination are carbons 7 and 8 in equal extent (Chart 5).[44] Second, the

presence of aryl groups at the 10- and 15-positions (e.g., **FbC-M^{10}P^{15}**) results in preference for bromination at the 7-position.[43] Third, the zinc chelate of a 5,10-diaryloxochlorin (e.g., **OxoFbC-Ar^{5,10}**) undergoes bromination selectively at the 20-position.[51] Fourth, the 20-position is >6-times more reactive than the 15-position in a fully unsubstituted oxochlorin (**OxoFbC**) toward electrophilic deuteration.[52] Here, we investigated bromination of both the zinc chelate and free base forms of a 10-phenyl-17-oxochlorin.

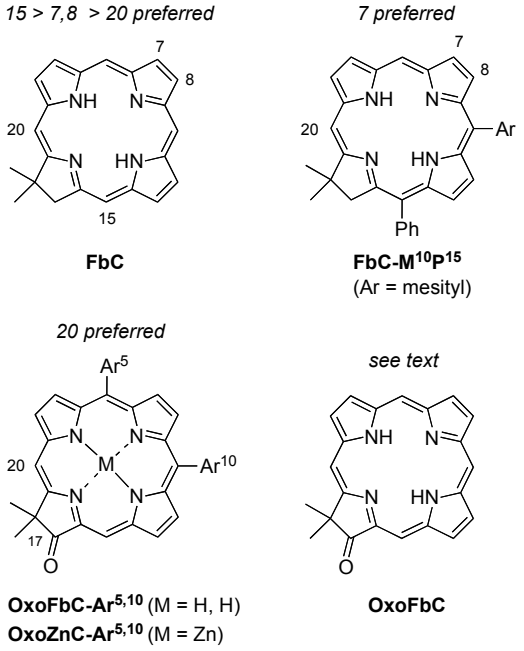

Chart 5. Preferred sites of bromination of chlorins and oxochlorins.

The 10-phenyl-17-oxochlorin (**OxoZnC-P^{10}**) was prepared in 52% yield from chlorin[53] **ZnC-P^{10}** via a two-step oxidation procedure[50] [basic alumina (activity I) in toluene at 60 °C, DDQ for 5 min at room temperature] (Scheme 4). Treatment of **OxoZnC-P^{10}** with one mol equiv of NBS in THF at room temperature gave a mixture of several brominated products that was not separable by column chromatography. Demetalation of the mixture with TFA in CH_2Cl_2 enabled separation of the free base products. The major product was identified by NOESY as

OxoFbC-P^{10}Br^{20} rather than the desired 7-bromo derivative required for the target oxochlorin analogue of the chlorosomal bacteriochlorophylls. On the other hand, demetalation of **OxoZnC-P^{10}** with TFA followed by treatment of the resulting free base **OxoFbC-P^{10}** with 1 mol equiv of NBS in THF at room temperature afforded the desired 7-bromo-17-oxochlorin **OxoFbC-Br^{7}P^{10}** in 58% yield (Scheme 4). The strong preference for 7- versus 8-substitution stems from shielding of the latter site by the 10-phenyl substituent.[43] The position of the bromo group in **OxoFbC-Br^{7}P^{10}** was established by NOESY. In summary, for the 10-phenyl-substituted macrocycles, the free base oxochlorin exhibits a bromination pattern (7 > 15, 20) that is distinct from that of the zinc oxochlorin (20 > 15, 7) and the free base chlorin (15 > 7 > 20).

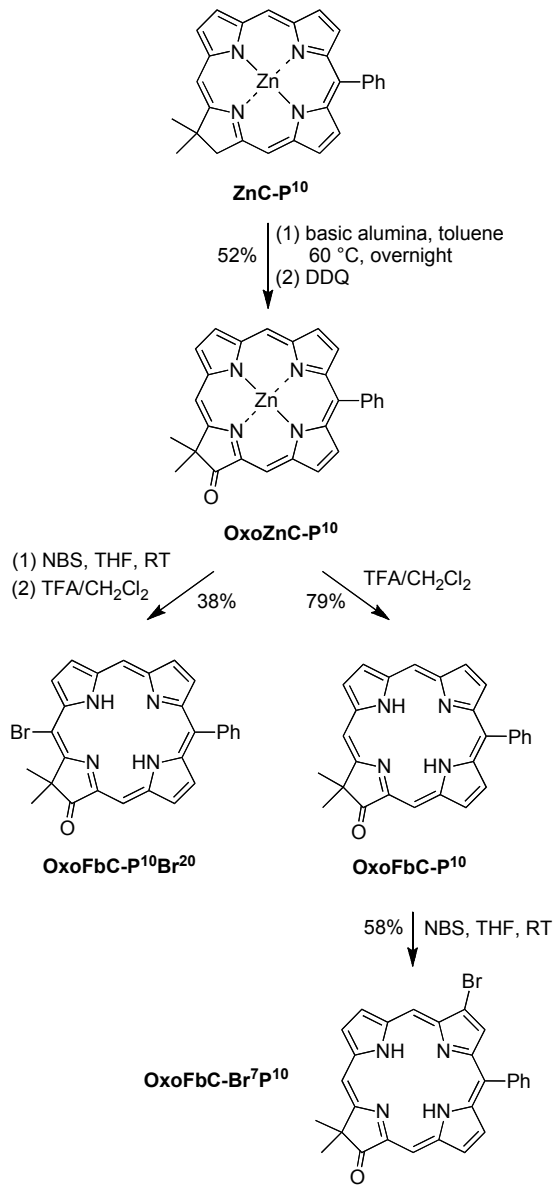

Scheme 4. Regioselective bromination of a 10-phenyl-17-oxochlorin.

(ii) Selective Reduction. The 7-acetyl group was introduced through palladium-coupling of **OxoFbC-Br^{7}P^{10}** with tributyl(1-ethoxyvinyl)tin[41] in the presence of 14 mol% of $(Ph_3P)PdCl_2$ in CH_3CN/DMF for 3 h at 85 °C followed by acidic hydrolysis to give 7-acetyl-oxochlorin **OxoFbC-A^{7}P^{10}** in 55% yield (Scheme 5). The reduction of the 7-acetyl group of **OxoFbC-A^{7}P^{10}** was first examined under conditions used for selective reduction of the aforementioned 3-acetyl-13^{1}-oxophorbines, namely treatment of **OxoFbC-A^{7}P^{10}** with 6 mol equiv of $BH_3 \cdot {}^{t}BuNH_2$

in $CHCl_3$ at room temperature. The conditions afforded the 17-hydroxychlorin **FbC-A^{7}P^{10}HO^{17}** in 70% yield. The mixture of diastereomers (**FbC-He^{7}P^{10}HO^{17}**) was isolated as a trace byproduct, but no presence of the desired 7-(1-hydroxyethyl)-17-oxochlorin **OxoFbC-He^{7}P^{10}** was observed by TLC analysis and ^{1}H NMR spectroscopy. The decreased reactivity of the carbonyl group adjacent to the C_7=C_8 double bond was discussed previously by Tamiaki.[25] The C_7=C_8 double bond is relatively isolated from the chlorin 18π-electron aromatic system, which increases the conjugation of the carbonyl group. The presence of diastereomers of **FbC-He^{7}P^{10}HO^{17}** and the absence of **OxoFbC-He^{7}P^{10}** together indicate that the 7-acetyl group in **OxoFbC-A^{7}P^{10}** can be reduced with a stronger reductant, albeit sacrificing selectivity.

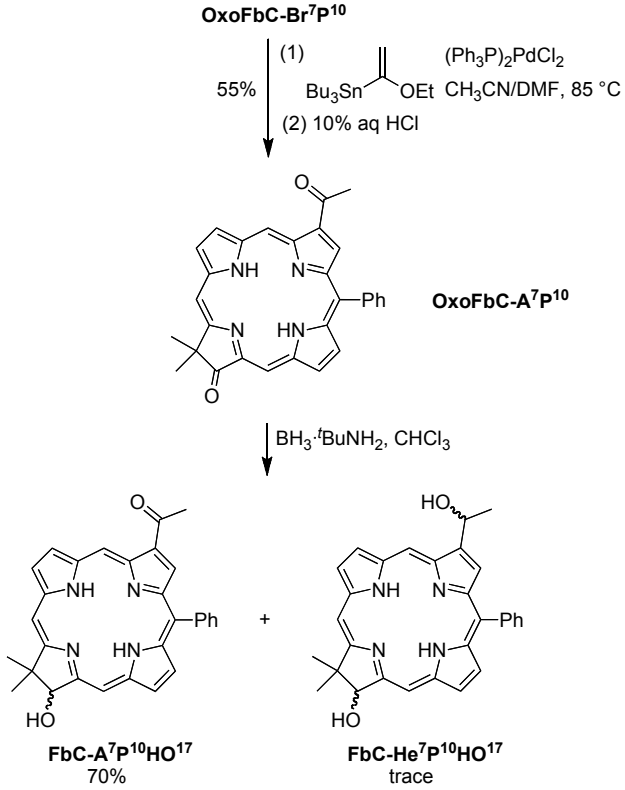

Scheme 5. Reduction of a 7-acetyl-10-phenyl-17-oxochlorin.

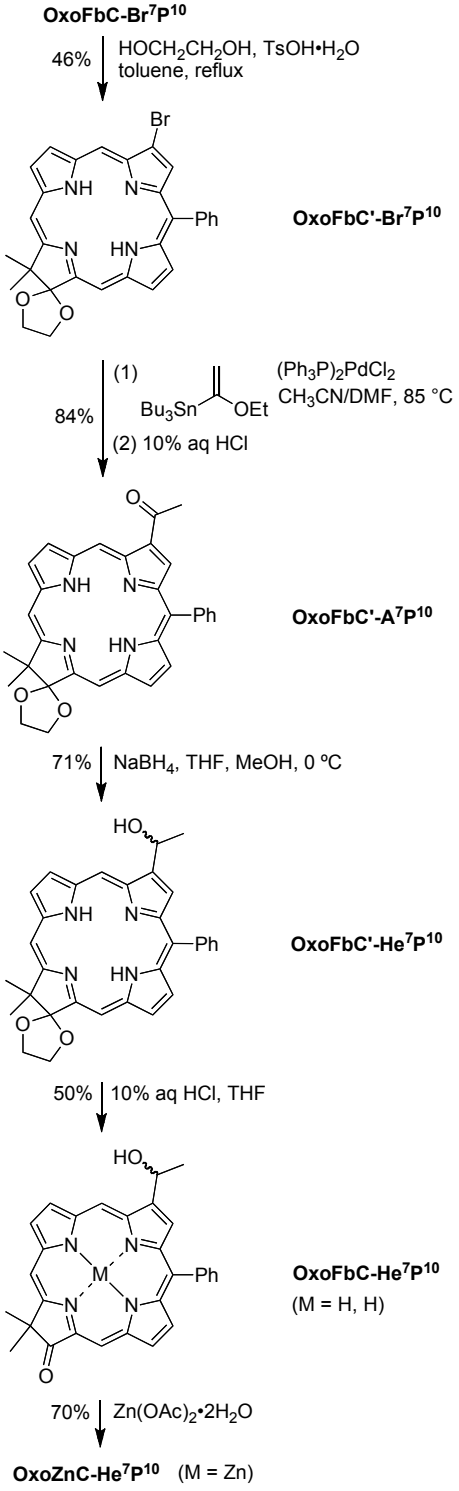

Scheme 6. Formation of the target 7-(1-hydroxyethyl)-17-oxochlorin.

To overcome the problem of the reduction of the 7-acetyl group of **OxoFbC-A^{7}P^{10}**, the 17-keto group was protected (Scheme 6). Thus, following a procedure for ketalization,[54] **OxoFbC-Br^{7}P^{10}** was heated under reflux with ethylene glycol and TsOH·H_2O in toluene for 20 h to afford **OxoFbC′-Br^{7}P^{10}** in 46% yield. Subsequent Pd-mediated acetylation in the manner described for **OxoFbC-A^{7}P^{10}** afforded **OxoFbC′-A^{7}P^{10}** (84% yield), which upon treatment with excess $NaBH_4$ in THF at room temperature afforded **OxoFbC′-He^{7}P^{10}** in 71% yield. Deprotection using reported conditions with some modifications[55] (10% aqueous HCl in THF at room temperature for 1.5 days) gave the desired **OxoFbC-He^{7}P^{10}** in 50% yield. The oxochlorin **OxoFbC-He^{7}P^{10}** was metalated with $Zn(OAc)_2·2H_2O$ to afford **OxoZnC-He^{7}P^{10}** in 70% yield.

C. Chemical Characterization. Altogether, 30 new macrocycles (chlorin, oxochlorin, oxophorbine and derivatives thereof) were prepared and 4 macrocyclic byproducts were isolated. Each macrocycle was characterized by low-resolution (LD-MS) and high-resolution (ESI-MS) mass spectrometry, and by UV-Vis absorption spectroscopy. Each macrocycle also was characterized by ^{1}H NMR spectroscopy, with the exception of **ZnOP-He^{3}Pf^{10}**, for which a solvent that afforded sufficient solubility was not identified. In each mesityl-substituted chlorosomal mimic, the hydroxy proton was not observed. ^{13}C NMR spectroscopy was attempted in a number of cases; in many cases satisfactory spectra were obtained whereas in other cases only a subset of the expected set of signals was observed. Such cases have been noted in the Experimental section.

The synthetic oxophorbine bearing the 10-mesityl group (**ZnOP-He^{3}M^{10}**) was characterized by the aforementioned set of techniques as well as by ^{13}C NMR and NOESY methods. The ^{1}H NMR spectrum of **ZnOP-He^{3}M^{10}** exhibits a doublet at δ = 2.04 ppm, attributed to the protons from the CH_3 unit of the 3-(1-hydroxyethyl) group, as well as a

multiplet at δ = 6.15–6.70 ppm, attributed to the proton from the CH unit of the same substituent. The NOESY spectrum exhibited the characteristic NOE between the CH in the 1-hydroxyethyl substituent and aromatic proton at the 2-position of the macrocycle.

In general, the three other target macrocycles with the requisite structural features for self-assembly (zinc(II) chelate and apposite keto and 1-hydroxyethyl groups) proved difficult to fully characterize by NMR methods. (i) The free base analogue of the 10-phenyl substituted oxophorbine (**FbOP-He^{3}P^{10}**) gave a satisfactory ^{1}H and ^{13}C NMR spectrum, whereas the zinc chelate was only characterized by ^{1}H NMR spectroscopy. (ii) The free base analogue of the immediate precursor to the 10-(pentafluorophenyl) substituted oxophorbine (**FbOP-A^{3}Pf^{10}**) gave a satisfactory ^{1}H and ^{13}C NMR spectrum, whereas the zinc chelate target compound (**ZnOP-He^{3}Pf^{10}**) was quite insoluble and was not characterized by any form of NMR spectroscopy. (iii) The free base analogue of the protected precursor to the oxochlorin (**OxoFbC′-He^{7}P^{10}**) gave a satisfactory ^{1}H and ^{13}C NMR spectrum, whereas the zinc chelate target compound (**OxoZnC-He^{7}P^{10}**) was only characterized by ^{1}H NMR spectroscopy. Regardless of the lack of NMR spectroscopic characterization, the mass spectra were as expected throughout the series of compounds that constitute each synthetic pathway.

D. Photophysical Properties. The electronic absorption spectra of representative free base oxophorbines are shown in Figure 2. Reduction of the acetyl group results in a significant hypsochromic shift of the Q_y band (603 cm^{-1}, λ_{max} = 656 nm for **FbOP-He^{3}M^{10}** versus 683 nm for **FbOP-A^{3}M^{10}**). The position of the wavelength maximum and the relative intensity of the Q_y and B_x bands in **FbOP-He^{3}M^{10}** are similar to those reported for 3-unsubstituted **FbOP-M^{10}**.[44] The Q_y band maximum in isomeric **FbHP-A^{3}M^{10}** appears at 662 nm and has a lower relative intensity. The spectral band positions and band intensity ratios are summarized in Table 2.

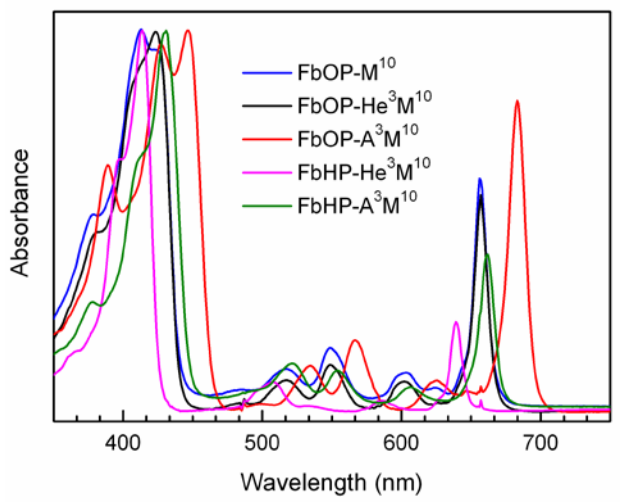

Figure 2. Absorption spectra (normalized at the B bands) in toluene at room temperature of free base species including the 3-alkylphorbine **FbHP-He^{3}M^{10}** (magenta), the 3-alkyl-13^1-oxophorbine **FbOP-He^{3}M^{10}** (black), the 3-unsubstituted 13^1-oxophorbine **FbOP-M^{10}** (blue), the 3-acetylphorbine **FbHP-A^{3}M^{10}** (green) and the 3-acetyl-13^1-oxophorbine **FbOP-A^{3}M^{10}** (red).

The fluorescence yield and singlet excited-state lifetimes for the target zinc oxophorbines **ZnOP-He^{3}M^{10}**, **ZnOP-He^{3}P^{10}** and **ZnOP-He^{3}Pf^{10}**, the corresponding free base oxophorbines **FbOP-He^{3}M^{10}**, **FbOP-He^{3}P^{10}** and **FbOP-He^{3}Pf^{10}**, and of several analogues are listed in Table 2. The various zinc oxophorbines have similar fluorescence yields (0.23–0.30) and excited-state lifetimes (5.1–6.3 ns). The various free base oxophorbines have comparable fluorescence yields to each other (0.26–0.32) and to the zinc chelates, but longer excited-state lifetimes (9.9–13.0 ns). Note that the sets of zinc and free base oxophorbines each include the parent compound for which the only substituents are the geminal dimethyl groups (**ZnOP** and **FbOP**);[56] thus, the results indicate that the substituents at the 3- and 13-positions have little effect on these photophysical properties. Similarly, replacement of the ring E keto group with a hydroxyl group gives compounds (**FbHP-A^{3}M^{10}** and **FbHP-He^{3}M^{10}**) that have photophysical properties comparable to the oxophorbines (**FbOP-A^{3}M^{10}** and **FbOP-He^{3}M^{10}**).

Turning to the oxochlorins, the unsubstituted free base compound **OxoFbC** studied previously[56] and used here as a benchmark has a fluorescence yield (0.12) that is 2.4-fold smaller than the average value for the free base oxophorbines (0.29) and a singlet excited-state lifetime (8.4 ns) that is only 1.4-fold shorter than the oxophorbine average (11.6 ns). On the other hand, zinc oxochlorin **OxoZnC-He^{7}P^{10}**, and the parent **OxoZnC** reported previously,[56] have an average fluorescence yield (0.031) and excited-state lifetime (0.84) that are both about 7-fold smaller than those for the zinc oxophorbines (Table 2). The latter values are comparable to those reported previously for 5,10-substituted zinc oxochlorins.[50,57]

Table 2. Photophysical Properties.[a]

Compound	B_{max} (nm)	$Q_y(0,0)$ abs (nm)	$Q_y(0,0)$ emis (nm)	$\frac{I_B}{I_{Q_y}}$ [b]	$\frac{\Sigma_B}{\Sigma_{Q_y}}$ [c]	Φ_f	τ_f (ns)
zinc chelates							
ZnOP-He^{3}M^{10}	426	642	644	1.9	2.4	0.24	5.7
ZnOP-He^{3}P^{10}	426	640	643	1.9	2.4	0.23	6.1
ZnOP-He^{3}Pf^{10}	426	648	653	1.7	2.7	0.25	5.7
ZnOP-A^{3}P^{10}	449	665	672	1.5	2.1	0.30	6.3
ZnOP [e]	419	637	639	1.6	2.4	0.23	5.1
OxoZnC-He^{7}P^{10}	419	609	612	4.8	4.2	0.032	0.86
OxoZnC [e]	411	602	604	3.4	4.3	0.030	0.82
free base cmpds							
FbOP-He^{3}M^{10}	423	657	660	1.9	4.3	0.30	12.3
FbOP-He^{3}P^{10}	423	656	659	2.0	4.8	0.29	12.0
FbOP-He^{3}Pf^{10}	422	663	667	1.9	4.4	0.27	9.9
FbOP-A^{3}M^{10}	446[f]	683	686	1.3	3.5	0.26	10.9
FbOP-A^{3}P^{10}	446[f]	682	686	1.3	4.2	0.28	10.5
FbOP-M^{10} [g]	413	656	659	1.7	4.4	0.32	13.0
FbOP [e]	408	654	656	1.5	4.1	0.30	11.5
OxoFbC [e]	400	634	636	4.6	11.1	0.12	8.4
FbHP-A^{3}M^{10}	430	661	664	3.2	6.3	0.32	10.5
FbHP-He^{3}M^{10}	413	639	641	4.4	8.0	0.35	10.7

[a]Data were acquired at room temperature for solutions in toluene, except for **ZnOP-He^{3}P^{10}**, **ZnOP-He^{3}Pf^{10}** and **ZnOP-A^{3}P^{10}**, which employed THF solutions. [b]Ratio of the peak intensities of the $Q_y(0,0)$ band to the Soret (B) maximum, which could be either the $B_y(0,0)$ or $B_x(0,0)$ band. [c]Ratio of the integrated intensities of the Q_y manifold [$Q_y(0,0)$, $Q_y(1,0)$] to the Soret manifold [$B_y(0,0)$, $B_y(1,0)$, $B_x(0,0)$, $B_x(1,0)$], for spectra plotted in cm^{-1}. [d]Comparable data are found in dilute solutions of the compound in THF and in toluene, with a small amount of assembly present in the latter case. [e]From ref 56. [f]Two peaks with comparable intensities are observed at 427 and 446 nm. [g]From ref 44.

E. Spectroscopic Studies on Self-Assembly of ZnOP-He^{3}M^{10}.

(i) Electronic Absorption Spectroscopy. The self-assembly of **ZnOP-He^{3}M^{10}** in solution was investigated using UV-Vis absorption spectroscopy and a variety of solution and preparative conditions, all at room temperature. The parameters varied included concentration of the compound, solvent (toluene, THF, *n*-hexane/THF mixture, Triton X-100 micellar solutions) and use of sonication. Somewhat limiting cases are illustrated in Figure 3, which shows absorption spectra of **ZnOP-He^{3}M^{10}** in THF or in *n*-hexane containing 0.3% THF. The spectra have been normalized to have the same integrated area (oscillator strength) across the spectral region shown (to reflect the same total pigment content; see also below).

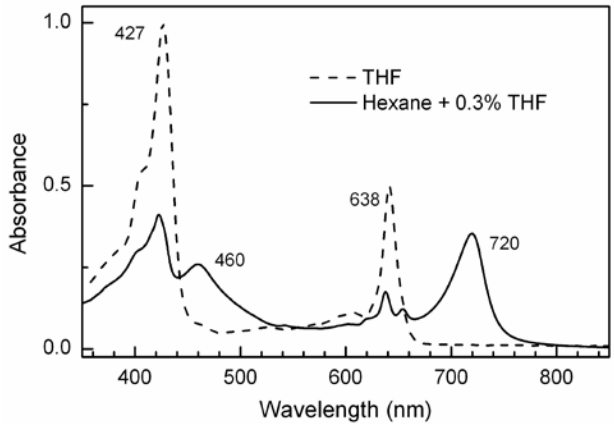

Figure 3. Absorption spectra at room temperature of 3-(1-hydroxyethyl)-13^1-oxophorbine **ZnOP-He^{3}M^{10}** in THF (dashed) and in *n*-hexane containing 0.3% THF (solid).

In THF solution, **ZnOP-He^{3}M^{10}** exhibits a strong, sharp Q_y band with maximum centered at 638 nm, characteristic for monomeric species. In *n*-hexane containing 0.3% THF (v/v), the Q_y band is intense and broad, and shifts to 720 nm (a bathochromic shift of 82 nm, or 1785 cm^{-1}). The Soret (B) band similarly shifts from 427 to 460 nm (33 nm; 1680 cm^{-1}). Such spectral shifts, particularly that in the Q_y band, are characteristic for self-assembled natural[58] and semisynthetic[27,59] analogues of the chlorosomal bacteriochlorophylls in nonpolar solvents.

The monomeric form and formation of the assemblies of **ZnOP-He^{3}M^{10}** were studied using a variety of conditions. Figure 4 shows spectra as a function of the concentration of this compound in THF, in which solvent coordination to the central zinc ion is expected to inhibit formation of the assembly. As expected, the spectra can be ascribed to the monomeric species throughout the concentration range studied; the absorbance at 637 nm depends linearly on **ZnOP-He^{3}M^{10}** concentration (Figure 4 inset). At the highest concentrations, which are far above those normally used for photophysical characterization studies, the sample is highly absorbant and virtually opaque, yet remains a solution of the monomeric species.

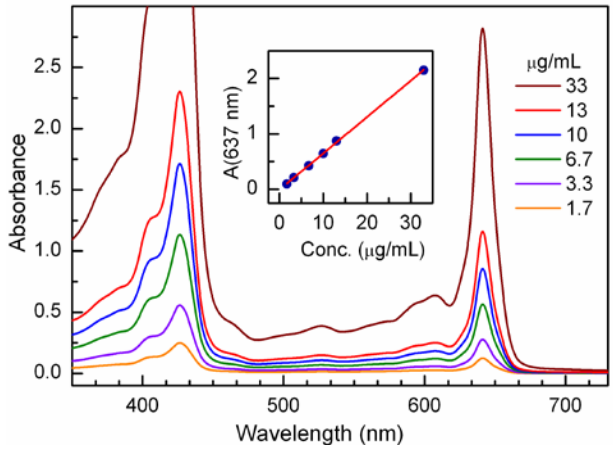

Figure 4. Absorption spectra as a function of concentration of **ZnOP-He^{3}M^{10}** in THF. The inset shows the absorbance at 637 nm as a function of concentration along with a linear fit. (Note that a 10 μg/mL solution of **ZnOP-He^{3}M^{10}** is 17 μM.)

As illustrated in Figure 3 (solid spectrum), the formation of assemblies (aggregates) is apparent for **ZnOP-He^{3}M^{10}** in *n*-hexane containing a small amount of THF to aid initial solubilization. Figure 5 shows absorption spectra for a 3.3 μg/mL (5.5 μM) solution as a function of the percentage of THF in the medium. With 7% THF the spectrum is that of the monomer and essentially equivalent to that in 100% THF. With 3.7% THF, the red-shifted absorption at 720 nm due to the assembly begins to be seen (Figure 5 inset). With 0.3% THF the

monomer feature at ~640 nm is dramatically reduced as one would expect due to greater formation of the assembly; however, a proportionate rise in the intensity of the long-wavelength feature at 720 nm is not observed, and in fact a diminution is observed. (Similarly the absorption of the 1% THF solution is slightly smaller than with 2% THF.) These observations reflect the inhomogeneous nature of the solutions with low THF concentrations due to the large fraction of assemblies that precipitate from solution and thus do not contribute to the associated red-region absorption feature.

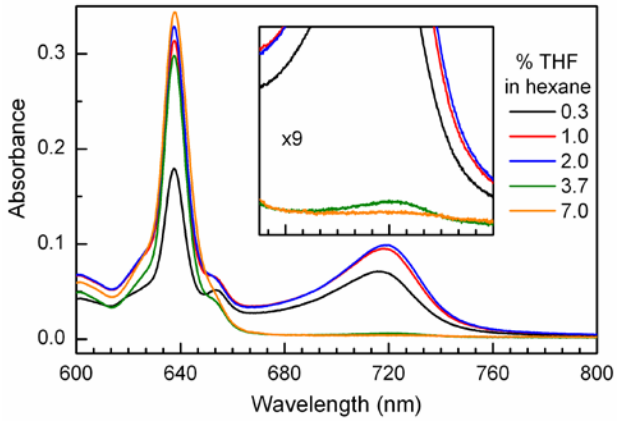

Figure 5. Absorption spectra of a 3.3 μg/mL (5.5 μM) solutions of **ZnOP-He^{3}M^{10}** as a function of %THF in *n*-hexane.

It was anticipated that the formation of the assemblies may depend on interplay between the amount of THF in the *n*-hexane solution and the concentration of the oxophorbine. To complement the %THF dependence depicted in Figure 5, a study was performed in which the concentration of **ZnOP-He^{3}M^{10}** was varied. The solvent consisted of *n*-hexane containing 3% THF, which is the approximate proportion at which the onset of formation of the assemblies was observed for a 3.3 μg/mL solution of **ZnOP-He^{3}M^{10}** (Figure 5). The results are shown in Figure 6A.

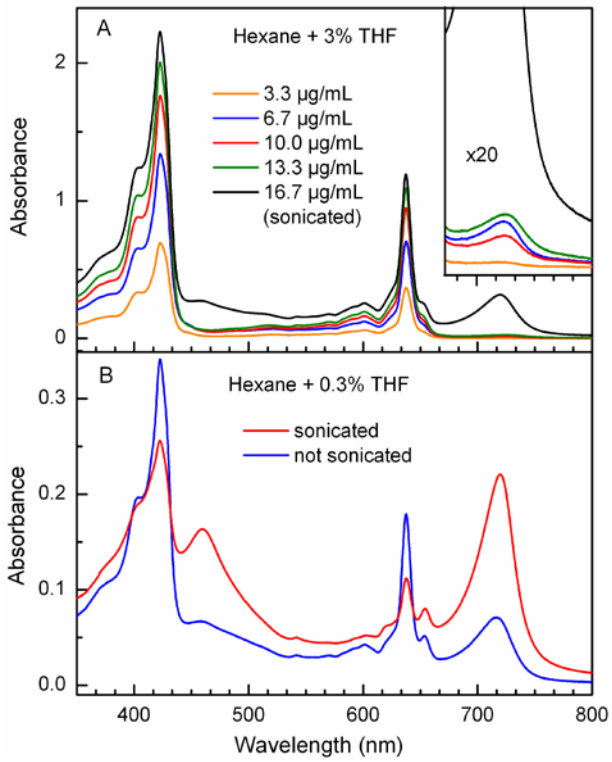

Figure 6. Absorption spectra of **ZnOP-He^{3}M^{10}** as a function of concentration in *n*-hexane containing 3% THF (A) and for two different preparations of a 3.3 µg/mL (5.5 µM) solution in *n*-hexane containing 0.3% THF with and without sonication (B).

The 3.3 µg/mL solution in Figure 6A is essentially the same as that observed in pure THF (Figure 3, dashed) and ascribed to monomeric **ZnOP-He^{3}M^{10}**. Increasing concentrations (6.7 µg/mL and above) show the presence of assemblies as is evidenced by the absorption at 720 nm (Figure 6A inset). However, quantitation of assembly formation on the basis of absorption in the red-region band is difficult. As noted above, the assemblies (aggregates) fall out of solution and adhere to the cuvette walls. The spectrum recorded depends on the extent of mixing upon preparation and the subsequent time to spectral acquisition. For example, the absorbance of the assembly at 720 nm (Figure 6A inset) for a 10 µg/mL solution (red) is less than that for a 6.7 µg/mL solution even though a larger amount of assemblies are produced in the former case, but

fall out of solution. Figure 6B shows that assemblies (or some fraction of them) can be returned to solution via sonication, greatly enhancing the red-region feature. Due to such issues concerning quantitation (and comparisons), the spectrum of the monomeric species and that dominated by the assembly in Figure 3A are normalized to the same integrated intensity over the near-UV and near-IR regions to correspond to approximately the same total pigment content.

Several other points regarding the formation of assemblies of **ZnOP-He^{3}M^{10}** can be noted. The assemblies formed in *n*-hexane with a small amount of THF can be returned significantly (but typically not completely) to the monomeric form by dilution in the same solvent. The assemblies can be formed in aqueous Triton X-100 micellar solutions (the compound is insoluble in water alone). The extent of formation of the assemblies (as expected) depends on the concentration of the oxophorbine and the detergent; starting near the CMC, appreciable assemblies are formed. Increasing the pigment concentration shifts the system towards assembly, while increasing the detergent concentration improves monomer solubility and shifts the system towards the monomeric form.

Zinc oxophorbine **ZnOP-He^{3}M^{10}** is also soluble in toluene to give solutions of the monomeric species. This point is illustrated in Figure 7 (dashed) for a 0.8 μg/mL (1.3 μM) solution. Upon increasing the concentration about 5-fold (Figure 7 solid), the formation of the assembly is apparent by the growth of the absorption at 720 nm relative to the 638-nm Q_y band of the monomeric species (and by the sloping baseline due to assembly particulates in the solution). Thus, for **ZnOP-He^{3}M^{10}** the photophysical properties (fluorescence yields and excited-state lifetimes) of the monomeric species could be investigated in dilute toluene solutions, as is our standard protocol for synthetic chlorins and related macrocycles (Table 2).[42,56,57] The replacement of the 10-mesityl group with a phenyl group in **ZnOP-He^{3}P^{10}** affords

a complex that is somewhat less soluble in toluene. This is evidenced for very dilute (~1 μM) solutions by the presence of a red-shifted feature similar to that found for **ZnOP-He^{3}M^{10}** in addition to pronounced features due to the monomeric form (data not shown). Incorporation of a 10-pentafluorophenyl group in **ZnOP-He^{3}Pf^{10}** affords a compound that is virtually insoluble in toluene and gives assemblies with little if any monomeric species even for very dilute (< 1 μM) solutions. On the other hand, the analogous zinc oxochlorin **OxoZnC-He^{7}P^{10}** is highly soluble in toluene. This compound remains in the monomeric form without the appearance of spectral manifestations (red shifted or broadened bands) or physical manifestations (precipitates, cloudy solutions) of aggregation at far higher concentrations than those at which **ZnOP-He^{3}M^{10}** or **ZnOP-He^{3}P^{10}** readily form assemblies.

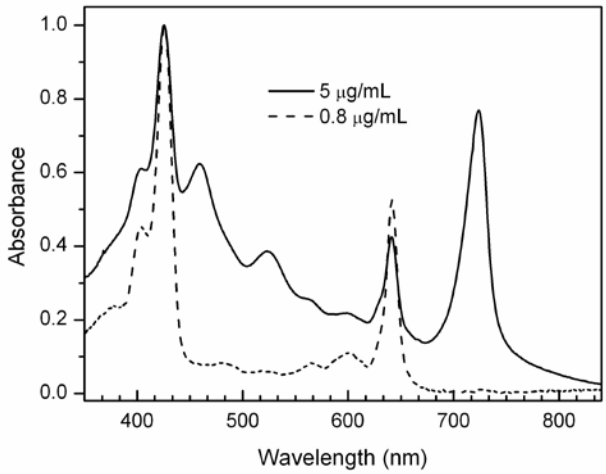

Figure 7. Absorption spectra of **ZnOP-He^{3}M^{10}** in toluene. The spectra are normalized at the Soret (B) maximum to facilitate comparisons.

The above-noted results indicate that the propensity for assembly formation increases in the following order **OxoZnC-He^{7}P^{10}** < **ZnOP-He^{3}M^{10}** < **ZnOP-He^{3}P^{10}** < **ZnOP-He^{3}Pf^{10}**. The presence of the geminal dimethyl unit in the same ring that bears the keto group in the zinc oxochlorin must provide substantial steric constraints toward assembly formation. This

particular inhibition is removed in the zinc oxophorbines, in which the geminal dimethyl group and keto group are in separate rings. In turn, the greater assembly formation for oxophorbines bearing a 10-phenyl versus 10-mesityl complex can be understood by diminished steric hindrance involving the aryl group. The greater extent of assembly for the 10-pentafluorophenyl-substituted oxophorbine likely arises from both decreased steric hindrance (versus 10-mesityl) and increased intermolecular interactions (e.g., π-stacking) derived from the electronic characteristics of the pentafluorophenyl rings. On the other hand, the free base analogues of all three zinc oxophorbines, **FbOP-He^{3}M^{10}**, **FbOP-He^{3}P^{10}** and **FbOP-He^{3}P^{10}** (like oxochlorin **OxoFbC-He^{7}P^{10}**) are soluble in toluene to give the monomeric species. Collectively, the results demonstrate the ability to tune the structural and electronic properties of the chlorosomal bacteriochlorophyll analogues toward the formation of assemblies for further study of light-harvesting and energy-transport properties.

(ii) Vibrational Spectroscopy. The assembly of **ZnOP-He^{3}M^{10}** was further investigated using both resonance Raman (RR) and IR spectroscopy. The focal point of these studies was the 13-keto substituent whose frequency is sensitive to hydrogen-bonding interactions such as those that would occur in the hypothetical assemblies shown in Figure 1. The initial aim of the vibrational spectroscopic studies was to probe the assemblies in solution using RR spectroscopy that parallel the absorption spectroscopic studies described above. However, examination of the RR spectra of **ZnOP-He^{3}M^{10}** in solution (and in solid films) revealed that the band associated with the 13-keto stretching vibration is too weak to identify with certainty (Figure S1, Supplementary Information). Consequently, the focus turned to the IR spectra of **ZnOP-He^{3}M^{10}**. The interpretation of the IR spectra of **ZnOP-He^{3}M^{10}** in solution is severely

compromised by interference from solvent bands. Thus, the IR spectra were acquired of solids, both in KBr pellets and neat films.

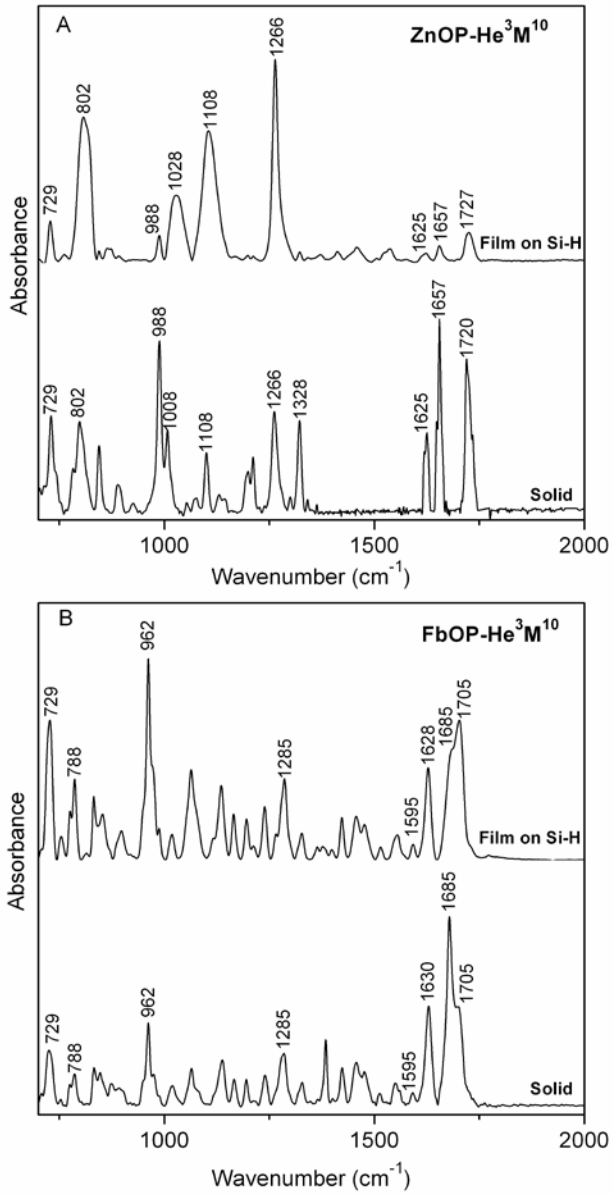

Figure 8. IR spectra at room temperature of (A) **ZnOP-He^{3}M^{10}** and (B) **FbOP-He^{3}M^{10}**.

The pellet and film IR spectra of **ZnOP-He^{3}M^{10}** are shown in Figure 8 (panel A). For comparison, the pellet and film IR spectra of the free base analogue, **FbOP-He^{3}M^{10}**, are also shown in Figure 8 (panel B). The key spectral region is 1650–1710 cm^{-1}, where the band

associated with the 13-keto stretching vibration is expected. [Note that the band in the 1720–1730 cm^{-1} region is not due to the 13-keto stretching vibration as this band is observed for complexes that lack the 13-keto group (unpublished results).]

In the case of **FbOP-He^{3}M^{10}**, the pellet and film samples exhibit bands near 1685 cm^{-1} and 1705 cm^{-1} that are assignable to the 13-keto stretching vibration. The relative intensity of these bands depends on the concentration of the samples in the pellet or in the solutions from which the films were deposited. Previous studies of chlorophylls have shown that 13-keto stretching frequencies near 1705 cm^{-1} are associated with 13-keto groups that are free from any type of interactions.[60] On the other hand, 13-keto stretching frequencies that are downshifted to the 1685 cm^{-1} region are indicative of a subset of molecules in the solid wherein the 13-keto group experiences hydrogen-bonding interactions. The downshifted 13-keto stretching vibrations observed for **FbOP-He^{3}M^{10}** could arise from hydrogen bonding of the 13-keto group on one molecule with the α-hydroxyethyl group of a neighboring molecule in the solid. This view is supported by the observation that the relative amounts of free versus interacting 13-keto groups in the solid samples are dependent on concentration in the pellet or the solution from which the film was deposited.

The pellet and film IR spectra of **ZnOP-He^{3}M^{10}** in the 13-keto region are quite different from those of **FbOP-He^{3}M^{10}**. In particular, the spectra of **ZnOP-He^{3}M^{10}** do not exhibit bands attributable to the 13-keto stretching vibrations in the 1680-1705 cm^{-1} region. Instead, a band attributable to this vibration is observed at near 1657 cm^{-1}. The frequency of this band does not depend on the concentration in the pellet or the solution from which the film was deposited. The much lower frequency for the 13-keto stretching vibration of **ZnOP-He^{3}M^{10}** versus **FbOP-He^{3}M^{10}** indicates that the nature of the interactions experienced by the 13-keto group are

different for the two complexes in the solids. One plausible explanation for the much lower 13-keto stretching frequency observed for the zinc chelate is that the keto group of one complex coordinates to the zinc ion of a neighboring complex. Another plausible explanation is that the hydrogen-bonding interaction is stronger for the zinc chelate than for the free base. Enhanced hydrogen bonding could arise if **ZnOP-He^{3}M^{10}** forms an assembly with the types of interactions shown in Figure 1. In particular, ligation of the hydroxy oxygen of one molecule to the zinc ion of a neighboring molecule would weaken the hydroxy bond owing to transfer of electron density from the oxygen atom to the metal ion. This in turn could result in a stronger hydrogen bond between the hydroxy group and the 13-keto group of an adjacent **ZnOP-He^{3}M^{10}** molecule.

Conclusions

The synthetic approaches developed previously to mimic chlorosomal assembly and function rely on (i) modification of naturally occurring tetrapyrrole macrocycles (pioneered chiefly by Tamiaki),[18] and (ii) synthesis and derivatization of porphyrins (pioneered chiefly by Balaban).[17,19] Here we have introduced a third approach that relies on *de novo* synthesis of chlorin macrocycles. While synthetically more intensive than the aforementioned methods, greater control over structure ultimately is available. This versatility is realized in the target synthetic zinc oxophorbines that differ in the 10-substituent (mesityl, phenyl, pentafluorophenyl), such compounds differ in the propensity to form assemblies, although all do so readily. The ability to tune the steric and electronic characteristics of the synthetic chlorosomal-bacteriochlorophyll mimics augurs well for the use of these constructs for bioinspired light-harvesting systems.

Experimental Section

General. ^{1}H NMR and ^{13}C NMR (100 MHz) spectra were collected at room temperature in $CDCl_3$ unless noted otherwise. All tetrapyrrole macrocycles were analyzed by laser desorption mass spectrometry (LD-MS) in the absence of a matrix. Electrospray ionization mass spectrometry (ESI-MS) data are reported for the molecular ion or protonated molecular ion. All commercially available materials were used as received. All of the Pd-mediated coupling reactions were carried out under argon using standard Schlenk-line procedures (e.g., three freeze-pump-thaw cycles were performed prior to and after the addition of the palladium reagent, for a total of six such cycles). Bromination reactions were performed using freshly recrystallized NBS (from water). Anhydrous solvents ($CHCl_3$, CH_2Cl_2, CH_3OH) were obtained from commercial suppliers and used as received. Chromatography often was performed with hexanes (a mixture of hexane isomers with bp ~68–70 °C). Sonication was performed in a benchtop bath.

Noncommercial Compounds. Compounds 8-bromo-2,3,4,5-tetrahydro-1,3,3-trimethyldipyrrin (**1**),[47] 8,9-dibromo-1-formyl-5-phenyldipyrromethane (**2a**),[48] 8,9-dibromo-1-formyl-5-mesityldipyrromethane (**2b**),[40] 1-formyl-5-(pentafluorophenyl)dipyrromethane[49] and oxochlorin[51] **OxoZnC-P^{10}** were prepared following literature procedures.

Static and Time-resolved Optical Spectroscopy. Argon-purged solutions of the samples in toluene (or THF for **ZnOP-He^{3}P^{10}**, **ZnOP-He^{3}Pf^{10}** and **ZnOP-A^{3}P^{10}**) with an absorbance of ≤0.10 at the excitation wavelength were used for the fluorescence spectral, quantum yield, and lifetime measurements. Solutions used for absorption studies in the same solvents contained ambient O_2. Solutions of **ZnOP-He^{3}M^{10}** in *n*-hexane containing a small percentage of THF (and ambient O_2) were prepared by adding a small amount of a concentrated pigment solution in THF to *n*-hexane followed by mixing. Static absorption (Varian Cary 100 or Shimadzu UV-1800) and fluorescence (Spex Fluorolog Tau 2 or PTI Quantamaster 40)

measurements were performed at room temperature, as were all other studies. Static emission measurements employed 2-4 nm excitation- and detection-monochromator bandwidths and 0.2 nm data intervals. Emission spectra were corrected for detection-system spectral response. Fluorescence quantum yields were determined relative to chlorophyll *a* in benzene[61] or toluene[56] (both with $\Phi_f = 0.325$). Fluorescence lifetimes were obtained by two methods (and typically averaged) as follows: (i) A phase-modulation technique in which samples were excited at various wavelengths in the Soret region and detected through appropriate colored glass filters (Spex Fluorolog Tau 2). Modulation frequencies from 4–250 MHz were utilized and both the fluorescence phase shift and modulation amplitude were analyzed. (ii) Decay measurements using time-correlated-single-photon-counting detection on an apparatus with an approximately Gaussian instrument response function with a full-width-at-half-maximum of ~0.5 ns (Photon Technology International LaserStrobe TM-3). Samples were excited in the Soret or Q regions using excitation pulses at 337 nm from a nitrogen laser or in the blue to green spectral regions from a dye laser pumped by the nitrogen laser. The fluorescence was detected via a monochromator with a bandpass of ≤ 2 nm.

FTIR Spectroscopy. The FTIR spectra of the solid compounds in either pellet or film forms were collected at room temperature using a Bruker Tensor 27 spectrometer with a spectral resolution of 4 cm^{-1}. The spectra of the solids in pellets were obtained in KBr (~1-2 wt % compound). These spectra were collected in transmission mode using a room-temperature DTGS detector, averaging over 32 scans. The spectra of the solids as films, deposited on a commercially available Si(100) substrate that was hydrogen-passivated, were obtained using a Harrick Scientific Ge attenuated total reflection accessory (GATR™, 65° incidence angle relative to the surface normal). The Si(100) substrates were placed in contact with the flat

surface of a semispherical Ge crystal that serves as the optical element. The IR spectra were collected with *p*-polarized light using a liquid-nitrogen cooled medium-bandwidth (600 – 4000 cm^{-1}) MCT detector, averaging over 256 scans. The spectra of the films were referenced against a bare hydrogen-passivated Si(100) substrate. The Ge crystal was cleaned with neat 2-butanone before every experiment, and the GATR™ accessory was purged with dry N_2 during data acquisition.

Resonance Raman Spectroscopy. Resonance Raman (RR) spectra were acquired for both solution and solid film samples. The solution measurements were made on samples dissolved in CH_2Cl_2; the sample cell was a sealed 4 mm i.d. NMR tube, which was spun to mitigate photodecomposition. The film measurements were made on samples deposited on a copper tip that was mounted in an evacuated chamber. All of the RR spectra were acquired at ambient temperature.

The RR spectra were acquired with a triple spectrograph (Spex 1877) equipped with a holographically etched 1200 or 2400 groove/mm grating in the first or third stage. The excitation wavelengths were provided by the discrete outputs of a krypton ion (Coherent Innova 200-K3) laser using 415 nm excitation. The scattered light was collected in a 90° configuration using a 50 mm f/1.4 Canon camera lens. A UV-enhanced charge-coupled device (CCD) was used as the detector (Princeton Instruments LN/CCD equipped with an EEV 1152-UV chip). The data acquisition times were typically 0.5 h (180 • 10 s frames). Cosmic spikes were removed prior to addition of the datasets. The laser power at the samples was 5–10 mW. The spectral resolution was ~2.5 cm^{-1}. The frequencies were calibrated using the known frequencies of indene, fenchone, and 50:50 toluene/acetonitrile.

Acknowledgment. This research was carried out as part of the Photosynthetic Antenna Research Center (PARC), an Energy Frontier Research Center funded by the U.S. Department of Energy, Office of Science, Office of Basic Energy Sciences under Award Number DE-SC0001035. We thank Ms. Rachel Williams and Ms. Kaitlyn Faries for assistance with some of the studies. Mass spectra were obtained at the Mass Spectrometry Laboratory for Biotechnology at North Carolina State University. Partial funding for the NCSU Facility was obtained from the North Carolina Biotechnology Center and the NSF.

Electronic Supplementary Information Available: Resonance Raman data for **ZnOP-He^{3}M^{10}** and **FbOP-He^{3}M^{10}** in CH_2Cl_2 solutions and solid films. ^{1}H NMR data for all new compounds.

References

(1) B. R. Green, J. M. Anderson and W. W. Parson, in *Light-Harvesting Antennas in Photosynthesis,* ed. B. R. Green and W. W. Parson, Kluwer Academic Publishers, The Netherlands, 2003, pp 1–28.

(2) R. E. Blankenship, J. M. Olson and M. Miller, in *Anoxygenic Photosynthetic Bacteria*, ed. R. E. Blankenship, M. T. Madigan and C. E. Bauer, Kluwer Academic Publishers, The Netherlands, 1995, pp 399–435.

(3) G. T. Oostergetel, H. van Amerongen and E. J. Boekema, *Photosynth. Res*., 2010, **104**, 245–255.

(4) H. Scheer, in *Chlorophylls and Bacteriochlorophylls: Biochemistry, Biophysics, Functions and Applications*; ed. B. Grimm, R. J. Porra, W. Rüdiger and H. Scheer, Kluwer Academic Publishers, The Netherlands, 2006, pp 1–26.

(5) J. Pšenčik, T. P. Ikonen, P. Laurinmäki, M. C. Merckel, S. J. Butcher, R. E. Serimaa and R. Tuma, *Biophys. J.*, 2004, **87**, 1165–1172.

(6) G. T. Oostergetel, M. Reus, A. Gomez Maqueo Chew, D. A. Bryant, E. J. Boekema and A. R. Holzwarth, *FEBS Lett.*, 2007, **581**, 5435–5439.

(7) J. Pšenčik, A. M. Collins, L. Liljeroos, M. Torkkelli, P. Laurinmäki, H. M. Ansink, T. P. Ikonen, R. E. Serimaa, R. E. Blankenship, R. Tuma and S. J. Butcher, *J. Bacteriol.*, 2009, **191**, 6701–6708.

(8) Y. Kakitani, Y. Koyama, Y. Shimoikeda, T. Nakai, H. Utsumi, T. Shimizu and H. Nagae, *Biochemistry*, 2009, **48**, 74–86.

(9) S. Furamaki, F. Vacha, S. Habuchi, Y. Tsukatani, D. A. Bryant and M. Vacha, *J. Am. Chem. Soc.*, 2011, **133**, 6703–6710.

(10) T. Nozawa, T. Noguchi and M. Tasumi, *J. Biochem.*, 1990, **108**, 737–740.

(11) A. Egawa, T. Fujiwara, T. Mizoguchi, Y. Kakitani, Y. Koyama and H. Akutsu, *Proc. Natl. Acad. Sci. U.S.A.*, 2007, **104**, 790–795.

(12) H. Akutsu, A. Egawa and T. Fujiwara, *Photosynth. Res.*, 2010, **104**, 221–231.

(13) T. S. Balaban, H. Tamiaki and A. R. Holzwarth, *Top. Curr. Chem.,* 2005, **258**, 1–38.

(14) T. Jochum, C. M. Reddy, A. Eichhöfer, G. Buth, J. Szmytkowski, H. Kalt, D. Moss and T. S. Balaban, *Proc. Natl. Acad. Sci. U.S.A.*, 2008, **105**, 12736–12741.

(15) S. Ganapathy, G. T. Oostergetel, P. K. Wawrzyniak, M. Reus, A. Gomez Maqueo Chew, F. Buda, E. J. Boekema, D. A. Bryant, A. R. Holzwarth and H. J. M. de Groot, *Proc. Natl. Acad. Sci. U.S.A.*, 2009, **106**, 8525–8530.

(16) T. S. Balaban, A. D. Bhise, G. Bringmann, J. Bürck, C. Chappaz-Gillot, A. Eichhöfer, D. Fenske, D. C. G. Götz, M. Knauer, T. Mizoguchi, D. Mössinger, H. Rösner, C. Roussel, M. Schraut, H. Tamiaki and N. Vanthuyne, *J. Am. Chem. Soc.*, 2009, **131**, 14480–14492.

(17) T. S. Balaban, *Acc. Chem. Res.,* 2005, **38**, 612–623.

(18) T. Miyatake and H. Tamiaki, *Coord. Chem. Rev.*, 2010, **254**, 2593–2602.

(19) T. S. Balaban, in *Handbook of Porphyrin Science,* ed. K. M. Kadish, K. M. Smith and R. Guilard, World Scientific Publishing Co., Singapore, vol. 1, 2010, pp 221–306.

(20) H. Tamiaki, M. Kouraba, K. Takeda, S.-i. Kondo and R. Tanikaga, *Tetrahedron: Asymmetry*, 1998, **9**, 2101–2111.

(21) T. Miyatake, H. Tamiaki, A. R. Holzwarth and K. Schaffner, *Helv. Chim. Acta*, 1999, **82**, 797–810.

(22) V. I. Prokhorenko, A. R. Holzwarth, M. G. Müller, K. Schaffner, T. Miyatake and H. Tamiaki, *J. Phys. Chem. B*, 2002, **106**, 5761–5768.

(23) Y. Saga, S. Akai, T. Miyatake and H. Tamiaki, *Chem. Lett.*, 2004, **33**, 544–545.
(24) S.-i. Sasaki and H. Tamiaki, *J. Org. Chem.*, 2006, **71**, 2648–2654.
(25) H. Tamiaki, K. Hamada and M. Kunieda, *Tetrahedron*, 2008, **64**, 5721–5727.
(26) C. Röger, M. G. Müller, M. Lysetska, Y. Miloslavina, A. R. Holzwarth and F. Würthner, *J. Am. Chem. Soc.*, 2006, **128**, 6542–6543.
(27) V. Huber, M. Lysetska and F. Würthner, *Small*, 2007, **3**, 1007–1014.
(28) C. Röger, Y. Miloslavina, D. Brunner, A. R. Holzwarth and F. Würthner, *J. Am. Chem. Soc.*, 2008, **130**, 5929–5939.
(29) V. Huber, S. Sengupta and F. Würthner, *Chem. Eur. J.*, 2008, **14**, 7791–7807.
(30) T. S. Balaban, A. Eichhöfer and J.-M. Lehn, *Eur. J. Org. Chem.*, 2000, 4047–4057.
(31) T. S. Balaban, A. D. Bhise, M. Fischer, M. Linke-Schaetzel, C. Roussel and N. Vanthuyne, *Angew. Chem. Int. Ed.*, 2003, **42**, 2140–2144.
(32) T. S. Balaban, M. Linke-Schaetzel, A. D. Bhise, N. Vanthuyne and C. Roussel, *Eur. J. Org. Chem.*, 2004, 3919–3930.
(33) T. S. Balaban, M. Linke-Schaetzel, A. D. Bhise, N. Vanthuyne, C. Roussel, C. E. Anson, G. Buth, A. Eichhöfer, K. Foster, G. Garab, H. Gliemann, R. Goddard, T. Javorfi, A. K. Powell, H. Rösner and T. Schimmel, *Chem. Eur. J.*, 2005, **11**, 2267–2275.
(34) M. C. Balaban, A. Eichhöfer, G. Buth, R. Hauschild, J. Szmytkowski, H. Kalt and T. S. Balaban, *J. Phys. Chem. B.*, 2008, **112**, 5512–5521.
(35) M. Kunieda and H. Tamiaki, *J. Org. Chem.*, 2009, **74**, 5803–5809.
(36) J. Szymtkowski, J. Conradt, H. Kuhn, C. M. Reddy, M. C. Balaban, T. S. Balaban and H. Kalt, *J. Phys. Chem. C*, 2011, **115**, 8832–8839.
(37) M. Ptaszek, Z. Yao, D. Savithri, P. D. Boyle and J. S. Lindsey, *Tetrahedron*, 2007, **63**, 12629–12638.
(38) G. P. Gurinovich, A. N. Sevchenko and K. N. Solov'ev, *Opt. Spectrosc.*, 1961, **10**, 396–401.
(39) M. Gouterman and L. Stryer, *J. Chem. Phys.* 1962, **37**, 2260–2266.
(40) J. K. Laha, C. Muthiah, M. Taniguchi, B. E. McDowell, M. Ptaszek and J. S. Lindsey, *J. Org. Chem.*, 2006, **71**, 4092–4102. *Ibid. J. Org. Chem.*, 2009, **74**, 5122.
(41) J. K. Laha, C. Muthiah, M. Taniguchi and J. S. Lindsey, *J. Org. Chem.*, 2006, **71**, 7049–7052.
(42) H. L. Kee, C. Kirmaier, Q. Tang, J. R. Diers, C. Muthiah, M. Taniguchi, J. K. Laha, M. Ptaszek, J. S. Lindsey, D. F. Bocian and D. Holten, *Photochem. Photobiol.*, 2007, **83**, 1110–1124.
(43) C. Muthiah, M. Ptaszek, T. M. Nguyen, K. M. Flack and J. S. Lindsey, *J. Org. Chem*. 2007, **72**, 7736–7749.
(44) C. Muthiah, D. Lahaye, M. Taniguchi, M. Ptaszek and J. S. Lindsey, *J. Org. Chem.*, 2009, **74**, 3237–3247.
(45) M. Ptaszek, D. Lahaye, M. Krayer, C. Muthiah and J. S. Lindsey, *J. Org. Chem*., 2010, **75**, 1659–1673.
(46) G. P. Moss, *Pure Appl. Chem.*, 1987, **59**, 779–832.
(47) M. Krayer, T. Balasubramanian, C. Ruzié, M. Ptaszek, D. L. Cramer, M. Taniguchi and J. S. Lindsey, *J. Porphyrins Phthalocyanines*, 2009, **13**, 1098–1110.
(48) O. Mass, M. Ptaszek, M. Taniguchi, J. R. Diers, H. L. Kee, D. F. Bocian, D. Holten and J. S. Lindsey, *J. Org. Chem*., 2009, **74**, 5276–5289.
(49) M. Ptaszek, B. E. McDowell and J. S. Lindsey, *J. Org. Chem.*, 2006, **71**, 4328–4331.

(50) M. Taniguchi, H.-J. Kim, D. Ra, J. K. Schwartz, C. Kirmaier, E. Hindin, J. R. Diers, S. Prathapan, D. F. Bocian, D. Holten and J. S. Lindsey, *J. Org. Chem.*, 2002, **67**, 7329–7342.
(51) M. Taniguchi, M. N. Kim, D. Ra and J. S. Lindsey, *J. Org. Chem*., 2005, **70**, 275–285.
(52) M. Taniguchi, M. Ptaszek, B. E. McDowell and J. S. Lindsey, *Tetrahedron*, 2007, **63**, 3840–3849.
(53) M. Ptaszek, B. E. McDowell, M. Taniguchi, H.-J. Kim and J. S. Lindsey, *Tetrahedron*, 2007, **63**, 3826–3839.
(54) E. M. Smith, G. F. Swiss, B. R. Neustadt, E. H. Gold, J. A. Sommer, A. D. Brown, P. J. S. Chiu, R. Moran, E. J. Sybertz and T. Baum, *J. Med. Chem*., 1988, **31**, 875–885.
(55) P. A. Grieco, M. Nishizawa, T. Oguri, S. D. Burke and N. Marinovic, *J. Am. Chem. Soc*., 1978, **99**, 5773–5780.
(56) O. Mass, M. Taniguchi, M. Ptaszek, J. W. Springer, K. M. Faries, J. R. Diers, D. F. Bocian, D. Holten and J. S. Lindsey, *New J. Chem*., 2011, **35**, 76–88.
(57) C. Kirmaier, E. Hinden, J. K. Schwartz, I. V. Sazanovich, J. R. Diers, K. Muthukumaran, M. Taniguchi, D. F. Bocian, J. S. Lindsey and D. Holten, *J. Phys. Chem. B*, 2003, **107**, 3443–3454.
(58) K. M. Smith, L. A. Kehres and J. Fajer, *J. Am. Chem. Soc*., 1983, **105**, 1387–1389.
(59) H. Tamiaki, H. Yoshimura, Y. Shimamura and M. Kunieda, *Photosynth. Res.*, 2008, **95**, 223–228.
(60) M. Lutz and B. Robert, in *Biological Applications of Raman Spectroscopy. Resonance Raman Spectra of Heme and Metalloproteins*, ed. T. G. Spiro, Wiley, New York, 1988, vol. 3, pp 347–412.
(61) G. Weber and F. W. J. Teale, *Trans. Faraday Soc.*, 1957, **53**, 646–655.

Chapter 5.

Effects of Substituents on Synthetic Analogs of Chlorophylls. Part 3: The Distinctive Impact of Auxochromes at the 7- versus 3-Positions

Reprinted with permission from Photochemistry and Photobiology. Springer, J. W., Faries, K. M., Diers, J. R., Muthiah, C., Mass, O., Kee, H. L., Kirmaier, C., Lindsey, J. S., Bocian, D. F. and Holten, D. (2012). Photochemistry and Photobiology, 88: 651–674.

ABSTRACT

Assessing the effects of substituents on the spectra of chlorophylls is essential for gaining a deep understanding of photosynthetic processes. Chlorophyll *a* and *b* differ solely in the nature of the 7-substituent (methyl versus formyl) whereas chlorophyll *a* and *d* differ solely in the 3-substituent (vinyl versus formyl), yet have distinct long-wavelength absorption maxima: 665 (*a)* 646 (*b*), and 692 nm (*d*). Here, the spectra, singlet excited-state decay characteristics, and results from DFT calculations are examined for synthetic chlorins and 13^1-oxophorbines that contain ethynyl, acetyl, formyl and other groups at the 3-, 7- and/or 13-positions. Substituent effects on the absorption spectra are well accounted for using Gouterman's four-orbital model. Key findings are that (1) the dramatic difference in auxochromic effects of a given substituent at the 7- versus 3- or 13-positions primarily derives from relative effects on the LUMO+1 and LUMO; (2) formyl at the 7- or 8-position effectively "porphyrinizes" the chlorin; and (3) the substituent effect increases in the order of vinyl < ethynyl < acetyl < formyl. Thus, the spectral properties are governed by an intricate interplay of electronic effects of substituents at particular sites on the four frontier MOs of the chlorin macrocycle.

INTRODUCTION

Chlorophyll *a* (**Chl *a***) and chlorophyll *b* (**Chl *b***) are the two green pigments that underlie the photosynthetic process in plants and many cyanobacteria. **Chl *a*** and **Chl *b*** each bear a 3-vinyl group, an isocyclic ring spanning the 13-15 positions, and a 7-methyl versus 7-formyl group, respectively, attached to the chlorin macrocycle (1). **Chl *a*** in toluene exhibits an intense B (Soret) band at 432 nm and a Q_y band at 665 nm of nearly comparable intensity (Figure 1); similar spectra are found in a variety of solvents (2-5). **Chl *b*** exhibits a B band at 458 nm and a Q_y band at 646 nm; the former is more intense than that of **Chl *a*** while the latter is less intense (2-5). The respective metal-free analogs pheophytin *a* (**Pheo *a***) and pheophytin *b* (**Pheo *b***) exhibit similar spectral differences (Figure 1). Thus, the presence of the 7-formyl versus 7-methyl group causes a bathochromic shift of the B band but a hypsochromic shift of the Q_y band, and also alters the ratio of the B and Q_y band intensities. Quite different behavior is observed for **Chl *d*** (and **Pheo *d***) wherein 3-formyl replaces the 3-vinyl of **Chl *a***. This change engenders a bathochromic shift (665 to 697 nm) and hyperchromic effect on the red-region absorption band, precisely the opposite of **Chl *b*** versus **Chl *a*** (Figure 1). **Chl *d*** is a primary pigment of the cyanobacterium *Acarychloris marina*, which grows on didemnid ascidians below layers of the symbiont *Prochlorin didemni* (also a cyanobacterium) whose rich **Chl *a*** content filters out most of the light at wavelengths shorter than about 690 nm (6). The spectral distinctions between the three native photosynthetic chromophore classes thus derive in large measure from whether a formyl group is present at the 7-position (**Chl *b***), the 3-position (**Chl *d***) or not at all (**Chl *a***).

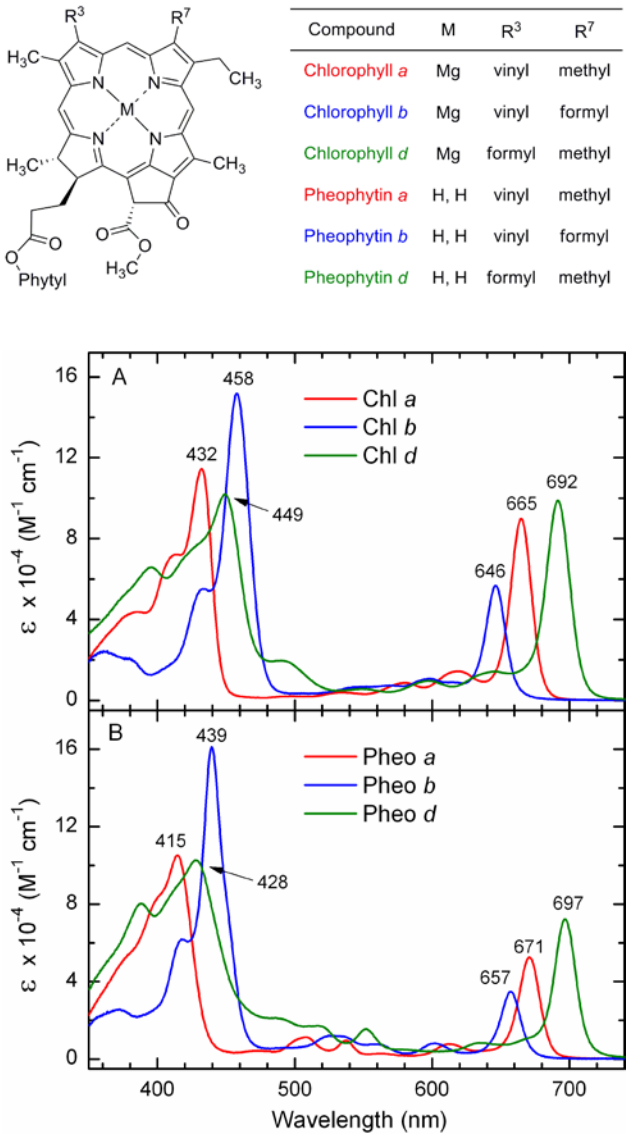

Figure 1. Chemical structure and absorption spectra of (A) chlorophyll *a* (red), chlorophyll *b* (blue), and chlorophyll *d* (green) and (B) the pheophytin analogues in toluene at room temperature. The spectra utilize the molar absorption coefficients reported in Ref 5 (the ordinate has been multiplied by 10^{-4}). (The small absorption near 500 nm for Chl *d* and Pheo *d* is due to carotenoid.)

The hypsochromic effect of the formyl group at the 7-position stands in stark contrast to a widespread maxim in organic photochemistry that the presence of a conjugative group causes a bathochromic effect on the absorption spectrum. The term auxochrome to describe conjugative

groups originated in late 19th-century efforts to understand the relation between color and constitution of synthetic dyes, where only bathochromic effects were typically observed (7–10). Similarly, mid-20th-century tables of empirical rules for calculating absorption spectra of substituted dienes and dienones typically only show bathochromic increments for incorporation of diverse functional groups (11). Thus, the classic book by Jaffé and Orchin (12) – consistent with Gillam and Stern (13) a decade earlier – defined an auxochrome as *"an atom or group of atoms which, alone, does not give rise to absorption in the ultraviolet but which, when conjugated to a chromophore, causes a bathochromic shift and hyperchromic effect."* On the other hand, Calvert and Pitts (11) offered a more guarded definition of auxochromes as groups that *"appreciably intensify and shift the absorption"* and stated that the shift can be bathochromic or hypsochromic. Mason (14) also mentioned that substitution of arenes with a conjugating substituent is *"usually, but not invariably, accompanied by a red-shift of the absorption band."* Attempts to explain the origin of the effect of auxochromes of dyes became interwoven with early concepts of resonance delocalization (15). Indeed, Lewis and Calvin (16) stated that the effect of an auxochrome *"may be described as providing, through resonance, entirely new electronic paths."* Such concepts were consistent with one-electron particle-in-a-box treatments of absorption in π-electron systems [wherein the lowest excited state derives solely from electron promotion from the highest occupied molecular orbital (HOMO) to the lowest unoccupied molecular orbital (LUMO)]. While the maxim still persists that a conjugative group causes a bathochromic effect, the origin of the absorption spectrum of cyclic polyenes including tetrapyrrole macrocycles is now known to be comprehensible only by consideration of the interplay of the four frontier molecular orbitals [in which the lowest excited state derives from an admixture of two one-electron configurations, such as HOMO → LUMO and HOMO-1

→ LUMO+1] (17–19). Thus, the effects of substituents on spectra stem from interactions of the substituents to differing extent with the four orbitals. Such interactions depend on the nature and position of the substituent.

Chart 1. Nomenclature of chlorins (left) and 13^1-oxophorbines (right).

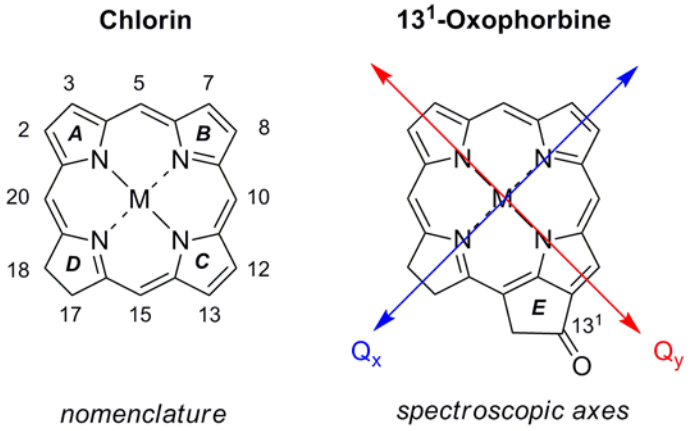

In our earlier studies (Parts 1 and 2) of synthetic analogs of the chlorophylls, we analyzed the spectral and photophysical properties of large sets of zinc and free base chlorins bearing a variety of substituents (e.g., acetyl, ethynyl, alkyl) at the 3- and/or 13-positions in terms of the four-orbital model (20,21). The studies also encompassed a few chlorins that contain the fifth 'isocyclic' ring (i.e., 13^1-oxophorbines). The nomenclature for chlorins and 13^1-oxophorbines, of which the chlorophylls are members, is shown in Chart 1. Several analogs with a subset of these groups (i.e., ethynyl and acetyl) at the 3,12- versus 3,13- position were also investigated (22). Sparsely substituted parent macrocycles [chlorins, oxochlorins, phorbines, and oxophorbines (23–26)] were probed to elucidate the minimal structural and electronic characteristics necessary to answer the question "what structural features make chlorophyll *a* green?" (26). However, none of these studies utilized a formyl substituent, which is relevant to

Chl *b* and **Chl *d***. Additionally, although 7-substituted chlorins and oxophorbines (relevant to **Chl *b***) have been prepared (27,28), the electronic and excited-state characteristics have not been analyzed and compared with the same substituents (e.g., formyl, acetyl, ethynyl) at other macrocycle sites.

Herein we report the results of studies of the spectral and photophysical properties of chlorins bearing formyl and other common substituents at the 7- versus 3,13-positions, as well as of the corresponding 7-substituted 13^1-oxophorbines (Charts 2 and 3). We also studied **Chl *a***, **Chl *b***, and **Chl *d*** as well as **Pheo *a***, **Pheo *b***, and **Pheo *d*** in the same (non-coordinating) solvent toluene to facilitate comparisons with the properties of synthetic chromophores examined under the same conditions. Collectively, the goals of these studies are to (i) gain insights into the architectural and electronic characteristics that underpin the distinctive spectral properties of **Chl *a***, **Chl *b***, and **Chl *d***, and (ii) strengthen the foundation for the utilization of tunable synthetic hydroporphyrin analogs in bioinspired light-harvesting and charge-transfer systems for solar-energy conversion.

MATERIALS AND METHODS

Compounds. The previously synthesized chlorins include zinc chlorins **ZnC-E^{3}E^{12}** (29,30), **ZnC-E^{3}A^{12}** (29,30), **ZnC-E^{3}M^{10}E^{13}** (29), **ZnC-M^{10}** (29), **ZnC-M^{10}A^{13}** (29), **ZnC-M^{10}E^{13}** (29), **ZnC-V^{3}M^{10}** (29), **ZnC** (23), **ZnC-P^{10}** (23), **ZnC-T^5** (23), **ZnC-P^{15}** (20), **ZnC-A^{3}M^{10}A^{13}** (29), **ZnC-M^{10}F^{13}** (31), **ZnC-F^{3}M^{10}F^{13}** (31), **ZnC-T^{10}** (27), **ZnC-F^{7}T^{10}** (27), **ZnC-A^{7}T^{10}** (27), **ZnC-E^{7}T^{10}** (27), **ZnC-E^{3}E^{13}** (22), **ZnC-E^{3}A^{13}** (22), **ZnC-A^{12}** (22) and **ZnC-A^{13}** (26); free base chlorins **FbC** (24), **FbC-P^{10}** (24), **FbC-T^5** (24), **FbC-P^{15}** (24), **FbC-M^{10}** (24), **FbC-M^{10}E^{13}** (20) and **FbC-M^{10}Es^{13}** (32); free base oxophorbines **FbOP-M^{10}** (28), **FbOP-A^{3}M^{10}** (28), **FbOP-**

F^{7}M^{10} (28), **FbOP-A^{7}M^{10}** (28), **FbOP-E^{7}M^{10}** (28) and **FbOP** (26); and zinc oxophorbine **ZnOP** (26). **Chl *a*** and **Chl *b*** were obtained from Aldrich. **Chl *d*** was isolated from *Chlorobium vibroforme*.

Synthesis procedures provided access to one new chlorin (**ZnC-M^{10}Es^{13}**) and increased amounts of valuable precursors (**ZnC-Br^{3}M^{10}Br^{13}**, **FbC-A^{3}M^{10}A^{13}**) to other chlorins. The prior synthesis of **FbC-A^{3}M^{10}A^{13}** was carried out by treatment of **ZnC-Br^{3}M^{10}Br^{13}** to demetalation, introduction of the acetyl groups via Stille coupling, and metalation to form **ZnC-A^{3}M^{10}A^{13}** followed by demetalation (20,29). Here, the synthesis of **FbC-A^{3}M^{10}A^{13}** was achieved by treatment of **ZnC-Br^{3}M^{10}Br^{13}** to demetalation and Stille coupling on the crude free base product to introduce the acetyl groups. Due to greater simplicity and larger scale, a 7.5-fold larger quantity (46 mg) of **FbC-A^{3}M^{10}A^{13}** was obtained versus the prior report (20).

Preparation of Zn(II)-17,18-dihydro-10-mesityl-13-methoxycarbonyl-18,18-dimethylporphyrin (**ZnC-M^{10}Es^{13}**). Application of a literature procedure for metalation (26) to the free base chlorin **FbC-M^{10}Es^{13}** afforded the title compound: ^{1}H NMR δ (300 MHz, $CDCl_3$) 1.84 (s, 6H), 2.02 (s, 6H), 2.60 (s, 3H), 4.15 (s, 3H), 4.52 (s, 2H), 7.25 (s, 2H), 8.35 (d, J = 4.4 Hz, 1H), 8.53 (s, 1H), 8.72–8.74 (m, 2H), 9.01–9.03 (m, 2H), 9.45 (s, 1H), 9.73 (s, 1H); LD-MS obsd 577.7; calcd 578.1660 ($C_{33}H_{30}N_4O_2Zn$); λ_{abs} (toluene) 415, 627 nm.

Preparation of Zn(II)-3,13-dibromo-17,18-dihydro-18,18-dimethyl-10-mesitylporphyrin (**ZnC-Br^{3}M^{10}Br^{13}**) (29). Following a streamlined procedure (23,27), a solution of 8,9-dibromo-1-formyldipyrromethane (29) (301 mg, 0.668 mmol) and 2,4,5,6-tetrahydro-1,3,3-trimethyldipyrrin (33) (150 mg, 0.557 mmol) in anhydrous CH_2Cl_2 (16 mL) was treated with a solution of *p*-TsOH·H_2O (530 mg, 2.78 mmol) in anhydrous methanol (4.0 mL) under argon. The red reaction mixture was stirred at room temperature for 40 min. A sample of 2,2,6,6-

tetramethylpiperidine (1.04 mL, 6.11 mmol) was added. The reaction mixture was concentrated. The crude solid was dissolved in CH_3CN (55.7 mL) and subsequently treated with 2,2,6,6-tetramethylpiperidine (2.36 mL, 13.9 mmol), $Zn(OAc)_2$ (1.53 g, 8.35 mmol), and AgOTf (429 mg, 1.67 mmol). The resulting suspension was refluxed for 20 h exposed to air. The crude mixture was filtered through a pad of silica (CH_2Cl_2) followed by column chromatography of the resulting solid [silica, hexanes, then hexanes/CH_2Cl_2 (1:1)] to afford a green solid (136.2 mg, 36%). The data obtained by ^{1}H NMR spectroscopy (400 MHz), laser-desorption mass spectrometry (LD-MS), fast-atom bombardment mass spectrometry (FAB-MS) and absorption spectroscopy were consistent with the reported data for the title compound obtained previously at lower scale (29).

Preparation of 3,13-diacetyl-17,18-dihydro-18,18-dimethyl-10-mesitylporphyrin (**FbC-A^{3}M^{10}A^{13}**) (20,34). A solution of **ZnC-Br^{3}M^{10}Br^{13}** (78.0 mg, 0.115 mmol) in CH_2Cl_2 (3.0 mL) was treated dropwise with trifluoroacetic acid (266 μL, 22.2 mmol) over a 2 min period. The solution was stirred at room temperature for 4 h. CH_2Cl_2 was added, and the organic layer was washed (saturated aqueous $NaHCO_3$ and water) and then dried (Na_2SO_4). The organic layer was concentrated to afford a purple solid. Following a procedure for Stille coupling on chlorins (29), a mixture of the crude free base chlorin, tributyl(1-ethoxyvinyl)tin (311 μL, 0.92 mmol) and $(PPh_3)_2PdCl_2$ (16.1 mg, 0.0230 mmol) was refluxed in THF (5.5 mL) for 20 h in a Schlenk line. The reaction mixture was treated with 10% aqueous HCl (30 mL) at room temperature for 2 h. CH_2Cl_2 was added. The organic layer was separated, washed (saturated aqueous $NaHCO_3$, water, and brine), dried (Na_2SO_4), and concentrated. The resulting residue was chromatographed [silica, hexanes/CH_2Cl_2 (1:1), then CH_2Cl_2] to afford a purple solid (46 mg, 74%): ^{1}H NMR (400 MHz, $CDCl_3$) δ –1.26 (brs, 2H), 1.85 (s, 6H), 2.03 (s, 6H), 2.63 (s, 3H), 3.06 (s, 3H), 3.27 (s,

3H), 4.60 (s, 2H), 7.25 (s, 2H), 8.35 (d, J = 4.4 Hz, 1H), 8.82 (s, 1H), 8.87 (d, J = 4.4 Hz, 1H), 8.93 (s, 1H), 9.30 (s, 1H), 10.10 (s, 1H), 10.60 (s, 1H); LD-MS obsd 542.6; FAB-MS obsd 542.2691, calcd 542.2682 ($C_{35}H_{34}N_4O_2$); λ_{abs} (toluene) 431, 687 nm.

Preparation of Pheophytin a. Following a reported procedure (35), a sample of **Chl *a*** (0.5 mg, 0.0006 mmol) was dissolved in a drop of cold (–18 °C) THF, and the solution was immediately diluted with hexanes (11 mL). The solution was treated with 11 mL of aqueous trichloroacetic acid (prepared by dissolving 25 g of trichloroacetic acid in 100 mL of H_2O). The solution was vigorously stirred for 15 min. The organic phase was washed with water (2 x 40 mL), 5% aqueous $NaHCO_3$ (1 x 40 mL), again with water (2 x 40 mL), and concentrated to a solid under reduced pressure at 30 °C. Acetone (5 mL) was added, and the mixture was concentrated so as to remove a trace of water. TLC analysis revealed a single green-brown spot [R_f = 0.67, ethyl acetate/hexanes (1:2)] with a small amount of a by-product. **Chl *a*** [a bright emerald green streaking spot, R_f = 0.5, ethyl acetate/hexanes (1:2)] was not observed by TLC analysis. The title compound was used as obtained: LD-MS obsd 870.6, calcd 870.5659 ($C_{55}H_{74}N_4O_5$); λ_{abs} (ethanol) 410, 507, 537, 609, 667 nm.

Preparation of Pheophytin b. Following a reported procedure (35), a sample of **Chl *b*** (2.5 mg, 0.0028 mmol) was dissolved in a drop of cold (–18 °C) THF, and the solution was immediately diluted with hexanes (50 mL). The solution was treated with 50 mL of aqueous trichloroacetic acid (prepared by dissolving 25 g of trichloroacetic acid in 100 mL of H_2O). The solution was vigorously stirred for 15 min. Water (50 mL) was added. The organic phase was washed with water (4 x 50 mL), and concentrated to a solid under reduced pressure at 30 °C. Acetone was added, and the mixture was concentrated so as to remove a trace of water. TLC analysis revealed a single spot [R_f = 0.7, ethyl acetate/hexanes (1:1) or R_f = 0.3, ethyl

acetate/hexanes (1:2)] with faint traces of two by-products. The title compound was used as obtained: LD-MS obsd 883.9, calcd 884.5452 ($C_{55}H_{72}N_4O_6$); λ_{abs} (ethanol) 437, 654 nm.

Preparation of Pheophytin d. Due to limited amount of material, a solution of the compound was prepared by addition of a trace amount of trifluoroacetic acid to a solution of **Chl *d*** in toluene. The resulting spectrum matched that reported for **Pheo *d*** (5), and the solution was used directly for photophysical studies.

Photophysical measurements. Static absorption (Varian Cary 100 or Shimadzu UV-1800) and fluorescence (Spex Fluorolog Tau 2 or PTI Quantamaster 40) measurements were performed at room temperature, as were all other studies. Measurement of the fluorescence quantum yield (Φ_f) and singlet excited-state lifetimes (τ_S) utilized dilute (μM) Ar-purged toluene solutions. Samples for Φ_f measurements had an absorbance ≤0.1 at the excitation wavelength. Static emission measurements employed 2-4 nm excitation- and detection-monochromator bandwidths and 0.2 nm data intervals. Emission spectra were corrected for detection-system spectral response. Fluorescence quantum yields were determined relative to several different standards depending on the spectral characteristics. These standards are (i) chlorophyll *a* in deoxygenated toluene (Φ_f = 0.325) (26), which is the value measured in benzene (36), and (ii) free base *meso*-tetraphenylporphyrin (**FbTPP**) in nondegassed toluene, for which Φ_f = 0.070 was established with respect to the zinc chelate **ZnTPP** in nondegassed toluene (Φ_f = 0.030) (37), consistent with prior results on **FbTPP** (38). Fluorescence lifetimes were obtained by two methods (and typically averaged) as follows: (i) A phase-modulation technique in which samples were excited at various wavelengths in the Soret region and detected through appropriate colored glass filters (Spex Fluorolog Tau 2). Modulation frequencies from 10–200 MHz were typically utilized and both the fluorescence phase shift and modulation amplitude were analyzed. (ii) Decay

measurements using time-correlated-single-photon-counting detection on an apparatus with an approximately Gaussian instrument response function with a full-width-at-half-maximum of *ca* 1 ns (Photon Technology International LaserStrobe TM-3). Samples were excited in the near-UV region using excitation pulses at 337 nm from a nitrogen laser or in the blue to green spectral regions from a dye laser pumped by the nitrogen laser. Note that some of the Φ_f and τ_S values from Ref 21 reported herein (Tables 1-3) were updated (changes typically <15%) to reflect averaging with additional repeat measurements. The additional studies included using the second technique for the τ_S determinations to complement the results from the first technique, which was used exclusively in the earlier study.

Density functional theory calculations. DFT calculations were performed in parallel mode (39) with either Spartan ′08 for windows version 1.2.0 or Spartan ′10 for windows version 1.1.0 on a PC equipped with an intel i7-975 cpu, 24 GB ram and three 300GB 10K rpm hard drives. The hybrid B3LYP functional and the 6-31G* basis set were employed. The equilibrium geometries were fully optimized using the default parameters of the Spartan program.

TDDFT calculations were performed in parallel mode (40) with Gaussian ’09 version B.01 64-bit for linux using OpenSUSE version 11.4. One of two PC systems was used for Gaussian runs. The hardware for the first PC system used for Gaussian runs is the same as that used for the Spartan calculations and the second is a PC equipped with an intel i7-980 cpu, 24 GB ram and two 600 GB 10k rpm hard drives. Geometries used for the TDDFT calculations were from optimizations at the B3LYP/6-31+G(d,p) level. TDDFT single point calculations were performed at the wB97xD/6-311+G(2d,2p) level. The models used for TDDFT calculations and geometry optimizations were selected based on a recent study published by Tian

et al. (41). Except for the occasional use of keyword scf=qc, default parameter settings were used for Gaussian calculations.

Chart 2. Chlorins and 13[1]-oxophorbines characterized here.

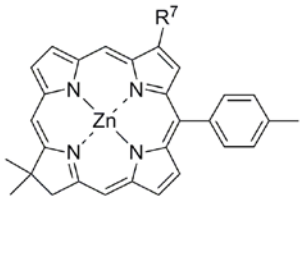

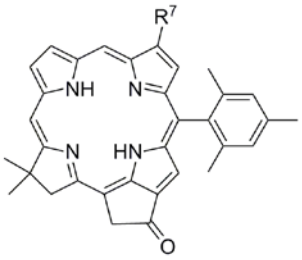

ZnC-X^{7}T^{10} Series

Cmpd	R^7
ZnC-T^{10}	H
ZnC-F^{7}T^{10}	-CHO
ZnC-A^{7}T^{10}	$-COCH_3$
ZnC-E^{7}T^{10}	—≡—TIPS

FbOP-X^{7}M^{10} Series

Cmpd	R^7
FbOP-M^{10}	H
FbOP-F^{7}M^{10}	-CHO
FbOP-A^{7}M^{10}	$-COCH_3$
FbOP-E^{7}M^{10}	—≡—TIPS

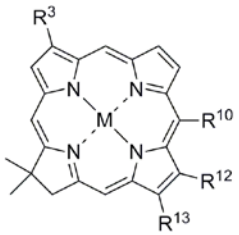

Diverse Substituted Chlorins

Cmpd	M	R^3	R^{10}	R^{12}	R^{13}
ZnC-M^{10}F^{13}	Zn	H	mesityl	H	-CHO
ZnC-F^{3}M^{10}F^{13}	Zn	-CHO	mesityl	H	-CHO
ZnC-M^{10}Es^{13}	Zn	H	mesityl	H	$-CO_2CH_3$
FbC-M^{10}Es^{13}	H,H	H	mesityl	H	$-CO_2CH_3$
ZnC-A^{12}	Zn	H	H	$-COCH_3$	H
ZnC-A^{13}	Zn	H	H	H	$-COCH_3$

Chart 3. Previously studied chlorins and 13[1]-oxophorbines used here for comparisons.

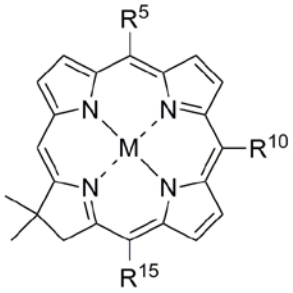

Cmpd	M	R^5	R^{10}	R^{15}
ZnC	Zn	H	H	H
FbC	H, H	H	H	H
ZnC-P^{10}	Zn	H	phenyl	H
FbC-P^{10}	H, H	H	phenyl	H
ZnC-T^{5}	Zn	*p*-tolyl	H	H
FbC-T^{5}	H, H	*p*-tolyl	H	H
ZnC-P^{15}	Zn	H	H	phenyl
FbC-P^{15}	H, H	H	H	phenyl

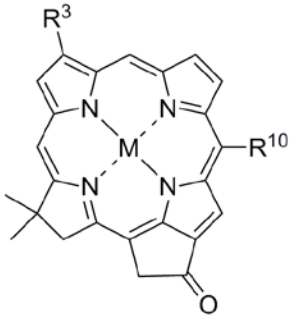

Cmpd	M	R^3	R^{10}
ZnOP	Zn	H	H
FbOP	H, H	H	H
FbOP-M^{10}	H, H	H	mesityl
FbOP-A^{3}M^{10}	H, H	-$COCH_3$	mesityl

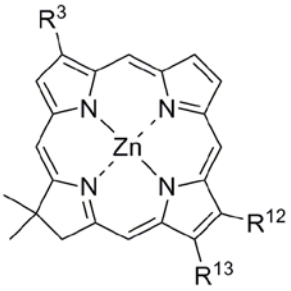

Cmpd	R^3	R^{12}	R^{13}
ZnC-E^{3}A^{12}	—≡—TIPS	-$COCH_3$	H
ZnC-E^{3}A^{13}	—≡—TIPS	H	-$COCH_3$
ZnC-E^{3}E^{12}	—≡—TIPS	—≡—TIPS	H
ZnC-E^{3}E^{13}	—≡—TIPS	H	—≡—TIPS

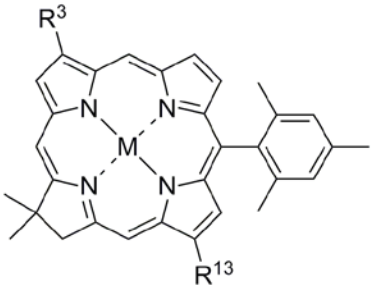

Cmpd	M	R^3	R^{13}
ZnC-M^{10}	Zn	H	H
FbC-M^{10}	H, H	H	H
ZnC-V^{3}M^{10}	Zn	vinyl	H
ZnC-M^{10}A^{13}	Zn	H	-$COCH_3$
ZnC-M^{10}E^{13}	Zn	H	—≡—TIPS
FbC-M^{10}E^{13}	H, H	H	—≡—TIPS
ZnC-E^{3}M^{10}E^{13}	Zn	—≡—TIPS	—≡—TIPS
ZnC-A^{3}M^{10}A^{13}	Zn	-$COCH_3$	-$COCH_3$

RESULTS AND DISCUSSION

Overview

The following sections first address the effects of substituents on the spectral and photophysical properties of the new chlorins and oxophorbines, along with comparisons to the properties of selected analogs studied previously as well as the native photosynthetic pigments. The results are then related to the effects on the electron densities and energies of the frontier molecular orbitals (MOs). This comparison is followed by a closer examination of the absorption profiles in terms of the four-orbital model, wherein the positions and intensities of the spectral features are related to linear combinations of simple one-electron promotions between the MOs. The four-orbital analysis provides simple guidelines as to how substituent patterns generally affect spectral properties; such insights give a general perspective of the spectral properties of the photosynthetic pigments and are useful from a molecular-design perspective.

Spectral and photophysical properties

General observations. Electronic ground-state absorption spectra of the new chlorins and oxophorbines (Chart 2), relevant analogs studied previously (Chart 3), and native chromophores (Figure 1) are shown in Figure 2. Each spectrum contains four main features with maxima that range approximately as follows: $Q_y(0,0)$ (598–670 nm), $Q_x(0,0)$ (520–560 nm) and overlapping $B_x(0,0)$ and $B_y(0,0)$ (the Soret bands; 390–440 nm). These bands reflect optical transitions from the ground state S_0 to excited states S_1, S_2, S_3, and S_4, respectively. Weaker (1,0) features are often seen roughly 1300 cm^{-1} to shorter wavelength than the origin bands. Note that the Soret region also appears to contain contributions from additional transitions, and that the relative wavelength ordering of the $B_x(0,0)$ and $B_y(0,0)$ features may differ among compounds (and the bands may not be of strictly pure x- and y-polarization). The spectra in Figure 2 show that the

$B_x(0,0)$ and $B_y(0,0)$ are coalesced into one feature (and similarly for the weaker $B_x(1,0)$ and $B_y(1,0)$ when resolved) for the sparsely substituted zinc chlorins (e.g., **ZnC**, **ZnC-F^{7}T^{10}**, **ZnC-M^{10}F^{13}**). Reflecting a progressive decrease in symmetry, the splitting of the B_x and B_y components increases as the number of substituents is increased for the zinc chlorins (e.g., **ZnC-F^{3}M^{10}F^{13}**), for the free base chlorins, and for the oxophorbines. Figure 3 shows representative fluorescence spectra. The emission spectra are dominated by the $Q_y(0,0)$ band, with weaker vibronic features to longer wavelengths. Peak absorption and fluorescence positions are listed in Tables 1 and 2. The wavelength of the Soret maximum (B_{max}) for each compound may reflect the $B_x(0,0)$, $B_y(0,0)$ or a combined feature.

Tables 1 and 3 list the measured fluorescence yields (Φ_f) and singlet excited-state lifetimes (τ_S). These observables are connected via the relationships $\tau_S = (k_f + k_{ic} + k_{isc})^{-1} = (k_f + k_{nr})^{-1}$ and $\Phi_f = k_f \bullet \tau_S$, which contain the rate constants for the decay pathways of the S_1 excited state (the Q_y state). The rate constants are for $S_1 \rightarrow S_0$ fluorescence (k_f), $S_1 \rightarrow S_0$ internal conversion (k_{ic}), and $S_1 \rightarrow T_1$ intersystem crossing (k_{isc}). The sum of the two nonradiative rate constants (k_{ic} and $k_{isc,}$) is denoted k_{nr}. The inverses of the values of k_f and k_{nr} (in units of ns) derived from the observed τ_S and Φ_f values are also listed as the last two columns in Tables 1 and 3. The relationships of the Einstein coefficients (42) indicate that a greater radiative rate constant for spontaneous fluorescence (k_f) implies an increased oscillator strength for the corresponding $S_1 \rightarrow S_0$ (i.e., Q_y) absorption transition. In turn, trends in the $Q_y(0,0)$ absorption intensity with substituent or macrocycle type are generally reflected in the $B/Q_y(0,0)$ peak intensity ratio, and similarly in the integrated intensities of the B and Q manifolds (origin plus vibronic features). These absorption-intensity ratios are listed in Tables 1 and 2.

Table 1. Spectral and Photophysical Properties of Synthetic and Native Chromophores.[a]

Compound	Source[b]	B_{max} abs (nm)	$Q_y(0,0)$ abs (nm)	$Q_y(0,0)$ emis (nm)	I_B/I_{Q_y}[c]	Σ_B/Σ_{Q_y}[d]	Φ_f	τ_f (ns)	k_f^{-1} (ns)	k_{nr}^{-1} (ns)
7-chlorins										
ZnC-F^{7}T^{10}	1	429	598	601	7.0	10.5	0.029	1.1	38	1.1
ZnC-A^{7}T^{10}	1	426	598	601	6.5	10.1	0.030	1.0	33	1.0
ZnC-E^{7}T^{10}	1	421	605	608	5.7	6.3	0.039	1.3	33	1.4
ZnC-T^{10}	1	405	605	608	4.2	3.9	0.057	1.6	28	1.7
7-oxophorbines										
FbOP-F^{7}M^{10}	1	441	653	655	4.6	6.5	0.17	9.0	53	11
FbOP-A^{7}M^{10}	1	439	654	656	4.1	6.1	0.17	9.4	55	11
FbOP-E^{7}M^{10}	1	434	660	662	2.7	6.0	0.28	13.2	47	18
3,12,13-chlorins										
ZnC-F^{3}M^{10}F^{13}	1	439	667	672	1.4	2.2	0.31	6.3	20	9.1
ZnC-M^{10}F^{13}	1	418	633	637	2.0	2.9	0.25	5.3	21	7.1
ZnC-M^{10}Es^{13}	1	415	627	630	2.4	3.4	0.24	4.8	20	6.3
FbC-M^{10}Es^{13}	1	405	653	656	1.9	5.2	0.29	9.8	34	14
ZnC-A^{13}	1	411	627	631	1.9	2.5	0.23	4.3	19	5.6
ZnC-A^{12}	1	418	636	641	1.8	2.4	0.19	4.4	23	5.4
prior chlorins										
ZnC	2	398	602	604	3.4	4.1	0.057	1.5	26	1.6
ZnC-P^{10}	2	404	605	608	4.1	4.7	0.060	1.5	28	1.7
ZnC-M^{10}	2	405	606	608	4.3	4.4	0.060	1.5	28	1.7
ZnC-T^{5}	2	405	605	608	4.2	4.2	0.060	1.6	28	1.7
ZnC-P^{15}	2	403	607	609	3.6	4.1	0.069	1.6	28	1.7
ZnC-V^{3}M^{10}	2	412	620	624	3.4	3.6	0.075	1.8	1.9	19
ZnC-M^{10}E^{13}	2	412	625	628	2.2	3.0	0.18	3.0	17	3.7
ZnC-M^{10}A^{13}	2	418	632	635	2.2	3.1	0.24	5.1	21	6.7
ZnC-E^{3}M^{10}E^{13}	2	423	646	649	1.6	2.5	0.23	4.1	18	5.3
ZnC-A^{3}M^{10}A^{13}	2	436	662	668	1.5	2.2	0.32	6.0	19	8.8
FbC	2	389	633	635	2.4	5.2	0.20	9.4	47	12
ZnC-E^{3}E^{13}	3	416	643	646	1.3	2.2	0.23	3.7	16	4.8
ZnC-E^{3}E^{12}	3	420	645	648	1.5	2.2	0.18	3.1	17	3.8
ZnC-E^{3}A^{13}	3	420	648	652	1.3	2.2	0.24	4.6	19	6.1
ZnC-E^{3}A^{12}	3	428	655	659	1.2	2.0	0.22	4.1	19	5.3

FbC-M^{10}	2	396	637	639	2.7	7.2	0.22	10.0	45	13
FbC-P^{10}	2	403	636	638	2.8	7.8	0.20	9.7	49	12
FbC-T^{5}	2	402	636	638	2.9	8.1	0.22	10.0	45	13
FbC-P^{15}	2	394	638	640	2.7	6.8	0.17	9.4	55	11
FbC-M^{10}E^{13}	2	418	654	656	1.6	5.0	0.30	9.8	33	14
prior oxophorbines										
ZnOP	4	419	637	639	1.6	2.4	0.23	5.1	22	6.6
FbOP	4	408	654	656	1.5	4.1	0.30	11.5	38	16
FbOP-M^{10}	5	413	656	659	1.7	4.4	0.32	13.0	41	19
FbOP-A^{3}M^{10}	5	446 [e]	683	686	1.3	3.5	0.26	10.9	42	15
native chromophores										
Chl *a*	4	432	665	671	1.3	1.6	0.33	6.2	19	9.2
Chl *b*	1	458	646	651	2.7	3.1	0.19	3.4	18	4.2
Chl *d*	1	449	692	697	1.0	2.9	0.24	6.7	28	8.8
Pheo *a*	1	415	671	676	2.0	3.8	0.24	7.6	32	10
Pheo *b*	1	439	657	662	4.6	6.1	0.15	7.5	50	8.8
Pheo *d*	1	428	697	702	1.4	4.0	0.16	6.5	41	7.7

[a] All data at room temperature in toluene unless noted otherwise.

[b] Source of the original data. (1) this study; (2) Ref 21; (3) Ref 22; (4) Ref 26; (5) Ref 34. Some of the Φ_f and τ_S values from Ref 21 were changed (by <15%) to reflect averaging with additional repeat measurements (including using a second technique for the τ_S measurements as noted in Materials and Methods).

[c] Ratio of the peak intensities of the $Q_y(0,0)$ band to the Soret (B) maximum, which could be either the $B_y(0,0)$ or $B_x(0,0)$ band.

[d] Ratio of the integrated intensities of the Q_y manifold [$Q_y(0,0)$, $Q_y(1,0)$] to the Soret manifold [$B_y(0,0)$, $B_y(1,0)$, $B_x(0,0)$, $B_x(1,0)$], for spectra plotted in cm^{-1}.

[e] Two peaks with comparable intensity are observed at 427 and 446 nm.

Table 2. Comparisons of Spectral Properties of New Compounds, Analogues Studied Previously and Native Chromophores.[a]

Entry	Compound	Source[b]	Δ reference[c]	B_{max}			$Q_y(0,0)$			I_B/I_{Q_y}		ΣB/ΣQ	
				λ (nm)	Δλ (nm)	Δν (cm^{-1})	λ (nm)	Δλ (nm)	Δν (cm^{-1})	value	Δ %	value	Δ %
1	**ZnC**	2		398			602			3.4		4.1	
2	**ZnC-T^{10}**	1	**ZnC**	405	7	–434	605	3	–82	4.2	24	3.9	-5
3	**ZnC-M^{10}**	2	**ZnC**	405	7	–434	606	4	–110	4.3	26	4.4	7
4	**ZnC-P^{10}**	2	**ZnC**	404	6	–373	605	3	–82	4.1	21	4.7	15
5	**ZnC-T^{5}**	2	**ZnC**	405	7	–434	605	3	–82	4.2	24	4.2	2
6	**ZnC-P^{15}**	2	**ZnC**	403	5	–312	607	5	–137	3.6	6	4.1	0
7	**ZnC-F^{7}T^{10}**	1	**ZnC-T^{10}**	429	24	–1381	598	-7	193	7.0	67	11	169
8	**ZnC-A^{7}T^{10}**	1	**ZnC-T^{10}**	426	21	–1217	598	-7	193	6.5	55	10	159
9	**ZnC-E^{7}T^{10}**	1	**ZnC-T^{10}**	421	16	–938	605	0	0	5.7	36	6.3	62
10	**ZnC-V^{3}M^{10}**	2	**ZnC-M^{10}**	412	7	–420	620	14	–373	3.4	–21	3.6	-18
11	**ZnC-M^{10}F^{13}**	1	**ZnC-M^{10}**	418	13	–768	633	27	–704	2.0	–53	2.9	-34
12	**ZnC-M^{10}A^{13}**	2	**ZnC-M^{10}**	418	13	–768	632	26	–679	2.2	–49	3.1	-30
13	**ZnC-M^{10}E^{13}**	2	**ZnC-M^{10}**	412	7	–420	625	19	–502	2.2	–49	3.0	-32
14	**ZnC-M^{10}Es^{13}**	1	**ZnC-M^{10}**	415	10	–595	627	21	–553	2.4	–44	3.4	-23
15	**ZnC-F^{3}M^{10}F^{13}**	1	**ZnC-M^{10}F^{13}**	439	21	–1144	667	34	–805	1.4	–30	2.2	-24
16	**ZnC-A^{3}M^{10}A^{13}**	2	**ZnC-M^{10}A^{13}**	436	18	–988	662	30	–717	1.5	–32	2.2	-29
17	**ZnC-E^{3}M^{10}E^{13}**	2	**ZnC-M^{10}E^{13}**	423	11	–631	646	21	–520	1.6	–27	2.5	-17
18	**ZnC-E^{3}E^{13}**	3		416			643			1.3		2.2	
19	**ZnC-E^{3}E^{12}**	3	**ZnC-E^{3}E^{13}**	420	4	–229	645	2	–48	1.5	15	2.2	0
20	**ZnC-E^{3}A^{13}**	3		420			648			1.3		2.2	
21	**ZnC-E^{3}A^{12}**	3	**ZnC-E^{3}A^{13}**	428	8	–445	655	7	–165	1.2	–8	2.0	–9

22	**ZnC-A^{13}**	1	**ZnC**	411	13	–795	627	25	–662	1.9	–44	2.5	–39
23	**ZnC-A^{12}**	1	**ZnC-A^{13}**	418	7	–407	636	9	–226	1.8	–5	2.4	–4
24	**ZnOP**	4	**ZnC**	419	21	–1259	637	35	–913	1.6	–53	2.4	-41
25	**FbC**	2		389			633			2.4		5.2	
26	**FbC-M^{10}**	2	**FbC**	396	7	–454	637	4	–99	2.7	13	7.2	38
27	**FbC-P^{10}**	2	**FbC**	403	14	–893	636	3	–75	2.8	17	7.8	50
28	**FbC-T^{5}**	2	**FbC**	402	13	–831	636	3	–75	2.9	21	8.1	56
29	**FbC-P^{15}**	2	**FbC**	394	5	–326	638	5	–124	2.7	13	6.8	31
30	**FbC-M^{10}E^{13}**	2	**FbC-M^{10}**	418	22	–1329	654	17	–408	1.6	–41	5.0	-31
31	**FbC-M^{10}Es^{13}**	1	**FbC-M^{10}**	405	9	–561	653	16	–385	1.9	–30	5.2	-28
32	**FbOP**	4	**FbC**	408	19	–1197	654	21	–507	1.5	–38	4.1	-21
33	**FbOP-M^{10}**	5	**FbOP**	413	5	–297	656	2	–47	1.7	13	4.4	7
34	**FbOP-F^{7}M^{10}**	1	**FbOP-M^{10}**	441	28	–1537	653	–3	70	4.6	171	6.5	48
35	**FbOP-A^{7}M^{10}**	1	**FbOP-M^{10}**	439	26	–1434	654	–2	47	4.1	141	6.1	39
36	**FbOP-E^{7}M^{10}**	1	**FbOP-M^{10}**	434	21	–1172	660	4	–92	2.7	59	6.0	36
37	**FbOP-A^{3}M^{10}**	5	**FbOP-M^{10}**	446	33	–1792	683	27	–603	1.3	–24	3.5	-20
38	**Chl *a***	1	**ZnOP**	432	13	–718	665	28	–661	1.3	–19	1.6	–33
39	**Chl *b***	1	**Chl *a***	458	26	–1314	646	–19	442	2.7	108	3.1	94
40	**Chl *d***	1	**Chl *a***	449	17	–876	692	27	–587	1.0	–23	2.9	81
41	**Pheo *a***	1	**FbOP**	415	7	–413	671	17	–387	2.0	33	3.8	–7
42	**Pheo *b***	1	**Pheo *a***	439	24	–1317	657	–14	318	4.6	130	6.1	61
43	**Pheo *d***	1	**Pheo *a***	428	13	–732	697	26	–556	1.4	–30	4.0	5

[a] All data at room temperature in toluene unless noted otherwise.
[b] Source of the original data. (1) This study; (2) Ref 21; (3) Ref 22; (4) Ref 26; (5) Ref 34.
[c] The reference compound used for calculation of the Δ values for each of the spectral and photophysical parameters.

Table 3. Comparisons of Photophysical Properties of New Compounds, Analogues Studied Previously and Native Chromophores.[a]

Entry	Compound	Source[b]	Δ reference[c]	Φ_f		τ_f		k_f^{-1}		k_{nr}^{-1}	
				value	Δ %	value (ns)	Δ %	value (ns)	Δ %	Value (ns)	Δ %
1	**ZnC**	2		0.057		1.5		26		1.6	
2	**ZnC-T^{10}**	1	**ZnC**	0.057	0	1.6	7	28	8	1.7	6
3	**ZnC-M^{10}**	2	**ZnC**	0.060	5	1.5	0	25	–4	1.6	0
4	**ZnC-P^{10}**	2	**ZnC**	0.060	5	1.5	0	25	–4	1.6	0
5	**ZnC-T^{5}**	2	**ZnC**	0.060	5	1.6	7	27	4	1.7	6
6	**ZnC-P^{15}**	2	**ZnC**	0.069	21	1.6	7	23	–12	1.7	6
7	**ZnC-F^{7}T^{10}**	1	**ZnC-T^{10}**	0.029	–49	1.1	–31	38	36	1.1	–35
8	**ZnC-A^{7}T^{10}**	1	**ZnC-T^{10}**	0.030	–47	1.0	–38	33	18	1.0	–41
9	**ZnC-E^{7}T^{10}**	1	**ZnC-T^{10}**	0.039	–32	1.3	–19	33	18	1.4	–18
10	**ZnC-V^{3}M^{10}**	2	**ZnC-M^{10}**	0.075	25	1.8	20	24	–4	1.9	19
11	**ZnC-M^{10}F^{13}**	1	**ZnC-M^{10}**	0.25	317	5.3	253	21	–16	7.1	344
12	**ZnC-M^{10}A^{13}**	2	**ZnC-M^{10}**	0.24	300	5.1	240	21	–16	6.7	319
13	**ZnC-M^{10}E^{13}**	2	**ZnC-M^{10}**	0.18	200	3.0	100	17	–32	3.7	131
14	**ZnC-M^{10}Es^{13}**	1	**ZnC-M^{10}**	0.24	300	4.8	220	20	–20	6.3	294
15	**ZnC-F^{3}M^{10}F^{13}**	1	**ZnC-M^{10}F^{13}**	0.31	24	6.3	19	20	–5	9.1	28
16	**ZnC-A^{3}M^{10}A^{13}**	2	**ZnC-M^{10}A^{13}**	0.32	33	6.0	18	19	–10	8.8	31
17	**ZnC-E^{3}M^{10}E^{13}**	2	**ZnC-M^{10}E^{13}**	0.23	28	4.1	37	18	6	5.3	43
18	**ZnC-E^{3}E^{13}**	3		0.23		3.7		16		4.8	
19	**ZnC-E^{3}E^{12}**	3	**ZnC-E^{3}E^{13}**	0.18	–22	3.1	–16	17	6	3.8	–21
20	**ZnC-E^{3}A^{13}**	3		0.24		4.6		19		6.1	
21	**ZnC-E^{3}A^{12}**	3	**ZnC-E^{3}A^{13}**	0.22	–8	4.1	–11	19	0	5.3	–13

22	**ZnC-A^{13}**	1	**ZnC**	0.23	304	4.3	187	19	–29	5.6	251
23	**ZnC-A^{12}**	3	**ZnC-A^{13}**	0.19	–17	4.4	2	23	24	5.4	–4
24	**ZnOP**	4	**ZnC**	0.23	304	5.1	240	22	–15	6.6	313
25	**FbC**	2		0.20		9.4		47		12	
26	**FbC-M^{10}**	2	**FbC**	0.22	10	10	6	45	–4	13	8
27	**FbC-P^{10}**	2	**FbC**	0.20	0	9.7	3	49	4	12	0
28	**FbC-T^{5}**	2	**FbC**	0.22	10	10	6	45	–4	13	8
29	**FbC-P^{15}**	2	**FbC**	0.17	–15	9.4	0	55	17	11	–8
30	**FbC-M^{10}E^{13}**	2	**FbC-M^{10}**	0.30	36	9.8	–2	33	–27	14	8
31	**FbC-M^{10}Es^{13}**	1	**FbC-M^{10}**	0.29	32	9.8	–2	34	–24	14	8
32	**FbOP**	4	**FbC**	0.30	50	12	22	38	–19	16	33
33	**FbOP-M^{10}**	5	**FbOP**	0.32	7	13	13	41	8	19	19
34	**FbOP-F^{7}M^{10}**	1	**FbOP-M^{10}**	0.17	–47	9.0	–31	53	29	11	–42
35	**FbOP-A^{7}M^{10}**	1	**FbOP-M^{10}**	0.17	–47	9.4	–28	55	34	11	–42
36	**FbOP-E^{7}M^{10}**	1	**FbOP-M^{10}**	0.28	–13	13	2	47	15	18	–5
37	**FbOP-A^{3}M^{10}**	5	**FbOP-M^{10}**	0.26	–19	11	–16	42	2	15	–21

38	**Chl *a***	1	**ZnOP**	0.33	41	6.2	22	19	–14	9.2	39
39	**Chl *b***	1	**Chl *a***	0.19	–42	3.4	–45	18	–6	4.2	–54
40	**Chl *d***	1	**Chl *a***	0.24	–26	6.7	8	28	46	8.8	-4
41	**Pheo *a***	1	**FbOP**	0.24	–20	7.6	–34	32	–17	10	–39
42	**Pheo *b***	1	**Pheo *a***	0.15	–85	7.5	–1	50	58	8.8	–12
43	**Pheo *d***	1	**Pheo *a***	0.16	–33	6.5	–14	41	28	7.7	–23

[a] All data at room temperature in toluene unless noted otherwise.

[b] Source of the original data. (1) this study; (2) Ref 21; (3) Ref 22; (4) Ref 26; (5) Ref 34. Some of the Φ_f and τ_S values from Ref 21 were changed (by <15%) to reflect averaging with additional repeat measurements (including using a second technique for the τ_S measurements as noted in Materials and Methods).

[c] The reference compound used for calculation of the Δ values for each of the spectral and photophysical parameters.

In the following subsections, comparisons are made concerning the effects of different substituents at various positions of the chlorin and oxophorbine macrocycles. Note that the spectral data presented in Table 1 are also given in Table 2, which includes comparisons with the most suitable benchmark for each set of compounds. Such data aid assessment of the impact of peripheral substituents on the spectral characteristics (λ_{max} values and intensity ratios) of a given compound relative to the benchmark. Table 3 is similarly designed to aid in quantitation of the substituent effects on the photophysical properties (Φ_f, τ_S, k_f, k_{nr}).

Effects of meso-aryl groups. For synthetic utility, construction of chlorins and oxophorbines studied here (Chart 2) and close analogs studied previously (21) generally contained a 10-aryl group [*p*-tolyl (T), mesityl (M), phenyl (P)] that may differ for the various sets of compounds (e.g., sets **ZnC-X^{7}T^{10}** and **FbOP-X^{7}M^{10}** with variable 7-substituent X) (Chart 3). Aryl groups have been similarly placed at the other (e.g., 5, 15) meso-positions (21,22,34). A key result is that essentially the same properties are found for a given macrocycle and pattern of β-pyrrole substituents independent of the nature and location of a single meso-aryl group (Tables 2 and 3; entries 2–6 and 26–29). For example, **ZnC-T^{10}** reported here and analogs studied previously bearing a 10-mesityl, 5-*p*-tolyl, or 5-phenyl group have the same $Q_y(0,0)$ position within 2 nm (e.g., **ZnC-T^{10}** and **ZnC-M^{10}** in Figures 2A and D), and Φ_f and τ_s values that differ by <10%. Thus, the nature of the 10-aryl group is irrelevant in comparisons given below concerning the effects of substituents at different β-pyrrole positions, or comparisons of chlorins or oxophorbines, either zinc chelates or free base forms.

Furthermore, on an absolute basis, the addition of one meso-aryl ring (for synthetic utility) causes only minor perturbations to the photophysical characteristics relative to the parent chlorins (**ZnC** or **FbC**) or oxophorbines (**ZnOP** or **FbOP**) (Tables 2 and 3; entries 1–6, 25-29,

32 and 33). The parent compounds lack any peripheral substituents other than the geminal dimethyl group. The spectral manifestations for the zinc chlorins include a small (typically 3-4 nm) bathochromic shift of $Q_y(0,0)$, a modest (~25%) decrease in $Q_y(0,0)$ intensity relative to the Soret (*e.g.* **ZnC-T^{10}** versus **ZnC**; Figure 2A), and <10% effects on Φ_f and τ_s (Tables 2 and 3). Collectively, these results show that the impacts of a single meso-aryl group are sufficiently small that they can be effectively ignored in making comparisons of synthetic chlorophyll analogs (e.g., bearing a 10-substituent) with the native photosynthetic pigments, which generally lack meso-substituents.

Impact of a 7-formyl group in free base oxophorbine. The absorption spectra in Figures 2B and 2C and the data listed in Table 2 show that incorporation of a 7-formyl group in a synthetic oxophorbine has significant spectral manifestations. Quantitation of the effects with the synthetic compounds entails a two-step process. First, in keeping with the above-noted points, the addition of a 10-mesityl group to the parent **FbOP** to form **FbOP-M^{10}** has relatively small effects, which include a 2 nm (–47 cm^{-1}) bathochromic shift (654 to 656 nm) of $Q_y(0,0)$ and a 13% increase of the B/Q_y peak-intensity ratio (Figure 2B and Table 2 entry 33). Subsequent addition of the 7-formyl group to produce **FbOP-F^{7}M^{10}** gives an opposing (hypsochromic) shift in $Q_y(0,0)$ (656 to 653 nm; –3 nm; 70 cm^{-1}) and a substantial (171%) increase in the B/Q_y peak-intensity ratio, namely a relative decrease in the $Q_y(0,0)$ intensity (Table 2 entry 34). Turning to other photophysical properties, the Φ_f and τ_S values for **FbOP-M^{10}** (0.32, 13.0 ns) are slightly larger than those for **FbOP** (0.30, 11.5 ns) and then decrease substantially upon addition of the 7-formyl group to give **FbOP-F^{7}M^{10}** (0.17, 9.0 ns) (Table 3 entry 34). The latter diminution in Φ_f and τ_S can be traced in part to the diminution in k_f, which in turn reflects the hypochromic effect on the $Q_y(0,0)$ absorption due to incorporation of the 7-

formyl group (Table 2).

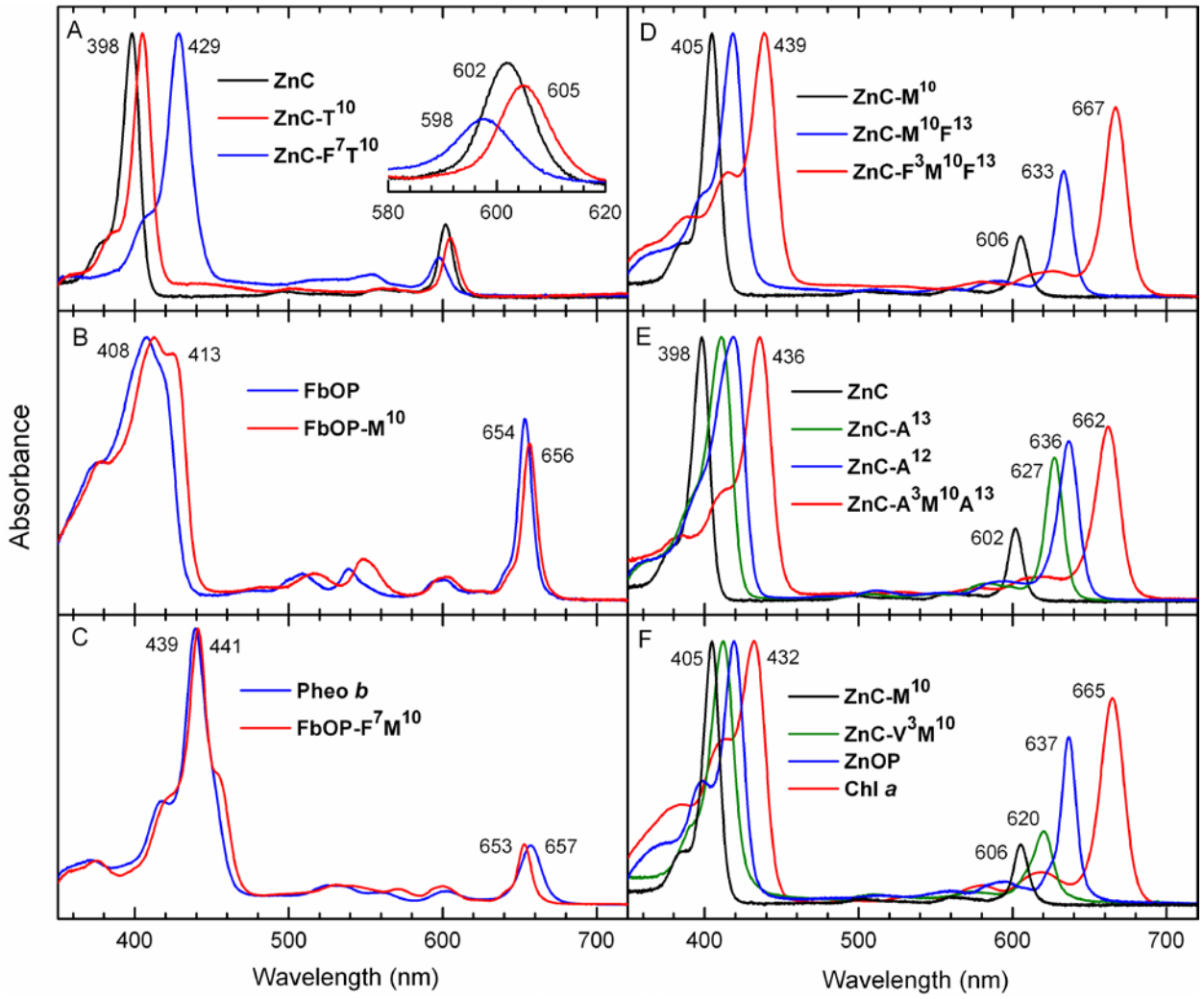

Figure 2. Absorption spectra of selected chlorins and oxophorbines.

Figure 2C also shows that the spectrum of synthetic oxophorbine **FbOP-F^{7}M^{10}** is remarkably close to that of the native chromophore **Pheo *b***, except that the latter has slightly longer wavelength Soret and $Q_y(0,0)$ absorption maxima. The photophysical properties of **FbOP-F^{7}M^{10}** ((Φ_f = 0.17, τ_S = 9.0 ns) are also reasonably close to those of **Pheo *b*** (Φ_f = 0.15 and τ_S = 7.5 ns). The 10-mesityl group of **FbOP-F^{7}M^{10}** has little impact on these comparisons (Figure 2B and Tables 2 and 3). The results indicate that starting with the parent chlorin (**FbC**),

incorporation of the keto-containing 5-membered ring (ring E; Chart 2) followed by the 7-formyl group gives a close spectral representation of the native chromophore (26). On the basis of prior results (21) for **ZnC-V^{3}M^{10}** versus **ZnC-M^{10}** (Figure 2F), the addition of a 3-vinyl group to **FbOP-F^{7}M^{10}** would be expected to give an almost perfect spectral match with **Pheo *b***. Similarly, the data in Figure 2F (and Table 2) suggest (26) that the combination of the keto-bearing 5-membered ring and a 3-vinyl group alone in the corresponding metal chelate should give a close spectral match with **Chl *a***, which lacks the 7-formyl group.

Nature of the 7-substituent. The spectral and photophysical properties engendered by different 7-substituents were examined for a set of free base oxophorbines **FbOP-X^{7}M^{10}** and a set of zinc chlorins **ZnC-X^{7}T^{10}**, where the substituent X is formyl (F), acetyl (A), or ethynyl (E). Consider the spectral effects for the two sets (each referenced to the relevant 7-unsubstituted benchmark) given by entries 7-9 and 34-36, respectively, in Table 2. The bathochromic shift in the Soret band (B_{max}) increases in the order ethynyl < acetyl < formyl, with acetyl closer to formyl than ethynyl for both sets. The shifts are 16, 21 and 24 nm (–938, –1217 and –1381 cm^{-1}) for the **ZnC-X^{7}T^{10}** series, and 21, 26, and 28 nm (–1172, –1434 and –1537 cm^{-1}) for the **FbOP-X^{7}M^{10}** series. Turning to the $Q_y(0,0)$ band, for **ZnC-X^{7}T^{10}** ethynyl gives no shift whereas acetyl and formyl both give a 7 nm (193 cm^{-1}) hypsochromic shift; for **FbOP-X^{7}M^{10}** ethynyl gives a 4 nm (–92 cm^{-1}) bathochromic shift whereas acetyl and formyl give hypsochromic shifts of 2 nm (47 cm^{-1}) and 3 nm (70 cm^{-1}). For both sets, the peak-intensity ratio of the Soret and $Q_y(0,0)$ bands (I_B/I_{Qy} in Table 2) increases along the series ethynyl < acetyl < formyl. The percent increases from the 7-unsubstituted benchmark are 36%, 55%, and 67% for the **ZnC-X^{7}T^{10}** series, and 59%, 141%, and 171% for the **FbOP-X^{7}M^{10}** series. Turning to the photophysical properties, with a few exceptions the Φ_f and τ_S are reduced 20-50% from the

values for the benchmark lacking a 7-substituent.

Effect of a 13- versus 7-formyl substituent. A 13-formyl group has dramatically different effects than a 7-formyl group. This point can be seen from the data for the addition of a 13-formyl group to **ZnC-M^{10}** to give **ZnC-M^{10}F^{13}** versus those described above for the addition of a 7-formyl group to **ZnC-T^{10}** to give **ZnC-F^{7}T^{10}** (entries 11 versus 7 in Tables 2 and 3). Spectral distinctions are shown in Figures 2D versus 2A. The 13- versus 7-formyl group gives a smaller bathochromic shift in B_{max} [13 nm (–768 cm^{-1}) versus 24 nm (–1381 cm^{-1})], a bathochromic shift in $Q_y(0,0)$ [27 nm (–704 cm^{-1})] versus a hypsochromic shift [-7 nm (193 cm^{-1})], a decrease (53%) versus an increase (67%) in the B/Q_y peak-intensity ratio, and a corresponding decrease (34%) versus an increase (169%) in the B/Q_y integrated-intensity ratio. Stated differently, a 13-formyl group gives an increase in the relative $Q_y(0,0)$ intensity along with a shift of the band to longer wavelength whereas the 7-formyl group causes just the opposite effects on both $Q_y(0,0)$ intensity and wavelength.

The differences extend to the photophysical characteristics. While a 13-formyl group increases Φ_f from 0.060 to 0.25 and τ_S from 1.5 ns to 5.3 ns, the opposite derives from a 7-formyl group, namely decreases in Φ_f from 0.057 to 0.029 and τ_S from 1.6 ns to 1.1 ns (entries 11 and 7 of Table 3). The differential effects of 13- versus 7-formyl groups result in part from a 16% increase versus a 36% decrease in k_f, consistent [via the relationships of the Einstein coefficients (42)] with the above-noted effects on the relative $Q_y(0,0)$ absorption intensities. A 13- versus 7-formyl group gives rise to a decrease versus an increase in the overall nonradiative decay rate constant $k_{nr} = (k_{ic} + k_{isc})$ of the Q_y (i.e., S_1) excited state (Table 3). The energy-gap law for nonradiative decay (42) would suggest that the $S_1 \rightarrow S_0$ internal conversion should show the opposite effect because of the lower excited-state energy with 13- versus 7-formyl. Thus, the

differential effect on k_{nr} is likely associated mainly with $S_1 \rightarrow T_1$ intersystem crossing, and in particular how a formyl group at the two positions leads to a difference in the electron-density distribution in the molecule. The latter point is addressed below in the context of the MO calculations. Collectively, these observations underscore the broad, profoundly different consequences of a formyl group at the 13- versus 7-positions of the chlorin macrocycle. The same is true, but with smaller impacts, for other auxochromes at the two positions. The latter point is illustrated by comparisons given in the next subsection.

Formyl versus other groups at the 13-position. With zinc chlorin **ZnC-M^{10}F^{13}** in hand, trends in properties with 13-substituents analogous to those given above for the 7-position can be made with the same groups (formyl, acetyl, ethynyl). Such comparisons make use of compounds **ZnC-M^{10}A^{13}** and **ZnC-M^{10}E^{13}** studied previously (20,21) and can be extended to include the 13-ester analog **ZnC-M^{10}Es^{13}** characterized here and oxophorbine **ZnOP** studied previously (26), which contains the 13-keto group integral to ring E (Chart 1). The properties of these compounds (each with respect to the appropriate reference) are given under entries 11-14 and 24 of Tables 2 and 3. The tables also list data for several free base analogs including **FbC-M^{10}Es^{13}** characterized here (entries 30–31). The main findings are as follows:

(1) Acetyl or ethynyl at the 13-position results in substantial differences from the same group at the 7-position, analogous to the above-noted differences for formyl.

(2) In analogy with the results for the 7-position, the impact of a 13-substituent on spectral properties generally follows the trend: ethynyl < acetyl < formyl, with the effect of acetyl being closer to formyl than ethynyl.

(3) Formyl and acetyl groups at the 13-position have comparable effects on Φ_f and τ_S.

(4) A 13-ester group has somewhat smaller effects on spectral and photophysical

properties than a 13-acetyl group.

(5) Starting with the parent chlorin, addition of the keto-containing 5-membered ring to give the oxophorbine engenders spectral changes that are slightly larger than 13-formyl, and changes in excited-state properties (Φ_f and τ_S) that are slightly smaller and closer to the effects of 13-acetyl (entries 11, 12, and 24 in Tables 2 and 3).

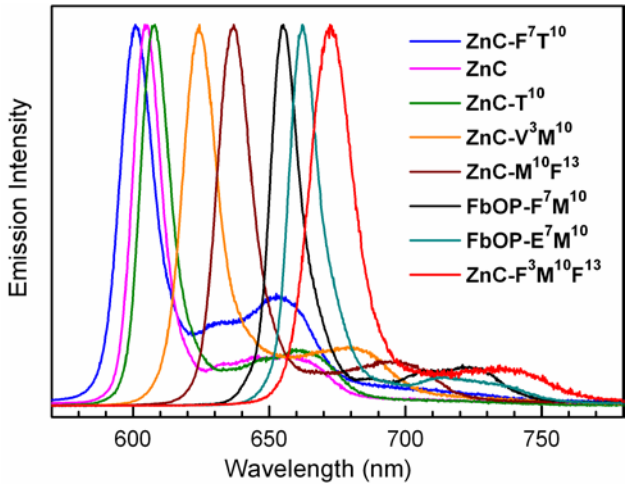

Figure 3. Fluorescence spectra of selected chlorins and oxophorbines.

Formyl versus other substituents at the 3-position. Assessment of the properties of **ZnC-F^{3}M^{10}F^{13}** versus **ZnC-M^{10}F^{13}** (entries 15 and 11 of Tables 2 and 3) gives insight into the effect of a 3-formyl group, just as the above comparison of the latter compound (**ZnC-M^{10}F^{13}**) versus **ZnC-M^{10}** reveals the effect of a 13-formyl group. The spectral evolution for this trio of chlorins is shown in Figure 2D. The collective data allow comparisons with analogous sets studied previously (21), namely **ZnC-A^{3}M^{10}A^{13}** versus **ZnC-M^{10}A^{13}** versus **ZnC-M^{10}** for acetyl and **ZnC-E^{3}M^{10}E^{13}** versus **ZnC-M^{10}E^{13}** versus **ZnC-M^{10}** for ethynyl (entries 16/12 and 17/13 in Tables 2 and 3). The main results for addition of a 3-substituent to give a 3,13-disubstituted zinc chlorin are as follows:

(1) Paralleling the results described above for the 7- and 13-positions, formyl at the 3-

position has a somewhat greater impact than acetyl which in turn has a more substantial impact than ethynyl.

(2) For each group, addition of the 3-substituent to give a 3,13-substituted complex generally has a greater impact on spectral properties than for the 13-substiutent. For example, comparing **ZnC-F^{3}M^{10}F^{13}** (referenced to **ZnC-M^{10}F^{13}**) versus **ZnC-M^{10}F^{13}** (referenced to **ZnC-M^{10}**), the former has a larger bathochromic shift in B_{max} [21 nm (–1144 cm^{-1}) versus 13 nm (–768 cm^{-1})] and a larger bathochromic shift in $Q_y(0,0)$ [34 nm (–805 cm^{-1}) versus 27 nm (–704 cm^{-1})]. Analogous results are found for the acetyl- and ethynyl-substituted chlorins (Table 2).

(3) Comparison of the above results with those obtained previously (20,21) for **ZnC-V^{3}M^{10}** versus **ZnC-M^{10}** (Table 2 entry 10) indicates that a 3-formyl (or 13-formyl) group gives larger bathochromic shifts in the Soret and Q_y bands than a 3-vinyl group.

(4) The spectral consequences of a 3-substituent parallel those for a 13-substituent (bathochromic shifts in Soret and Q_y, and decrease in the B/Q_y intensity ratio) in being profoundly different than for a 7-substituent (bathochromic shift in Soret, hypsochromic shift in Q_y and increase in the B/Q_y intensity ratio). The comparative properties of the synthetic chlorins (and oxophorbines) thus mimic the similar functionally significant differences in spectral properties of **Chl *d*** versus **Chl *a*** (formyl versus vinyl at the 3-position) and **Chl *b*** versus **Chl *a*** (formyl versus methyl at the 7-position), as shown in Figure 1.

(5) It was noted above concerning the spectra in Figure 2F (and the data in Table 2) that the addition of a keto-bearing 5-membered ring to a zinc chlorin to form the corresponding 13^{1}-oxophorbine (**ZnOP**) plus the addition of a 3-vinyl group will be expected to give a close spectral match with **Chl *a***, which bears both of these structural elements (in addition to many others; Figure 1). Comparison of Figures 2D-F also reveals that the $Q_y(0,0)$ bands of **ZnC-**

F^{3}M^{10}F^{13} and **ZnC-A^{3}M^{10}A^{13}** lie at wavelengths 2-3 nm longer and shorter, respectively than that of **Chl *a***, and the Soret bands are only 4-8 nm longer. Thus these two synthetic chlorins also give a good spectral representation of **Chl *a***, and have comparable photophysical properties (τ_S ~ 6 ns, Φ_f ~ 0.3) as well. The spectral match makes sense considering the relative effects of the key substitutions along the Q_y axis (rings A and C; Chart 1), namely keto-bearing 5-membered ring > formyl > acetyl > vinyl. Thus, for applications in which a spectrum and photophysical characteristics similar to those of **Chl *a*** are required, the 3,13-disubstituted zinc chlorins provide relatively simple alternatives.

Photophysical properties of the native chromophores. The photophysical properties of the native chromophores have been investigated previously in a variety of solvents, with **Chl *a*** being the most widely studied. The ranges of values and average for τ_S (in ns) at room temperature (unless noted otherwise) are as follows: **Chl *a*** (4.6 to 7.8; average 5.9) (43–56); **Chl *b*** (3.2 to 6.3; average 4.0) (43–45,48,49,54–59); **Chl *d*** (6.2) (55); **Pheo *a*** (5.3 to 8.1; average 6.5) (48,50,56,58,60); **Pheo *b*** (7.3 at 77 K, 7.7 at 4.2 K) (56). The ranges of values and average for Φ_f at room temperature are as follows: **Chl *a*** (0.07 to 0.50; average 0.30) (36,38,44,45,48,49,61–68); **Chl *b*** (0.06 to 0.17; average 0.11) (36,44,45,49,54,57,59,61,62,64,65,67,68); **Pheo *a*** (0.11 to 0.29; average 0.20) (36,61,64,65,67–69); **Pheo *b*** (0.07 to 0.14; average 0.10) (64,65,67,68). Here we have studied all six native chromophores in the same solvent (toluene) that we have used previously (20–22,26) with the synthetic analogs in order to facilitate comparisons. The τ_S and Φ_f values that we have found here for the chromophores in toluene fall within the range of values observed previously and are in good agreement with the values in the same or similar (e.g., benzene) media where comparisons can be made. Specific comparisons are as follows.

A very important parameter for the function of the native photosynthetic chromophores is the singlet excited-state lifetime (τ_S) because the inverse of this quantity is the total intrinsic decay rate with which energy or charge transfer competes in the native antenna or reaction-center complexes. Related and of interest is the fluorescence yield (Φ_f), which is given by the product of τ_S and the radiative decay rate constant k_f. The latter can be related to the strength of the Q_y absorption manifold.

For **Chl *b*** versus **Chl *a*** versus **Chl *d***, the τ_S value is 3.4 ns versus 6.2 ns versus 6.7 ns, and the Φ_f value is 0.19 versus 0.33 versus 0.24 (entries 38–40 of Table 3). These measured quantities in turn reflect a radiative rate constant k_f of $(18\ ns)^{-1}$ versus $(19\ ns)^{-1}$ versus $(28\ ns)^{-1}$ and net (internal conversion plus intersystem crossing) nonradiative decay rate constant k_{nr} of $(4.2\ ns)^{-1}$ versus $(9.2\ ns)^{-1}$ versus $(8.8\ ns)^{-1}$. The most significant change is that **Chl *b*** has a roughly two-fold increased k_{nr} versus **Chl *a***, which results in the two-fold reduction in excited-state lifetime. The enhanced nonradiative decay is likely associated with enhanced intersystem crossing. This is so because the higher energy Q_y state of **Chl *b*** versus **Chl *a*** would be expected to decrease the contribution from internal conversion. A similar effect was described above for the incorporation of a 7-formyl group in **ZnC-T^{10}** to give **ZnC-F^{7}T^{10}** (Table 3). Again, one consideration here is the effect of the formyl group on the electron density distribution in the molecule and thus on the intersystem crossing rate.

For **Pheo *b*** versus **Pheo *a*** versus **Pheo *d***, the τ_S value is 7.5 ns versus 7.6 ns versus 6.5 ns and the Φ_f value is 0.15 versus 0.24 versus 0.16 (entries 41–43 of Table 3). These measured quantities in turn reflect radiative rate constant k_f of $(50\ ns)^{-1}$ versus $(32\ ns)^{-1}$ versus $(41\ ns)^{-1}$ and net nonradiative decay rate constant k_{nr} of $(8.8\ ns)^{-1}$ versus $(10\ ns)^{-1}$ and $(7.7\ ns)^{-1}$. Thus, the excited-state lifetimes are comparable for all three native free base chromophores and only

modestly longer than the Mg-containing chlorophyll analogs (except for **Chl *a***). The radiative rate constants are all diminished compared to the chlorophyll analogs, consistent with the reduced $Q_y(0,0)$ absorption intensity (relative to the Soret) of the pheophytins compared to the chlorophylls (Figure 1).

For a direct comparison between native and synthetic analogs it was noted above that the absorption spectrum of **Pheo *b*** is mimicked well by that of oxophorbine **FbOP-F^{7}M^{10}** except that the former has slightly longer wavelength absorption maxima (Figure 2C). The photophysical properties of **Pheo *b*** (Φ_f =0.15 and τ_S = 7.5 ns) are also mimicked reasonably well by those of **FbOP-F^{7}M^{10}** (0.17, 9.0 ns). The 10-mesityl group in the synthetic compound has little impact on photophysical properties (Figure 2B and Tables 2 and 3).

Molecular orbital characteristics

Figure 4 gives the electron-density distributions and energies of the frontier MOs of representative chlorins and 13^{1}-oxophorbines. The MOs are the highest occupied (HOMO), the lowest unoccupied (LUMO), the HOMO-1 and the LUMO+1. These four orbitals are the most relevant to the optical and photophysical characteristics of the molecules. Table 4 lists the MO energies for all new chlorins and oxophorbines studied here, selected analogs studied previously, and native chromophores to aid in the assessment of the effects of individual substituents. In this section, the effects of the nature and position of substituents on the individual frontier MOs are described. Connections to the spectral properties are analyzed in the next section. Key findings are as follows:

(1) A single meso-aryl group has only small effects on the frontier MOs for both the zinc chelates and free base forms (entries 2-6 and 26-29 in Table 4). The effects are generally

destabilizing (energy shifts to less negative values relative to **ZnC** and **FbC**, respectively). The energy shifts are ≤0.04 eV for the LUMO+1, LUMO and HOMO. The shifts are somewhat larger (up to 0.09 eV) for the HOMO-1, which places considerable electron density at the meso-positions (Figure 4).

(2) Addition of a 7-substituent to a zinc chlorin (**ZnC-X^{7}T^{10}** set; entries 7-9 in Table 4) or a free base oxophorbine (**FbOP-X^{7}M^{10}** set; entries 34-36) shifts all four MOs to more negative energies, with the degree of stabilization in the order formyl > acetyl > ethynyl.

(3) For both sets of complexes noted in point (2), the energy shift upon 7-substitution is significantly larger (by roughly two- to three-fold) for the LUMO+1 than the other three MOs. The magnitudes of the energy shifts for all three substituents (formyl, acetyl, ethynyl) for the **ZnC-X^{7}T^{10}** series (exemplified by values for **ZnC-F^{7}T^{10}** versus **ZnC-T^{10}**) decrease in the order LUMO+1 (–0.50 eV) > HOMO (–0.26 eV) > HOMO-1 (–0.19 eV) ~ LUMO (–0.18 eV). The magnitudes of the energy shifts for all three substituents for the **FbOP-X^{7}M^{10}** series (exemplified by values for **FbOP-F^{7}M^{10}** versus **FbOP-M^{10}**) decrease in the order LUMO+1 (–0.48 eV) > HOMO-1 (–0.21 eV) > HOMO (–0.18 eV) > LUMO (–0.14 eV).

(4) Addition of a 13-substituent to a zinc chlorin (**ZnC-M^{10}X^{13}** set; entries 11-14 in Table 4) shifts all four frontier MOs to more negative energies, with the degree of stabilization in the order formyl > acetyl > ester > ethynyl.

(5) The orbital stabilization for each 13-substituent in the **ZnC-M^{10}X^{13}** series noted in point (4) follows the order LUMO > HOMO > HOMO-1 ~ LUMO+1. For example, the values (in eV) are –0.37, –0.24, –0.19 and –0.19 for **ZnC-M^{10}F^{13}** and –0.30, –0.17, –0.12 and –0.13 for **ZnC-M^{10}A^{13}** (both versus **ZnC-M^{10}**).

(6) Addition of a 3-substituent (formyl, acetyl, ethynyl) to a 13-substituted zinc chlorin

(**ZnC-X^{3}M^{10}X^{13}** series; entries 15-17 in Table 4) shifts all four MOs to more negative energies, with the degree of stabilization in the order formyl > acetyl > ethynyl.

(7) The orbital stabilization (energy shifts) for each 3-substituent in the **ZnC-X^{3}M^{10}X^{13}** series noted in point (6) follows the order LUMO > LUMO+1 >HOMO > HOMO-1. For example, the values (in eV) are –0.36, –0.29, –0.21 and –0.18 for **ZnC-F^{3}M^{10}F^{13}** (versus **ZnC-M^{10}F^{13}**) and –0.27, –0.21, –0.14 and –0.10 for **ZnC-A^{3}M^{10}A^{13}** (versus **ZnC-M^{10}A^{13}**).

(8) The above-noted calculated orbital energy shifts for the addition of a 3-formyl group to **ZnC-M^{10}F^{13}** (to form **ZnC-F^{3}M^{10}F^{13}**) parallel the following values for addition of a 3-formyl group to **ZnC-M^{10}** (to form the fictive chlorin **ZnC-F^{3}M^{10}**, which has MO energies of –5.31, –5.01, –2.54, and –1.38 eV): LUMO (–0.42), LUMO+1 (–0.27), HOMO (–0.23), HOMO-1 (–0.20). For each orbital, the shift is 0.18–0.32 eV greater than those for the analogous addition of a 3-vinyl group to **ZnC-M^{10}** [to form the chlorin **ZnC-V^{3}M^{10}** studied previously (21)] of –0.10, –0.05, –0.01, and –0.02 eV, respectively (Table 4). These comparisons exemplify the more substantial stabilization of each frontier MO by 3-formyl versus 3-vinyl. This point will be explored further below in relation to the observed spectral effects.

(9) The trends in LUMO energies reflect trends in (but not absolute values of) the reduction potentials, and similarly for the HOMO energies and oxidation potentials, as we have found for a large series of zinc chlorins (21). In particular, the more negative LUMO and HOMO energies (Table 4) for **ZnC-F^{7}T^{10}** (–2.28 and –5.01 eV) versus **ZnC-T^{10}** (–2.10 and –4.75 eV) indicate that the addition of a 7-formyl group makes the chlorin easier to reduce and harder to oxidize. A similar conclusion is reached for the free base oxophorbines **FbOP-F^{7}M^{10}** (–2.72 and –5.35 eV) versus **FbOP-M^{10}** (–2.58 and –5.17 eV).

Name	ZnC	ZnC-F^{7}T^{10}	ZnC-M^{10}F^{13}	ZnC-F^{3}M^{10}F^{13}	FbC	FbOP	FbOP-F^{7}M^{10}
Structure	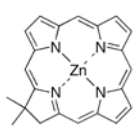	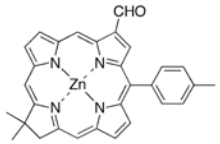	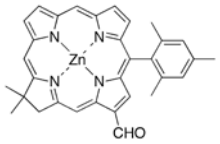	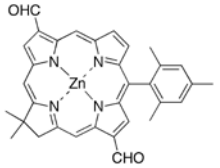	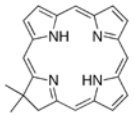	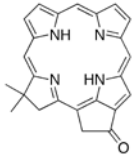	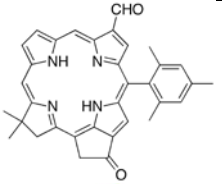
LUMO+1 (eV)	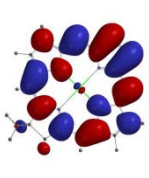	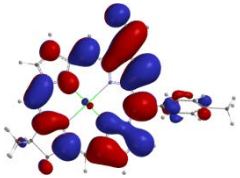	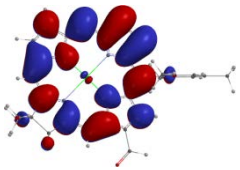	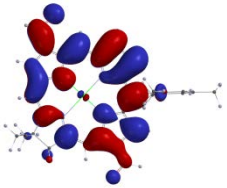	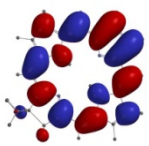	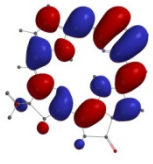	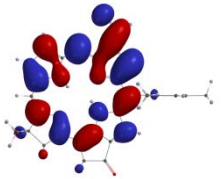
	–1.55	–2.03	–1.75	–2.04	–1.67	–1.93	–2.39
LUMO (eV)	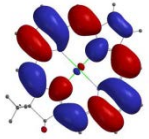	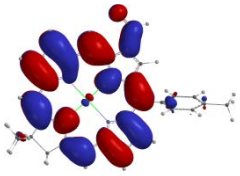	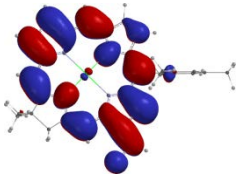	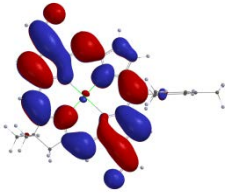	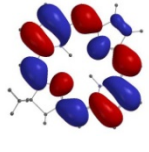	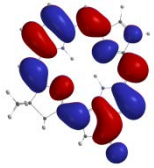	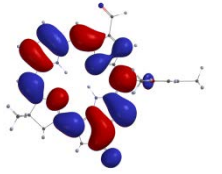
	–2.12	–2.28	–2.49	–2.85	–2.20	–2.62	–2.72
HOMO (eV)	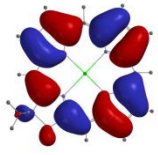	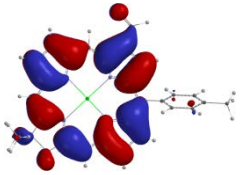	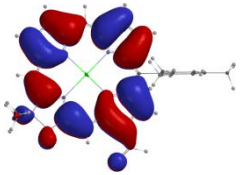	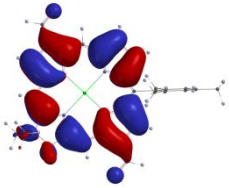	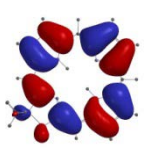	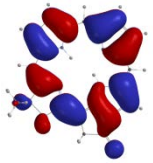	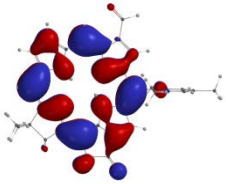
	–4.79	–5.01	–5.02	–5.23	–4.89	–5.20	–5.35
HOMO-1 (eV)	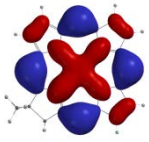	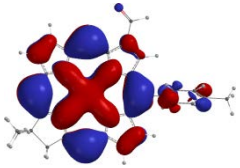	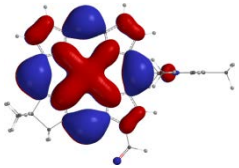	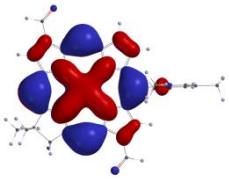	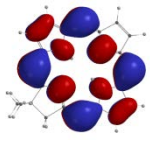	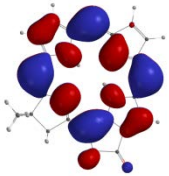	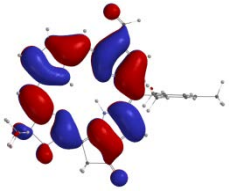
	–5.16	–5.26	–5.30	–5.48	–5.07	–5.26	–5.40

Figure 4. Electron densities and energies (eV) of frontier MOs of representative chlorins and oxophorbines.

Table 4. Molecular Orbital Energies and Energy Gaps for Chlorins and Oxophorbines.[a]

Entry	compound	code [b]	HOMO-1	HOMO	LUMO	LUMO+1	LUMO – HOMO	LUMO+1 – HOMO-1	ΔE_{avg}	ΔE_{dif}
	Zinc Chelates									
1	**ZnC**	a	–5.16	–4.79	–2.12	–1.55	2.67	3.61	3.14	0.94
2	**ZnC-T^{10}**	X	–5.07	–4.75	–2.10	–1.53	2.65	3.54	3.10	0.89
3	**ZnC-M^{10}**	r	–5.11	–4.78	–2.12	–1.56	2.66	3.55	3.11	0.89
4	**ZnC-P^{10}**	b	–5.12	–4.77	–2.11	–1.55	2.66	3.57	3.12	0.91
5	**ZnC-T^{5}**		–5.08	–4.75	–2.10	–1.53	2.65	3.55	3.10	0.90
6	**ZnC-P^{15}**		–5.13	–4.78	–2.14	–1.55	2.64	3.58	3.11	0.94
7	**ZnC-F^{7}T^{10}**	F	–5.26	–5.01	–2.28	–2.03	2.73	3.23	2.98	0.50
8	**ZnC-A^{7}T^{10}**	A	–5.26	–4.99	–2.30	–1.96	2.69	3.30	3.00	0.61
9	**ZnC-E^{7}T^{10}**	E	–5.15	–4.83	–2.18	–1.74	2.65	3.41	3.03	0.76
10	**ZnC-V^{3}M^{10}**	c	–5.13	–4.79	–2.22	–1.61	2.57	3.52	3.05	0.95
11	**ZnC-M^{10}F^{13}**	d	–5.30	–5.02	–2.49	–1.75	2.53	3.55	3.04	1.02
12	**ZnC-M^{10}A^{13}**	e	–5.23	–4.95	–2.42	–1.69	2.53	3.54	3.04	1.01
13	**ZnC-M^{10}E^{13}**	f	–5.19	–4.85	–2.27	–1.64	2.58	3.55	3.07	0.97
14	**ZnC-M^{10}Es^{13}**	g	–5.20	–4.92	–2.36	–1.65	2.56	3.55	3.06	0.99
15	**ZnC-F^{3}M^{10}F^{13}**	h	–5.48	–5.23	–2.85	–2.04	2.38	3.44	2.91	1.06
16	**ZnC-A^{3}M^{10}A^{13}**	i	–5.33	–5.09	–2.69	–1.90	2.40	3.43	2.92	1.03
17	**ZnC-E^{3}M^{10}E^{13}**	j	–5.26	–4.91	–2.42	–1.75	2.49	3.51	3.00	1.02
18	**ZnC-E^{3}E^{13}**	p	–5.32	–4.94	–2.43	–1.75	2.51	3.57	3.04	1.06

19	**ZnC-E^{3}E^{12}**	o	–5.31	–4.94	–2.43	–1.79	2.51	3.52	3.02	1.01
20	**ZnC-E^{3}A^{13}**	n	–5.36	–5.04	–2.57	–1.81	2.47	3.55	3.01	1.08
21	**ZnC-E^{3}A^{12}**	m	–5.36	–5.02	–2.58	–1.88	2.44	3.48	2.96	1.04
22	**ZnC-A^{13}**	k	–5.28	–4.97	–2.44	–1.69	2.53	3.60	3.07	1.07
23	**ZnC-A^{12}**	l	–5.29	–4.95	–2.45	–1.74	2.50	3.54	3.02	1.04
24	**ZnOP**	q	–5.34	–5.12	–2.57	–1.83	2.55	3.51	3.03	0.96
	Free Bases									
25	**FbC**		–5.07	–4.89	–2.20	–1.67	2.69	3.40	3.05	0.71
26	**FbC-M^{10}**		–5.02	–4.87	–2.18	–1.68	2.69	3.34	3.02	0.65
27	**FbC-P^{10}**		–5.01	–4.87	–2.19	–1.68	2.68	3.33	3.01	0.65
28	**FbC-T^{5}**		–4.98	–4.85	–2.17	–1.65	2.68	3.33	3.01	0.65
29	**FbC-P^{15}**		–5.04	–4.87	–2.20	–1.66	2.67	3.38	3.03	0.71
30	**FbC-M^{10}E^{13}**		–5.10	–4.93	–2.33	–1.75	2.60	3.35	2.98	0.75
31	**FbC-M^{10}Es^{13}**		–5.11	–5.01	–2.42	–1.77	2.59	3.34	2.97	0.75
32	**FbOP**		–5.26	–5.20	–2.62	–1.93	2.58	3.33	2.96	0.75
33	**FbOP-M^{10}**	OX	–5.19	–5.17	–2.58	–1.91	2.59	3.28	2.94	0.69
34	**FbOP-F^{7}M^{10}**	OF	–5.40	–5.35	–2.72	–2.39	2.63	3.01	2.82	0.38
35	**FbOP-A^{7}M^{10}**	OA	–5.32	–5.28	–2.66	–2.29	2.62	3.03	2.83	0.41
36	**FbOP-E^{7}M^{10}**	OE	–5.27	–5.22	–2.64	–2.10	2.58	3.17	2.88	0.59
37	**FbOP-A^{3}M^{10}**		–5.30	–5.29	–2.84	–2.13	2.45	3.17	2.81	0.72

[a] Obtained from DFT calculations. All values are in eV.
[b] Compound designation code for data points in Figures 5-7.

Spectral analysis using the four-orbital model

The basic model. In this section, the substituent effects on the energies of the frontier MOs (HOMO−1, HOMO, LUMO, LUMO+1) of the synthetic chlorins and oxophorbines are explored further using Gouterman's four-orbital model (17–19). Within this model, the B_y and Q_y states are comprised of linear combinations of the (y-polarized) electronic configurations that result from HOMO → LUMO and HOMO−1 → LUMO+1 one-electron promotions. (Similarly B_x and Q_x are derived from HOMO → LUMO+1 and HOMO-1 → LUMO.) The B_y state reflects the symmetric combination and the Q_y state the antisymmetric combination of the configurations. The respective constructive versus destructive interference of the associated transition dipole moments results in a strong $B_y(0,0)$ band (in the Soret manifold) and a weaker $Q_y(0,0)$ band, consistent with the observed spectra (Figures 1 and 2).

The key parameters that are most closely tied to the optical properties are the average energy (ΔE_{avg}) and difference in energy (ΔE_{dif}) of the [LUMO – HOMO] and [LUMO+1 – HOMO-1] energy gaps given in Eqs. 1.

$$\Delta E_{avg} = [\Delta E(\text{LUMO+1} - \text{HOMO-1}) + \Delta E(\text{LUMO} - \text{HOMO})]/2 \quad (1a)$$

$$\Delta E_{dif} = [\Delta E(\text{LUMO+1} - \text{HOMO-1}) - \Delta E(\text{LUMO} - \text{HOMO})] \quad (1a)$$

Parameter ΔE_{avg} places the energy center of gravity of the $B_y(0,0)$ and $Q_y(0,0)$ bands. The $Q_y(0,0)$ band lies lower and the $B_y(0,0)$ band higher than the average energy by one-half the magnitude of a splitting parameter (σ_y) that in turn depends on ΔE_{dif} and the configuration interaction energy (δ) as given by Eqs. 2 and 3.

$$E_{By} = \Delta E_{avg} + \sigma_y/2 \quad (2a)$$

$$E_{Qy} = \Delta E_{avg} - \sigma_y/2 \quad (2b)$$

$$\sigma_y = \Delta E_{dif} / [\sin(2\eta_y)] \quad (2c)$$

$$\eta_y = [\tan^{-1}(\Delta E_{dif}/2\delta)]/2 \quad (3)$$

The configuration-interaction energy derives from the electron-density distribution in the molecule (and thus electron-electron repulsion) and should be relatively constant for a series of related molecules. In addition to the $B_y - Q_y$ splitting (σ_y; Eq. (2c)), the relative intensities of the B_y and Q_y bands is driven by ΔE_{dif} via Eq. (4), using η_y in Eq. (3).

$$\Sigma_{Q_y}/\Sigma_{B_y} = [1-\cos(2\eta_y)]/[1+\cos(2\eta_y)] \quad (4)$$

The intensity relationship follows because the constructive (B_y) versus destructive (Q_y) interference of the (nominally equal) transition-dipole moments associated with the HOMO-1 → LUMO+1 and HOMO → LUMO configurations dictates the relative oscillator strengths of the B_y and Q_y absorption transitions. In particular, as ΔE_{dif} increases (e.g., due to substituents), the transition-dipole cancellation for the Q_y state decreases and intensity is shifted from B_y to Q_y, and vice versa. Mathematically, as ΔE_{dif} increases, η_y in Eq. (2) increases, $\cos(2\eta_y)$ decreases and the numerator in Eq. (4) grows at the expense of the denominator, and vice versa. According to Eqs. (2), this same increase in ΔE_{dif} increases the energy spacing between B_y and Q_y, and vice versa.

It is useful to note the contribution of the (HOMO → LUMO) and (HOMO-1 → LUMO+1) configurations to the states responsible for the main optical features. For porphyrins, the two configurations are effectively degenerate and contribute equally to the B_y and Q_y states. For chlorins, prior DFT calculations (70–72), prior other theoretical work (73–75), and our own DFT calculations using Spartan (39) and Gaussian (40) give a (HOMO → LUMO):(HOMO-1 → LUMO+1) composition of the Q_y state in the range 65:35 to 80:20 for chlorins (depending on the molecule and calculation).

Spectral analysis for the synthetic chlorins and oxophorbines. In this section, the four-orbital model is used to analyze the spectral properties of the new 7-substituted chlorins and oxophorbines, and 3,13-disubstituted chlorins (Chart 2). The scope is broadened by the inclusion of effects of selected additional substituents utilized previously at the 3,13-positions (Chart 3) (20–22,26). Figures 5 and 6 show the MO energies (top panels), energy gaps (middle panels), and four-orbital parameters (bottom panels) plotted against the energy/wavelength (Table 2) of the Soret maximum (B_{max}; left panels) and $Q_y(0,0)$ band (right panels) for the various compounds. The intensity ratio of the Q_y and B_y manifolds simulated using Eq. (4) and a configuration interaction energy of 0.4 eV is plotted against the observed integrated intensity ratio of the Q_y manifold and the entire Soret manifold in Figure 7. Note that for the synthetic chlorins, B_{max} defines the position of the $B_y(0,0)$ band, which is intimately connected with the $Q_y(0,0)$ band within the four-orbital model, because splitting with $B_x(0,0)$ is typically negligible. The splitting of the two bands increases as the symmetry is diminished and is quite apparent for the free base oxophorbines (Figures 1 and 2). However, the consistent use of the B_{max} rather than relying on specific (and in some cases uncertain) assignments of the $B_y(0,0)$ and $B_x(0,0)$ bands for the latter compounds does not alter any conclusions drawn here from the analysis. In the following, the effects of substituents at the 3- and 13-positions of the synthetic zinc chlorins are analyzed first, followed by discussion of the 7-substituted zinc chlorins and free base oxophorbines.

Figure 5 shows that the trends in B_{max} and $Q_y(0,0)$ absorption energy/wavelength with MO-related properties for formyl (and ester) at the 13- or 3,13-positions are in keeping with those for other substituents (acetyl, ethynyl, vinyl; Tables 2 and 4) that were part of an extended set of analogs studied previously (21). As noted above, formyl, acetyl and other substituents

employed at the 3- and 13-positions stabilize the frontier MOs to varying degrees. The plots in Figures 5A and 5D show that stabilization of each orbital accompanies the bathochromic shifts in the $B_y(0,0)$ and $Q_y(0,0)$ bands. In particular, the plot for each orbital (and also each plot in panels B, C, E and F) has the unsubstituted reference zinc chlorin **ZnC** (labeled "a") at the top right (highest MO and spectral energy), the diformyl complex **ZnC-F^{3}M^{10}F^{13}** (labeled "h") at the lower left (lowest MO and spectral energy), and the mono-formyl analog **ZnC-M^{10}F^{13}** (labeled "d") in between. However, for both bands, the slope of the trend line for the LUMO (m = 2.6 or 3.2) is much greater than that for the HOMO (m = 1.6 or 1.8) and the slope for the LUMO+1 (m = 1.7 or 2.1) is modestly greater than that for the HOMO-1 (m = 1.3 or 1.6). Figures 5B and 5E show that these differences translate into a more steep decrease of the [LUMO – HOMO] energy gap (m = 1.0 or 1.4) than the [LUMO+1 – HOMO-1] energy gap (m = 0.4 or 0.6) with the two spectral positions. In turn, the unequal slopes of the two MO energy gaps translate into an increase in ΔE_{dif} that accompanies the decrease (bathochromic shift) in the center of gravity parameter ΔE_{avg} (right to left in Figures 5C and F). The increase in ΔE_{dif} with 3- and 13-substituents also correlates with the increase in $Q_y(0,0)$ intensity relative to the Soret manifold (Figure 7, circles) as predicted by the four-orbital model.

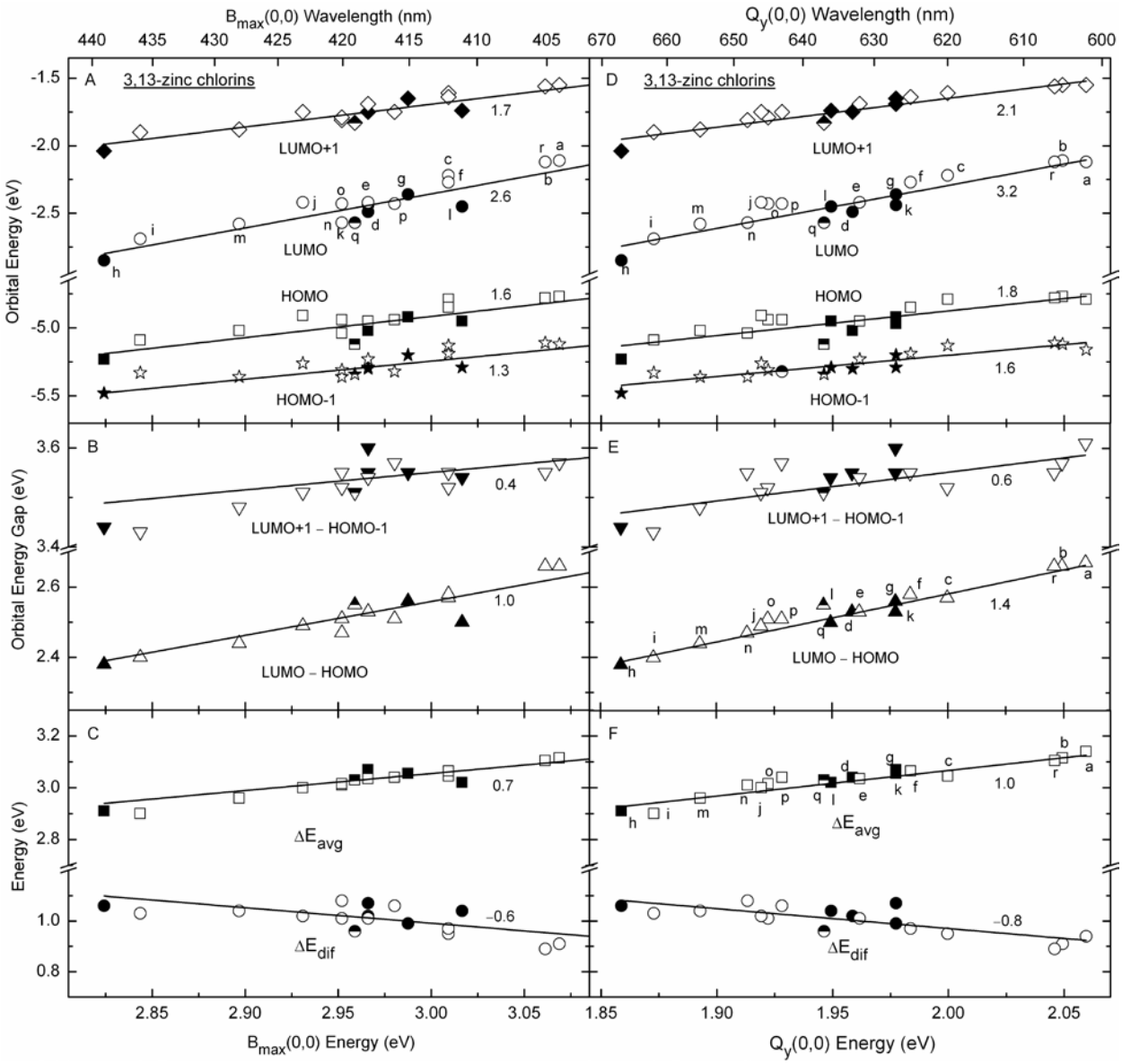

Figure 5. Calculated frontier MO energies (top panels), energy gaps (middle panels), and four-orbital parameters (bottom panels) versus the measured B_{max} (left panels) and $Q_y(0,0)$ (right panels) absorption energy (bottom axis) and wavelength (top axis) for 3,13-disubstituted zinc chlorins characterized here (closed symbols), a selection of 3,13-disubstituted zinc chlorins studied previously (open symbols), and oxophorbine **ZnOP** (half-filled symbols). Top: energies LUMO+1 (diamonds), LUMO (circles), HOMO (squares), HOMO-1 (stars). Middle: energy gaps LUMO+1 – HOMO-1 (down triangles), and LUMO – HOMO (up triangles). Bottom: ΔE_{avg} (squares) and ΔE_{dif} (circles). The indicated values are the slopes of the trend lines. The compound code for the data points is given in the third column of Table 4.

Figure 6 shows the analogous plots of MO-related parameters versus spectral positions for the 7-substituted zinc chlorins (solid lines and closed symbols) and free base oxophorbines (open symbols and dashed lines). Figure 7 (squares and diamonds) shows the associated plots for the relative spectral intensities. Although there are fewer 7-substituted compounds in each set (unsubstituted and mono-formyl, -acetyl and -ethynyl), differences from the effects of 3- and 13-substituents (Figure 5) are quite apparent. It is simplest in viewing each plot in Figure 6 to compare the position of the 7-formyl zinc chlorin (labeled "F") or 7-formyl free base oxophorbine (labeled "OF") with that for the unsubstituted zinc chlorin (labeled "X") or free base oxophorbine (labeled "OX"). Additionally, for the $Q_y(0,0)$ bands, the 7-ethynyl group (labeled "E" or "OE") causes a shift that is either in the opposite direction (free base oxophorbines) or minimal (zinc chlorins) compared to formyl (or acetyl). In the following we focus on the effects of 7-formyl (labeled "F" or "OF") and the similar but typically modestly smaller effects of 7-acetyl (labeled "A" or "OA").

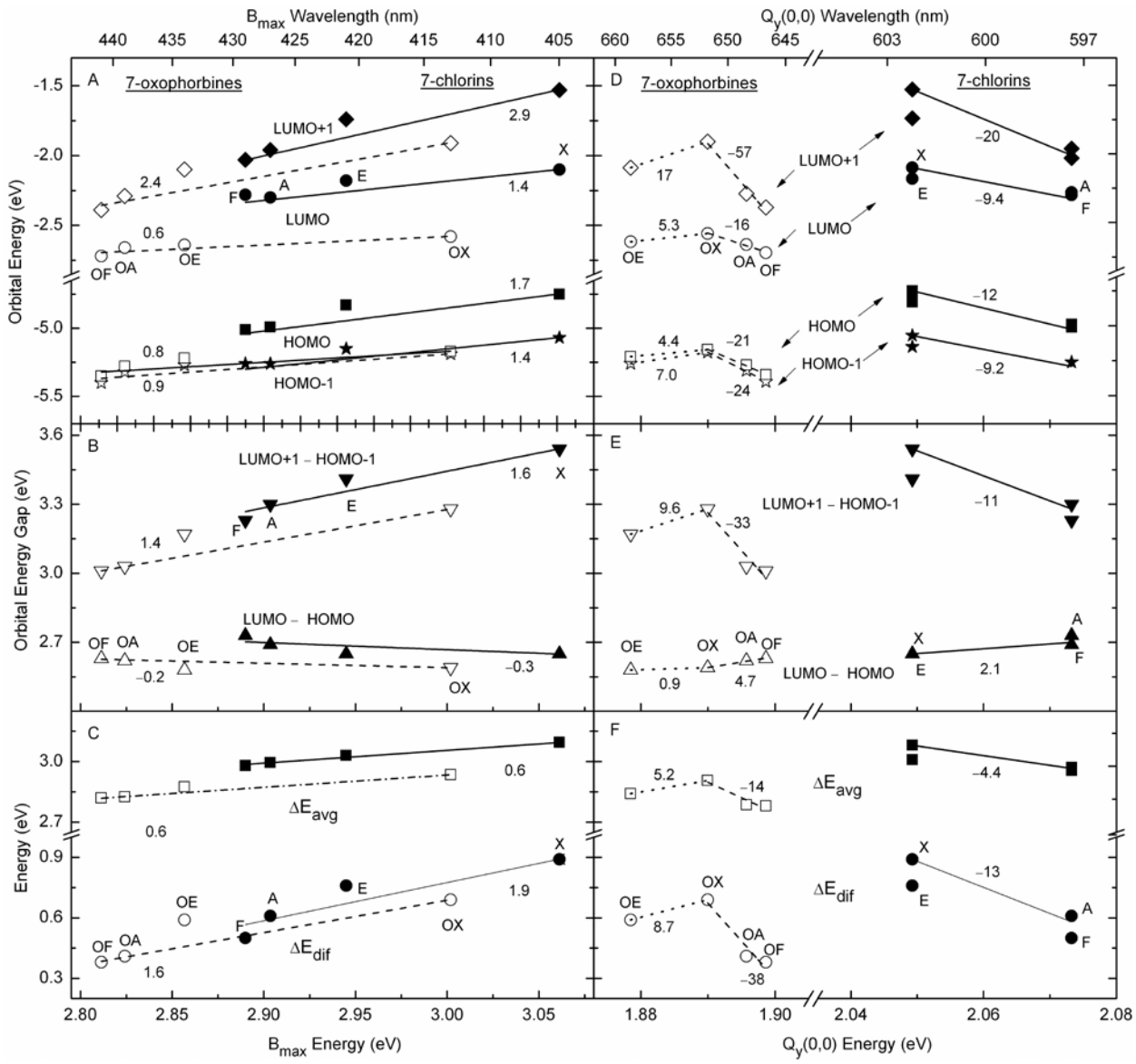

Figure 6. Calculated frontier MO energies (top panels) and energy gaps (middle panels) and four-orbital parameters (bottom panels) versus the measured B_{max} (left) and $Q_y(0,0)$ (right) absorption-band energy (bottom axis) and wavelength (top axis) for 7-substituted zinc chlorins (closed symbols) and 7-substituted free base oxophorbines (open symbols) (Chart 1). Top: energies LUMO+1 (diamonds), LUMO (circles), HOMO (squares), HOMO-1 (stars). Middle: energy gaps LUMO+1 – HOMO-1 (down triangles), and LUMO – HOMO (up triangles). Bottom: ΔE_{avg} (squares) and ΔE_{dif} (circles). The indicated values are the slopes of the trend lines for 7-unsubstituted, 7-acetyl, and 7-formyl chlorins (solid lines) and oxophorbines (dashed lines) and in the right panels for 7-unsubstituted and 7-ethynyl oxophorbines (dotted). The compound code for the data points is given in the third column of Table 4.

Stabilization of the MO by incorporation of a 7-formyl group is connected with the observed bathochromic shift in B_{max} and a hypsochromic shift in $Q_y(0,0)$. The slopes of the trend lines in Figures 6A and 6D reveal these shifts are associated with a substantially greater substituent effect on the LUMO+1 than the other three MOs, with the effect of the LUMO being comparable to the HOMO-1, which is modestly smaller than that for the HOMO. These trends can be compared with those described above for 3- and 13-substituents (Figure 5), where the substituent dependence of the LUMO has the greatest impact, with the effects of the LUMO+1 being comparable to that of the HOMO (as opposed to HOMO–1). The MO shifts for 7-formyl (and 7-acetyl) translate into opposing slopes of the trendlines for the LUMO+1 – HOMO-1 versus LUMO – HOMO for B_{max} (Figure 6B) and a reversal in both slopes for $Q_y(0,0)$ relative to B_{max} (Figure 6E versus 6B). In turn, the resulting effect of these two 7-substituents to bathochromically shift B_{max} and hypsochromically shift $Q_y(0,0)$ is connected with a decrease in the average MO energy gap parameter ΔE_{avg} combined with a decrease in the MO energy-gap difference parameter ΔE_{dif}. The decreased ΔE_{dif} is connected with a reduced $B_y(0,0) - Q_y(0,0)$ splitting and a decrease in the relative $Q_y(0,0)$ intensity [via Eqs. (3) and (4)], the latter being shown in Figure 7 (squares and diamonds).

Collectively, these considerations show that the dramatic difference in the spectral impact of the same substituent, especially formyl, at the 7- versus 3- or 13-positions primarily derives from the differential impacts on the LUMO+1 and LUMO orbitals, and the resulting differences in the MO energy gaps that underlie the spectral properties. Tracing the origins of the spectral properties to the effects of the substituents and sites on the energies of specific MOs has been aided by analysis using the four-orbital model.

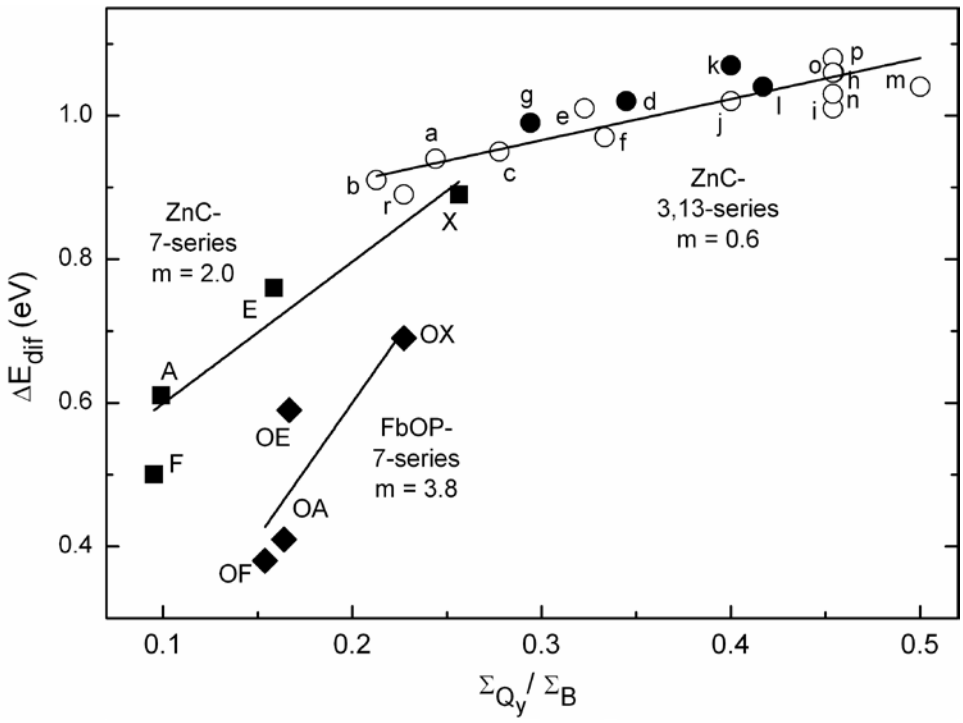

Figure 7. Simulated (using Eq. 4 and $\delta = 0.4$ eV) versus observed integrated intensities of the Q_y and B absorption manifolds for 7-substituted free base oxophorbine series (filled diamonds), 7-substituted zinc chlorin series (filled squares) and zinc chlorins studied here (filled circles) and previously (open circles) substituted at the 3-, 13- or 3,13-positions (along with controls, such as containing a common 10-aryl group). The designations of the compounds (data points) are indicated in the third column of Table 4.

Walking a given substituent around the macrocycle

The pronounced difference in the spectral impact of a formyl group at the 7- versus 3- or 13-positions prompted us to inquire as to whether such differences also pertain to other macrocycle positions, and in particular whether there are unique characteristics of the 7-position (or 8-position), which lies in the pyrrole ring trans to the reduced ring in the chlorins (Chart 1). To this end DFT calculations were performed in which either a single formyl, acetyl, vinyl or ethynyl group was walked around a zinc chlorin lacking any substituent other than the geminal dimethyl group in the reduced ring. The results are shown in Figures 8-10.

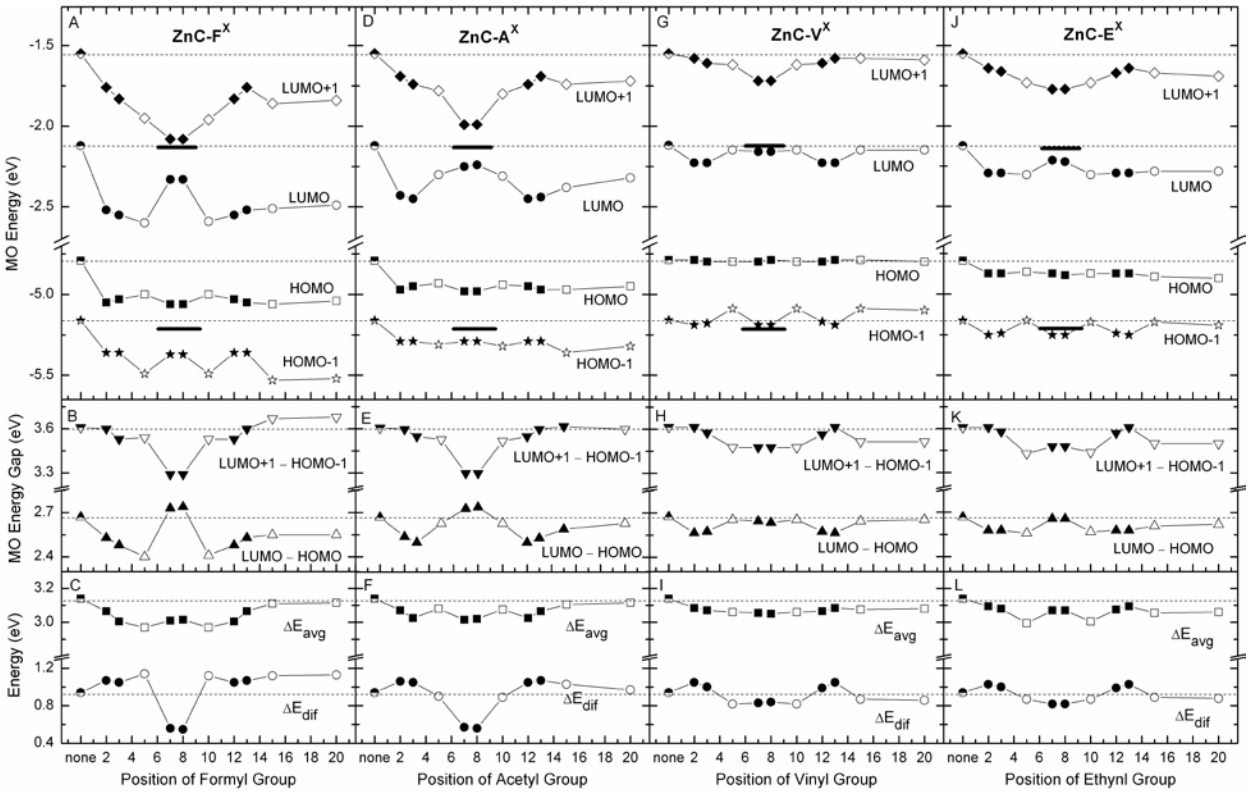

Figure 8. MO energies (top panels), energy gaps (middle panels) and four-orbital parameters (bottom panels) for a zinc chlorin containing a single formyl (A-C), acetyl (D-F), vinyl (G-I) or ethynyl (J-L) group at various macrocycle sites. The solid bar at –2.14 eV (under the points for the 7- and 8-positions) denotes the energy of the degenerate "LUMOs" of the unsubstituted zinc porphyrin and the solid bar at –5.21 eV denotes the energy of the accidentally degenerate porphyrin "HOMOs". The horizontal dashed lines denote the reference values for **ZnC** with no substituents.

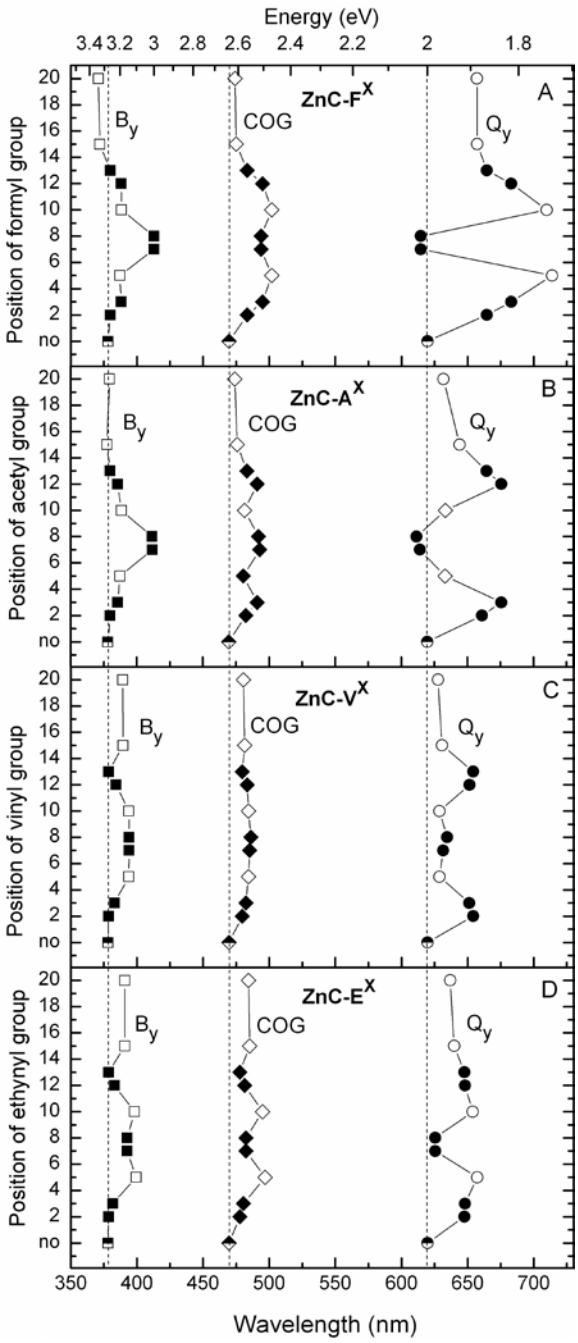

Figure 9. Simulations of the $B_y(0,0)$ and $Q_y(0,0)$ band positions and the energy center of gravity (COG) obtained from the four-orbital parameters depicted in the bottom panels of Figure 8 for a zinc chlorin containing a single formyl (F), acetyl (A), vinyl (V), or ethynyl (E) group at various macrocycle sites. The dashed lines denote the wavelength (bottom axis) or energy (top axis) for no substituent (vertical axis position "no"). For all simulations, a value of the $\delta = 0.4$ eV was used and an energy correction of $\Delta E_{corr} = 0.5$ eV was applied to ΔE_{avg} to place the center of gravity in the typical spectral region.

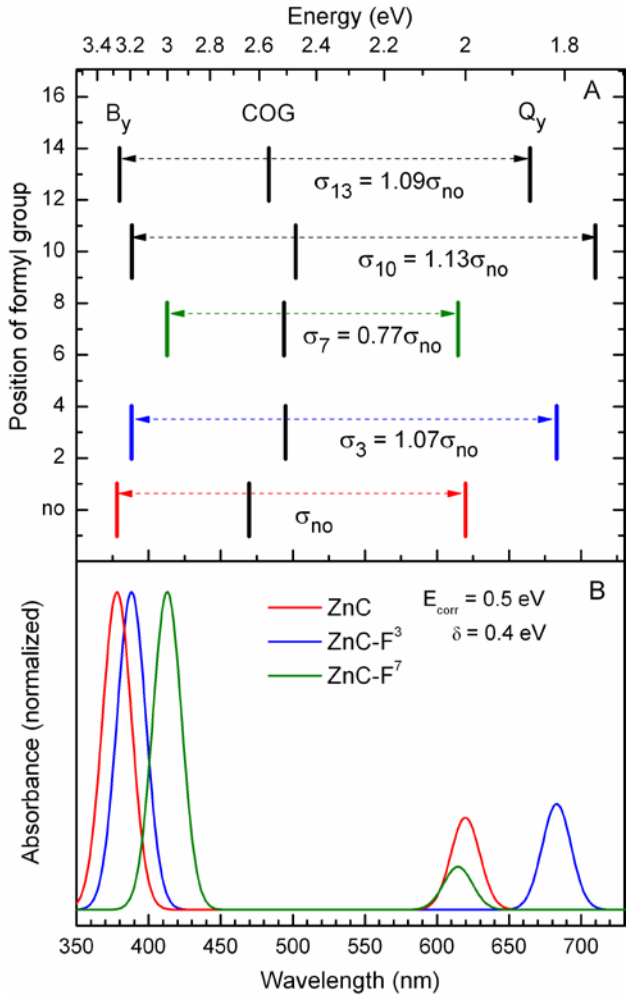

Figure 10. (A) Simulations of the $B_y(0,0)$ and $Q_y(0,0)$ band positions and the energy center of gravity (COG) obtained from the four-orbital parameters depicted in the bottom panels of Figure 9 for a zinc chlorin containing no substituents or a single formyl group at the 3-, 7-, 10- and 13-positions. (B) The same data as in panel A for three cases but with the bands given 20-nm wide Gaussian skirts. The intensities of $B_y(0,0)$ bands are normalized to unity and the intensities of the $Q_y(0,0)$ bands are given by the result in Eq. 4 times the measured **ZnC** $Q_y(0,0)/B_y(0,0)$ peak intensity ratio of 0.29, which serves as a reference.

In Figure 8, the top panels (A,D,G,J) show the energies of the individual MOs, the middle panels (B,E,H,K) the MO energy gaps [LUMO+1 – HOMO-1] and [LUMO – HOMO], and the bottom panels (C,F,I,L) the four-orbital parameters ΔE_{avg} and ΔE_{dif}. Figures 9 and 10 show simulated positions of the $B_y(0,0)$ and $Q_y(0,0)$ bands and their center of gravity (COG) based solely on ΔE_{avg} and ΔE_{dif} and a constant value of $\delta = 0.4$ eV for the configuration-interaction energy (rounded from the values of 0.42 eV found by Gouterman (17) for porphyrins and 0.49 eV found by Kee et al. (21) for a set of zinc chlorins). A constant energy correction of $\Delta E_{cor} = 0.5$ eV was used to shift the MO ΔE_{avg} to lie within the typical $B_{max} – Q_y$ spectral center of gravity range for zinc chlorins. It is noteworthy that the purpose of such simulations is not to predict absolute spectral characteristics, but rather to elucidate the origins of trends and contrasting properties with substituent, which are independent of the exact values of δ and ΔE_{cor} employed.

The simulations in Figures 9 and 10 generally correctly predict the effects of a formyl, acetyl, vinyl, or ethynyl group at the 7- versus 3- or 13-positions of the synthetic zinc chlorins (Tables 1 and 2 and Figure 2). This agreement is expected on the basis of the four-orbital analysis given in the preceding section that utilized the calculated MO energies for the exact compounds studied (Figures 5-7). However, the origins of the primary effects may be more readily apparent using fictive macrocycles with a single auxochrome. For example the simulations given in Figure 10B correctly predict that 3-formyl gives a bathochromic shift in $B_y(0,0)$ and a bathochromic shift and small hyperchromic effect on $Q_y(0,0)$; Figure 10A shows that these effects arise from a reduced energy (bathochromic shift) of the center of gravity (ΔE_{avg}) coupled with an increase in ΔE_{dif}, the latter driving the increased band splitting (Eqs. 2) and intensity ratio (Eq. 4). The simulations given in Figure 10B also correctly predict that 7-

formyl gives a larger bathochromic shift in $B_y(0,0)$ and hypochromic effect on $Q_y(0,0)$; Figure 10A shows that these effects arise from a comparable (to 3-formyl) reduction in the center of gravity (ΔE_{avg}) coupled with a reduction (rather an the increase for 3-formyl) in ΔE_{dif}. Inspection of Figure 10A reveals how the relative signs and magnitudes of substituent-induced changes in ΔE_{avg} and ΔE_{dif} ultimately dictate whether the $B_y(0,0)$ and $Q_y(0,0)$ bands will undergo shifts in the same or opposite directions (and the ΔE_{dif}-driven change in relative intensities). These basic insights also apply to the analogous effects of 3-formyl in **Chl *d*** versus 7-formyl in **Chl *b*** relative to no formyl in **Chl *a*** (Figure 1).

Although the simulations correctly predict an increase or decrease in the $Q_y(0,0)/B_y(0,0)$ intensity ratio, making quantitative intensity comparisons with the observed spectra are difficult for the following reasons:

(1) A change in ΔE_{dif} reflects a change in the ratio of integrated intensities (oscillator strengths) of the Q_y and B_y manifolds; this ratio may be obscured when spectra are normalized to the Soret peak intensity (because there are uncertainties in extinction coefficients) if the bands have different bandwidths.

(2) The Soret region of the observed spectra contains overlapping contributions from the $B_y(0,0)$, $B_x(0,0)$, $B_y(1,0)$, and $B_x(1,0)$ and likely from other non-four-orbital transitions.

Nonetheless, these points do not diminish the fact that the four-orbital simulations generally correctly predict both the substituent effects on the $Q_y(0,0)$ and $B_y(0,0)$ positions and relative intensities. Furthermore, starting at the observed spectra (Figures 1 and 2) and simulated spectra (Figures 9 and 10), it is a straightforward path via the two key four-orbital parameters (ΔE_{avg} and ΔE_{dif}; Figure 8 bottom panels) and the two associated MO energy gaps (Figure 8 middle panels) to the MOs themselves (Figure 8 top panels), thereby tracing the effects of the

nature and position of a substituent on the spectral characteristics to their root origin. Specific insights gleaned from walking a single substituent around the periphery of a zinc chlorin are given in the following.

In the top panels of Figure 8, the solid bar at –2.14 eV (under the points for the 7- and 8-positions) denotes the energy of the two degenerate "LUMOs" of the unsubstituted zinc porphyrin, and the solid bar at –5.21 eV denotes the energy of the two accidentally degenerate porphyrin "HOMOs". Reduction of ring D (Chart 1) destabilizes one porphyrin orbital of each pair, which become the chlorin LUMO+1 and HOMO, while two other porphyrin orbitals are far less affected, translating into the chlorin LUMO and HOMO–1. These effects are seen in the top panels in Figure 8 by comparing the MO energies for the unsubstituted chlorin (left-most, half filled points) with those for the porphyrin analog (solid bars).

Relative to the unsubstituted chlorin, MO shifts generally increase in the following order: vinyl (Figure 8G) < ethynyl (Figure 8J) < acetyl (Figure 8D) < formyl (Figure 8A). The electronic properties of the formyl group accentuates the contrasting effects at the 7- and 8-positions versus other sites, which are summarized as follows:

(1) Formyl at all positions stabilizes the LUMO+1 compared to the unsubstituted chlorin, with the effect at the 7- and 8-positions being so substantial as to return the energy level essentially back down to that of the unsubstituted porphyrin.

(2) Formyl at all positions stabilizes the LUMO, although the minimum effect is for the 7- and 8-positions such that only a modest stabilization is observed compared to the unsubstituted chlorin *and* porphyrin.

(3) Formyl at all positions stabilizes the HOMO, albeit slightly more so at the β-pyrrole (closed symbols) versus meso sites (open symbols), and for the 7- and 8-positions the shift brings the level ~65% of the way back down toward that of the unsubstituted porphyrin.

(4) Formyl at all positions stabilizes the HOMO−1, but the effect is about half as large at the β-pyrrole- (including 7- and 8-) positions versus the meso-positions and thus keeps the level closest to that of the unsubstituted chlorin *and* porphyrin.

(5) Analogous but slightly smaller effects generally occur for acetyl at the β-pyrrole positions. The more substantial differences of acetyl versus formyl at the meso positions (open symbols) likely derive from the precise orientations with respect to the macrocycle plane; the DFT-minimized structures have the C=O basically in-plane for 5-, 10-, or 15-formyl, slightly out-of-plane for 20-formyl, and substantially out-of-plane for 5-, 10-, 15-, or 20-acetyl. Further refinement on this point is beyond the level of the present calculations.

(6) The effects of vinyl or ethynyl can be in the same or opposite direction than formyl or acetyl depending on the site of macrocycle substitution.

In effect, of all macrocycle sites, the 7- and 8-positions are unique in allowing maximal effects on the LUMO+1 and minimal effects on the LUMO, as well as generally comparable (all positions) and small to modest effects on the HOMO and HOMO-1. In contrast, the maximal effect of 3- and 13- substituents is typically on the LUMO. Furthermore, the distinguishing characteristics of the 7- and 8- positions are emphasized by the electronically hot yet structurally compact formyl group compared to other auxochromes such as acetyl, vinyl and ethynyl. A simplified view is that the distinguishing characteristics of the 7- or 8-positions and the formyl (or acetyl) group combine to effectively “porphyrinize” the chlorin. If not exactly true in terms of the precise effects on all frontier MOs (top panels in Figure 8), this perspective is appropriate

when considering the relevant MO energy gaps (middle panels) and four-orbital parameters (bottom panels) that underlie the spectral properties (Figures 9 and 10). This analysis thus traces in a relatively straightforward manner the molecular origins of the distinguishing spectral characteristics of incorporation of a formyl (or acetyl) group at the 7- versus 3- (or 13-) positions of synthetic chlorins and oxophorbines, as well as the distinguishing spectral features of the native photosynthetic pigments **Chl *a***, **Chl *b***, and **Chl *d***.

Walking a formyl substituent around the chlorin versus 13^1-oxophorbine macrocycle.

The MO-based analysis in the prior section has elucidated the molecular origins of the spectral consequences of placing a single substituent (formyl, acetyl, vinyl, ethynyl) at various sites around the perimeter of a zinc chlorin. The analysis invites the question as to whether the similar behavior or deviations can be expected for the free base chlorin analogues, and for the related zinc and free base 13^1-oxophorbines. The oxophorbines are more directly relevant to the native chlorophylls and pheophytins, which also contain the keto-bearing five-membered ring. Figures 11 and 12 give the results of walking a formyl group around all four molecules (**ZnC**, **FbC**, **ZnOP**, **FbOP**); the results for **ZnC** given above (Figures 8 and 9) are reproduced here for ease of comparison with the other three cases.

Figure 11 gives the MO energies (top panels), MO energy gaps (middle panels) and resulting four-orbital parameters (bottom panels) on which the spectral characteristics depend. The left-hand panels in Figure 12 give the simulated wavelengths (and energies) of the $B_y(0,0)$ and $Q_y(0,0)$ bands and their center of gravity. The right-hand panels give schematic stick spectra showing the $Q_y(0,0)$ position and the integrated intensity of the Q_y manifold normalized (in each case) to the integrated intensity of the B_y manifold. In Figure 11 panels A,D,G, and J, the solid

bars give the energies of the frontier MOs of the unsubstituted porphyrin analog. The analogs for 13[1]-oxophorbines **ZnOP** and **FbOP** are the respective zinc and free base porphyrin with an annulated keto-bearing five-membered ring, in other words 17,18-didehydro-13[1]-oxophorbines given that a phorbine is a chlorin (Chart 4). The "porphyrinic" MO values are as follows: zinc porphyrin [−5.22 eV (HOMO-1), −5.21 eV (HOMO), −2.14 eV (LUMO and LUMO+1)]; free base porphyrin [−5.30 eV (HOMO-1), −5.15 eV (HOMO), −2.24 eV (LUMO), −2.22 eV (LUMO+1)]; zinc 17,18-didehydro-13[1]-oxophorbine [−5.53 eV (HOMO-1), −5.40 eV (HOMO), −2.60 eV (LUMO), −2.40 eV (LUMO+1)]; free base 17,18-didehydro-13[1]-oxophorbine [−5.60 eV (HOMO-1), −5.33 eV (HOMO), −2.67 eV (LUMO), −2.48 eV (LUMO+1)]. The main points that emerge are as follows.

Chart 4. Porphyrin analogues of the chlorins and 13[1]-oxophorbines.

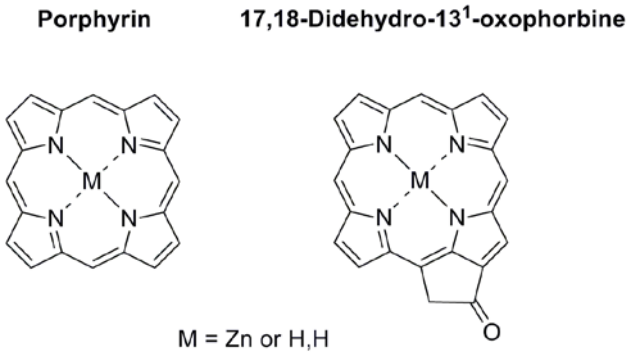

(1) All four molecules (**ZnC**, **FbC**, **ZnOP**, **FbOP**) show the same dramatic difference in the impact of a formyl group at the 7- and 8-positions compared to other sites, namely a bathochromic shift in $B_y(0,0)$ and a hypsochromic shift (zinc chelates) or virtually no change (free bases) in $Q_y(0,0)$ and the hypochromic effect on the $Q_y(0,0)$ band (Figure 12). Again, these effects arise from substantial LUMO+1stabilization by 7- or 8-formyl with less change in the other orbitals, particularly the LUMO (Figure 11). In this regard, the "porphyrinization" of the chlorin or oxophorbine by 7- or 8-formyl is even more pronounced for **FbC** and **FbOP** than for

ZnC and **ZnOP**, respectively, as can be seen from the individual MOs and the low ΔE_{dif} value (which is at a minimum for porphyrins).

(2) The presence of the oxophorbine unit makes the above-noted effects [decreased $B_y(0,0) - Q_y(0,0)$ splitting and decreased $Q_y(0,0)/B_y(0,0)$ intensity ratio] to be slightly emphasized for 7- versus 8-formyl, and more so for **ZnOP** than **FbOP** (Figures 12 C,D,G and H). Thus, **Chl *b*** has the formyl group placed at the position of greatest impact for such major spectral distinctions from **Chl *a***.

(3) In general, the $B_y(0,0)$ band is bathochromically shifted, the $Q_y(0,0)$ band is hypsochromically shifted, and the $Q_y(0,0)/B_y(0,0)$ intensity ratio is reduced for the free base chlorin or oxophorbine compared to the zinc chelate.

(4) The presence of the oxophorbine unit in **ZnOP** versus **ZnC** and **FbOP** versus **FbC** diminishes the magnitude of the bathochromic shift caused by a 5-formyl group and enhances that due to a 10-formyl group.

Inspection of Figures 11 and 12 shows that these effects can be traced to the effects of the formyl group at the various positions in the various macrocycles on the individual MOs, particularly the LUMO+1 relative to the LUMO (and the HOMO and HOMO-1) for the 7- and 8-substituents. Where comparisons can be made, the main effects depicted by the simulations are consistent with the observed spectra of the synthetic chlorins (Figure 2) and the native chromophores (Figure 1). Collectively, the results indicate that the differential effects of a strong auxochrome at various macrocycle positions are generally similar for the chlorins and oxochlorins, and for the zinc chelates and free base forms; differences do exist (and origins traced) that can be utilized by judicious choice of substituent site, such as the 7-position (versus the 8- position, etc.) of the formyl group in **Chl *b***.

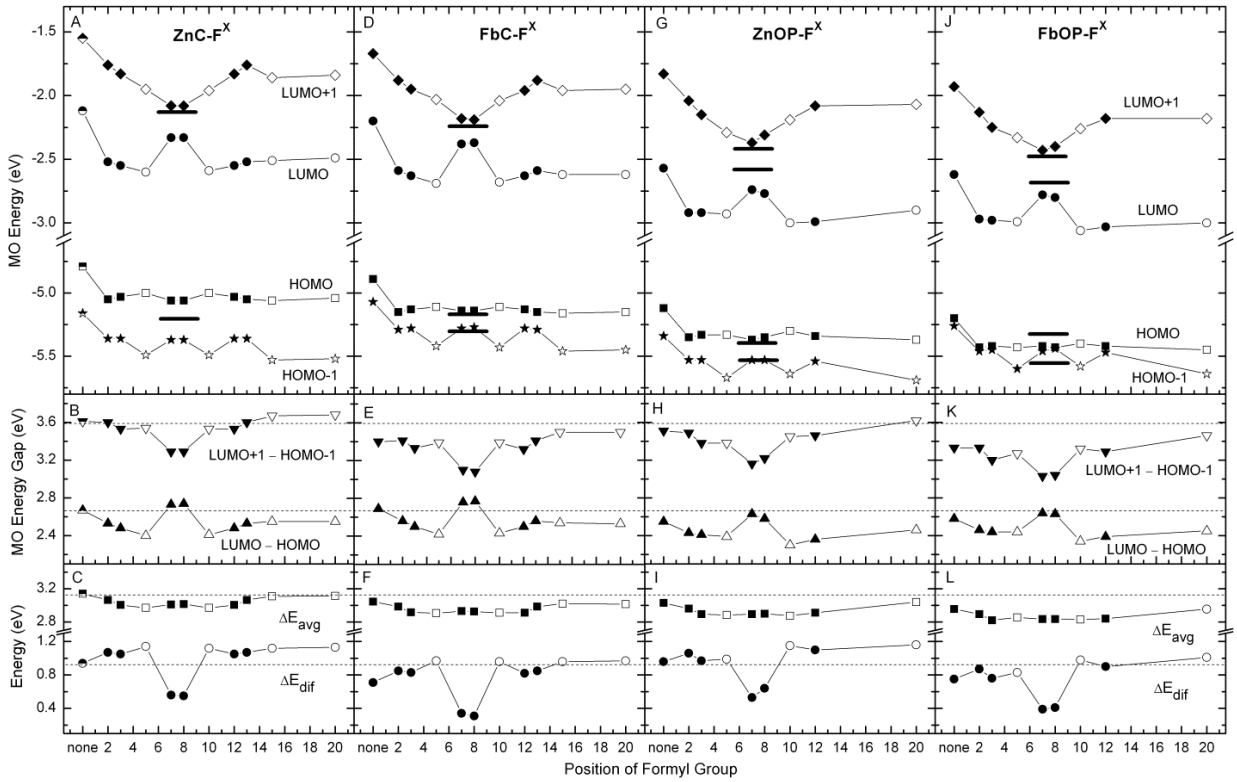

Figure 11. MO energies (top panels), energy gaps (middle panels) and four-orbital parameters (bottom panels) for four fictive compounds bearing a single formyl group at various macrocycle positions. The compounds are zinc (A-C) and free base (D-F) chlorin and zinc (G-I) and free base (J-L) 13^1-oxophorbine unit. The solid bars in each panel denote the energies of the frontier MOs (LUMO+1, LUMO, HOMO, HOMO-1) of the unsubstituted porphyrin analog; fewer than four orbitals are shown for **ZnC** and **FbC** because pairs of orbitals are degenerate or effectively so (see text for details). The horizontal dashed lines denote the reference values for **ZnC** with no substituents.

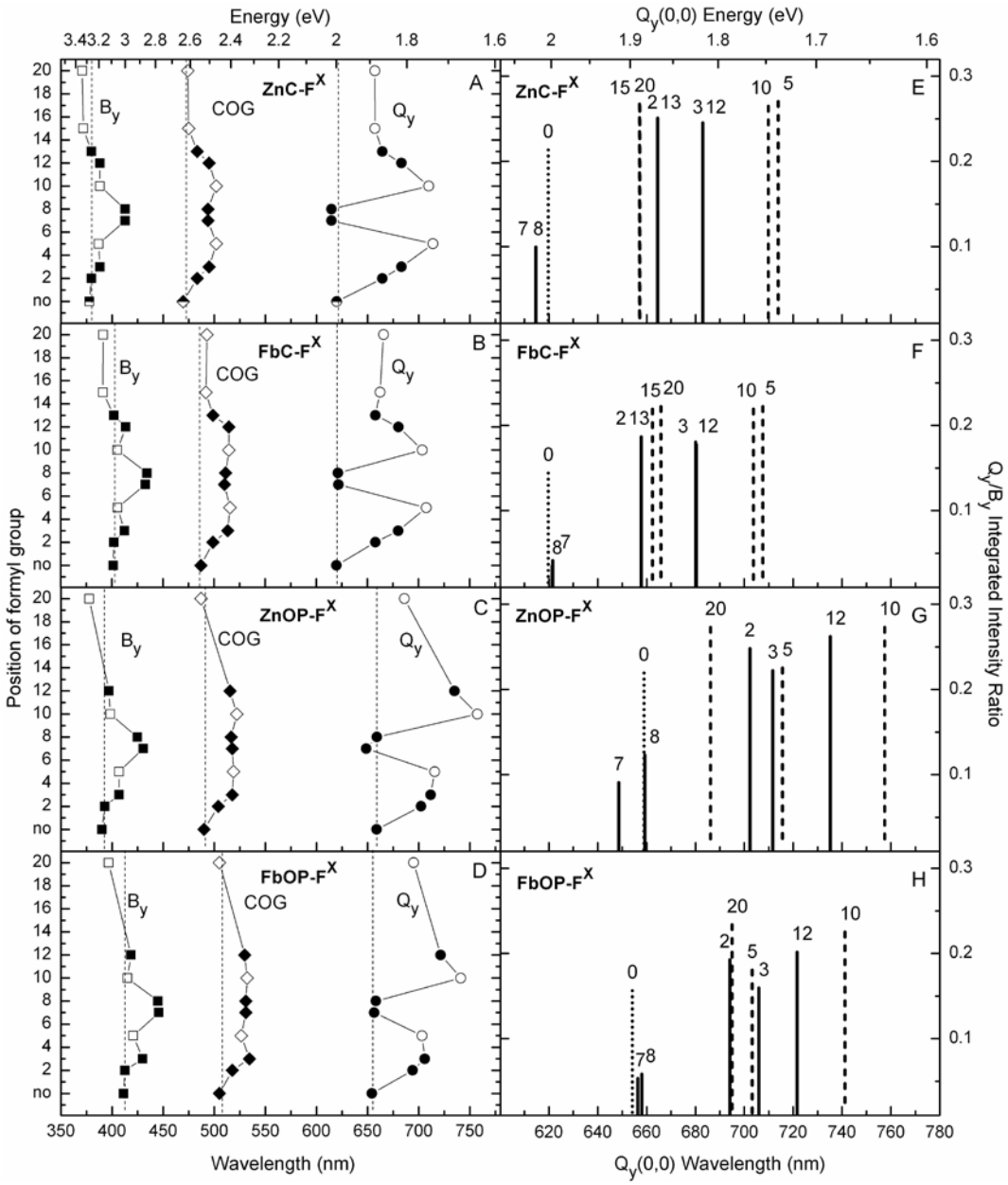

Figure 12. Simulations of the $B_y(0,0)$ and $Q_y(0,0)$ band positions and the energy center of gravity (COG) obtained from the four-orbital parameters depicted in the bottom panels of Figure 11 for four fictive molecules bearing a single formyl group at various macrocycle positions. The compounds are zinc (A) and free base (B) chlorin and zinc (C) and free base (D) 13^1-oxophorbine unit. The dashed line for each case denotes the wavelength (bottom axis) or energy (top axis) for no substituent (vertical axis position "no"). For all simulations, a value of the δ = 0.4 eV was used and an energy correction of ΔE_{corr} = 0.5 eV was applied to ΔE_{avg} to place the center of gravity in the typical spectral region. Panels E-H give analogous stick spectra showing the $Q_y(0,0)$ position and integrated intensity of the Q_y manifold normalized to that of the B_y manifold.

Effect of the same substituent at the 12- versus 13-positions

The spectral simulations shown in Figure 9 for fictive zinc chlorins bearing formyl or acetyl at various macrocycle positions predict that such groups at the 12- versus 13-positions should give small yet measurable differences in spectral properties. It is of interest to compare such a prediction with observation as a calibration on the ability of the four-orbital approach to give insights into the origins of such modest changes in spectral characteristics. To this end, zinc chlorins **ZnC-A^{12}** and **ZnC-A^{13}** were prepared. Absorption spectra are shown in Figure 2E and the spectral and photophysical parameters are listed in Tables 2 and 3 (entries 22 and 23). For additional comparisons, the tables (entries 18-21) also list data for two previously studied (22) pairs of analogs **ZnC-E^{3}A^{12}** versus **ZnC-E^{3}A^{13}** and **ZnC-E^{3}E^{12}** versus **ZnC-E^{3}E^{13}**. The main results are as follows:

(1) The simulations (Figures 8 and 9) suggest that both 12- and 13-acetyl will give a bathochromic shift in both the $B_y(0,0)$ and $Q_y(0,0)$ bands, and an hyperchromic effect on the latter with respect to the former, in agreement with observations on **ZnC-A^{12}** and **ZnC-A^{13}** (Figure 2 and Table 2).

(2) The simulations suggest that the bathochromic shifts in both the $B_y(0,0)$ and $Q_y(0,0)$ bands will be larger (by ~10 nm) for 12- versus 13-acetyl, in agreement with observation. The comparable shifts for the two bands for both compounds arise because both 12- and 13-acetyl engender comparable shifts in the center-of-gravity (via ΔE_{avg}) without a significant difference in the splitting (via ΔE_{dif}).

(3) The comparable ΔE_{dif} in turn predicts that 12- and 13-acetyl groups should give comparable $Q_y(0,0)$ intensities relative to $B_y(0,0)$, consistent with observations. Closer examination of this point indicates that the simulated intensity (and splitting) should be about 2%

lower for 12- vs 13-acetyl, which is reversed from the small observed difference in relative intensities (Figure 2E). However, this small difference is understandable considering the above-noted points concerning detailed comparisons of simulated and observed intensity ratios.

(4) The observed spectral differences for **ZnC-E^{3}E^{12}** versus **ZnC-E^{3}E^{13}** are smaller than those for **ZnC-E^{3}A^{12}** versus **ZnC-E^{3}A^{13}** and **ZnC-A^{12}** versus **ZnC-A^{13}** (Table 2, entries 18–23). This observed smaller 12- versus 13-position difference for ethynyl compared to acetyl is predicted by the four-orbital simulations given in Figure 9D compared to Figure 9B.

(5) All three pairs of compounds show a ~20% reduction in Φ_f and variable impact on τ_S for the same substituent (acetyl or ethynyl) at the 12- versus 13-position.

(6) The above noted differences ultimately arise from the inequivalence of the chlorin 12- and 13-positions (Chart 1). Inspection of Figure 8 indicates that the inequivalence does not significantly affect the HOMO-1, and causes reversed effects for 12- versus 13-substitution on the HOMO compared to the LUMO and LUMO+1. As a consequence, differences in the spectral and electronic properties of the lowest singlet excited state of the 12-versus 13-substituted chlorins originate more from the [LUMO–HOMO] configuration than the [LUMO+1 – HOMO-1] contribution.

Collectively, these observations indicate that the four-orbital simulations of the effects of acetyl (or ethynyl) at the 12- versus 13-positions reproduce the key spectral differences and give insights into their origin. Further inspection of Figures 8 and 9 suggest that analogous differences are to be expected for a substituent (e.g., acetyl, formyl, vinyl) at the 2- versus 3-positions. The latter considerations are relevant to the spectral properties of native chlorophylls and bacteriochlorophylls, which typically differ in the substituent pattern at these two positions.

CONCLUSIONS AND OUTLOOK

A widespread view in organic photochemistry is that the incorporation of a conjugative group in a chromophore causes a bathochromic shift of the absorption spectrum. While correct in many instances, the spectra of **Chl *a*** versus **Chl *b*** provide a prominent exception to this (simplistic) view. The long-wavelength absorption band of the "less-conjugated" **Chl *a*** (7-methyl) appears at 665 nm whereas that of the "more-conjugated" **Chl *b*** (7-formyl) absorbs at 646 nm. Thus, the effects of substituents on chlorin absorption spectra cannot be satisfactorily addressed by a simple "particle-in-a-box" method [in which the lowest excited state is composed solely of the (LUMO – HOMO) configuration] but rather can be understood with Gouterman's four-orbital model [in which the lowest excited state is composed of a linear combination of the (LUMO – HOMO) and (LUMO+1 – HOMO-1) configurations]. The results gathered here show that the presence of a potent auxochrome at the 7-position primarily stabilizes the LUMO+1 but has little effect on the LUMO, and gives modest effects on the HOMO and HOMO-1. The resulting differences in the MO energy gaps are at the heart of the observed spectral differences of **Chl *b*** versus **Chl *a***. Thus, the spectral change caused by the 7-formyl group stems not from a change in the path or extent of π-conjugation, as was once believed to be the origin of auxochromic effects (7,8,12,13,15,16), but rather by stabilization preferentially of one of the four frontier orbitals of the cyclic polyene.

Upon consideration of all possible sites for incorporation of a formyl group, the 7- and 8-positions are most susceptible to this pattern of effects on orbital energies. The overall impact of the 7-formyl group is to "porphyrinize" the chlorin in terms of the resulting spectra and the relative energies of the frontier orbitals. Indeed, the major absorption bands of **Chl *b*** are positioned "inside" (i.e., the B and Q_y bands appear at longer and shorter wavelengths,

respectively) those of **Chl *a***. On the other hand, **Chl *d*** can be regarded as a somewhat more extreme form of **Chl *a*** given the presence of a formyl group in lieu of a vinyl group at the 3-position.

The availability of a set of >30 synthetic chlorins, which were prepared to probe the effects of substituents, in conjunction with DFT calculations on these and other fictive chlorins, has enabled the insights delineated above. Understanding the interplay of the four frontier molecular orbitals with substituents at diverse sites should facilitate the rational design of chlorins for specific photochemical purposes and deepen understanding of photosynthetic processes in general.

Acknowledgment–This work was supported by grants from the Division of Chemical Sciences, Geosciences, and Biosciences, Office of Basic Energy Sciences of the U.S. Department of Energy to D.F.B. (DE-FG02-05ER15660), D.H. (DE-FG02-05ER15661) and J.S.L. (DE-FG02-96ER14632). We thank Dr. Michael Krayer for preparation of chlorin **ZnC-M^{10}Es^{13}**, Drs. Jayeeta Bhaumik, Marcin Ptaszek, and Masahiko Taniguchi for gifts of synthetic chlorins, and Drs. Dariusz Niedzwiedzki and Robert Blankenship for a gift of **Chl *d***.

REFERENCES

1. Scheer, H. (1991) Structure and occurrence of chlorophylls. In *Chlorophylls* (Edited by H. Scheer), pp 3–30. CRC Press, Boca Raton, FL, USA.
2. Smith, J. H. C. and A. Benitez (1955) Chlorophylls: Analysis in plant materials. In *Modern Methods of Plant Analysis* (Edited by K. Paech and M. V. Tracey), Vol. IV, pp 142–196. Springer-Verlag, Berlin.
3. Strain, H. H., M. R. Thomas and J. J. Katz (1963) Spectral absorption properties of ordinary and fully deuteriated chlorophylls *a* and *b*. *Biochim. Biophys. Acta* **75**, 306–311.
4. Rowan, K. S. (1989) *Photosynthetic Pigments of Algae*, pp 65–111. Cambridge University Press, Cambridge.
5. Kobayashi, M., M. Akiyama, H. Kano and H. Kise (2006) Spectroscopy and structure determination. In *Chlorophylls and Bacteriochlorophylls: Biochemistry, Biophysics, Functions and Applications* (Edited by B. Grimm, R. J. Porra, W. Rüdiger and H. Scheer), pp 79–94. Springer, Dordrecht, The Netherlands.
6. Larkum, A. W. D. and M. Kühl (2005) Chlorophyll *d*: The puzzle resolved. *Trends Plant Sci.* **10**, 355–357.
7. Maccoll, A. (1947) Colour and constitution. *Quart. Rev*. **1**, 16–58.
8. Ferguson, L. N. (1948) Relationships between absorption spectra and chemical constitution of organic molecules. *Chem. Rev*. **43**, 385–446.
9. Venkataraman, K. (1952) *The Chemistry of Synthetic Dyes,* Vol. 1, pp 323–400. Academic Press, New York.
10. Dähne, S. (1978) Color and constitution: One hundred years of research. *Science* **199**, 1163–1167.
11. Calvert, J. G. and J. N. Pitts, Jr. (1966) *Photochemistry*, pp 263–268. John Wiley and Sons, Inc., New York.
12. Jaffé, H. H. and M. Orchin (1962) *Theory and Applications of Ultraviolet Spectroscopy*, pp 175–177, 587. John Wiley and Sons, Inc., New York.
13. Gillam, A. E. and E. S. Stern (1954) *An Introduction to Electronic Absorption Spectroscopy in Organic Chemistry,* pp 44–45. Edward Arnold (Publishers) Ltd., London.
14. Mason, S. F. (1970) Color and the electronic states of organic molecules. In *The Chemistry of Synthetic Dyes,* Vol 3 (Edited by K. Venkataraman), pp 169–221. Academic Press, New York.
15. Bury, C. R. (1935) Auxochromes and resonance. *J. Am. Chem. Soc.* **57**, 2115–2117.
16. Lewis, G. N. and M. Calvin (1939) The color of organic substances. *Chem. Rev.* **25**, 273–328.
17. Gouterman, M. (1959) Study of the effects of substitution on the absorption spectra of porphin. *J. Chem. Phys.* **30**, 1139–1161.
18. Gouterman, M. (1961) Spectra of porphyrins. *J. Mol. Spectroscopy* **6**, 138–163.
19. Gouterman, M. (1978) Optical spectra and electronic structure of porphyrins and related rings. In *The Porphyrins* Vol. 3 (Edited by D. Dolphin), pp 1–165. Academic Press, New York.
20. Kee, H. L., C. Kirmaier, Q. Tang, J. R. Diers, C. Muthiah, M. Taniguchi, J. K. Laha, M. Ptaszek, J. S. Lindsey, D. F. Bocian and D. Holten (2007) Effects of substituents on synthetic analogs of chlorophylls. Part 1: Synthesis, vibrational properties and excited-state decay characteristics. *Photochem. Photobiol*. **83**, 1110–1124.

21. Kee, H. L.; C. Kirmaier, Q. Tang, J. R. Diers, C. Muthiah, M. Taniguchi, J. K. Laha, M. Ptaszek, J. S. Lindsey, D. F. Bocian and D. Holten (2007) Effects of substituents on synthetic analogs of chlorophylls. Part 2: Redox properties, optical spectra and electronic structure. *Photochem. Photobiol*. **83**, 1125–1143.
22. Mass, O., M. Ptaszek, M. Taniguchi, J. R. Diers, H. L. Kee, D. F. Bocian, D. Holten and J. S. Lindsey (2009) Synthesis and photochemical properties of 12-substituted versus 13-substituted chlorins. *J. Org. Chem*. **74**, 5276–5289.
23. Ptaszek, M., B. E. McDowell, M. Taniguchi, H.-J. Kim and J. S. Lindsey (2007) Sparsely substituted chlorins as core constructs in chlorophyll analogue chemistry. Part 1: Synthesis. *Tetrahedron* **63**, 3826–3839.
24. Taniguchi, M., M. Ptaszek, M., B. E. McDowell and J. S. Lindsey (2007) Sparsely substituted chlorins as core constructs in chlorophyll analogue chemistry. Part 2: Derivatization. *Tetrahedron* **63**, 3840–3849.
25. Taniguchi, M., M. Ptaszek, B. E. McDowell, P. D. Boyle and J. S. Lindsey (2007) Sparsely substituted chlorins as core constructs in chlorophyll analogue chemistry. Part 3: Spectral and structural properties. *Tetrahedron* **63**, 3850–3863.
26. Mass, O., M. Taniguchi, M. Ptaszek, J. W. Springer, K. M. Faries, J. R. Diers, D. F. Bocian, D. Holten and J. S. Lindsey (2011) Structural characteristics that make chlorophylls green: Interplay of hydrocarbon skeleton and substituents. *New J. Chem*. **35**, 76–88.
27. Muthiah, C., M. Ptaszek, T. M. Nguyen, K. M. Flack and J. S. Lindsey **(**2007) Two complementary routes to 7-substituted chlorins. Partial mimics of chlorophyll *b*. *J. Org. Chem*. **72**, 7736–7749.
28. Muthiah, C., D. Lahaye, M. Taniguchi, M. Ptaszek and J. S. Lindsey (2009) Regioselective bromination tactics in the de novo synthesis of chlorophyll *b* analogues. *J. Org. Chem*. **74**, 3237–3247.
29. Laha, J. K., C. Muthiah, M. Taniguchi, B. E. McDowell, M. Ptaszek and J. S. Lindsey (2006) Synthetic chlorins bearing auxochromes at the 3- and 13-positions. *J. Org. Chem.* **71**, 4092–4102.
30. Laha, J. K., C. Muthiah, M. Taniguchi, B. E. McDowell, M. Ptaszek and J. S. Lindsey (2009) Additions and corrections: Synthetic chlorins bearing auxochromes at the 3- and 13-positions. *J. Org. Chem.* **74**, 5122.
31. Muthiah, C., J. Bhaumik and J. S. Lindsey (2007) Rational routes to formyl-substituted chlorins. *J. Org. Chem*. **72**, 5839–5842.
32. Ptaszek, M., D. Lahaye, M. Krayer, C. Muthiah and J. S. Lindsey (2010) De novo synthesis of long-wavelength absorbing chlorin-13,15-dicarboximides. *J. Org. Chem*. **75**, 1659–1673.
33. Krayer, M., T. Balasubramanian, C. Ruzié, M. Ptaszek, D. L. Cramer, M. Taniguchi and J. S. Lindsey (2009) Refined syntheses of hydrodipyrrin precursors to chlorin and bacteriochlorin building blocks. *J. Porphyrins Phthalocyanines* **13**, 1098–1110.
34. Mass, O., D. R. Pandithavidana, M. Ptaszek, K. Santiago, J. W. Springer, J. Jiao, Q. Tang, C. Kirmaier, D. F. Bocian, D. Holten and J. S. Lindsey (2011) De novo synthesis and properties of analogues of the self-assembling chlorosomal bacteriochlorophylls. *New J. Chem.* **35**, 2671–2690.
35. Lötjönen, S. and P. H. Hynninen (1983) An improved method for the preparation of (10*R*)- and (10*S*)-pheophytins *a* and *b*. *Synthesis* 708–710.

36. Weber, G. and F. W. J. Teale (1957) Determination of the absolute quantum yield of fluorescent solutions. *Trans. Faraday Soc.* **53**, 646–655.
37. Seybold, P. G. and M. Gouterman (1969) Porphyrins XIII: Fluorescence spectra and quantum yields. *J. Mol. Spectrosc.* **31**, 1–13.
38. Gradyushko, A. T., A. N. Sevchenko, K. N. Solovyov and M. P. Tsvirko (1970) Energetics of photophysical processes in chlorophyll-like molecules. *Photochem. Photobiol.* **11**, 387–400.
39. Except for molecular mechanics and semi-empirical models, the calculation methods used in Spartan ′08 or ′10 have been documented in: Shao, Y., L. F. Molnar, Y. Jung, J. Kussmann, C. Ochsenfeld, S. T. Brown, A. T. B. Gilbert, L. V. Slipchenko, S. V. Levchenko, D. P. O'Neill, R. A. DiStasio Jr., R. C. Lochan, T. Wang, G. J. O. Beran, N. A. Besley, J. M. Herbert, C. Y. Lin, T. Van Voorhis, S. H. Chien, A. Sodt, R. P. Steele, V. A. Rassolov, P. E. Maslen, P. P. Korambath, R. D. Adamson, B. Austin, J. Baker, E. F. C. Byrd, H. Dachsel, R. J. Doerksen, A. Dreuw, B. D. Dunietz, A. D. Dutoi, T. R. Furlani, S. R. Gwaltney, A. Heyden, S. Hirata, C.-P. Hsu, G. Kedziora, R. Z. Khalliulin, P. Klunzinger, A. M. Lee, M. S. Lee, W. Liang, I. Lotan, N. Nair, B. Peters, E. I. Proynov, P. A. Pieniazek, Y. M. Rhee, J. Ritchie, E. Rosta, C. D. Sherrill, A. C. Simmonett, J. E. Subotnik, H. L. Woodcock III, W. Zhang, A. T. Bell, A. K. Chakraborty, D. M. Chipman, F. J. Keil, A. Warshel, W. J. Hehre, H. F. Schaefer III, J. Kong, A. I. Krylov, P. M. W. Gill and M. Head-Gordon (2006) Advances in methods and algorithms in a modern quantum chemistry program package. *Phys. Chem. Chem. Phys.* **8**, 3172–3191.
40. The calculation methods used in Gaussian ′09, Revision **B.01** have been documented in: Frisch, M. J., G. W. Trucks, H. B. Schlegel, G. E. Scuseria, M. A. Robb, J. R. Cheeseman, G. Scalmani, V. Barone, B. Mennucci, G. A. Petersson, H. Nakatsuji, M. Caricato, X. Li, H. P. Hratchian, A. F. Izmaylov, J. Bloino, G. Zheng, J. L. Sonnenberg, M. Hada, M. Ehara, K. Toyota, R. Fukuda, J. Hasegawa, M. Ishida, T. Nakajima, Y. Honda, O. Kitao, H. Nakai, T. Vreven, J. A. Montgomery, Jr., J. E. Peralta, F. Ogliaro, M. Bearpark, J. J. Heyd, E. Brothers, K. N. Kudin, V. N. Staroverov, R. Kobayashi, J. Normand, K. Raghavachari, A. Rendell, J. C. Burant, S. S. Iyengar, J. Tomasi, M. Cossi, N. Rega, J. M. Millam, M. Klene, J. E. Knox, J. B. Cross, V. Bakken, C. Adamo, J. Jaramillo, R. Gomperts, R. E. Stratmann, O. Yazyev, A. J. Austin, R. Cammi, C. Pomelli, J. W. Ochterski, R. L. Martin, K. Morokuma, V. G. Zakrzewski, G. A. Voth, P. Salvador, J. J. Dannenberg, S. Dapprich, A. D. Daniels, Ö. Farkas, J. B. Foresman, J. V. Ortiz, J. Cioslowski and D. J. Fox, Gaussian, Inc., Wallingford CT, 2009.
41. Tian, B., E. S. E. Eriksson and L. A. Eriksson, (2010) Can range-separated and hybrid DFT functionals predict low-lying excitations? A Tookad case study. *J. Chem. Theory Comput.* **6**, 2086–2094.
42. Birks, J. B. (1970) in *Photophysics of Aromatic Molecules*, pp 142–192. Wiley-Interscience, London.
43. Brody, S. S. (1957) Instrument to measure fluorescence lifetimes in the millimicrosecond region. *Rev. Sci. Instr*. **28**, 1021–1026.
44. Brody, S. S. and E. Rabinowitch (1957) Excitation lifetime of photosynthetic pigments in vitro and in vivo. *Science* **125**, 555.
45. Brody, S. S. (1960) Delay in intermolecular and intramolecular energy transfer and lifetimes of photosynthetic pigments. *Z. Elektrochem*. **64**, 187–194.

46. Butler, W. L. and K. H. Norris (1963) Lifetime of the long-wavelength chlorophyll fluorescence. *Biochim. Biophys. Acta* **66**, 72–77.
47. Müller, A., R. Lumry and H. Kokubun (1965) High performance phase fluorometer constructed from commercial subunits. *Rev. Sci. Instrum*. **36**, 1214–1226.
48. Dzhagarov, B. M. (1972) Effect of structural factors on intramolecular transitions in tetrapyrrole molecules. *Izv. Akad. Nauk SSSR, Ser. Fiz*. **36**, 1093–1096 (English translation: *Bull. Acad. Sci. USSR* (1972) **36**, 984–986).
49. Hindman, J. C., R. Kugel, M. R. Wasielewski and J. J. Katz (1978) Coherent stimulated light emission (lasing) in covalently linked chlorophyll dimers. *Proc. Natl. Acad. Sci. USA* **75**, 2076–2079.
50. Yuen, M. J., L. L. Shipman, J. J. Katz and J. C. Hindman (1980) Concentration quenching of fluorescence from chlorophyll-*a*, pheophytin-*a*, pyropheophytin-*a* and their covalently-linked pairs. *Photochem. Photobiol.* **32**, 281–296.
51. Kaplanova, M. and K. Cermak (1981) Effect of reabsorption on the concentration dependence of fluorescence lifetimes of chlorophyll *a*. *J. Photochem*. **15**, 313–319.
52. Connolly, J. S., A. F. Janzen and E. B. Samuel (1982) Fluorescence lifetimes of chlorophyll *a*: Solvent, concentration and oxygen dependence. *Photochem. Photobiol.* **36**, 559–563.
53. Natarajan, L.V., J. E. Ricker, R. E. Blankenship and R. Chang (1984) Solvent influences on the singlet quenching of chlorophyll *a* by 2,5-dimethyl-*p*-benzoquinone. *Photochem. Photobiol.* **39**, 301–306.
54. Jabben, M., N. A. Garcia, S. E. Braslavsky and K. Schaffner (1986) Photophysical parameters of chlorophylls *a* and *b* – fluorescence and laser-induced optoacoustic measurements. *Photochem. Photobiol.* **43**, 127–131.
55. Niedzwiedzki, D. and R. Blankenship (2010) Singlet and triplet excited state properties of natural chlorophylls and bacteriochlorophylls. *Photosyn. Res.* **106**, 227–238.
56. Avarmaa, R. A. and R. P. Tamkivi (1978) Dependence of decay times of chlorophyll fluorescence on luminescence and excitation wavelengths. *Optik. Spektrosk.* **45**, 247–254.
57. Kelly, A. R. and L. K. Patterson (1971) Model systems for photosynthesis II. Concentration quenching of chlorophyll *b* fluorescence in solid solutions. *Proc. Roy. Soc. Lond. A* **324**, 117–126.
58. Avarmaa, R., T. Soovik, R. Tamkivi and V. Tonissoo (1977) Fluorescence life-times of chlorophyll *a* and some related compounds at low temperatures. *Studia Biophysica* **65**, 213–218.
59. Pfarrherr, A., K. Teuchner and D. Leupold (1991) Chlorophyll *b* in solution: fluorescence lifetimes, absorption and emission spectra as criteria of purity. *J. Photochem. Photobiol. B: Biol.* **9**, 35–41.
60. Dmitrievsky, O. D., V. L. Ermolaev and A. N. Terenin (1957) Direct life-time measurements of excited molecules of chlorophyll and analogous pigments in different media. *Dokl. Akad. Nauk SSSR* **114**, 751.
61. Forster, L. S. and R. Livingston (1952) The absolute quantum yields of the fluorescence of chlorophyll solutions. *J. Chem. Phys*. **20**, 1315–1320.
62. Latimer, P., T. T. Bannister and E. Rabinowitch (1956) Quantum yields of fluorescence of plant pigments. *Science* **124**, 585–586.
63. Broyde, S. B. and S. S. Brody (1967) Emission spectra of chlorophyll-*a* in polar and nonpolar solvents. *J. Chem. Phys*. **46**, 3334–3340.

64. Dvornikov, S. S., V. N. Knyukshto, K. N. Solovev and M. P. Tsvirko (1979) Phosphorescence of chlorophyllis *a* and *b* and their pheophytins. *Opt. Spectrosc. (USSR)* **46**, 385–388.
65. Kelly, A. R. and G. Porter (1970) Model systems for photosynthesis I. Energy transfer and light harvesting mechanisms. *Proc. Roy. Soc. Lond. A* **315**, 149–161.
66. Leupold, D., A. Struck, H. Stiel, K. Teuchner, S. Oberländer and H. Scheer (1990) Excited-state properties of 20-chloro-chlorophyll *a*. *Chem. Phys. Lett*. **170**, 478–484.
67. Kawai, N. and K. Morishige (1994) Absorption and fluorescence properties of chlorophyll *a* and *b* and pheophytin *a* and *b* in aqueous solutions of nonionic surfactants. *Bunseki Kagaku* **43**, 791–797.
68. Kawai, N. and K. Morishige (1994) Visible absorption and fluorescence properties of chlorophyll *a* and *b* and pheophytin *a* and *b* in the nonionic surfactant-nonaqueous solvent system. *Bunseki Kagaku* **43**, 1155–1162.
69. Gurinovich, G. P., A. N. Sevchenko and K. N. Solov'ev (1971) *Spectroscopy of Chlorophyll and Related Compounds,* pp 134–364. National Technical Information Service, US Department of Commerce, Springfield, VA.
70. Linnanto, J. and J. Korppi-Tommola (2006) Quantum chemical simulation of excited states of chlorophylls, bacteriochlorophylls and their complexes. *Phys. Chem. Chem. Phys*. **8**, 663–687.
71. Petit, L., A. Quartarolo, C. Adamo and N. Russo (2006) Spectroscopic properties of porphyrin-like photosensitizers: Insights from theory. *J. Phys. Chem. B* **110**, 2398–2404.
72. Balaban, T. S.; Braun, P. Hättig, C.;Hellweg, A.; Kern, J.; Saenger, W.; Zouni, A. (2009) *Biochimica et Biophysica Acta* **1787**, 1254–1265.
73. Weiss, C., Jr. (1972) The pi electron structure and absorption spectra of chlorophylls in solution. *J. Mol. Spectrosc.* **44**, 37–80.
73. Petke, J. D., G. M. Maggiora, L. L. Shipman and R. E. Christoffersen (1978) Stereoelectronic properties of photosynthetic and related systems. *Ab initio* configuration interaction calculations on the ground and lower excited singlet and triplet states of magnesium chlorin and chlorin. *J. Mol. Spectrosc.* **73**, 311–331.
74. Petke, J. D., G. M. Maggiora, L. Shipman and R. E. Christoffersen (1979) Stereoelectronic properties of photosynthetic and related systems–V. *Ab initio* configuration interaction calculations on the ground and lower excited singlet and triplet states of ethyl chlorophyllide *a* and ethyl pheophorbide *a*. *Photochem. Photobiol*. **30**, 203–223.

Chapter 6.

Amphiphilic Chlorins and Bacteriochlorins Partitioned in Micellar Environments. Molecular Design, De novo Synthesis, and Photophysical Properties

Under review at *Chemical Science.*

Abstract

The deployment of amphiphilic tetrapyrrole macrocycles in organized media is of great value for a variety of fundamental photochemical studies, yet work to date has chiefly employed porphyrins rather than chlorins or bacteriochlorins. The latter absorb strongly in the red or near-infrared spectral region, respectively. Here, eight amphiphilic macrocycles (six chlorins and two bacteriochlorins) have been designed, synthesized and characterized; the compounds differ in long wavelength absorption (610–745 nm) and peripheral substituents (type of auxochrome, hydrophobic/hydrophilic groups). A methyl pyridinium or benzoic acid substituent at the 15-position provides a polar "tail" whereas hydrophobic groups distal thereto provide a lipophilic "head" for the spontaneous incorporation into organized media. The eight (bacterio)chlorins are characterized by static and time-resolved absorption and fluorescence spectroscopy in dimethylformamide (DMF) and three micellar environments (TX-100, CTAB, and SDS) as well as ultrafast transient absorption studies in DMF. In most cases, a robust excited singlet state was observed [free base chlorins (Φ_f = 0.14–0.20; τ_S = 7.9–12.1 ns; Φ_{isc} = 0.5), zinc chlorins (Φ_f = 0.08–0.19; τ_S = 2.0–3.4 ns; Φ_{isc} = 0.6–0.8) and free base bacteriochlorins (Φ_f = 0.06–0.16; τ_S = 1.8–4.6 ns; Φ_{isc} = 0.4)]. In the case of bacteriochlorins, minimal medium dependence was observed whereas changing the hydrophilic group from methyl pyridinium to benzoic acid increases the fluorescence yield and excited-state lifetime by 50%. In the case of chlorins, the zinc chelate with methyl pyridinium substitution exhibits substantial environmental dependence due to interaction of the solvent with the methyl pyridinium group and the central zinc metal. Collectively, the studies provide valuable information for the design of red or near-infrared absorbing chromophores for incorporation into amphiphilic environments such as proteins, membranes, or micelles.

Introduction

One of the great distinguishing features of photosynthetic systems is the exquisite 3-dimensional organization of the photo-active and redox-active constituents. The constituents, which include diverse tetrapyrrole macrocycles, are typically arranged in proteins which themselves are embedded in bilayer lipid membranes. Studies to elicit photosynthetic-like function have employed diverse approaches to emulate the molecular organization of the native systems, ranging from the synthesis of covalent multicomponent architectures[1,2] to studies of molecules in non-covalent assemblies. The former approach creates a molecular scaffolding to serve the organizing role of the photosynthetic protein, whereas the latter relies on non-covalent interactions between the component and the medium for organization.

A very attractive means of non-covalent organization entails incorporation of an amphiphilic molecule into a micelle or bilayer membrane. Protoporphyrin IX – Nature's amphiphilic ligand for iron in diverse biological processes (Chart 1) – and analogues thereof have been widely studied in such surfactant assemblies.[3] Protoporphyrin IX is amphiphilic due to the presence of two alkanoic acid groups on one edge of the essentially planar macrocycle, and hydrophobic groups attached to the distal edge. Bonellin, a naturally occurring chlorin found in the marine eucharian worm, is amphiphilic but also far less accessible than protoporphyrin IX.[4,5] Surfactant-based micelles and bilayer membranes in aqueous solution are characterized by a profound change in polarity in moving from the aqueous medium to the core of the assembly; the static dielectric constant changes from ~80 in bulk water to ~2–4 deep in the hydrophobic milieu.[6] Accordingly, an amphiphilic molecule such as protoporphyrin IX is predisposed to organize with the polar, carboxylic acids (or carboxylates) at the aqueous–

surfactant interface, and the remainder of the molecule projects into the core of the hydrophobic surfactact media.

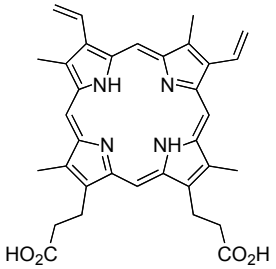

Protoporphyrin IX

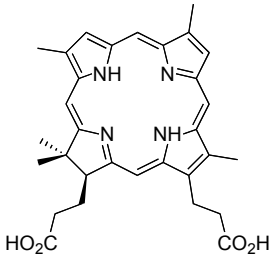

Bonellin

Chart 1. Naturally occurring amphiphilic porphyrin and chlorin

The vast majority of amphiphilic tetrapyrrole macrocycles that have been studied in surfactant media contain the porphyrin chromophore.[3,7,8] Chlorins and bacteriochlorins differ from porphyrins in having strong absorption in the red and near-infrared (NIR) spectral region, and form the basis for chlorophylls and bacteriochlorophylls in photosynthetic phenomena, respectively.[9] Chlorophyll *a* itself is regarded as somewhat amphiphilic (due to the three carbonyl groups on one edge of the molecule) and has been employed in surfactants (e.g., micelles, bilayer membranes) for studies of interfacial photoreactions,[10-12] but our focus here is on amphiphilic hydroporphyrins that contain a fully ionized (or ionizable) moiety. A sizable number of such amphiphilic chlorins have been prepared by semisynthetic methods and examined in surfactant media.[13-36] The starting point in the semisynthesis typically relies on chlorophyll *a*,[13-30] chlorophyll *b*,[31] or protoporphyrin IX.[32-36] Far fewer amphiphilic

bacteriochlorins have been prepared by semisynthesis, and all such compounds are derived from bacteriochlorophyll *a*.[24,37-42] Representative structures of such (bacterio)chlorins are shown in Chart 2. While photosynthetic mimicry provided the initial motivation for study of amphiphilic tetrapyrrole macrocycles in surfactant media, the field of photodynamic therapy has added impetus given that the efficacy of tetrapyrroles as photosensitizers depends in part on interaction with, diffusion through, or transport across bilayer membranes.

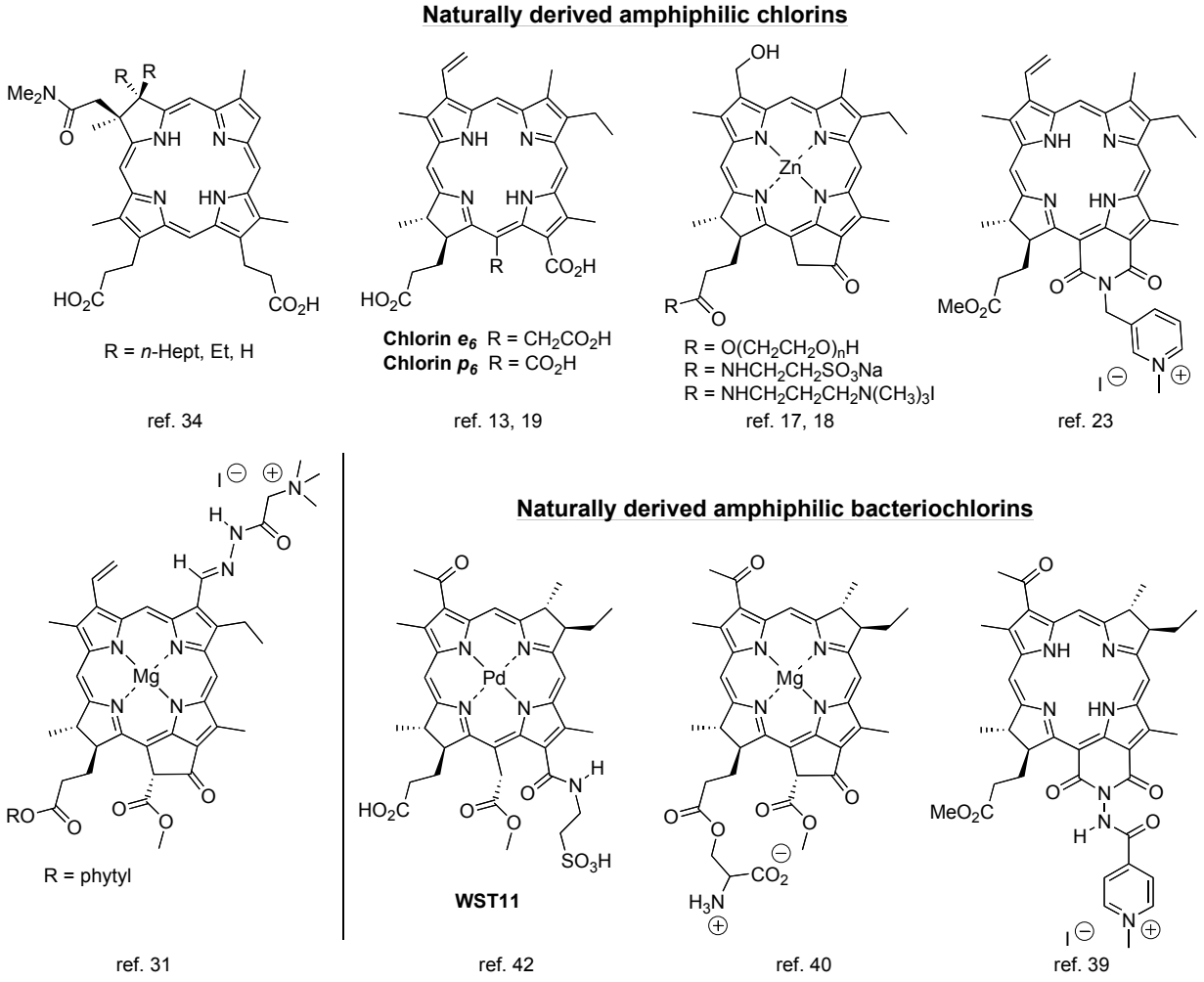

Chart 2. Naturally derived, amphiphilic chlorins and bacteriochlorins

Semisynthetic methods are quite attractive in requiring limited synthetic manipulation from an advanced, naturally occurring substance, but often are equally constrained by the inevitable patterns and types of substituents present therein.[43-46] By contrast, *de novo* synthetic methods require more extensive laboratory work but in principle afford complete freedom of design concerning the type and patterns of peripheral substituents. Considerable advances have occurred in the past two decades concerning the synthesis of chlorins and bacteriochlorins.[47-53] Still, the *de novo* synthesis of amphiphilic (bacterio)chlorins has been exercised to far lesser extent than have the semisynthetic methods.[54-61] Representative synthetic amphiphilic (bacterio)chlorins prepared previously are shown in Chart 3.

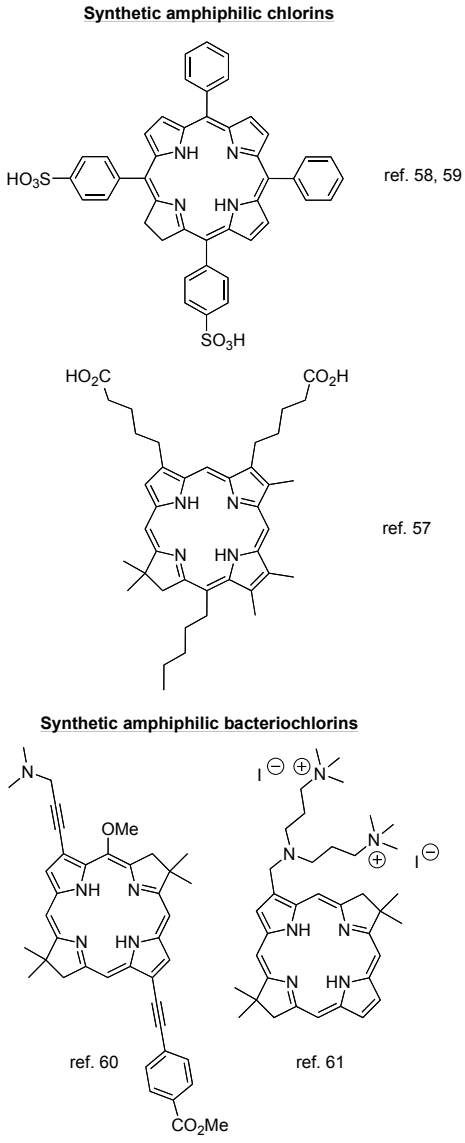

Chart 3. Synthetic, amphiphilic chlorins and bacteriochlorins

In this paper, we report the design, *de novo* synthesis, and photophysical characterization of eight amphiphilic (bacterio)chlorins (Chart 4). The chlorins and bacteriochlorins are equipped with (i) a geminal dimethyl group in each pyrroline ring to stabilize the macrocycle against adventitious dehydrogenation; (ii) a benzoic acid or methyl pyridinium substituent at the 15-position to provide a polar "tail". The chlorins are further diversified by a lipophilic *p*-tolyl group (5-position) or auxochromic and lipophilic phenylethynyl group (3-position) to provide a lipophilic "head", and the use of a zinc chelate versus free base. The compounds are characterized using static and time-resolved absorption and fluorescence spectroscopy in dimethylformamide (DMF) and in aqueous micellar solution containing a neutral, cationic, or anionic surfactant: Triton X-100 (TX-100), cetyl (hexadecyl) trimethylammonium bromide (CTAB), or sodium dodecyl sulfate (SDS); such surfactants have been employed previously with chlorophyll *a*,[62] chlorophyll derivatives,[16,63] and bacteriochlorophyll *a*.[64] The studies provide a roadmap of the interplay between spectral and photophysical properties and the specific environment, macrocycle type (chlorin, bacteriochlorin), central metal (zinc, free base), and substituent groups (hydrophobic, hydrophilic). The insights aid the rational design of amphiphilic photosynthetic-chromophore analogues for target environments (proteins, membranes, micelles, etc.) to maintain tunable red and NIR absorption, modest fluorescence yield and long singlet excited-state lifetime.

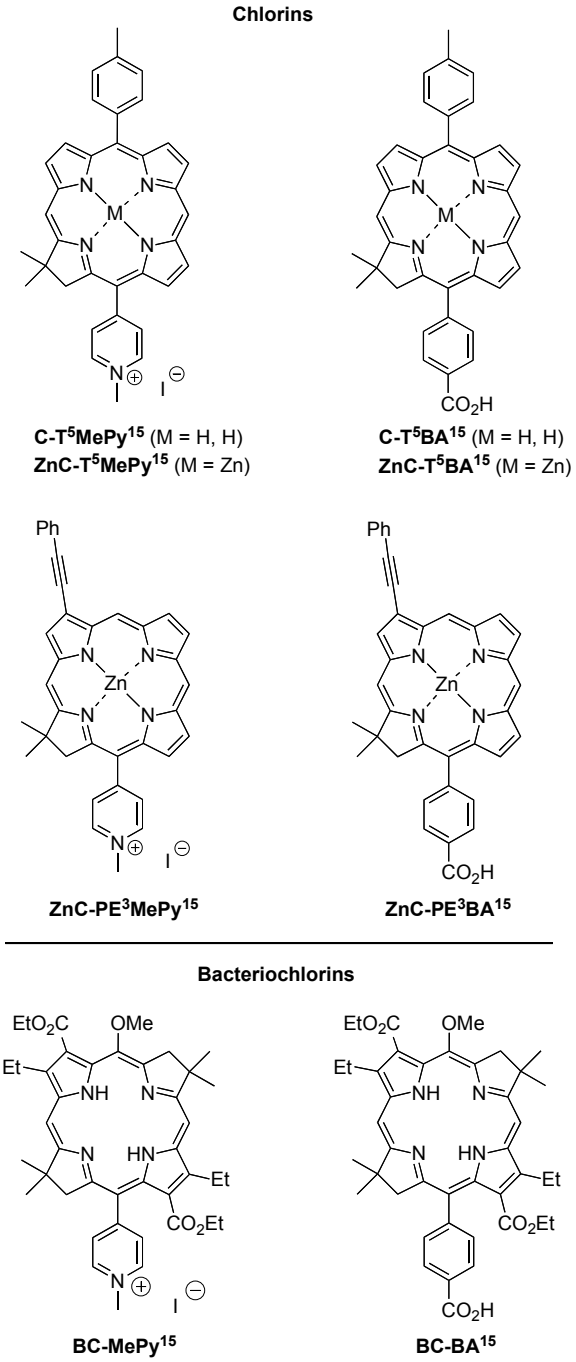

Chart 4. Set of amphiphilic chlorins and bacteriochlorins

Results

I. Synthesis. Synthetic amphiphilic chlorins and bacteriochlorins are available through *de novo* methods that enable introduction of substituents at desired sites about the perimeter of the macrocycle. In the case of chlorins, the methodology entails acid-promoted condensation of a dipyrromethane (Eastern half) and a tetrahydrodipyrrin (Western half) followed by metal-mediated oxidative cyclization,[65-67] whereas bacteriochlorins are prepared by self-condensation of two dihydrodipyrrin–acetal molecules.[68,69] The selective introduction of substituents relies on (i) use of substituted precursors in macrocycle formation;[69,70] or (ii) bromination of the (bacterio)chlorin macrocycle followed by Pd-mediated coupling reaction.[71,72] In the synthesis of the 5,15- and 3,15-chlorins, both strategies were utilized.

A. 5,15-Chlorins. The synthesis of the 5,15-disubstituted chlorins relies on the derivatization of free base 5-*p*-tolyl-15-bromochlorin **C-T^{5}Br^{15}** via palladium coupling. The chlorin **C-T^{5}Br^{15}** was synthesized previously by coupling of Western and *p*-tolyl-containing Eastern halves followed by regioselective 15-bromination.[73] A benzoic acid group at the 15-position was introduced by Suzuki coupling. Thus, treatment of **C-T^{5}Br^{15}** with 8 equivalents of 4-(4,4,5,5-tetramethyl-1,3,2-dioxaborolan-2-yl)benzoic acid (**1**) in the presence of $Pd(PPh_3)_4$ (25 mol %) and 5 equivalents of Cs_2CO_3 at 95 °C under argon afforded chlorin–benzoic acid **C-T^{5}BA^{15}** in 62% yield. Treatment of **C-T^{5}BA^{15}** with excess $Zn(OAc)_2 \cdot 2H_2O$ in $CHCl_3$/MeOH at room temperature gave **ZnC-T^{5}BA^{15}** in 91% yield (Scheme 1).

Synthesis of **C-T^{5}MePy^{15}** started with the treatment of **C-T^{5}Br^{15}** with 4-(4,4,5,5-tetramethyl-1,3,2-dioxaborolan-2-yl)pyridine (**2**) in the presence of $Pd(PPh_3)_4$ (25 mol %) and 5 equivalents of Cs_2CO_3 to afford the corresponding chlorin–pyridine **C-T^{5}Py^{15}** in 85% yield. Quaternization with excess iodomethane in $CHCl_3$ at room temperature afforded the zwitterion

C-T^{5}MePy^{15} in 95% yield. Finally, chlorin **C-T^{5}MePy^{15}** was metalated with 15 equivalents of $Zn(OAc)_2 \cdot 2H_2O$ in $CHCl_3$/MeOH to afford zinc chlorin **ZnC-T^{5}MePy^{15}** in 89% yield. The opposite sequence of quaternization and metalation steps was not successful because of very poor solubility of **ZnC-T^{5}Py^{15}** in organic solvents and partial demetalation upon subsequent treatment with iodomethane (Scheme 1).

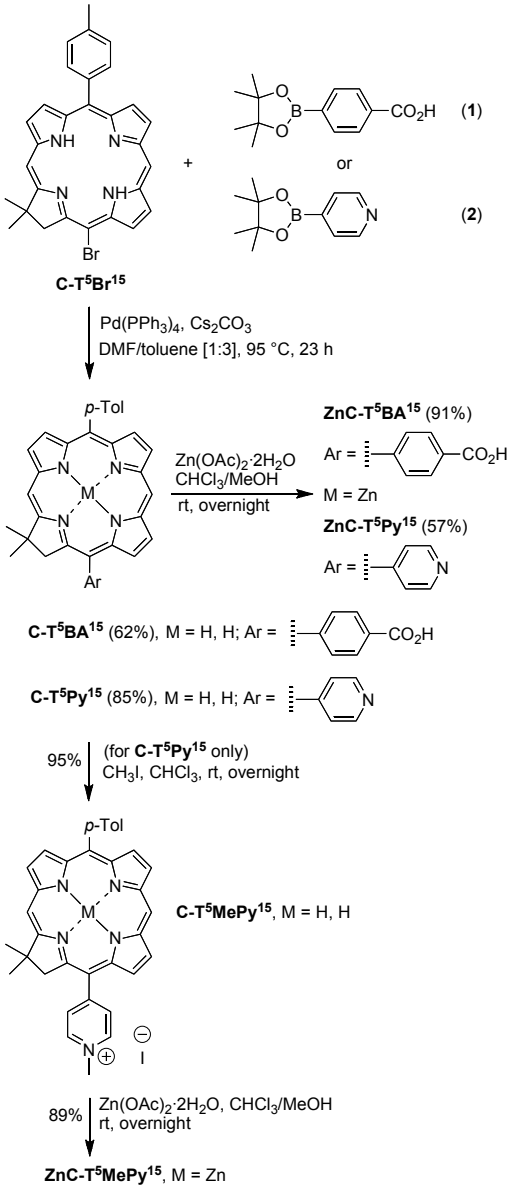

Scheme 1. Synthesis of 5,15-substituted amphiphilic chlorins

B. 3,15-Chlorins. For the synthesis of 3,15-substituted chlorins, we considered functionalizing the Western half as a means of installing the desired auxochrome prior to the chlorin-forming reaction. The synthesis of a Western half bearing a phenylethynyl group is shown in Scheme 2. The Sonogashira coupling of Western half **3**[74] with phenylacetylene was carried out under conditions that have been used with pyrrolic compounds [20 mol% each of $(PPh_3)_2PdCl_2$ and CuI in THF containing diisopropylamine],[70,75,76] thereby affording **4** in 69% yield. The detosylation[74] was achieved by stirring a mixture of **4** and TBAF in THF at reflux for 1 h, affording phenylethynyl Western half **5** in 71% yield (Scheme 2).

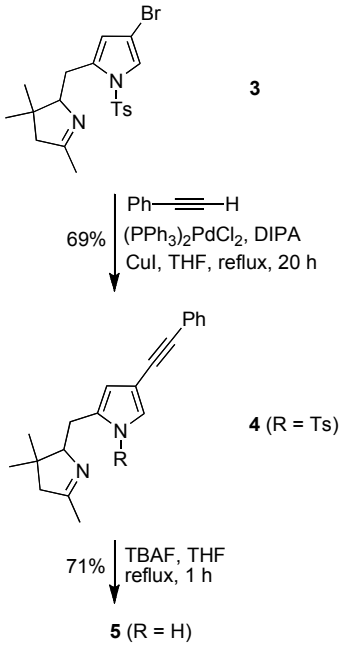

Scheme 2. Synthesis of a phenylethynyl-substituted Western half

The general chlorin-forming reaction[67,70] entails an acid-catalyzed condensation of a 2,3,4,5-tetrahydro-1,3,3-trimethyldipyrrin species (Western half) and a 9-bromo-1-formyl-dipyrromethane species (Eastern half), followed by zinc-mediated oxidative cyclization, as shown in Scheme 3. The phenylethynyl-substituted Western half (**5**) was condensed with an

Eastern half (**6**)[70] in anhydrous CH_2Cl_2 upon treatment with $TsOH \cdot H_2O$ in anhydrous MeOH followed by oxidative cyclization with 2,2,6,6-tetramethylpiperidine, $Zn(OAc)_2$, and AgOTf in refluxing acetonitrile open to air. Subsequent treatment with TFA in CH_2Cl_2 provided the 3-(phenylethynyl)chlorin **C-PE^3** in 6% yield. Chlorin **C-PE^3** was subjected to regioselective bromination (under neutral conditions[77]) at the 15-position to give **C-PE^{3}Br^{15}** in 61% yield. Two-dimensional NMR characterization (HH-NOESY) confirmed the bromine atom at the 15-position.

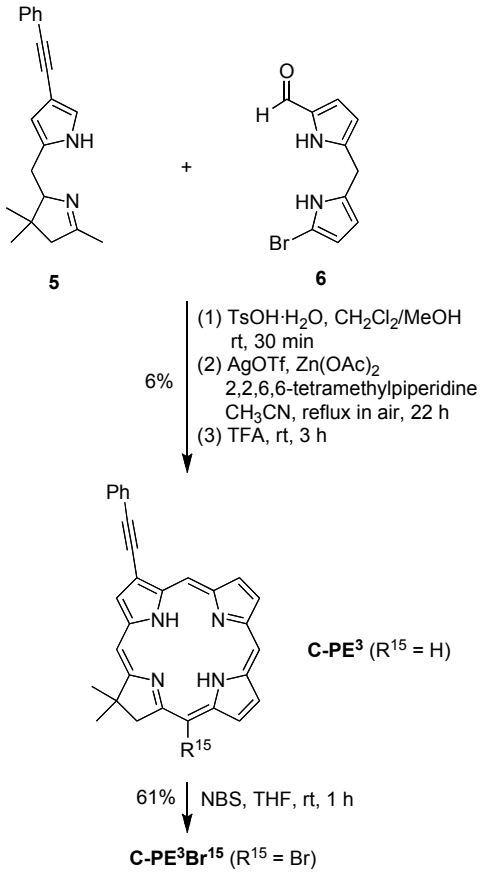

Scheme 3. Synthesis of **C-PE^{3}Br^{15}**

Suzuki coupling of chlorin **C-PE^{3}Br^{15}** and **1** in the presence of $Pd(PPh_3)_4$ and Cs_2CO_3 afforded the chlorin–benzoic acid **C-PE^{3}BA^{15}** in 46% yield. Treatment of **C-PE^{3}BA^{15}** with

excess $Zn(OAc)_2 \cdot 2H_2O$ in $CHCl_3$/MeOH at room temperature gave **ZnC-PE^{3}BA^{15}** in 72% yield (Scheme 4). Similarly, reaction of **C-PE^{3}Br^{15}** and **2** in the presence of $Pd(PPh_3)_4$ and Cs_2CO_3 afforded the 3-(phenylethynyl)chlorin–pyridine **C-PE^{3}Py^{15}** in 76% yield. Quaternization with excess iodomethane in $CHCl_3$ at room temperature afforded the zwitterion **C-PE^{3}MePy^{15}** in 82% yield. Finally, chlorin **C-PE^{3}MePy^{15}** was metalated with 15 equivalents of $Zn(OAc)_2 \cdot 2H_2O$ in $CHCl_3$/MeOH to afford the zinc chlorin **ZnC-PE^{3}MePy^{15}** in 72% yield.

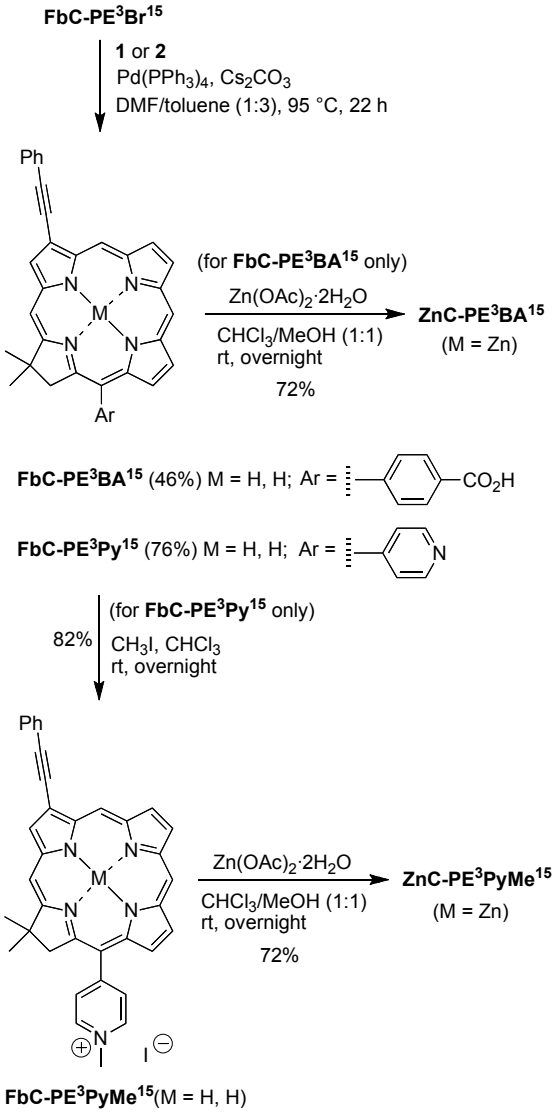

Scheme 4. Synthesis of 3,15-substituted amphiphilic chlorins

C. Bacteriochlorins. To obtain tetrapyrroles with NIR absorption, we chose one set of bacteriochlorins (Chart 4), which absorb strongly in the 700–800 nm region. The synthesis of amphiphilic bacteriochlorins relies on the Suzuki coupling[72] of a 15-bromobacteriochlorin[69] (**BC-Br**^{15}, Scheme 5). Thus, treatment of **BC-Br**^{15} with 5 equivalents of **1** in the presence of $Pd(PPh_3)_4$ (30 mol%) and 6 equivalents of Cs_2CO_3 at 95 °C under argon gave the corresponding bacteriochlorin–benzoic acid **BC-BA**^{15} in 20% yield. The use of a stoichiometric amount of $Pd(PPh_3)_4$ gave the product **BC-BA**^{15} in 63% yield. No palladiation of the bacteriochlorin was observed under these conditions. Similarly, Suzuki coupling of **BC-Br**^{15} with 5 equivalents of **2** gave the bacteriochlorin–pyridine **BC-Py**^{15} in 74% yield. Quaternization with excess MeI gave quantitative conversion to give methyl pyridinium bacteriochlorin **BC-MePy**^{15}.

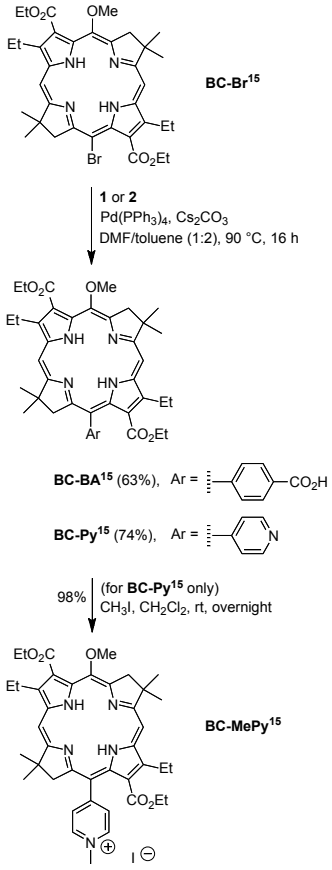

Scheme 5. Synthesis of amphiphilic bacteriochlorins

II. Photophysical characterization. Studies of each amphiphilic chlorin and bacteriochlorin were performed in the organic solvent DMF and in three aqueous micellar solutions: CTAB (cationic), SDS (anionic) and TX-100 (neutral). Each micellar solution contained phosphate buffer (pH 7) with surfactant at a concentration (~3 mM, TX-100; ~10 mM, CTAB; ~80 mM, SDS) that is about 10-times the critical micelle concentration (cmc) (~0.2 mM, TX-100; ~1 mM for CTAB; ~8 mM for SDS).[78] Assuming roughly 100 surfactant molecules per micelle and Poisson statistics,[16,62,79] for a chlorin or bacteriochlorin concentration of roughly 1 μM, there typically will be one or a few chromophores per micelle (with many empty micelles) under the conditions of the experiments. This estimate is consistent with the finding that the photophysical properties (absorption and fluorescence spectra, fluorescence yields, singlet excited-state lifetimes) of both bacteriochlorins are essentially unchanged when the surfactant concentration is reduced to the cmc level, and the same is true for select chlorin/surfactant combinations. Note that the Poisson model may not rigorously hold if there are specific interactions between the chromophores and the charged head groups of the surfactant. This point has been raised in studies of chlorophyll *a* and analogues, nominally at 10-fold the chromophore concentrations (e.g., 10 μM) and 0.1-fold the surfactant concentration (e.g., 1 mM CTAB, near the cmc) used here.[16] The possibility of such interactions for the select amphiphilic chlorins and charged surfactants (CTAB, SDS) is discussed below.

A. Absorption and fluorescence spectra. Fig. 1 shows absorption and fluorescence spectra for the three pairs of amphiphilic chlorins (**ZnC-T^{5}MePy^{15}** and **ZnC-T^{5}BA^{15}**; **ZnC-PE^{3}MePy^{15}** and **ZnC-PE^{3}BA^{15}**; **C-T^{5}MePy^{15}** and **C-T^{5}BA^{15}**) in DMF and the three micellar solutions. Fig. 2 shows the analogous data for a pair of amphiphilic bacteriochlorins (**BC-MePy^{15}** and **BC-BA^{15}**) in the same four media.

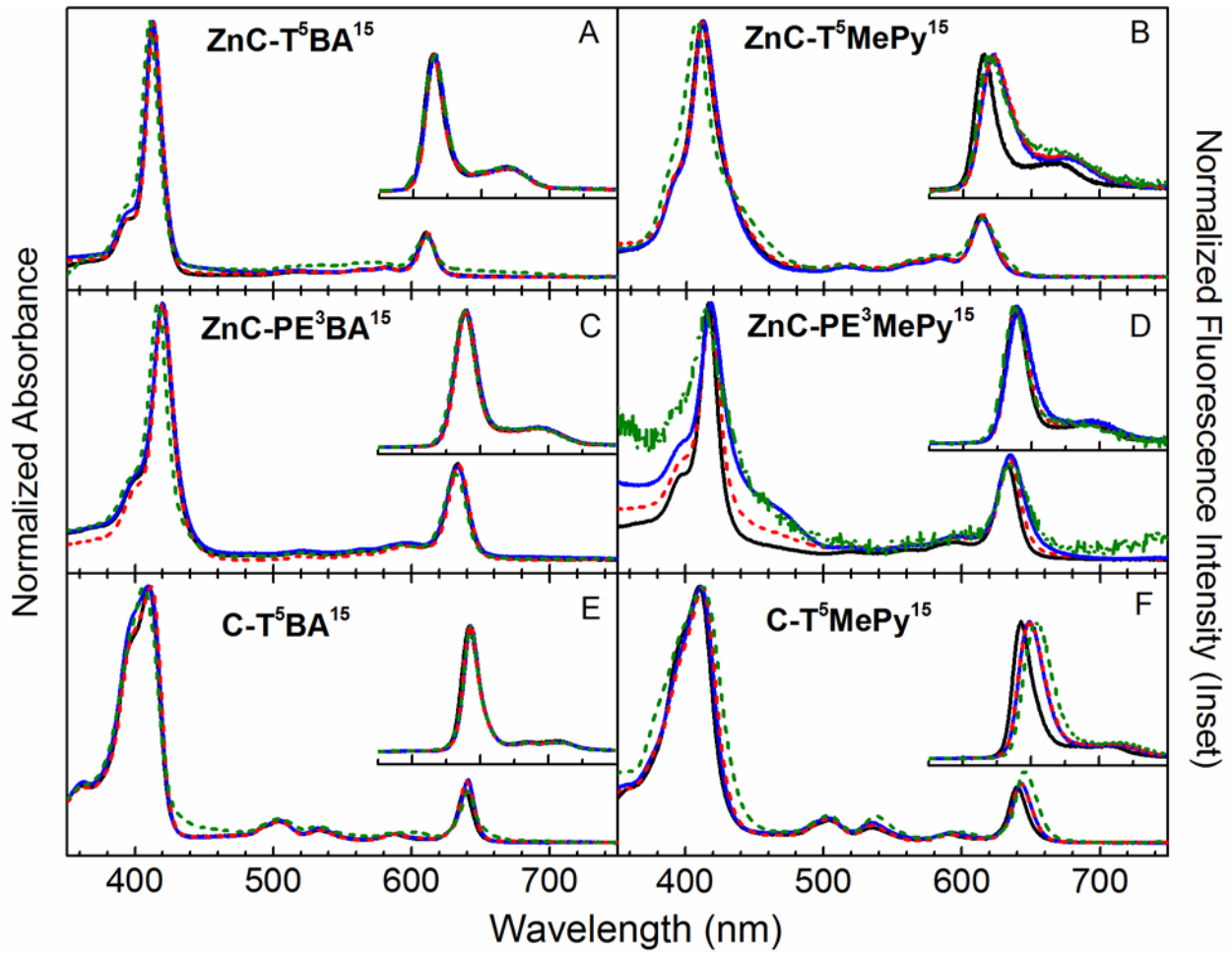

Fig. 1 Normalized absorbance (main) and fluorescence (inset) for chlorins **ZnC-T^{5}BA^{15}** (A), **ZnC-T^{5}MePy^{15}** (B), **ZnC-PE^{3}BA^{15}** (C), **ZnC-PE^{3}MePy^{15}** (D), **C-T^{5}BA^{15}** (E) and **C-T^{5}MePy^{15}** (F) in DMF (black), TX-100 (red dash), CTAB (blue), and SDS (green dash).

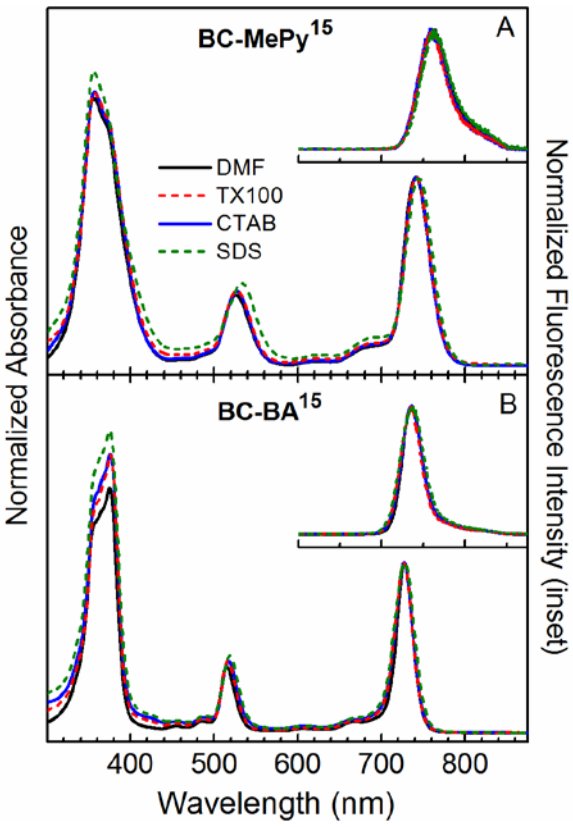

Fig. 2 Normalized absorbance (main panels) and fluorescence (insets) for bacteriochlorins **BC-MePy**[15] (A) and **BC-BA**[15] (B) in DMF (black), TX-100 (red dash), CTAB (blue), and SDS (green dash).

The absorption spectrum of each amphiphilic (bacterio)chlorin shows the expected features in three spectral regions. These are the near-ultraviolet (NUV) Soret bands (B_y and B_x) that coalesce in some cases, the green-orange Q_x bands for which both the (1,0) and (0,0) transitions are prominent in some cases, and the Q_y band, which is dominated by the (0,0) transition. The $Q_y(0,0)$ band lies in the red region for chlorins and the NIR for bacteriochlorins; the band is more intense for bacteriochlorins than for chlorins. Table 1 lists the peak positions of the B (B_y and B_x where resolved), Q_x (origin and overtone bands where apparent) and Q_y (origin band). The table also includes the Q_y/B peak-intensity ratio, the position of the Q_y fluorescence maximum, and the full-width-at-half-maximum (FWHM) of the Q_y absorption and fluorescence bands. As noted above, the data in Table 1 (and Figs. 1 and 2) for the amphiphilic

(bacterio)chlorins in micellar solutions utilized surfactants at ~10 times the cmc in phosphate buffer (pH7). Table 2 shows that, for the bacteriochlorins, similar results were obtained in the micellar solutions with surfactants at the cmc with or without the buffer.

Table 1. Spectral and photophysical properties of amphiphilic (bacterio)chlorins.[a]

Compound	Solvent	B Abs (nm)[b]	Q_x Abs (nm)[c]	Q_y Abs (nm)	Q_y Abs FWHM (nm)	I_{Qy}/I_B	Q_y Em (nm)	Q_y Em FWHM (nm)	Φ_f	τ_S (ns)
ZnC-T^{5}MePy^{15}	DMF	411	518	614	20	0.25	615	18	0.007	0.04[d]
ZnC-T^{5}BA^{15}	DMF	413	516	610	15	0.18	615	16	0.08	2.0
ZnC-PE^{3}MePy^{15}	DMF	417	519	633	18	0.38	639	18	0.16	3.2
ZnC-PE^{3}BA^{15}	DMF	420	521	633	18	0.37	639	18	0.19	3.3
C-T^{5}MePy^{15}	DMF	410	503/535	640	15	0.22	643	17	0.15	9.5
C-T^{5}BA^{15}	DMF	410	505/533	639	13	0.21	642	15	0.20	11.1
BC-MePy^{15}	DMF	356/371	526	741	35	0.70	762	43	0.06	1.8
BC-BA^{15}	DMF	357/375	515	728	24	0.70	736	28	0.16	4.6
ZnC-T^{5}MePy^{15}	TX-100	412	515	615	21	0.26	622	28	0.02	0.48[d]
ZnC-T^{5}BA^{15}	TX-100	413	516	611	14	0.18	615	15	0.07	2.0
ZnC-PE^{3}MePy^{15}	TX-100	418	519	634	20	0.40	639	19	0.13	3.1
ZnC-PE^{3}BA^{15}	TX-100	421	520	634	17	0.36	639	18	0.17	3.2
C-T^{5}MePy^{15}	TX-100	412	504/535	643	17	0.25	649	23	0.15	9.9
C-T^{5}BA^{15}	TX-100	412	505/533	640	12	0.24	642	13	0.18	11.9
BC-MePy^{15}	TX-100	357/374	527	742	35	0.69	760	41	0.09	3.1
BC-BA^{15}	TX-100	359/376	517	727	25	0.61	734	29	0.13	4.7
ZnC-T^{5}MePy^{15}	CTAB	412	515	614	21	0.23	623	26	0.02	0.37[d]
ZnC-T^{5}BA^{15}	CTAB	413	517	611	16	0.17	616	17	0.07	2.1
ZnC-PE^{3}MePy^{15}	CTAB	419	518	635	23	0.41	640	21	0.10	2.4
ZnC-PE^{3}BA^{15}	CTAB	420	521	633	20	0.36	640	19	0.16	3.1
C-T^{5}MePy^{15}	CTAB	411	503/535	643	17	0.24	649	22	0.14	7.9
C-T^{5}BA^{15}	CTAB	409	504/533	641	12	0.25	643	13	0.18	11.7
BC-MePy^{15}	CTAB	357/372	528	742	34	0.69	760	40	0.07	2.7
BC-BA^{15}	CTAB	358/376	517	727	26	0.61	736	29	0.12	4.4
ZnC-T^{5}MePy^{15}	SDS	407	516	615	27	0.24	619	27	0.002	0.02[d]
ZnC-T^{5}BA^{15}	SDS	411	*e*	610	17	0.19	615	20	0.04	2.1
ZnC-PE^{3}MePy^{15}	SDS	415	*e*	635	28	0.38	638	20	~0.03[f]	0.1/3.0[d,f]
ZnC-PE^{3}BA^{15}	SDS	417	519	632	20	0.34	639	19	0.16	3.4
C-T^{5}MePy^{15}	SDS	412	504/538	645	18	0.29	654	25	0.15	8.4
C-T^{5}BA^{15}	SDS	406	505/533	641	14	0.21	642	13	0.14	12.1
BC-MePy^{15}	SDS	356	533	745	37	0.64	763	42	0.06	2.6
BC-BA^{15}	SDS	359/375	518	728	29	0.56	736	34	0.11	4.1

[a]All data were acquired at room temperature. The typical error is ±15% for the fluorescence quantum yield (Φ_f) and ±20% for the singlet excited-state lifetime (τ_S). [b]The B absorption bands merge to one feature with partially resolved bands for. [c]The features for the zinc chlorins are very weak and potentially complicated by interference from higher order vibronic Q_y bands. The Q_x absorption for free base chlorins is $Q_x(1,0)/Q_x(0,0)$ and is $Q_x(0,0)$ for bacteriochlorins. [d]Decay time was determined by transient absorption spectroscopy, with primary component(s) listed in table. The full set of decay components are for **ZnC-T^{5}MePy^{15}** in the four media are as follows: DMF [40 ps (98%), ~1 ns (2%); TX-100 [70 ps (23%), 480 ps (52%), 1.3 ns (25%)]; CTAB [66 ps (20%), 370 ps (60%), 1.1 ns (20%); SDS [20 ps (70%), 60 ps (25%), 1.4 ns (5%)]. [e]Q_x features are too weak to be identified. [f]**ZnC-PE^{3}MePy^{15}** is sparingly soluble in SDS. The Φ_f value is approximate and τ_S is biphasic with components of 100 ps (65%) and 3 ns (35%).

Table 2. Spectral and photophysical properties of amphiphilic bacteriochlorins.[a]

Compound	Solvent	x-cmc conc	buffer	B Abs (nm)[b]	Q_x Abs (nm)[c]	Q_y Abs (nm)	Q_y Abs FWHM (nm)	I_{Qy}/I_B	Q_y Em (nm)	Q_y Em FWHM (nm)	Φ_f	τ_S (ns)
BC-MePy^{15}	DMF	na	na	356/371	526	741	35	0.70	762	43	0.06	1.8
	TX-100	10	+	357/374	527	742	35	0.69	760	41	0.09	3.1
		1	+	357/374	526	742	35	0.70	760	42	0.09	3.1
		1	–	357/373	528	742	35	0.70	760	42	0.07	2.9
	CTAB[d]	10	+	357/372	528	742	34	0.69	760	40	0.07	2.7
		1	+	357/371	528	742	33	0.67	760	40	0.07	2.7
		1	–	356/372	528	743	35	0.67	762	38	0.04	1.9
	SDS	10	+	356	533	745	37	0.64	763	42	0.06	2.6
BC-BA^{15}	DMF	na	na	357/375	515	728	24	0.70	736	28	0.16	4.6
	TX-100	10	+	359/376	517	727	25	0.61	734	29	0.13	4.7
		1	+	358/376	517	727	25	0.63	734	29	0.14	4.6
		1	–	359/377	517	727	26	0.61	735	28	0.14	4.6
	CTAB	10	+	358/376	517	727	26	0.61	736	29	0.12	4.4
		1	+	358/376	518	726	27	0.59	736	30	0.10	4.3
		1	–	357/376	517	724	31	0.56	734	29	0.05	3.5
	SDS[d]	10	+	359/375	518	728	29	0.56	736	34	0.11	4.1
		1	–	359/375	518	723	29	0.53	733	33	0.09	3.9

[a]All data were acquired at room temperature. Column 3 for the micellar solutions indicates whether the surfactant is at 1- or 10-fold the cmc. Column 4 indicates whether (+) or not (–) the micellar solution was prepared using phosphate buffer (pH 7) or simply deionized water. In columns 3 and 4, na means the parameter is not applicable for DMF. [b] The B absorption bands are nominally B_y/B_x. [c] The Qx absorption is $Q_x(0,0)$. [d]Aggregation is significant in this case.

The amphiphilic (bacterio)chlorins are generally soluble in the four media to concentrations of (at least) tens of micromolar, far in excess of the ~1 μM level typical for the spectroscopic measurements. Cases with severely limited solubility are **ZnC-PE^{3}MePy^{15}** in

SDS, TX-100 and CTAB; **ZnC-T^{5}BA^{15}** in SDS; and **ZnC-PE^{3}BA^{15}** in SDS. The resulting (filtered) solution for **ZnC-T^{5}BA^{15}** shows a normal sharp Soret band with only minor spectral distortion in the Q_x and Q_y region, which is visible as a slightly elevated baseline (Fig. 1A, green dash). In the case of **ZnC-PE^{3}MePy^{15}** in CTAB and SDS, broadening of the Soret band is observed with only modest change in the Q_y absorption (Fig. 1D, blue and green-dash). The Soret broadening is accompanied by formation of a separate feature at ~460 nm that is further revealed in a multi-Gaussian fit (Fig. 3B). The elevated baseline in the NUV region of the micellar solution indicates some light scattering in the sample.

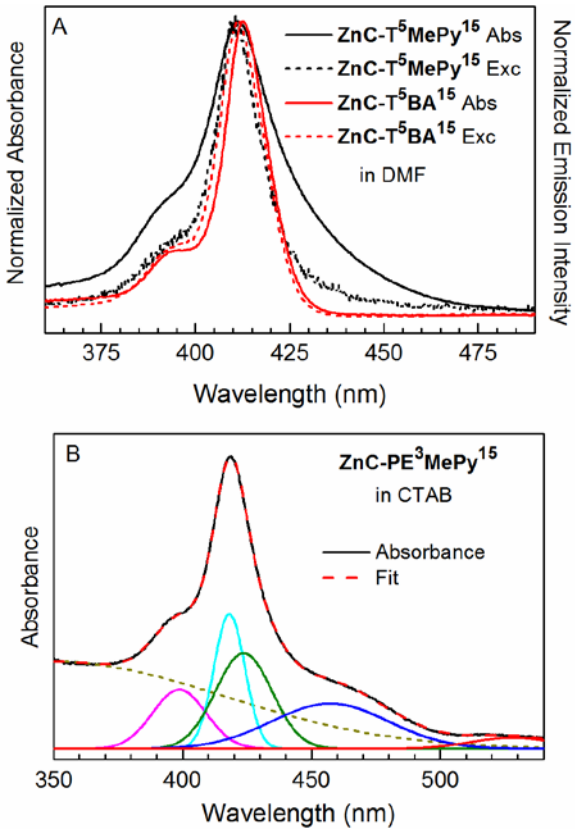

Fig. 3 (A) Normalized Soret region absorption spectra (solid lines) and fluorescence excitation spectra (dashed lines) for **ZnC-T^{5}MePy^{15}** (black) and **ZnC-T^{5}BA^{15}** (red) in DMF; for the excitation spectra, the fluorescence was detected at 615 and 642 nm for the two compounds, respectively. (B) Soret-region absorbance for **ZnC-PE^{3}MePy^{15}** in CTAB (black), six fit Gaussian components, and cumulative fit (red dashed); the absorbance scale is 0–0.06.

In contrast, the absorption spectrum of **ZnC-PE^{3}BA^{15}** is normal in all four media (Fig. 1C). The same is true for analogue **ZnC-T^{5}BA^{15}** (Fig. 1A), wherein the 3-phenylethyne group is replaced by a 5-*p*-tolyl group. The effects of the 15-benzoic acid substituent of **ZnC-T^{5}BA^{15}** are readily compared with those of the methyl pyridinium group (referred to hereafter as benzoate and pyridinium, respectively); the methyl pyridinium-containing **ZnC-T^{5}MePy^{15}** retains good solubility but broadened Soret-region absorption in all solvents (Fig. 1B). An expanded Soret-region view in DMF is given in Fig. 3A. The broadened absorption of **ZnC-T^{5}MePy^{15}** extends to 475 nm whereas that for **ZnC-T^{5}BA^{15}** has reached the baseline by ~430 nm despite the similar position of the maximum for the two compounds. The fluorescence excitation spectra for the two compounds closely resemble the relatively narrow absorption band of **ZnC-T^{5}BA^{15}** (Fig. 3A). These comparisons show that the states/species responsible for the Soret broadening of **ZnC-T^{5}MePy^{15}** do not give rise to fluorescence. The analogous bacteriochlorins **BC-MePy^{15}** and **BC-BA^{15}** both show normal Soret-region absorption characterized by overlapping but discernible B_y and B_x components (Fig. 2).

B. Excited-state properties. The fluorescence quantum yield (Φ_f) and singlet excited-state lifetime (τ_S) were measured for each of the eight compounds in the four different media (Table 1). The τ_S values were typically measured using two fluorescence techniques (frequency domain, and time domain with ~1 ns instrument response function) and averaged. For zinc chlorins **ZnC-T^{5}MePy^{15}** in all media and **ZnC-PE^{3}MePy^{15}** in SDS, ultrafast transient absorption spectroscopy (~100 fs resolution) was also used to determine lifetimes (or components) not resolvable by the other techniques.

Ultrafast transient absorption studies were performed for all eight compounds in DMF to obtain an estimate of the yield of $S_1 \rightarrow T_1$ intersystem crossing (Φ_{isc}), also called the triplet yield.

Representative data for **ZnC-T^{5}BA^{15}** in DMF are shown in Fig. 4A. The spectrum at 50 ps is due to the S_1 excited state and contains $Q_y(0,0)$ ground-state absorption bleaching and excited-state stimulated emission at ~615 nm along with a relatively flat excited-state absorption between 450 and 600 nm. At 5 ns (the data extend to ~8 ns), the feature at ~615 nm has decayed and has almost reached an asymptotic value reflecting Q_y bleaching due to the population of molecules that remain out of the ground state and in the long-lived T_1 excited state. From these data a value of $\Phi_{isc} \sim 0.8$ is obtained. The inset to Fig. 4A shows the S_1 decay profile ($\tau \sim 1.8$ ns), which is consistent with the τ_s value of 2.0 ns obtained by fluorescence measurements. Except for positions of the ground-state bleaching features and the time scales of the S_1 decay, the transient absorption data for **ZnC-T^{5}BA^{15}** are representative of the other compounds in DMF except for **ZnC-T^{5}MePy^{15}**, which is described below.

For each compound in DMF, the Φ_{isc} value together with Φ_f affords the yield of $S_1 \rightarrow S_0$ internal conversion (Φ_{ic}) via the relationship $\Phi_{ic} = 1 - \Phi_{isc} - \Phi_f$. The three yields along with τ_S give the rate constants for S_1 excited-state decay via fluorescence (k_f), intersystem crossing (k_{isc}), and internal conversion (k_{ic}) via the expression $k_i = \Phi_i / \tau_S$. The yields and rate constants for the six chlorins and two bacteriochlorins in DMF are collected in Table 3.

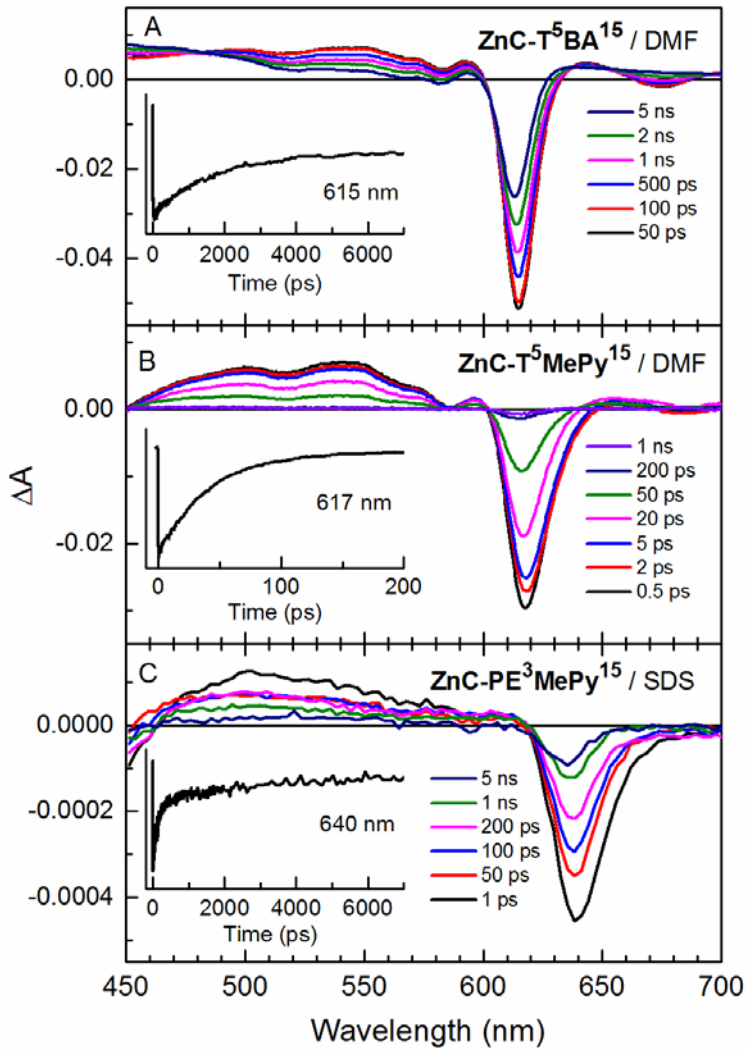

Fig. 4. Transient absorption data of select compounds and media using excitation with 100 fs flashes at 415 nm. Each panel shows representative spectra as a function of time, with an inset giving a representative kinetic profile at the indicated probe wavelength. (A) **ZnC-T^{5}BA^{15}** in DMF, (B) **ZnC-T^{5}MePy^{15}** in DMF, and (C) **ZnC-PE^{3}MePy^{15}** in SDS. Note the shorter time scale of the inset in (B) and the smaller amplitude of ΔA in (C), which is limited by the solubility of the compound in SDS.

Table 3. Photophysical and kinetic properties of amphiphilic tetrapyrroles in DMF.[a]

Compound	τ_S (ns)	Φ_f	Φ_{isc}	Φ_{ic}	k_f^{-1} (ns)	k_{isc}^{-1} (ns)	k_{ic}^{-1} (ns)
ZnC-T^{5}MePy^{15}	0.04	0.007	0.01	0.98[b]	6	4	0.04[b]
ZnC-T^{5}BA^{15}	2.0	0.08	0.84	0.08	30	2	20
ZnC-PE^{3}MePy^{15}	3.2	0.16	0.61	0.23	20	5	10
ZnC-PE^{3}BA^{15}	3.3	0.19	0.71	0.10	20	5	30
C-T^{5}MePy^{15}	9.5	0.15	0.51	0.34	60	20	30
C-T^{5}BA^{15}	11.1	0.20	0.45	0.35	60	20	30
BC-MePy	1.8	0.06	0.39	0.55	30	5	3
BC-BA^{15}	4.6	0.16	0.41	0.43	30	10	10

[a]All data were obtained at room temperature. Φ_{isc} values are ±15%. [b]Facilitated by a process such as charge transfer.

The S_1 excited-state decay characteristics of the amphiphilic chlorins and bacteriochlorins in DMF are generally similar to those of synthetic lipophilic chlorin[80-82] and bacteriochlorin[83] analogues studied previously in organic solvents (typically toluene). For example, the values of $\tau_S \sim 4.6$ ns, $\Phi_f \sim 0.16$ and $\Phi_{isc} \sim 0.4$ for bacteriochlorin **BC-BA^5** are typical of synthetic free base bacteriochlorins that have the Q_y absorption band in the 720–780 nm region, which defines the energy of the S_1 excited state.[83] Analogue **BC-MePy^{15}** has modestly lower τ_S (~1.8 ns) and Φ_f (~0.06) values. Free base chlorins **C-T^{5}BA^{15}** and **C-T^{5}MePy^{15}** exhibit $\tau_S \sim 10$ ns, Φ_f = 0.15–0.20 and $\Phi_{isc} \sim 0.5$. Zinc chlorins **ZnC-T^{5}BA^{15}**, **ZnC-PE^{5}BA^{15}** and **ZnC-PE^{5}MePy^{15}** have τ_S values reduced to 2.0–3.2 ns, Φ_f in the range 0.08–0.19 and Φ_{isc} increased to 0.6–0.8. Differences between the zinc chelates and free base analogues can be traced largely to the heavy atom effect on intersystem crossing rate constant k_{isc}. The outlier is **ZnC-T^{5}MePy^{15}** in DMF, for which Φ_f is reduced to 0.007 and $\tau_s \sim 40$ ps. In the simple trifurcation model for S_1 excited-state decay, **ZnC-T^{5}MePy** exhibits an effectively greater yield and rate constant of $S_1 \rightarrow S_0$ internal conversion, perhaps due to a contribution from charge transfer (*vide infra*).

Consider now the consequences of pyridinium versus benzoate as the 15-hydrophilic group on the S_1 excited-state decay properties of the amphiphilic (bacterio)chlorins spanning DMF and the three micellar media (CTAB, SDS, TX-100) (Table 1). Bacteriochlorin **BC-BA**[15] has Φ_f and τ_S values (0.11–0.16; 4.1–4.7 ns) that are increased about two-fold compared to those for **BC-MePy**[15] (0.06–0.09; 1.8–3.1 ns). The increases for the bacteriochlorin pair are more substantial than those for the pair of free base chlorin analogues, are in the mid-range of those found for the zinc chlorins, and show less medium dependence, as noted in the following.

The change in the 15-hydrophilic substituent from pyridinium to benzoate for the chlorins also consistently increases Φ_f and τ_S, with varying magnitudes dependent on the medium and other chromophore design variables (hydrophobic substituent/site and metalation state) (Table 1). For the free base chlorins, Φ_f and τ_S values of **C-T**[5]**BA**[15] (0.14–0.20, 11.1–12.1 ns) are only modestly larger than those for **C-T**[5]**MePy**[15] (0.14–0.15, 7.9–9.9 ns), one exception being effectively the same Φ_f in SDS. Similarly, for the 3-phenylethynyl pair, the Φ_f and τ_S values of **ZnC-PE**[3]**BA**[15] in DMF, TX-100 and CTAB (0.16–0.19, 3.1–3.2 ns) are only modestly increased compared to those of **ZnC-PE**[3]**MePy**[15] (0.10–0.16, 2.4–3.2 ns). The values for **ZnC-PE**[3]**BA**[15] in SDS are in accord with the other media (0.16, 3.4 ns). However, **ZnC-PE**[3]**MePy**[15] in SDS (for which the solubility is low) has dramatically reduced Φ_f (~0.03) and biphasic S_1 decay with a fast (~100 ps) component (*vide infra*). The Φ_f of **ZnC-T**[5]**BA**[15] is increased ten-fold in DMF and two-fold in SDS compared to **ZnC-T**[5]**MePy**[15], along with parallel increases in τ_S. Similar but less dramatic increases in Φ_f and τ_S are observed for **ZnC-T**[5]**BA**[15] versus **ZnC-T**[5]**MePy**[15] in CTAB and TX-100. In general, the singlet excited-state (e.g., fluorescence) decay profile for **ZnC-T**[5]**MePy**[15] in each medium is multi-exponential, requiring ultrafast transient absorption to resolve the fast components as follows.

The transient absorption spectrum for **ZnC-T^{5}MePy^{15}** in DMF is shown in Fig. 4B. Like **ZnC-T^{5}BA^{15}** (Fig. 4A), the spectrum at 0.5 ps contains $Q_y(0,0)$ ground-state absorption bleaching and excited-state stimulated emission at ~615 nm. Compared to **ZnC-T^{5}BA^{15}**, the early-time spectrum for **ZnC-T^{5}MePy^{15}** appears to have more pronounced excited-state absorption in the 450–600 nm region with a small dip at ~525 nm that likely represents bleaching of a Q_x vibronic component. An even greater difference is that unlike the modest τ_s (~2 ns) and large Φ_{isc} for **ZnC-T^{5}BA^{15}** (Fig. 4A and Table 3), the entire spectrum for **ZnC-T^{5}MePy^{15}** effectively (~95%) decays to $\Delta A = 0$, reflecting the return of molecules to the ground state, with a 40 ps time constant (Fig. 4B inset). The short τ_S parallels the low Φ_f (0.007) observed for **ZnC-T^{5}MePy^{15}** DMF. Similar results are obtained for this chlorin in SDS, which also has a substantially reduced Φ_f (0.002) along with a shortened S_1 excited-state decay (Table 1).

Another special, somewhat intermediate, case is **ZnC-PE^{3}MePy^{15}** in SDS (Fig. 4C). The combination of this chlorin and medium results in limited solubility and a reduced Φ_f (~0.03) compared to this compound in other media (0.10-0.16) (Table 1). The excited-state decay and ground-state recovery profile includes a prompt ~100 ps and longer-lived ~3 ns components in a roughly 2:1 ratio. The slower phase is consistent with the τ_s value measured via fluorescence decay. The fast phase is consistent with the reduced Φ_f and a route for facile deactivation of the S_1 excited-state to the ground state in a fraction of the sample.

Discussion

A. Overview. Rational synthetic methods now provide access to amphiphilic (bacterio)chlorins. Amphiphilicity facilitates organized deployment of molecules in micelles, membranes, liposomes, proteins and other such environments wherein a largely hydrophobic compartment is surrounded by a largely hydrophilic region and/or aqueous phase. Amphiphilic chlorins have been accessible previously via the *de novo* approach of Jacobi,[54,55,57] but far fewer amphiphilic bacteriochlorins have been prepared. The three primary design variables explored in the set of six amphiphilic chlorins (**ZnC-PE^{3}MePy^{15}**, **ZnC-PE^{3}BA^{15}**, **ZnC-T^{5}MePy^{15}**, **ZnC-T^{5}BA^{15}**, **C-T^{5}MePy^{15}**, **C-T^{5}BA^{15}**) are (1) the identity of the hydrophilic group at the 15-position (pyridinium and benzoate), (2) identity and position of the hydrophobic group (*p*-tolyl and phenylethynyl), and (3) macrocycle metalation state (zinc or free base). The two bacteriochlorins (**BC-MePy^{15}** and **BC-BA^{15}**) differ in the 15-hydrophilic group.

A chief recent use of amphiphilic hydroporphyrins in membranes has been in photodynamic therapy. Fundamental studies with amphiphilic hydroporphyrins in membranes include the following: examination of the yield of singlet oxygen as a function of tetrapyrrole depth in the membrane;[57] probing the effects of surfactant composition and tetrapyrrole structure in determining tetrapyrrole assembly and aggregation[16,56,63] including formation of light-harvesting antennae;[17,18] and examination of interfacial photoreactions such as photoinduced electron-transfer processes.[19,31] The photophysical studies performed herein establish the foundation for use of the synthetic (bacterio)chlorins for such applications as well as with biohybrid photosynthetic light-harvesting architectures,[84,85] which are typically examined in surfactant assemblies. While our chief interests lie in artificial photosynthesis, the findings also may be germane for developing active sensitizers for photodynamic therapy.[86]

In the following, comparisons of the key observations (Figs. 1 and 2 and Tables 1 and 3) upon variation in molecular characteristics are described first for the bacteriochlorins and then for chlorins. The discussion highlights differences in properties of specific compounds with medium and a few cases that represent outliers from general behavior.

B. Effect of hydrophilic group on the properties of amphiphilic bacteriochlorins. The absorption and fluorescence spectra of the free base bacteriochlorins **BC-MePy**[15] and **BC-BA**[15] show minimal medium (DMF, CTAB, TX-100, SDS) dependence. Upon a change in the 15-hydrophilic group from pyridinium to benzoate, the following characteristics are consistently observed across all solvents: (1) Φ_f and τ_s increase by roughly 50%, (2) the Q_x band hypsochromically shifts (10–15 nm), (3) the Q_y absorption band hypsochromically shifts (13–17 nm) and narrows (by 8–12 nm FWHM), (4) the relative intensities of the nominal B_y and B_x bands reverse, (5) the combined Soret feature narrows (by ~12 nm FWHM), (6) the Q_y fluorescence band narrows (by 8–15 nm FWHM), and (7) the spacing (Stokes shift) between the Q_y absorption and fluorescence maxima decreases.

C. Effect of hydrophilic group on spectral properties of amphiphilic chlorins. Upon a change in the 15-hydrophilic group from pyridinium to benzoate, the Q_y absorption and emission bands consistently hypsochromically shift (3 nm average) and narrow (5 nm average FWHM). The effects are minimized with the 3-phenylethynyl group installed, the presence of which outweighs the more subtle effects from variation of the hydrophilic 15-substituent.

Collectively the effects of a change in the 15-hydrophilic group from pyridinium to benzoate for the three pairs of chlorins are smaller than those observed for the pair of bacteriochlorins **BC-MePy**[15] and **BC-BA**[15]. The rather modest effects of the identity of the hydrophilic group on the spectral properties of the amphiphilic chlorins is consistent with prior

observation on primarily hydrophobic synthetic chlorins, wherein the presence of one or two meso (e.g., 15-position) substituents has relatively small effects on the optical spectra, especially relative to β-pyrrole (e.g., 3-position) substituents.[80-82]

There are two notable outliers in the general excellent solubility and/or spectral and photophysical characteristics of the amphiphilic (bacterio)chlorins, both of which stem from the zinc chlorins with certain combinations of hydrophobic and hydrophilic groups, and medium. The first class of outliers appears to derive at least in part from reduced solubility. Dimers or larger aggregates are formed that are partly soluble and contribute to the spectral and excited-state properties. **ZnC-PE^{3}MePy^{15}** in CTAB and SDS shows substantially broadened Soret-region absorption (Figs. 1D and 3B), and in SDS a reduced Φ_f and τ_S (*vide infra*). In comparison, **ZnC-PE^{3}MePy^{15}** in DMF and **ZnC-PE^{3}BA^{15}** in all media exhibit Soret absorption and photophysical properties (Fig. 1 and Table 1) typical[80-82] of predominantly hydrophobic zinc chlorins. The absorption spectra of **ZnC-T^{5}BA^{15}** in the micellar solutions and DMF are normal, although the Φ_f and τ_S are modestly reduced (*vide infra*). The absorption spectra of free base chlorins **C-T^{5}BA^{15}** and **C-PE^{3}BA^{15}** and their bacteriochlorin counterparts in all four media are typical of hydrophobic analogues.

Comparisons are given below of the spectral characteristics of the amphiphilic (bacterio)chlorins and those for the photosynthetic chromophores chlorophyll *a* and bacteriochlorophyll *a* in micellar solutions. In those cases the formation of dimers or aggregates results in broadened or split Soret features, and a new distinct feature well separated from the monomer Q_y band in the red or NIR region. The perturbation to the Q_y relative to the Soret can be estimated assuming the coupling of two transition dipoles. For a dimer, this coupling is proportional to the square of the transition moment of the monomer. Translating this logic to the

case of **ZnC-PE^{3}MePy^{15}** in CTAB, a new feature at ~460 nm lies ~2000 cm^{-1} to lower energy than the monomer band at ~420 nm. Together with the Q_y/B peak-intensity ratio of ~0.4 (Table 1), a shift in the Q_y band of ~330 cm^{-1} is predicted, which places the transition ~15 nm to lower energy than the monomer Q_y band at 635 nm. This shift is comparable to the ~20 nm FWHM of the monomer Q_y band (Table). Thus, only modest asymmetric broadening of the Q_y band is expected. This prediction is generally consistent with the ground-state absorption spectrum (Fig. 1D) and Q_y bleaching in the transient absorption spectrum for **ZnC-PE^{3}MePy^{15}** in CTAB and SDS (Fig. 4C) relative to that for **ZnC-T^{5}BA^{15}** (Fig. 4A).

The second class of outliers appears to involve some excited-state charge-transfer (CT) character (e.g., macrocycle ↔ pyridinium). Solubility is not a primary issue although dimers or aggregates could contribute to the spectral (and excited-state) properties. This class involves **ZnC-T^{5}MePy^{15}** in all four media. Compared to **ZnC-T^{5}BA^{15}** and most of the other chlorin cases, **ZnC-T^{5}MePy^{15}** exhibits a broadened Soret-region absorption such that the wings do not contribute significantly to fluorescence (Fig. 1B and 3A).

D. Effect of hydrophilic group on excited-state properties of amphiphilic chlorins and bacteriochlorins. Most of the amphiphilic chlorins and bacteriochlorins in the four media display excited-state characteristics (Φ_f, τ_S, Φ_{isc}, etc.) comparable to the largely hydrophobic analogues studied previously. In this section, attention is given to the photophysical outliers (compound/medium), in analogy to the discussion in the previous section on spectral outliers. The specific cases relate primarily to the choice of the 15-hydrophilic group in the zinc chlorins.

Zinc chlorin **ZnC-T^{5}MePy^{15}** in all four media exhibits dramatically reduced Φ_f and τ_S values (Table 1). The compound also shows the above-noted broadened Soret-region absorption (Figs. 1D and 3B) along with a broad and more distinct excited-state absorption profile between

450 and 650 nm (Fig. 4A). One interpretation is that these collective deviations from the norm reflect macrocycle ↔ pyridinium CT character to the Soret excited-states, to the Q_y excited state, or underlie a state at still lower energy. Additionally, dimers or other small aggregates may be present to some degree in the ground state or form following excitation (excimers). One or more of such factors would enhance internal conversion and reduce the radiative probability as indicated by the excited-state decay rate constants for **ZnC-T^{5}MePy^{15}** in DMF (Table 3) and the reduced Φ_f and τ_S values indicated in all media, along with the medium dependence of these quantities (Table 1).

A change in the 15-hydrophilic group from pyridinium to benzoate to produce **ZnC-T^{5}BA^{15}** gives rise to much greater Φ_f and τ_S values. The values are still modestly lower than those of **ZnC-PE^{3}BA^{15}** in all four media, and of **ZnC-PE^{3}MePy^{15}** in all media except SDS, but parallel the photophysical properties observed previously for other zinc chlorins bearing aryl rings at the meso (e.g., 5- and 15-) positions and lacking β-pyrrole substituents.[80-82] Like **ZnC-T^{5}MePy^{15}**, the analogue **ZnC-PE^{3}MePy^{15}** exhibits a reduced Φ_f and a short τ_S component (in addition to a monomer-like component) in SDS (Table 1 and Fig. 4C). The perturbed excited-state properties for **ZnC-PE^{3}MePy^{15}** may arise in part from solubility and thus from partly soluble dimers or aggregates, including those formed in the excited state (excimers). Another possibility is interaction of the positively charged quaternary nitrogen of the pyridinium group with the negatively charged head group of SDS. Normal behavior is observed for **ZnC-PE^{3}MePy^{15}** in the other media. Free base chlorins **C-T^{5}BA^{15}** and **C-T^{5}MePy^{15}** show less dependence on the nature of the 15-hydrophilic group (and less medium dependence) than the analogous zinc chelates.

Collectively, the findings regarding the use of a pyridinium versus benzoate group show

large variation in photophysical properties of the zinc chelates with medium compared to relatively solvent-insensitive properties of the free base (bacterio)chlorins that bear a pyridinium substituent. The results suggest that the source of the solvent dependence for the zinc chelates involves a complex interaction of the solvent environment with the pyridinium group (or the pyridinium-substituted macrocycle) and central zinc metal. This behavior could involve the negative or partial negative charges on SDS and DMF solvents, respectively, or involve inter-chromophore interactions facilitated by the medium such as the distribution of chromophores in the micellar systems.

The findings have implications for the selection of chromophores for incorporation into environments such as proteins, membranes, or micelles. Such environments may lead to medium-chromophore interactions or foster chromophore–chromophore interactions, or both, that are much more extensive when the compound bears a pyridinium rather than benzoate group, especially when the central metal ion (e.g., $Zn^{2+)}$ is present. If a central metal ion is required, the similarity of the optical spectra and excited-state properties of **ZnC-T^{5}BA^{15}** in all three micellar media and DMF and those obtained previously for hydrophobic analogues in organic solvents indicates that through appropriate design zinc chlorins can be rendered amphiphilic without compromising desirable photophysical characteristics.

If apical binding to a central metal is not a requisite, the combination of pyridinium with either free base chlorin or bacteriochlorin macrocycles can produce versatile amphiphilic chromophores with desirable photophysical properties for energy or electron transfer. For compounds containing a benzoate group the modest variations in Φ_f and τ_S with medium and with variation in distal hydrophobic group (*p*-tolyl or phenylethynyl), metalation state (zinc or free base), and reduction state of the macrocycle (chlorin or bacteriochlorin) bodes well for using

this substituent to produce amphiphilic chromophores that have photophysical properties that are relatively independent of the environment.

E. Effect of distal hydrophobic group on the properties of chlorins. Prior work has shown that meso (e.g., 5-position) aryl groups of synthetic chlorins have limited effects on the spectral and photophysical properties, whereas β-pyrrole (e.g., 3-position) substituents commonly evoke bathochromic shifts, intensification of the Q_y absorption band, and increased Φ_f.[80-82] Similarly for the amphiphilic chlorins studied here, a change in the hydrophobic group from 5-*p*-tolyl (**ZnC-T^{5}MePy^{15}** and **ZnC-T^{5}BA^{15}**) to 3-phenylethynyl (**ZnC-PE^{3}MePy^{15}** and **ZnC-PE^{3}BA^{15}**) gives rise to bathochromic shifts in Soret (B) absorption (6–8 nm), Q_y absorption (19–23), and fluorescence (17–24 nm), intensification (by 50–100%) of Q_y peak absorption relative to the Soret (I_{Qy}/I_B), and increases in both Φ_f and τ_S, regardless of solvent or hydrophilic substituent (Fig. 1 and Table 1). Thus, the identity and placement of the hydrophobic group is a useful variable for tuning spectral and photophysical properties of the amphiphilic chlorins.

F. Effect of the central metal (zinc chelate versus free base) in chlorins. The effect of the central metal of chlorins is explored by comparison of **ZnC-T^{5}MePy^{15}** versus **C-T^{5}MePy^{15}** and **ZnC-T^{5}BA^{15}** versus **C-T^{5}BA^{15}**. A change in metalation state from zinc to free base gives rise to a bathochromic shift in the Q_y absorption (26–31 nm) and fluorescence (26–35 nm) features, accentuated absorption in the Q_x region, and increases in both Φ_f and τ_S. For example, **ZnC-T^{5}BA^{15}** averaged over all the solvents has nearly a three-fold decrease in Φ_f and nearly a five-fold decrease in τ_s compared to that of **C-T^{5}BA^{15}**. The comparison is even more dramatic for the solvent averaged **ZnC-T^{5}MePy^{15}**, with an ~10-fold decrease in Φ_f and even larger decrease in τ_s compared to **C-T^{5}MePy^{15}**. In general, the free base chlorins show only modest solvent dependence compared to the zinc chelates.

G. Comparison with studies of native photosynthetic chromophores in micelles. The observations made herein can be compared with the results of prior studies on chlorophyll *a* and bacteriochlorophyll *a* and derivatives thereof in micellar media.[16,62-62,79] Those studies utilized surfactants bearing positive, negative, or neutral surfactant head groups, including those used here (CTAB, SDS, TX-100). The studies, by design, generally employed conditions to foster the incorporation of multiple chromophores per micelle and thus inter-chromophore interactions (aggregation). In contrast, the studies performed herein – aimed at obtaining photophysical characteristics of the synthetic amphiphilic (bacterio)chlorins in the absence of aggregation – used roughly one-tenth the chromophore concentration (e.g., 1 μM versus 10 μM) and ten-times the surfactant concentration (e.g. 10-fold versus 1-fold the cmc value). Regardless, in most cases no significant changes in properties were observed here for all bacteriochlorin/medium combinations and for select chlorin/medium cases when the surfactant concentration was reduced to the cmc level.

The prior studies of the photosynthetic chromophores and analogues in micellar media were motivated in part to investigate the formation of bathochromically shifted absorption features in the red (chlorophyll *a*) or NIR (bacteriochlorophyll *a*) similar to those observed in native light-harvesting complexes versus that of the monomer Q_y band. Such shifted positions are typically ascribed to exciton coupling between the chromophores. An additional motivation was to examine the potential effects of charged head groups of the surfactants to mimic a similar role of ionized amino acids in proteins that had been suggested by theoretical work.[87-89]

In the case of bacteriochlorophyll *a*, a new feature bathochromically shifted from the monomer position (780 nm) was observed in TX-100 (~850 nm)[79] and CTAB (~970 nm)[64] corresponding to Q_y shifts of roughly 1000 and 2500 cm^{-1}, respectively Additionally shifted,

broadened or split Soret features were observed. For chlorophyll *a* in TX-100, a feature at ~750 nm is found, corresponding to a bathochromic shift from the monomer Q_y band (~665 nm) of about 1700 cm^{-1}.[62] The magnitude of these Q_y shifts are substantially greater than those of <400 cm^{-1} expected for select amphiphilic chlorin/medium combinations. As noted above, the predicted Q_y shifts are based on the extent of broadening (or splitting) observed in the Soret band of **ZnC-PE^{3}MePy^{15}** in CTAB, consistent with observations for this case and others (e.g., Fig. 3).

The differences between the prior studies of the native photosynthetic (bacterio)chlorophylls and the present study of synthetic amphiphilic (bacterio)chlorins may arise from several sources, including the following.

(1) Relative concentrations. The surfactant/chromophore ratios used in the prior studies are 10-100-fold lower than those used here resulting (by design) in greater chromophore loading per micelle. Such loading increases the possibility of inter-chromophore interactions, and the extent of spectral shifts because the magnitude will increase (to a point) with the number of interacting units. The spectral and photophysical properties (Table 2) basically did not change for the amphiphilic bacteriochlorins studied here when the surfactant concentration was reduced 10-fold to the cmc level.

(2) Isocyclic ring. Chlorophyll *a* and close analogues have a keto-bearing five-membered ("isocyclic") ring that increases the Q_y oscillator strength (relative to the Soret)[90] compared to the synthetic chlorins studied here. This difference can lead to 2–3-fold increase in Q_y intensity (relative to B) and thus an increase in Q_y shift/splitting by a factor of 4 or more. A related difference is expected for bacteriochlorophyll *a* versus the synthetic amphiphilic bacteriochlorins,[91] but to a lesser extent than the chlorins.

(3) Point charges. Direct interactions can occur between the surfactant molecules and the

keto-bearing annulated ring (and other functional groups) present on the native photosynthetic chromophores. For example, in the case of chlorophyll *a* in CTAB, such interaction with the positively charged ammonium group of CTAB results in an absorption feature that is shifted hypsochromically from the monomer position (~640 versus ~665 nm).[64] This oxophorbine motif is absent in the synthetic (bacterio)chlorins studied here but could be incorporated or mimicked[90,91] with other auxochromes to attain similar Q_y positions and intensities.[80-83] For the synthetic amphiphilic (bacterio)chlorins studied here there is generally no clear evidence for such direct chromophore-surfactant interactions (or effects of surfactant head group charge) on spectral properties, except in specific cases such as the zinc chelates with certain substituents (e.g., **ZnC-T^{5}MePy^{15}** and **ZnC-PE^{3}MePy^5**).

A major finding that emerges from these studies and comparisons is that considerable leeway is available in the design of the synthetic (bacterio)chlorins to achieve amphiphilicity and tune spectral properties while retaining favorable photophysical properties such as long excited-state lifetimes. As shown herein, where an outlier that has unfavorable excited-state (or chemical) properties for a specific environment is encountered, an alternative can be designed to achieve the desired outcome.

Outlook

Amphiphilic tetrapyrrole macrocycles are of interest in fields ranging from artificial photosynthesis to photodynamic therapy given that such molecules assemble spontaneously in surfactant media. Amphiphilic porphyrins have long been accessible via diverse synthetic methods, whereas amphiphilic (bacterio)chlorins have heretofore rarely been prepared other than via semisynthesis from native macrocycles. Advances in the *de novo* synthesis of (bacterio)chlorins now open the door to the design and rational synthesis of amphiphilic tetrapyrrole macrocycles with wavelength-tunable absorption in the red or NIR characteristic of naturally occurring chlorophylls or bacteriochlorophylls, respectively. While the studies to date concern surfactant media, such amphiphilic macrocycles can also be employed in conjunction with surfaces or proteins. With regards to the latter, additional noncovalent interactions can be exploited such as apical coordination by a ligand to the central metal such as zinc (to preserve photoactivity), in the same manner as that for the redox-active iron chelate of protoporphyrin IX upon incorporation to give a heme protein.[92,93] Partitioning of amphiphilic (bacterio)chlorins into surfactant media or peptides is a complementary approach to that of covalent attachment (i.e., bioconjugation) to a scaffolding with the added allure of spontaneity and a certain extent of orientation control. Taken together, the ability to design and synthesize wavelength-tunable amphiphilic (bacterio)chlorins should afford a versatile platform for light-harvesting and solar-energy conversion in the valuable red and NIR spectral regions.

Experimental Section

General Methods. ^{1}H NMR (400 MHz) and ^{13}C NMR (100 MHz) spectra were collected at room temperature unless noted otherwise. Absorption spectra were obtained at room

temperature. All commercially available materials were used as received. Silica gel (40 μm average particle size) was used for column chromatography. THF was freshly distilled from sodium/benzophenone ketyl. Laser-desorption mass spectrometry was performed without a matrix. Electrospray ionization mass spectrometry (ESI-MS) data are reported for the molecular ion or protonated molecular ion. The palladium-coupling reactions were carried out using Schlenk-line techniques.

Noncommercial Compounds. Compounds **3**,[74] **6**,[70] **C-T^{5}Br^{15}** (ref 73) and **BC-Br^{15}** (ref 69) were prepared following literature procedures.

Static and time-resolved optical spectroscopy. Measurements to determine fluorescence yields, singlet excited-state lifetimes, and intersystem-crossing (triplet) yields were performed as described previously.[82,83] In short, fluorescence lifetimes are typically the average value from measurements using a phase-modulation technique and a time-resolved instrument with an instrument response function of ~1 ns using Soret or Q_x excitation. Transient absorption studies typically utilized ~130-fs excitation pulses (in the Soret, Q_x or Q_y regions) with an energy of 0.5 μJ and a diameter of 1 mm. The Φ_{isc} values (triplet yields) were obtained using transient absorption spectroscopy. The extent of bleaching of the ground-state bands (relative to a relatively flat transient absorption) due to the S_1 excited state measured immediately after excitation was compared with that due to the T_1 excited state at the asymptote of the S_1 decay. When probing the $Q_y(0,0)$ band, the contribution of S_1 stimulated emission was taken into account. The standards for fluorescence quantum yields include (i) chlorophyll *a* in deoxygenated toluene ($\Phi_f = 0.325$),[90] which is the value measured in benzene,[94] and (ii) free base *meso*-tetraphenylporphyrin (**FbTPP**) in nondegassed toluene, for which $\Phi_f = 0.070$ was established with respect to the zinc chelate **ZnTPP** in nondegassed toluene ($\Phi_f = 0.030$),[95]

consistent with prior results on **FbTPP**.[96] For the chlorins the Φ_f values were typically measured using Soret (B) excitation and for the bacteriochlorins using both Soret and Q_x excitation and the values found to be the same within ±15% and averaged. Samples used for static absorption and fluorescence studies typically had a chlorin or bacteriochlorin concentration of 0.2-0.7 μM and used in a 1 cm path cuvette ($A \leq 0.15$ at the excitation wavelength) and those for transient absorption studies about 3-fold more concentrated in a 2 mm path cuvette.

Sample Preparation. TX-100 and CTAB were prepared at 1.96 g/L (3.01 mM) and 3.64 g/L (9.97 mM), respectively in 100 mM potassium phosphate buffer pH = 7.0. SDS was prepared at 23.1 g/L (80.0 mM) in 10 mM potassium phosphate buffer, pH = 7.0. The approximate cmc of each surfactant was as follows: TX-100, 0.2 mM; CTAB, 1 mM; and SDS, 8 mM.[78] Hence, each surfactant was employed at a concentration ~10 times that of the cmc. SDS at 10X the cmc was relatively insoluble in 100 mM potassium phosphate buffer, pH = 7.0 at room temperature (heating with stirring produced an optically clear solution but precipitation ensued upon cooling).

The sample solution resulting from the addition of the chlorin or bacteriochlorin to a TX-100 or CTAB solution (particularly the latter) could become slightly cloudy and show minor NUV (<400 nm) light scattering that could be eliminated or largely reduced by passing through a 0.2 μM nylon syringe filter. Any particulate removed was un-colored indicating the absence of chromophore, consistent with an unchanged absorption profile other than a reduction of the minor NUV light scattering. Samples were immediately deoxygenated by passing water-saturated Ar over the solution surface of a vented but otherwise sealed cuvette while stirring. Samples that would become slightly cloudy at this point again showed no change in the visible (chlorins) or NIR (bacteriochlorin) Q_y absorption profile but only minor increase in NUV (Soret-

region) absorption baseline.

Acknowledgment. This research was carried out as part of the Photosynthetic Antenna Research Center (PARC), an Energy Frontier Research Center funded by the U.S. Department of Energy, Office of Science, Office of Basic Energy Sciences, under Award No. DE-SC0001035. Mass spectra were obtained at the Mass Spectrometry Laboratory for Biotechnology at North Carolina State University. Partial funding for the facility was obtained from the North Carolina Biotechnology Center and the National Science Foundation.

References

1 P. D. Harvey, In *The Porphyrin Handbook*, eds. K. M. Kadish, K. M. Smith and R. Guilard, Academic Press, San Diego, CA, 2003; vol. 18, pp. 63–250.

2 P. D. Harvey, C. Stern and R. Guilard, In *Handbook of Porphyrin Science,* eds. K. M. Kadish, K. M. Smith and R. Guilard, World Scientific Publishing Co., Singapore, vol. 11, 2011, pp. 1–179.

3 F. Ricchelli, *J. Photochem. Photobiol. B: Biol.,* 1995, **29**, 109–118.

4 L. Agius, J. A. Ballantine, V. Ferrito, V. Jaccarini, P. Murray-Rust, A. Pelter, A. F. Psaila and P. J. Schembri, *Pure Appl. Chem.*, 1979, **51**, 1847–1864.

5 P. H. Hynninen, J. Helaja, F.-P. Montforts and C. M. Müller, *J. Porphyrins Phthalocyanines*, 2004, **8**, 1376–1382.

6 H. G. L. Coster, In *Planar Lipid Bilayers (BLMs) and their Applications*, ed. H. T. Tian and A. Ottova-Leitmannova, Elsevier Science B.V., Amsterdam, 2003, pp. 75–108.

7 M. Kepczynski, R. P. Pandian, K. M. Smith and B. Ehrenberg, *Photochem. Photobiol.,* 2002, **76**, 127–134.

8 A. R. M. Soares, Y. Thanaiah, M. Taniguchi and J. S. Lindsey, *New J. Chem.,* 2013, **37***,* 1087–1097.

9 H. Scheer, In *Chlorophylls and Bacteriochlorophylls. Biochemistry, Biophysics, Functions and Applications,* eds. B. Grimm, R. J. Porra, W. Rüdiger and H. Scheer, Advances in Photosynthesis and Respiration, vol. 25; Springer, Dordrecht, The Netherlands, pp. 1–26.

10 B. R. Masters and D. Mauzerall, *J. Membrane Biol*., 1978, **41**, 377–388.

11 K. Kalyanasundaram and G. Porter, *Proc. R. Soc. Lond. A*., 1978, **364**, 29–44.

12 A. Ilani and D. Mauzerall, *Biophys. J.*, 1981, **35**, 79–92.

13 G. P. Gurinovich, T. E. Zorina, S. B. Melnov, N. I. Melnova, I. F. Gurinovich, L. A. Grubina, M. V. Sarzhevskaya and S. N. Cherenkevich, *J. Photochem. Photobiol. B: Biol.,* 1992, **13**, 51–57.

14 J. D. Spikes and J. C. Bommer, *J. Photochem. Photobiol. B: Biol.*, 1993, **17**, 135–143.

15 G. Zheng, A. Graham, M. Shibata, J. R. Missert, A. R. Oseroff, T. J. Dougherty and R. K. Pandey, *J. Org. Chem.,* 2001, **66**, 8709–8716.

16 A. Agostiano, L. Catucci, G. Colafemmina and H. Scheer, *J. Phys. Chem. B,* 2002, **106**, 1446–1454.

17 T. Miyatake, H. Tamiaki, H. Shinoda, M. Fujiwara and T. Matsushita, *Tetrahedron,* 2002, **58**, 9989–10000.

18 T. Miyatake, H. Tamiaki, M. Fujiwara and T. Matsushita, *Bioorg. Med. Chem.,* 2004, **12**, 2173–2178.

19 T. K. Mukherjee, P. P. Mishra and A. Datta, *Chem. Phys. Lett.*, 2005, **407**, 119–123.

20 L. O. Cinteza, T. Y. Ohulchanskyy, Y. Sahoo, E. J. Bergey, R. K. Pandey and P. N. Prasad, *Mol. Pharmaceut.* 2006, **3**, 415–423.

21 F. Postigo, M. L Sagristá, M. A. De Madariaga, S. Nonell and M. Mora, *Biochim. Biophys. Acta,* 2006, **1758**, 583–596.

22 H. Taima, A. Okubo, N. Yoshioka and H. Inoue, *Chem. Eur. J.*, 2006, **12**, 6331–6340.

23 A. V. Nechaev and A. F. Mironov, *Russ. J. Bioorg. Chem.,* 2008, **34**, 245–251.

24 A. F. Mironov and M. A. Grin, *J. Porphyrins Phthalocyanines,* 2008, **12**, 1163–1172.

25 J. A. S. Cavaleiro, M. A. F. Faustino and J. P. C. Tomé, *Carbohydr. Chem.,* 2009, **35**, 199–231.

26 J. F. Lovell, C. S. Jin, E. Huynh, H. Jin, C. Kim, J. L. Rubinstein, W. C. W. Chan, W. Cao, L. V. Wang and G. Zheng, *Nature Mater.*, 2011, **10**, 324–332.

27 L. Huang, T. Zhiyentayev, Y. Xuan, D. Azhibek, G. B. Kharkwal and M. R. Hamblin, *Lasers Surg. Med.,* 2011, **43**, 313–323.

28 F. Li and K. Na, *Biomacromolecules,* 2011, **12**, 1724–1730.

29 R. G. W. Jinadasa, X. Hu, M. G. H. Vicente and K. M. Smith, *J. Med. Chem.*, 2011, **54**, 7464–7476.

30 D. Bauer, F.-P. Montforts, A. Losi and H. Görner, *Photochem. Photobiol. Sci.,* 2012, **11**, 925–930.

31 A. Losev and D. Mauzerall, *Photochem. Photobiol*., 1983, **38**, 355–361.

32 F.-P. Montforts and G. Zimmermann, *Angew. Chem. Int. Ed. Engl.,* 1986, **25**, 458–459.

33 A. M. Richter, E. Waterfield, A. K. Jain, B. Allison, E. D. Sternberg, D. Dolphin and J. G. Levy, *Br. J. Cancer,* 1991, **63**, 87–93.

34 D. Kusch, A. Meier and F.-P. Montforts, *Liebigs Ann.,* 1995, 1027–1032.

35 A. F. Uchoa, K. T. de Oliveira, M. S. Baptista, A. J. Bortoluzzi, Y. Iamamoto and O. A. Serra, *J. Org. Chem.,* 2011, **76**, 8824–8832.

36 A. Szurko, M. Rams, A. Sochanik, K. Sierón-Stoltny, A. M. Kozielec, F.-P. Montforts, R. Wrzalik and A. Ratuszna, *Bioorg. Med. Chem.,* 2009, **17**, 8197–8205.

37 Q. Chen, Z. Huang, D. Luck, J. Beckers, P.-H. Brun, B. C. Wilson, A. Scherz, Y. Salomon and F. W. Hetzel, *Photochem. Photobiol.,* 2002, **76**, 438–445.

38 A. F. Mironov, M. A. Grin, A. G. Tsiprovskii, A. V. Segenevich, D. V. Dzardanov, K. V. Golovin, A. A. Tsygankov and Y. K. Shim, *Russ. J. Bioorg. Chem.,* 2003, **29**, 190–197.

39 A. F. Mironov, M. A. Grin, A. G. Tsiprovskii, R. A. Titeev, E. A. Nizhnik and I. S. Lonin, *Mendeleev Commun.,* 2004, **14**, 204–207.

40 I. G. Meerovich, I. Y. Kubasova, N. A. Oborotova, G. A. Meerovich, S. A. Demura, A. Brandis, V. Rosenbach-Belkin, A. Y. Baryshnikov and A. Scherz, *Proc. SPIE,* 2005, **5973**, 59730G1–12.

41 Z. Huang, Q. Chen, K. C. Dole, A. B. Barqawi, Y. K. Chen, D. Blanc, B. C. Wilson and F. W. Hetzel, *Photochem. Photobiol. Sci.,* 2007, **6**, 1318–1324.

42 I. Ashur, R. Goldschmidt, I. Pinkas, Y. Salomon, G. Szewczyk, T. Sarna and A. Scherz, *J. Phys. Chem. A,* 2009, **113**, 8027–8037.

43 P. H. Hynninen, In *Chlorophylls*, ed. H. Scheer, CRC Press: Boca Raton, FL, USA 1991; pp. 145–209.

44 Y. Chen, G. Li and R. K. Pandey, *Curr. Org. Chem*., 2004, **8**, 1105–1134.

45 V. Y. Pavlov and G. V. Ponomarev, *Chem. Heterocyclic Cmpds.,* 2004, **40**, 393–425.

46 M. A. Grin, A. F. Mironov and A. A. Shtil, *Anti-Cancer Agents Med. Chem*., 2008, **8**, 683–697.

47 W. Flitsch, *Adv. Heterocyclic Chem*., 1988, **43**, 73–126.

48 F.-P. Montforts, B. Gerlach and F. Höper, *Chem. Rev.,* 1994, **94**, 327–347.

49 F.-P. Montforts and M. Glasenapp-Breiling, *Prog. Heterocyclic Chem.,* 1998, **10**, 1–24.

50 S. Fox and R. W. Boyle, *Tetrahedron,* 2006, **62**, 10039–10054.

51 M. Galezowski and D. T. Gryko, *Curr. Org. Chem*., 2007, **11**, 1310–1338.

52 A. M. G. Silva and J. A. S. Cavaleiro, In *Progress in Heterocyclic Chemistry,* eds. G. W. Gribble and J. A. Joule, Elsevier, Amsterdam, 2008, vol. 19, pp. 44–69.

53 C. Brückner, L. Samankumara and J. Ogikubo, In *Handbook of Porphyrin Science*, eds. K. M. Kadish, K. M. Smith and R. Guilard, World Scientific Publishing Co., Singapore, World Scientific, Singapore, 2012, vol. 17, pp. 1–112.

54 W. G. O'Neal, W. P. Roberts, I. Ghosh, H. Wang and P. A. Jacobi, *J. Org. Chem.*, 2006, **71**, 3472–3480.

55 W. G. O'Neal and P. A. Jacobi, *J. Am. Chem. Soc.*, 2008, **130**, 1102–1108.

56 J. Gravier, B. Korchowiec, R. Schneider and E. Rogalska, *Chem. Phys. Lipids,* 2009, **158**, 102–109.

57 S. B. Dror, I. Bronshtein, Y. Garini, W. G. O'Neal, P. A. Jacobi and B. Ehrenberg, *Photochem. Photobiol. Sci.*, 2009, **8**, 354–361.

58 K. Berg, S. Nordstrand, P. K. Selbo, D. T. T. Tran, E. Angell-Petersen and A. Høgset, *Photochem. Photobiol. Sci.*, 2011, **10**, 1637–1651.

59 M. Lilletvedt, G. Smistad, H. H. Tønnesen, A. Høgset and S. Kristensen, *Eur. J. Pharm. Sci.*, 2011, **43**, 180–187.

60 Z. Yu and M. Ptaszek, *Org. Lett*., 2012, **14**, 3708–3711.

61 S. Sharma, M. Krayer, F. F. Sperandio, L. Huang, Y.-Y. Huang, D. Holten, J. S. Lindsey and M. R. Hamblin, *J. Porphyrins Phthalocyanines,* 2013, **17**, 73–85.

62 A. Agostiano, L. Catucci, G. Colafemmina and M. Della Monica, *Biophys. Chem.*, 1996, **60**, 17–27.

63 P. P. Mishra, J. Bhatnagar and A. Datta, *J. Phys. Chem. B*, 2005, **109**, 24225–24230.

64 J. Gottstein, A. Scherz and H. Scheer, *Biochim. Biophys. Acta,* 1993, **1183**, 413–416.

65 J.-P. Strachan, D. F. O'Shea, T. Balasubramanian and J. S. Lindsey, *J. Org. Chem.,* 2000, **65**, 3160–3172.

66 M. Taniguchi, D. Ra, G. Mo, T. Balasubramanian and J. S. Lindsey, *J. Org. Chem.,* 2001, **66**, 7342–7354.

67 M. Ptaszek, B. E. McDowell, M. Taniguchi, H.-J. Kim and J. S. Lindsey, *Tetrahedron,* 2007, **63**, 3826–3839.

68 H.-J. Kim and J. S. Lindsey, *J. Org. Chem.,* 2005, **70**, 5475–5486.

69 M. Krayer, M. Ptaszek, H.-J. Kim, K. R. Meneely, D. Fan, K. Secor and J. S. Lindsey, *J. Org. Chem*., 2010, **75**, 1016–1039.

70 J. K. Laha, C. Muthiah, M. Taniguchi, B. E. McDowell, M. Ptaszek and J. S. Lindsey, *J. Org. Chem.,* 2006, **71**, 4092–4102. *Ibid.*, *J. Org. Chem.* 2009, **74**, 5122.

71 M. Taniguchi, M. N. Kim, D. Ra and J. S. Lindsey, *J. Org. Chem*., 2005, **70**, 275–285.

72 D. Fan, M. Taniguchi and J. S. Lindsey, *J. Org. Chem.,* 2007, **72**, 5350–5357.

73 C. Muthiah, M. Ptaszek, T. M. Nguyen, K. M. Flack and J. S. Lindsey, *J. Org. Chem*., 2007, **72**, 7736–7749.

74 M. Krayer, T. Balasubramanian, C. Ruzié, M. Ptaszek, D. L. Cramer, M. Taniguchi and J. S. Lindsey, *J. Porphyrins Phthalocyanines,* 2009, **13**, 1098–1110.

75 A. Alvarez, A. Guzmán, A. Ruiz, E. Velarde and J. M. Muchowski, *J. Org. Chem.,* 1992, **57**, 1653–1656.

76 M. Bergauer, H. Hübner and P. Gmeiner, *Bioorg. Med. Chem. Lett.* 2002, **12**, 1937–1940.

77 C. Muthiah, D. Lahaye, M. Taniguchi, M. Ptaszek and J. S. Lindsey, *J. Org. Chem*., 2009, **74**, 3237–3247.

78 P. Mukerjee and K. J. Mysels, Nat. Stand. Ref. Data Ser., Nat. Bur. Stand. (U.S.), 1971, **36**, 1–222.

79 A. Scherz, V. Rosenbach-Belkin and J. R. E. Fisher, *Proc. Natl. Acad. Sci. USA*, 1990, **87**, 5430–5434.

80 H. L. Kee, C. Kirmaier, Q. Tang, J. R. Diers, C. Muthiah, M. Taniguchi, J. K. Laha, M. Ptaszek, J. S. Lindsey, D. F. Bocian and D. Holten, *Photochem. Photobiol*., 2007, **83**, 1110–1124.

81 H. L. Kee, C. Kirmaier, Q. Tang, J. R. Diers, C. Muthiah, M. Taniguchi, J. K. Laha, M. Ptaszek, J. S. Lindsey, D. F. Bocian and D. Holten, *Photochem. Photobiol*., 2007, **83**, 1125–1143.

82 J. W. Springer, K. M. Faries, H. L. Kee, J. R. Diers, C. Muthiah, O. Mass, C. Kirmaier, J. S. Lindsey, D. F. Bocian and D. Holten, *Photochem. Photobiol.,* 2012, **88**, 651–674.

83 E. Yang, C. Kirmaier, M. Krayer, M. Taniguchi, H.-J. Kim, J. R. Diers, D. F. Bocian, J. S. Lindsey and D. Holten, *J. Phys. Chem. B,* 2011, **115**, 10801–10816.

84 J. W. Springer, P. S. Parkes-Loach, K. R. Reddy, M. Krayer, J. Jiao, G. M. Lee, D. M. Niedzwiedzki, M. A. Harris, C. Kirmaier, D. F. Bocian, J. S. Lindsey, D. Holten and P. A. Loach, *J. Am. Chem. Soc.,* 2012, **134**, 4589−4599.

85 K. R. Reddy, J. Jiang, M. Krayer, M. A. Harris, J. W. Springer, E. Yang, J. Jiao, D. M. Niedzwiedzki, D. Pandithavidana, P. S. Parkes-Loach, C. Kirmaier, P. A. Loach, D. F. Bocian, D. Holten and J. S. Lindsey, *Chem. Sci.,* 2013, **4**, 2036–2053.

86 E. Yang, J. R. Diers, Y.-Y. Huang, M. R. Hamblin, J. S. Lindsey, D. F. Bocian and D. Holten, *Photochem. Photobiol.,* 2013, **89**, DOI: 10.1111/php.12021.

87 R. C. Davis, S. L. Ditson, A. F. Fentiman and R. M. Pearlstein, *J. Am. Chem. Soc*., 1981, **103**, 6823–6826.

88 J. Eccles and B. Honig, *Proc. Natl. Acad. Sci. USA*, 1983, **80**, 4959-4962.

89 L. K. Hanson, In *Chlorophylls*, ed. H. Scheer, CRC Press, Boca Raton, 1991, pp. 993–1014.

90 O. Mass, M. Taniguchi, M. Ptaszek, J. W. Springer, K. M. Faries, J. R. Diers, D. F. Bocian, D. Holten and J. S. Lindsey, *New J. Chem*., 2011, **35**, 76–88.

91 M. Krayer, E. Yang, J. R. Diers, D. F. Bocian, D. Holten and J. S. Lindsey, *New J. Chem*., 2011, **35**, 587–601.

92 T. Xu, S. P. Wu, I. Miloradovic, M. J. Therien and J. K. Blasie, *Nano Lett*., 2006, **6**, 2387–2394.

93 D. Noy, B. M. Discher, I. V. Rubstov, R. M. Hochstrasser and P. L. Dutton, *Biochem*., 2005, **44**, 12344–12354.

94 G. Weber and F. W. J. Teale, *Trans. Faraday Soc.,* 1957, **53**, 646–655.

95 P. G. Seybold, and M. Gouterman, *J. Mol. Spectrosc.,* 1969, **31**, 1–13.

96 A. T. Gradyushko, A. N. Sevchenko, K. N. Solovyov and M. P. Tsvirko, *Photochem. Photobiol.,* 1970, **11**, 387–400.

Chapter 7.

Spectral and Photophysical Properties of Chlorin Chalcones

INTRODUCTION

Novel chlorins have been developed which contain 13-substituents inspired by natural carotenoids. These have been termed chlorin chalcones. The substituents explored contain a single double bond in the short phenyl chalcone moiety (phCh), and six double bonds in the extended retinyl moiety (Ret1). Both substituents are explored in free base and zinc chlorin macrocycles.

MATERIALS AND METHODS

Synthesis. Novel chlorin chalcones (Chart 1) and simplified benchmarks (Chart 2) were analyzed as received from the Lindsey lab, North Carolina State University. The chlorin chalcones described herein were prepared previously[1] with the exception of **ZnC-M^{10}Ret1^{13}**, which was obtained by zincation of the free base chlorin **FbC-M^{10}Ret1^{13}**.

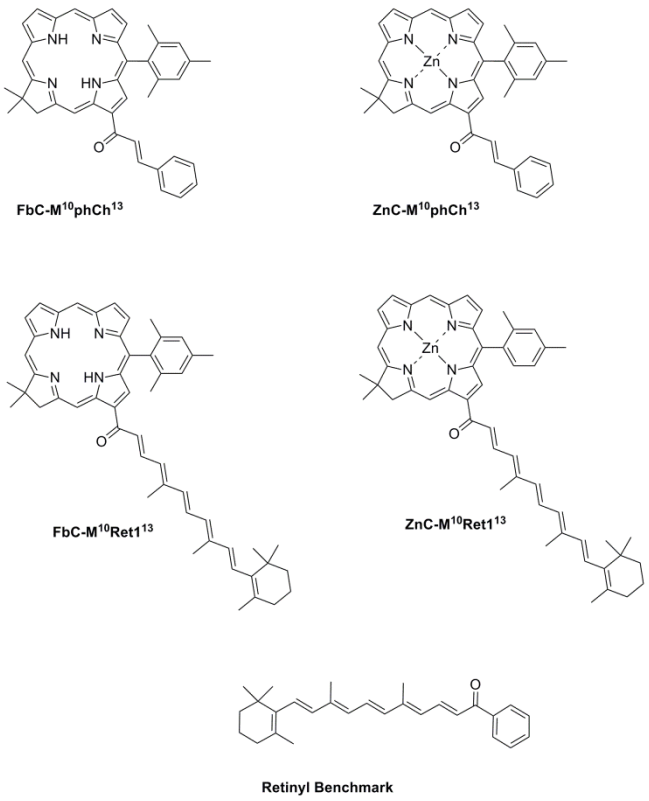

Chart 1. Novel chlorin chalcones and retinyl benchmark.

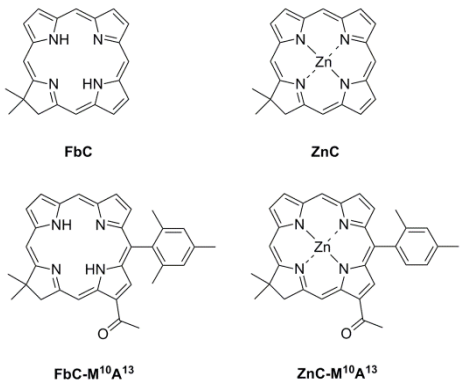

Chart 2. Simplified benchmarks.

Photophysical measurements. Measurements to determine fluorescence yields, singlet excited-state lifetimes, and intersystem-crossing (triplet) yields were performed as described previously.[2,3] In short, fluorescence lifetimes are typically the average value from measurements using a phase-modulation technique and a time-resolved instrument with an instrument response function of ~1 ns using Soret excitation. Transient absorption studies typically utilized ~130-fs excitation pulses (in the Soret, Q_x or Q_y regions) with an energy of 0.5 μJ and a diameter of 1 mm. The standard for fluorescence quantum yields was chlorophyll *a* in deoxygenated toluene ($\Phi_f = 0.325$),[4] which is the value measured in benzene.[5] Samples used for static absorption and fluorescence studies typically had a chlorin concentration of 0.2-0.7 μM and used a 1 cm path cuvette ($A \leq 0.1$ at the excitation wavelength) and those for transient absorption studies about 3-fold more concentrated in a 2 mm path cuvette.

RESULTS AND DISCUSSION

Absorption Spectra

The absorption spectrum of a typical zinc chlorin and free base chlorin, such as the unsubstituted **ZnC**, the 10,13-substituted **ZnC-M^{10}A^{13}**, and their free base analogues studied

previously is normally comprised of four main features (Fig. 1). Progressing from longer to shorter wavelengths, these bands (and general spectral ranges) are Q_y (600–670 nm), Q_x (475–550 nm), B_x (390–430 nm), and B_y (390–430 nm). The Q_x band is generally very weak for zinc chlorins, sometimes undistinguishable, becoming more prominent with a change to the free base macrocycle. Free base chlorins typically display the $Q_x(1,0)$ vibronic overtone feature found roughly 500–1500 cm^{-1} to higher energy than the Q_x origin transition, with relatively equal absorbance. The B_x and B_y features are also known collectively as the Soret band, and are substantially overlapping for zinc chlorins, with only slight separation in the case of free base chlorins. Vibronic overtones of B_x and B_y also overlap with the origin transitions. Due to the extreme overlap of the B bands for chlorins, actual B_x and B_y assignments in the spectra are rarely made. Additional features may also contribute to the Soret-region absorption. The relative intensity of the Q_y absorption band can vary immensely.

The absorption spectra of the novel zinc and free base chlorin-chalcones studied here possess the same overall absorption characteristics of the simpler benchmarks provided for comparison, but with some interesting differences noted below. Spectra obtained in toluene are shown in Figure 1. The spectra are similar to those measured in dimethylsulfoxide (DMSO). All studies were performed at room temperature.

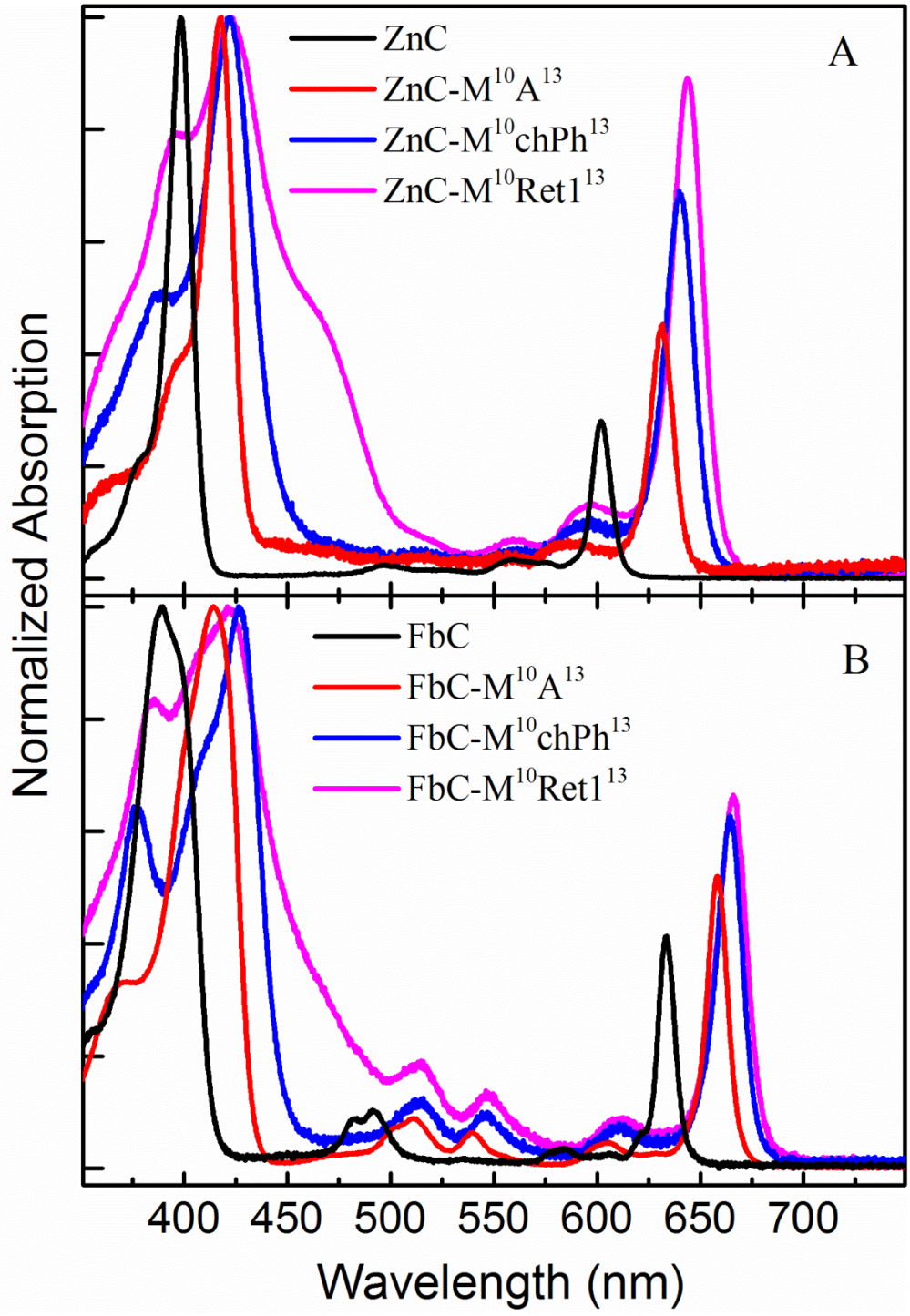

Figure 1. Absorption spectra in toluene of zinc chlorins (A) and free base chlorins (B), normalized at the Soret band.

Similar spectral trends are observed for the zinc and free base sets. The Q_y absorption band bathochromically shifts, intensifies, and has increased FWHM as the 13-substituent changes along the series: no substituent, acetyl, chalcone-phenyl (chPh), retinyl1 (ret1). The increase in the relative Q_y absorption is dramatic for the chlorin-chalcones, especially for **ZnC-M^{10}Ret1^{13}**, where the I_{Qy}/I_B ratio approaches unity (0.89) and is the most intense chlorin Q_y band observed.[2,6,7] The 13-retinyl substituent also has dramatic effects at the edge of the Soret region, displaying prominent shoulders in both **ZnC-M^{10}Ret1^{13}** and **FbC-M^{10}Ret1^{13}** consistent with the underlying absorption from the retinyl benchmark auxochrome discussed in a subsequent section. There are some subtle changes in the spectral properties as the solvent is changed from toluene to DMSO. There is a slight bathochromic shift in the absorption maximum of the B band, along with peak shape changes of the Q_y absorption band. The greater FWHM of the Q_y absorption band is paralleled by a corresponding decrease in relative Q_y peak intensity (I_{Qy}/I_B) upon changing from toluene to DMSO. The compensating effects of bandwidth and peak height indicate that the integrated intensity (oscillator strength) of the Q_y band generally does not change appreciably with solvent. Similar results were observed in a recent, similar study with bacteriochlorin chalcones.[8] The following spectral characteristics are summarized in Table 1: peak positions of the B and Q_y (origin) bands, the Q_y/B peak-intensity ratio, the position of the Q_y fluorescence maximum, and the full-width-at-half-maximum (FWHM) of the Q_y absorption and fluorescence bands.

Table 1. Spectral Properties of Chlorin Chalcones and Associated Benchmarks.

Compound	Solvent	B_{max} Abs (nm)	Q_y Abs (nm)	Q_y Abs FWHM (nm)	I_{Qy}/I_{Bmax}	Q_y Em (nm)	Q_y Em FWHM (nm)
ZnC	Toluene	398	602	11	0.28	604	12
ZnC-M^{10}A^{13}	Toluene	418	631	14	0.45	635	15
ZnC-M^{10}chPh^{13}	Toluene	422	640	17	0.69	646	18
ZnC-M^{10}Ret1^{13}	Toluene	423	644	20	0.89	648	23
FbC	Toluene	389	633	10	0.42	635	12
FbC-M^{10}A^{13}	Toluene	414	658	12	0.52	661	14
FbC-M^{10}chPh^{13}	Toluene	426	665	15	0.62	669	16
FbC-M^{10}Ret1^{13}	Toluene	421	666	17	0.67	670	18
ZnC	DMSO	403	604	14	0.16	608	15
ZnC-M^{10}A^{13}	DMSO	423	636	19	0.32	642	20
ZnC-M^{10}chPh^{13}	DMSO	429	645	28	0.59	658	31
ZnC-M^{10}Ret1^{13}	DMSO	402/427[a]	650	31	0.72	650	33
FbC	DMSO	395	631	12	0.31	633	14
FbC-M^{10}A^{13}	DMSO	414	655	15	0.36	660	17
FbC-M^{10}chPh^{13}	DMSO	424	661	20	0.48	668	21
FbC-M^{10}Ret1^{13}	DMSO	418	663	24	0.53	665	25

[a]Two peaks of nearly identical intensity in the Soret region, with maxima at 402 nm and 427 nm.

Fluorescence Spectra

The fluorescence spectrum of each chlorin–chalcone and associated simpler benchmarks, presented in Figure 2, is dominated by the Q_y origin band and is quite typical of previously studied chlorins. For the zinc chlorins, the Q_y fluorescence maximum is bathochromically shifted 2–8 nm in DMSO compared to toluene, paralleling the same solvent effect on the Q_y absorption maximum. The opposite effect is seen for the free base chlorins, with a 1–5 nm hypsochromic shift in DMSO compared to toluene, also consistent with Q_y absorption changes. Both the zinc and free base chlorins exhibit broader emission peaks (as measured by FWHM) in DMSO compared to toluene, with the largest change observed for the zinc-chalcones (11–13 nm FWHM increase).

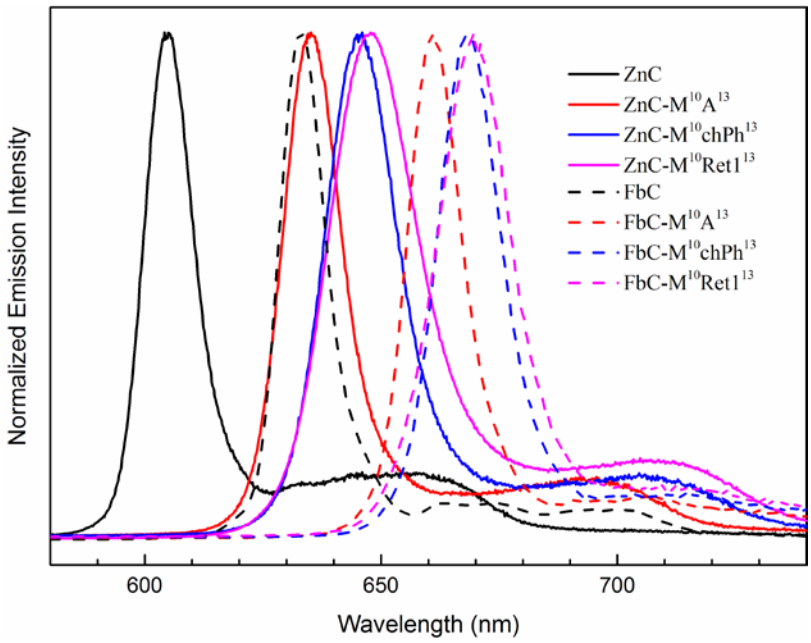

Figure 2. Fluorescence spectra of zinc chlorins (solid lines) and free base chlorins (dashed lines).

Photophysical Properties

Fluorescence quantum yields (Φ_f) and first singlet excited-state lifetimes (τ_s) are presented in Table 2 for each compound in toluene and DMSO. In toluene, the chlorin chalcones exhibit some of the highest fluorescence yields (0.24-0.30) observed in synthetic chlorins studied within the group,[2,6,7] approaching the native chlorophyll *a* (0.325). Unlike the static absorption and fluorescence spectra, the photophysical properties of the chlorin chalcones have strong solvent dependencies. Fluorescence quenching and lifetime reduction in DMSO are observed for all the chlorin chalcones, but not observed in the simpler benchmarks. The solvent effect is more pronounced for the longer retinyl substituent, particularly in conjunction with the zinc central metal in compound **ZnC-M^{10}Ret1^{13}**.

Table 2. Photophysical Properties of Chlorin Chalcones.

Compound	Φ_f	τ_s (ns)	Φ_f	τ_s (ns)
	Toluene		DMSO	
ZnC	0.06	1.7	0.07	1.8
ZnC-M^{10}A^{13}	0.24	4.7	0.25	5.6
ZnC-M^{10}chPh^{13}	0.26	4.6	0.15	3.2
ZnC-M^{10}Ret1^{13}	0.28	3.7	0.006	0.015/0.4[a]
FbC	0.20	8.8	0.17	9.3
FbC-M^{10}A^{13}	0.26	9.9	0.24	9.3
FbC-M^{10}chPh^{13}	0.30	8.4	0.24	7.3
FbC-M^{10}Ret1^{13}	0.24	7.2	0.13	1.0/7.4[b]

[a] Measured by transient absorption, dual exponential fit reveals 0.015 and 0.4 ns lifetimes with relative amplitudes of 96% and 4%, respectively.
[b] Two component decay with equal amplitude.

The broad absorption effected by the retinyl substituent, in conjunction with the impressive fluorescence yields for both **ZnC-M^{10}Ret1^{13}** and **FbC-M^{10}Ret1^{13}** make this a very interesting candidate for light-harvesting. Looking at **ZnC-M^{10}Ret1^{13}** in toluene, the broad absorption in the 450-500 nm range (typically lacking in chlorins) is reproduced in the fluorescence excitation spectrum (Figure 3), indicating that the absorption advantage of the retinyl substituent is translated into fluorescence, and could be made available for excitation energy transfer.

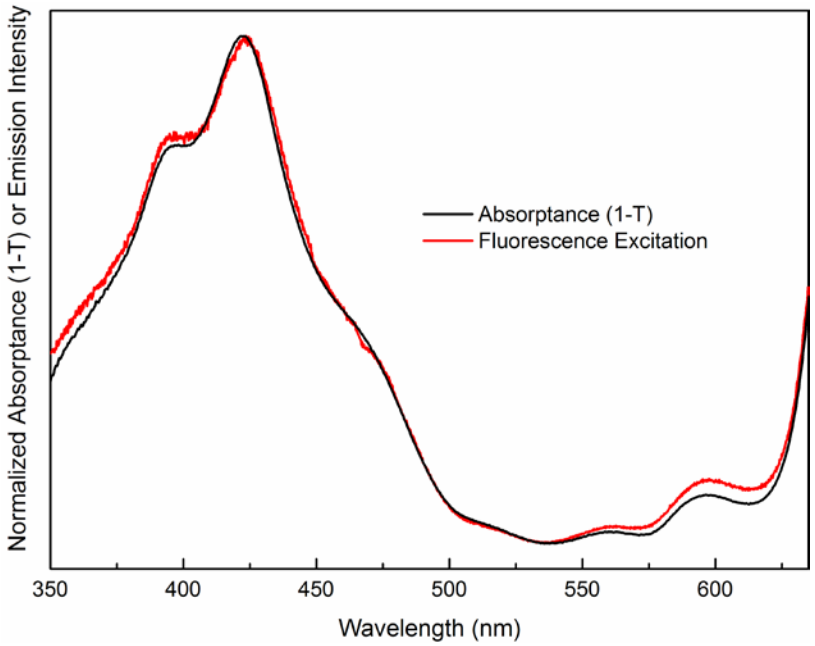

Figure 3. Absorptance (1-T) spectrum vs fluorescence excitation spectrum (λ_{em} = 650 nm) for **ZnC-M^{10}Ret1^{13}**.

The dramatic reduction in Φ_f and τ_s with the polar solvent DMSO suggests that these attractive light-harvesting characteristics exhibited by the compound in toluene are quite dependent on the environment. Transient absorption spectroscopy was employed to resolve the fast decay kinetics of **ZnC-M^{10}Ret1^{13}** in DMSO, and representative spectra are presented in Figure 4 for this compound in both DMSO and toluene. In addition to the prompt decay kinetics in DMSO (15 ps and 400 ps components with relative amplitudes of 96% and 4%, respectively), there is a prominent positive absorption feature in the 500-600 nm range, similar to the retinyl benchmark discussed in the next section. The dominant 15 ps component is similar to the lifetime of the retinyl benchmark in DMSO, and the 400 ps component is consitent with the observed Φ_f of 0.006.

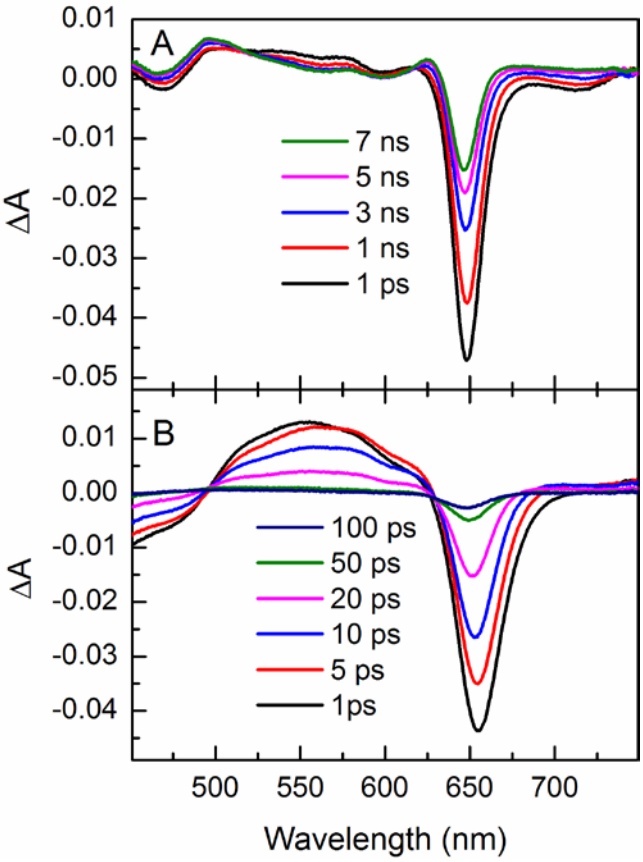

Figure 4. Transient absorption spectra of **ZnC-M[10]Ret1[13]** using excitation with ~130 fs flashes at ~420 nm. Each panel shows representative spectra as a function of time, (A) in toluene, (B) in DMSO. Note the dramatically shorter time scale of panel B .

Retinyl Benchmark

Static absorption spectra of the retinyl benchmark are presented in Figure 5. There is some subtle broadening in DMSO, but the spectra are relatively similar. No fluorescence is observed from the retinyl benchmark in either solvent.

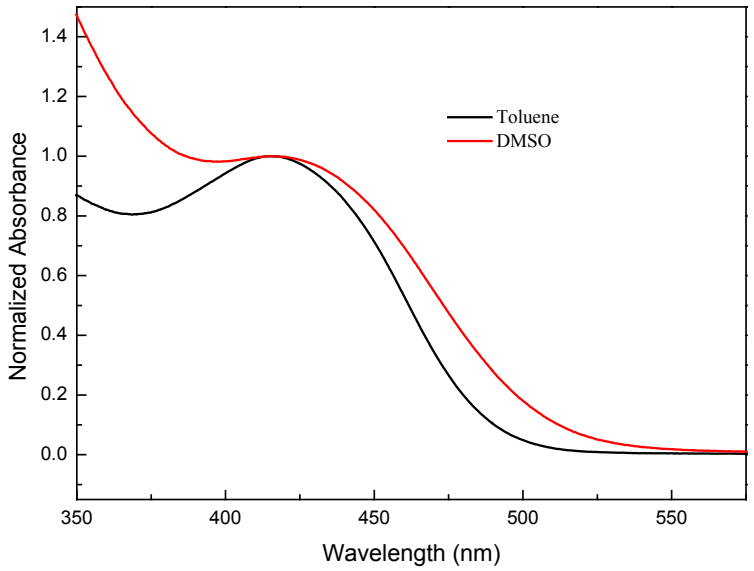

Figure 5. Absorption spectra of the retinyl benchmark in toluene (black) and DMSO (red), normalized at the local maxima at approximately 415 nm.

Transient absorption spectra are generally similar for the retinyl benchmark between the two solvents (Figure 6). Each display broad positive absorption from 500-700 nm, with the negative ground state bleaching feature dominating at lower wavelengths. Kinetics fits of the peak wavelength traces return lifetimes of 6.5 ps and 60 ps (1:1 ratio) in toluene, and 15 ps in DMSO.

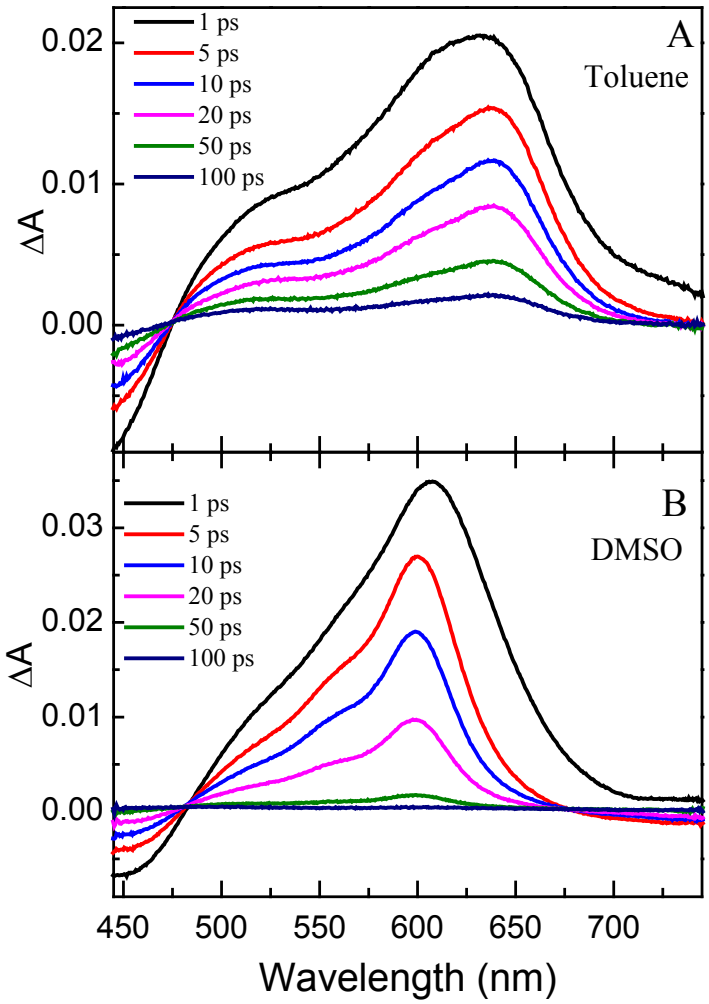

Figure 6. Transient absorption spectra obtained following excitation at 420 nm of the retinyl benchmark in toluene (A) and DMSO (B).

CONCLUSIONS and OUTLOOK

The novel chlorin chalcones exhibit consistently high fluorescence yields in non-polar solvent (0.26-0.30), which approach that of native chlorophyll *a* (0.325). They also exhibit the most red-shifted Q_y bands for chlorins studied thus far. Incorporation of chalcone substituents at the 3- and 13-positions are expected to red-shift this band even further, as the effects of substituents at these positions are typically additive.[6,7] Thus, chalcone substituents can be successfully incorporated into the chlorin macrocycle, with additional absorption in the 450-500 nm region and strong absorption in red regions of the solar spectrum not previously accessible with our synthetic chlorins. In highly polar solvent, fluorescence yields are substantially reduced, especially with the longer retinyl substituent, with concomitant reduction in the first singlet excited state lifetime. These synthetic chlorin chalcones could emulate the dichotomous roles that carotenoids play by varying the local environmental conditions, performing great light-harvesting functions in a non-polar environment and excitation energy quenching in a quite polar setting. Both modalities are likely to be of use in artificial photosynthesis; devising schemes to manipulate and controllably switch between the divergent properties could be a future pursuit.

The analysis herein can be extended with estimates of the yield of $S_1 \rightarrow T_1$ intersystem crossing (Φ_{isc}), also called the triplet yield. Along with τ_S the rate constants for the S_1 excited-state decay via fluorescence (k_f), intersystem crossing (k_{isc}), and internal conversion (k_{ic}) can all be determined via the expression $k_i = \Phi_i / \tau_S$. The spectral properties could also be correlated to calculated molecular orbital energies within Gouterman's four-orbital model[9-11] for additional insights.

REFERENCES

(1) Ruzié, C.; Krayer, M.; Lindsey, J. S. *Org. Lett*. **2009**, *11*, 1761–1764.

(2) J. W. Springer, K. M. Faries, H. L. Kee, J. R. Diers, C. Muthiah, O. Mass, C. Kirmaier, J. S. Lindsey, D. F. Bocian and D. Holten, *Photochem. Photobiol.,* 2012, **88**, 651–674.

(3) E. Yang, C. Kirmaier, M. Krayer, M. Taniguchi, H.-J. Kim, J. R. Diers, D. F. Bocian, J. S. Lindsey and D. Holten, *J. Phys. Chem. B,* 2011, **115**, 10801–10816.

(4) O. Mass, M. Taniguchi, M. Ptaszek, J. W. Springer, K. M. Faries, J. R. Diers, D. F. Bocian, D. Holten and J. S. Lindsey, *New J. Chem*., 2011, **35**, 76–88.

(5) D. Noy, B. M. Discher, I. V. Rubstov, R. M. Hochstrasser and P. L. Dutton, *Biochem*., 2005, **44**, 12344–12354.

(6) Kee, H. L., C. Kirmaier, Q. Tang, J. R. Diers, C. Muthiah, M. Taniguchi, J. K. Laha, M. Ptaszek, J. S. Lindsey, D. F. Bocian and D. Holten. *Photochem. Photobiol*. **83**, 1110–1124.

(7) Kee, H. L.; C. Kirmaier, Q. Tang, J. R. Diers, C. Muthiah, M. Taniguchi, J. K. Laha, M. Ptaszek, J. S. Lindsey, D. F. Bocian and D. Holten. *Photochem. Photobiol*. **83**, 1125–1143.

(8) Yang, E., Ruzié, C., Krayer, M., Diers, J. R., Niedzwiedzki, D. M., Kirmaier, C., Lindsey, J. S., Bocian, D. F. and Holten, D. *Photochem. Photobiol*. **89**: 586–604.

(9) Gouterman, M. (1959) Study of the effects of substitution on the absorption spectra of porphin. *J. Chem. Phys.* **30**, 1139–1161.

(10) Gouterman, M. (1961) Spectra of porphyrins. *J. Mol. Spectroscopy* **6**, 138–163.

(11) Gouterman, M. (1978) Optical spectra and electronic structure of porphyrins and related rings. In *The Porphyrins* Vol. 3 (Edited by D. Dolphin), pp 1–165. Academic Press, New York.

Chapter 8.

Biohybrid Photosynthetic Antenna Complexes for Enhanced Light-Harvesting

Reprinted with permission from *Journal of the American Chemical Society*. J. W. Springer, P. S. Parkes-Loach, K. R. Reddy, M. Krayer, J. Jiao, G. M. Lee, D. M. Niedzwiedzki, M. A. Harris, C. Kirmaier, D. F. Bocian, J. S. Lindsey, D. Holten and P. A. Loach, *J. Am. Chem. Soc.,* 2012, **134**, 4589−4599.

Abstract

Biohybrid antenna systems have been constructed that contain synthetic chromophores attached to 31mer analogs of the bacterial photosynthetic core light-harvesting (LH1) β-polypeptide. The peptides are engineered with a Cys site for bioconjugation with maleimide-terminated chromophores, which include synthetic bacteriochlorins (**BC1**, **BC2**) with strong near-infrared absorption and commercial dyes Oregon Green (**OGR**) and Rhodamine Red (**RR**) with strong absorption in the blue-green to yellow-orange regions. The peptides place the Cys 14 (or 6) residues before a native His site that binds bacteriochlorophyll *a* (BChl *a*) and, like the native LH proteins, have high helical content as probed by single-reflection IR spectroscopy. The His residue associates with BChl *a* as in the native LH1 β-polypeptide to form dimeric ββ-subunit complexes $[31mer(-14Cys)X/BChl]_2$, where X is one of the synthetic chromophores. The native-like BChl-*a* dimer has Q_y absorption at 820 nm and serves as the acceptor for energy from light absorbed by the appended synthetic chromophore. The energy-transfer characteristics of biohybrid complexes have been characterized by steady-state and time-resolved fluorescence and absorption measurements. The quantum yield of energy transfer from a synthetic chromophore located 14 residues from the BChl-coordinating His site are as follows: **OGR** (0.30) < **RR** (0.60) < **BC2** (0.90). Oligomeric assemblies of the subunit complexes $[31mer(-14Cys)X/BChl]_n$ are accompanied by a bathochromic shift of the Q_y absorption of the BChl-*a* oligomer as far as the 850-nm position found in cyclic native photosynthetic LH2 complexes. Room-temperature stabilized oligomeric biohybrids have energy-transfer quantum yields comparable to those of the dimeric subunit complexes as follows: **OGR** (0.20) < **RR** (0.80) < **BC1** (0.90). Thus, the new biohybrid antennas retain the energy-transfer and self-

assembly characteristics of the native antenna complexes, offer enhanced coverage of the solar spectrum, and illustrate a versatile paradigm for the construction of artificial LH systems.

I. Introduction

The quest for renewable energy has prompted substantial interest in evaluating the attributes and limitations of natural photosynthetic processes.[1] Both plant and bacterial photosynthetic systems employ light-harvesting antenna systems that collect light and funnel energy to the reaction centers. The antennas are generally multi-subunit complexes that simultaneously (i) hold the light-absorbing cofactors – (bacterio)chlorophylls and accessory chromophores – at fixed relative distances and orientations, (ii) tune the absorption wavelengths of these chromophores, and (iii) achieve directional energy funneling.[2,3] These combined features give rise to nearly quantitative delivery of the energy quanta to the photochemical reaction centers. Despite this high quantum yield, the overall photoconversion efficiency is limited at the outset because a given photosynthetic antenna system utilizes only a fraction (typically less than half) of the photon-rich visible and near-infrared (NIR) regions of the solar spectrum.[1] Thus, in the construction of highly efficient artificial solar-conversion systems, it is important to maximize solar coverage while maintaining near-quantitative delivery to the target sites.

The mainstream efforts over the past few decades to build fully synthetic light-harvesting systems have required constructing both the chromophores and scaffolding *de novo*.[4,5] The challenges associated with such syntheses have chiefly restricted focus to architectures containing chromophores that are relatively few in number (*e.g.,* <10) and have readily accessible synthetic chemistry (*e.g.*, porphyrins, which lack red and NIR absorption).[6] A complementary approach entails development of biohybrid light-harvesting systems. The

biohybrid approach builds upon the burgeoning structural knowledge of the natural light-harvesting (bacterio)chlorophyll-protein complexes,[7-10] the ability to reconstitute bacterial antenna systems from the component parts *in vitro*,[11-14] and the recent availability of red- and NIR-absorbing, stable synthetic (bacterio)chlorins.[15-19] The bacteriochlorins are distinguished by wavelength tunability of a sharp and intense absorption band in the NIR region, a reasonable degree of synthetic tailorability (for solubility, bioconjugation, etc.), robustness on routine handling, and spectral features that are quite insensitive to medium and environmental polarity.[15] Few if any other classes of pigments afford this combination of features,[20] and few bioconjugatable bacteriochlorins have previously been prepared.[6,21,22]

A foundation for developing biohybrid antenna complexes relies on modifications of the αβ-subunit (Figure 1A) common to cyclic oligomeric light-harvesting complexes LH1 and LH2 (Figure 1B) of photosynthetic bacteria.[7-9] The subunit consists of two polypeptides (α and β), both of which are typically 40–50 amino acids in length,[2,12] and contribute a histidine residue (Figure 1A, black) as an apical ligand to the central Mg of one of two bacteriochlorophyll *a* (BChl *a*) molecules in the subunit complex (Figure 1A, purple). Electronic interactions between the two BChl *a* molecules shift the intense Q_y absorption band from ~780 nm for monomeric BChl *a* to ~820 nm for the dyad. The αβ-subunit readily self-assembles from the native components (α and β polypeptides and BChl *a*) *in vitro*.[11-14]

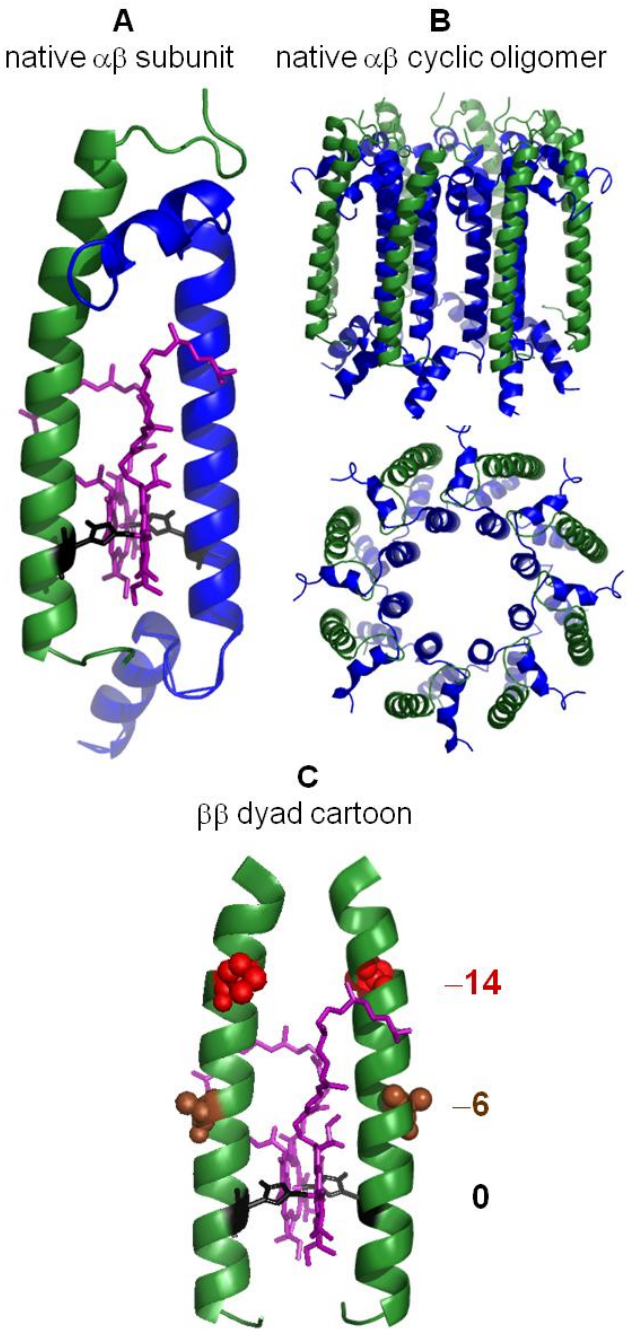

Figure 1. (A) The αβ-subunit of the LH2 (B800-850) complex of *Rs. molischianum*.[9] (B) Side and top views of the full LH2 complex showing polypeptides without BChl-*a* for clarity. (C) Cartoon of the 31mer ββ-complex showing two possible sites (–14, –6) for chromophore attachment and the BChl-*a* dimer B820 (purple). The BChl-coordinated His (black) is defined as position 0.

In this paper, we describe the design, assembly and energy-transfer characteristics of biohybrid antenna complexes. For the construction of these complexes, polypeptide analogs containing the last 31 amino acids of the β polypeptide of *Rb. sphaeroides* LH1[11,23,24] have been utilized. These polypeptides lack 17 residues from the N-terminus of the native peptide and have the sequence ELHSVY**M**$^{-14}$SGLWLFS**A**$^{-6}$VAIVA**H**^{0}LAVYIWRPWF. (Three key sites are emboldened and underlined with positions superscripted.) Prior work has shown that the 31mer readily associates with BChl *a* to form a homodimeric ββ-subunit complex (illustrated in Figure 1C) in which the BChl-*a* dimer (denoted B820) has a Q_y absorption band near 820 nm.[11,23,24] Oligomeric forms can be produced in which the BChl-*a* Q_y band is bathochromically shifted to up to 850 nm (and thus denoted B850). In our studies, two peptide analogs were prepared in which either −6Ala (Figure 1C, brown) or −14Met (Figure 1C, red) is replaced by Cys to allow designer-chromophore attachment at that site. The modified 31mers (without attached chromophore) are denoted 31mer(−6Cys) and 31mer(−14Cys). The chromophores chosen for covalent attachment to the peptides include two synthetic bacteriochlorins (**BC1**, **BC2**) and two commercial dyes [Oregon green (**OGR**) and rhodamine red (**RR**)] (Figure 2). Each chromophore bears a maleimide-terminated linker for bioconjugation with the Cys site of 31mer(−6Cys) and 31mer(−14Cys). These four chromophores have spectral properties that are complementary to each other and to the BChl-*a* energy-acceptor complex in the biohybrid antennas. The biohybrid complexes thus afford a modular design and synthesis, can draw on a palette of diverse bioconjugatable dyes, exploit natural self-assembling peptides, and afford the possibility to tailor the desired absorption spectral features in the creation of antenna systems with enhanced light-harvesting capacity.

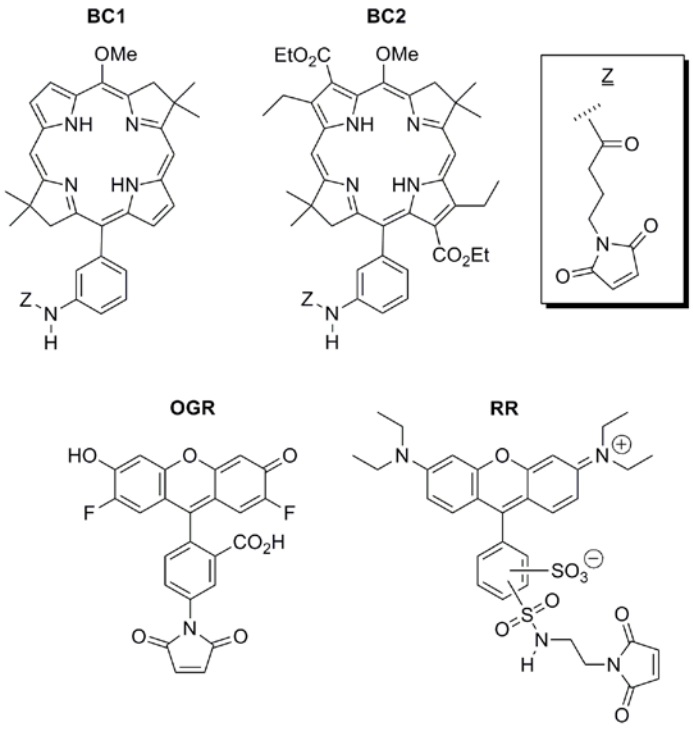

Figure 2. Bioconjugatable bacteriochlorins (**BC1**, **BC2**) and commercial dyes (**OGR**, **RR**).

II. Experimental Procedures

Two synthetic polypeptides (Bio-Synthesis, Lewisville, TX) were used in these studies. Each contained 31 amino acids with a sequence identical to that of the last 31 amino acids in the β polypeptide of LH1 of *Rb. sphaeroides* except for the substitution of a Cys in place of either Met-14 or Ala-6. Purity was >90% according to HPLC data, and the mass spectrometry results were consistent with the expected product: *m/z* = 3633 observed versus 3634 calculated for the 31mer(−14Cys) and *m/z* = 3694 observed versus 3696 calculated for the 31mer(−6Cys). BChl *a* with a geranyl-geraniol esterifying alcohol was isolated from membranes of the G9 carotenoidless mutant of *Rhodospirillum rubrum*.[24] *n*-Octyl *β*-D-glucopyranoside (referred to as octyl glucoside from Sigma) and the dyes Oregon Green 488 maleimide (**OGR**) and Rhodamine Red maleimide (**RR**) from Invitrogen:Molecular Probes were used as received. The synthesis of the bacteriochlorins **BC1** and **BC2** will be described elsewhere. The synthetic chromophores

were tethered to the peptides in *N,N*-dimethylformamide via standard procedures to afford 1:1 complexes of dye:peptide on the basis of extinction coefficients for each of **BC2**, **OGR** and **RR** (see Supporting Information). For **BC1**, limited solubility in the HPLC solvents precluded rigorous removal of unreacted 31mer(–14Cys) from 31mer(–14Cys)BC1. If any **BC1**-free peptide were incorporated into the biohybrid complexes, the amount and effect are small on the basis of the agreement of the energy-transfer efficiency determined from fluorescence-excitation spectra versus two other measurements, as described below.

The conditions for forming B820- and B850-type complexes have been previously described.[11,23,24] In general, 0.05-0.20 mg of each polypeptide was dissolved in 5-10 μL of hexafluoroacetone trihydrate. To this solution was added 0.50 mL of 4.5% (w/v) octyl glucoside in 50 mM potassium phosphate buffer (pH 7.5) followed by 2.0 mL of 100 mM potassium phosphate buffer (pH 7.5) to bring the octyl glucoside concentration to 0.90%. Increasing amounts of BChl *a* were then added to the sample by injecting 5-20 μL of a degassed acetone solution to approach the same BChl-*a* concentration as that of the polypeptide. In general, this resulted in a combined absorbance (A_{780nm} + A_{820nm}) between 0.1 and 0.2. The sample was then diluted to 0.75% octyl glucoside and again to 0.66% octyl glucoside to optimize subunit formation. After each dilution, an absorption spectrum was recorded. In some cases, complete formation of the B820 complex required cooling the sample to about 6 °C for 1 h. For formation of B850-type complexes, the sample was kept overnight at 4–8 °C, after which a final absorption spectrum was taken. For evaluation of the B850-type complex stability, the samples (after chilling overnight) were brought to room temperature and the absorption spectra recorded over time to follow the conversion to B820 and/or BChl *a*. For study of the B850-type complexes at room temperature, the samples that were chilled overnight were diluted with an equal volume of

cold 100 mM potassium phosphate buffer (pH 7.5) to bring the octyl glucoside concentration to 0.33% and then warmed to room temperature. Prior to reconstitution, protein concentrations were determined by dissolving the protein in 20 μL of hexafluoroacetone trihydrate followed by 1.00 mL of 0.1 % TFA in 2:1 (v/v) acetonitrile/2-propanol,[24] recording the UV absorption spectrum, and calculating the concentration assuming an extinction coefficient at 287 nm of 3400 $M^{-1}cm^{-1}$ per Trp residue.[25] Where necessary a correction was made for the absorbance of the attached chromophores. Aliquots were dried under argon and vacuum. The B820- and B850-type complexes were prepared at Northwestern University and shipped overnight on ice (in their B850 state) to Washington University where they were stored at 4-8 °C.

Procedures for single-reflection infrared spectroscopy, ellipsometry, and steady-state and time-resolved optical spectroscopy are described in the Supporting Information.

III. Results and Discussion

A. Synopsis

In the following, the assembly of the new biohybrid architectures from the component parts is described first (Section B). The energy-transfer properties of the dimeric ββ-subunit complexes are then given (Section C), followed by a description of the results of studies of energy flow in oligomeric assemblies based on the same components (Section D). A general analysis of the results for the various biohybrid complexes is then given and related to the Förster theory for energy transfer (Section E). Finally, conclusions and an outlook for future directions are presented (Section F).

B. Assembly of Biohybrid Light-Harvesting Complexes

1. Properties of the components. The synthetic analogs of the native antenna peptides, both with and without attached chromophores, were examined to ensure that they retained helical structures (like the native β polypeptide[26-28]). Figure 3 shows single-reflection FTIR spectra of 31mer(−14Cys), 31mer(−6Cys), both peptides with attached **OGR**, the native β peptide, and myoglobin in films on gold, as well as **OGR** in a KBr pellet. Myoglobin serves as a model for a prototypical α-helical system and exhibits two strong bands at 1664 and 1546 cm^{-1}, assignable to the amide I and amide II vibrations. The various peptides, with and without the conjugated **OGR**, exhibit similar spectra, consistent with an α-helical structure. Comparisons among the spectra lead to several conclusions: (i) Deposition on the metal substrate does not disrupt the structure of the peptide. (ii) The comparable spectra for 31mer(−14Cys) versus 31mer(−14Cys)OGR and 31mer(−6Cys) versus 31mer(−6Cys)OGR indicate that attachment of **OGR** does not significantly perturb the α-helical content of the peptide. (iii) The similarity in the spectra of the 31mer peptides and full-length native β indicates that the 31mers retain significant α-helical content despite removal of 17-residues from the N-terminus of the native sequence. Finally, no bands are apparent in the IR spectra of peptides 31mer(−14Cys)OGR and 31mer(−6Cys)OGR that might be attributed to **OGR**. This observation is not surprising given that there is a single dye molecule attached to the protein and that all the amino acid residues collectively contribute to the IR spectrum. The high α-helical content of the polypeptides and their conjugated derivatives in films is consistent with NMR studies of the native β-polypeptide in organic solvents[26,28] and in aqueous detergent solutions[27] as well as the crystal structures for LH2 of *Rs. molischianum*[9] (Figure 1), *Rps. acidophila*[7] and the RC-LH1 complex[8] of *Rps.*

palustris. Thus, the backbone structures of the 31mer polypeptides and their chromophore-tethered forms are essentially known in their B820- and oligomeric-type complexes.

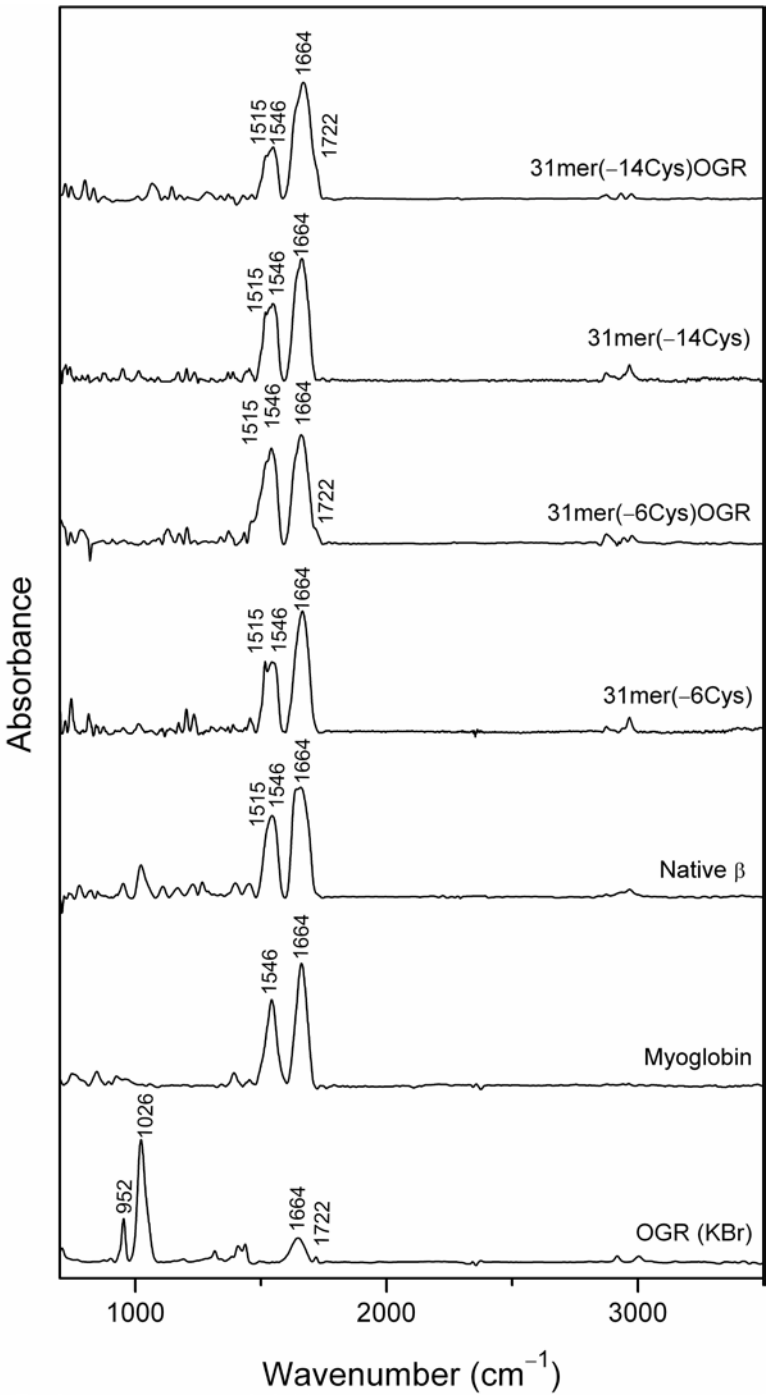

Figure 3. Single-reflection FTIR spectra of antenna peptides and myoglobin in films on gold (15 h deposition time) and **OGR** in KBr pellet.

One long-term objective of the studies of the biohybrid systems is to form extended assemblies on solid substrates. Consequently, other properties of the peptides on the surface were investigated. These properties included the thickness of the films formed as a function of deposition time and the helicity of the peptides as a function of film thickness. Elipsometric measurements as a function of deposition time (10 min – 15 h) revealed that the average film thickness increases as a function of deposition time and maximizes at ~5-7 nm (Figure S-2). This thickness corresponds to an extremely thin film of ~10 peptides if the peptides lie flat on the surface, or a single monolayer if the peptides assemble vertically. Regardless of film thickness, the α-helicity of the peptides does not change, as judged by the frequencies of the amide I and II vibrations.

The chromophores for bioconjugation to the synthetic peptides have complementary optical properties. Figure 4 shows the longest wavelength absorption band and the fluorescence profile for chromophores **BC1**, **BC2**, **OGR** and **RR** (normalized for clarity). The bacteriochlorins have an intense ($\varepsilon \sim 120{,}000\ M^{-1}cm^{-1}$)[15,19] NIR Q_y band plus weaker Q_x bands (500–560 nm) and strong near-UV Soret bands (not shown). **OGR** ($\varepsilon \sim 77{,}000\ M^{-1}cm^{-1}$) and **RR** ($\varepsilon \sim 126{,}000\ M^{-1}cm^{-1}$) absorb and fluoresce strongly in the blue-green and yellow-orange spectral regions, respectively (450–650 nm) (see Supporting Information).

2. Formation of B820- and oligomeric-type complexes. Both 31mer(–14Cys) and 31mer(–6Cys) associate with BChl *a* to form ββ-subunit complexes $[31mer(-14Cys)BChl]_2$ and $[31mer(-6Cys)BChl]_2$ with a Q_y band at ~820 nm and a weaker Q_x band at ~590 nm (Figure 4, black). The spectrum is essentially the same as that for the BChl-*a* dyad in either the native-sequence 31mer ββ-subunit complex or the native αβ-subunit complex.[11,12] The key steps in forming the biohybrid complexes include (i) bioconjugation of chromophore X (**BC1**, **BC2**, **RR**,

OGR) to 31mer(−14Cys) to form constructs 31mer(−14Cys)X, followed by (ii) interaction with BChl *a* to assemble B820-type complexes [31mer(−14Cys)X/BChl]$_2$. The biohybrid complex [31mer(−6Cys)OGR/BChl]$_2$ was also assembled (see Experimental Section and Supporting Information).

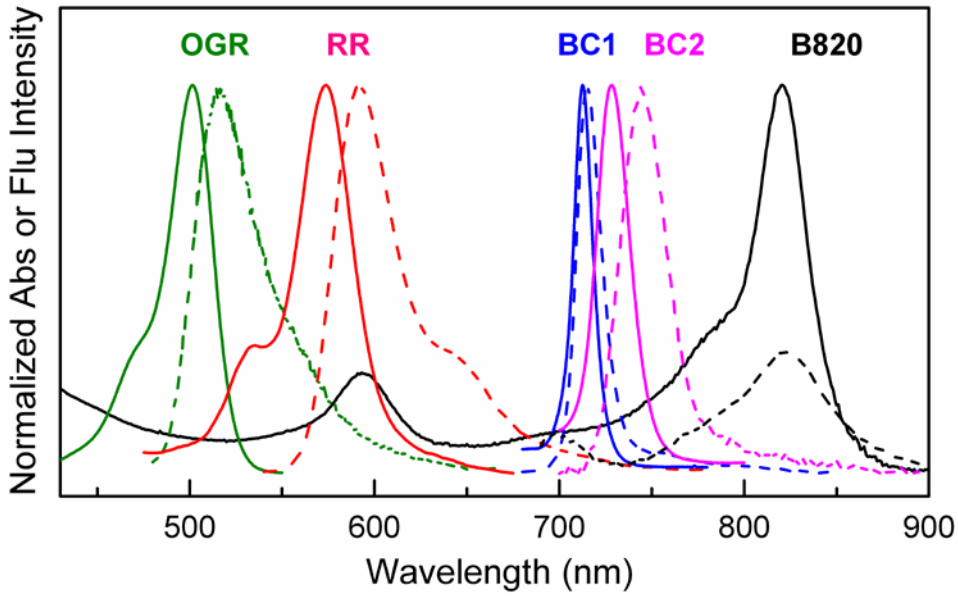

Figure 4. Normalized absorption (solid) and fluorescence (dashed) spectra of bioconjugatable dyes (colored) and of BChl-*a* dimer B820 in subunit complex [31mer(−14Cys)BChl]$_2$ (black). The B820 fluorescence is scaled arbitrarily for clarity.

Figure 5A shows part of the spectral evolution (black → green → red) obtained for the formation of biohybrid complex [31mer(−14Cys)OGR/BChl]$_2$. Comparison with Figure 4 shows that the complex combines the characteristic native-like B820 absorption and that of **OGR** at ~500 nm. Figure 5A also illustrates that chilling (typically overnight) results in association of ββ-subunits to form an oligomeric complex [31mer(−14Cys)OGR/BChl]$_n$ that has the Q_y absorption shifted to ~850 nm; thus, the interacting BChls of the oligomeric complex are generically denoted B850. The ββ-subunit complex is reformed by warming to room temperature. The oligomeric complex also can be stabilized at room temperature by first diluting

the cold sample of the ββ-subunit complex with cold buffer to decrease the detergent concentration to below its critical micelle concentration (CMC) and then warming the sample to room temperature. Formation of the analogous **BC2**-containing ββ-subunit complex [31mer(−14Cys)BC2/BChl]$_2$ is shown in Figure 5B; **BC2** contributes the strong Q_y band at 730 nm and modest Q_x band at 515 nm. Similar behavior is found for constructs with **RR** and **BC1**, except that for the latter the oligomeric complex is stabilized at room temperature with the detergent concentration still slightly above the CMC.

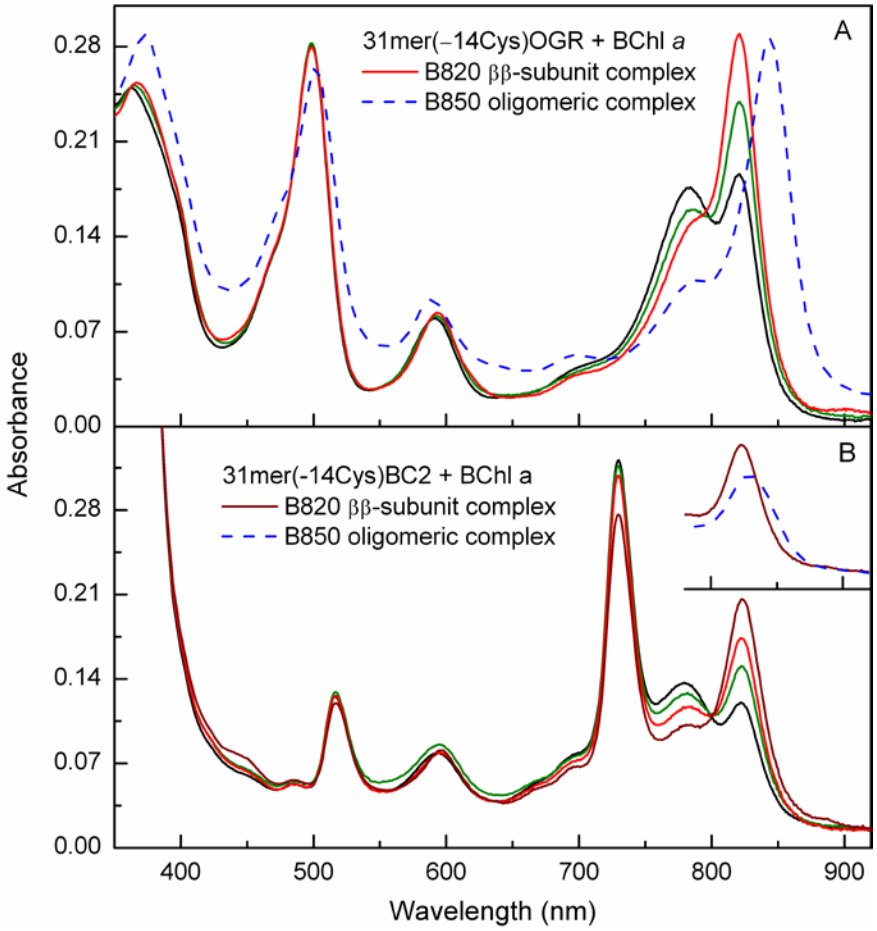

Figure 5. Absorption spectra for formation of B820- and B850-type complexes. (A) The solution contains 31mer(−14Cys)OGR and BChl *a* at 0.90% (black), 0.75% (green) and 0.66% (red) octyl glucoside; the latter is then chilled overnight (dashed blue). (B) The solution contains 31mer(−14Cys)BC2 and BChl *a* at 0.90% (black), 0.75% (green) and 0.66% (red) octyl glucoside; the latter is then chilled for 1 h (brown) or overnight (dashed blue).

The subunit and oligomeric complexes may contain extra absorption in the 780-800 nm and Soret regions (Figure 5) due in part to excess BChl *a* sometimes used to saturate assembly formation. Additionally, the spectra of the ββ-subunit complexes necessarily contain small amounts of free BChl *a* and free peptide with bound pigment X [*e.g.*, 31mer(−14Cys)X] because the formation/dissociation of the subunit complex is an equilibrium process. The equilibrium disassembly is substantially diminished upon formation of the oligomeric architectures.

C. Energy-Transfer Characteristics of Dimeric Subunit (B820-type) Complexes

1. Overview. In this section, measurements are described on the B820-type ββ-subunit complexes. The inherent properties of photoexcited B820 (B820*) in $[31mer(-14Cys)BChl]_2$ (no attached synthetic chromophore) are given first as a benchmark for results on the analogs $[31mer(-14Cys)X/BChl]_2$ that contain chromophore X (**OGR**, **RR**, **BC1** or **BC2**). The homodimeric B820-type ββ-subunit complexes can be sufficiently stabilized to be studied in detail, which has the following advantages. First and foremost, structural knowledge about the B820-type complex stems from extensive spectroscopic characterization[11,12,27-33] and crystal structures of two LH2 complexes[7,9] and that of an RC-LH1 core complex.[8] Any significant perturbation of the structure by a covalently added chromophore would be easily observable in the association constant[11,12] and spectroscopic properties of the B820 complex. While the flexible hydrocarbon tether permits some conformational freedom of the covalently attached chromophores, positions −14 and −6 were chosen for attachment because they are on a part of the polypeptide that must be α-helical for appropriate BChl-*a* binding to form B820 (Figure 1). Secondly, the B820-type complex is in equilibrium with the "free" polypeptides and BChl *a* so

that thermodynamic measurements are possible.[11,12] Thirdly, studies of the B820 complexes provides a benchmark for assembling and investigating oligomeric species (Section D).

2. Control B820-type complexes. Figure 6 shows time-resolved absorption data for [31mer(−14Cys)BChl]$_2$ obtained using a 0.1-ps excitation flash in the Q_x band at 590 nm. The data reveal an instrument-limited rise and subsequent evolution in the combined feature associated with the bleaching in the B820 Q_y absorption and B820* stimulated emission (fluorescence stimulated by the white light probe pulse). Figure 6A shows that B820* has completely decayed to the ground state ($\Delta A = 0$) by 4 ns. Figure 6B and the short-time inset show kinetic traces representative of those acquired at 1.5-nm intervals from 800 to 900 nm. The data were globally analyzed using a triple-exponential function, resulting in best-fit time constants of 3 ps, 50 ps, and 600 ps.

The raw spectral data in Figure 6A, along with principal-component and global analysis, indicates that the 3-ps component has little decay of B820 Q_y bleaching and thus little return of B820* to the ground state. Thus, this fast component likely reflects relaxation (vibrational, conformation, electronic) on the excited-state potential-energy surface, accompanied by a change in spectral shape (*e.g.*, a shift in the stimulated-emission position). The 50-ps and 600-ps components (relative amplitudes of 0.2 and 0.8 at 820 nm) both contribute to the time evolution across the 800–900 nm region, and involve bleaching decay and thus deactivation of B820* to the ground state. One interpretation is that the major 600-ps component reflects the inherent decay of B820* and the minor 50-ps component reflects energy transfer followed by exciton annihilation (and ground-state recovery) involving two ββ-subunit complexes in close contact. Such assignments would parallel those for decay components on these timescales for the excited BChl-*a* complex B850* in native LH2 complexes, with the shorter component reflecting LH2

clusters (which form depending on conditions such as detergent concentration).[34] Another interpretation, or a contribution to the B820* decay in [31mer(–14Cys)BChl]$_2$ on both time scales, is that there is more than one chromophore–peptide conformer with small differences in the spatial relationship of the two BChl *a* that comprise B820, leading to multiple decay times.

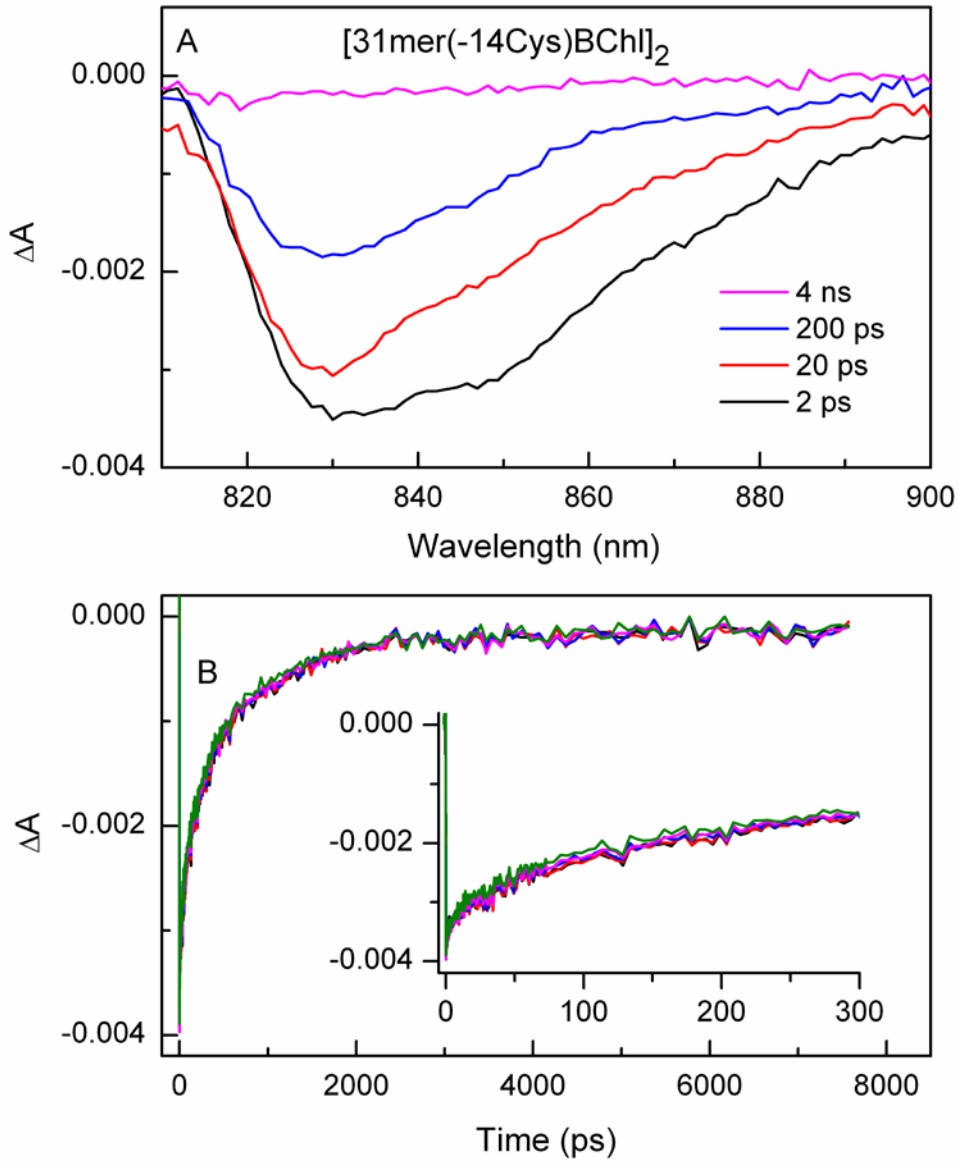

Figure 6. Time-resolved absorption spectra (A) and five kinetic traces between 829 and 834 nm (B) for [31mer(–14Cys)BChl]$_2$ (λ_{exc} = 590 nm).

The dominant 600-ps lifetime component of B820* decay in [31mer(−14Cys)BChl]$_2$ as well as the amplitude-weighted value of (0.2)(50 ps) + (0.8)(600 ps) ~ 500 ps, are considerably shorter than the average (for many solvents) singlet excited-state lifetime of 3 ns for monomeric BChl *a*.[35] Similarly the B820 fluorescence yield of roughly 0.01 measured here for [31mer(−14Cys)BChl]$_2$ is smaller than the average value of 0.17 for BChl *a*.[35] The inherent decay (largely by internal conversion) of photoexcited BChl-*a* dimer (P870*) in the bacterial photosynthetic reaction center (measured when electron transfer is blocked) is also relatively short (100–200 ps) and heterogeneous in that the apparent lifetime varies about two-fold with probe wavelength.[36] The shorter inherent B870* lifetime versus that for monomeric BChl *a* has been ascribed to enhanced nuclear-electronic coupling (Born-Oppenheimer breakdown).[37] The rationale stems from the fact that the excited state of two tightly coupled BChl molecules (B_a and B_b) is comprised of a linear combination of locally-excited (B_a* and B_b*) and charge-transfer ($B_a^+ B_b^-$ and $B_a^- B_b^+$) configurations. The latter configurations are sensitive to motions that modulate the distance (and Coulombic interaction) between the two BChl *a* molecules, resulting in vibration-induced fluctuations in the electronic character of B870* that enhance non-radiative deactivation. These same characteristics almost certainly apply to B820* in the biohybrid antenna complexes.

3. OGR-containing B820-type complexes. Representative data for the **OGR**-containing complexes are shown in Figure 7. The right inset shows B820 fluorescence at ~825 nm elicited by excitation of **OGR** at 494 nm in biohybrid complex [31mer(−14Cys)OGR/BChl]$_2$ (magenta). That this emission is not due to direct excitation of B820 is demonstrated by its absence in the **OGR**-free control complex [31mer(−14Cys)BChl]$_2$ (teal) studied under the same conditions (λ_{exc}, concentrations). The left inset of Figure 7 shows the excitation spectrum (430–650 nm) of

the B820 fluorescence (orange) normalized to the absorption spectrum (dashed blue) in the B820 Q_x band. The ratio of excitation to absorption signals (integrated intensities) at 500 nm for **OGR** gives $\Phi_{ENT} = 0.40$.

Companion time-resolved fluorescence data are shown in the main part of Figure 7. The OGR* lifetime is reduced from 4.1 ns in 31mer(–14Cys)OGR control (red) to 3.2 ns in [31mer(–14Cys)OGR/BChl]$_2$ biohybrid (blue). The lifetime reduction gives $\Phi_{ENT} = 0.22$. This result together with that from steady-state emission give an average value of $\Phi_{ENT} = 0.3$ for **OGR** → B820 energy transfer. Figure 7 also shows that more rapid energy transfer shortens the excited-state lifetime to ~0.2 ns for **OGR** at the –6 position in [31mer(–6Cys)OGR/BChl]$_2$. A small ~4 ns component is due to 31mer(–6Cys)OGR formed by dissociation of the complex.

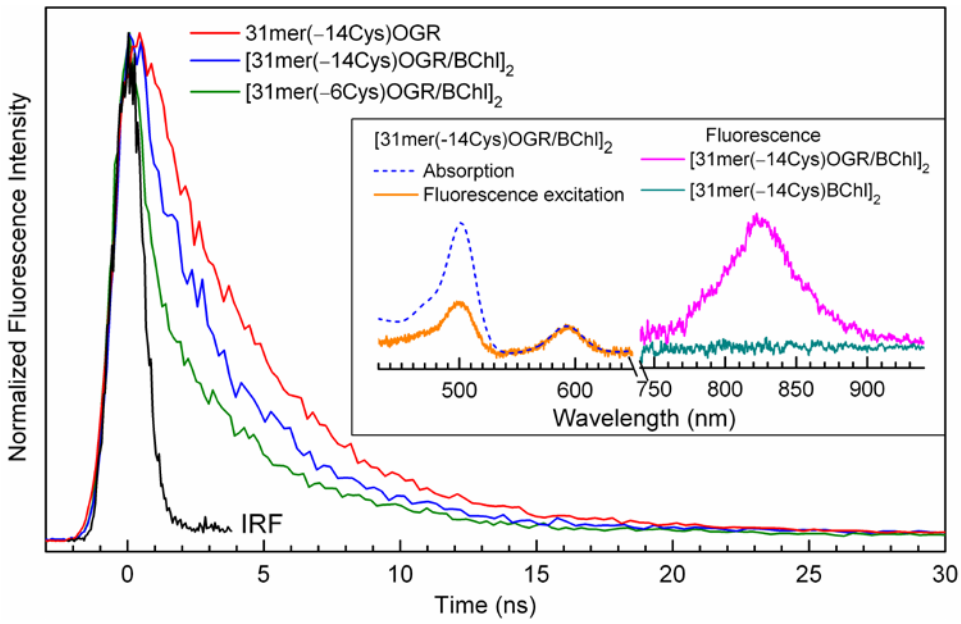

Figure 7. Photophysical data for OGR-containing controls and B820-type ββ-subunit complexes. The main panel shows fluorescence decays (λ_{exc} = 499 nm, λ_{det} = 520 nm) for the control peptide (red) and biohybrids (blue, green) along with the instrument response function (IRF; black). The insets show fluorescence (λ_{exc} = 494 nm), fluorescence excitation (λ_{det} = 825 nm) and absorption spectra (see text).

Although the OGR* decay profile for [31mer(−14Cys)OGR/BChl]$_2$ in Figure 7 is well described by a single-exponential with τ = 3.2 ns, a small 4.1-ns component due to free 31mer(−14Cys)OGR complex would not cause a detectable deviation from a single-exponential fit. For example, simulated data generated with a dual-exponential function, a small 4.1 ns component for free 31mer(−14Cys)OGR and a major 2.9 ns component for [31mer(−14Cys)OGR/BChl]$_2$, are fit well by a single exponential with τ = 3.2 ns (the same as observed). If the true lifetime for [31mer(−14Cys)OGR/BChl]$_2$ were 2.9 ns, the energy-transfer yield would then increase to 0.29 (from 0.22), which would be closer to the value of 0.40 obtained from fluorescence-excitation spectra. Such considerations exemplify the good agreement of the two measurements of the energy-transfer efficiency within experimental uncertainty.

4. BC2-containing B820 complexes. Representative data for **BC2**-containing complexes are shown in Figures 8 and 9. Figure 8A shows fluorescence spectra for [31mer(−14Cys)BC2/BChl]$_2$ (red) and 31mer(−14Cys)BC2 (blue) obtained using excitation in the Q_x band of **BC2** at 516 nm. The feature at 740 nm is **BC2** fluorescence. As expected, no emission is observed from **BC2**-free [31mer(−14Cys)BChl]$_2$ (green). The fluorescence intensity of each sample was divided by the (similar) absorbance at λ_{exc}. The ratio of the integrated (690–770 nm) intensities reveals that the **BC2** fluorescence from [31mer(−14Cys)BC2/BChl]$_2$ is 8% of that from 31mer(−14Cys)BC2. This reduction corresponds to Φ_{ENT} = 0.92 for **BC2** $\rightarrow$ B820 energy transfer in the biohybrid.

Figure 8A (and inset) also shows that excitation of **BC2** at 516 nm gives rise to B820 fluorescence at ~830 nm in [31mer(−14Cys)BC2/BChl]$_2$ but not in the controls, again reflecting energy transfer in the biohybrid. Figure 8B shows the fluorescence-excitation spectrum (λ_{det} =

830 nm) normalized to the absorption spectrum at 590 nm. Comparison of the integrated (490–550 nm) areas of the Q_x band of **BC2** in the excitation versus absorption spectra gives $\Phi_{ENT} = 0.75$ for **BC2** $\rightarrow$ B820 energy transfer. This value is modestly lower than that obtained from the **BC2** fluorescence quenching.

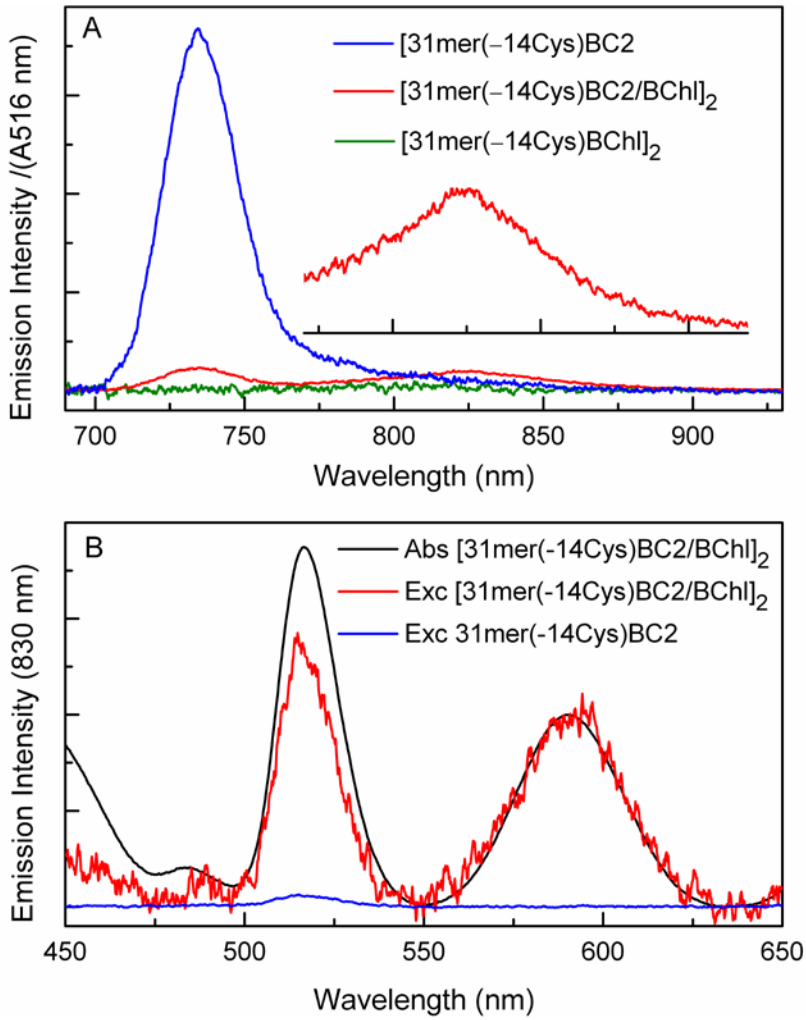

Figure 8. (A) Fluorescence spectra (λ_{exc} = 516 nm) for peptide 31mer(–14Cys)BC2 (blue) and B820-type complexes [31mer(–14Cys)BC2/BChl]$_2$ (red) and [31mer(–14Cys)BChl]$_2$ (green). The intensities are divided by the absorbance at λ_{exc}. The inset is a blowup of the NIR emission of [31mer(–14Cys)BC2/BChl]$_2$. (B) Fluorescence excitation spectrum (λ_{det} = 830 nm) of [31mer(–14Cys)BC2/BChl]$_2$ (red) normalized to the absorption spectrum at 590 nm (black). The excitation spectrum of peptide 31mer(–14Cys)BC2 (blue), scaled by the BC2 fluorescence yield relative to that in [31mer(–14Cys)BC2/BChl]$_2$.

A third estimate for Φ_{ENT} is provided by transient absorption measurements of the BC2* lifetime in the absence and presence of energy transfer. Figure 9A shows representative spectra (λ_{exc} = 512 nm) that contain combined **BC2** Q_y bleaching and stimulated emission. Figure 9B and the short-time inset show time profiles at 730 nm for biohybrid [31mer(−14Cys)BC2/BChl]$_2$ (red) and control peptide 31mer(−14Cys)BC2 (blue). The BC2* decay profile for the control peptide is well described by a single exponential with τ = 4 ns, similar to that obtained from fluorescence decay for this same peptide as well as for **BC2** in buffer solution by both techniques. For [31mer(−14Cys)BC2/BChl]$_2$, about 15% of BC2* decay also has $\tau \sim 4$ ns, which can be attributed to free 31mer(−14Cys)BC2 formed by dissociation of the complex.

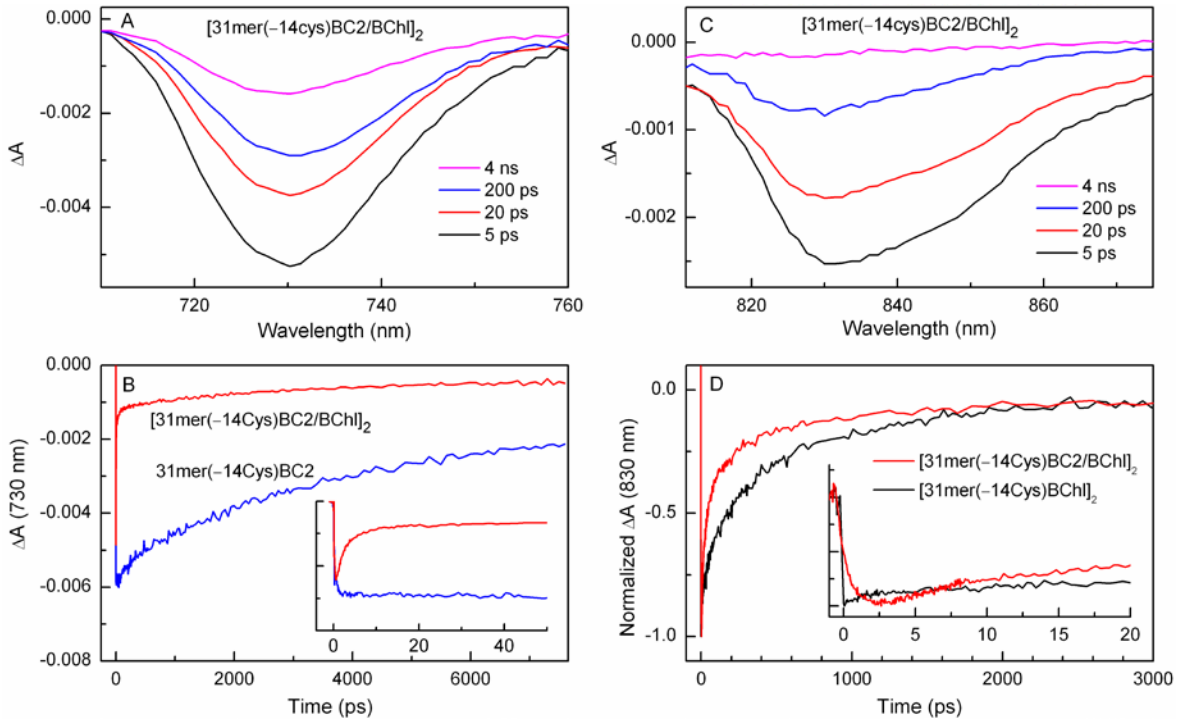

Figure 9. Time-resolved absorption spectra for [31mer(−14Cys)BC2/BChl]$_2$ in the Q_y bleach and stimulated emission for **BC2** (A) and B820 (C) and corresponding kinetic traces at 730 nm (B) and 830 nm (D) for [31mer(−14Cys)BC2/BChl]$_2$ (red), 31mer(−14Cys)BC2 (blue) using λ_{exc} = 512 nm. The kinetic trace in D for [31mer(−14Cys)BChl]$_2$ (black) utilizes λ_{exc} = 590 nm and λ_{det} = 830 nm.

Most of the BC2* decay occurs in <100 ps, with time constants (and relative fractions) of 3 ps (0.60) and 30 ps (0.25). The non-single-exponential BC2* decay in the biohybrid likely reflects more than one conformation of **BC2** with respect to B820 due to linker mobility. The rapid (<100 ps) decay compared to 4 ns in the control peptide indicates that **BC2** → B820 energy transfer in [31mer(−14Cys)BC2/BChl]$_2$ has $\Phi_{ENT} > 0.95$. This estimate together with 0.92 from **BC2** fluorescence quenching and 0.75 from excitation-spectrum analysis give a collective $\Phi_{ENT} = 0.9$.

Energy transfer from **BC2** to B820 produces B820* and associated B820 Q_y bleaching and B820* stimulated emission (Figure 9C). The B820* time profile for [31mer(−14Cys)BC2/BChl]$_2$ (Figure 9D and inset, red) shows an ~1 ps (non-instantaneous) rise followed by components of roughly 3, 30 and 600 ps. Although simple B820* rise and fall kinetics are not expected in the biohybrid because the BC2* decay in this system is multi-exponential (3 and 30 ps) and the inherent time evolution of B820* (obtained in [31mer(−14Cys) BChl]$_2$) is multi-exponential (3, 50 and 600 ps), the time profile contains recognizable characteristics. The B820* rise in [31mer(−14Cys)BC2/BChl]$_2$ (Figure 9D inset, red) occurs in ~1 ps, which is a manifestation of **BC2** → B820 energy transfer, compared to the instantaneous (<150 fs) response obtained upon direct excitation (λ_{exc} = 590 nm) of B820 in [31mer(−14Cys)BChl]$_2$ (Figure 9D, inset black). This rise and the subsequent ~3 ps component reflect the convolution of the early time decay components of BC2* decay and the inherent B820* time evolution, and similarly for the overlapping components over tens of picoseconds. The decay component on the time scale of hundreds of picoseconds in the biohybrid is similar to the component of the inherent decay of B820*. The presence of this longer-time phase for

$[31mer(-14Cys)BC2/BChl]_2$ suggests that B820* does not undergo significant (and unwanted) quenching by **BC2** following **BC2** $\rightarrow$ B820 energy transfer.

5. RR-containing B820-type complexes. Energy transfer from **RR** to B820 was probed in ββ-subunit complex $[31mer(-14Cys)RR/BChl]_2$. The analysis for most measurements parallels that for the **OGR**- and **BC2**-containing analogs. For example, excitation of **RR** at 526 nm leads to B820 fluorescence at 830 nm (Figure S-3A). This process results in quenching of the **RR** fluorescence at 580 nm compared to control peptide 31mer(−14Cys)RR, affording Φ_{ENT} = 0.70. Comparison of the normalized and integrated B820 fluorescence excitation spectrum and the absorption spectrum across the **RR** profile centered at 580 nm gives Φ_{ENT} = 0.55 (Figure S-3B). Time-resolved absorption studies (Figures S-4 and S-5) show that the RR* decay in $[31mer(-14Cys)RR/BChl]_2$, control peptide 31mer(−14Cys)RR and RR alone in solution all require fitting by three exponentials. The reduced amplitude-weighted lifetime for the biohybrid versus the control affords Φ_{ENT} = 0.60 (see Supporting Information). The three independent assays give consistent results and an average of Φ_{ENT} = 0.6.

D. Energy-Transfer Characteristics of Oligomeric (B850-type) Complexes.

1. Overview. The studies described above have focused on homodimeric B820-type complexes. We now turn to the study of oligomeric species, for which there are some advantageous properties exhibited by native systems. In the reconstitution of LH1 and LH2 with native polypeptides and BChl,[11,12] the bathochromically shifted Q_y absorption and circular dichroism spectra reproduce the values observed *in vivo* and therefore the reconstituted systems very likely have cyclic structures as observed in crystal structures and atomic-force microscopy of these complexes.[7-9] The native LH1 and LH2 complexes are oligomers of αβ-heterodimeric

B820 subunits in which there are specific stabilizing interactions between the two polypeptides in their N-terminal regions.[38] The polypeptides studied here do not have the full N-terminal portion of the native *Rb. sphaeroides* LH1 β-polypeptide and thus, would not form native oligomeric structures with a native α-polypeptide.[11,12] However, the homodimeric ββ-B820 species do associate when the detergent concentration is lowered below the CMC and form oligomeric species with bathochromically shifted Q_y bands compared to the B820 subunit form.[23,24,39] The extent of this bathochromic shift has been related to the number of interacting BChl *a* in the oligomeric species.[40] Whether the oligomers form rings of 8 or 9 subunits (16 or 18 BChl *a*) like LH2 when the Q_y maximum is near 850 nm, or whether smaller numbers of subunits are associated to form "arcs"[40] is not known at this time. The oligomeric forms of the ββ-homodimers are usually very stable at low temperature (at 0.66% octyl glucoside) or at room temperature when the octyl glucoside concentration is lowered to below the CMC (*e.g.*, 0.33%).

The biohybrids containing **OGR**, **RR**, and **BC1** form oligomers that have a substantially bathochromically shifted Q_y band (847, 845 and 844 nm; see Figures 5A and S-9 for the **OGR** and **BC1** complexes), whereas for **BC2** the absorption maximum shifts to between 830 and 835 nm; see Figure 5B). The bathochromic shift in the Q_y band simplifies photophysical studies compared to B820-type complexes due to (i) reduced overlap with the absorption and emission bands of free BChl *a* (absorbing at 780 nm) and (ii) a greater shift from the 800-nm light used to generate the continuum probe pulses in ultrafast absorption studies. In the following, results are presented concerning the oligomeric assemblies, first those containing B850 without a bioconjugated chromophore and then with attached **OGR** or **RR**. These B850-type complexes are stabilized at room temperature (by dilution of the detergent rather than chilling alone) to

facilitate comparisons with the results presented above on the B820-type analogs studied at the same temperature.

2. The BChl-a oligomer B850. The time-resolved absorption data for the B850 Q_y bleach and B850* stimulated emission decay in oligomer [31mer(−14Cys)BChl]$_n$ are given in Figure S-8. The characteristics are generally similar to those for B820 in the ββ-subunit complex [31mer(−14Cys)BChl]$_2$ (Figure 6) except for a bathochromic shift in the spectral features and more rapid overall decay to the ground state. The time-evolution for B850* (like B820*) requires fitting with (minimally) three exponentials, giving time constants of 6 ps, 40 ps and 500 ps. The 6-ps component for B850*, like the 3-ps component for B820*, is attributed to relaxation (vibrational, conformational, electronic) on the excited-state potential energy surface with little if any decay to the ground state. The 40-ps and 500-ps components (relative amplitudes of 0.7 and 0.3 at 850 nm) both contribute to the time evolution across the 800–900 nm region, and involve bleaching decay and thus deactivation of B850* to the ground state. Heterogeneity in the decay kinetics of B850* is analogous to that discussed above for B820*.

The chief finding is that B850* in oligomer complex [31mer(−14Cys)BChl]$_n$ decays more rapidly than B820* in ββ-subunit complex [31mer(−14Cys)BChl]$_2$. This observation is in keeping with the fluorescence yields of ~0.001 for B850 and ~0.01 for B820 determined here. Enhanced nonradiative deactivation driving diminished τ_S* and Φ_f for B850* versus B820* (and versus 3 ns and 0.17 for monomeric BChl *a*) could arise from (i) nuclear-electronic coupling as described above for B820* but now involving a greater number and perhaps more highly interacting BChl *a* molecules, (2) the energy-gap law for nonradiative decay[41] associated with the lower excited-state energy, and (3) greater effective clustering of the complexes leading to increased exciton annihilation.

3. OGR-containing oligomeric complexes. The results of photophysical measurements on [31mer(-14Cys)OGR/BChl]$_n$ are shown in Figure 10. The data can be compared directly with those described above for [31mer(–14Cys)OGR/BChl]$_2$ (Figure 7) and are analyzed similarly. The OGR* lifetime of 3.4 ns for [31mer(-14Cys)OGR/BChl]$_n$ versus 4.1 ns for 31mer(–14Cys)OGR gives $\Phi_{ENT} = 0.17$. The normalized fluorescence excitation and absorption spectra gives $\Phi_{ENT} = 0.22$. The average value is 0.2. The values of ββ-subunit complex determined above for the B820-type complex are 0.22 (fluorescence lifetimes) and 0.40 (excitation/absorption spectra) for an average of 0.3. Thus, the efficiency of energy transfer from **OGR** to B850 in the oligomeric biohybrid is comparable to or slightly lower than that from **OGR** to B820 in the ββ-subunit form.

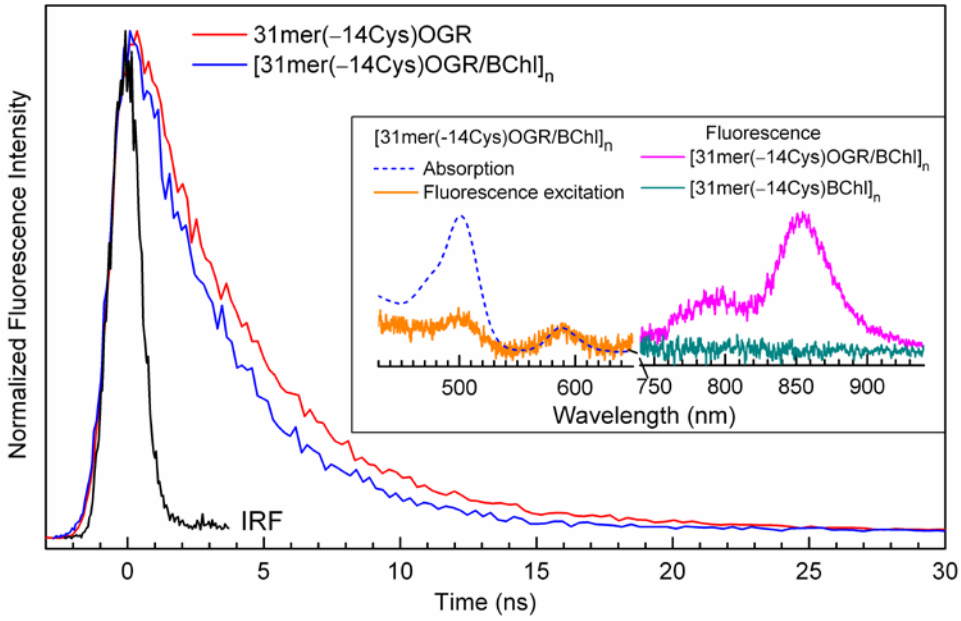

Figure 10. Photophysical data for OGR-containing controls and B850-type oligomeric complex. The main panel shows fluorescence decays (λ_{exc} = 499 nm, λ_{det} = 520 nm) for the control peptide (red) and the biohybrid (blue) along with the instrument response function (IRF; black). The insets show fluorescence, fluorescence excitation and absorption data as indicated and described in the text.

4. RR-containing oligomeric complexes. Photophysical studies were performed on **RR**-containing oligomeric complexes and controls (Figures S-6 and S-7) that are analogous to those described above for the **RR**-containing ββ-subunit complexes (Figures S-3 and S-5). The reduction of **RR** fluorescence in $[31mer(-14Cys)RR/BChl]_n$ versus 31mer(-14Cys)RR gives $\Phi_{ENT} = 0.90$. The normalized fluorescence-excitation and absorption spectra give $\Phi_{ENT} = 0.58$. Time-resolved absorption studies afford $\Phi_{ENT} = 0.93$ (see Supporting Information for analysis). The three measurements afford an average value of $\Phi_{ENT} \sim 0.8$ for **RR** $\rightarrow$ B850 energy transfer in oligomeric assembly $[31mer(-14Cys)RR/BChl]_n$. This result can be compared with the average value of $\Phi_{ENT} = 0.6$ for **RR** $\rightarrow$ B820 energy transfer in ββ-subunit complex $[31mer(-14Cys)RR/BChl]_2$. Collectively, the results indicate that the efficiency of energy transfer is comparable to or somewhat greater in the oligomeric assembly than in the subunit complex.

5. BC1-containing oligomeric complexes. Oligomeric complexes containing **BC1** are very stable at room temperature even with the detergent concentration still slightly above the CMC and heating (e.g., at 35 °C) is required for conversion to the subunit form (see Figure S-9 for absorption spectra). Thus, studies on these systems focused on oligomeric complexes $[31mer(-14Cys)BC1/BChl]_n$. Measurements similar to those described above were used to determine the yield of **BC1** $\rightarrow$ B850 energy transfer, which give values of 0.87 from the **BC1** fluorescence-intensity quenching (Figure S-10A), 0.79 from **BC1** fluorescence excitation versus absorption spectra (Figure S-10B), and 0.94 from BC1* decay kinetics in the oligomer versus the peptide control. The average value is $\Phi_{ENT} = 0.9$. Following excitation of **BC1**, B850 bleaching and decay is observed (Figure S-11). Thus, oligomeric complexes based on the synthetic

bacteriochlorins combine strong NIR absorption and a high-energy transfer efficiency to the BChl-*a* acceptor complex.

E. Comparison of the Energy Transfer Characteristics of the Various Biohybrids

All of the ββ-subunit complexes exhibit energy transfer from the synthetic chromophore to the native-like BChl-*a* dimer B820. The energy-transfer efficiencies (Φ_{ENT} ± 0.1) for biohybrids [31mer(−14Cys)X/BChl]$_2$ increase in the following order for tethered chromophore X: **OGR** (0.3) < **RR** (0.6) < **BC2** (0.9). Similarly, the energy-transfer efficiencies observed in the oligomeric assemblies [31mer(−14Cys)X/BChl]$_n$ investigated increase in the order **OGR** (0.2) < **RR** (0.8) < **BC1** (0.9). The latter results show that the energy-transfer efficiencies in the oligomeric architectures are comparable to those in the subunit complexes. Additionally, Φ_{ENT} increases from 0.3 for **OGR** at the −14 position in [31mer(−14Cys)OGR/BChl]$_2$ to 0.8 for **OGR** at the −6 position in [31mer(−6Cys)OGR/BChl]$_2$.

These trends in the measured Φ_{ENT} values are consistent with a Förster through-space mechanism for energy transfer. Calculated Φ_{ENT} values obtained using PhotochemCad[42] are given for a range of distances in Table 1. Inspection of the calculated values using a 40 Å donor-acceptor center-to-center distance for the sake of discussion, shows that the trend in calculated Φ_{ENT} for the series of chromophores at the −14 position reproduces the trend in measured values on the basis of the following parameters: (i) spectral overlap (J) of the chromophore (donor) fluorescence with the B820 (acceptor) absorption, and (ii) the chromophore radiative rate constant $k_{rad} = \Phi_f \bullet \tau_S$, which is driven largely by the differences in Φ_f. A greater Φ_{ENT} value for **OGR** at the −6 versus −14 positions is expected due to the shorter distance from the B820 energy acceptor (e.g., 25 versus 40 Å).

Table 1. Förster Energy-Transfer Parameters for B820-Type Biohybrid Complexes[a]

Biohybrid System	donor Φ_f	donor τ_S (ns)	$(k_{rad})^{-1}$ (ns)	J $x10^{-13}$ (cm^6)	R (Å)	Φ_{ENT}
$[31mer(-14Cys)BC2/BChl]_2$	0.19	4.2	22	13	50	0.83
					40	0.95
					30	0.99
					20	>0.99
$[31mer(-14Cys)BC1/BChl]_2$	0.10	4.7	47	9.4	50	0.65
					40	0.88
					30	0.98
					20	0.99
$[31mer(-14Cys)RR/BChl]_2$	0.14	2.4	17	4.4	50	0.55
					40	0.82
					30	0.96
					20	0.99
$[31mer(-14Cys)OGR/BChl]_2$	0.058	4.1	71	1.5	50	0.15
					40	0.40
					30	0.79
					20	0.98
$[31mer(-6Cys)OGR/BChl]_2$	0.058	4.1	71	1.5	25	0.92

[a]The energy-transfer efficiency (Φ_{ENT}) for each of the biohybrid ββ-subunit complexes $[31mer(-14Cys)X/BChl]_2$ (X = **OGR**, **RR**, **BC1**, **BC2**) and $[31mer(-6Cys)OGR/BChl]_2$ was calculated using PhotochemCad.[42] The input parameters for the energy are the fluorescence quantum yield (Φ_f) and emission spectrum of the control peptide 31mer(−14Cys)X that contain chromophores X. The input parameters for the energy acceptor include the absorption spectrum of the BChl-*a* dimer B820 in the synthetic chromophore-free complex $[31mer(-14Cys)BChl]_2$. The calculations did not make use of the donor singlet excited-state lifetime (τ_S) in the absence of the acceptor, which was used only to calculate the radiative rate constant $k_{rad} = \Phi_f/\tau_S$ listed in the Table. Because k_{rad} reflects the optical transition dipole-strength of the donor, it is a useful parameter in gauging the relative effectiveness of the four chromophores in the Förster through-space dipole-dipole mechanism. See the Supporting Information for further information.

The effective chromophore-B820 distance is uncertain due to factors that include the flexibility (and nature) of the linker. A distance of 35-40 Å would be consistent with a fully extended 10 Å linker and the chromophore centered at 270° from the peptide axis (with 0° pointing from the –14Cys to the 0His site). The calculations also assume a dynamically averaged orientation factor of 1.125, which may not be correct and could differ for the various chromophores (and linkers). Thus, the calculations are not meant to serve as a structural probe. Collectively, the consistency of the trends in measured and calculated values is good and provides additional foundation for engineering the chromophores and assemblies to provide efficient energy transfer and solar coverage.

IV. Conclusions and Outlook

The finding of rapid and highly efficient energy transfer (Φ_{ENT} ~90%) from tethered bacteriochlorins **BC1** and **BC2** to the native-like BChl-*a* acceptor complex, and the good yields for accessory chromophores (**OGR** and **RR**), augurs well for the use of such constructs as a foundation for producing more elaborate biohybrid light-harvesting architectures. For example, the simple 31mer ββ-subunits of the type studied here could be employed in liposomes for improved stability, or the full-length α and β polypeptides could be engineered to incorporate synthetic chromophores. The co-recognition of the α and β polypeptides to form αβ-subunits and assembly of the latter affords highly stable native-like cyclic oligomeric architectures in which the Q_y band of the BChl-*a* acceptor complex is at ~870 nm. This wavelength is bathochromically shifted even farther versus that of the ββ-subunit complexes (~820 nm) or the oligomers assembled from the 31-mer β polypeptide (~850 nm). Such stable oligomeric complexes provide a platform for further manipulations to achieve long-range directed energy

flow, including patterning on surfaces as has been achieved with native antenna.[43] For biohybrid designs, dozens of stable, synthetic hydroporphyrins (chlorins, bacteriochlorins, and analogs) that together have absorption and fluorescence bands spaced in fine increments spanning the orange-red into the NIR regions (610 nm to 820 nm) are now available[15-19] and can be adapted for bioconjugation, as exemplified for **BC1** and **BC2** in Figure 4. This palette of chromophores enables the construction of a variety of oligomeric multi-subunit biohybrid architectures with various subunits housing distinct (bacterio)chlorins with complementary absorption spectra. Such constructs rely on the natural light-harvesting antenna protein for the architectural scaffold. While our chief focus has concerned use of bioconjugatable bacteriochlorins given their attractive spectral and photophysical features, a very broad range of pigments should be amenable to this biohybrid approach. In summary, the ability to retain the superb features of native photosynthetic antenna complexes and achieve wide tunability in solar coverage via incorporation of synthetic chromophores, including the recently available NIR-absorbing bacteriochlorins, together may open new horizons in artificial photosynthesis.

Acknowledgement

This research was carried out as part of the Photosynthetic Antenna Research Center (PARC), an Energy Frontier Research Center funded by the U.S. Department of Energy, Office of Science, Office of Basic Energy Sciences under Award Number DE-SC0001035.

Supporting Information Available: Additional experimental procedures; analysis of data for RR-containing constructs; parameters for Förster calculations; and additional data. This material is available free of charge via the Internet at http://pubs.acs.org.

References

(1) Blankenship, R. E.; et al. *Science* **2011**, *332*, 805–809.

(2) Gabrielsen, M.; Gardiner, A. T.; Cogdell, R. J. In *The Purple Phototrophic Bacteria*; Hunter, C. N.; Daldal, F.; Thurnauer, M. C.; Beatty, J. T., Eds.; Springer: Dordrecht, The Netherlands; Advances in Photosynthesis and Respiration; 2009, pp 135–153.

(3) Bullough, P. A.; Qian, P.; Hunter, C. N. In *The Purple Phototrophic Bacteria*; Hunter, C. N.; Daldal, F.; Thurnauer, M. C.; Beatty, J. T., Eds.; Springer: Dordrecht, The Netherlands; Advances in Photosynthesis and Respiration; 2009, pp 155–179.

(4) (a) Harvey, P. D.; Stern, C.; Guilard, R. In *Handbook of Porphyrin Science*; Kadish, K. M.; Smith, K. M., Guilard, R., Eds.; World Scientific Publishing Co.: Singapore; Vol. 11, 2011, pp 1–179. (b) Aratani, N.; Osuka, A. In *Handbook of Porphyrin Science;* Kadish, K. M.; Smith, K. M., Guilard, R., Eds.; World Scientific Publishing Co.: Singapore; Vol. 1, 2010, pp 1–132. (c) Moore, T. A.; Moore, A. L.; Gust, D. *Phil. Trans. R. Soc. Lond. B* **2002**, *357*, 1481–1498. (d) Wasielewski, M. R. In *Chlorophylls*; Scheer, H. Ed.; CRC Press, Boca Raton, FL, USA, 1991, pp 269–286.

(5) (a) Noy, D.; Moser, C. C.; Dutton, P. L. In *Chlorophylls and Bacteriochlorophylls: Biochemistry, Biophysics, Functions and Applications*; Grimm, B.; Porra, R. J.; Rüdiger, W.; Scheer, H., Eds.; Springer: Dordrecht, The Netherlands, 2006, pp 349–363. (b) Nango, M. *Ibid.*, pp 365–373.

(6) Lindsey, J. S.; Mass, O.; Chen, C.-Y. *New J. Chem.* **2011**, *35*, 511–516.

(7) Papiz, M. Z.; Prince, S. M.; Howard, T.; Cogdell, R. J.; Isaacs, N. W. *J. Mol. Biol.* **2003**, *326*, 1523–1538.

(8) Roszak, A. W.; Howard, T. D.; Southall, J.; Gardiner, A. T.; Law, C. J.; Isaacs, N. W.; Cogdell, R. J. *Science* **2003**, *302*, 1969–1972.

(9) Koepke, J.; Hu, X.; Muenke, C.; Schulten, K.; Michel, H. *Structure* **1996**, *4*, 581–597.

(10) (a) Sturgis, J. N.; Tucker, J. D.; Olsen, J. D.; Hunter, C. N.; Niederman, R. A. *Biochemistry* **2009**, *48*, 3679–3698. (b) Sener, M. K.; Olsen, J. D.; Hunter, C. N.; Schulten, K. *Proc. Natl. Acad. Sci. USA* **2007**, *104*, 15723–15728.

(11) Loach, P. A.; Parkes-Loach, P. S. In *Anoxygenic Photosynthetic Bacteria*; Blankenship, R. E.; Madigan, M. T.; Bauer, C. E., Eds.; Kluwer Academic Publishers: Boston, MA, 1995, pp 437–471.

(12) Loach, P. A.; Parkes-Loach, P. S. In *The Purple Phototrophic Bacteria*; Hunter, C. N.; Daldal, F.; Thurnauer, M. C.; Beatty, J. T., Eds.; Springer: Dordrecht, The Netherlands; Advances in Photosynthesis and Respiration; 2009, pp 181–198.

(13) Law, C. J.; Chen, J.; Parkes-Loach, P. S.; Loach, P. A. *Photosynth. Res.* **2003**, *75*, 193–210.

(14) Paulsen, H. In *Chlorophylls and Bacteriochlorophylls: Biochemistry, Biophysics, Functions and Applications*; Grimm, B.; Porra, R. J.; Rüdiger, W.; Scheer, H., Eds.; Springer: Dordrecht, The Netherlands; 2006, pp 375–385.

(15) Yang, E.; Kirmaier, C.; Krayer, M.; Taniguchi, M.; Kim, H.-J.; Diers, J. R.; Bocian, D. F.; Lindsey, J. S.; Holten, D. *J. Phys. Chem. B* **2011**, *115*, 10801–10816.

(16) Krayer, M.; Yang, E.; Diers, J. R.; Bocian, D. F.; Holten, D.; Lindsey, J. S. *New J. Chem.* **2011**, *35*, 587–601.

(17) Taniguchi, M.; Cramer, D. L.; Bhise, A. D.; Kee, H. L.; Bocian, D. F.; Holten, D.; Lindsey, J. S. *New J. Chem.* **2008**, *32*, 947–958.

(18) Kee, H. L.; Kirmaier, C.; Tang, Q.; Diers, J. R.; Muthiah, C.; Taniguchi, M.; Laha, J. K.; Ptaszek, M.; Lindsey, J. S.; Bocian, D. F.; Holten, D. *Photochem. Photobiol.* **2007**, *83*, 1125–1143.

(19) Kim, H.-J.; Lindsey, J. S. *J. Org. Chem.* **2005**, *70*, 5475–5486.

(20) Wagner, R. W.; Lindsey, J. S. *Pure Appl. Chem.* **1996**, *68*, 1373–1380.

(21) Sutton, J. M.; Clarke, O. J.; Fernandez, N.; Boyle, R. W. *Bioconjugate Chem.* **2002**, *13*, 249–263.

(22) Mironov, A. F.; Grin, M. A. *J. Porphyrins Phthalocyanines* **2008**, *12*, 1163–1172.

(23) Meadows, K. A.; Parkes-Loach, P. S.; Kehoe, J. W.; Loach P. A. *Biochemistry* **1998**, *37*, 3411–3417.

(24) Meadows, K. A.; Iida, K.; Tsuda, K.; Recchia, P. A.; Heller, B. A.; Antonio, B.; Nango, M.; Loach, P. A. *Biochemistry* **1995**, *34*, 1559–1574.

(25) Parkes-Loach, P. S.; Sprinkle, J. R.; Loach, P. A. *Biochemistry* **1988**, *27*, 2718–2727.

(26) Wang, Z.-Y.; Gokan, K.; Kobayashi, M.; Nozawa, T. *J. Mol. Biol.* **2005**, *347*, 465–477.

(27) Sorgen, P. L.; Cahill, S. M.; Krueger-Koplin, R. D.; Krueger-Koplin, S. T.; Schenck, C. C.; Girvin, M. E. *Biochemistry* **2002**, *41*, 31–41.

(28) Conroy, M. J.; Westerhuis, W. H. J.; Parkes-Loach, P. S.; Loach, P. A.; Hunter, C. N.; Williamson, M. P. *J. Mol. Biol.* **2000**, *298*, 83–94.

(29) Robert, B. In *The Purple Phototrophic Bacteria*; Hunter, C. N.; Daldal, F.; Thurnauer, M. C.; Beatty, J. T., Eds.; Springer: Dordrecht, The Netherlands; Advances in Photosynthesis and Respiration; 2009, pp 199–212.

(30) Sturgis, J. N.; Olsen, J. D.; Robert, B.; Hunter, C. N. *Biochemistry* **1997**, *36*, 2772–2778.

(31) van Mourik, F.; van der Oord, C. J. R.; Visscher, K. J.; Parkes-Loach, P. S.; Loach, P. A.; Visschers, R. W.; van Grondelle, R. *Biochim. Biophys. Acta* **1991**, *1059*, 111–119.

(32) Visschers, R. W.; Chang, M. C.; van Mourik, F.; Parkes-Loach, P. S.; Heller, B. A.; Loach, P. A.; van Grondelle, R. *Biochemistry* **1991**, *30*, 5734–5742.

(33) Chang, M. C.; Callahan, P. M.; Parkes-Loach, P. S.; Cotton, T. M.; Loach, P. A. *Biochemistry* **1990**, *29*, 421–429.

(34) (a) Pflock, T.; Dezi, M.; Venturoli, G.; Cogdell, R. J.; Köhler, J.; Oellerich, S. *Photosynth. Res.* **2008**, *95*, 291–298. (b) Shubert, A.; Stenstam, A.; Beenken, W. J. D.; Herek, J. L.; Cogdell, R. J.; Pullerits, T.; Sundström, V. *Biophys. J.* **2004**, *86*, 2363–2373.

(c) Hunter, C. N.; Bergström, H.; van Grondelle, R.; Sundström, V. *Biochemistry* **1990**, *29*, 3203–3207.

(35) (a) Niedzwiedzki, D. M.; Blankenship, R. E. *Photosynth. Res.* **2010**, *106*, 227–238. (b) Musewald, C.; Hartwich, G.; Pöllinger-Dammer, F.; Lossau, H.; Scheer, H.; Michel-Beyerle, M. E. *J. Phys. Chem B* **1998** *102*, 8336–8342. (c) Becker, M.; Nagarajan, V.; Parson, W. W. *J. Am. Chem. Soc.* **1991** *113*, 6840–6848. (d) Losev, A. P.; Sagun, E. I.; Kochubeev, G. A.; Nichiporovich, I. N. *J. Appl. Spectrosc.* **1986**, *45*, 798–803. (e) Connolly, J. S.; Samuel, E. B.; Janzen, A. F. *Photochem. Photobiol.* **1982**, *36*, 565–574.

(36) Chuang, J. I.; Boxer, S. G.; Holten, D.; Kirmaier, C. *J. Phys. Chem. B* **2008**, *112*, 5487–5499.

(37) McDowell, L. M.; Kirmaier, C.; Holten, D. *Biochim. Biophys. Acta* **1990**, *1020*, 239–246.

(38) Parkes-Loach, P. S.; Majeed, A. P.; Law, C. J.; Loach, P. A. *Biochemistry* **2004**, *43,* 7003–7016.

(39) Kehoe, J. W.; Meadows, K. A.; Parkes-Loach, P. S.; Loach, P. A. *Biochemistry* **1998**, *37*, 3418–3428.

(40) Westerhuis, W. H. J.; Sturgis, J. N.; Ratcliffe, E. C.; Hunter, C. N.; Niederman, R. A. *Biochemistry* **2002**, *41*, 8698–8707.

(41) Birks, J. B. *Photophysics of Aromatic Molecules*, Wiley-Interscience: London, 1970, pp 142–192.

(42) Dixon, J. M.; Taniguchi, M.; Lindsey, J. S. *Photochem. Photobiol.* **2005**, *81*, 212–213.

(43) (a) Iida, K.; Dewa, T.; Nango, M. In *The Purple Phototrophic Bacteria*; Hunter, C. N.; Daldal, F.; Thurnauer, M. C.; Beatty, J. T., Eds.; Springer: Dordrecht, The Netherlands; Advances in Photosynthesis and Respiration; 2009, pp 861–875. (b) Escalante, M.; Zhao Y.; Ludden M. J. W.; Vermeij, R.; Olsen, J. D.; Berenschot, E.; Hunter, C. N.; Huskens, J.; Subramaniam, V.; Otto, C. *J. Am. Chem. Soc.* **2008**, *130*, 8892–8893.

Supporting Information

Additional Experimental Procedures

Preparation of Polypeptides with Covalently Attached Chromophores. The procedure followed was essentially that recommended by Invitrogen:Molecular Probes (Handbook of Fluorescent Probes and Research Products 2001) and is summarized here for conjugation of **BC2** to the 31mer(–14Cys) polypeptide. A sample of the polypeptide (3.0 mg) was dissolved in 230 μL of *N,N*-dimethylformamide (DMF), and 70 μL of 100 mM Tris buffer (pH 7.3) was added with stirring. A sample of **BC2** (2.0 mg) was dissolved in 230 μL of DMF, and 70 μL of 100 mM Tris buffer (pH 7.3) was added. This latter solution was slowly added to the former with stirring and under a gentle flow of Argon. The sample was stoppered and stirred for 2 h at room temperature in the dark. The reaction mixture was then dried under vacuum and stored at –20 °C. A portion of the dried material was dissolved in 35 μL of hexafluoroacetone trihydrate (HFA) to which was added 35 μL of 1:1 HPLC A:B solvent, and the sample injected into a Waters Breeze HPLC system with a Rheodyne manual injector and a Waters 2487 UV detector. Perkin-Elmer HCODS C18 columns (150 x 4.6 mm) were used for all purifications. The HPLC solvent system consisted of (A) 0.1% trifluoroacetic acid (TFA) as the aqueous solvent and (B) 0.1 % TFA in 2:1 (v/v) acetonitrile/2-propanol as the organic solvent.[24] Typical results are shown in Figure S-1. On the basis of extinction coefficients for **BC2** at 730 nm (120,000 $M^{-1}cm^{-1}$ at the 730-nm Q_y maximum) and for the 31mer(–14Cys) at 289 nm (10,200 $M^{-1}cm^{-1}$), the material in the peak at 60 min exhibited a 1:1 ratio of **BC2**:polypeptide.

FTIR spectroscopy. The FTIR spectra of the peptides were collected at room temperature on solid films deposited on an Au substrate (200 nm Au atop a 20 nm Cr adhesion layer on a Si substrate). The films were prepared by depositing 50 μL of the peptide in solution

(either DMF or DMSO/CH_2Cl_2 (1:1)) onto the substrate contained in a sealed vial under Ar. The deposited droplet was then allowed to sit on the substrate for times varying from 10 min to 15 h after which the substrate was washed three times with CH_2Cl_2 and dried under a stream of Ar.

The FTIR spectrometer was a Bruker Tensor 27 equipped with a Harrick Scientific Ge attenuated total reflection accessory (GATR™, 65° incidence angle relative to the surface normal). The substrates were placed in contact with the flat surface of a semispherical Ge crystal that serves as the optical element. The IR spectra were collected with *p*-polarized light using a liquid-nitrogen cooled medium-bandwidth (600–4000 cm^{-1}) MCT detector, averaging over 256 scans; the spectral resolution was 4 cm^{-1}. The spectra of the films were referenced against a bare Au substrate. The Ge crystal was cleaned with neat 2-butanone before every experiment, and the GATR™ accessory was purged with dry N_2 during data acquisition.

Ellipsometry. Ellipsometric measurements on the peptide films (prepared as described above) were carried out on a Jobin-Yvon Uvisel Model M200 phase modulated bench top unit using a Xenon lamp as the light source (maximum intensity at 450 nm). The incident angle was fixed at 70° and the wavelength was changed from 300 nm to 800 nm in 5-nm increments. The ellipsometric parameters were fitted using the Levenberg-Marquardt regression method. The film thickness was calculated using a modified polyimide model wherein the values of the refractive index ranged from 1.45 to 1.50.[S1]

Static and time-resolved optical spectroscopy. Static absorption measurements employed a Varian Cary 50 or 100 or Shimadzu UV-1800 spectrometer. Static fluorescence measurements employed a Spex Fluorolog Tau 2 or PTI Quantamaster 40 spectrofluorometer. Fluorescence lifetimes were obtained via decay measurements using a Photon Technology International LaserStrobe TM-3, composed of a GL-3300 nitrogen laser with a GL-302 dye laser

unit and time-correlate-single-photon-counting detection. The apparatus has an approximately Gaussian instrument response function with a full-width-at-half-maximum of ~1 ns. Excitation pulses were provided by the nitrogen-pumped dye laser (350-650 nm). Static emission measurements employed 0.2-nm data intervals and typical monochromator bandwidths of 2–4 nm. Most measurements (500 nm to ≥1100 nm) utilized a setup consisting of an InGaAs detector with lock-in detection and excitation light chopped at 30 Hz; the detection monochromator bandwidth was increased to up to 8 nm for some measurements of weak B820 NIR emission. Some experiments (450–850 nm) utilized a setup containing a Hamamatsu R928 photomultiplier tube. For both setups, emission spectra were corrected for detection-system spectral response. The fluorescence yield determinations, depending on the absorption and emission wavelengths involved, employed a number of different standards whose yields were cross-checked with respect to each other. These standards were (1) free base *meso*-tetraphenylporphyrin (**FbTPP**) in nondegassed toluene, for which $\Phi_f = 0.070$ was established with respect to the zinc chelate **ZnTPP** in nondegassed toluene ($\Phi_f = 0.030$),[S2] consistent with prior results on **FbTPP**,[S3] and (2) 8,8,18,18-tetramethylbacteriochlorin[15] in Argon-purged toluene, for which $\Phi_f = 0.14$ was established with respect to **FbTPP** and chlorophyll *a* (**Chl *a***) in deoxygenated benzene[S4] or toluene[S5] (both with $\Phi_f = 0.325$). Measurements of fluorescence spectra, fluorescence excitation spectra, fluorescence quantum yields, and fluorescence lifetimes employed samples having an absorbance (A) ≤ 0.1 at the excitation wavelength(s). Under these conditions, the pertinent regions (e.g., 450-650 nm) of the absorption and absorptance spectra have the same shapes; the latter spectrum is the most relevant for quantitative comparisons with the excitation spectra to estimate the energy-transfer efficiencies in the biohybrid complexes. Samples of **OGR** and **RR** (in 1:1 DMF/Tris-buffer and phosphate buffer, respectively) and **BC1**

and **BC2** (in toluene) were typically purged (bubbled) with argon in septum-stoppered cuvettes. Samples of the peptide-bound chromophores and biohybrid complexes in detergent solutions were typically purged by passing Argon over the stirred solution.

Time-resolved pump-probe absorption experiments were carried out using a Helios femtosecond transient absorption spectrometer (Ultrafast Systems) coupled to a femtosecond laser system (Newport/Spectra-Physics). The one-box Solstice amplified ultrafast laser system consists of a Mai-Tai femtosecond oscillator whose output goes to a Spitfire Pro XP regenerative amplifier that is pumped by an Empower diode-pumped solid state pulsed green laser. The amplifier produces 800 nm pulses (~3.5 mJ, ~90 fs) at 1 kHz. The output beam is split into two and used to generate (i) the pump beam (90%) in a Topas-C optical parametric amplifier (Light Conversion, Lithuania) and (ii) probe pulses (10%) for the Helios transient-absorption spectrometer. The pump (excitation) pulses pass through a depolarizer to provide isotropic excitation of the sample and avoid pump-probe polarization effects. Individual ΔA spectra are acquired using excitation light chopped at 0.5 kHz (to provide alternate accumulations of the probe light with and without excitation) and averaged over 1-5 s (typically 2 s). Final ΔA spectra represent the average of 1000 such individual spectra. For the experiments reported here, the excitation pulses (typically of energy 2 μJ/pulse) were adjusted to have a spot diameter of 1 mm. For some experiments, studies of the signal characteristics as a function of excitation-pulse energies up to 6 μJ/pulse were examined to insure that multiphoton effects were avoided at the lower energies normally used.

The samples were typically excited near the peaks of the main absorption features shown in the spectra below and in the paper. For example, for bacteriochlorin **BC2**, and the peptide or biohybrids containing that chromophore, experiments were performed that utilized excitation in

either the Q_x band (~515 nm) or the Q_y band (~720 nm). Samples were contained in 2-mm or 1-cm path cuvettes and were mixed continuously using a magnetic micro-stirrer to minimize photo-degradation. Control samples consisting of a chromophore-attached peptide or biohybrid antenna complex typically had an absorbance of ≤0.15 in the main absorbance feature.

Studies of RR.

Time-resolved absorption data for **RR** in solution (Figure S-4) and biohybrid $[31mer(-14Cys)RR/BChl]_2$ and control peptide 31mer(−14Cys)RR (Figure S-5) were obtained using a 0.1 ps flash at 526 nm. The data in Figures S-4, S-5A and S-5B probe decay of RR* in the region of **RR** bleaching and RR* stimulated emission at 580 nm. The RR* decay for **RR** in buffer solution (Figure S-4) is clearly not single exponential and is described well by a dual exponential with components of 215 ps (0.24) and 1510 ps (0.76) or a triple exponential with time constants of 1 ps (0.07), 260 ps (0.24), and 1570 ps (0.69). Similarly, in Figure S-5B, a fit to the decay profile (following the instrument-limited rise) for $[31mer(-14Cys)RR/BChl]_2$ (black line) requires a triple exponential with time constants (and relative fractions) of 2.1 ps (0.41), 43 ps (0.31), and 1355 ps (0.28). The decay profile for control peptide 31mer(−14Cys)RR (red line) is also triple exponential with components of 4.1 ps (0.25), 78 ps (0.20), and 1860 ps (0.52).

The multi-phasic decay of RR* even when the dye is not appended to a peptide indicates that more than one form (conformation, etc.) is present in solution. The forms may be modified in a number of properties when **RR** is attached to the peptide in 31mer(−14Cys)RR. For example, RR* may be sensitive to different environments sampled by motion of the chromophore with respect to the peptide, some of which could slightly lengthen a lifetime component or lead to quenching interactions with amino acids. Some of the same locales would

be sampled by **RR** in [31mer(−14Cys)RR/BChl]$_2$, in which energy transfer from **RR** to B820 provides an additional avenue for RR* decay for each form. Energy transfer no doubt underlies the reduced time constants and increased weightings of the middle and short components for [31mer(−14Cys)RR/BChl]$_2$ versus 31mer(−14Cys)RR. The amplitude-weighted decay time constant for [31mer(−14Cys)RR/BChl]$_2$ is (2.1 ps)(0.41)+(43 ps)(0.31)+(1355 ps)(0.28) = 394 ps while that for 31mer(−14Cys)RR is (4.1 ps)(0.25)+(78 ps)(0.20)+(1860 ps)(0.52) = 984 ps. These values afford Φ_{ENT} = 1 − (394 ps / 984 ps) = 0.60.

Additional support for energy transfer in [31mer(−14Cys)RR/BChl]$_2$ is derived from the data in Figures S5-C and D. Figure S-5C shows that following excitation of **RR** (λ_{exc} = 535 nm) energy transfer from RR* to B820 produces B820* and thus B820 Q_y bleaching and stimulated emission. Figure S-5D shows a clear lag/rise in the development of the B820 bleaching for [31mer(−14Cys)RR/BChl]$_2$ (black) compared to the instrument-limited rise observed for direct excitation (λ_{exc} = 590 nm) of B820 in [31mer(−14Cys)BChl]$_2$ (blue). The development of B820* in the biohybrid has a time constant of ~5 ps, although good fits are obtained with a rise time in the range 3–8 ps. This lag can be associated with the fast components to the RR* decay (and thus energy transfer) convolved with the fast components of the B820* dynamics expected from the time profile for B820* in the absence of **RR** in [31mer(−14Cys)BChl]$_2$, which minimally includes 3 ps relaxation and 50 ps decay components (Figure S5-D). The slower phase(s) of B820* decay extending to hundreds of picoseconds for [31mer(−14Cys)RR/BChl]$_2$ are also consistent with the inherent 600 ps B820* decay component observed in [31mer(−14Cys)BChl]$_2$. Thus, the overall B820* time profile in the biohybrid complex is reasonably understood considering the inherent multi-component decays of the donor and acceptor even in the absence of each other.

Analogous time-resolved absorption studies of the RR* decay profile via Q_y bleaching were performed on oligomeric subunit complex [31mer(-14Cys)RR/BChl]$_n$ (Figure S-7). The RR* decay time constants (and relative amplitudes) of 1.3 ps (0.65), 20 ps (0.24), and 583 ps (0.11) for oligomer [31mer(-14Cys)RR/BChl]$_n$ and 4.1 ps (0.25), 78 ps (0.23), and 1860 ps (0.52) for control peptide 31mer(−14Cys)RR; comparison of the amplitude-weighted average lifetimes gives $\Phi_{ENT} = 100[1 - (70 \text{ ps} / 984 \text{ ps})] = 0.93$.

Time-resolved NIR absorption measurements on the B850 Q_y bleaching of [31mer(−14Cys)RR/BChl]$_n$ (Figure S-7D) show a non-instrument limited ~1 ps rise consistent with the 1.3 ps component of RR* decay followed by decay components of 10 and 40 ps of comparable amplitude and a minor (10%) phase lasting several hundred picoseconds.. The latter are consistent with a convolution of the slower component of RR* decay and the inherent B850* decay components measured in control oligomer [31mer(−14Cys)BChl]$_n$ (Figure 8).

Förster Calculations

The energy-transfer efficiency (Φ_{ENT}) for each of the biohybrid ββ-subunit complexes [31mer(−14Cys)X/BChl]$_2$ (X = **OGR**, **RR**, **BC1**, **BC2**) and [31mer(−6Cys)OGR/BChl]$_2$ was calculated using PhotochemCad.[42] The calculations use the "R_0 method" in which R_0 is the distance at when the efficiency is 50%. The expression for the energy-transfer efficiency is $\Phi_{ENT} = R_0^6 / (R^6 + R_0^6)$, where $R_0^6 = (8.8 \times 10^{23}) \kappa^2 \Phi_f J n^{-4}$. (See the PhotochemCad documentation for the development of the expression.) Here, n is solvent refractive index; κ^2 is the orientation term for which the dynamically averaged value of 1.125 was used; R is the center to center (in Å) distance of the energy-donor chromophore and the BChl-*a* acceptor complex B820; Φ_f is the fluorescence quantum yield of the chromophore in the absence of the acceptor (given in Table 1

of the manuscript); J is the spectral overlap integral and is calculated using the emission spectrum of the control peptide 31mer(−14Cys)X that contains chromophore X and the absorption spectrum of the BChl-*a* dimer B820 in the synthetic chromophore-free complex $[31mer(-14Cys)BChl]_2$, for which the molar absorptivity at 820 nm is ε = 172,000 $M^{-1}cm^{-1}$. Note that the equation used in the calculation does not use the lifetime of the donor chromophore in either the absence or presence of the acceptor. This is advantageous if one does not know the lifetime, or when the excited-state decay profile is multi-exponential, as it is for **RR** even in solution and not attached to the 31mer peptide (both in the absence of acceptor).

References

(1) Blankenship, R. E.; Tiede, D. M.; Barber, J.; Brudvig, G. W.; Fleming, G.; Ghirardi, M.; Gunner, M. R.; Junge, W.; Kramer, D. M.; Melis, A.; Moore, T. A.; Moser, C. C.; Nocera, D. G.; Nozik, A. J.; Ort, D. R.; Parson, W. W.; Prince, R. C.; Sayre, R. T. *Science* **2011**, *332*, 805–809.

(S1) Vörös, J. *Biophys. J.* **2004**, *87*, 553–561.

(S2) Seybold, P. G.; Gouterman, M. *J. Mol. Spectrosc.* **1969**, *31*, 1–13.

(S3) Gradyushko, A. T.; Sevchenko, A. N.; Solovyov, K. N.; Tsvirko, M. P. *Photochem. Photobiol.* **1970**, *11*, 387–400.

(S4) Weber, G.; Teale, F. W. J. *Trans. Faraday Soc.* **1957**, *53*, 646–655.

(S5) Mass, O.; Taniguchi, M.; Ptaszek, M.; Springer, J. W.; Faries, K. M.; Diers, J. R.; Bocian, D. F.; Holten, D.; Lindsey, J. S. *New J. Chem*. **2011**, *35*, 76–88.

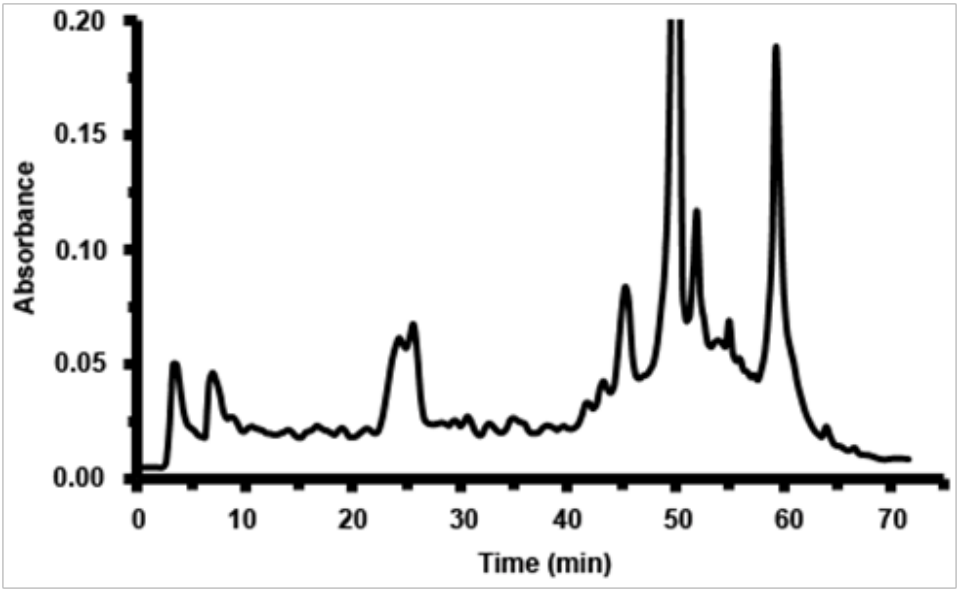

Figure S-1. HPLC chromatogram of 31mer(−14Cys)BC2 (λ_{det} = 280 nm). The peak at 60 min is the 31mer(−14Cys)BC2 product and that at 50 min is free **BC2**. (For some preparations, the dried sample was first extracted twice with methanol to remove free **BC2**, dried under a stream of Argon and then dried overnight under vacuum. Subsequent HPLC analysis showed little free **BC2**.) Fractions of the 60-min peak were cut and collected to give the sample of 31mer(−14Cys)BC2 that was examined in the spectroscopic studies described herein.

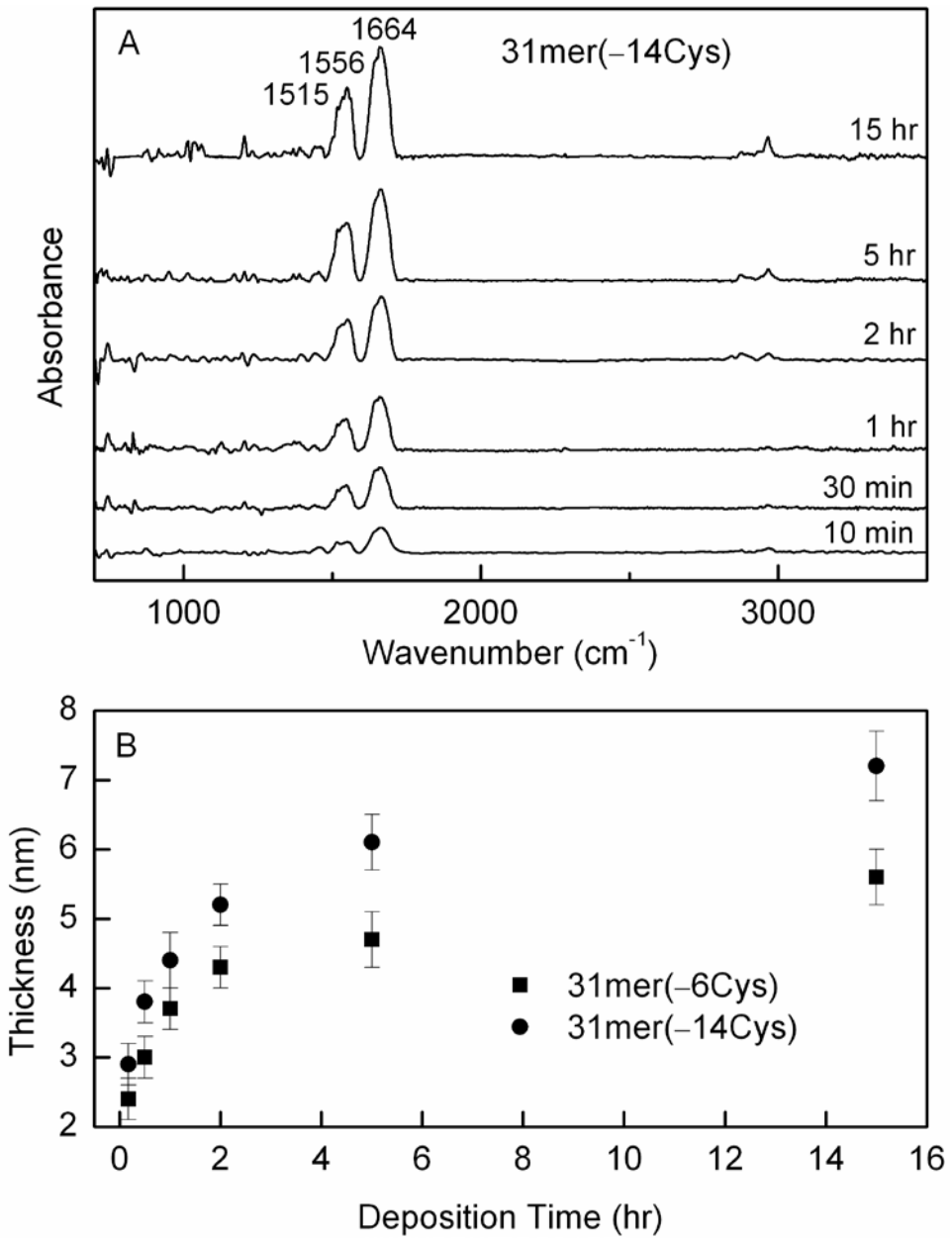

Figure S-2. (A) Single-reflection infrared data for films of peptides as a function of deposition time: (A) spectra of 31mer(–14Cys) and (B) thickness of films of 31-mer(–14Cys) (circles) and 31-mer(–6Cys) (squares).

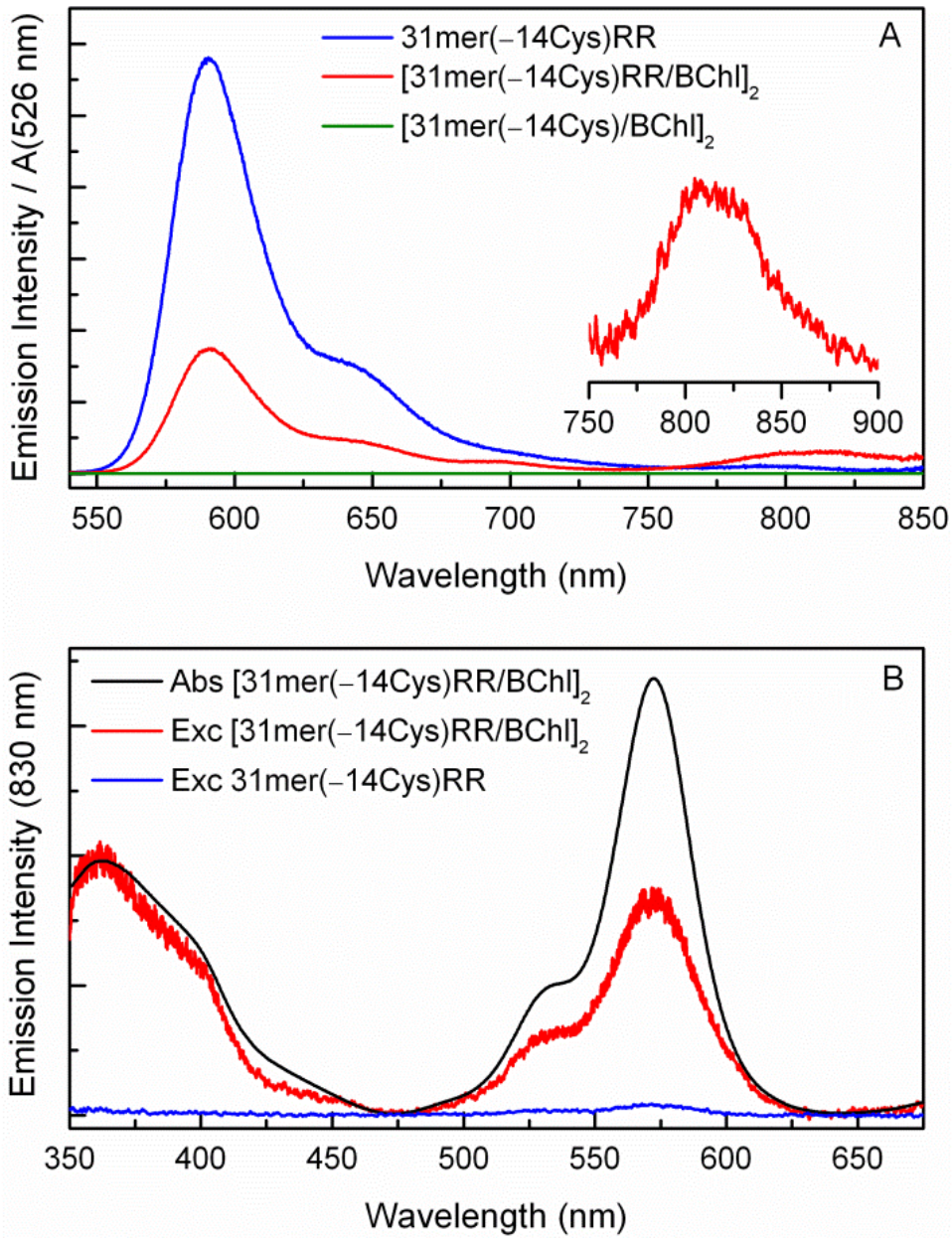

Figure S-3. (A) Fluorescence spectra (λ_{exc} = 526 nm) for peptide 31mer(−14Cys)RR (blue) and complexes [31mer(−14Cys)RR/BChl]$_2$ (red) and [31mer(−14Cys)BChl]$_2$ (green). The intensities are divided by the absorbance at λ_{exc} = 526 nm for (A) and 830 nm for (B). The inset shows the emission spectrum of [31mer(−14Cys)RR/BChl]$_2$ obtained using a NIR-enhanced detection system. (B) Fluorescence excitation spectrum for [31mer(−14Cys)RR/BChl]$_2$ (λ_{det} = 830 nm) (red) normalized to the absorption spectrum at 365 nm (black). Fluorescence excitation spectrum for 31mer(−14Cys)RR (λ_{det} = 830 nm) (blue) scaled by the **RR** fluorescence yield in that complex relative to that for [31mer(−14Cys)RR/BChl]$_2$.

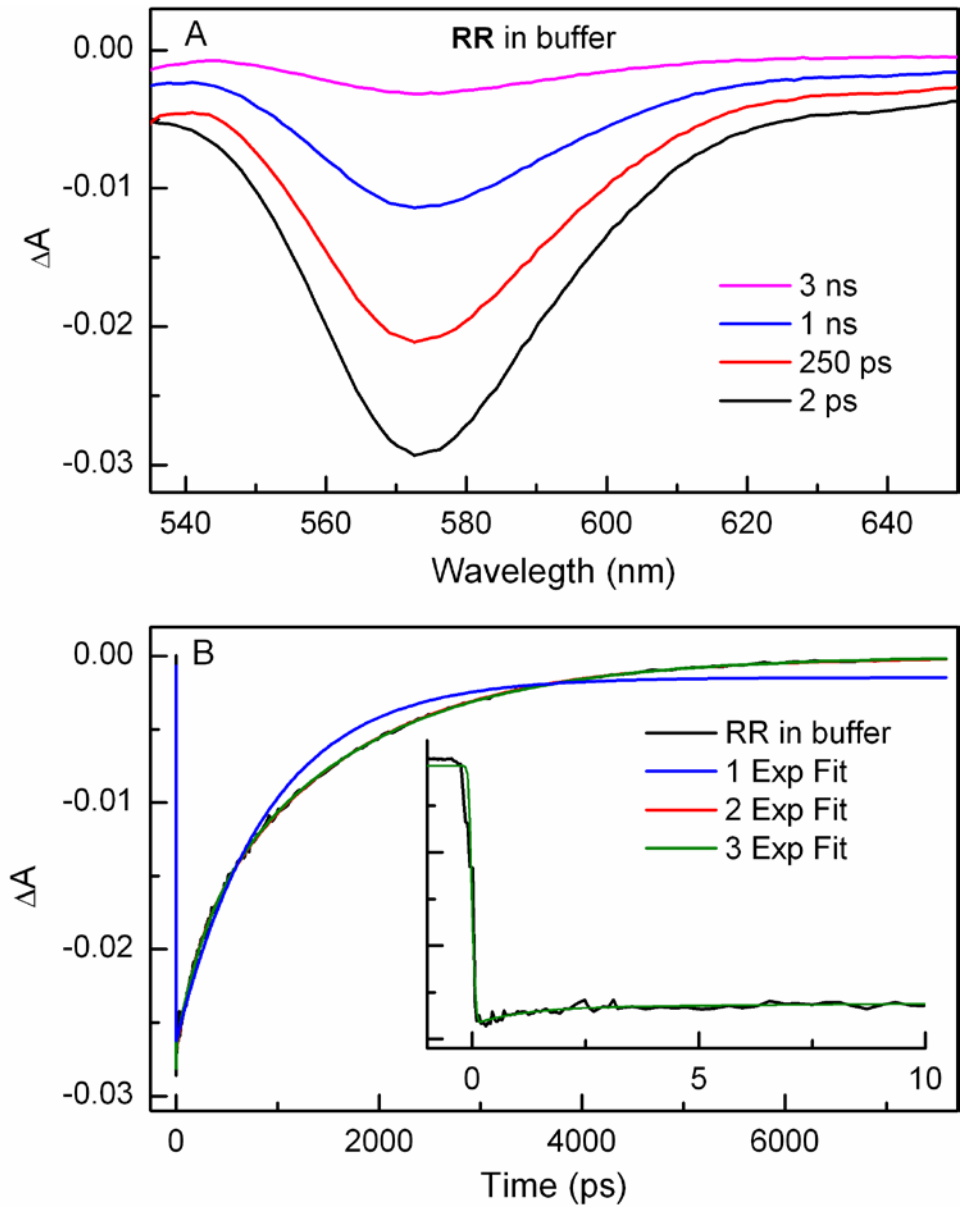

Figure S-4. Time-resolved absorption data using λ_{exc} = 535 nm for **RR** in 100 mM phosphate buffer (pH 7.5). Panel (A) gives spectra and panel (B) shows a kinetic trace at 580 nm (black) and fits to a single- (blue), double- (red) or triple (green) exponential.

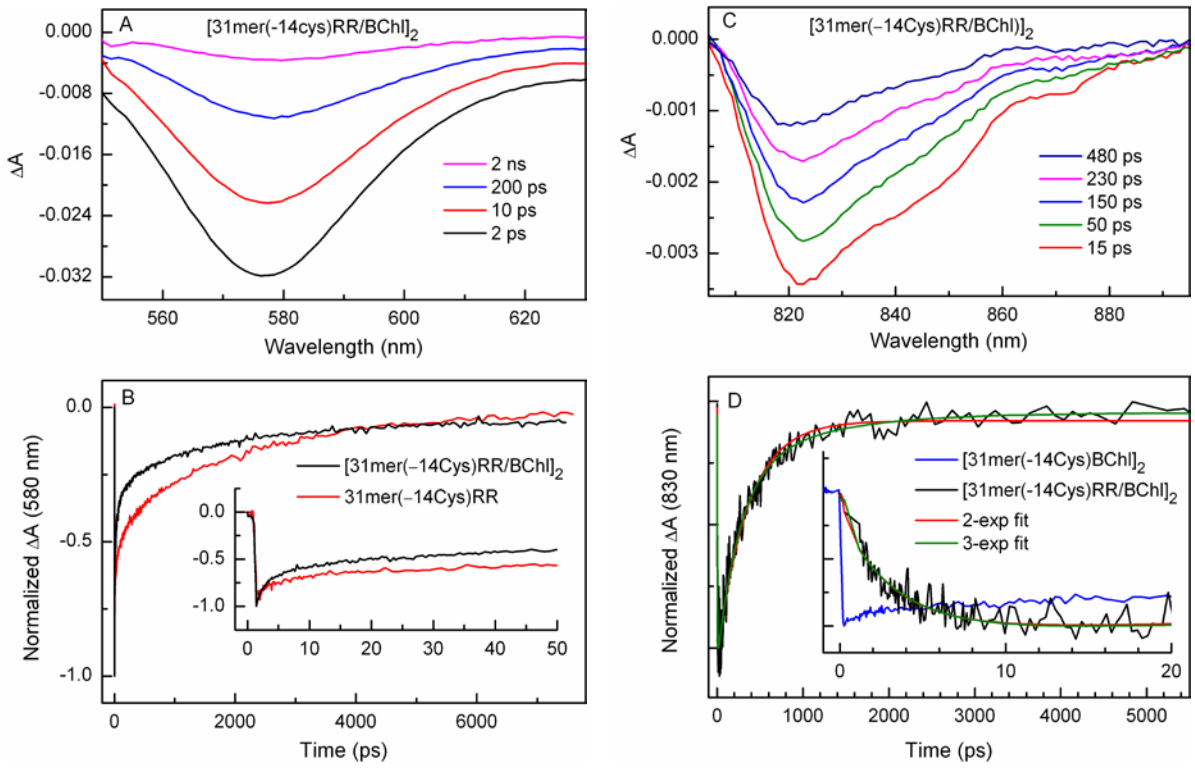

Figure S-5. Time-resolved absorption data for [31mer(–14Cys)RR/BChl]$_2$ in the Q_y region using λ_{exc} = 535 nm. Panel (A) shows combined bleaching and stimulated emission for **RR** and panel (C) for B820 (C). Panel (B) shows a kinetic traces at 580 nm for RR and panel (D) for B820 at 830 nm for [31mer(–14Cys)RR/BChl]$_2$ (black), 31mer(–14Cys)RR (red), and [31mer(–14Cys)BChl]$_2$ (blue) Panel D (lower right) shows dual- (red) and triple- (green) exponential function for [31mer(–14Cys)RR/BChl]$_2$.

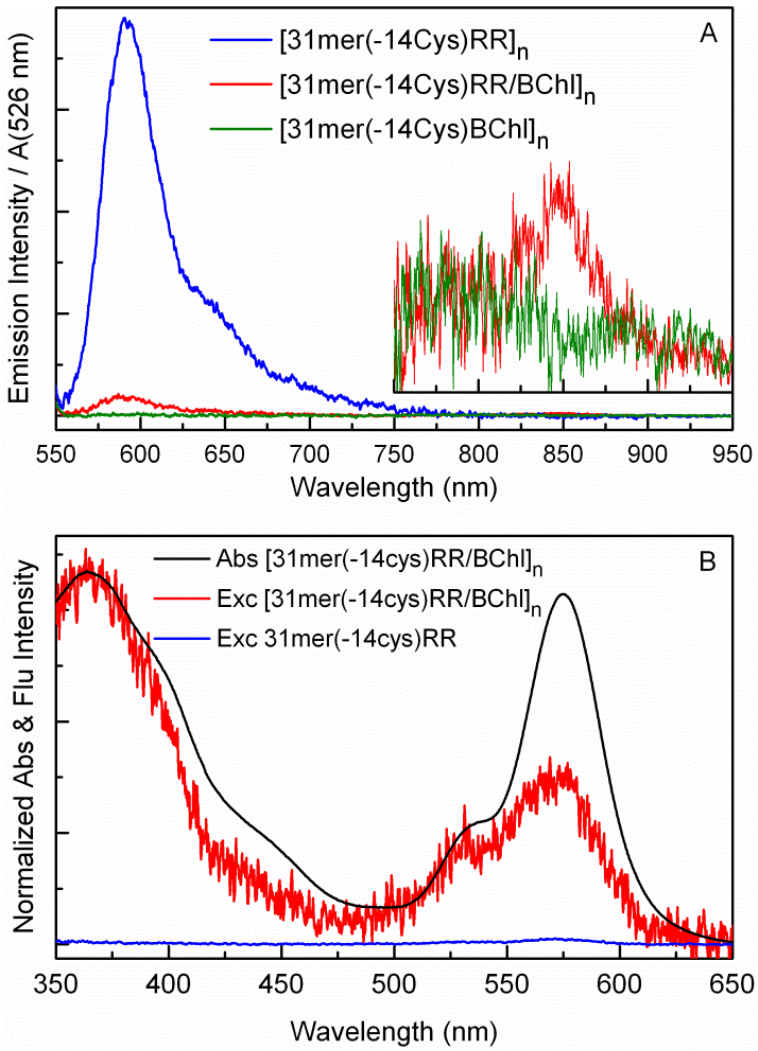

Figure S-6. (A) Fluorescence spectra (λ_{exc} = 526 nm) for 31mer(–14Cys)RR (blue), [31mer(–14Cys)RR/BChl]$_n$ (red) and [31mer(–14Cys)BChl]$_n$ (green). The intensities are divided by the absorbance at λ_{exc} = 526 nm. The inset shows the spectrum of [31mer(–14Cys)RR/BChl]$_n$ for the same sample and λ_{exc} with a red-enhanced detection system. (B) Fluorescence excitation spectrum (λ_{det} = 850 nm) for [31mer(–14Cys)RR/BChl]$_n$ (red) and 31mer(–14Cys)RR (blue), with the latter scaled by the **RR** fluorescence yield in that complex relative to that for [31mer(–14Cys)RR/BChl]$_n$. The absorption spectrum (black) and excitation spectrum of [31mer(–14Cys)RR/BChl]$_n$ are normalized at 365 nm.

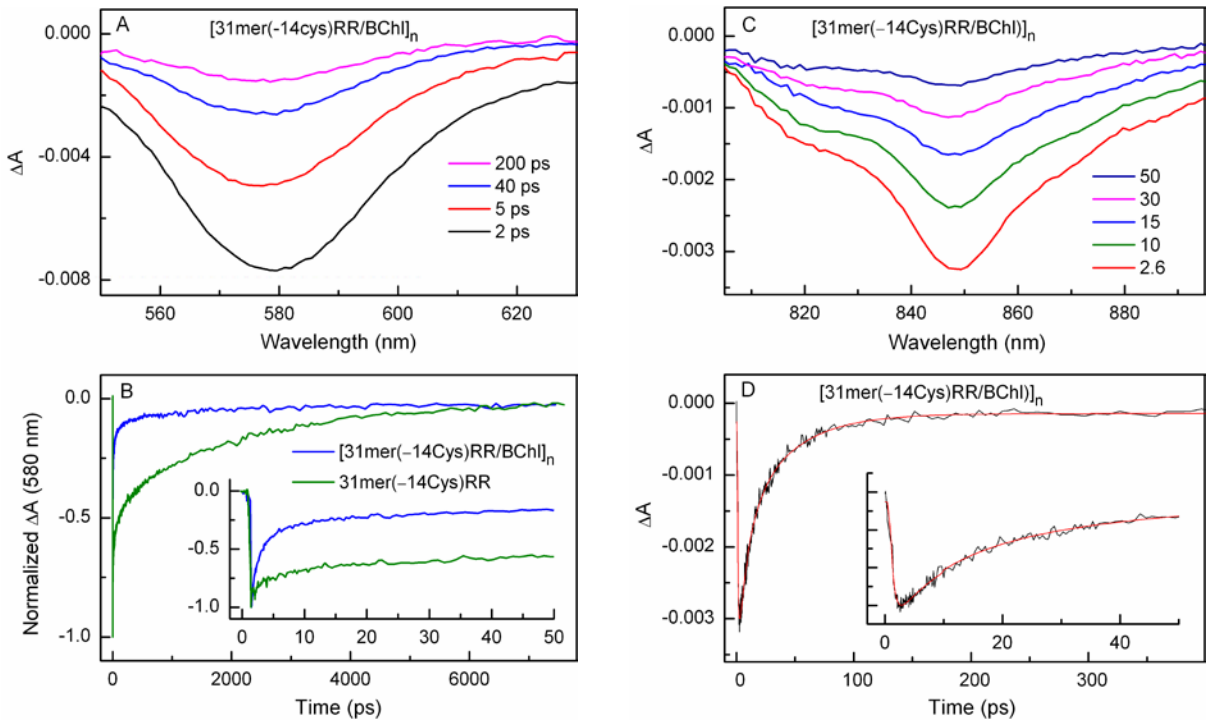

Figure S-7. (A) Time-resolved absorption spectra for $[31mer(–14Cys)RR/BChl]_n$ and (B) kinetic traces at 580 nm for $[31mer(–14Cys)RR/BChl]_n$ (blue) and 31mer(–14Cys)RR (green) using λ_{exc} = 535 nm. (C) Time-resolved absorption spectra for $[31mer(–14Cys)RR/BChl]_n$ and (D) kinetic trace at 850 nm and a fit to a triple-exponential function using λ_{exc} = 535 nm.

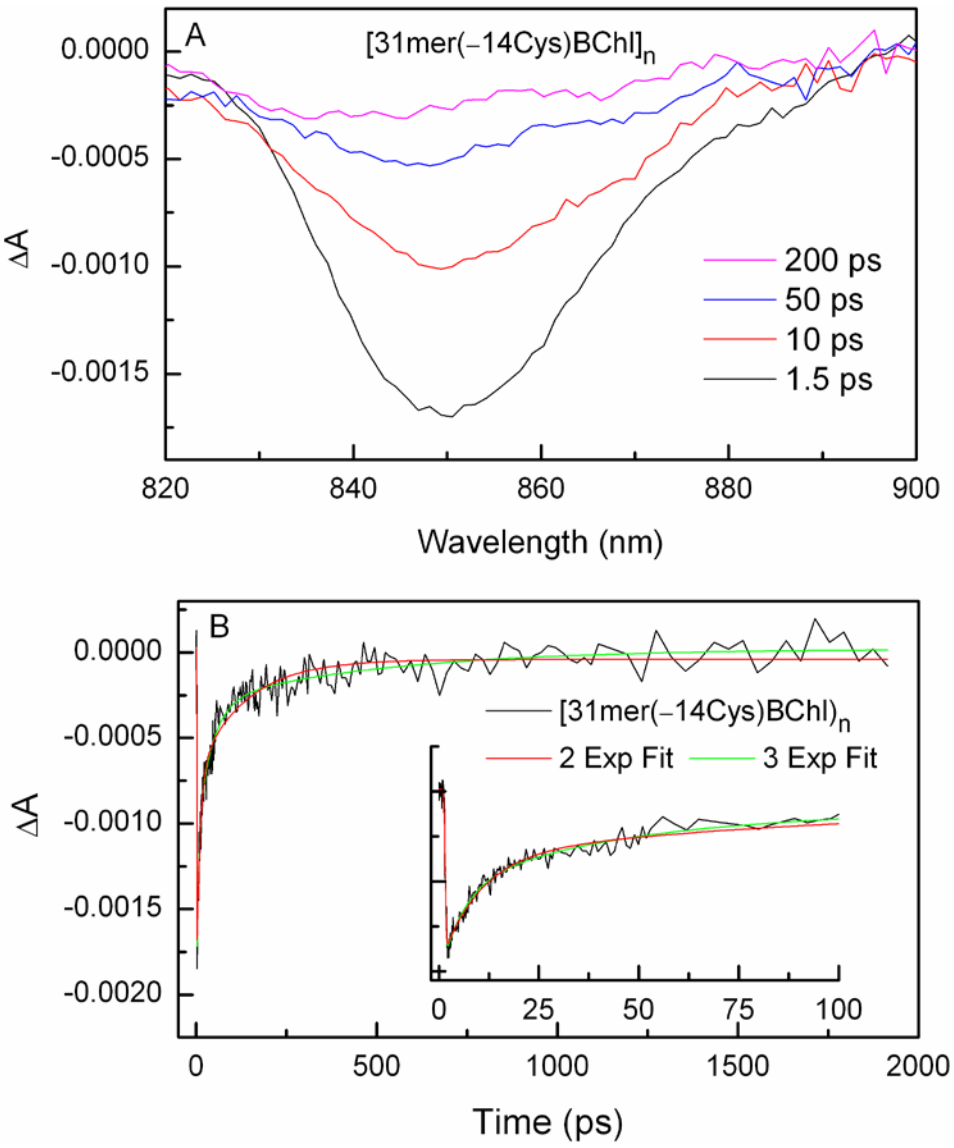

Figure S-8. (A) Time-resolved absorption spectra and (B) kinetic trace at 850 nm (black) and fits to two exponentials (red) and three exponentials (green) for [31mer(–14Cys)BChl]$_n$ (λ_{exc} = 590 nm) at room temperature.

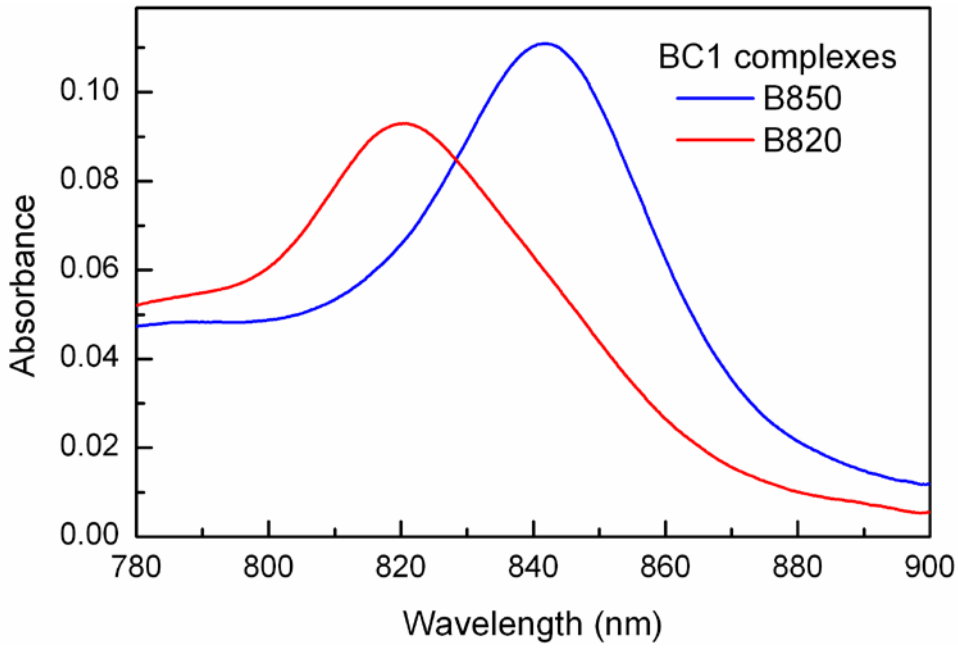

Figure S-9. NIR absorption spectra of oligomeric complex $[31mer(-14cys)BC1/BChl]_n$ (0.66% octyl glucoside solution) at room temperature (blue) and ββ-subunit complex $[31mer(-14cys)BC1/BChl]_2$ obtained by heating the solution of the oligomeric complex at 39 °C (red).

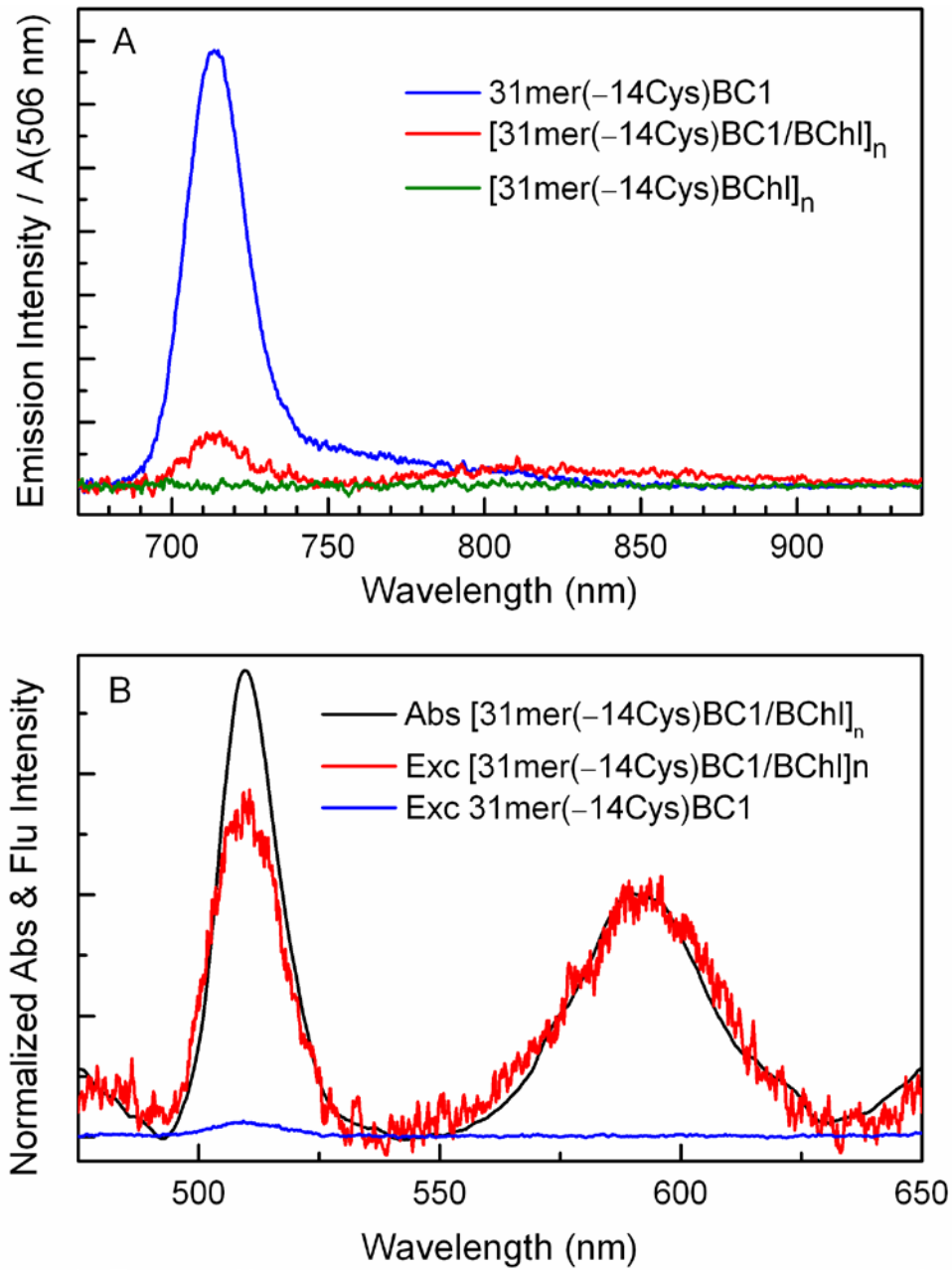

Figure S-10. (A) Fluorescence spectra (λ_{exc} = 506 nm) for peptide 31mer(–14Cys)BC1 (blue) and complexes [31mer(–14Cys)BC1/BChl]$_n$ (red) and [31mer(–14Cys)BChl]$_n$ (green). The intensities are divided by the absorbance at λ_{exc} – 506 nm. (B) Fluorescence excitation spectrum for [31mer(–14Cys)BC1/BChl]$_n$ (λ_{det} = 850 nm) (red) normalized to the absorption spectrum at 590 nm (black). Fluorescence excitation spectrum for 31mer(–14Cys)BC1 (λ_{det} = 850 nm) (blue scaled by the BC1 fluorescence yield in that complex relative to that for [31mer(–14Cys)BC1/BChl]$_n$.

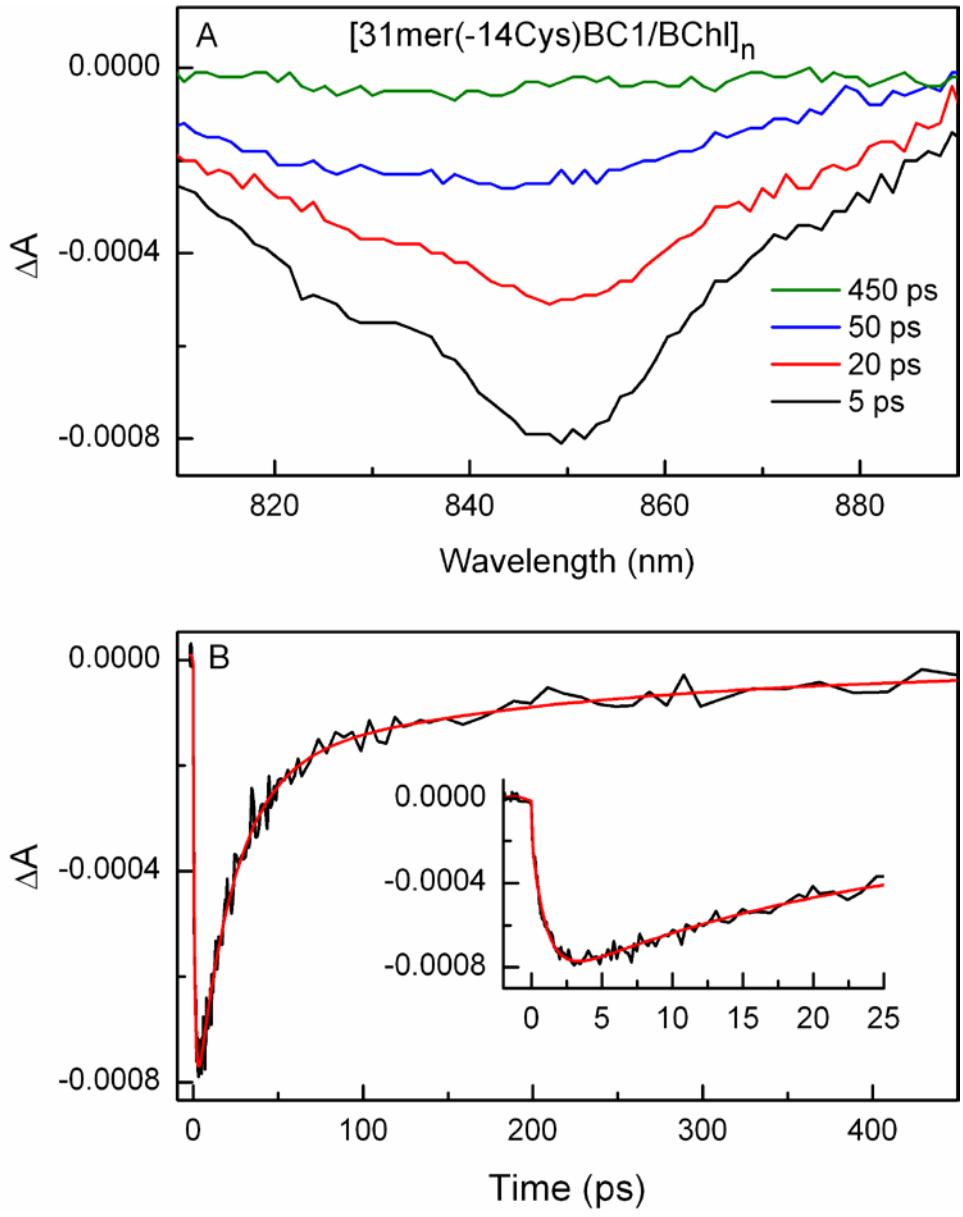

Figure S-11. (A) Time-resolved absorption spectra and (B) kinetic trace at 850 nm (black) and a fit to three exponentials (red) for $[31mer(-14Cys)BC1/BChl]_n$ (λ_{exc} = 506 nm) at room temperature.

Chapter 9.

Palette of Lipophilic Bioconjugatable Bacteriochlorins for Construction of Biohybrid Light-Harvesting Architectures

Reprinted with permission from *Chemical Science*. Reddy, K. R.; Jiang, J. Krayer, M.; Harris, M. A.; Springer, J. W.; Yang, E.; Jiao, J.; Niedzwiedzki, D. M.; Pandithavidana, D.; Parkes-Loach, P. S.; Kirmaier, C.; Loach, P. A.; Bocian, D. F.; Holten, D.; Lindsey, J. S. *Chem. Sci.*, 2013, **4**, 2036-2053.

Abstract

The challenge of creating both pigment building blocks and scaffolding to organize a large number of such pigments has long constituted the central impediment to the construction of artificial light-harvesting architectures. Light-harvesting (LH) antennas in photosynthetic bacteria are formed in a two-tiered self-assembly process wherein (1) a peptide dyad containing two bacteriochlorophyll *a* molecules forms, and (2) the dyads associate to form cyclic oligomers composed of 8 or 9 dyads in LH2 and 15 or 16 in LH1 of purple photosynthetic bacteria. While such antenna systems generally have near-quantitative transfer of excitation energy among pigments, only a fraction of the solar spectrum is typically absorbed. A platform architecture for study of light-harvesting phenomena has been developed that employs native photosynthetic peptide analogs, native bacteriochlorophyll *a*, and synthetic near-infrared-absorbing bacteriochlorins. Herein, the syntheses of 10 lipophilic bacteriochlorins are reported, of which 7 contain bioconjugatable handles (maleimide, iodoacetamide, formyl, carboxylic acid) for attachment to the peptide chassis. The bioconjugatable bacteriochlorins typically exhibit a long-wavelength absorption band in the range 710 to 820 nm, fluorescence yield of 0.1–0.2, and lifetime of the lowest singlet excited state of 2–5 ns. The α-helical structure of the native-like peptide is retained upon conjugation with a synthetic bacteriochlorin, as judged by single-reflection infrared studies. Static and time-resolved optical studies of the oligomeric biohybrid architectures in aqueous detergent solution reveal efficient (~90%) excitation energy transfer from the attached bacteriochlorin to the native-like bacteriochlorophyll *a* sites. The biohybrid light-harvesting architectures thus exploit the self-constituting features of the natural systems yet enable versatile incorporation of members from a palette of synthetic chromophores, thereby opening the door to a wide variety of studies in artificial photosynthesis.

Introduction

The initial stages of energy conversion in both natural photosynthesis and artificial systems involve harvesting solar photons and delivering the excitation energy to sites for photochemistry or photocurrent production.[1,2] The light-harvesting (LH) units of photosynthetic systems typically include hundreds to thousands of pigments.[3] In most cases, the light-harvesting units are composed of pigments (chlorophylls, bacteriochlorophylls, carotenoids) organized in protein assemblies. A chief challenge to the construction of fully synthetic light-harvesting architectures is the necessity to construct both the pigment building blocks and the scaffolding to organize the pigments. The problems of constructing and stitching together scaffolding and chromophores have largely limited the size of synthetic architectures that have been created,[4-6] although a few exceptions exist of covalently linked arrays of porphyrins that encompass >100 chromophores.[7,8] Analogous architectures that incorporate hydroporphyrins (i.e., chlorins and bacteriochlorins) have not yet been developed.[9] Use of such hydroporphyrins is essential because a large fraction of available solar radiation lies in the red and near-infrared (NIR) spectral region, where hydroporphyrins absorb strongly yet porphyrins absorb poorly if at all.[10,11]

The formation of the light-harvesting pigment-protein complexes (LH1 and LH2) of bacterial photosynthetic systems entails a two-tiered self-assembly process. In the first tier, two bacteriochlorophyll *a* (BChl *a*) molecules associate (via magnesium–histidine dative bonds) with one α-peptide and one β-peptide, each of which is ~50 amino acids in length, to give an αβ-subunit (Fig. 1A).[1,12] In the second tier, the αβ-subunits associate with each other to give cyclic oligomers (Fig. 1B).[13-16] Although variation is observed among bacterial species, the number of αβ-subunits in the LH2 rings is typically 8 or 9, as observed in *Phaeospirillum (Phs.)*

molischianum (Fig. 1B)[13] or *Rhodopseudomonas (Rps.) acidophila*,[15] respectively. Similarly, the number of αβ-subunits in the LH1 rings is typically 15 or 16, as is observed in *Rhodopseudomonas (Rps.) palustris*[16] or *Rhodospirillum (Rds.) rubrum*,[14] respectively.

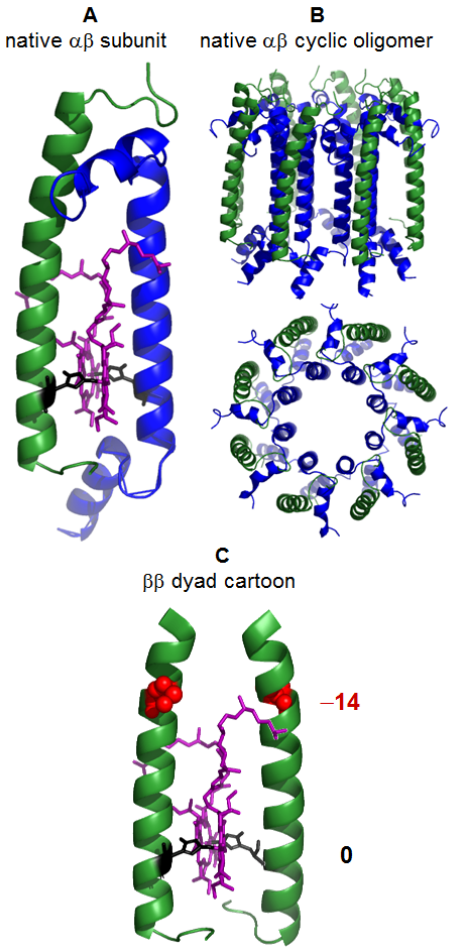

Fig. 1. Structures of subunits and oligomeric photosynthetic light-harvesting complexes. (A) αβ-subunit consisting of the α-peptide (blue), β-peptide (green) and a pair of BChl *a* molecules (purple) coordinated via the central magnesium ion to histidine residues (black) of the peptides. (B) Side and top views of the LH2 complex of *Phs. molischianum*;[13] some peptides in the side view, and all the BChl *a* molecules in both views are omitted for clarity. (C) Cartoon of the truncated ββ-subunit complex formed by association of two BChl *a* with two 31mer β-peptides. The –14 site is used here for incorporation of a cysteine (see text).

The two-tiered assembly processes result in spectral changes in the NIR region owing to the interaction of the embedded BChl *a* molecules with each other and the protein environment.

The solar spectrum (air-mass 1.5) is shown in Fig. 2A.[11] Monomeric BChl *a* in organic media has a long-wavelength Q_y absorption at ~780 nm (Fig. 2B, green), whereas the absorption of the pigments in an αβ-subunit shifts to ~820 nm (Fig. 2B, orange dots) due to the interaction of the two BChl *a* molecules. Upon formation of the cyclic oligomer in LH2, the number of interacting BChl *a* molecules is increased to 16 or 18 resulting in a further shift of the absorption to ~850 nm (Fig. 2C, blue). The LH2 complexes also contain a third BChl *a* per subunit (for a total of 8 or 9 additional chromophores) that resides between adjacent β-peptides in the oligomeric assembly; these effectively monomeric BChl *a* absorb at ~800 nm (Fig. 2C, blue), which represents a modest protein-induced shift from the spectral position *in vitro*. [The native light-harvesting systems also contain carotenoid, which is spheroidene (440–550 nm absorption) in the *Rb. sphaeroides* LH1 and LH2 complexes for which spectra are shown in Fig. 2C.[17]] In the LH1 complexes of *Rps. palustris*[16] and *Rds. rubrum*,[14] the cyclic architectures are increased to 15 or 16 subunits and the number of interacting BChl *a* to 30 or 32, giving rise to an additional bathochromic shift in Q_y absorption to ~875 nm (Fig. 2C, red). In the bacterial photosynthetic membranes, LH2 complexes border LH1, which encapsulates the photochemical reaction center.[1,2] This structural arrangement along with the spectral properties (e.g., Fig. 2C) provides both a spatial and energy gradient for directional energy flow from LH2 to LH1 to reaction center. These characteristics illustrate the essential feature of the protein scaffolding in organizing a very large number of native BChl *a* pigments for light-harvesting.

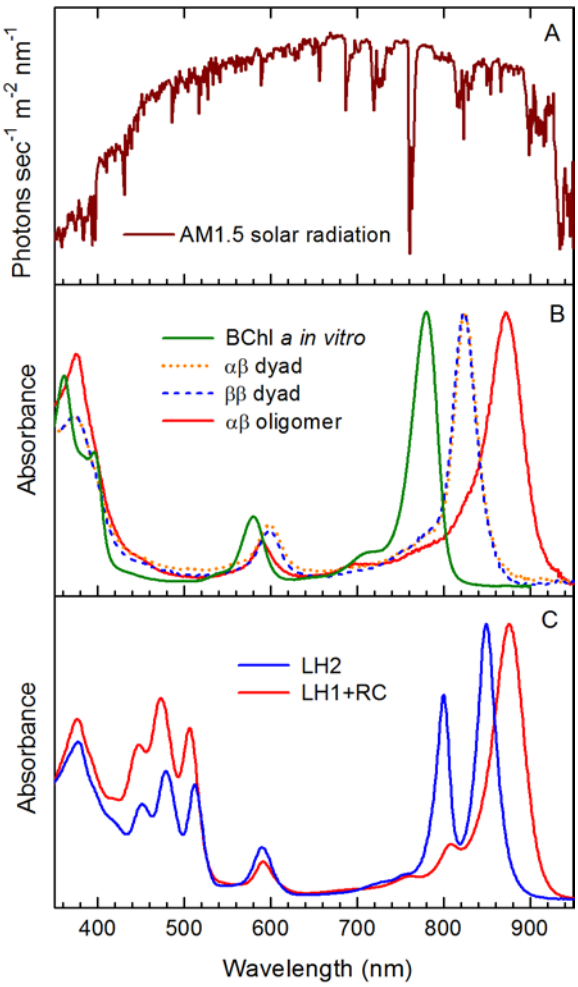

Fig. 2. (A) Photon flux density spectrum of light reaching the earth through an airmass of 1.5 atmospheres thickness (the AM1.5 solar-radiation standard); the ordinate values have been multiplied by 10^{-18}. (B) Absorption spectra of BChl *a* in toluene (green), the αβ-subunit (orange dots), the ββ-subunit obtained by association of BChl *a* with the truncated, 31mer β-peptide (blue dashes), and the oligomer obtained by reconstitution of the full length *Rb. sphaeroides* peptides with BChl *a* (red). (C) Absorption spectra of LH2 (blue) and LH1+RC (red) from *Rb. sphaeroides* complexes that have sphaeroidene as the only carotenoid.[17]

We have been working to develop an architectural platform for light-harvesting that combines biological (or bioinspired) and synthetic constituents and thus affords design versatility and facile assembly. This biohybrid architecture employs analogues of the native light-harvesting pigments of bacterial photosynthetic systems in conjunction with synthetic chromophores. The synthetic chromophores piggyback on the self-forming chassis generated by

the peptides and the embedded BChl *a* molecules. A key rationale for such biohybrid light-harvesting architectures is to overcome limitations of synthetic chemistry for creation of scaffolding to accommodate large numbers of pigments. A second rationale is to redress shortcomings of the natural system such as limited coverage of the solar spectrum.[18] Indeed, although the quantum efficiencies of energy transfer within and between the antenna complexes (and reaction center) approach 100%, LH1 and LH2 individually or even together (Fig. 2C) absorb across only a fraction of the photon-rich visible and NIR regions of the solar spectrum (Fig. 2A). The development of such biohybrid constructs extends prior work on the reconstitution of native or native-like peptides with chromophores,[12,19-21] provides an entrée into the study of self-assembling supramolecular protein oligomers,[22-24] and complements bioinspired systems such as chromophore arrays or maquettes that combine synthetic peptide scaffolds with synthetic or native chromophores.[25-29]

Our initial biohybrid constructs[18] entailed covalent attachment of a bioconjugatable bacteriochlorin (or commercial dye) to a cysteine residue in a 31mer peptide that is a truncated analogue[19,30,31] of the *Rb. sphaeroides* LH1 β-peptide. Like the native β-peptide, the truncated β-peptide dimerizes with incorporation of two BChl *a* molecules to give ββ-subunit complexes (Fig. 1C)[31] with absorption spectrum nearly identical to that of the native αβ-dyad (Fig. 2B). The resulting dyads of the truncated β-peptide (but not the native β-peptide) self-associate to give β_n-oligomeric assemblies that contain 2*n* BChl *a*.[31] The chromophore-attached peptides similarly associate with each other and BChl *a* to form ββ-subunit complexes or β_n-oligomeric assemblies that contain 2 or 2*n* BChl *a*, respectively. The appended chromophores have complementary absorption to the native-like BChl *a* dyad in the subunit complex or BChl *a* array in the oligomeric complex and transfer energy to the BChl *a* sites with efficiencies that range

from ~20% to ≥90% depending on the chromophore and attachment site.[18] The success of this approach requires access to wavelength-tunable, bioconjugatable bacteriochlorins, which heretofore have only rarely been reported.[32-37]

Herein, we report the synthesis and photophysical characterization of a palette of seven bioconjugatable bacteriochlorins and corresponding model compounds bearing similar substituent patterns but lacking bioconjugatable groups. The lipophilicity of the bacteriochlorins enables incorporation of the resulting biohybrid complexes in membranes, micelles, or similar environments. One bacteriochlorin was bioconjugated to an analogue of a native photosynthetic peptide (31 residues). The conjugate gave oligomeric assemblies in detergent solution. The energy-transfer characteristics of the oligomers were characterized using static and time-resolved absorption and emission spectroscopy. Infrared studies were performed to ensure that the α-helical structure of the peptides is not compromised by a conjugated bacteriochlorin. Collectively, the results illustrate the versatility of this approach for assembling light-harvesting architectures that exhibit high (≥90%) energy-transfer efficiencies and broad coverage of the solar spectrum.

Results and Discussion

Synthetic Bacteriochlorins

Design. Recent advances in synthesis by a number of groups have provided entrées to analogues of the naturally occurring bacteriochlorophylls.[35,36,38-47] The resulting synthetic bacteriochlorins contain the tetrahydroporphyrin π-system characteristic of bacteriochlorophylls but differ with regards to key structural features. Our own work in synthetic methodology has led to bacteriochlorins of the type shown in Chart 1.[48,49] One key structural element consists of a

geminal dimethyl group in each reduced, pyrroline ring to provide stability toward adventitious dehydrogenation. The synthetic bacteriochlorins are stable towards diverse reaction conditions (e.g., Pd-coupling, aldol condensation, reductive amination).[50-55] The synthesis of the bacteriochlorins entails self-condensation of a 1-(1,1-dimethoxymethyl)-3,3-dimethyl-2,3-dihydrodipyrrin (i.e., a dihydrodipyrrin–acetal). The reliance on self-condensation to give two equivalent halves of the resulting bacteriochlorins limits the possibilities to install a single bioconjugatable group because the substituents at positions 2 and 12 are identical with each other, as are those at positions 3 and 13. Rational approaches for installing one bioconjugatable group onto the synthetic bacteriochlorins include: (i) bromination of the 15-position of a 5-alkoxybacteriochlorin followed by derivatization,[50] (ii) installation of a 6-membered imide ring spanning the 13,15-positions and derivatization of the *N*-imide moiety,[55] (iii) elaboration of the 5-alkoxy site,[56] and (iv) rational[36] or statistical[53] access to the 3-position.

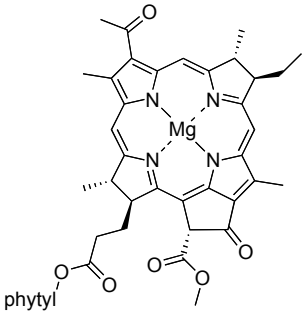

bacteriochlorophyll *a*

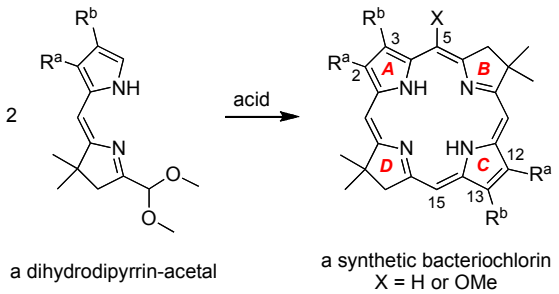

a dihydrodipyrrin-acetal

a synthetic bacteriochlorin
X = H or OMe

Chart 1. BChl *a* (top) and route to stable synthetic bacteriochlorins (bottom).

Fundamental spectroscopic studies on the synthetic bacteriochlorins[51,55,57] have afforded an understanding of substituent effects on electronic-structure, optical, redox, and excited-state characteristics. Through these studies, it is possible to tune the wavelength (and intensity) of the NIR region absorption from 700–800 nm with ≤10 nm precision, and with less control from 800–900 nm. The position of the Q_y band of a photochemically active species defines not only a spectral region where absorption occurs but also the energy of the initially formed lowest energy singlet excited state. The next step is to retain this tunability, and maintain other favorable photophysical characteristics such as long excited-state lifetimes, while utilizing additional macrocycle sites for incorporation of a bioconjugatable linker.

The palette shown in Chart 2 contains seven bioconjugatable bacteriochlorins, including four with maleimide groups (**BC1-4**), a formyl–bacteriochlorin (**BC5**), a bacteriochlorin bearing an iodoacetamide group (**BC6**), and a carboxy–bacteriochlorin (**BC7**). Bacteriochlorins **BC1** and **BC2** were used to prepare earlier biohybrid architectures (but their syntheses were not described),[18] and mono-formylbacteriochlorin (**BC5**) has been prepared[53] and characterized[57] previously. A corresponding set of seven benchmark bacteriochlorins lacking bioconjugatable groups includes five new compounds (**BC9** and **BC10** have been prepared and characterized previously[55]). The availability of benchmark bacteriochlorins was particularly important for the compounds containing either iodine (**BC6**) or maleimide (**BC1-4**) due to the potential of such groups to modify excited-state decay properties via the heavy-atom effect or electron-transfer quenching, respectively. Carboxy–bacteriochlorin **BC7** is both bioconjugatable and a benchmark for bacteriochlorin **BC1**.

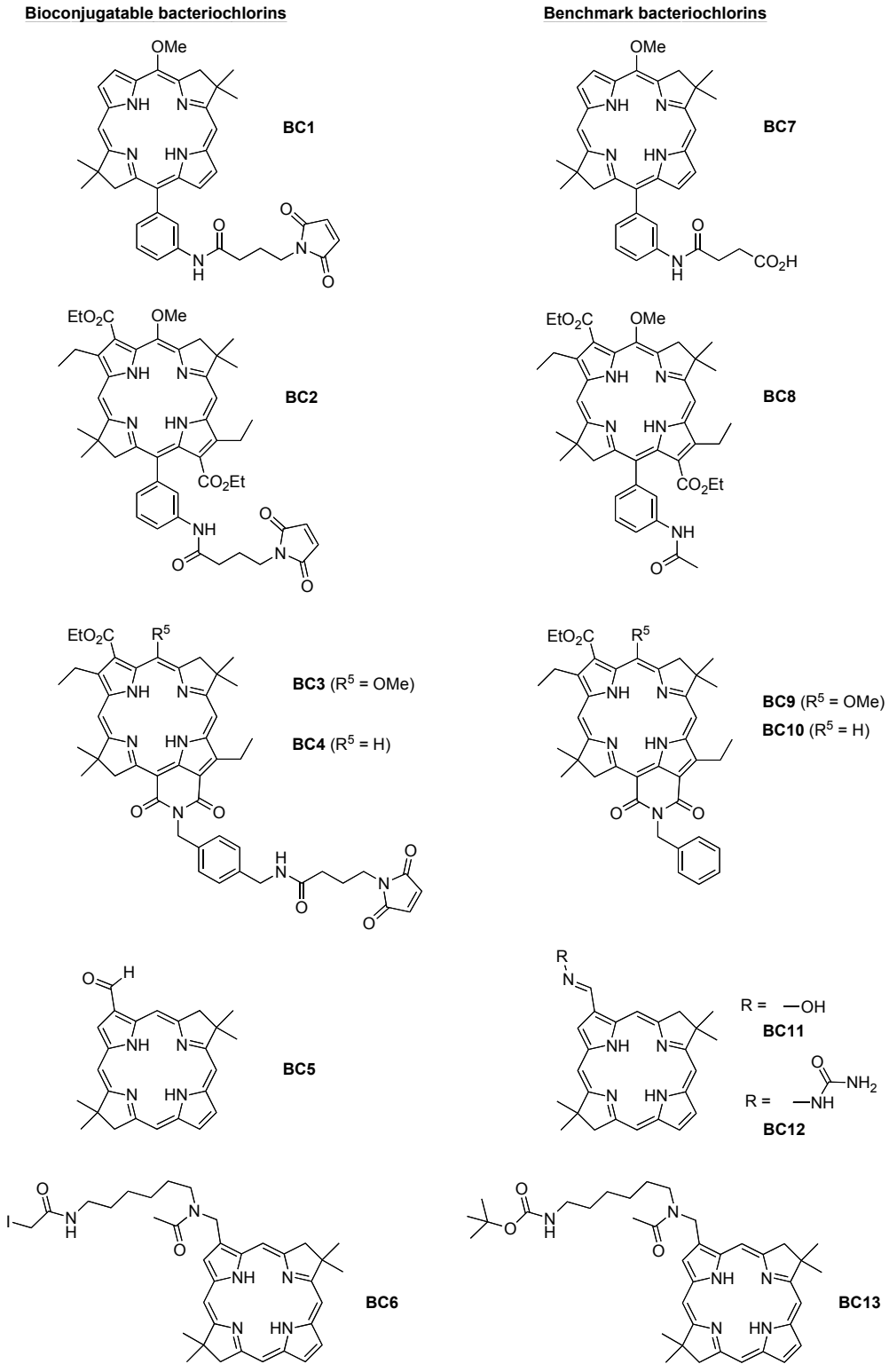

Chart 2. Bioconjugatable bacteriochlorins (left panel) and benchmarks (right panel). **BC7** serves both capacities.

Synthesis. Bacteriochlorins bearing a 5-methoxy group undergo regioselective 15-bromination, which provides an attractive means of introducing a single group into the bacteriochlorin skeleton.[50] Accordingly, Suzuki coupling of bacteriochlorin[49] **MeOBC-Br^{15}** with 3-aminophenylboronic acid pinacol ester (**1**) gave the anilino–bacteriochlorin **MeOBC-An^{15}** in excellent yield (Scheme 1). Treatment of **MeOBC-An^{15}** with succinic anhydride (**2**) gave the amide with a propionic acid tether (**BC7**), whereas coupling with 4-maleimidobutyric acid (**3**) mediated by dicyclohexylcarbodiimide (DCC) afforded the maleimide-terminated bacteriochlorin **BC1**.

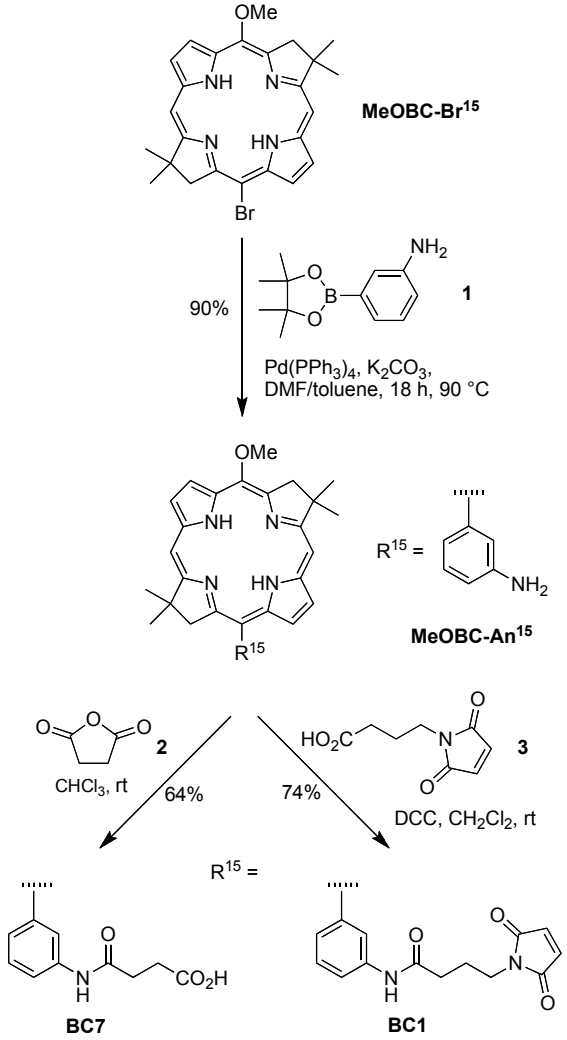

Scheme 1. Carboxy- or maleimide-substituted bacteriochlorins via an anilino building block.

In a similar manner, Suzuki coupling of bacteriochlorin[49] **MeOBC-EtEs-Br**[15] with **1** provided bacteriochlorin **MeOBC-EtEs-An**[15] in good yield. Treatment with acetic anhydride in the presence of 4-(dimethylamino)pyridine (DMAP) afforded model compound **BC8** in 71% yield, whereas DCC-mediated coupling with **3** gave bacteriochlorin **BC2** in 32% yield (Scheme 2).

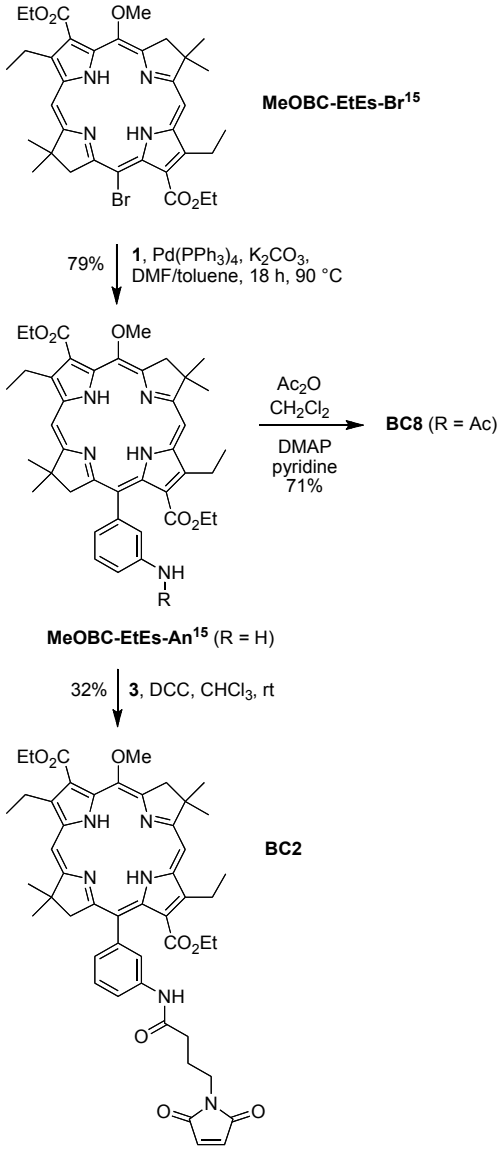

Scheme 2. Maleimide-substituted bacteriochlorin and acetamide-substituted bacteriochlorin benchmark.

The synthesis of **BC3** and **BC4** also used the known bacteriochlorin[49] **MeOBC-EtEs-Br^{15}** and bacteriochlorin[55] **HBC-EtEs-Br^{15}**, respectively. Tandem carbonylation followed by intramolecular imidation has recently been demonstrated using benzylamine to give the corresponding *N*-benzyl bacteriochlorin-13,15-dicarboximide.[55] Here, the reaction with several equivalents of *p*-xylylenediamine (**4**) gave bacteriochlorin **MeOBC-Im** and **HBC-Im** in 47% and 21% yield, respectively. Again, DCC-mediated coupling with **3** gave **BC3** and **BC4** in 73% and 63% yield, respectively (Scheme 3).

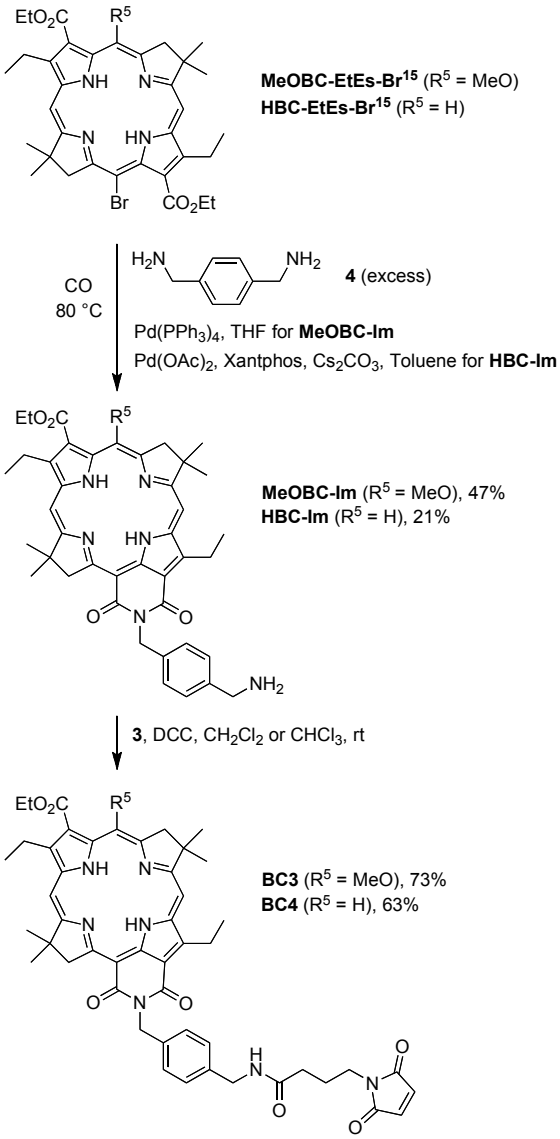

Scheme 3. Maleimide-substituted bacteriochlorin-13,15-dicarboximides.

BC5 was obtained as previously described by the statistical Pd-mediated carbonylation of 3,13-dibromobacteriochlorin.[53] The formyl group of bacteriochlorin **BC5** can be derivatized by imination or by reductive amination. Two examples of imination include microwave-mediated reaction with hydroxylamine or semicarbazide to give **BC11** (48%) or **BC12** (36%), respectively (Scheme 4). Reductive amination of **BC5** using *N*-Boc-1,6-diaminohexane (**5**) gave **BC13-H** in good yield. To avoid any photoinduced quenching processes, the secondary amine was acylated (with acetic anhydride) to afford **BC13**. Treatment with TFA cleaved the Boc group, and subsequent reaction with iodoacetic anhydride (**6**) gave bacteriochlorin **BC6**. The iodoacetamide group is well suited for potential attachment to cysteine residues on a target protein.

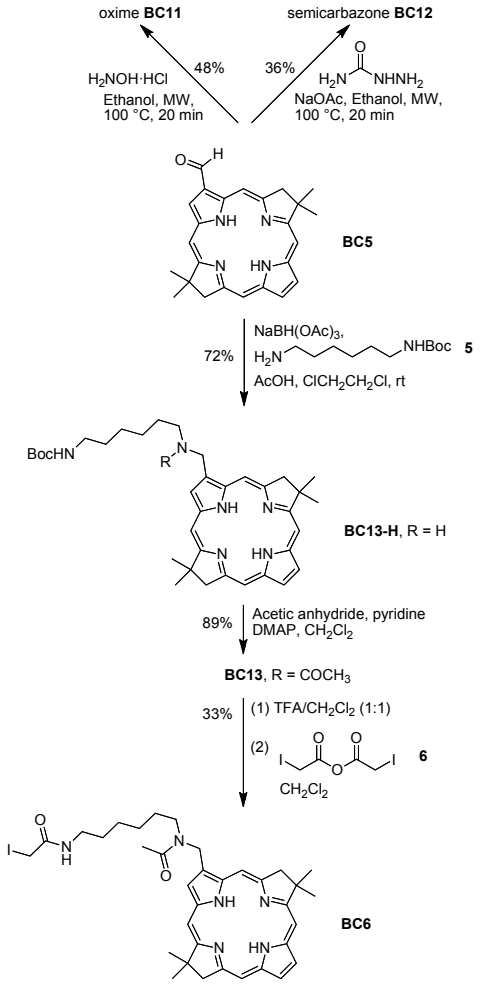

Scheme 4. Iodoacetamide-substituted bacteriochlorin and imine-bacteriochlorin benchmarks.

Formation of Bacteriochlorin–Peptide Bioconjugates

Maleimido–bacteriochlorins **BC1** and **BC2** were used previously to prepare bioconjugates for incorporation into biohybrid light-harvesting architectures.[18] Here, the iodoacetamide-substituted bacteriochlorin **BC6** was employed to prepare a conjugate with a cysteinyl-peptide that is an analogue of a native photosynthetic light-harvesting peptide. The peptide (previously termed **31mer(–14Cys)**,[18] here denoted **P1**) employed has the sequence ELHSVY**C**$^{-14}$SGLWLFSAVAIVA**H**^{0}LAVYIWRPWF. This sequence is identical to that of the 31 amino acids at the carboxy terminus of the β-peptide of LH1 of *Rb. sphaeroides*[19,30,31] except that the Met at −14 is replaced by Cys for chromophore conjugation (Fig. 1C). The His at position 0 to which BChl *a* is coordinated and the Cys at −14 are emboldened and underlined with positions superscripted.

Bacteriochlorin **BC6** was conjugated to −14Cys of **P1** in aqueous *N,N*-dimethylformamide (DMF) solution containing Tris buffer (pH 7.3 or 8.6)[22] to give bacteriochlorin–peptide conjugate **BC6-P1**, following methods established for bacteriochlorins **BC1** and **BC2**.[18] The hydrophobicity of the peptide,[58] the bacteriochlorin, and resulting conjugate presented challenges in purification. The crude reaction mixture was purified by reverse-phase HPLC with elution with aqueous–organic solvent mixtures including use of isopropanol and butanol.[59,60] Initially, the **BC6-P1** conjugate was isolated in ~2% yield (by spectroscopic determination of the amount of bacteriochlorin in the starting material and the product). Subsequent improvements afforded the **BC6-P1** conjugate in 17% isolated yield, which was estimated to stem from the product of synthetic yield (inferred 30%), chromatographic recovery (80%), and fraction cut on the HPLC (70%). The **BC6-P1** conjugate was characterized by HPLC, absorption spectroscopy, ESI-MS, and MALDI-MS. The results

were consistent with expectation for the bacteriochlorin–peptide conjugate. A full description of the conjugation, purification, and characterization is provided in the Supplementary Information.

Physicochemical Characterization

We first describe the photophysical characterization of the bacteriochlorin benchmarks and the bacteriochlorin conjugate **BC6-P1**, and then turn to explore the energy-transfer properties of the assemblies derived from the bacteriochlorin–peptide conjugate.

Bacteriochlorin Absorption and Emission Spectra. The Q_y absorption band of each synthetic bacteriochlorin described herein spans from ~710 to ~820 nm. Fig. 3 shows representative absorption and fluorescence spectra. The fluorescence maxima are typically shifted 5–10 nm to longer wavelength than the Q_y absorption peak. The absorption spectra of the bioconjugatable bacteriochlorins obtained after conjugation to the 31mer peptide (in aqueous buffer solution) are similar to those of the peptide-free bioconjugatable bacteriochorin (in toluene) and to those of the bacteriochlorin prior to addition of the bioconjugatable linker (in toluene). The peak absorption and fluorescence positions are listed in Table 1.

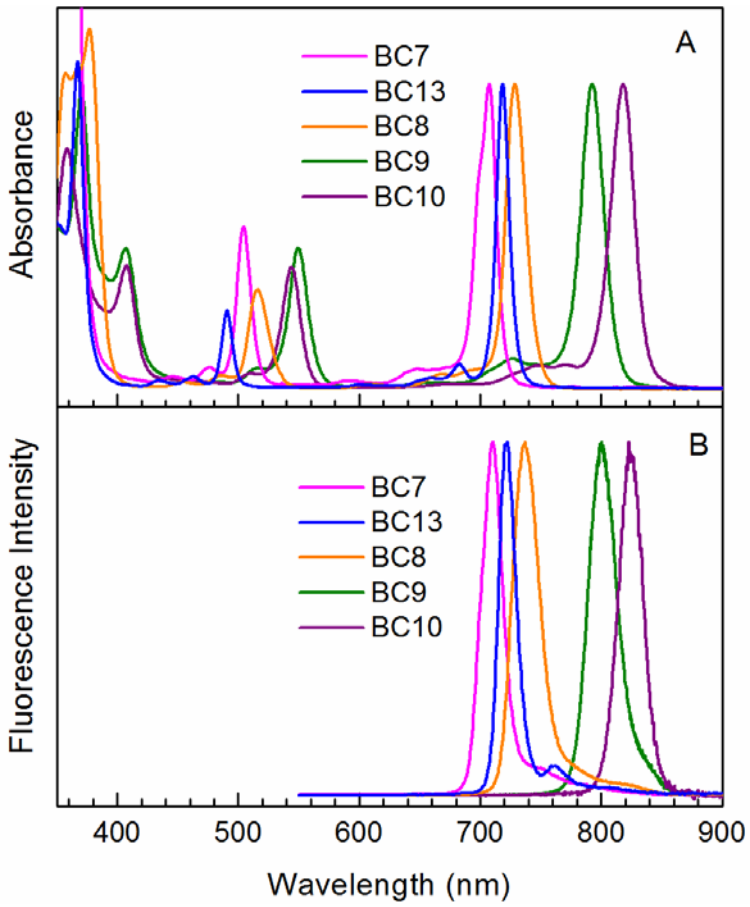

Fig. 3. Absorption (A) and fluorescence (B) spectra of representative synthetic bacteriochlorins.

Bacteriochlorin Photophysical Properties. The fluorescence yield (Φ_f), singlet excited-state lifetime (τ_S) and yield of intersystem crossing to the triplet excited state (Φ_T) were determined for the bacteriochlorins that lack or contain an iodoacetamide or maleimide group (Table 1). The data for the compounds lacking the bioconjugatable group are discussed first. The results indicate that as the Q_y absorption shifts to longer wavelength (and the S_1 excited state shifts to lower energy), there is a general decrease in Φ_f and τ_S values but no clear variation in Φ_T. These findings are consistent with prior results on a much larger (~30) set of synthetic free base bacteriochlorins.[57] Given the smaller set studied here, some of the data are best considered in groups. The first group (**BC7**, **BC8**, **BC13**) have Q_y bands at 707–729 nm, Φ_f values of

0.11–0.20 (0.15 average) and τ_S values of 3.8–4.7 ns (4.3 ns average). The second group (**BC5**, **BC11**, **BC12**) have Q_y bands at 733–739 nm, Φ_f values of 0.11–0.12 and τ_S values of 3.1–3.2 ns. At lower S_1 energy is **BC9**, with Q_y at 793 nm, $\Phi_f = 0.052$, and $\tau_S = 2.2$ ns. At lowest S_1 energy is **BC10** with Q_y at 818 nm, $\Phi_f = 0.036$, and $\tau_S = 1.8$ ns. The average Φ_T value for all these bacteriochlorins is 0.65, which is modestly greater than the average of 0.52 found for the set of ~30 analogues.[57] The general decrease in $\tau_S = 1/(k_f + k_{ic} + k_{isc})$ and $\Phi_f = k_f \bullet \tau_S$ values with decreasing S_1 energy is due in part to an increasing rate constant for $S_1 \rightarrow S_0$ internal conversion (k_{ic}) associated with the energy-gap law of nonradiative decay.[61] However, such effects are sufficiently modest that even the bacteriochlorin with the lowest S_1 energy (1.51 eV) and the longest-wavelength Q_y band (818 nm) has an excited-state lifetime that is sufficiently long (~2 ns) to drive efficient energy- (and charge-) transfer process in biohybrid architectures.

The photophysical properties of the bacteriochlorins with the bioconjugatable iodoacetamide (**BC6**) or maleimide (**BC1-4**) group were also characterized to facilitate comparisons with the benchmarks. The conjugates **BC1-P1** and **BC2-P1** were studied previously and the Φ_f and τ_S values determined in aqueous detergent (with no BChl *a* added to promote assembly formation).[18] The maleimide-terminated bacteriochlorins (in toluene or peptide-attached and in aqueous buffer) generally have Φ_f and τ_S values comparable to those of the benchmark in toluene (Table 1).

Table 1. Photophysical data for diverse bacteriochlorins.[a]

Cmpd	Linker group[b]	Solvent	λB_y abs (nm)	λB_x abs (nm)	λQ_x abs (nm)	λQ_y abs (nm)	λQ_y em (nm)	I_{Qy}/I_B	Φ_f[c]	τ_s[d] (ns)	Φ_T[e]
BC1	Maleimide	Toluene	349	370	508	713	715	0.74	0.16	4.8	0.67
BC1-P1[f]		Aqueous[g]	348	370	508	712	714	0.85	0.10	4.7	
BC7	Carboxy	Methanol	345	366	504	707	710	0.53	0.14	4.7	0.63
BC2	Maleimide	Toluene	357	377	516	729	735	0.84	0.18	3.7	0.56
BC2-P1[f]		Aqueous[g]	357	375	516	730	744	0.73	0.19	4.2	
BC8	None	Toluene	357	377	516	729	737	0.85	0.20	4.3	0.51
BC3	Maleimide	Toluene	370	407	549	792	800	1.01	0.070	1.9	0.54
BC9	None	Toluene	371	407	550	793	798	1.02	0.052	2.2	0.79
BC4	Maleimide	Toluene	359	408	545	818	825	1.15	0.052	1.4	0.34
BC10	None	Toluene	358	408	544	818	823	1.28	0.036	1.8	0.51
BC5	Formyl	Toluene	352	359	513	733	739	0.87	0.12	3.2	0.80
BC11	None	Toluene	352	372	502	734	739	1.25	0.11	3.1	0.55
BC12	None	Toluene	351	373	505	739	745	1.03	0.12	3.1	0.68
BC6	Iodide	Toluene	342	367	491	719	721	0.95	0.082	2.4	0.65
BC6-P1		Aqueous[g]	341	366	490	717	719	0.83	0.001[h]	0.04[h]	
BC13	None	Toluene	342	367	491	718	722	0.93	0.11	3.8	0.59

[a]All studies at room temperature. [b]Terminating group on the linker for bioconjugation (see Chart 2). [c]Fluorescence quantum yield. [d]Singlet excited-state lifetime typically measured by both fluorescence and transient absorption and the results averaged. [e]Yield of the intersystem crossing to the triplet excited state (e.g., the triplet yield). The value for **BC7** was measured in THF. [f]Data from ref. 18. [g]Potassium phosphate buffer (100 mM, pH = 7.5) containing 0.66% octyl glucoside. [h]The Φ_f and τ_S values listed are the smallest values found for different preparations. The highest Φ_f value found is 0.04. For all preparations, the singlet excited-state decay profiles have components ~0.04 ns and ~3 ns measured by transient absorption and ≤0.3 ns and ~3 ns measured by fluorescence (with lower time resolution), with the amplitude ratio depending on sample. The shortest lifetime value for the conjugate was used for calculation of the energy-transfer efficiency in the biohybrid complex.

The iodoacetamide-terminated bacteriochlorin **BC6** in toluene has somewhat reduced Φ_f and τ_S values compared to the benchmark **BC13** in the same solvent (0.082 versus 0.11; 2.4 versus 3.8 ns). These values together with the respective yields of intersystem crossing to the triplet excited state (0.65 and 0.59) suggest a contribution from a modest (iodine) heavy atom effect to increase k_{isc}. For the **BC6-P1** conjugate in aqueous detergent solution, the Φ_f value is reduced to 0.001. The singlet decay profile is dominated (90%) by a 0.04 ns component with a minor ~3 ns component as determined by transient absorption spectroscopy; in agreement with values of ≤0.3 ns and ~3 ns measured by fluorescence (with lower time resolution). The amplitude ratio of the slow to fast lifetime components and the Φ_f value depends on preparation. The shorter Φ_f and τ_S values may reflect quenching of the bacteriochlorin by the peptide and the longer values either a bacteriochlorin–peptide conformer with effectively no quenching or free chromophore. Regardless, as described below, the excited-state lifetime is sufficiently long to support a near-quantitative energy-transfer efficiency in oligomeric assemblies.

Bacteriochlorin and Bacteriochlorin–Peptide Conjugate Infrared Spectra. The synthetic analogs of the native antenna peptides, both with and without conjugated bacteriochlorin, were examined to ensure retention of helical structures (like the native β-peptide[62-64]). Fig. 4 shows single-reflection FTIR spectra of films of complexes on Au substrates. The complexes are bacteriochlorin–peptide conjugate **BC6-P1**, the native β-peptide, a synthetic native-length β-peptide that contains −14Cys in place of the native −14Met, a truncated 31mer β-peptide that contains −14Cys (**P1**), and myoglobin. Also shown are data for benchmark bacteriochlorin **BC13** in a KBr pellet. Myoglobin serves as a model for a prototypical α-helical system and exhibits two strong bands at 1664 and 1546 cm^{-1}, assignable to the amide I and amide II vibrations, respectively. The various peptides, with and without the

conjugated bacteriochlorins, exhibit similar spectra, consistent with an α-helical structure. Similar results were obtained in our prior study[18] except that data for bacteriochlorin–peptide conjugates were not available. Comparisons among the spectra indicate that the helical structure of the peptide is not compromised by truncation of the native-length peptide to give the 31mer, incorporation of a bacteriochlorin, or deposition on the metal surface. No bands associated with the bacteriochlorin are apparent in the IR spectra of the bacteriochlorin–peptide conjugate, which is not surprising given that there is a single chromophore attached to the protein and that all the amino acid residues collectively contribute to the IR spectrum. The higher optical density of the bacteriochlorin in a KBr pellet allows the resolution of bands associated with the chromophore, including various macrocycle skeletal vibrations (e.g., 1018, 1611 cm^{-1}) and the N-H stretching mode (3383 cm^{-1}). The high α-helical content of the peptides and their conjugated derivative in films is consistent with NMR studies of the native β-peptide in organic solvents[62,64] and in aqueous detergent solutions[63] as well as the crystal structures for LH2 of *Phs. molischianum*[13] Fig. 1) and *Rps. acidophila*[15] and the RC-LH1 complex[16] of *Rps. palustris*. IR spectra for the 31mer conjugates of bacteriochlorins **BC1** and **BC2**, along with their benchmarks **BC7** and **BC8**, gave results comparable to those for **BC6-P1** and **BC13** (see Fig. S1 in the Supplementary Information).

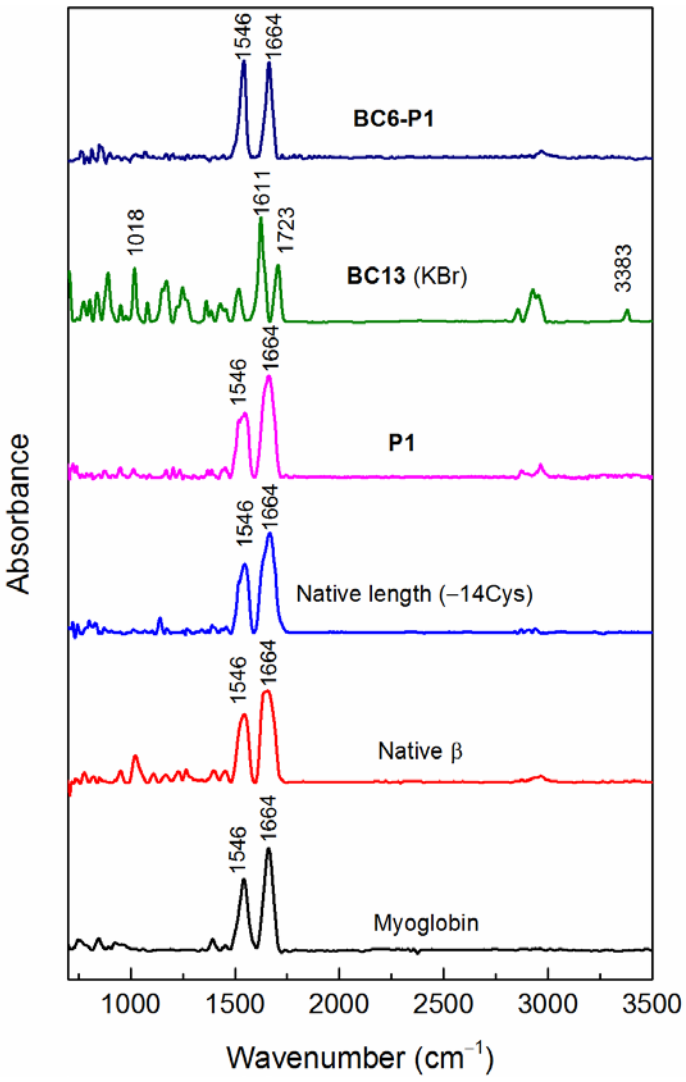

Fig. 4. Single-reflection FTIR spectra (from top to bottom) of bacteriochlorin–peptide conjugate **BC6-P1**, a truncated 31mer β-peptide that contains –14Cys (**P1**), a synthetic native-length β-peptide that contains –14Cys, the native β-peptide, and myoglobin in films on Au substrates (15 h deposition time). The spectrum (second from top) of the bacteriochlorin **BC13** (benchmark for **BC6**) in a KBr pellet is also shown.

Studies of Bacteriochlorin-Containing Biohybrid Assemblies

Formation of Oligomeric Biohybrid Antenna Complexes. The conditions for forming ββ-subunit (B820-type) and β-oligomeric (B850-type) complexes have been described previously[18,19,30,31] and are summarized in the Experimental Methods section. Three preparations

of bacteriochlorin-peptide conjugate **BC6-P1** were performed: β-oligomeric complexes were assembled from two of them (Preps I and III) and the other (Prep II) was used for methods development and in-depth chemical characterization. The different preparations were performed in order to refine procedures and ensure consistency in properties and energy-transfer characteristics of the biohybrid resulting complexes, which was achieved.

For preparations I and III of β-oligomeric complexes, a solution of **BC6-P1** was prepared in potassium phosphate buffer (100 mM, pH 7.5–7.6) containing 0.90–1.35% *n*-octyl β-D-glucopyranoside (OG). Increasing amounts of BChl *a* were then added. The resultant sample was then diluted to 0.75% OG and again to 0.66% OG to optimize the formation of the ββ-subunit complex, which has the Q_y band at ~820 nm. The sample was then chilled overnight at 4–8 °C to form the β-oligomeric complex, for which the Q_y band is shifted to 835–840 nm.

For clarity the oligomeric assembly is referred to as a B850-type complex, and is denoted **[(BC6-P1-BChl)$_2$]$_n$**. The control oligomeric complex that does not contain an appended synthetic bacteriochlorin is denoted **[(P1-BChl)$_2$]$_n$**. The steady-state and time-resolved absorption and emission studies described below were carried out on samples held at 9 °C to afford stable complexes. Prior studies[18] on the oligomeric assemblies of **BC1** and **BC2** were carried out at room temperature; **BC1** affords stable β_n-oligomeric complexes at room temperature whereas those of **BC2** are less stable and slowly dissociate to give ββ-subunits. Bacteriochlorin **BC6**, like **BC1** and **BC2**, form stable oligomeric assemblies at 9 °C.

Figure 5 shows the absorption spectra of conjugate **BC6-P1** (panel A) and β-oligomeric complex denoted **[(BC6-P1-BChl)$_2$]$_n$** from Prep III that were used for energy-transfer studies described in the following section. Virtually the same spectral characteristics and the same near-

quantitative (~90%) energy-transfer efficiency were obtained for the complexes from Prep I, for which photophysical data are shown in Supplementary Information.

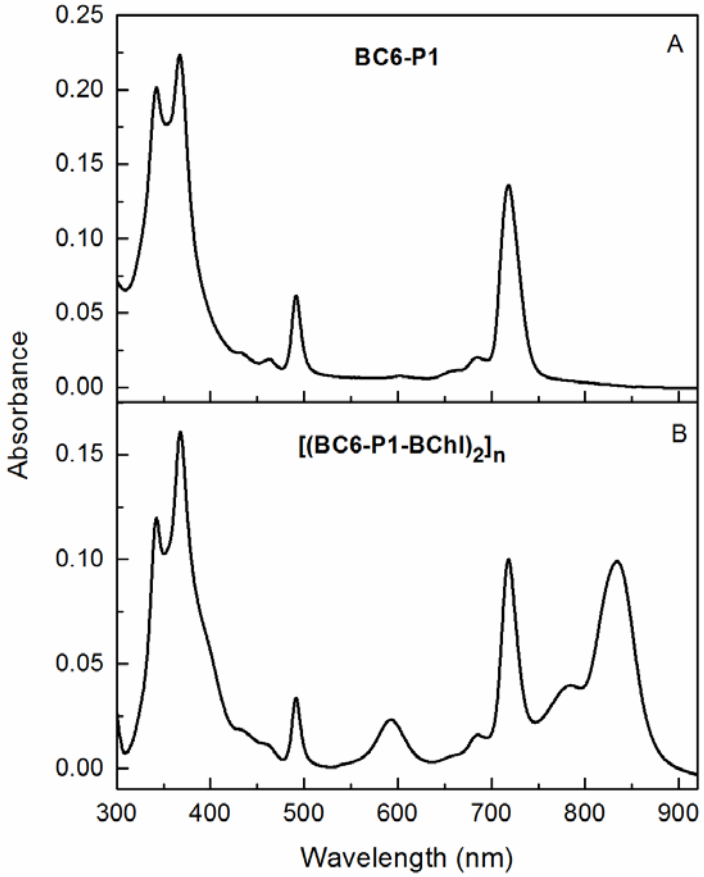

Fig. 5. Absorption spectrum of (A) bacteriochlorin–peptide conjugate **BC6-P1** and (B) oligomeric biohybrid **$[(BC6\text{-}P1\text{-}BChl)_2]_n$** from Prep III (corrected for light scattering) that were used for photophysical studies.

Energy-Transfer in Biohybrid Antenna Complexes. Highly efficient energy transfer was observed for the oligomeric biohybrid assembly containing bacteriochlorin **BC6**. The bacteriochlorin in toluene or on the peptide in aqueous buffer solution (Fig. 5A and Table 1) or in the oligomeric assembly (Fig. 5B) has the Q_y band at ~720 nm. Energy transfer from **BC6** to the BChl *a* array (denoted B850) in the biohybrid assembly **[(BC6-P1-BChl)$_2$]$_n$** to produce excited state B850* was probed by excitation spectra (Fig. 6A) of the fluorescence from B850 (Fig. 6B), and by quenching of the fluorescence from **BC6** (Fig. 6B). Fluorescence from B850* in this assembly is observed (as expected) at ~850 nm upon direct excitation of B850 (e.g., in the BChl *a* Q_x band at ~600 nm). Excitation of **BC6** in its Q_x band at 490 nm (or Q_y band at 718 nm) also produces B850* fluorescence for **[(BC6-P1-BChl)$_2$]$_n$** (Fig. 6B black) but not, as expected, for oligomer control **[(P1-BChl)$_2$]$_n$** that has no **BC6** (Fig. 6B, green). These results indicate that energy transfer occurs from excited **BC6** (BC6*) to B850 in the oligomeric biohybrid complex. The energy-transfer efficiency (Φ_{ENT}) was determined by comparing the amplitudes of the **BC6** features in the fluorescence-excitation versus absorptance (i.e., 1−transmittance) spectra (Fig. 6A, teal and red, respectively). A value of 0.85 is obtained from such comparisons in the **BC6** Q_y band (718 nm) and Q_x band (490 nm) when the two types of spectra are normalized in the B850 Q_x band at ~600 nm. A second determination gives Φ_{ENT} = 0.93 on the basis of the fluorescence yield of B850* fluorescence in the biohybrid complex **[(BC6-P1-BChl)$_2$]$_n$** (7×10^{-5}) compared to the oligomer control **[(BC6-P1)$_2$]$_n$** (0.001).

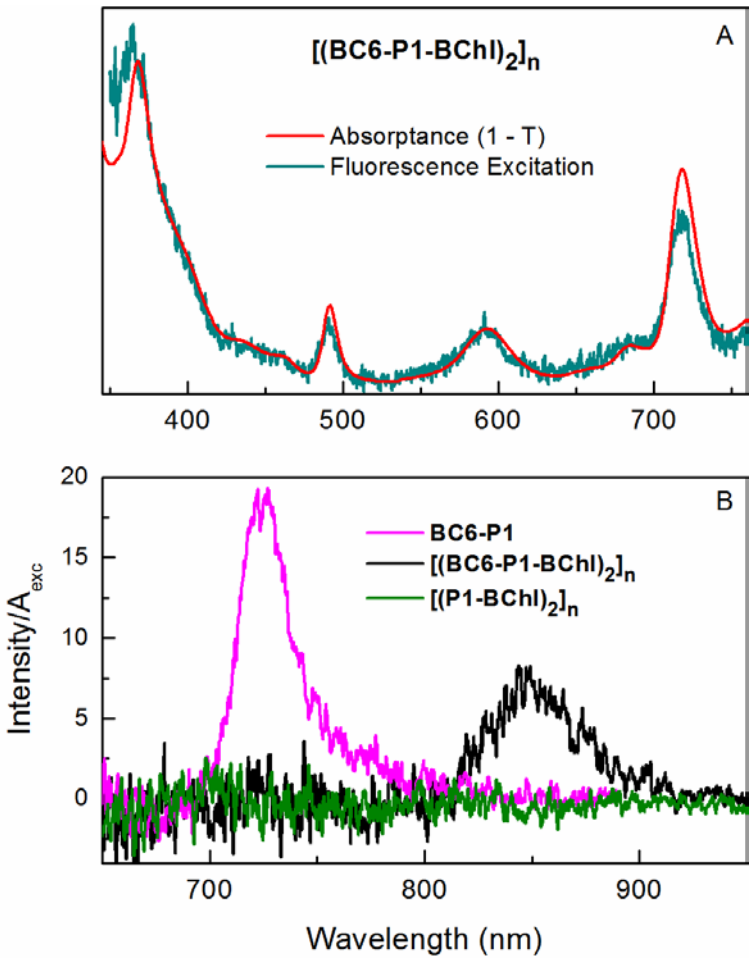

Fig. 6. Steady-state fluorescence data of oligomeric biohybrid **[(BC6-P1-BChl)$_2$]$_n$**, oligomeric control **[(P1-BChl)$_2$]$_n$**, and bacteriochlorin–peptide conjugate **BC6-P1** at 9 °C. (A) Absorptance (1–T) and fluorescence excitation spectra (λ_{det} = 850 nm) for the biohybrid normalized at the 590-nm BChl Q_x maximum. The absorptance spectrum was corrected for light scattering and the excitation spectrum for instrument parameters. (B) Fluorescence spectra of the biohybrid (black), control peptide conjugate (magenta) and oligomeric control (green), with the intensities divided by the absorbance at λ_{exc} = 490 nm.

A high efficiency of energy transfer is also reflected in the substantial quenching of the **BC6** fluorescence in biohybrid **[(BC6-P1-BChl)$_2$]$_n$** versus control peptide conjugate **BC6-P1**. The **BC6** fluorescence (~720 nm) elicited by excitation of this chromophore in the Q_x band (490 nm) in the biohybrid complex (Fig. 6B, black) is only a few percent of that in the control peptide conjugate (magenta); as expected, oligomeric control **[(P1-BChl)$_2$]$_n$** does not show any **BC6**

emission (Fig. 6B, green). The **BC6** fluorescence-quenching results indicate a high efficiency (0.95) of energy transfer from BC6* to the $BChl_n$ array (B850) in the biohybrid assembly.

Biohybrid complex **$[(BC6\text{-}P1\text{-}BChl)_2]_n$** and oligomer control **$[(P1\text{-}BChl)_2]_n$** were also studied using ultrafast transient absorption spectroscopy. As expected, excitation of the BChl *a* array (B850) in the oligomer control with an ~100-fs flash produces an instrument-limited (<300 fs) rise in the combined NIR B850 absorption bleaching and B850* stimulated emission. This instantaneous spectral response is shown in Fig. 7A and the instantaneous appearance of the signal at 845 nm is shown in the inset to Fig. 8 (blue). Subsequently, B850* in the oligomer control **$[(P1\text{-}BChl)_2]_n$** decays (Fig. 7B and 8) with time constants of 5, 30 and 300 ps. The time constants were determined from global analysis wherein the data at each wavelength were fit with a function consisting of the convolution of the instrument response plus three exponential terms (n = 1,2,3) of the form $A_n \bullet \exp(-t/\tau_n)$ plus a constant (ΔA_∞). Possible origins of the multiple B850* decay components have been described[18] and could involve (1) several forms of B850* if there is more than one conformer, each of which could have shorter inherent decay characteristics than ~3 ns for monomeric BChl* due to inter-BChl interactions, and (2) excited-state annihilation involving multiple excitations in the same biohybrid assembly or two assemblies in close proximity (analogous to considerations for LH2[65-67]). Contributions due to excited-state annihilation are expected to depend on the details of the experimental conditions such as the intensity of the excitation flashes.

In contrast, excitation of **BC6** (at 720 nm) in biohybrid complex **$[(BC6\text{-}P1\text{-}BChl)_2]_n$** results in a non-instantaneous rise in the formation of the combined B850 bleaching and B850* stimulated emission. The comparatively slow growth (τ = 1–2 ps) in the spectral features is shown in Fig. 7C and the slow rise in the signal at 845 nm is shown in the inset to Fig. 8 (red).

This lag in the formation of B850* reflects energy transfer from BC6* to the BChl *a* array (B850) in the biohybrid. [Subsequently B850* decays in the biohybrid **[(BC6-P1-BChl)$_2$]$_n$** primarily with a time constant of ~40 ps, with a smaller phase >100 ps.] A similar time (~2 ps) is found for decay bleaching in the Q_x band of **BC6** (not shown). The 1–2 ps kinetic component observed at these wavelengths and others across the visible and NIR regions reflects the BC6* lifetime in the biohybrid complex **[(BC6-P1-BChl)$_2$]$_n$**. Values in this range when compared with the shortest **BC6** excited-state lifetime component of 40 ps in control peptide **BC6-P1** give an energy-transfer efficiency of 0.95.

Thus, four complementary measurements are in excellent agreement in giving an efficiency of Φ_{ENT} = 0.9 for energy transfer from excited **BC6** to the BChl *a* array (B850) in biohybrid complex **[(BC6-P1-BChl)$_2$]$_n$**. The measurements (and Φ_{ENT} values) are (1) analysis of fluorescence-excitation versus absorptance spectra (0.85), (2) fluorescence yield in the biohybrid versus oligomeric control **[(P1-BChl)$_2$]$_n$** (0.93), (3) quenching for BC6* fluorescence in the biohybrid versus control peptide conjugate **BC6-P1** (0.95), and (4) **BC6** excited-state lifetime in the biohybrid versus control peptide conjugate (0.95).

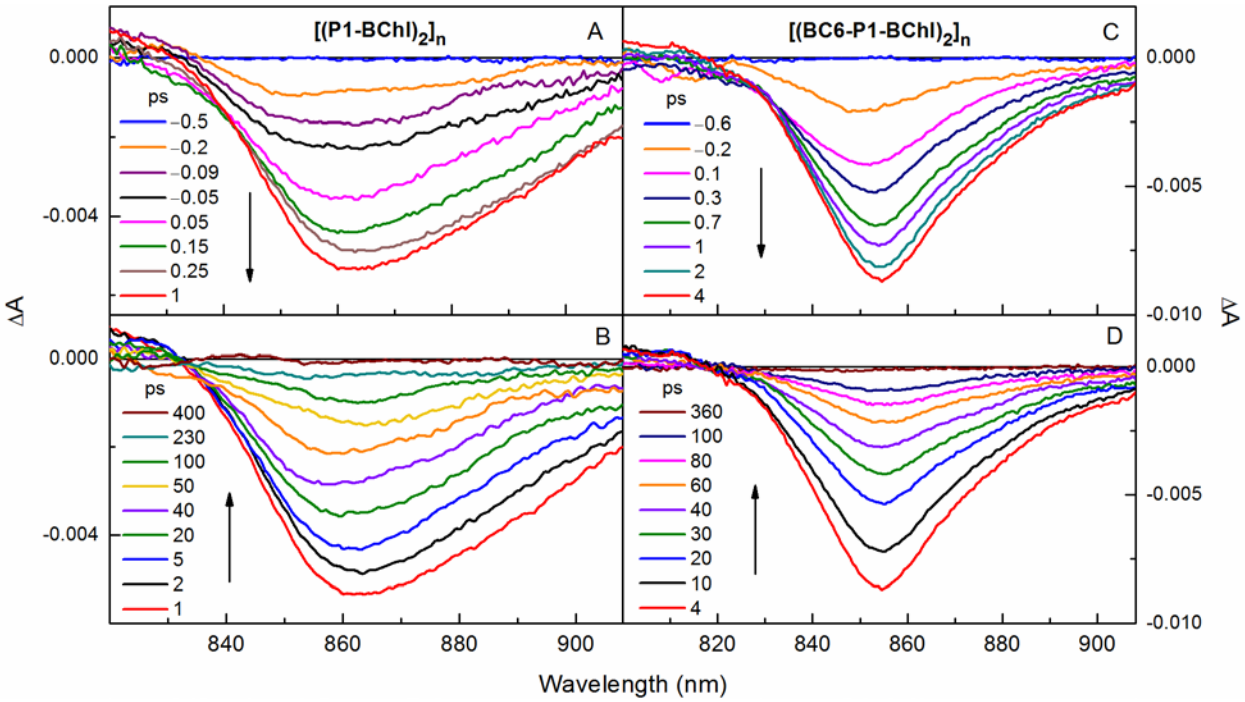

Fig. 7. NIR transient absorption spectra at 9 °C of the BChl *a* complex (B850) in oligomeric control **[(P1-BChl)$_2$]$_n$** using excitation at 590 nm (left panels) and oligomeric biohybrid **[(BC6-P1-BChl)$_2$]$_n$** using excitation of **BC6** at 720 nm (right panels). Panel (A) shows the instrument-limited rise and panel (B) the decay of the combined B850 bleaching and B850* stimulated emission for the oligomeric control. Panel (C) shows non-instrument-limited growth and panel (D) decay of the features for the biohybrid.

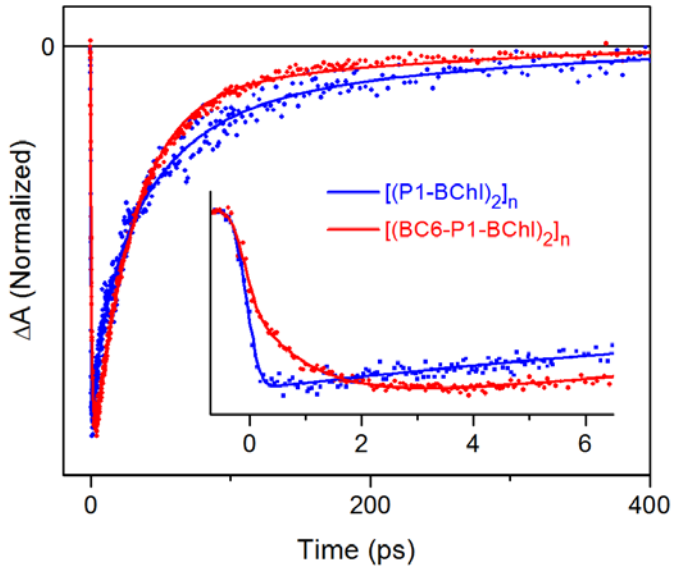

Fig. 8. Time-evolution of the bleaching/stimulated-emission (850 nm) for prep III of oligomeric biohybrid **[(BC6-P1-BChl)$_2$]$_n$** and oligomeric control **[(P1-BChl)$_2$]$_n$** at 9 °C. The inset shows the 1-2 ps growth of bleaching for the biohybrid and the instrument-limited rise for the control. The line through each data set is a fit to a function consisting of three exponentials plus a long-time constant convolved with the instrument response; see text for further details.

Analogous studies on the oligomeric biohybrid complex **[(BC2-P1-BChl)$_2$]$_n$**, which contains bacteriochlorin **BC2**, were carried out at 9 °C to stabilize the oligomeric complex, thereby complementing the prior work on the same construct carried out at room temperature.[18] The biohybrid containing **BC2** exhibits ≥90% energy transfer as deduced from analysis of steady-state fluorescence data and transient absorption data (see Supplementary Information). The efficient energy transfer observed herein for both **BC2** and **BC6** is attributed to the Förster dipole-dipole mechanism, where fluorescence of bacteriochlorins that absorb in the 700–840 nm spectral region overlaps either the Q_y origin transition or higher-energy vibronic components of the BChl *a* constituents of the ββ-subunit and β-oligomeric biohybrid assemblies.[18] The collective results show that the appended synthetic bacteriochlorin in the assemblies enhances solar coverage and exhibits highly efficient (≥90%) energy transfer to the native-like BChl *a* sites in the biohybrid architectures.

Outlook

The development of photosynthetic model systems that rival the natural systems in architectural complexity has long been stymied by the challenge of organizing large numbers of constituents. Such architectures typically have overall dimension spanning tens of nanometers yet require well-defined and tightly controlled organization of individual pigments at the few or even sub-Angstrom length scale. The challenge is perhaps most pronounced in the light-harvesting arena, where pigments in large numbers – from a few 10s to >1000 – must be deployed to gather sunlight and funnel excitation energy to the reaction centers, which are much fewer in number. Synthetic chemistry has made enormous strides over the past decades in the *de novo* construction of light-harvesting architectures but has generally fallen far short of the architectural elegance of the natural light-harvesting systems.

The biohybrid approach wherein natural constituents (or derivatives therefrom) are combined with synthetic components provides one strategy for overcoming the limitations of present synthetic chemistry while accommodating the objective of creating tailored artificial light-harvesting systems. In the present work, seven bioconjugatable bacteriochlorins were prepared by extension of established synthetic routes. The photophysical properties are generally comparable to those of benchmarks lacking the bioconjugation group, and generally are not appreciably altered upon attachment to a peptide. Oligomeric biohybrid architectures that contain such bacteriochlorins exhibit enhanced solar coverage compared to natural photosynthetic antenna complexes and show near-quantitative yields of energy transfer to the native-like BChl *a* target sites. Such multichromophore biohybrid assemblies are made possible by access to the suite of stable synthetic bacteriochlorins. The past lack of availability of such chromophores has resulted in only limited reports on bacteriochlorin-containing arrays (typically

dyads) for photochemical studies.[9] A key challenge to the ultimate success of the biohybrid approach entails the practical matter of learning how to handle and purify the synthetic peptide constructs, which in the case reported here are very hydrophobic. Approaches may include use of the full-length β-peptide (rather than the truncated, 31-mer employed herein), alternative purification methods, and/or more polar bacteriochlorins. Regardless, the self-assembly approach provides an intrinsic culling out of defective units and thereby affords a powerful paradigm for formation of elaborate multicomponent molecular architectures.[68] The ability to tune the optical properties of the biohybrid assemblies allows exploration of solar-conversion systems that extend the overall functional properties of the natural photosynthetic systems while maintaining proven, robust architectural characteristics.

Acknowledgment. This work was supported by the Photosynthetic Antenna Research Center (PARC), an Energy Frontier Research Center funded by the U.S. Department of Energy, Office of Science, Office of Basic Energy Sciences under Award Number DE-SC0001035. We thank Profs. Richard Cogdell and Neil Hunter for stimulating discussions, and Dr. Pu Qian and Prof. Neil Hunter for the absorption spectra shown in Fig. 2C. Mass spectra were obtained at the NCSU Department of Chemistry Mass Spectrometry Facility. Funding for the facility was obtained from the North Carolina Biotechnology Center and the NCSU Department of Chemistry.

Experimental Section

General Methods. ^{1}H NMR spectra (300 MHz) and ^{13}C NMR spectra (100 MHz) were collected at room temperature in $CDCl_3$ unless noted otherwise. Silica gel (40 μm average particle size) was used for column chromatography. All solvents were reagent grade and were used as received unless noted otherwise. THF was freshly distilled from sodium/benzophenone ketyl. Laser-desorption mass spectrometry (LD-MS) was performed without any matrix or with a matrix (MALDI-MS) of 1,4-bis(5-phenyl-2-oxaxol-2-yl)benzene (POPOP).[69] Electrospray ionization mass spectrometry (ESI-MS) data are reported for the molecular ion, protonated molecular ion, or sodium-cationized molecular ion. Known bacteriochlorins **BC5**,[53] **MeOBC-Br**[15] (ref. 49), **MeOBC-EtEs-Br**[15] (ref. 49), and **HBC-EtEs-Br**[15] (ref. 55) were prepared according to literature procedures, as were bacteriochlorin–imides **BC9** and **BC10**.[55]

Formation of Biohybrid Assemblies. A synthetic peptide (Bio-Synthesis, Lewisville, TX) was used that contained 31 amino acids with a sequence identical to that of the 31 amino acids at the carboxy terminus of the β-peptide of LH1 of *Rb. sphaeroides* except for the substitution of a Cys in place of Met-14 (~80% purity). Three preparations (I–III) of bacteriochlorin-peptide conjugate **BC6-P1** were performed: Preps I and III were used to prepare β-oligomeric complexes whereas Prep II was used for methods development and in-depth chemical characterization. For Prep I, BChl *a* with a geranyl-geraniol esterifying alcohol was isolated from membranes of the G9 carotenoidless mutant of *Rds. rubrum*;[30] for Prep III, BChl *a* with a phytol esterifying alcohol was obtained from Sigma. *n*-Octyl *β*-D-glucopyranoside (OG) was used as received from Sigma. Bacteriochlorin **BC6** was conjugated to the peptide in aqueous DMF to afford a 1:1 complex of bacteriochlorin–peptide using an extinction coefficient of 120,000 $M^{-1}cm^{-1}$ for the bacteriochlorin (see Supplementary Information). Protein

concentrations were determined by dissolving the bacteriochlorin–peptide conjugate (**BC6-P1**) in 20 μL of hexafluoroacetone trihydrate followed by 1.00 mL of 2:1 (v/v) acetonitrile/2-propanol containing 0.1% TFA,[30] recording the absorption spectrum, and calculating the concentration assuming an extinction coefficient at 287 nm of 3400 $M^{-1}cm^{-1}$ per Trp residue.[70] Where necessary, a correction was made for the absorbance of the conjugated bacteriochlorin. Aliquots were dried under argon and then vacuum.

The conditions for forming ββ-subunit (B820-type) and β-oligomeric (B850-type) complexes have been previously described.[18,19,30,31] In general, a solution of 0.05–0.20 mg of peptide in 5–10 μL of hexafluoroacetone trihydrate was treated with 0.50 mL of 4.5% (w/v) OG in 50 mM potassium phosphate buffer (pH 7.5) followed by 2.0 mL of 100 mM potassium phosphate buffer (pH 7.5) to bring the OG concentration to 0.90%. Increasing amounts of BChl *a* were then added to the sample by injecting 5–20 μL of a degassed acetone solution to approach the same BChl *a* concentration as that of the peptide. In general, this resulted in a combined absorbance ($A_{780nm} + A_{820nm}$) between 0.1 and 0.2. The sample was then diluted to 0.75% OG and again to 0.66% OG to optimize ββ-subunit (B820) formation. After each dilution, an absorption spectrum was recorded. In some cases, complete formation of the B820 complex required cooling the sample to about 6 °C for 1 h. For formation of β-oligomeric (B850) complexes, the sample was kept overnight at 4–8 °C, after which a final absorption spectrum was taken. The B850-type complexes were prepared at Northwestern University or North Carolina State University and shipped overnight on ice (in their B850 state) to Washington University or University of California at Riverside where they were stored at 4–8 °C for studies at 9 °C.

FTIR Spectroscopy. The FTIR spectra of myoglobin, the peptides, and the bacteriochlorin–peptide conjugates were collected at room temperature on solid films deposited

on a Au substrate (200 nm Au atop a 20 nm Cr adhesion layer on a Si substrate). The films were prepared by depositing 50 μL of the sample in buffer solution onto the substrate contained in a sealed vial under Ar. The deposited droplet was then allowed to sit on the substrate for 15 h after which the substrate was washed three times with water and dried under a stream of argon. The spectra of the benchmark bacteriochlorins were collected at room temperature on solids in KBr pellets.

The FTIR spectrometer was a Bruker Tensor 27 equipped with a Harrick Scientific Ge attenuated total reflection accessory (GATR™, 65° incidence angle relative to the surface normal). The substrates were placed in contact with the flat surface of a semispherical Ge crystal that serves as the optical element. The IR spectra were collected with *p*-polarized light using a liquid-nitrogen cooled medium-bandwidth (600–4000 cm^{-1}) MCT detector, averaging over 256 scans; the spectral resolution was 4 cm^{-1}. The spectra of the films were referenced against a bare Au substrate. The Ge crystal was cleaned with neat 2-butanone before every experiment, and the GATR™ accessory was purged with dry N_2 during data acquisition.

Static and Time-Resolved Optical Spectroscopy. Static absorption measurements employed a Varian Cary 50 or 100 or Shimadzu UV-1800 spectrometer. Static fluorescence measurements employed a Spex Fluorolog Tau 2 or PTI Quantamaster 40 spectrofluorometer. Fluorescence lifetimes were obtained via decay measurements using a Photon Technology International LaserStrobe TM-3, composed of a GL-3300 nitrogen laser with a GL-302 dye laser unit and time-correlate-single-photon-counting detection. The apparatus has an approximately Gaussian instrument response function with a full-width-at-half-maximum of ~1 ns. Excitation pulses were provided by the nitrogen-pumped dye laser (350-650 nm). Static emission measurements employed 0.2-nm data intervals and typical monochromator bandwidths of 2–4

nm. Most measurements (500 nm to ≥1100 nm) utilized a setup consisting of an InGaAs detector with lock-in detection and excitation light chopped at 30 Hz; the detection monochromator bandwidth was increased to up to 8 nm for some measurements of weak B820 NIR emission. Some experiments (450–850 nm) utilized a setup containing a Hamamatsu R928 photomultiplier tube. For both setups, emission spectra were corrected for detection-system spectral response. The fluorescence yield determinations, depending on the absorption and emission wavelengths, employed a number of different standards whose yields were cross-checked with respect to each other. These standards were (1) free base *meso*-tetraphenylporphyrin (**FbTPP**) in nondegassed toluene, for which $\Phi_f = 0.070$ was established with respect to the zinc chelate **ZnTPP** in nondegassed toluene ($\Phi_f = 0.030$),[71] consistent with prior results on **FbTPP**,[72] (2) 8,8,18,18-tetramethylbacteriochlorin[57] in argon-purged toluene, for which $\Phi_f = 0.14$ was established with respect to **FbTPP** and chlorophyll *a* (**Chl *a***) in deoxygenated benzene[73] or toluene[74] (both with $\Phi_f = 0.325$), and (3) 2,12-di-*p*-tolyl-8,8,18,18-tetramethylbacteriochlorin[48] in argon-purged toluene for which $\Phi_f = 0.16$ was established as noted above for 8,8,18,18-tetramethylbacteriochlorin (this value is updated from 0.18 reported previously[57]), and (4) BChl *a* in toluene (0.12,[75] which is similar to values reported in other solvents[76,77]). Measurements of fluorescence spectra, fluorescence excitation spectra, fluorescence quantum yields, and fluorescence lifetimes employed samples having an absorbance (A) ≤ 0.1 at the excitation wavelength(s). Under these conditions, the pertinent regions (e.g., 450–650 nm) of the absorption and absorptance spectra have the same shapes; the latter spectrum is the most relevant for quantitative comparisons with the excitation spectra to estimate the energy-transfer efficiencies in the biohybrid complexes. Samples of bacteriochlorin (in toluene) were typically purged (bubbled) with argon in septum-stoppered cuvettes. Samples

of the bacteriochlorin–peptide and biohybrid complexes in detergent solutions were typically purged by passing argon over the stirred solution.

Time-resolved pump-probe absorption experiments were carried out using a Helios femtosecond transient absorption spectrometer (Ultrafast Systems) coupled to a femtosecond laser system (Newport/Spectra-Physics). The one-box Solstice amplified ultrafast laser system consists of a Mai-Tai femtosecond oscillator whose output goes to a Spitfire Pro XP regenerative amplifier that is pumped by an Empower diode-pumped solid state pulsed green laser. The amplifier produces 800 nm pulses (~3.5 mJ, ~90 fs) at 1 kHz. The output beam is split into two and used to generate (i) the pump beam (90%) in a Topas-C optical parametric amplifier (Light Conversion, Lithuania) and (ii) probe pulses (10%) for the Helios transient-absorption spectrometer. The pump (excitation) pulses pass through a depolarizer to provide isotropic excitation of the sample and avoid pump-probe polarization effects. Individual ΔA spectra are acquired using excitation light chopped at 0.5 kHz (to provide alternate accumulations of the probe light with and without excitation) and averaged over 1–5 s (typically 2 s). Final ΔA spectra represent the average of 1000 such individual spectra. For the experiments reported here, the excitation pulses (typically of energy 0.5 μJ/pulse) were adjusted to have a spot diameter of 1 mm.

The samples were typically excited near the peaks of the main absorption features. For example, for bacteriochlorin **BC6**, and the peptide or biohybrids containing that chromophore, experiments were performed that utilized excitation in either the Q_x band (~540 nm) or the Q_y band (~720 nm). Samples were contained in 2-mm or 1-cm path cuvettes and were mixed continuously using a magnetic micro-stirrer to minimize photo-degradation. Control samples

consisting of a bacteriochlorin–peptide or biohybrid antenna complex typically had an absorbance of ≤0.15 in the main absorbance feature.

The Φ_T (triplet yield) values were obtained using a transient-absorption technique in which the extent of bleaching of the ground-state Q_x and Q_y bands due to the lowest singlet excited state was measured immediately following an 0.1 ps flash (in the Q_x or Q_y bands) and compared with that due to the lowest triplet excited state at the asymptote of the singlet excited-state decay. For the Q_y region, the contribution of stimulated emission was taken into account. For both states and spectral regions, the extent of bleaching in the presence of excited-state absorption in the transient difference spectra was determined by various methods (to encompass a reasonable range of spectral shapes) including Gaussian fitting, integrations, and linear interpolation of the excited-state absorption across the ground-state bleaching region. An average value of the triplet yields obtained by these methods is reported for each bacteriochlorin.

Electronic supplementary information (ESI) available: preparation and characterization data of bacteriochlorin–peptide conjugate **BC6-P1**; selected spectroscopic data for **BC1-P1**, **BC2-P1**, and **BC6-P1** and oligomers thereof; chemical characterization data for 15 synthetic bacteriochlorins. See DOI: 10.1039/c2scXXXX.

References

1 M. Gabrielsen, A. T. Gardiner and R. J. Cogdell, in *The Purple Phototrophic Bacteria*, ed. C. N. Hunter, F. Daldal, M. C. Thurnauer and J. T. Beatty, Springer, Dordrecht, The Netherlands; Advances in Photosynthesis and Respiration; 2008, pp 135–153.

2 P. A. Bullough, P. Qian and C. N. Hunter, in *The Purple Phototrophic Bacteria*, ed. C. N. Hunter, F. Daldal, M. C. Thurnauer and J. T. Beatty, Springer, Dordrecht, The Netherlands; Advances in Photosynthesis and Respiration; 2008, pp 155–179.

3 D. Mauzerall and N. L. Greenbaum, *Biochim. Biophys. Acta,* 1989, **974**, 119–140.

4 P. D. Harvey, in *The Porphyrin Handbook*, ed. K. M. Kadish, K. M. Smith and R. Guilard, Academic Press, San Diego, CA, 2003, Vol. 18, pp 63–250.

5 N. Aratani and A. Osuka, in *Handbook of Porphyrin Science,* ed. K. M. Kadish, K. M. Smith and R. Guilard, World Scientific Publishing Co., Singapore, 2010, Vol. 1, pp 1–132.

6 P. D. Harvey, C. Stern and R. Guilard, in *Handbook of Porphyrin Science*, ed. K. M. Kadish, K. M. Smith and R. Guilard, World Scientific Publishing Co., Singapore, 2011, Vol. 11, pp 1–179.

7 N. Aratani and A. Osuka, *Macromol. Rapid Commun*., 2001, **22**, 725–740.

8 N. Aratani, D. Kim and A. Osuka, *Acc. Chem. Res.,* 2009, **42**, 1922–1934.

9 J. S. Lindsey, O. Mass and C.-Y. Chen, *New J. Chem*., 2011, **35***,* 511–516.

10 G. M. Hasselman, D. F. Watson, J. S. Stromberg, D. F. Bocian, D. Holten, J. S. Lindsey and G. J. Meyer, *J. Phys. Chem. B,* 2006, **110**, 25430–25440.

11 J. R. Stromberg, A. Marton, H. L. Kee, C. Kirmaier, J. R. Diers, C. Muthiah, M. Taniguchi, J. S. Lindsey, D. F. Bocian, G. J. Meyer and D. Holten, *J. Phys. Chem. C,* 2007, **111**, 15464–15478.

12 P. A. Loach and P. S. Parkes-Loach, in *The Purple Phototrophic Bacteria*, ed. C. N. Hunter, F. Daldal, M. C. Thurnauer and J. T. Beatty, Springer, Dordrecht, The Netherlands; Advances in Photosynthesis and Respiration; 2008, pp 181–198.

13 J. Koepke, X. Hu, C. Muenke, K. Schulten and H. Michel, *Structure,* 1996, **4**, 581–597.

14 S. J. Jamieson, P. Wang, P. Qian, J. Y. Kirkland, M. J. Conroy, C. N. Hunter and P. A. Bullough, *EMBO J.,* 2002, **21**, 3927–3935.

15 M. Z. Papiz, S. M. Prince, T. Howard, R. J. Cogdell and N. W. Isaacs, *J. Mol. Biol.,* 2003, **326**, 1523–1538.

16 A. W. Roszak, T. D. Howard, J. Southall, A. T. Gardiner, C. J. Law, N. W. Isaacs and R. J. Cogdell, *Science,* 2003, **302**, 1969–1972.

17 V. Slouf, P. Chábera, J. D. Olsen, E. C. Martin, P. Qian, C. N. Hunter and T. Polivka, *Proc. Natl. Acad. Sci. U.S.A.,* 2012, **109**, 8570–8575.

18 J. W. Springer, P. S. Parkes-Loach, K. R. Reddy, M. Krayer, J. Jiao, G. M. Lee, D. M. Niedzwiedzki, M. A. Harris, C. Kirmaier, D. F. Bocian, J. S. Lindsey, D. Holten and P. A. Loach, *J. Am. Chem. Soc.,* 2012, **134**, 4589−4599.

19 P. A. Loach and P. S. Parkes-Loach, in *Anoxygenic Photosynthetic Bacteria*, ed. R. E. Blankenship, M. T. Madigan and C. E. Bauer, Kluwer Academic Publishers, Boston, MA, 1995, pp 437–471.

20 C. J. Law, J. Chen, P. S. Parkes-Loach and P. A. Loach, *Photosynth. Res.,* 2003, **75**, 193–210.

21 H. Paulsen, in *Chlorophylls and Bacteriochlorophylls: Biochemistry, Biophysics, Functions and Applications*, ed. B. Grimm, R. J. Porra, W. Rüdiger and H. Scheer, Springer, Dordrecht, The Netherlands, 2006, pp 375–385.

22 H. Kitagishi, K. Oohora, H. Yamaguchi, H. Sato, T. Matsuo, A. Harada and T. Hayashi, *J. Am. Chem. Soc.,* 2007, **129**, 10326−10327.

23 K. Oohora, A. Onoda, H. Kitagishi, H. Yamaguchi, A. Harada and T. Hayashi, *Chem. Sci.*, 2011, **2**, 1033–1038.

24 J. K. Staples, K. M. Oshaben and W. S. Horne, *Chem. Sci*., 2012, **3**, 3387–3392.

25 H. Mihara, K.-Y. Tomizaki, T. Fujimoto, S. Sakamoto, H. Aoyagi and N. Nishino, *Chem. Lett.,* 1996, 187−188.

26 K. Tomizaki, T. Murata, K. Kaneko, A. Miike and N. Nishino, *J. Chem. Soc*., *Perkin Trans. 2,* 2000, 1067–1074.

27 D. Noy, C. C. Moser and P. L. Dutton, in *Chlorophylls and Bacteriochlorophylls: Biochemistry, Biophysics, Functions and Applications*, ed. B. Grimm, R. J. Porra, W. Rüdiger and H. Scheer, Springer, Dordrecht, The Netherlands, 2006, pp 349–363.

28 M. Nango, in *Chlorophylls and Bacteriochlorophylls: Biochemistry, Biophysics, Functions and Applications*, ed. B. Grimm, R. J. Porra, W. Rüdiger and H. Scheer, Springer, Dordrecht, The Netherlands, 2006, pp 365–373.

29 I. Cohen-Ofri, M. van Gastel, J. Grzyb, A. Brandis, I. Pinkas, W. Lubitz and D. Noy, *J. Am. Chem. Soc.,* 2011, **133**, 9526–9535.

30 K. A. Meadows, K. Iida, K. Tsuda, P. A. Recchia, B. A. Heller, B. Antonio, M. Nango and P. A. Loach, *Biochemistry,* 1995, **34**, 1559–1574.

31 K. A. Meadows, P. S. Parkes-Loach, J. W. Kehoe and P. A. Loach, *Biochemistry,* 1998, **37**, 3411–3417.

32 J. M. Sutton, N. Fernandez and R. W. Boyle, *J. Porphyrins Phthalocyanines,* 2000, **4**, 655–658.

33 J. M. Sutton, O. J. Clarke, N. Fernandez and R. W. Boyle, *Bioconjugate Chem*., 2002, **13**, 249–263.

34 J. R. McCarthy, J. Bhaumik, N. Merbouh and R. Weissleder, *Org. Biomol. Chem.,* 2009, **7**, 3430–3436.

35 S. Singh, A. Aggarwal, S. Thompson, J. P. C. Tomé, X. Zhu, D. Samaroo, M. Vinodu, R. Gao and C. M. Drain, *Bioconjugate Chem*., 2010, **21**, 2136–2146.

36 Z. Yu and M. Ptaszek, *Org. Lett.,* 2012, **14**, 3708–3711.

37 V. M. Alexander, K. Sano, Z. Yu, T. Nakajima, P. L. Choyke, M. Ptaszek and H. Kobayashi, *Bioconjugate Chem.,* 2012, **23**, 1671–1679.

38 Y. Chen, G. Li and R. K. Pandey, *Curr. Org. Chem.,* 2004, **8**, 1105–1134.

39 A. M. G. Silva, A. C. Tomé, M. G. P. M. S. Neves, A. M. S. Silva and J. A. S. Cavaleiro, *J. Org. Chem.,* 2005, **70**, 2306–2314.

40 M. Galezowski and D. T. Gryko, *Curr. Org. Chem.,* 2007, **11**, 1310–1338.

41 M. A. Grin, A. F. Mironov and A. A. Shtil, *Anti-Cancer Agents Med. Chem.,* 2008, **8**, 683–697.

42 A. C. Tomé, M. G. P. M. S. Neves and J. A. S. Cavaleiro, *J. Porphyrins Phthalocyanines,* 2009, **13**, 408–414.

43 N. A. M. Pereira, S. M. Fonseca, A. C. Serra, T. M. V. D. Pinho e Melo and H. D. Burrows, *Eur. J. Org. Chem*., 2011, 3970–3979.

44 J. M. Dąbrowski, K. Urbanska, L. G. Arnaut, M. M. Pereira, A. R. Abreu, S. Simões and G. Stochel, *ChemMedChem,* 2011, **6**, 465–475.

45 A. Kozyrev, M. Ethirajan, P. Chen, K. Ohkubo, B. C. Robinson, K. M. Barkigia, S. Fukuzumi, K. M. Kadish and R. K. Pandey, *J. Org. Chem.,* 2012, **77**, 10260–10271.

46 L. P. Samankumara, S. Wells, M. Zeller, A. M. Acuña, B. Röder and C. Brückner, *Angew. Chem. Int. Ed.,* 2012, **51**, 5757–5760.

47 C. Brückner, L. Samankumara and J. Ogikubo, in *Handbook of Porphyrin Science*, ed. K. M. Kadish, K. M. Smith and R. Guilard, World Scientific, Singapore, 2012, Vol. 17, pp 1–112.

48 H.-J. Kim and J. S. Lindsey, *J. Org. Chem.,* 2005, **70**, 5475–5486.

49 M. Krayer, M. Ptaszek, H.-J. Kim, K. R. Meneely, D. Fan, K. Secor and J. S. Lindsey, *J. Org. Chem*., 2010, **75**, 1016–1039.

50 D. Fan, M. Taniguchi and J. S. Lindsey, *J. Org. Chem.,* 2007, **72**, 5350–5357.

51 M. Taniguchi, D. L. Cramer, A. D. Bhise, H. L. Kee, D. F. Bocian, D. Holten and J. S. Lindsey, *New J. Chem.,* 2008, **32**, 947–958.

52 K. E. Borbas, C. Ruzié and J. S. Lindsey, *Org. Lett.,* 2008, **10**, 1931–1934.

53 C. Ruzié, M. Krayer, T. Balasubramanian and J. S. Lindsey, *J. Org. Chem*., 2008, **73**, 5806–5820.

54 C. Ruzié, M. Krayer and J. S. Lindsey, *Org. Lett.,* 2009, **11**, 1761–1764.

55 M. Krayer, E. Yang, J. R. Diers, D. F. Bocian, D. Holten and J. S. Lindsey, *New J. Chem*., 2011, **35**, 587–601.

56 O. Mass and J. S. Lindsey, *J. Org. Chem.,* 2011, **76**, 9478–9487.

57 E. Yang, C. Kirmaier, M. Krayer, M. Taniguchi, H.-J. Kim, J. R. Diers, D. F. Bocian, J. S. Lindsey and D. Holten, *J. Phys. Chem. B,* 2011, **115**, 10801–10816.

58 H. Zuber and R. J. Cogdell in *Anoxygenic Photosynthetic Bacteria*, ed. R. E. Blankenship, M. T. Madigan and C. E. Bauer, Kluwer Academic Publishers, Boston, MA, 1995, pp 315–348.

59 K. J. Glover, P. M. Martini, R. R. Vold and E. A. Komives, *Anal. Biochem.,* 1999, **272**, 270−274.

60 F. Shen, Y.-C. Huang, S. Tang, Y.-X. Chen and L. Liu, *Isr. J. Chem.,* 2011, **51**, 940−952.

61 J. B. Birks, *Photophysics of Aromatic Molecules*, Wiley-Interscience, London, 1970, pp 142–192.

62 M. J. Conroy, W. H. J. Westerhuis, P. S. Parkes-Loach, P. A. Loach, C. N. Hunter and M. P. Williamson, *J. Mol. Biol.,* 2000, **298**, 83–94.

63 P. L. Sorgen, S. M. Cahill, R. D. Krueger-Koplin, S. T. Krueger-Koplin, C. C. Schenck and M. E. Girvin, *Biochemistry,* 2002, **41**, 31–41.

64 Z.-Y. Wang, K. Gokan, M. Kobayashi and T. Nozawa, *J. Mol. Biol.,* 2005, **347**, 465–477.

65 C. N. Hunter, H. Bergström, R. van Grondelle and V. Sundström, *Biochemistry,* 1990, **29**, 3203–3207.

66 A. Schubert, A. Stenstam, W. J. D. Beenken, J. L. Herek, R. J. Cogdell, T. Pullerits and V. Sundström, *Biophys. J.,* 2004, **86**, 2363–2373.

67 T. Pflock, M. Dezi, G. Venturoli, R. Cogdell, J. Köhler and S. Oellerich, *Photosynth. Res.* 2008, **95**, 291–298.

68 J. S. Lindsey, *New J. Chem.,* 1991, **15**, 153–180.

69 N. Srinivasan, C. A. Haney, J. S. Lindsey, W. Zhang and B. T. Chait, *J. Porphyrins Phthalocyanines,* 1999, **3**, 283−291.

70 P. S. Parkes-Loach, J. R. Sprinkle and P. A. Loach, *Biochemistry*, 1988, **27**, 2718–2727.
71 P. G. Seybold and M. Gouterman, *J. Mol. Spectrosc.,* 1969, **31**, 1–13.
72 A. T. Gradyushko, A. N. Sevchenko, K. N. Solovyov and M. P. Tsvirko, *Photochem. Photobiol.,* 1970, **11**, 387–400.
73 G. Weber and F. W. J. Teale, *Trans. Faraday Soc.,* 1957, **53**, 646–655.
74 O. Mass, M. Taniguchi, M. Ptaszek, J. W. Springer, K. M. Faries, J. R. Diers, D. F. Bocian, D. Holten and J. S. Lindsey, *New J. Chem*., 2011, **35**, 76–88.
75 C.-Y. Chen, E. Sun, D. Fan, M. Taniguchi, B. E. McDowell, E. Yang, J. R. Diers, D. F. Bocian, D. Holten and J. S. Lindsey, *Inorg. Chem.,* 2012, **51***,* 9443–9464.
76 J. S. Connolly, E. B. Samuel and A. F. Janzen, *Photochem. Photobiol.,* 1982, **36**, 565–574.
77 A. P. Losev, E. I. Sagun, G. A. Kochubeev and I. N. Nichiporovich, *J. Appl. Spectrosc.,* 1986, **45**, 798–803.

Supplementary Information

1. FTIR spectra of bacteriochlorin–peptide conjugates.

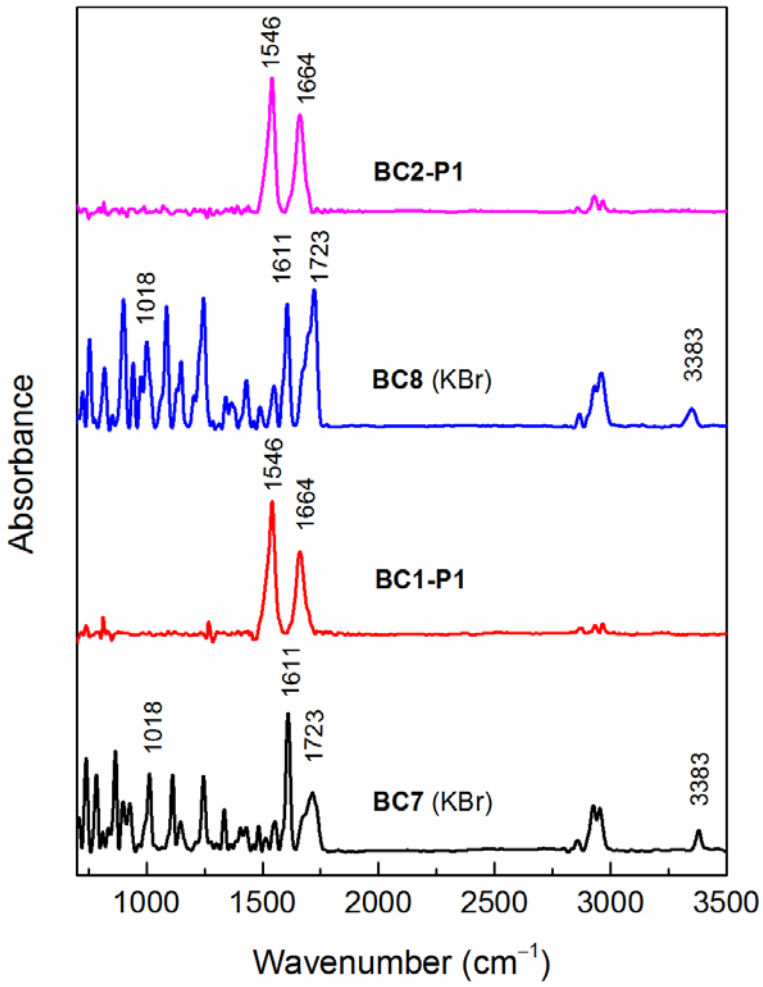

Figure S1. Single-reflection FTIR spectra of bacteriochlorin–peptide conjugates in films on Au substrates (15 h deposition time) and benchmark bacteriochlorins in KBr pellets. The feature at 1723 cm^{-1} is likely a peripheral-group C=O vibration. Other bands are identified in the body of the paper.

2. Spectroscopic data for oligomeric biohybrid complexes of BC2.

Studies analogous to those described for **[(BC6-P1-BChl)$_2$]$_n$** were performed on the oligomeric biohybrid complex **[(BC2-P1-BChl)$_2$]$_n$**, which contains bacteriochlorin **BC2** in place of **BC6**. As noted, the present studies on **[(BC2-P1-BChl)$_2$]$_n$**, which were carried out at 9 °C to stabilize the oligomeric complexes, complement the prior work on the same constructs carried out at room temperature.[18] The biohybrid containing **BC2** exhibits ≥90% energy transfer as deduced from analysis of steady-state fluorescence data similar to those shown in Fig. 6 and transient absorption data similar to those shown in Fig. 7 and Fig. 8 for the biohybrid containing **BC6**. For example, Fig. S2 shows that the energy transfer results in diminished amplitude of the **BC2** emission in the biohybrid complex **[(BC2-P1-BChl)$_2$]$_n$**; the amplitude is ~10 % of that in the control peptide conjugate **BC2-P1**, which lacks the BChl *a* acceptor array (B850).

Fig. S3 shows that excitation of **BC2** followed by energy transfer to B850 in **[(BC2-P1-BChl)$_2$]$_n$** results in a 1–2 ps rise component in the B850 bleaching and B850* stimulated-emission features. This finding is analogous to the rise phase found after excitation of **BC6** in **[(BC6-P1-BChl)$_2$]$_n$** (Fig. 8). Thus, the transient absorption data for biohybrids containing either bacteriochlorin **BC6** or **BC2** reveal a fast kinetic phase not present in the oligomer control **[(P1-BChl)$_2$]$_n$** that can be attributed to energy transfer from the excited bacteriochlorin to B850. Such findings are in harmony with the results of the steady-state fluorescence quenching and fluorescence excitation versus absorptance spectral analyses for both biohybrids. The collective results show that the appended synthetic bacteriochlorin in the assemblies enhances solar coverage and exhibits efficient (≥90%) energy transfer to the native-like BChl *a* sites in the biohybrid architectures.

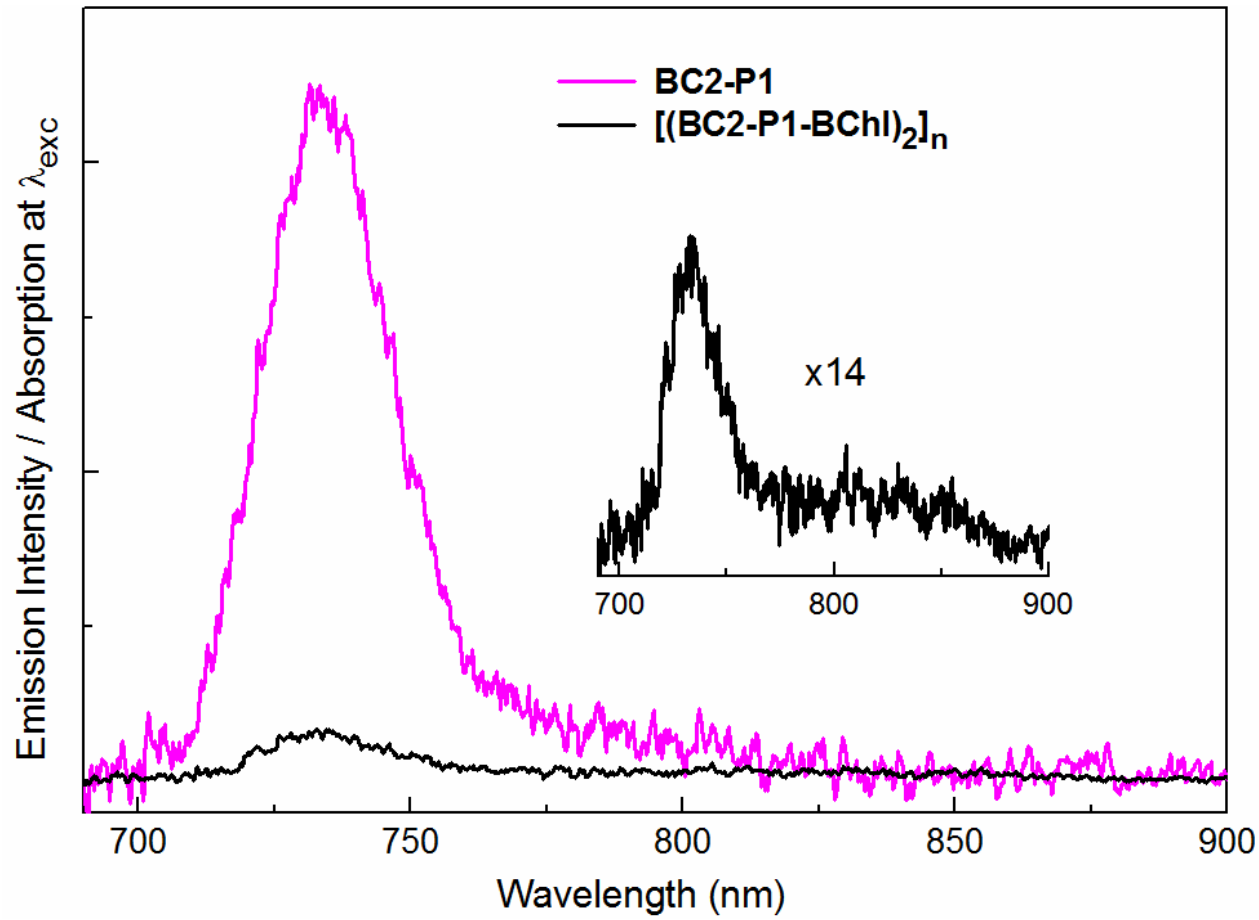

Figure S2. Emission intensity normalized to the absorption value at the excitation wavelength (516 nm) for control peptide **BC2-P1** (magenta) and oligomeric biohybrid complex **[(BC2-P1-BChl)$_2$]$_n$** (black). The inset (an expanded view for the biohybrid assembly) shows residual **BC2** fluorescence (734 nm), fluorescence from the BChl *a* array B850 (850 nm) and possible trace emission from free BChl *a* (780–800 nm).

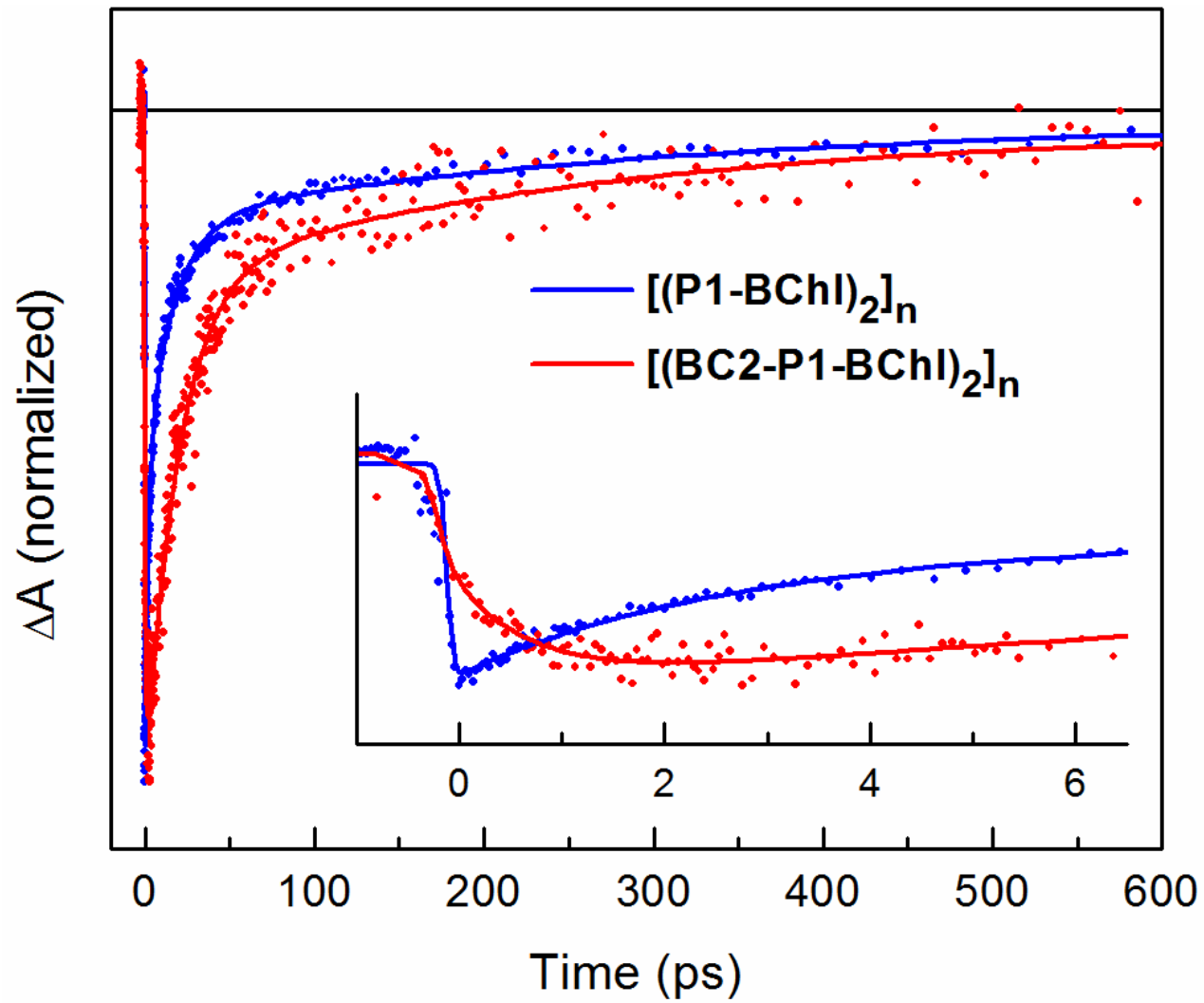

Figure S3. Time-evolution of the bleaching/stimulated-emission for oligomeric biohybrid **[(BC2-P1-BChl)$_2$]$_n$** (λ_{exc} = 516 nm, λ_{det} = 835 nm) (red) and oligomeric control **[(P1-BChl)$_2$]$_n$** (λ_{exc} = 590 nm, λ_{det} = 855 nm) (blue) at 9 °C normalized to the same maximum amplitude. The inset shows the 1–2 ps growth of bleaching for the biohybrid and the instrument-limited rise for the control. The line through each data set is a fit to a function consisting of three exponentials plus a long-time constant convolved with the instrument response.

4. Spectroscopic data for BC6-P1 (from Prep I).

Highly efficient energy transfer was observed for the β-oligomeric biohybrid complexes containing bacteriochlorin **BC6**. These complexes were obtained from both Prep I and Prep III and studied by the full array of static and time-resolved spectroscopic measurements. Figs. S4–S6 given below for Prep I parallel Figs. 6-8 in the body of the paper. The descriptions of

these results for Prep I parallel those given in the body of the paper for Prep III and thus are not reproduced here. Only a few specific comments on the data for Prep I are given.

Energy transfer from **BC6** to the BChl *a* array (denoted B850) in the biohybrid assembly **[(BC6-P1-BChl)$_2$]$_n$** to produce excited state B850* was first probed by excitation spectra (Fig. S4A) of the fluorescence from B850 (Fig. S4B). Fluorescence from B850* in this assembly is observed (as expected) at ~850 nm upon direct excitation of B850 in the Q_x band at 590 nm. Fluorescence from **[(BC6-P1-BChl)$_2$]$_n$** is also obtained using excitation in the Q_y band of **BC6** at ~718 nm (Fig. S4B and inset, black). An energy-transfer efficiency (Φ_{ENT}) value of 0.9 ± 0.1 was determined by comparing the amplitudes of the **BC6** features in the fluorescence-excitation versus absorptance spectra (Fig. 6A, blue and magenta, respectively). A similarly high (≥0.9) efficiency of energy transfer is also reflected by the observation that the **BC6** fluorescence (λ_{det} = 720 nm; λ_{exc} = 490 nm) in biohybrid **[(BC6-P1-BChl)$_2$]$_n$** (Fig. S4C, black) is only a few percent of that in the control peptide conjugate (magenta). Similar quenching is observed upon excitation of **BC6** in the Q_y band (718 nm) for biohybrid **[(BC6-P1-BChl)$_2$]$_n$** versus peptide control **BC6-P1**, where in this case the scan cannot reveal the Q_y(0,0) fluorescence peak but only the vibronic features to longer wavelengths (Fig. S4B, black versus magenta).

Fig. 5B and inset reveal that excitation of **BC6** gives rise to not only B850* fluorescence at ~850 nm, but also fluorescence at shorter wavelengths extending to <800 nm due in part to energy transfer to species present in small amounts relative to the biohybrid. Such contributions include (i) a tail of emission from free **BC6** (λ_{max} ~720 nm) or **BC6-P1** from which BChl *a* has dissociated, (ii) free BChl *a* (λ_{max} ~780 nm) that has dissociated from the complex, (iii) a small fraction of ββ-subunit subunit complexes or less extended oligomers (λ_{max} ~830 nm). The fluorescence yields (Φ_f) are on the order of 0.1 for monomeric synthetic bacteriochlorins

(bioconjugatable and benchmarks) and BChl *a* (Table 1), on the order of 0.01 for the BChl *a* dimer (B820) in ββ-subunits, and on the order of 0.001 for the BChl *a* array (B850) in oligomeric assemblies (with or without conjugated bacteriochlorin), as found here for **BC6** complexes and previously[18] for **BC1** and **BC2** complexes. Thus, very small amounts of monomeric chromophores or subunits will give rise to detectable fluorescence (780–840 nm) in addition to that for B850 (~850 nm) in the biohybrid assemblies even if the latter is the overwhelmingly dominant species present. An additional preparation of **[(BC6-P1-BChl)$_2$]$_n$** is largely free of such emission at shorter wavelength (Fig. 6 in the body of the paper). The latter sample also gives a high (≥0.9) yield of energy transfer from **BC6** to B850. This comparison shows that the presence of a small amount of relatively highly emitting species such as free BChl *a* or synthetic chromophore (or bacteriochlorin–peptide conjugate) does not compromise the photophysical measurements on or the functionality of the oligomeric assembly.

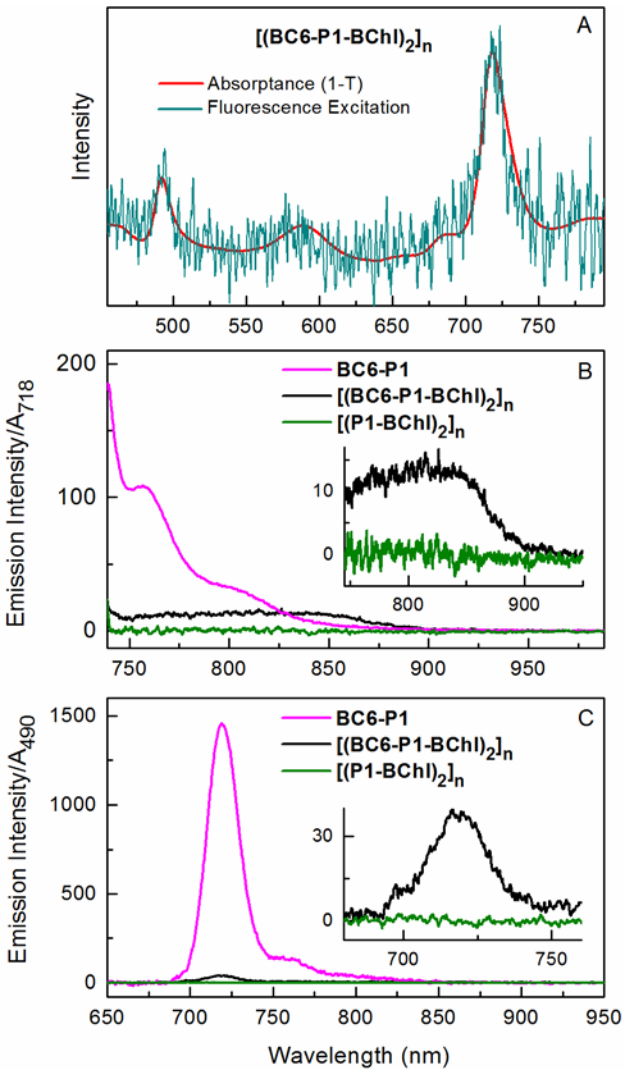

Figure S4. Steady-state fluorescence data for oligomeric biohybrid **[(BC6-P1-BChl)$_2$]$_n$**, oligomer control **[(P1-BChl)$_2$]$_n$**, and control peptide **BC6-P1** at 9 °C. (A) Absorptance (1-T) and fluorescence excitation spectra (λ_{det} = 850 nm) for the biohybrid normalized at the 590-nm BChl Q_x maximum. The absorptance spectrum was corrected for light scattering and the excitation spectrum for instrument parameters. (B) Fluorescence spectra of the biohybrid (black), control peptide (magenta) and oligomer control (green), with the intensities divided by the absorbance at λ_{exc} = 718 nm. (C) Fluorescence spectra of the biohybrid (black) and control peptide (magenta) and control oligomer (green) with the intensities divided by the absorbance at λ_{exc} = 490 nm.

Biohybrid complex **[(BC6-P1-BChl)$_2$]$_n$** and oligomer control **[(P1-BChl)$_2$]$_n$** were also studied using ultrafast transient absorption spectroscopy. The data shown in Figs. S5 and S6 are similar to those shown for Prep I in Figs. 7 and 8 of the body of the paper, with a few small differences in spectra/kinetic detail. For Prep III, B850* shows decay time constants of ~4, ~30

and ~600 ps for oligomeric control **[(P1-BChl)$_2$]$_n$** and ~40 and ~300 ps for biohybrid **[(BC6-P1-BChl)$_2$]$_n$**. The main finding is that B850 bleaching and B850* stimulated emission show an instantaneous (<300 fs) overall rise for the oligomeric control but comparatively slow growth (1–2 ps) as are shown in Fig. S6. These rise-time data are the same as those found for the complexes from Prep I shown in Fig. 8 of the body of the paper. The 1–2 ps lag in the formation of B850* reflects energy transfer from BC6* to the BChl *a* array (B850) in the biohybrid. The B850* rise-time constant, which reflects the BC6* lifetime in the biohybrid, is significantly shorter than the lifetime of BC6* in the control peptide conjugate or organic media and the benchmark bacteriochlorin (Table 1 in the body of the paper). This comparison again reflects the near-quantitative yield of energy transfer from excited **BC6** to the BChl *a* array (B850) in the biohybrid complex.

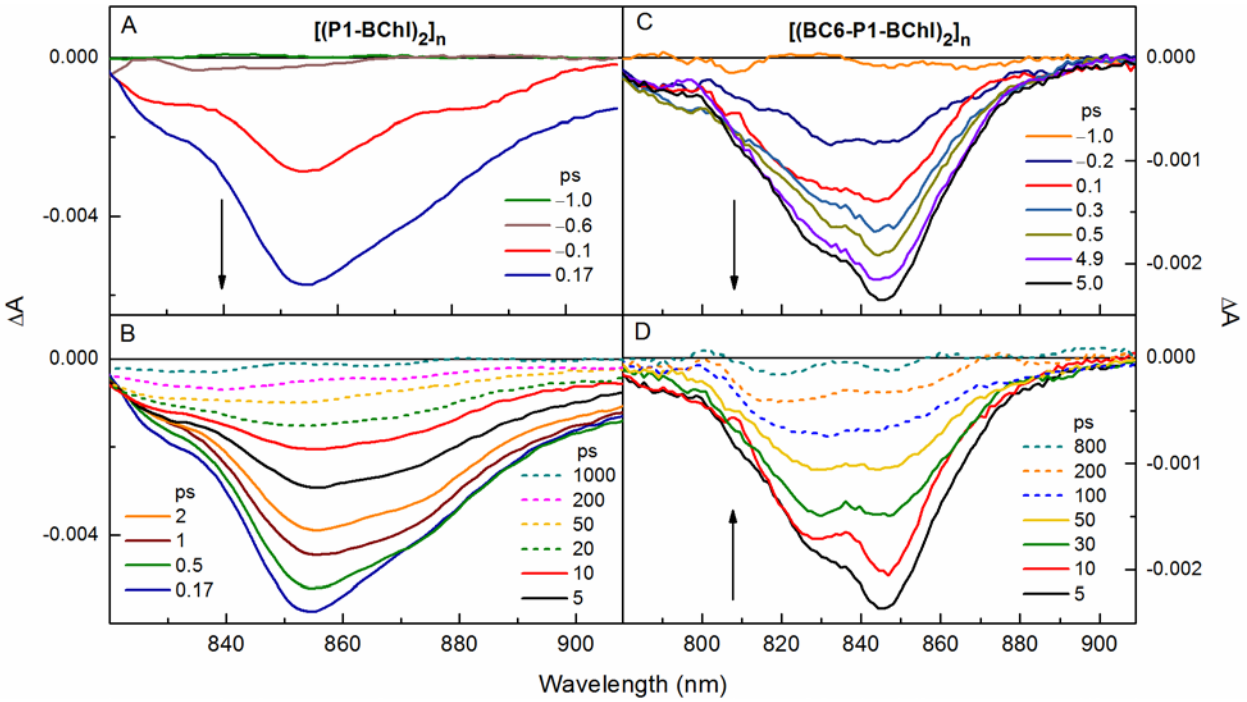

Figure S5. NIR transient absorption spectra at 9 °C of the BChl complex in oligomeric control **[(P1-BChl)$_2$]$_n$** using excitation at 590 nm (left panels) and oligomeric biohybrid **[(BC6-P1-BChl)$_2$]$_n$** using excitation of **BC6** at 718 nm (right panels). Panel (A) shows the instrument-limited rise and panel (B) the decay of the combined B850 bleaching B850* stimulated emission for the oligomeric control. Panel (C) shows non-instrument-limited growth and panel (D) decay of the features for the biohybrid.

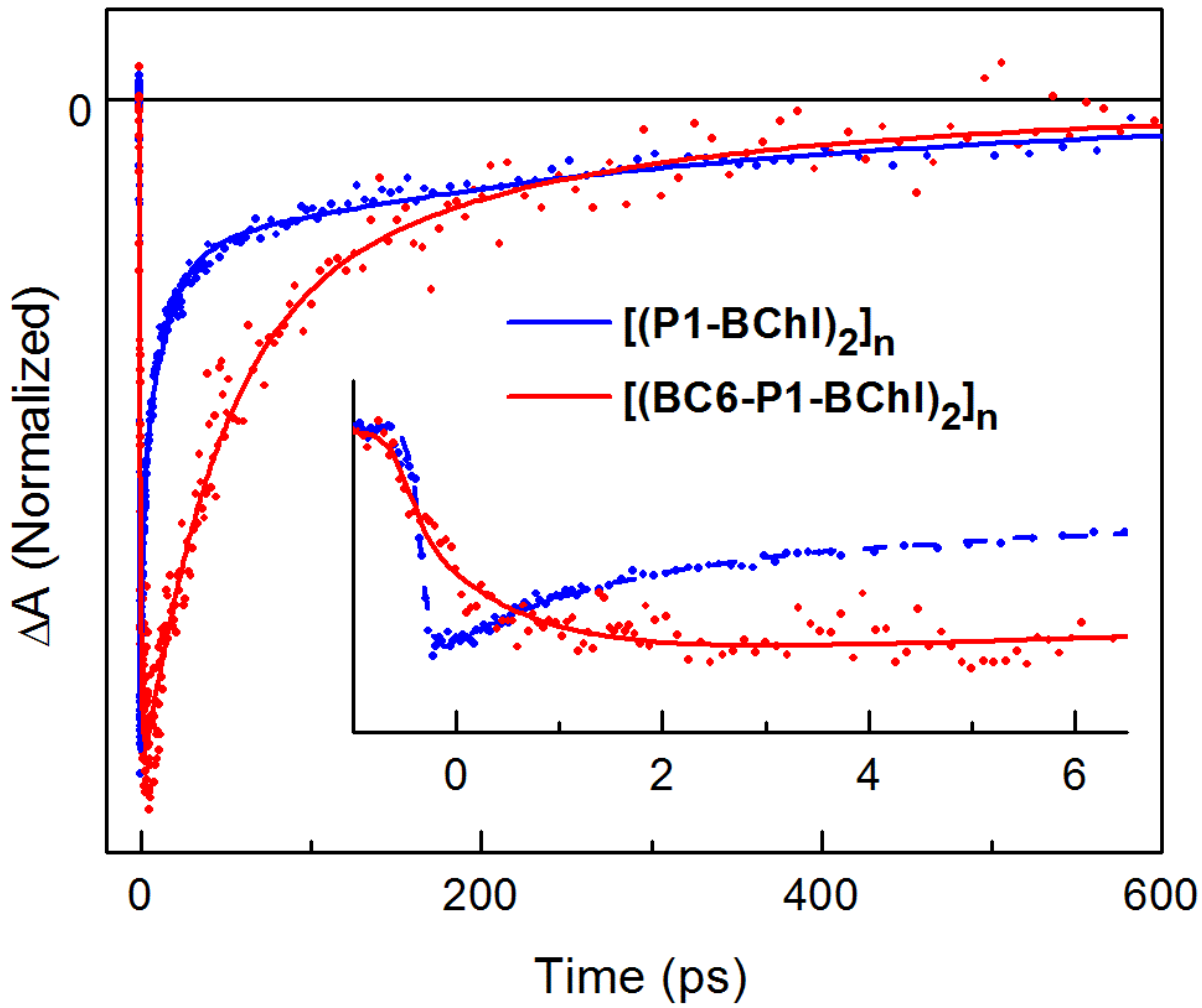

Figure S6. Time-evolution of the bleaching/stimulated-emission (845 nm) for oligomeric biohybrid **$[(BC6\text{-}P1\text{-}BChl)_2]_n$** and oligomeric control **$[(P1\text{-}BChl)_2]_n$** at 9 °C. The inset shows the 1–2 ps growth of bleaching for the biohybrid and the instrument-limited rise for the control. The line through each data set is a fit to a function consisting of three exponentials plus a long-time constant convolved with the instrument response.